

# 1997 Digest of the LEOS Summer Topical Meetings

11-15 August 1997

**VERTICAL-CAVITY LASERS**

**TECHNOLOGIES FOR A GLOBAL  
INFORMATION INFRASTRUCTURE**

**WDM COMPONENTS TECHNOLOGY**

**ADVANCED SEMICONDUCTOR  
LASERS AND APPLICATIONS**

TECHNICALLY CO-SPONSORED BY THE  
OPTICAL SOCIETY OF AMERICA

**GALLIUM NITRIDE MATERIALS,  
PROCESSING, AND DEVICES**

at

**THE QUEEN ELIZABETH HOTEL**

**MONTREAL, QUEBEC, CANADA**



IEEE



**DISTRIBUTION STATEMENT A**

Approved for public release;  
Distribution Unlimited

# REPORT DOCUMENTATION PAGE

Form Approved  
OMB NO. 0704-0188

Public reporting burden for this collection of information is estimated to average 1 hour per response, including the time for reviewing instructions, searching existing data sources, gathering and maintaining the data needed, and completing and reviewing the collection of information. Send comment regarding this burden estimates or any other aspect of this collection of information, including suggestions for reducing this burden, to Washington Headquarters Services, Directorate for Information Operations and Reports, 1215 Jefferson Davis Highway, Suite 1204, Arlington, VA 22202-4302, and to the Office of Management and Budget, Paperwork Reduction Project (0704-0188), Washington, DC 20503.

1. AGENCY USE ONLY (Leave blank)

2. REPORT DATE

January 1998

3. REPORT TYPE AND DATES COVERED

Final Report 13Aug97 - 12Aug98

4. TITLE AND SUBTITLE

1997 IEEE/LEOS Summer Topical Meeting on Gallium Nitride Materials, Processing and Devices

5. FUNDING NUMBERS

DAAG55-97-1-0388

6. AUTHOR(S)

Edward F. Labuda

7. PERFORMING ORGANIZATION NAMES(S) AND ADDRESS(ES)

IEEE Lasers and Electro-Optics Society  
455 Hoews Lane  
PO Box 1331  
Piscataway, NJ 08854

8. PERFORMING ORGANIZATION  
REPORT NUMBER

9. SPONSORING / MONITORING AGENCY NAME(S) AND ADDRESS(ES)

U.S. Army Research Office  
P.O. Box 12211  
Research Triangle Park, NC 27709-2211

10. SPONSORING / MONITORING  
AGENCY REPORT NUMBER

ARO 37712.1-EL-CF

11. SUPPLEMENTARY NOTES

The views, opinions and/or findings contained in this report are those of the author(s) and should not be construed as an official Department of the Army position, policy or decision, unless so designated by other documentation.

12a. DISTRIBUTION / AVAILABILITY STATEMENT

Approved for public release; distribution unlimited.

12 b. DISTRIBUTION CODE

13. ABSTRACT (Maximum 200 words)

ABSTRACT NOT AVAILABLE

14. SUBJECT TERMS

15. NUMBER OF PAGES

16. PRICE CODE

17. SECURITY CLASSIFICATION  
OF THIS PAGE

UNCLASSIFIED

18. SECURITY CLASSIFICATION  
OF THIS PAGE

UNCLASSIFIED

19. SECURITY CLASSIFICATION  
OF ABSTRACT

UNCLASSIFIED

20. LIMITATION OF ABSTRACT

UL

**1997 DIGEST  
of the IEEE/LEOS  
Summer Topical Meetings  
11-15 August 1997**

**Vertical-Cavity Lasers**

**Technologies For A Global Information Infrastructure**

**WDM Components Technology**

**Advanced Semiconductor Lasers And Applications**

Technically Co-Sponsored by the Optical Society of America

**Gallium Nitride Materials, Processing, And Devices**

**at**

***THE QUEEN ELIZABETH HOTEL  
MONTREAL, QUEBEC, CANADA***

**IEEE Catalog Number: 97TH8276**

**Library of Congress: 97-70754**

**DTIC QUALITY INSPECTED 2**

**19980519 059**

*The 1997 Summer Topicals would like to  
acknowledge support from the following  
corporations*

AIXTRON  
&  
EMCORE



**1997 DIGEST  
of the IEEE/LEOS  
Summer Topical Meetings  
11-13 August 1997**

**Vertical-Cavity Lasers**

**at  
*THE QUEEN ELIZABETH HOTEL  
MONTREAL, QUEBEC, CANADA***

**IEEE Catalog Number: 97TH8276**

**Library of Congress: 97-70754**

The papers in this book make up the digest of the meeting mentioned on the cover and title page. They reflect the authors' opinions and are published as presented and without change in the interest of timely dissemination. Their inclusion in this publication does not necessarily constitute endorsement by the editors, the Institute of Electrical and Electronics Engineers, Inc.

Copyright and reprint permissions: Abstracting is permitted with credit to the source. Libraries are permitted to photocopy beyond the limits of U.S. copyright law for private use of patrons those articles in this volume that carry a code at the bottom of the first page, provided the per-copy fee indicated in the code is paid through the Copyright Clearance Center, 222 Rosewood Drive, Danvers MA 01923. Instructors are permitted to photocopy isolated articles for noncommercial classroom use without fee. For other copying, reprint or republication permission, write to IEEE Copyrights Manager, IEEE Service Center, 445 Hoes Lane, P.O. Box 1331, Piscataway NJ 08855-1331.

© 1997 by The Institute of Electrical and Electronics Engineers, Inc. All right reserved.

IEEE Catalog Number: 97TH8276

ISBN:	0-7803-3891-X	Softbound Edition
	0-7803-3892-8	Microfiche Edition

Library of Congress: 97-70754

Additional copies can be ordered from:

IEEE Service Center  
445 Hoes Lane  
P.O. Box 1331  
Piscataway, NJ 08855-1331  
Tel: (732) 981-1393  
Fax: (732) 981-9667



# **VERTICAL-CAVITY LASERS**

## **Co-Chairs:**

Constance Chang-Hasnain, *University of California - Berkely, Berkeley, CA*  
Larry Coldren, *University of California Santa Barbara, Santa Barbara, CA*

## **Program Committee:**

Kent Choquette, *Sandia National Laboratories, Albuquerque, NM*  
Dennis Deppe, *University of Texas, Austin, TX*  
Karl Ebeling, *Universitat Ulm, Ulm Germany*  
Mary Hibbs-Brenner, *Honeywell, Bloomington, MN*  
Jack Jewell, *Picolight Inc., Boulder, CO*  
Fumio Koyama, *Tokyo Institute of Technology, Yokohama, Japan*  
S.-Y. Wang, *Hewlett Packard, Palo Alto, CA*



# TABLE OF CONTENTS

## Monday, 11 August 1997

### Session MA: Perspectives

MA1	New Materials and Process Technologies for Vertical Cavity Surface Emitting Lasers .....	3
MA2	VCSEL Research, Development and Applications at Honeywell .....	5
MA3	Future Prospects of VCSELs: Industrial View .....	7

### Session MB: High Efficiency

MB1	Towards Microcavity Vertical Cavity Lasers: Aperture and Cavity Design for High Efficiency and Low Threshold .....	9
MB2	Uniform and High Power Selectively Oxidized 8x8 VCSEL Array .....	11
MB3	High Efficiency 850 nm Wavelength GaAs VCSELs .....	13
MB4	850nm VCSEL's with Buried Al <sub>x</sub> O <sub>y</sub> Current Apertures .....	15

### Session MC: Towards Data Storage

MC1	Visible VCSELs: Recent Advances and Applications. ....	17
MC2	VCSELs for Compact Disk Players .....(paper not available)	
MC3	Self-Pulsating VCSEL With Controllable Quantum-Well Saturable Absorber .....	19
MC4	Tera Bytes Optical Disk With Electric Tracking Control Using Micro-Cavity VCSEL Array and PD Array .....	21

### Session MD: Applications in Switching

MD1	Integrated VCL/PIN Arrays for Optical Computing Applications .....	23
MD2	Hybrid Integration of VCSELs to Foundry Fabricated Smart Pixels .....	25
MD3	4x4 Broadband Optoelectronic Switch Using VCSELs .....	27
MD4	VCSEL Based High Performance ATM Switch .....	29

## Tuesday, 12 August 1997

### Session TuA: Novel Material Technologies

TuA1	Low-Threshold Continuous-Wave Operation of an Oxide-Confined Vertical-Cavity Surface-Emitting Laser Based on a Quantum Dot Active Region and Half-Wave Cavity .....	33
TuA2	Dynamically Stable Polarization Characteristics of Oxide-Confinement Vertical-Cavity Surface-Emitting Lasers Grown on GaAs(311) A Substrate .....	35
TuA3	Multiple-Wavelength VCSEL Arrays on Patterned Substrates .....	37
TuA4	P-type Modulation Carbon-Doping to InGaAs/AlGaAs Quantum Wells by MOCVD Auto-Doping for Surface-Emitting Lasers .....	39
TuA5	AlGaAsSb/AlAsSb Bragg Mirrors on InP for 1.3 and 1.55 $\mu$ m Vertical Cavity Surface Emitting Lasers. ....	41

# TABLE OF CONTENTS

## **Session TuB: Long Wavelength VCSELs**

TuB1	120°C Pulsed Operation From a 1.55 $\mu\text{m}$ Vertical-Cavity Laser .....	43
TuB2	High Performance 1.3 $\mu\text{m}$ Vertical-Cavity Surface-Emitting Lasers with Oxygen-Implanted Confinement Regions and Wafer-Bonded Mirror .....	45
TuB3	Long Wavelength VCSELs With Monolithic Integrated GaInAsP/InP Mirror .....	47
TuB4	Metamorphic GaAs/AlAs Bragg Mirrors Deposited on InP for 1.3/1.55 $\mu\text{m}$ Vertical Cavity Lasers .....	49

## **Wednesday, 13 August 1997**

## **Session WA: High Speed Devices and Data Links**

WA1	High-Speed Vertical Cavity Surface Emitting Lasers .....	53
WA2	Turn-on Jitter in Zero-Biased Single-Mode Vertical Cavity Surface Emitting Lasers ..	55
WA3	Vertical Cavity Lasers for Datalinks .....	57
WA4	Using VCSELs and Multicore Fiber for Multi-Channel Transmission .....	59

## **Session WB: Structures and Analysis**

WB1	Diode Cascade Quantum Well VCSEL .....	61
WB2	A High Performance Continuously Tunable Top-Emitting VCSEL .....	63
WB3	Diffraction Loss of Confined Modes in Microcavities .....	65
WB4	Analysis of Three Dimensionally Confined Microcavity Surface Emitting Lasers Using Vector Finite Elements .....	67
WB5	Microcavity LEDs with an overall efficiency of 4 % into a numerical aperture of 0.5 ..	69

## **Session WC: Single Mode Applications and Characterization**

WC1	Vertical Cavity Lasers for Printing .....	71
WC2	High Power Single Transverse Mode Selectively Oxidized VCSELs .....	73
WC3	Single-mode Vertical-Cavity Surface-Emitting Laser With Cavity Induced Antiguiding .....	75
WC4	Failure Analysis of 850 nm Proton-Implanted VCSELs .....	77
WC5	Structural Dependence of The Thermal Resistance of Vertical Cavity Surface Emitting Lasers .....	79

# **VERTICAL-CAVITY LASERS**

**Monday, 11 August 1997**

## **Sessions:**

- MA: Perspectives**
- MB: High Efficiency**
- MC: Towards Data Storage**
- MD: Applications in Switching**

## **Monday Papers Not Available**

MC2      “VCSELs for Compact Disk Players”, *H.K. Shin, Samsung Electronics Co., Kyungki-do, Korea*



MA1 (Invited)  
8:30am - 9:00am

## New Materials and Process Technologies for Vertical Cavity Surface Emitting Lasers

K. Iga

Tokyo Institute of Technology  
4259 Nagatsuta, Midoriku, Yokohama, Japan 226  
Fax +81-45-924-5014 kiga@pi.titech.ac.jp

Surface emitting (SE) lasers[1] or vertical cavity SE lasers (VCSELs) are now considered to be utilized as devices in various optical systems as in networks, optical parallel interconnects, laser printers, and ultra-parallel optoelectronics[2]. We like to review the progress of VCSELs in wide range of optical spectra based on GaInAsP, GaIn(N)As, GaAlAs, AlGaInP, ZnSe, GaN, and related compounds and discuss on some new aspects.

The materials for semiconductor lasers are now covering most of III-V compound alloys as shown in Fig 1. The problems which should be seriously considered for making vertical cavity SE lasers will be ;

- (A) Highly reflective and transparent DBR's
- (B) Minimization of optical losses
- (C) Maximization of optical-field and gain overlap
- (D) Electrode-formation to reduce the resistivity for high efficiency operation
- (E) Heat sinking for high temperature and high power operation.

Some of the present technical status of VCSELs are reviewed in various spectral regions.

(a) 1550 nm: The epitaxial bonding of GaInAsP-InP/GaAs-AlAs mirrors have been exhibiting CW operation up to 64 °C[3] Further development may be necessary to compete with edge emitters employing DFB and spotsizer transformer(SST) structures.

(b) 1300 nm: A buried structure is utilized together with thermally conductive MgO/Si mirror demonstrating the first room temperature (RT) cw operation[4]. The highest operation is up to 34 °C[5].

The introduction of GaInNAs/GaAs and AlGaInAs/InP may be a solution to material bottle neck of GaInAsP/InP system, i.e. temperature characteristics, AlAs oxidation capability, the use of GaAs/AlAs DBRs, etc. It would be extremely important to develop 1300 nm VCSELs for short distance optical links due to low cost chip and modulating capability. It may readily replace any edge emitters for optical interconnects and links, if 1 mW devices can be realized.

(c) 980 nm: The GaInAs/GaAs strained pseudo-morphic system grown on a GaAs exhibits a high laser gain and has been introduced into VCSELs together with using GaAlAs/AlAs DBRs. The native oxide of AlAs is successfully used for current confinement. The typical size made in the author's group[6] is 20 micron core starting from 30 micron mesa diameter. We have achieved about 1 mW of power output and submicro-ampere threshold. A smaller diameter device having 5 micron started from 20 micron mesa exhibited a threshold of 70  $\mu$ A at room temperature cw operation. This value is the third world-record for SE lasers. More recently, an even lower threshold (10 $\mu$ A, 40 $\mu$ A) has been reported[7],[8]. The power conversion efficiency of 50 % was achieved. Also, near 200 mW has been demonstrated.

However, due to the unavailability of low cost detectors in this wavelength, it is difficult to find real applications. This

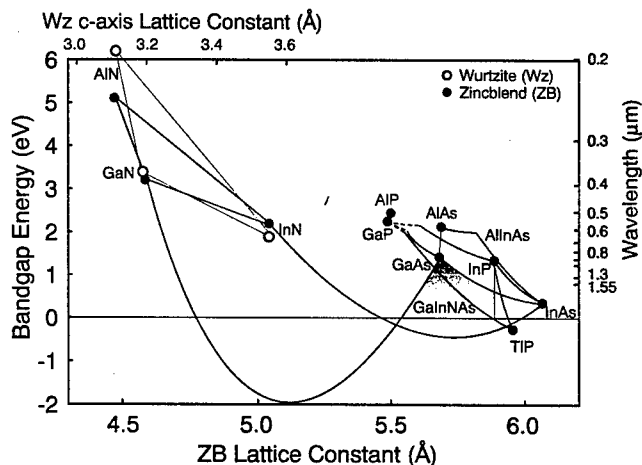


Fig. 1 Bandgaps and lattice constants for III-V semiconductors

wavelength might be bearing as a "headline" device.

(d) 850 nm: Sub-mA thresholds and 10 mW outputs have been achieved. The power conversion efficiency of 57% has been demonstrated[9]. Some commercial optical links have already been in markets. The price of low-skew multimode fiber ribbons may be a key issue for inexpensive multimode-fiber-based data links.

(e) 780 nm: The device having 200  $\mu$ A threshold and 1.1 mW output has been reported aiming at CD player application[10]. A VCSEL-loaded pickup is being commercialized.

(f) 670-650 nm: AlGaInP/GaAs SE lasers are developed and room temperature operation exhibiting submilliampere threshold and a few mW outputs have been obtained[12]. The best application of red color VCSELs may be laser printers and the first generation DVDs.

(g) 555 nm: The ZnSe system is still only the material to provide CW operation of green-blue semiconductor lasers operating beyond 100 hours. Some trials for green surface emitters were attempted. There may be difficult to find a good application for green VCSELs since GaN devices look more promising.

(h) 470-340 nm: The GaN and related materials including Al, In, and B can cover wide spectral ranges green to UV. The reported reliability of GaN based LEDs and LDs[12] looks to indicate a good material potentiality for VCSELs as well[13]. The estimation of threshold for GaN/Al<sub>0.1</sub>Ga<sub>0.9</sub>N quantum well lasers is carried out using the density-matrix theory with intraband broadening[14].

The trial for realizing blue to UV VCSELs has just started. Some of optical pumping experiments have been reported. We have made a preliminary study to search for MOCVD selective area growth and dry etch of a GaN system by Chlorine-based reactive ion beam etch. These may be crucial technologies for GaN-based devices[14].

The application area of blue-UV VCSELs is huge. It may provide the next generation DVD's, laser printers incorporating blue-sensitive drums, full color displays, high efficiency illuminations together with green and red devices, and so on.

In order to further achieve substantial innovations in VCSEL performances, the following technical issues are remaining unsolved or still non-optimized;

- (a) AlAs oxidation and its application to current confinement and optical beam focusing, in particular, for long wavelength devices.
- (b) Modulation doping, p-type and n-type modulation doping to quantum wells/barriers.
- (c) Quantum wires and dots for active engines.
- (d) Strained quantum wells and strain-compensation.
- (e) Angled substrates such as (311A), (311B), (411), etc for polarization control [15].
- (f) New material combinations such as GaInNAs/GaAs or AlGaInAs/InP for long wavelength emission.
- (g) Reproducible water fusion technique to achieve optimum combination of active region and mirrors.
- (h) Transparent mirrors to increase quantum efficiency and output power.
- (i) Multi-quantum barriers (MQBs) to prevent carrier leakage to p-cladding layer.
- (j) Wavelength controlling technologies such as tuning, steering, trimming, etc.
- (k) Arrays and high power technologies

## References

- [1] K. Iga, F. Koyama, and S. Kinoshita, IEEE J. Quant. Electron., Vol. QE-24, pp.1845-1855, Sept. 1988.
- [2] K. Iga, Gakujutu-Geppo(Monthly J. of MECSS), Vol. 49, pp.42-46, Jan. 1996.
- [3] D. I. Babic, K. Streubel, R. P. Mirin, J. Pirek, N. M. Margalit, J. E. Bowers, E. L. Hu, D. E. Mars, L. Yang, and K. Carey, IPRM'96 ThA1-2, April 1996.
- [4] T. Baba, Y. Yogo, K. Suzuki, F. Koyama, and K. Iga, Electron. Lett., Vol. 29, pp.913-914, May 1993.
- [5] S. Uchiyama, N. Yokouchi and T. Ninomiya, The 43th Spring Meeting of Jpn. Soc. Appl. Phys., no. 26p-C-7, March 1996.
- [6] Y. Hayashi, T. Mukaiharu, N. Hatori, N. Ohnoki, A. Matsutani, F. Koyama and K. Iga, Electron. Lett., Vol.31, pp.560-561, March 1995.
- [7] G. M. Yang, M. H. Macdougall, P. D. Dapkus, CLEO'95, Post Deadline Papers, CPD4-1, Baltimore, 1995.
- [8] D. L. Huffaker, D. G. Deppe, C. Lei, and L. A. Hodge, CLEO'96 (Anaheim), JTuH5, June 1996.
- [9] B. Weigl, G. Reiner, M. Grabherr, and K. Ebeling, CLEO'96 (Anaheim), JTuH2, June 1996.
- [10] H. E. Shin, Y. G. Zoo, and E. H. Lee: 16th Conference on Lasers and Electro-Optics (Anaheim), JTuH7 (1996)
- [11] J. A. Lott and R. P. Shneider, Jr.: Electron. Lett., 29, 830 (1993)
- [12] S. Nakamura, M. Senoh, S. Nagahama, N. Iwasa, T. Yamada, T. Matsushita, H. Kiyoku, and Y. Sugimoto, Jpn. J. Appl. Phys., Vol 35, pp.L14-L16, 15 Jan. 1996.
- [13] K. Iga, Int'l Symposium on Blue Laser and Light Emitting Diodes, Th-11, March 1996.
- [14] T. Honda, F. Koyama, and K. Iga, MRS'96, Dec. 1997, to be published in MRS 1996 Fall Meeting Symposia Proceedings, Materials Research Society, Pittsburgh, 1997..
- [15] K. Takahashi, P. O. Vaccaro, T. Watanabe, T. Mukaiharu, F. Koyama, and K. Iga, Jpn J. Appl. Phys., 35, pp. 6102-6107, Dec. 1996.

**MA2 (Invited)**  
**9:00am - 9:30am**

## **VCSEL research, development and applications at Honeywell**

Robert A. Morgan

Honeywell Technology Center, 12001 State Hwy. 55, Plymouth, MN 55441-4779

### I. Overview

Due to great strides in development and their numerous applications, producible vertical-cavity surface-emitting lasers (VCSELs) are now commercialized. The entrenched proton-implanted AlGaAs-based (emitting near 850 nm) technology platform is commonly utilized. Renditions of this VCSEL design not only exist in commercial products, but has enabled numerous system demonstrations. Commercial-grade performance on all fronts for high-speed optical data communications has been clearly established in our laboratory. Honeywell designs have more than adequately met producibility, performance, and robustness stipulations. Progress in performance include the elimination of the excessive voltage-drop that plagued VCSELs as recently as 2 to 3 years ago. Threshold voltages as low as  $V_{th} = 1.53$  V ( and routinely  $< 1.6$  V) are now commonplace. Operating Voltages, current and powers are typically,  $< 1.8$  V,  $\approx 10$  mA, and  $> 1$  mW. Even submilliamp threshold currents ( $I_{th} = 0.68$  mA, cw, RT) have been demonstrated with this planar all-AlGaAs structure. Moreover, continuous wave (cw) power  $P_{cw} > 59$  mW, and respectable wall-plug efficiencies ( $\eta_{wp} = 28\%$ ) have been demonstrated. Producibility milestones include  $> 99\%$  device yield across 3-in-dia metal-organic vapor phase epitaxy (MOVPE)-grown wafers (from a commercially-available chamber) and wavelength operation across  $> 100$ -nm range. VCSEL robustness is evidenced by maximum cw lasing temperature  $T = 200^\circ\text{C}$ , and temperature ranges of 10K - 400K, and  $-55^\circ\text{C}$  and  $155^\circ\text{C}$  on a single VCSEL. Moreover, demonstrated reliability is in excess of  $10^7$  hours MTTF (at room T) has been reported. Furthermore, preliminary radiation hardness tests indicate that these VCSELs exhibit an order of magnitude reduction in sensitivity to neutron flux damage compared to a qualified LED. These characteristics should enable great advances in VCSEL-based technologies and beckon the notion that "commercial-grade" VCSELs are viable in cryogenic and avionics/military environments.

The future may hold extensions of this platform to different wavelengths, increased integration, and advanced structures and novel applications. These includes low-threshold, high-speed, single-mode VCSELs, hybrid VCSEL transceivers, and self pulsating (decohered) or Frequency-Modulated (FM) VCSELs. Applications include serial and parallel optical interconnects. Present optical data links have focused on interconnections between computers. Honeywell has also developed technology to allow parallel interconnections within the processor. VCSEL-based interconnects within backplanes, board-to-board, and within and between Multi-Chip Modules (MCMs) have been demonstrated and offer promise for next generation processors. This has been made possible implementing polymer waveguide arrays together with VCSEL arrays. Applications are being expedited by the compatibility with the existing electronics packaging infrastructure.

### II. VCSELs for Data-Communications

We have evaluated VCSELs for use in high-speed optical data communication interconnects. The established proton-implanted AlGaAs-based (emitting near 850 nm) VCSEL exhibits three-decibel modulation bandwidths of  $\approx 15$  GHz ( $> 10$  GHz typical). Further more, we have also demonstrated a novel technique implementing a minor modification of the established platform to engineer low-threshold, high-speed, single-mode VCSELs. Said VCSELs are demonstrated in optical data links with bit error rates (BERs)  $< 10^{-12}$  under bias-free operation and exhibiting a Modulation Current Efficiency Factor (MCEF)  $\approx 10$  GHz/ $\sqrt{\text{mA}}$ . Data link issues such as compliance with engineering standards will be discussed further.

A comparison of the experimental results presented in this paper with the list of source requirements indicates that VCSELs are a viable replacement for edge-emitting lasers within datacom applications requiring data rates up to and conceivably beyond 2.5 Gbit/s. The VCSEL's large MCEF may permit below-threshold biasing and small modulation current drives. Issues with sub-threshold biasing relating to turn-on delay have been analyzed. Turn-on delay has the deleterious effect of closing the eye pattern, thus increasing the bit error rate. However, we have demonstrated zero-bias operation with acceptable results for Fiber Channel Standards at 1.062 Gbits/s, implementing a submilliamp-threshold VCSEL with an  $MCEF \approx 10 \text{ GHz}/\sqrt{\text{mA}}$ . The parameters that determine the laser bias are the threshold current, the modulation current, and the data pattern. The turn-on delay of a higher threshold laser can be reduced with a large modulation current. This, however, may lead to high output power exceeding the maximum power requirement of  $-4$  to  $-3$  dBm, and higher thermal dissipation. The data pulse history strongly affects turn-on delay for bit periods less than the minority carrier lifetime. If the pattern is Manchester encoded or is scrambled, both of which limit the number of preceding zeros, the deleterious consequences of turn-on delay are minimized. Finally, as the lasing threshold current is reduced, the turn-on delay is decreased. Further results and calculations will be presented.

Much of the impetus driving VCSEL laser research has been focused toward VCSEL arrays for high-speed optical interconnects. Parallel channel (1-D) interconnects may also prove to be an enabling technology in the foreseeable future. This includes densely-packed, 2-dimensional high-throughput free-space optical interconnects for advanced switching and processing architectures.

### III. VCSELs Within Backplanes and MCMs

We have demonstrated the use of a polymer waveguide ribbon interconnecting two MCMs. Each MCM was fabricated using an MCM-C (Ceramic) process with electrical interconnects implemented using wire bonds. Three independent channels were implemented, although the polymer waveguide ribbon was fabricated with 32 channels. Data rates up to 1 Gbit/s were demonstrated while independent operation of all channels was verified. A key feature of the packages is the low profile. The 90-deg directional change required to interface the VCSEL to the polymer waveguide is implemented using the 45-deg reflector and therefore occupies no additional height beyond the thickness of the polymer waveguides. Although the demonstration employed polymer waveguide ribbons as the interconnect medium, polymer waveguides can also be used to provide a manufacturable interface between VCSELs and optical fibers. The same MCM technology may therefore be used for polymer-waveguide-based intracabinet interconnects or fiber-based interconnect applications. Extensions of this technology are emerging.

### IV. Wrapup

The recent commercialization of VCSELs has opened up the possibility of VCSELs in numerous evolving technologies. Many of the present applications include optical links, LED and CD replacements in printing, storage, duplication, and sensors. As VCSEL components have exhibited "silicon-like" manufacturability, the ubiquity of VCSEL-based optoelectronic circuits appears bright. VCSEL-array-based smart pixel processors have the potential to enable ultrafast interconnect-intensive processors. VCSELs and VCSEL arrays appear promising between, and even within, computers, backplanes, and MCMs. The possibility of RF-VCSELs is speculated. Beyond present "commercial-grade" development, there have been a number of exciting research advancements in decreasing the threshold currents and speed of VCSELs. This may enable even lower power dissipation, higher speeds, and extensions to arrays, and expedite extensions to other spectral regions.

I wish to acknowledge my Honeywell coworkers on this research: M. Hibbs-Brenner, J. Bristow, S. Bounnak, J. Guenter, K. Johnson, R. Johnson, E. Kalweit, J. Lehman, Y. Liu, T. Marta, J. Nohava, R. Skogman, D. Smith, and R. Walterson. I also wish to acknowledge work funded in part by DARPA.

MA3 (Invited)  
9:30am - 10:00am

### Future Prospects of VCSELs: Industrial View

Yoshimasa Sugimoto and Kenichi Kasahara

*Opto-Electronics Research Laboratories, NEC Corporation*

*34, Miyukigaoka, Tsukuba, Ibaraki 305, Japan*

Research and development of vertical-cavity surface-emitting lasers (VCSELs) has made rapid progress in recent years. VCSEL array link modules have been developed with increasing speed by American consortiums such as OETC and POLO. On the other hand, high-performance VCSELs, such as low-threshold or high wall-plug efficiency ones, are being developed using AIAs selective oxidation. With this background, we describe the future prospects of VCSELs from an industrial viewpoint.

The future trends of VCSELs are shown in Fig. 1. The axes show the progress in Fiber to the Desk, which is expected to use single-channel VCSELs with high speed and high reliability, and Fiber to the CPU, which will require highly parallel VCSELs having at least 100 channels.

First, let us consider reliability. It has already been reported that the reliability of 0.85- $\mu\text{m}$  VCSELs is over  $10^4$  hours at 40 °C [1]. However, some applications may require an even higher level of reliability. One idea for making highly reliable VCSELs is to make the active region of the VCSELs from an Al-free structure[2].

Second, low-voltage and low-power operation will be required to match the trend in CMOS-

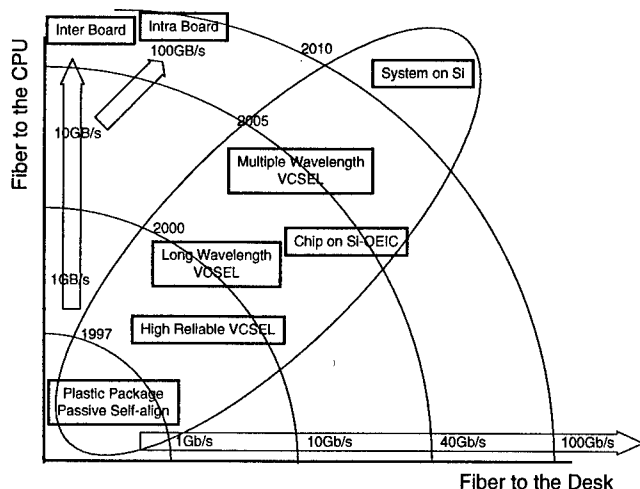


Fig. 1. Future trends of VCSELs.

LSIs. CMOS circuits currently operate at a voltage of 3.3 V, and will use 2 V by around 2002. Therefore, VCSELs will probably be fabricated from narrow-band-gap materials, which can inherently be operated at lower voltage. Long-wavelength VCSELs will be used for short-distance optical interconnections.

Third, module assembly techniques will become important for making highly parallel optical interconnections. The requirements are a low-cost plastic-based package and passive self-aligned assembly. Getting over 100 channels will also require a 2D array to raise the transmission-channel limit. Figure 2(a) shows a schematic diagram of a VCSEL-array module fabricated by our group [3]. This module has a  $2 \times 8 (=16)$ -channel 2D VCSEL array. The module uses a plastic-based receptacle package, directly joined to a push/pull fiber connector. The VCSEL-array was passively self-aligned to the package. Figure 2(b) shows the bit error rate (BER) performance at room temperature against receiver sensitivity. This module exhibits no noise floor BER performance at 1 Gbps per channel without an isolator and a sensitivity of  $-26.0 \text{ dBm} \pm 0.9 \text{ dB}$ . This structure has the potential to provide highly parallel interconnections with over 100 channels.

In summary, from the industrial viewpoint, we believe that the VCSEL is a promising device for achieving optical interconnections.

#### REFERENCES

- [1] M. Lebby, C. A. Gaw, W. Jiang, P. A. Kiely, C. L. Shieh, P. R. Claisse, J. Ramdani, D. H. Hartman, D. B. Schwartz, and J. Grula, Proc. 46th Electronic Components and Technology Conference (1996) 279.
- [2] H. Yi, J. Diaz, B. Lane, and M. Razeghi, Appl. Phys. Lett., **69**, (1996) 2983.
- [3] H. Kosaka, M. Kajita, M. Yamada, Y. Sugimoto, K. Kurata, T. Tanabe, and Y. Kasukawa, Electron. Lett., **32**, (1996) 1991.

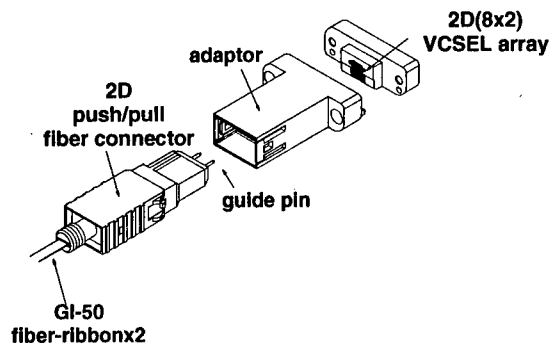


Fig. 2(a). Schematic diagram of VCSEL-array module

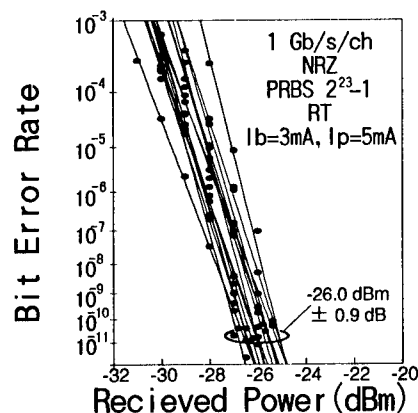


Fig. 2(b). Bit-error-rate performance of module

MB1 (Invited)

10:30am - 11:00am

## Towards microcavity vertical cavity lasers: aperture and cavity design for high efficiency and low threshold

Eric R. Hegblom, Brian J. Thibeault, and Larry A. Coldren

Department of Electrical and Computer Engineering, University of California,  
Santa Barbara, CA 93016

Lasers have long been expected to benefit from confinement of the mode to a microcavity. Reducing the laser size, however, typically leads to parasitic electrical and optical losses which overshadow any potential improvements. To possibly gain the benefits of microcavity effects, or more simply to obtain high efficiency devices with low threshold, one must eliminate these parasitic losses. The various effects preventing the scaling of device performance to small sizes are optical scattering losses, current spreading, carrier diffusion and heating. Figure 1 shows a schematic of a vertical cavity laser along with the different parasitics. Optical scattering losses can come from the aperture or the pillar sidewalls (when there is no aperture present). The low index aperture around the high index semiconductor behaves like a lens, but because its shape cannot be exactly parabolic it will scatter light out of the laser. Optical scattering losses for blunt apertures have been shown experimentally and theoretically to increase roughly as a power law ( $L_s \sim R^{-2.6}$ ) when the device radius,  $R$ , scales with the mode radius [1,2]. The excess losses will not only lower the differential efficiency of the device, but also impact the threshold in an exponential manner ( $J_{th} \sim \text{Exp}\{L_s\}$ ). In the absence of these losses, the threshold current in the device will be increased by current spreading between the aperture and the active region and by carrier diffusion within the quantum wells. The excess contribution to threshold,  $\Delta I_{th}$ , for either of these parasitics scales approximately linearly [2,3] with device size  $\Delta I_{th} \sim R_0 + R$ . Thus, they will add to threshold but not present a dramatic limit to scaling. Finally, heating of the device in the absence of other parasitics will decrease with size,  $\Delta T \sim 1/R$ ,  $J_{th} R^2 \sim J_{th} R$ . Optical scattering losses are clearly the most severe since they become larger at smaller sizes and amplify the other parasitics.

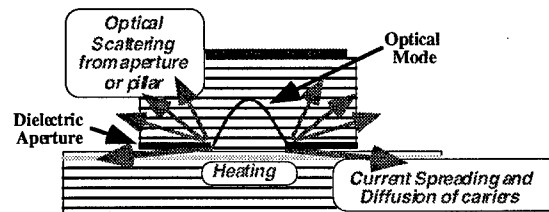


Figure 1: VCL schematic with parasitics

Optical scattering loss for small sizes have been lowered dramatically by confining the mode with apertures rather than the rough sidewalls of etched mesas [2]. However the losses for quarter-wave thick oxide aperture devices are still significant enough to prevent scaling below  $\sim 4\mu\text{m}$  [4]. As we have shown, excess loss in small oxide or air apertured devices can be addressed by using thinner apertures or an effectively weaker perturbation to the mode [5] or they can be partially addressed by using high contrast (dielectric) mirrors [6] which reduce the effective cavity length and consequently the amount of diffraction. Excess loss scales roughly with the same power for the effective optical thickness of the aperture or the cavity length [1]. However, it is much easier to reduce the effective optical thickness of the aperture than to reduce the cavity length since the spacer region must be at least  $\lambda/2$  and dielectric mirrors will require using intracavity contact layers. The optical thickness of the aperture depends critically on the location of the aperture in the standing-wave pattern. For apertures which are placed near the null, then the scattering loss becomes small, but the mode will not be well confined at the smallest aperture sizes as seen experimentally in  $1.55\mu\text{m}$  devices [7]. This effect promotes their single mode operation [7,8], but prevents scaling below  $\sim 2\text{-}3\mu\text{m}$ .

An alternative method to reduce scattering loss is to taper the oxidation front to create a more lens-like element within the cavity. When a thin AlAs layer is surrounded by AlGaAs and oxidized

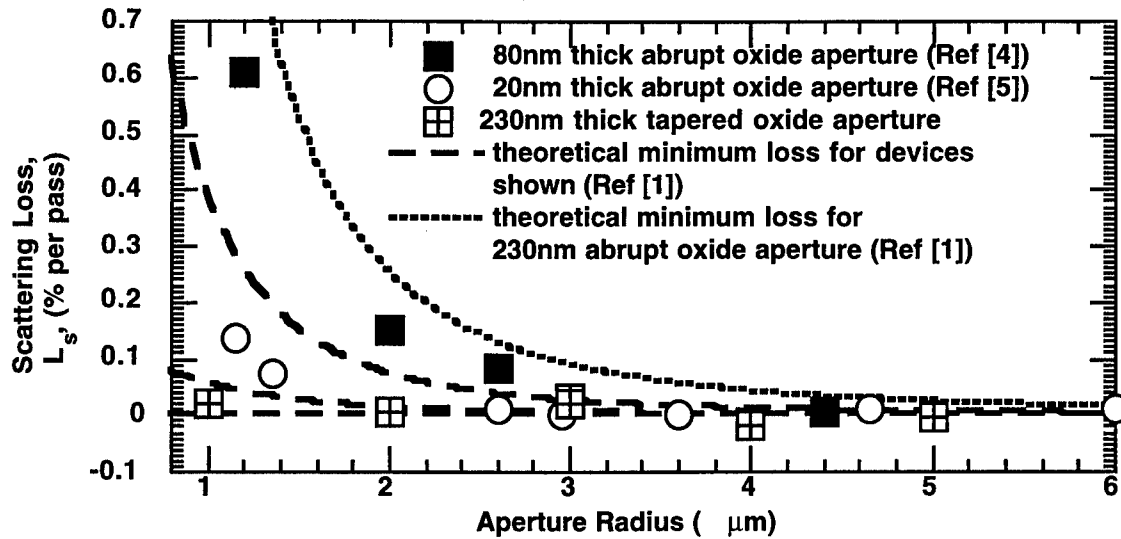


Figure 2: Scattering Losses: experiment and theory

from the edge, then the oxide front not only moves laterally but also transversely, producing a tapered profile.[9]

We have fabricated  $\lambda=980\text{nm}$  vertical cavity lasers with a tapered oxide profile which is produced by placing a 10.5nm layer of AlAs within the first p-mirror layer which is a 230nm ( $3/4 \lambda$ ) thick  $\text{Al}_{0.9}\text{Ga}_{0.1}\text{As}$  layer. In Fig. 2, we have plotted the scattering loss (as determined from the differential efficiency of tapered and abrupt apertured devices [4,5]) vs. the radius of the opening in the oxide. The dashed lines show the scattering loss theoretically predicted for the three devices based upon propagating the mode through the cavity and aperture [1]. The dotted line in Fig. 2 indicates the excess loss predicted if the 230nm thick aperture were abrupt instead of tapered.

Simulations of 980nm AlAs/GaAs VCLs with quarter-wave thick apertures[1] tapered over more than  $\sim 3\mu\text{m}$  show they have no excess loss. Although for a given mode size, scattering losses from such a "long" tapered aperture are much lower than for an abrupt aperture, the apertures close off before the mode size can shrink below a  $1/e^2$  radius of  $\sim 1.5\mu\text{m}$ . This situation is also representative of the data above. Tapering quarter-wave thick apertures over a shorter distance ( $\sim 1\mu\text{m}$ ) not only lowers scattering losses at the small aperture sizes, but also confines the mode to the smallest sizes.

Ultimately, the smallest size mode confined by a single aperture (obtained by using a parabolic (ideal lens) profile) is limited by the angular stop-band of the DBR mirror. For 980nm VCLs with AlAs/GaAs mirrors the smallest mode size has a  $1/e^2$  radius of  $\sim 0.6\mu\text{m}$ . To reduce this size further one would need to turn to dielectric mirrors or use multiple apertures which are thin so as not to introduce additional losses.

- [1] E. R. Hegblom *et al.*, IEEE J. Selected Topics in Quantum Electron. 3 (1997).
- [2] B. J. Thibeault *et al.*, SPIE Photonics West '97, San Jose, CA, 1997,
- [3] E. R. Hegblom *et al.*, SPIE Photonics West, San Jose, 1997, 3003.
- [4] P. D. Floyd *et al.*, IEEE Photon. Technol. Lett. 8, 590 (1996).
- [5] B. J. Thibeault *et al.*, IEEE Photon. Tech. Lett. 8, 593 (1996).
- [6] D. L. Huffaker *et al.*, IEEE Photon. Technol. Lett. 8, 974 (1996).
- [7] N. M. Margalit *et al.*, IEEE J. Selected Topics in Quantum Electron. 3 (1997).
- [8] J. W. Scott, Patent Pending #08,494,823 .
- [9] R. L. Naone *et al.*, Electron. Lett. 33, 300 (1997).



MB2

11:00am - 11:15am

## Uniform and High Power Selectively Oxidized 8x8 VCSEL Array

Kent D. Choquette, H. Q. Hou, K. M. Geib, and B. E. Hammons

Center for Compound Semiconductor Technology  
Sandia National Laboratories  
Albuquerque, NM 87185  
kdchoqu@sandia.gov

The compatibility to 2-dimensional array fabrication is an inherent attribute of vertical cavity surface emitting lasers (VCSELs).<sup>1</sup> High power 2-dimensional VCSEL arrays are of interest for optical display, imaging, and scanning applications. Uniformity of array characteristics such as threshold and operating current is an important consideration, particularly to simplify interfacing the array to microelectronic drive circuitry. Moreover, high power (albeit multimode) emission from each element is desirable, in spite of thermal management problems that may arise. We report the uniform characteristics of an 8x8 individually addressable high power 850 nm VCSEL array.

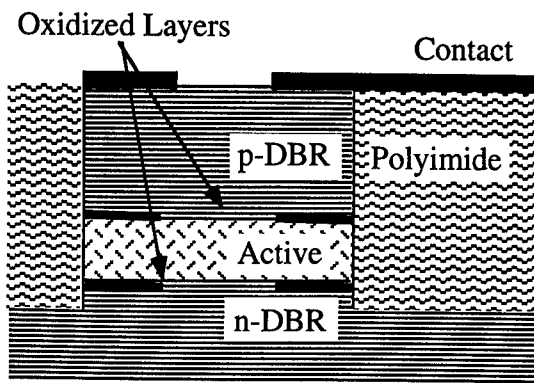
To achieve 2-dimensional array uniformity, both growth and fabrication uniformity issues must be considered. The VCSEL wafer is grown by metalorganic vapor phase epitaxy using an EMCORE reactor designed and calibrated for high growth uniformity.<sup>2</sup> The distributed Bragg reflector (DBR) mirrors are composed of  $\text{Al}_{0.16}\text{Ga}_{0.84}\text{As}/\text{Al}_{0.94}\text{Ga}_{0.06}\text{As}$  layers with continuous compositional grading at the interfaces. In the 6 DBR periods on each side of the optical cavity the doping profile is decreased to as low as  $5 \times 10^{17} \text{ cm}^{-3}$  for reduced optical absorption. This design enhances the output power at the expense of relatively higher threshold voltage. As shown in Fig. 1(a), quarterwave thick  $\text{Al}_{0.98}\text{Ga}_{0.02}\text{As}$  layers are converted to buried oxide apertures on each side of the optical cavity<sup>3</sup> which contains five 8 nm thick GaAs quantum wells. VCSEL mesas are etched  $\approx 3.5 \mu\text{m}$  deep to expose the layers for oxidation. Oxidation in steam at  $440^\circ\text{C}$  for 20 minutes produces  $15 \times 15 \mu\text{m}$  oxide apertures within the  $50 \times 50 \mu\text{m}$  mesas. During oxidation, the gas flow, water vapor partial pressure, and furnace temperature are held constant to maintain a reproducible and uniform oxidation process.<sup>4</sup> After oxidation, the array is planarized to the top of the VCSEL mesas using polyimide. This facilitates the deposition of the fan metal level providing contact to bonding pads around the perimeter of the array, as depicted in Fig. 1(b).

Fig. 2 shows cw light vs. current (L-I) curves for a typical VCSEL in the array. As evident from Fig. 3, the individual average threshold current is  $2.5 \pm 0.1 \text{ mA}$ ; the average threshold voltage is  $2.66 \pm 0.02 \text{ V}$ . For applications employing 2-dimensional arrays, it is necessary to have not only uniform threshold characteristics, but also uniform operating performance. Fig. 4 illustrates that uniform high output power (average  $15.2 \pm 0.4 \text{ mW}$ ) is found at a consistent drive current (average  $34.3 \pm 0.6 \text{ mA}$ ) for all elements of the 8x8 array. Hence for this array, the threshold current uniformity ( $\pm 5\%$ ) is surpassed by the output power uniformity ( $\pm 2.8\%$ ) and corresponding drive current uniformity ( $\pm 1.8\%$ ). Thermal issues in 2-dimensional arrays are also important, especially for simultaneous cw operation of multiple elements. In Fig. 2 are shown cw L-I curves arising from the center VCSEL with its four nearest neighbors (see inset) at various operating currents. As seen in Fig. 2, when all five elements are driven to their maximum output (33 mA), the output from each VCSEL is only reduced from  $\approx 15$  to 13 mW. Note the threshold current for each element increases by  $< 0.2 \text{ mA}$ . Further analysis of 2-dimensional VCSEL array performance, including thermal crosstalk, will be presented.

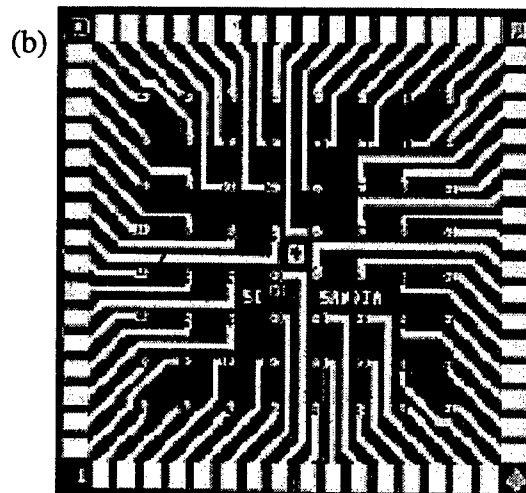
Sandia is a multiprogram laboratory operated by Sandia Corporation, a Lockheed Martin Company, for the United States Department of Energy under contract No. DE-AC04-94AL85000.

### References

- <sup>1</sup>A. Von Lehmen, et al., *Electron. Lett.* **27**, 583 (1991).
- <sup>2</sup>H. Q. Hou, et al., *Photon. Tech. Lett.* **8**, 1285 (1996).
- <sup>3</sup>K. D. Choquette, et al., *Photon. Tech. Lett.* **7**, 1237 (1995).
- <sup>4</sup>K. M. Geib, et al., *SPIE proceedings* **3003**, (1997).



(a)



(b)

Fig. 1. (a) sketch of planar oxide-confined VCSELs; (b) 8x8 individually addressed array where VCSEL are on 250  $\mu\text{m}$  pitch.

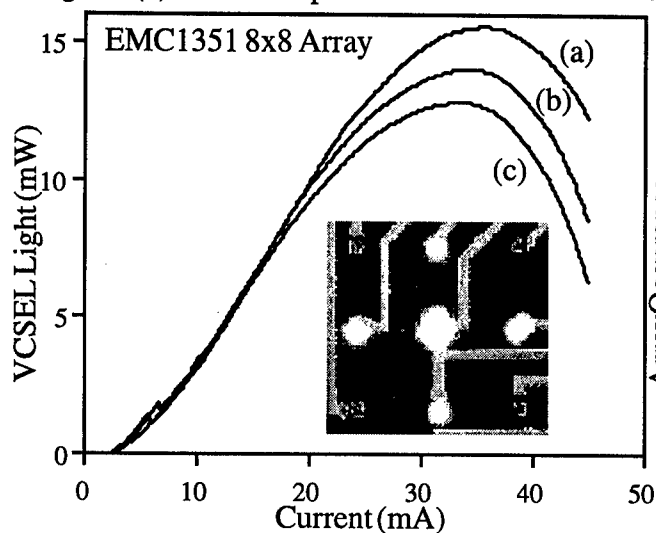


Fig. 2. L-I curves of center VCSEL with 4 surrounding nearest neighbors each driven at: (a) 0 mA; (b) 20 mA; and (c) 33 mA.

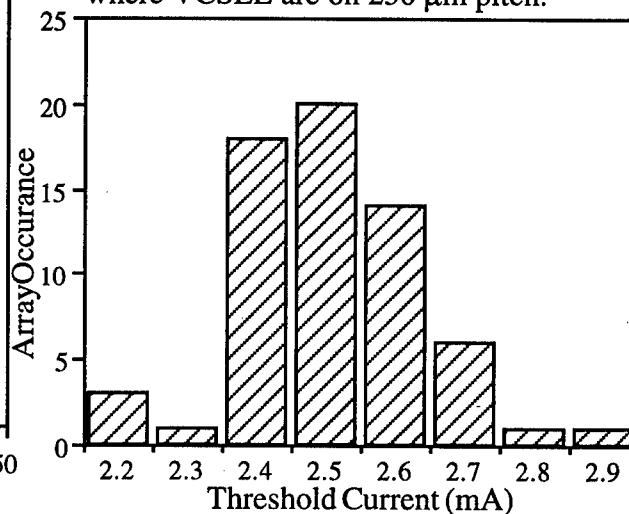


Fig. 3. Uniformity of array threshold current

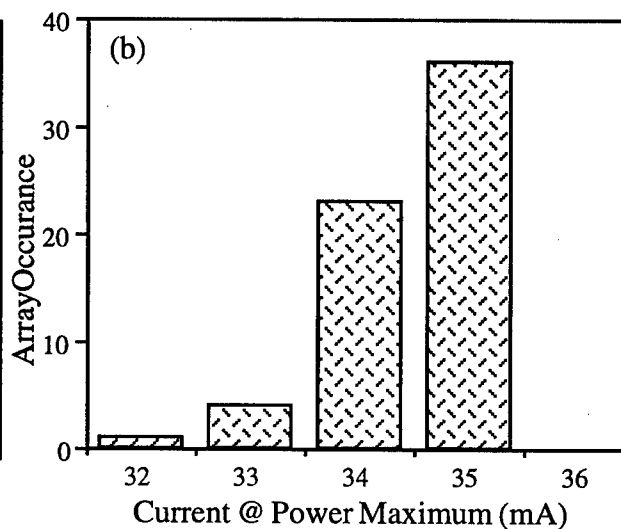
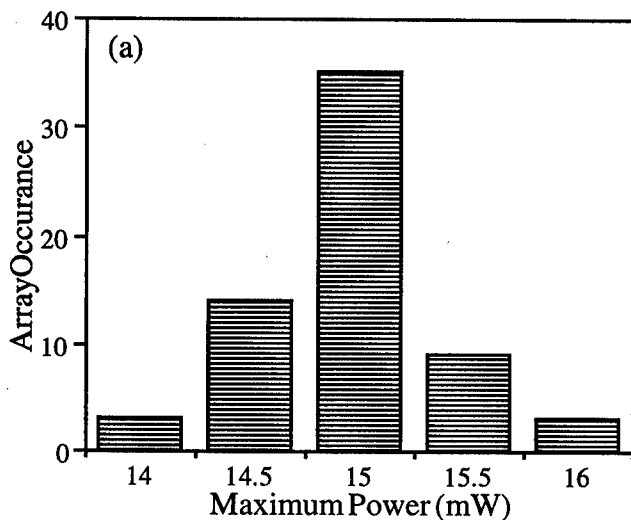


Figure 4. Uniformity of VCSEL array performance: (a) maximum power (average  $15.2 \pm 0.4$  mW); and (b) drive current at maximum power (average  $34.3 \pm 0.6$  mA).

# High Efficiency 850 nm Wavelength GaAs VCSELs

R. Michalzick, R. Jäger, B. Weigl, M. Grabherr, C. Jung, G. Reiner, and K.J. Ebeling  
University of Ulm, Dept. of Optoelectronics, D-89069 Ulm, Germany

**Abstract**— We report on the optimization of selectively oxidized VCSELs incorporating GaAs quantum wells for multimode emission around 850 nm wavelength. Devices with active diameters between 5 and 12  $\mu\text{m}$  show maximum wallplug efficiencies exceeding 55 %. Continuous wave operation is achieved up to +185 °C and the maximum single-mode output power corresponding to 30 dB sidemode suppression ratio is increased to 2.25 mW with layer structures exhibiting reduced index guiding of the optical wave.

## I. INTRODUCTION

OPTIMIZATION of vertical cavity surface emitting lasers (VCSELs) towards high conversion efficiencies from electrical to optical power is of great interest. Large one- or two-dimensional arrays for parallel optical communications or high power generation, smart pixel based switching networks [1] as well as bias-free data transmission schemes [2] are among the applications that would benefit most from the availability of such devices. For InGaAs quantum well (QW) based VCSELs emitting around 980 nm wavelength, a nearly twofold increase in the reported maximum wallplug efficiency over proton-implanted devices [3] was already achieved [4], [5] by employing the selective oxidation technique for current confinement. For optical interconnect applications, however, the interest is now focused mainly on GaAs QW VCSELs since the standard operation regime was defined to cover wavelengths between 820 and 860 nm. High performance devices with conversion efficiencies of about 30 % have already been demonstrated [3], [6]. In this paper we present a detailed study of optimized GaAs VCSELs exhibiting record high efficiencies up to 57 %.

## II. LAYER STRUCTURE

The layer structures are grown by solid source molecular beam epitaxy on n-GaAs substrates. The one-wavelength thick inner cavity contains three, each 8 nm thick GaAs QWs separated by 10 nm  $\text{Al}_{0.2}\text{Ga}_{0.8}\text{As}$  barriers. P-type top and n-type bottom mirrors consist of  $\text{Al}_{0.9}\text{Ga}_{0.1}\text{As}$ - $\text{Al}_{0.2}\text{Ga}_{0.8}\text{As}$  and  $\text{AlAs}$ - $\text{Al}_{0.2}\text{Ga}_{0.8}\text{As}$  quarter-wavelength Bragg stacks, respectively. After wet chemical mesa etching, selective oxidation of a single 30 nm thick AlAs layer incorporated in the first top Bragg reflector layer provides efficient current confinement as well as built-in effective index guiding.

## III. DEVICE OPTIMIZATION

First experiments were done with Beryllium as the p-type dopant and optimized devices with 6  $\mu\text{m}$  active diameter already showed differential quantum efficiencies of 73 %, maximum wallplug efficiencies slightly above 40 % at 2.55 mW output power, and maximum powers of 8.5 mW [7]. Despite of these encouraging results, we started to use Carbon as the p-type dopant. In comparison to Beryllium, Carbon is known for its low diffusion coefficient allowing for sharper doping profiles which are needed for further improvements of the current-voltage characteristics. A reduction of the overall doping concentration is in addition helpful to decrease the absorption losses and thus to increase the differential quantum efficiency. With this new approach, maximum wallplug efficiencies of VCSELs with nominally identical layer structures were enhanced up to 53 %.

Despite of the small oxide layer thickness, the refractive index discontinuity in the cavity gives rise to excess scattering losses which can be reduced by decreasing the spatial overlap between the standing wave and the oxide. Reduced index guiding, on the other hand, leads to a broadening of the transverse mode profiles and a better overlap between gain and intensity profiles in the active layer. Fig. 1 depicts the output characteristics of a 5  $\mu\text{m}$  diameter device processed from a wafer in which the oxide layer is shifted towards a node of the standing wave pattern [8]. Threshold current is about 0.8 mA and the threshold

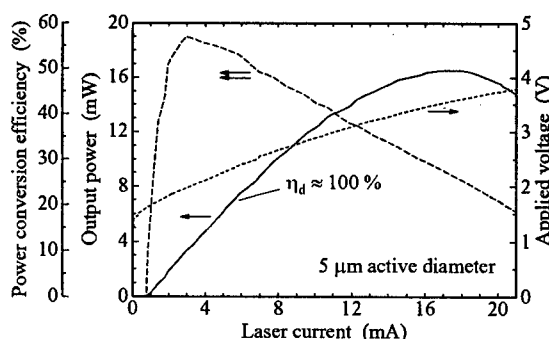


Fig. 1. Output characteristics of a 5  $\mu\text{m}$  diameter GaAs VCSEL emitting at 850 nm wavelength.

voltage of 1.58 V turns out to be only 120 mV larger than the voltage corresponding to the observed emis-

sion wavelength of 850 nm. The differential quantum efficiency is near to 100 % over a wide current range and maximum output power is limited to 16.6 mW by thermal rollover at 17.4 mA current. The peak conversion efficiency of 57 % is reached at 3 mA current and 3.3 mW optical power. The sharp decrease of efficiency is caused by the differential resistance of about 150  $\Omega$ . Nevertheless, the efficiency remains above 30 % for powers up to 16 mW.

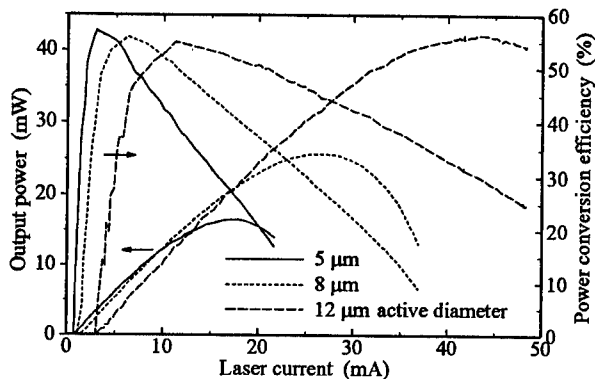


Fig. 2. Output power and conversion efficiency of oxidized GaAs VCSELs with different active diameters.

Fig. 2 shows that wallplug efficiencies over 55 % are achieved with VCSELs of 5 to 12  $\mu\text{m}$  active diameter. For smaller diameters, efficiencies begin to drop due to increased series resistances and larger devices eventually suffer from a nonideal current supply through the top ring contact. The more gradual efficiency rollover for increased diameter results from reduced differential resistances  $R_d$ . The 12  $\mu\text{m}$  diameter device with  $R_d$  below 50  $\Omega$  has optimum conversion at 11 mA current corresponding to 12 mW power and reaches its maximum output power of about 42 mW with 30 % conversion efficiency.

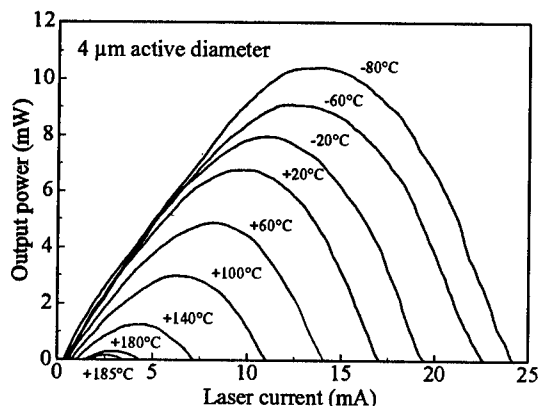


Fig. 3. Power-current curves of a 4  $\mu\text{m}$  diameter GaAs VCSEL for heat sink temperatures from  $-80$  to  $+185$   $^{\circ}\text{C}$ .

In Fig. 3, power-current characteristics are displayed for a VCSEL of 4  $\mu\text{m}$  diameter over a heat sink temperature range from  $-80$  to  $+185$   $^{\circ}\text{C}$ . At room temperature, maximum device efficiency is still 45 %. In a temperature range of technical interest from  $-40$  to  $+80$   $^{\circ}\text{C}$  the threshold current stays below 500  $\mu\text{A}$  and an output power of 1 mW is achieved with currents varying from 1.5 to 1.85 mA [8]. It is interesting to note that for all curves the turn-off at high currents occurs at an approximately constant internal temperature of about 195  $^{\circ}\text{C}$  [9].

Resulting from the oxide aperture induced effective index guiding in the VCSEL cavity, single-mode operation is relatively difficult to obtain. By comparing devices with different positions of the oxide layer in the standing wave pattern we have clear evidence for a beneficial effect of reduced index guiding on the maximum single-mode power and the side mode suppression ratio (SMSR). Single-mode conversion efficiencies of up to 43 % at 1.25 mW power in 4  $\mu\text{m}$  devices and maximum single-mode powers of 2.25 mW at 30 dB SMSR with 3  $\mu\text{m}$  diameter VCSELs have been achieved [10].

#### ACKNOWLEDGMENTS

This work was supported by the German Ministry of Research and Technology (BMBF) and the German Research Foundation (DFG).

#### REFERENCES

- [1] S. Matsuo et al., "A monolithically integrated smart pixel using an MSM-PD, MESFET's, and a VCSEL", *IEEE J. Sel. Top. Quantum Electron.*, vol. 2, pp. 121-127, 1996.
- [2] P. Schnitzer et al., "Bias-free 1 Gb/s data transmission using single-mode GaAs VCSELs at  $\lambda = 835$  nm", *Electron. Lett.*, vol. 32, pp. 2145-2146, 1996.
- [3] R.A. Morgan et al., "Producible GaAs-based MOVPE-grown vertical-cavity top-surface emitting lasers with record performance", *Electron. Lett.*, vol. 31, pp. 462-464, 1995.
- [4] K.L. Lear et al., "Selectively oxidized vertical cavity surface emitting lasers with 50 % power conversion efficiency", *Electron. Lett.*, vol. 31, pp. 208-209, 1995.
- [5] B. Weigl et al., "High efficiency selectively oxidised MBE grown vertical-cavity surface-emitting lasers", *Electron. Lett.*, vol. 32, pp. 557-558, 1996.
- [6] R.P. Schneider, et al., "Oxide-confined 850 nm vertical-cavity lasers for multimode-fibre data communications", *Electron. Lett.*, vol. 32, pp. 1300-1302, 1996.
- [7] B. Weigl et al., "Oxidised GaAs QW vertical-cavity lasers with 40 % power conversion efficiency", *Electron. Lett.*, vol. 32, pp. 1784-1786, 1996.
- [8] R. Jäger et al., "57 % wallplug efficiency oxide-confined 850 nm wavelength VCSELs", *Electron. Lett.*, vol. 33, 1997, in press.
- [9] B. Weigl et al., "High performance oxide confined GaAs VCSELs", submitted to *IEEE J. Sel. Top. Quantum Electron.*, 1997.
- [10] M. Grabherr et al., "Efficient single-mode oxide-confined GaAs VCSELs emitting in the 850 nm wavelength regime", submitted to *IEEE Photon. Technol. Lett.*, 1997.

### 850 nm VCSEL's with buried $\text{Al}_x\text{O}_y$ current apertures

Chao-Kun Lin, \*Michael H. MacDougal, Jon Geske, Aaron E. Bond, Won-Jin Choi and P. Daniel Dapkus

Department of Electrical Engineering/Electrophysics  
University of Southern California, Los Angeles, CA 90089-0483

\* Gore Photonics  
425 Commerce ct., Lompoc, CA 93436

Vertical cavity surface emitting lasers (VCSELs) with 850 nm emission wavelength are of great interest for short haul optical interconnections because of the compatibility with standard Si or GaAs based receivers. Low current and high wall plug efficiency VCSELs are needed. In this presentation, 850nm VCSELs using buried  $\text{Al}_x\text{O}_y$  current apertures with low threshold current and peak optical output of 1.2 mW are reported.

In this talk we will report on top contacted 850 nm VCSEL's with oxide apertures grown by MOCVD. The epitaxial structures were grown on  $n^+$  (100) GaAs substrates using an atmospheric MOCVD system equipped with an in-situ laser reflectometry for calibrating the various growth rates of GaAs and AlAs at the beginning of each growth run to control the layer thickness precisely and reproducibly. This tool is also used to monitor the growth of each layer and served to discover a small but important variation of the growth rates in n- and p-type GaAs

The device structure consists of 40.5 pairs n-type (Si doped) and 28 pairs p-type (Zn doped)  $\text{Al}_{0.93}\text{Ga}_{0.07}\text{As}/\text{Al}_{0.22}\text{Ga}_{0.78}\text{As}$  distributed Bragg reflector (DBR), and a one wavelength long cavity that is composed of three lattice matched GaAs/ $\text{Al}_{0.22}\text{Ga}_{0.78}\text{As}$  quantum wells and two  $\text{Al}_{0.6}\text{Ga}_{0.4}\text{As}$  cladding layers. A 190 Å linear composition grading layer is inserted between  $\text{Al}_{0.93}\text{Ga}_{0.07}\text{As}$  and  $\text{Al}_{0.22}\text{Ga}_{0.78}\text{As}$  layers of both n- and p-type DBR to reduce the series resistance of the device. The  $\text{Al}_{0.93}\text{Ga}_{0.07}\text{As}$  layer of the first p-DBR period is replaced by AlAs which has higher oxidation rate and will be selectively oxidized in the subsequent wet oxidation to form the current aperture. The calculated reflectivity of the n-DBR is 99.94% and 99.73% for p-DBR. A quarter wavelength thick  $p^+$  GaAs contact layer is grown on the top of the structure and the thickness of  $\text{Al}_{0.22}\text{Ga}_{0.78}\text{As}$  layer directly beneath this contact layer is adjusted to ensure the phase of optical waves matches at the adjacent interfaces.

Fig. 1 shows the light-current-voltage characteristics for VCSELs with square  $\text{Al}_x\text{O}_y$  current apertures of  $3.5 \times 3.5 \mu\text{m}^2$ ,  $8.9 \times 8.9 \mu\text{m}^2$  and  $14 \times 14 \mu\text{m}^2$ . The devices with smallest aperture ( $3.5 \times 3.5 \mu\text{m}^2$ ) exhibit threshold currents as low as 240  $\mu\text{A}$  and the peak optical power reaches 1.2 mW at 5 mA under room temperature cw operation on an un-cooled stage. The threshold currents of the devices with  $8.9 \times 8.9 \mu\text{m}^2$  and  $14 \times 14 \mu\text{m}^2$  apertures

are  $650\mu\text{A}$  and  $1.3\text{ mA}$ , respectively. The threshold voltage of these devices ranges from  $1.65$  to  $1.8\text{ V}$ . The external differential quantum efficiencies are  $25\%$  for the device of  $3.5\times 3.5\text{ }\mu\text{m}^2$  aperture and  $32\text{-}34\%$  for the other devices with larger aperture. The wall plug efficiencies are  $12\text{-}14\%$  owing to the typical series resistance of  $200\text{ }\Omega$  for  $14\times 14\text{ }\mu\text{m}^2$  aperture devices and  $400\text{ }\Omega$  for those with  $3.5\times 3.5\text{ }\mu\text{m}^2$  apertures.

The characteristics of these devices including modulation response and the effects of adding strain to the active region will be reported at the conference.

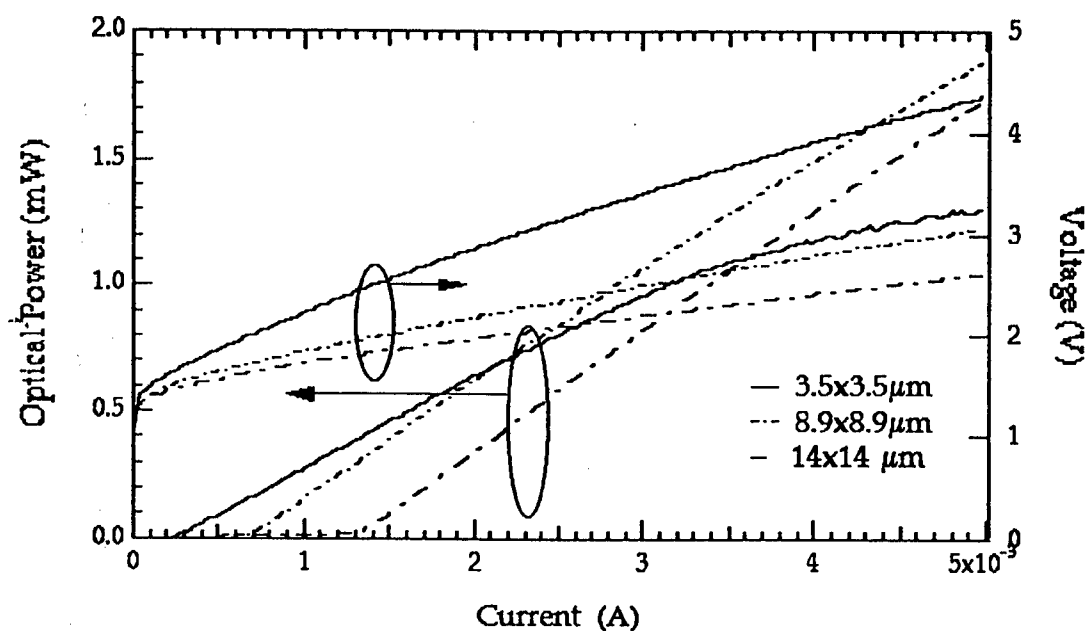


Fig. 1 Light-current-voltage characteristics of 850 nm VCSELs with various sizes of oxide current aperture.

MC1 (Invited)  
1:30pm - 2:00pm

## Visible VCSELs: Recent Advances and Applications

M. Hagerott Crawford\*, K. D. Choquette, H. Q. Hou, R. J. Hickman, K. M. Geib and  
B. E. Hammons

Sandia National Laboratories, Albuquerque, NM, 87185-0601

\*corresponding author e-mail: mhcrawf@sandia.gov

AlGaInP-based visible VCSELs fabricated by selective oxidation of AlGaAs have demonstrated enhanced performance in the form of lower thresholds and shorter wavelength operation [1]. While the oxide confinement layers provide enhanced electrical and optical confinement, the low index layers contribute to multimode operation at lower operating currents and to date visible VCSELs fabricated by ion implantation have demonstrated the highest single transverse mode powers [2]. In this talk, we will present results on recent improvements in the performance of both types of AlGaInP visible VCSEL structures brought about by new heterostructure designs.

One of the areas in which visible VCSEL performance has lagged behind that of near-IR VCSELs is in high temperature performance. Achieving continuous wave (CW) lasing from visible VCSELs at elevated temperatures is challenging due to enhanced carrier leakage in the AlGaInP-based active region as compared to the GaAs and InGaAs quantum well active regions of 850 nm and 980 nm VCSELs. While previously reported visible VCSEL designs incorporated  $(\text{Al}_{0.5}\text{Ga}_{0.5})_{0.5}\text{In}_{0.5}\text{P}$  barrier layers with no cladding layers [2], recent designs have included higher bandgap  $(\text{Al}_{0.7}\text{Ga}_{0.3})_{0.5}\text{In}_{0.5}\text{P}$  cladding layers. The temperature dependent performance of both implanted and selectively oxidized structures incorporating this design have been evaluated. CW lasing up to 75 °C has been achieved with ion implanted structures, as seen in Figure 1a. The performance of a 3  $\mu\text{m}$  x 3  $\mu\text{m}$  selectively oxidized VCSEL is shown in Figure 1b, where CW lasing up to 85 °C and low threshold voltages of 2.0 V over the 25-80 °C temperature range are seen.

Further studies have been performed on selectively oxidized AlGaInP visible VCSELs to optimize their performance, including an evaluation of device performance as a function of cavity reflectivity. In particular, VCSEL structures were grown with varying numbers of top mirror pairs: from 28 to 36 AlAs/  $\text{Al}_{0.5}\text{Ga}_{0.5}\text{As}$  pairs. CW lasing was achieved for all of the structures and a detailed evaluation of the optimal mirror design will be presented. Another area of device design that was explored was the number of oxide layers above the active region. Previous designs employed 5 oxide layers [5], while fewer pairs are expected to improve performance due to reduced scattering loss. In Figure 2, we present L-I-V data of a design employing 2 oxide layers where a record low threshold voltage of 1.980 V (135 meV above the photon energy) has been achieved. This device also demonstrates a peak wallplug efficiency of 12.2%, the highest value reported for visible VCSELs.

Recent progress has also been made in pushing AlGaAs-based VCSELs to shorter wavelengths, including the demonstration of room temperature, continuous wave operation in the 700 nm region [3]. In this talk, we will compare the capabilities and limitations of AlGaInP-based and AlGaAs-based visible wavelength VCSELs.

Visible VCSELs have several advantages over conventional edge emitting lasers for low optical power (< 10 mW) applications such as laser printing, plastic fiber based data communication, bar code scanning, optical data storage and chemical sensing. To date, prototype systems utilizing AlGaInP visible VCSELs have been evaluated for a number of applications, and critical performance specifications will be discussed. In addition, the results of recent device reliability studies will be presented.

This work has been supported by the United States Department of Energy under Contract DE-AC04-94AL85000. Sandia is a multiprogram laboratory operated by Sandia Corporation, a Lockheed Martin Company, for the United States Department of Energy.

- [1] K. D. Choquette, R. P. Schneider, M. H. Crawford, K. M. Geib and J. J. Figiel, *Electron. Lett.*, vol. 31, pp. 1145-1146, 1995.
- [2] M. H. Crawford, R. P. Schneider, Jr., K. D. Choquette and K. L. Lear, *IEEE Photon. Technol. Lett.*, vol. 7, pp. 724-726, 1995.
- [3] H. Q. Hou, M. H. Crawford, R. J. Hickman and B. E. Hammons, *Electron. Lett.*, vol. 32, pp. 1986-1987, 1996.

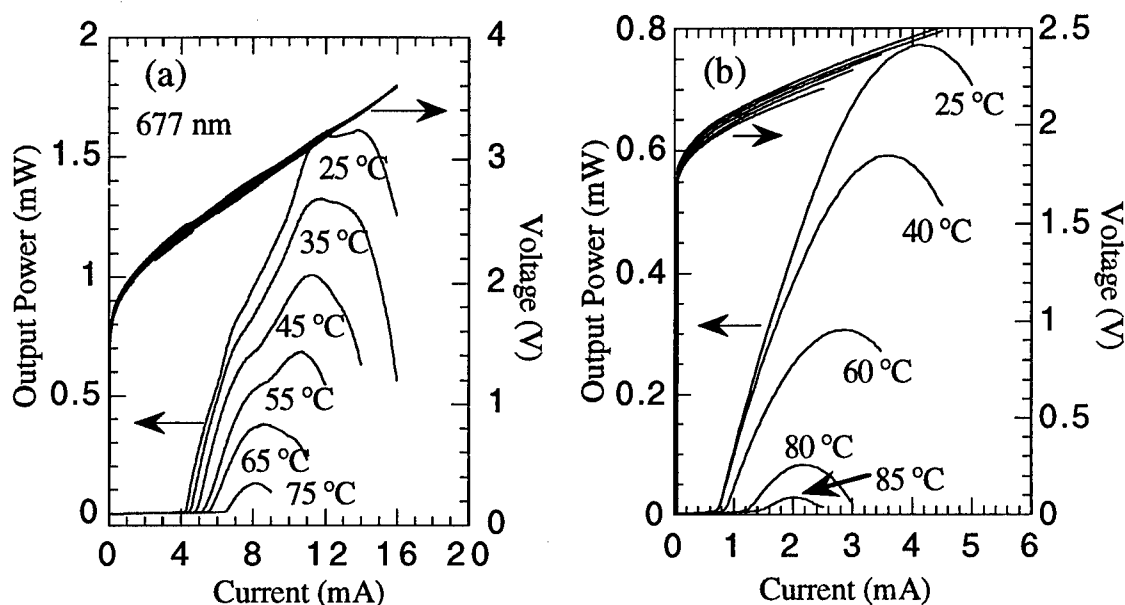


Figure 1: Temperature dependent L-I-V data for a (a) 10  $\mu\text{m}$  diameter ion implanted VCSEL with emission at 677 nm and a (b) 3  $\mu\text{m}$  x 3  $\mu\text{m}$  selectively oxidized VCSEL with emission at 683 nm. Both devices utilize  $(\text{Al}_{0.7}\text{Ga}_{0.3})_{0.5}\text{In}_{0.5}\text{P}$  cladding layers.

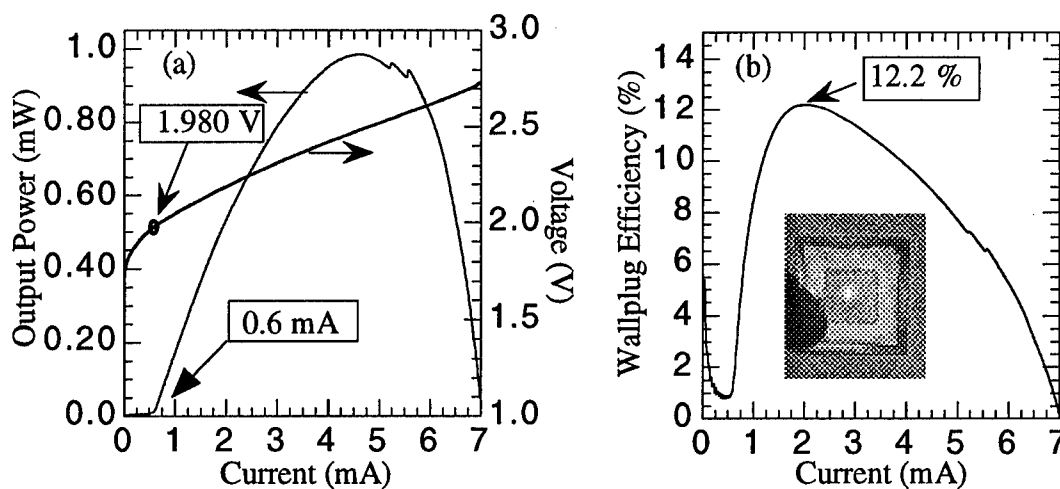


Figure 2: (a) L-I-V data for a 3  $\mu\text{m}$  x 3  $\mu\text{m}$  selectively oxidized VCSEL with 2 oxide apertures and emission at 672 nm. (b) Wallplug efficiency versus current for the same device. The inset shows a top view of the VCSEL with the oxide aperture illuminated below threshold. The mesa is approximately 50  $\mu\text{m}$  on a side.



## Self-Pulsating VCSEL with Controllable Quantum-Well Saturable Absorber

S. F. Lim\*, J. A. Hudgings, G. S. Li\*, W. Yuen\*, K. Y. Lau, and C. J. Chang-Hasnain  
211-196 Cory Hall, EECS Department, University of California, Berkeley, CA 94720

**Abstract:** We experimentally demonstrate the first self-pulsating VCSEL with a controllable quantum-well saturable absorber. Self-pulsation frequencies as high as 2 GHz were obtained.

**Introduction:** Self-pulsating lasers have proven extremely useful in applications where elimination of optical feedback and high-speed driving circuitry is needed. Most self-pulsating lasers demonstrated thus far have been edge-emitters. It is desirable to attain self-pulsating VCSELs because the surface-normal geometry facilitates 2D array configurations and wafer-scale fabrication. Though self-pulsation in VCSELs has been previously analyzed [1] and observed with kHz repetition rate [2], no VCSEL has yet been observed to self-pulsate with a controllable saturable absorber or at high frequency. In this work, we present the first demonstrated VCSEL with self-pulsations occurring through a voltage-controlled saturable absorber. The self-pulsating frequency ranges from 1.4 GHz to about 2 GHz with a FWHM of at most 10 MHz. The regime of self-pulsation extends over a range of laser and saturable absorber biases.

**Design and Fabrication:** The device schematic is shown in Fig. 1a. It is comprised of n-doped  $\text{Al}_x\text{Ga}_{1-x}\text{As}/\text{GaAs}$  distributed Bragg reflectors (DBR) on a GaAs substrate, a  $3\lambda/4$ -thick layer of AlAs for oxidation, a pair of n-doped  $\text{Al}_x\text{Ga}_{1-x}\text{As}/\text{GaAs}$  ( $x=0.7$ ) DBRs, followed by a  $1\lambda$  spacer that contains two 80-Å  $\text{In}_{0.2}\text{Ga}_{0.8}\text{As}$  quantum wells as the active region separated by 100-Å GaAs barriers, a pair of p-doped  $\text{Al}_x\text{Ga}_{1-x}\text{As}/\text{GaAs}$  ( $x=0.7$ ) DBRs, another  $3\lambda/4$ -thick layer of AlAs for oxidation, a p-doped  $\text{Al}_x\text{Ga}_{1-x}\text{As}/\text{GaAs}$  ( $x=0.7$ ) DBR stack that contains 6 mirror pairs, a  $5\lambda/4$  spacer with one 80-Å  $\text{In}_{0.2}\text{Ga}_{0.8}\text{As}$  quantum well as the saturable absorber, and n-doped  $\text{Al}_x\text{Ga}_{1-x}\text{As}/\text{GaAs}$  ( $x=0.7$ ) DBR pairs as well as a phase-matching layer on top. The fabrication involved etching down to oxidize the AlAs layers, evaporating the top n-contact, etching down to just below the absorber spacer, then evaporating an annular gold p-contact. The devices tested had approximately 26- $\mu\text{m}$  diameter oxide-defined apertures. The p-contact is used to forward bias the active region while the n-contact is used to control the voltage across the quantum-well saturable absorber. Fig. 1b shows the circuit used during measurement. The saturable absorber was biased with a voltage source in series with a variable resistor. A bias-T was used as shown to provide a path for any AC signal generated by the absorber.

**Results:** The power-current (L-I) trace of a typical device is depicted in Fig. 2. A noticeable discontinuity in  $dL/dI$  and hysteresis loop are observed at threshold, indicating bistable operation. This hysteresis can be measured over a large range of absorber bias voltages and resistances. As the absorber bias voltage and resistance are varied, the loop can be made to close, and the laser begins to self-pulsate. Typical threshold of a self-pulsating laser occurs at  $\sim 8.5$  mA with voltage  $\sim 3.3$  V and peak output power of  $\sim 1.5$  mW.

Negative differential resistance is obtained over a range of  $V_a$  and  $R$  as shown by the current-voltage ( $I_a$ - $V_a$ ) characteristic of the saturable absorber in Fig. 3. Depending on  $V_a$  and  $R$  (namely, the position and slope of the load line), the laser can operate in a bistable mode or self-pulsating mode.

Self-pulsation was measured using a high-speed detector and an RF spectrum analyzer. Fig. 4 shows a trace of the pulsation centered at 1.86 GHz with a FWHM (-3 dB) of at most 10 MHz for the laser bias current set at 9 mA, the saturable absorber voltage at 2 V, and the variable resistor at 10 k $\Omega$ . Self-pulsations with frequencies ranging from 1.4 GHz to about 2 GHz were also measured at other absorber voltages and resistances and laser bias currents. Detailed characterization of self-pulsating parameter ranges will be shown at the meeting.

**Summary:** We experimentally demonstrated the first VCSEL to self-pulsate using a voltage-controlled quantum-well saturable absorber. Self-pulsation frequencies as high as 2 GHz were observed over a range of absorber voltages and resistances. Such performance renders 2D arrays of self-pulsating VCSELs extremely feasible.

**Acknowledgments:** We gratefully acknowledge funding by ONR (Office of Naval Research) grant no. N00014-96-1-0583 as well as support from the UC Berkeley Microlab, Muthu Jeganathan for help with the theory, and Ta-Chung Wu for assistance with measurement.

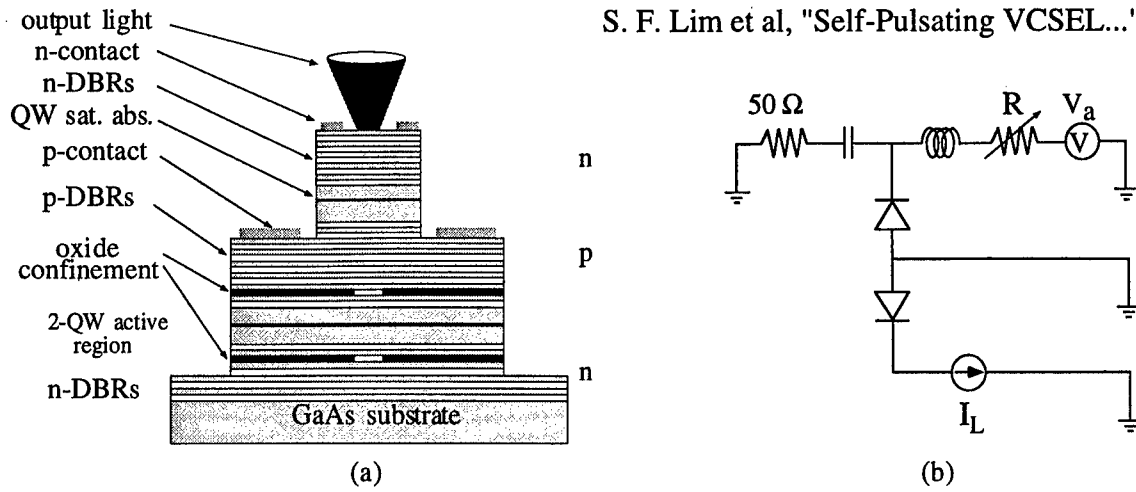


Fig. 1. (a) device schematic (b) driving circuit diagram

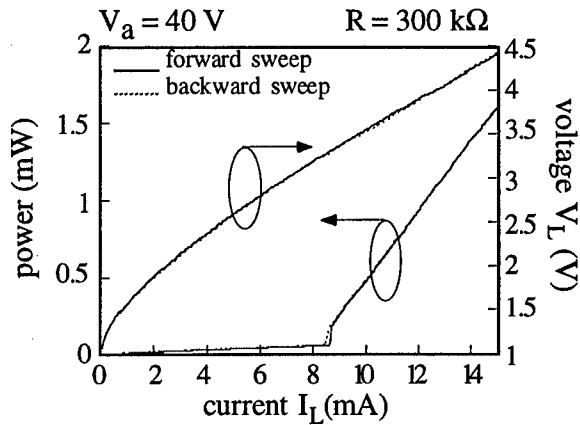


Fig. 2. Power-current ( $I_L$ - $I_L$ ) trace showing near-threshold kink and hysteresis; voltage-current ( $V_L$ - $I_L$ ) for laser.

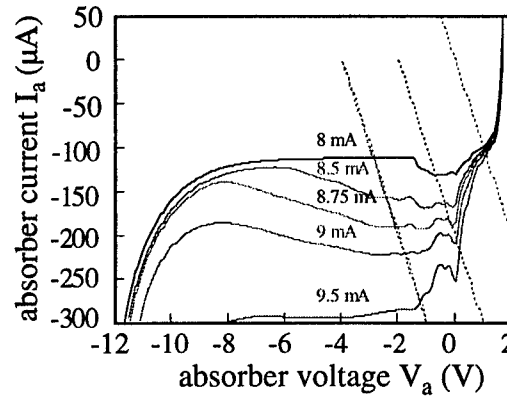


Fig. 3.  $I_a$ - $V_a$  for absorber at different laser bias currents. Dotted lines = load lines for  $R = 10$  kΩ.

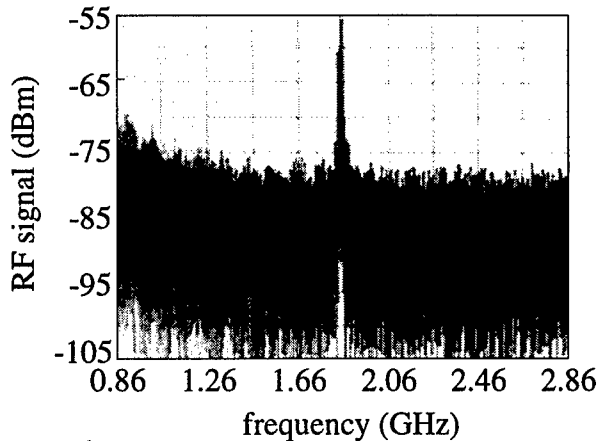


Fig. 4. Self-pulsation observed on RF spectrum analyzer

#### References

- [1] D. G. H. Nugent, R. G. S. Plumb, M. A. Fisher, and D. A. O. Davies, *Electronics Letters*, 1995, 31(1), p. 43-44.
- [2] K. D. Choquette, H. Q. Hou, K. L. Lear, H. C. Chui, K. M. Geib, A. Mar, and B. E. Hammons, *Electronics Letters*, 1996, 32(5), p. 459-460.

\* also affiliated with Stanford University

MC4

2:45pm - 3:00pm

## Tera Bytes Optical Disk with Electric Tracking Control Using Micro-cavity VCSEL Array and PD array

Kenya Goto

Dept. Information and Communication Technology, School of High-Technology for Human Welfare,  
Tokai University: Nishino 317, Numazu-city, Shizuoka 410-03, Japan  
Phone: +81-559-68-1111, Fax: +81-559-68-1155, e-mail:kenya@wing.ncc.u-tokai.ac.jp

### 1. Introduction

We have already developed a lensless optical floppy disk system<sup>1)</sup>. In this paper an ultra high density optical memory disk system of T bits/inch<sup>2</sup> with G bits/s data transfer rate is newly proposed using near field optics, of which tracks are electric controlled. The optical heads in this system use 100×100 micro-cavity VCSEL arrays. One track width on the disk is 20 nm which is fine controlled by an electrical method using a 150×150 photo-diode array and the whole head is controlled by a conventional optical and electro-mechanical method in seeking tracks.

### 2. VCSEL array writing head and electrical tracking method

The optical head in this system consists of a VCSEL<sup>2)</sup> array, a gimbals and a heat sink which has three contact pads<sup>3)</sup>. The pads closely contact to thin lubricant film on the optical disk surface. The VCSEL array consists of 100×100 micro-cavity VCSEL elements. The gimbals and the lubricant prevent the head from bouncing<sup>3)</sup>. They are very useful method to keep the spacing minimum and constant between an output face of the VCSEL array and the optical disk medium. The head can emits 10 thousand evanescent waves on the surface of optical disk medium from very small center holes of each output mirror of the micro-cavity VCSELs and can write information bits on the medium. In order to align the 10 thousand tracks the VCSEL array must be in position by about 0.57 degrees inclination<sup>4)</sup> toward to a tangential direction of the disk rotation, when the diameter of a micro-cavity VCSEL and each distance between VCSELs are one micron meter each shown as a schematic in Fig. 1.

Each track doesn't have any borderline between them, total 10 thousand tracks are in one group that is traced at once and fine track tuned by only electrical fine tracking method with no electro-mechanical aid. But in a seeking mode the conventional tracking method is used with the pre-formed sampling pits or with very narrow pre-grooves on the disk surface which are formed in every 200 micron meter apart in a radial direction of the disk. The evanescent waves from the VCSELs are irradiated to the optical disk surface with contact head technology<sup>3)</sup>, which keep the gap between medium and lasers within 10 nm including a protection coat on disk medium and a lubricant thin film over the protection coat as shown in Fig. 2a. The power density of the evanescent optical wave from 10 nm diameter windows size will be enough to write information on the disk (of either the phase change medium or the photon mode medium).

### 3. Reading head and electrical tracking error detection

The tracks are always irradiated in limited numbers (for example 100×100=10,000). On the other hand, the reading head consists of a high sensitive photo diode array and optical fiber tips

connected to each photo diode element. The number of their elements is more than 1.5 times that of the writing head in order to see the total track width in one group by knowing which diodes are detecting signal. The electrical tracking is down using only these photo diode array without any mechanical feedback.

#### 4. Optical disk and head interface

A compound ring target of GeSbTe for depositing disk medium on a polished glass disk and a silicon ring target for depositing dielectric thin film over the disk medium as a protection layer are used in an Electron Cyclotron Resonance sputtering. A lubricant such as PFPE (perfluoro polyether diol)<sup>3)</sup> which consists of a very thin movable polymer chains and a thinner coupling chains (as shown in Fig. 2b) to the protection layer of the optical disk is dip coated as thin as 1 nm. In order to prevent the head bouncing a gimbal is used to press the head toward the disk surface. The system can write and read information data as rapidly as G Byte/ sec and can store data up to 2 Tera Bytes on one surface of an 120mm optical disk.

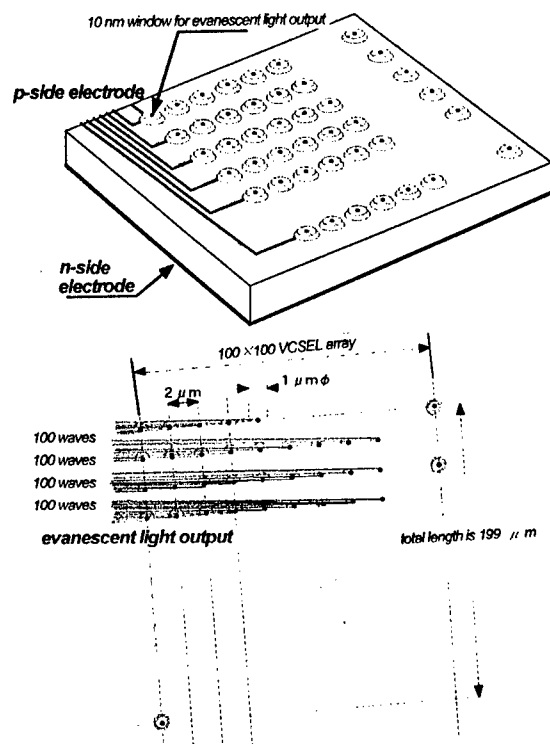


**Fig. 1** Ultra high density optical head consists of a VCSEL array, and its traced beams are shown

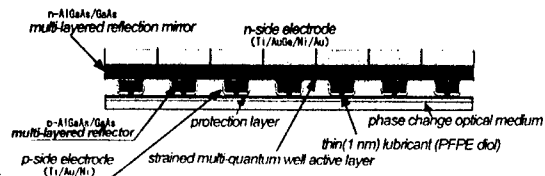


**Fig. 2a** The optical contact head with narrow gap between VCSEL array and disk surface

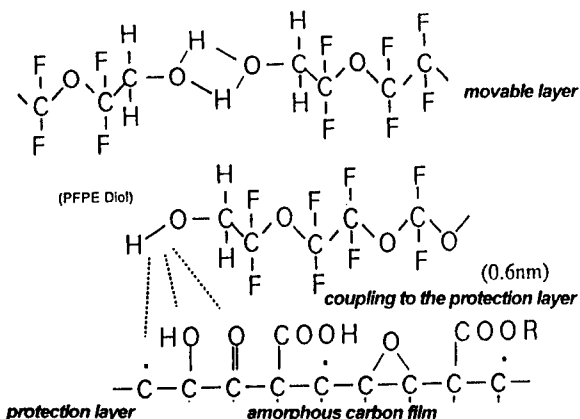


**Fig. 2b** The lubricant consists of both sticky polymer chain and movable polymer chain in PFPE diol

#### References

- 1) K. Goto, T. Sato: "Proposal Optical Floppy Disk Head & Preliminary Exp.," Jpn. J. Appl. Phys., **32**, #11B (Nov. 1993) 5459
- 2) M. Osikiri, F. Koyama, K. Iga: "Flat Surface Circular Buried Hetero-structure Surface Emitting Laser with Highly Reflective Si/SiO Mirrors", Electron. Lett., **27**, No. 22 (1991) 2038
- 3) M. Yanagisawa, A. Sato, K. Ajiki, F. Watanabe: "Design Concept for In-Contact HDI Systems," *TRIB*-Vol. 6, Tribology of Contact/ Near-Contact Recording for Ultra High Density Magnetic Storage, ASME (1996) 25-32
- 4) K. Goto: "Proposal of High Bit Rate 2T Bytes Optical Disk" Tech. Dig., Optical Data Storage '97, p3 (Tucson, April 7-9)

MD1 (Invited)  
3:30pm - 4:00pm

## Integrated VCL/PIN Arrays for Optical Computing Applications

John Wasserbauer, Jeffrey Scott, Stan Swirhun, David Lewis and Peter Kazlas\*

Vixel Corporation, 325 Interlocken Pkwy, Bldg. A, Broomfield, CO 80021

\*University of Colorado, Campus Box 525, Boulder, CO 80309-0525

### Introduction

High speed, dense arrays of vertical cavity lasers (VCLs) and detectors are at the core of many optically-interconnected computers and optical processors [1, 2]. In both applications, desired VCL properties include low threshold current and voltage, high single-mode power, high contrast and excellent array uniformity; desired detector characteristics include high speed and responsivity [3]. In this paper, we present a general purpose optical interconnect device for optical computing applications. The device is comprised of a monolithically integrated vertical-cavity laser (VCL) and PIN photodiode array. As an optical interconnect element, it functions as a bi-directional electro-optic interface; as an optical processing element or smart pixel, it can be coupled with external circuitry to provide arbitrary transfer functions. Device parameters and layout have been optimized for excellent overall performance and easy system insertion.

### Device Structure and Layout

The integrated VCL-PIN structure is depicted in Figure 1. The growth of the VCL/PIN wafer is accomplished by first growing the VCL structure and a stop etch layer followed by the photodiode in n-i-p configuration. The device fabrication includes a mesa etch to isolate the PIN from the VCL. Top contacts are provided for the PIN anode and cathode, while the VCL is contacted from opposite sides of the wafer.

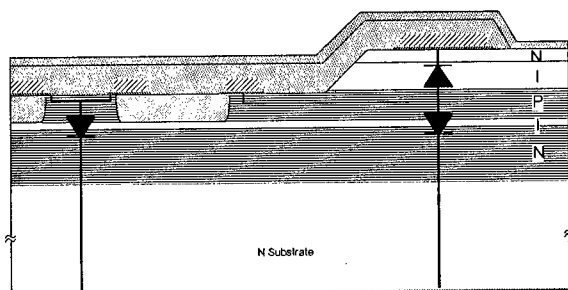


Figure 1. Layer structure of the integrated VCL-PIN.

The devices are laid out in a 2x16 array on a 250  $\mu\text{m}$  (horizontal) and 750  $\mu\text{m}$  (vertical) pitch with VCLs on the top row and PINs on the bottom row, as illustrated in Figure 2. The VCL wavelength is 850 nm with a maximum aperture dimension of 8  $\mu\text{m}$ . The PINs have an aperture of 140  $\mu\text{m}$ .

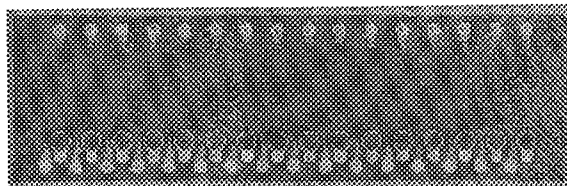


Figure 2. Layout of the integrated 2x16 VCL-PIN array.

### VCL and PIN Characteristics

VCL thresholds are typically 2.5 mA and 2.2 V. The lasers achieve maximum single-mode output powers of over 1 mW. The threshold is temperature-insensitive over a broad range of temperatures. Figure 3 illustrates the L-I response over the 0 to 90°C temperature range. No appreciable increase in threshold occurs from 0 to 60°C.

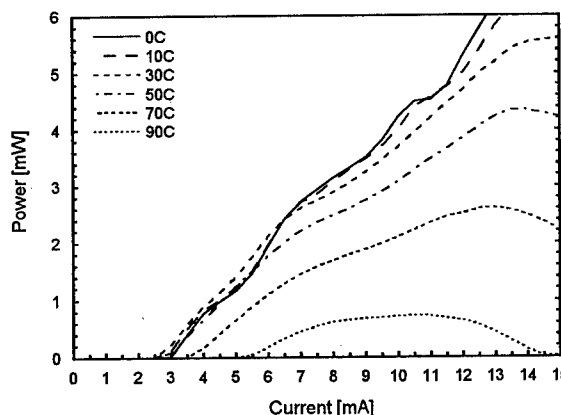


Figure 3. Temperature performance of an 8  $\mu\text{m}$  diameter VCL laser.

Optical interconnects require excellent power uniformity over the laser array. Figure 4 shows good VCL uniformity across a sixteen element array. In polarization-based optical processors, polarization control and uniformity are important device requirements [4]. Although single-mode lasers are naturally polarized with a large rejection ratio, the polarization direction can vary from laser to laser. We have demonstrated polarization control through the use of oval-shaped apertures. Figure 5 shows the polarized L-I characteristics of an oval aperture VCL. An average rejection ratio of 25 dB is achieved throughout the single-mode regime.

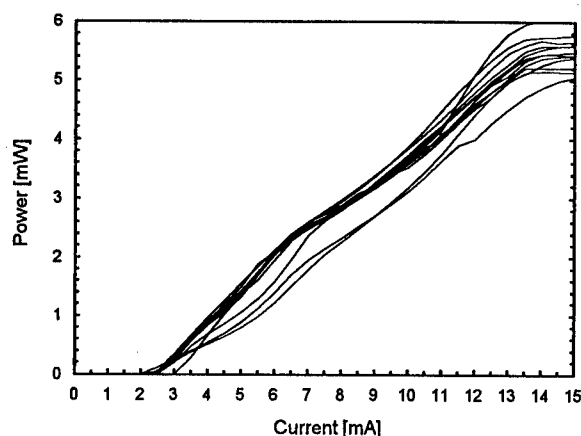


Figure 4. Uniformity of 1x16 array of 8  $\mu\text{m}$  diameter CLs.

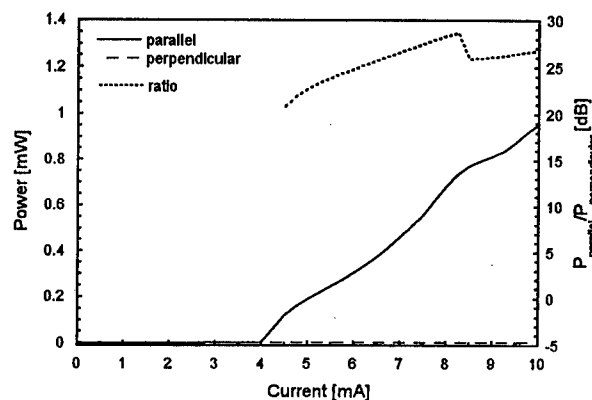


Figure 5. Polarization of an oval-shaped aperture VCL.

For optical data links, the lasers have been characterized for relative intensity noise (RIN). Figure 6 demonstrates that VCLs maintain a RIN below -120 dB/Hz for all currents above threshold.

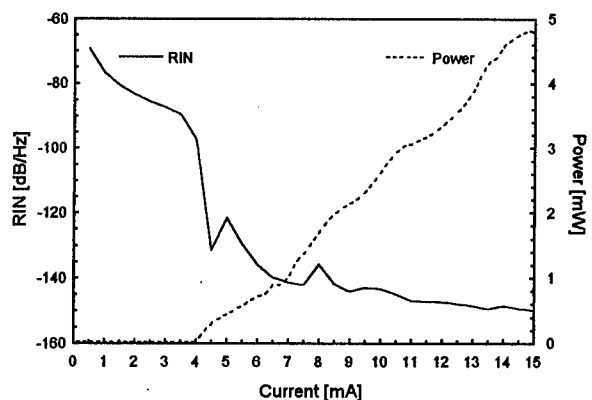


Figure 6. RIN and power versus current for a single-mode  $\mu\text{m}$  diameter VCL.

The PIN photodiodes exhibit a responsivity of 0.535 W/A, while maintaining a low dark current of 10 nA at a bias voltage of -5 V. The -3 dB bandwidth of the 140- $\mu\text{m}$  diameter detectors was measured to be 2.3 GHz. The frequency response is shown in Figure 7.

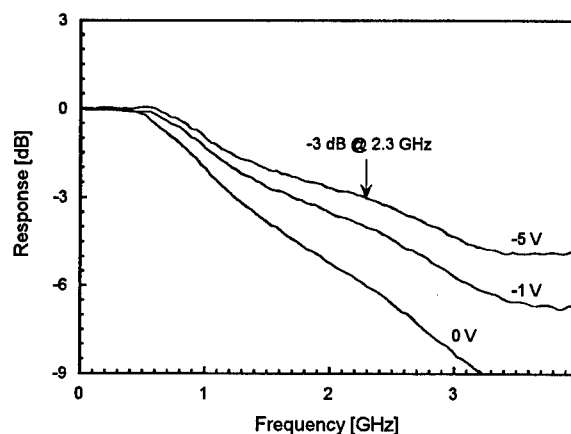


Figure 7. 40- $\mu\text{m}$  PIN photodetector frequency response at various levels of reverse bias.

## Conclusions

We have fabricated and characterized an integrated 2x16 VCL/PIN array. The device was designed to perform as a high performance, multi-functional electro-optic building block for optical computing applications. VCL arrays exhibit over 1 mW single-mode power with good power uniformity at low thresholds, while PIN arrays concurrently achieve 0.535 W/A responsivity.

This work is supported by the NAVY Small Business Innovation Research Program Contract N62269-93-C-0553.

## References

- [1] J. L. Jewell et al., "Surface-emitting Microlasers for Photonic Switching and Interchip Connections," *Optical Engineering*, 29(3): 210-214 (1990).
- [2] D. Paananen, J. Wasserbauer, J. Scott, P. Bruesenbach, D. Lewis, G. Simonis, "A 16x16 VCSEL Array Module for Optical Processing and Interconnect Applications," *1997 OSA Spring Topical Meetings - Optics in Computing*, March 17-21, 1997.
- [3] See *Digest IEEE/LEOS 1996 Summer Topical Meeting - Smart Pixels*, August 5-9, 1996, Keystone, CO.
- [4] M. G. Robinson and K. M. Johnson, "A Noise Analysis of Polarization-based Connectionist Machines," *Applied Optics* 31: 263-272 (1992).

**MD2**

**4:00pm - 4:15pm**

## **Hybrid Integration of VCSELs to Foundry Fabricated Smart Pixels**

R. Pu, E. M. Hayes and C. W. Wilmsen  
Department of Electrical Engineering  
Colorado State University  
Fort Collins, Colorado 80523

K. D. Choquette, K. M. Geib and  
H. Q. Hou  
Sandia National Laboratories  
Albuquerque, New Mexico 87185

An opto-electronic integrated circuit (OEIC) smart pixel is a structure composed of optical inputs and/or outputs interconnected to electronic processing circuitry. The optical I/O allows the data to be read in 2-D page oriented formats. This circumvents the bottlenecks in the electrical interconnections and improves speed by reducing the capacitance and inductance of the wirebonds. Recently, we have reported the successful hybrid integration of VCSELs to a foundry fabricated OEIC by flip-chip bump-bonding a backemitting VCSEL array [1] as shown in Figure 1. In this paper we will present the results of improved integration processing and VCSEL design that will increase yields and mechanical and electrical robustness. In addition, a new approach to bonding VCSELs directly to the smart pixels is presented

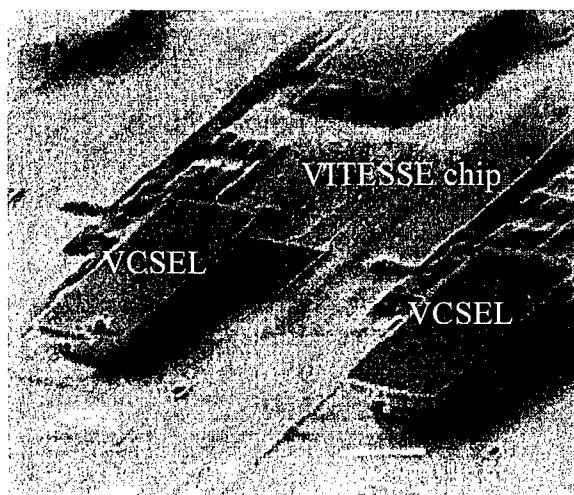


Figure 1: Flip-Chip Bump-Bonded VCSELs to an OEIC smart pixel.

To compete with electronic solutions optical interconnects must be reliable, reasonably priced, have good noise margin, and have low power consumption. To meet some of these requirements a standard foundry process is needed. We chose the Vitesse GaAs E/D MESFET foundry process offered through MOSIS since the metal-semiconductor-metal photodetector (MSM-PDs) can be fabricated along with the MESFETs. It also allows operating frequencies in the GHz range. We have designed and had fabricated an OEIC with MSMs, MESFETs and VCSEL bump bonding pads. We have shown in testing the MSM PDs that the frequency of operation is above 200 MHz. Figure 2 (a) shows the Vitesse fabricated smart pixel chip with VCSEL bonding pads and figure 2 (b) shows the smart pixel after VCSEL flip-chip bump-bonding.

Our current process is shown in figure 3. The problems encountered with this first attempt at the hybrid integration process involved the OEIC bond pads and the VCSEL wafer. First, we found that the OEIC bond pads needed to be processed before the solder deposition for the flip chip bonding. Also, problems with the substrate removal left a rough surface on the back side of the VCSEL which inhibited lasing efficiency. We also found that the contact resistance was much higher than desired. Therefore, we have redesigned the VCSEL wafer to allow for a much smoother substrate removal and provide better

electrical contacting to the n-mirror. The bond pads on the OEIC are also being redesigned to allow for easier deposition and improved electrical contact to the VCSEL.

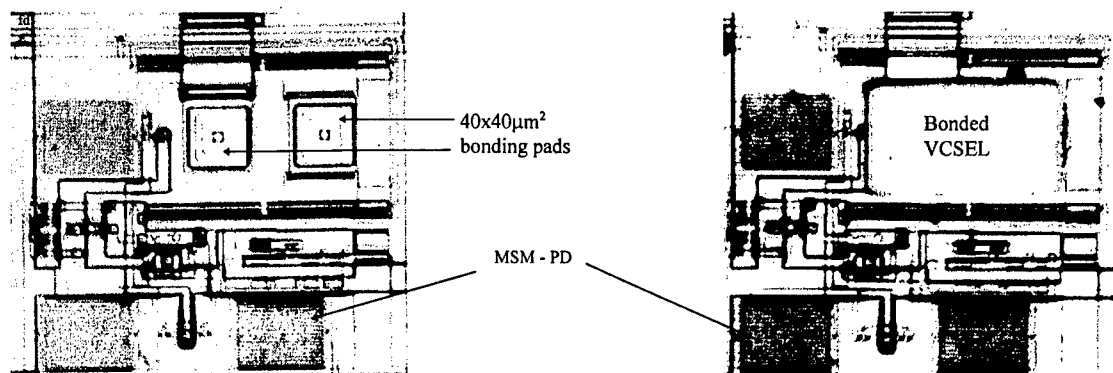


Figure 2 (a) : MSM, MESFETs, and VCSEL bump bonding pads on the smart pixel form Vitesse

(b) After Bump Bonding of VCSEL onto smart pixel.

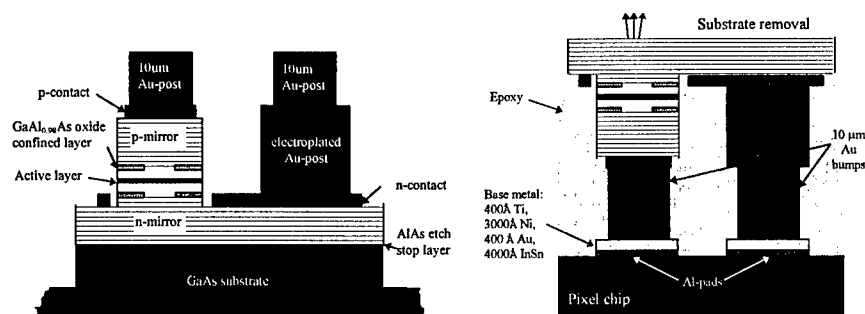


Fig.3 (a) The structure of flip-chip back-emitting VCSEL , (b) Bump bonding the VCSEL onto pixel chip

Finally, we will also present another approach to hybrid integration of VCSELs onto integrated circuits (Si-CMOS, Bipolar, or GaAs). This process should improve the yield, mechanical robustness, electrical connections, and simplify the processing. It will also allow for screening of the VCSEL arrays prior to bonding. The final product of this process is shown in figure 4. This technique should also allow for multiple bonding of VCSELs onto a single OEIC smart pixel array allowing larger arrays to be constructed from smaller pre-screened VCSEL arrays.

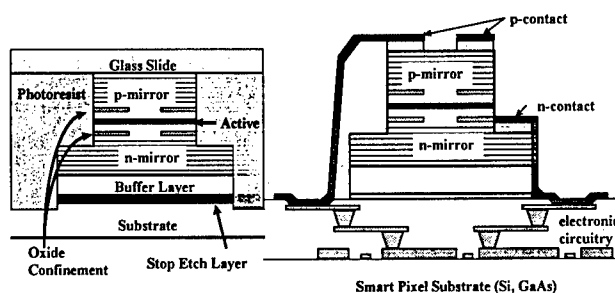


Figure 4: Another approach at hybrid integration of VCSELs onto a smart pixel circuit.

[1] R. Pu, R. Jurrat, E.M. Hayes, C.W. Wilmsen, K. Choquette, K. Geib, and H.Q. Hou, *IEEE/LEOS Spring Topical Meetings 1997, March 16-21 1997, Lake Tahoe, NV.*



MD3

4:15pm - 4:30pm

## 4x4 Broadband Optoelectronic Switch Using VCSELs

N. Rajkumar, J. N. McMullin

TRLabs, 800 Park Plaza, 10611-98 Ave., Edmonton, AB T5K 2P7, Canada

B. P. Keyworth

JDS FITEL Inc., 570 West Hunt Club Road, Nepean, ON, K2G 5W8, Canada

Future optical networks which employ wavelength division multiplexing (WDM) will require switches that are bit rate/code rate transparent, and allow spatial and wavelength reconfiguration of a channel. Optoelectronic cross-bar switches (OECBS) are able to perform all the required functionalities [1]-[3]. In a recent paper [3], a 3x3 OECBS using free-space optical distribution was described. In this paper we describe initial work on a free-space 4x4 OECBS which utilizes a 850nm VCSEL array on 500  $\mu\text{m}$  centers as the optical sources within the switch.

The layout of the 4x4 OECBS is shown in Fig. 1(a). 1x4 splitting of each VCSEL input is achieved using a 1:2 Dammann binary grating fabricated on quartz and a non-polarizing beam-splitter cube producing the 16 cross-points on the two output faces of the cube. F2.72 polymer microlenses [4] fabricated on the quartz plate focus the VCSEL beams on the output planes. The path of the 4 beams from one input is shown in Fig. 1(b). The output beams are detected by linear arrays of metal-semiconductor-metal (MSM) photodetectors mounted by flip-chip bonding on a separate glass submount which also holds the biasing and RF circuitry.

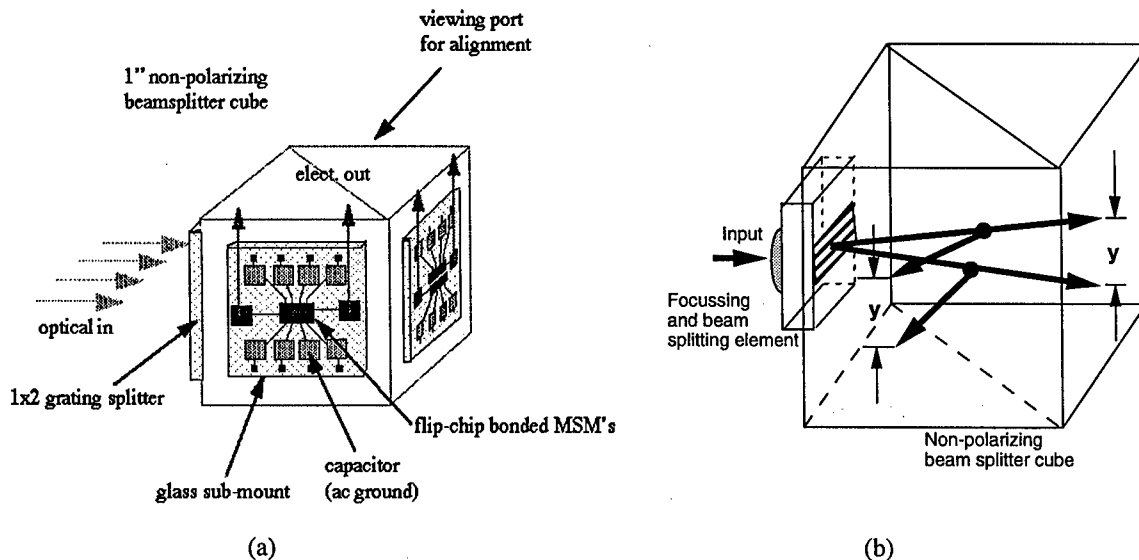


**Fig. 1 (a)** 4x4 free-space OECBS **(b)** trace of a single input beam illustrating the 1:4 split

A camera image of the optical distribution at one face of the beam splitter cube is shown in Fig. 2. The optical cross-talk was measured to be -44.8 dB electrical. The VCSELs and microwave drive circuitry were mounted on a heat-sinking aluminium nitride substrate. The frequency response of the VCSEL to a modulation applied at its input and the cross-talk due to a modulation applied in an adjacent VCSEL is shown in Fig. 3. The VCSELs were biased at an operating current of 11 mA for an output power of 1 mW and the 3 dB bandwidth of the laser is 2.64 GHz.

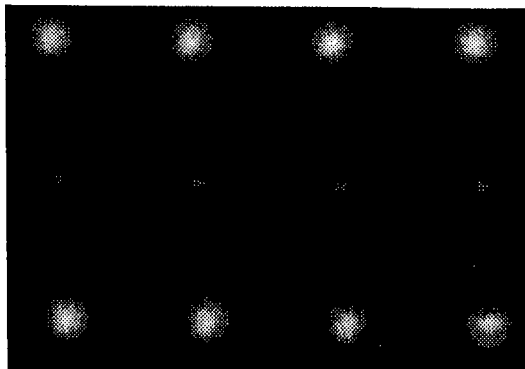
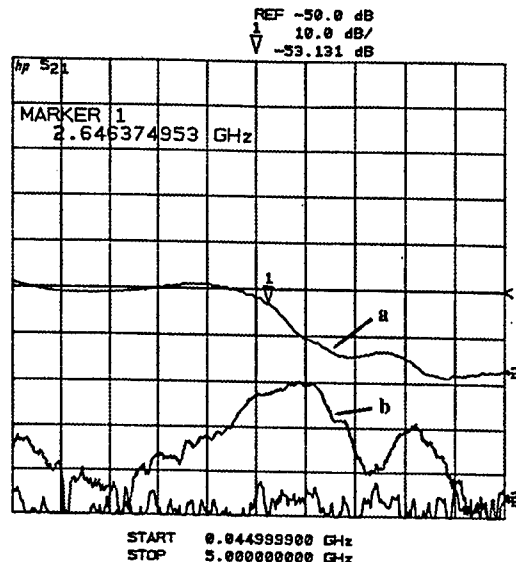


**Fig. 2** Image of the optical distribution at the beam splitter cube face.

**Fig. 3** (a) VCSEL response to a modulation at its input, and (b) to a modulation applied in the adjacent channel.



The average adjacent channel cross-talk in the VCSELs is approximately -35 dB. It has been experimentally verified that the cross-talk seen in the response of Fig. 3 is entirely due to the parasitics inherent in the device and not due to the limitations in the package. The MSM detector cross-points were fabricated on Corning 7059 glass and have a 3 dB device limited bandwidth of 2 GHz. The detectors are terminated in a low impedance 50  $\Omega$  front-end MMIC amplifier with a 50 dB gain. The ON-OFF contrast was measured to be -69.5 dB electrical.

The signal-to-noise ratio (SNR) of the entire system for a 2 GHz bandwidth calculated from the measured data is 24.84 dB. The principal noise source is the receiver thermal noise ( $\text{SNR}_{\text{TH}} = 26.43$  dB). The second dominant source of noise in the present system is the laser noise, both RIN ( $\text{SNR}_{\text{RIN}} = 31.98$ ) and adjacent channel electrical cross-talk noise ( $\text{SNR}_{\text{ECN}} = 35$  dB). By employing VCSELs with higher output powers and MSMs with better responsivity, it is possible to improve the S/N ratio to a level at which the laser noise would dominate, establishing a S/N ceiling. The S/N ceiling for the present system is estimated to be -30 dB. If further improvements in the S/N is desired, VCSELs with lower intrinsic RIN and lower device cross-talk would be required.

## References

1. M. Veilleux, R. I. MacDonald, "An optoelectronic switching Matrix with high isolation", *J. Lightwave Tech.*, vol. 10, pp. 988-991, 1992.
2. R. I. MacDonald, "Optoelectronic Switching for Virtual Wavelength Paths", Paper PThD1, Photonics in Switching Topical Meeting, April 2-4 1997, Stockholm.
3. N. Rajkumar, J. N. McMullin, B. P. Keyworth, "Optoelectronic cross-bar switching using free-space optical distribution", *IEEE Photon. Tech. Lett.*, vol. 8, no.11, pp. 1534-1536, 1996.
4. B. P. Keyworth, D. J. Corazza, J. N. McMullin, L. Mabbott, "Single-step fabrication of refractive microlens arrays", *Appl. Opt.*, in press.

MD4

4:30pm - 4:45pm

## VCSEL Based High Performance ATM Switch

C.W. Wilmsen and C. Duan

*Electrical Engineering Department, Colorado State University  
Fort Collins, Colorado 80523, USA*

J.R. Collington, M.P. Dames and W.A. Crossland

*Cambridge University Engineering Department  
Trumpington Street, Cambridge, UK, CB2 1PZ*

Large-broadband ATM switching nodes will require novel hardware solutions which could benefit from the inclusion of optical interconnect technology, since electronic solutions are limited by pin out and by the capacitance /inductance of the interconnections. This paper describes, analyzes and provides preliminary data from a new three stage free space optical switch which utilizes VCSELs for the optical interconnections, a liquid crystal spatial light modulator (SLM) as a reconfigurable shutter and relatively simple optics for fan out and fan in. A custom CMOS chip is required to introduce a time delay in the optical bit stream and to drive the VCSELs. Analysis shows that the switch should be scaleable to 1024 input and output channels. This size switch requires an array of 2048 VCSELs. A detailed optical power budget calculation indicates that each of the VCSELs in the array must have a maximum optical output of  $\sim 2$  mW.

The three stage switch, as illustrated in Fig. 1 is composed of a central routing switch (optical cross-bar ) which performs cross point routing of the inputs to the outputs. Figure 2 illustrates the general features of the proposed VCSEL/SLM based switch. The first stage is composed of the VCSEL arrays and their controlling electronics, the second stage is made up of the holographic fan-out optics and a SLM, and the third stage contains the fan-in optics, the output photodetector array and electronic queues/controls. The first stage electronically divides the  $N$  inputs into  $m$  sectors of size  $N/m$  in order to reduce the number of cross points. The output of these sectorized units drive the VCSELs.  $N/m$  copies of each of the optical bit streams emitted from the lasers are then made by the holographic fan-out optics and imaged onto the array of liquid crystal routing shutters. Only  $N$  of the  $N^2/m$  routing shutters are open; one for each output channel. The beams reflected from the shutter are then collected by the fan-in optics and directed onto a photodetector array prior to queuing for the output port.

The liquid crystal routing shutter pattern remains fixed for one ATM cell period, e.g.  $2.7\mu\text{s}$  for STM-1 (155Mbps), during which time the bit stream of that set of inputs cells is routed to the proper output. Since the next set of input ATM cells will be routed to different outputs, the routing shutter array must be reconfigured into another pattern before these new cells arrive. However, there is very little time between the incoming and the liquid crystal shutters switch slowly, therefore a delay between the cells must be introduced. This time delay can be gained by electronically multiplexing the odd and even incoming ATM cells between two spatially separated VCSEL arrays, as outlined in Fig. 3a. To accomplish this, each input channel has a multiplexing switch, two 424 bit shift registers (which provides a one cell delay between the cells streams) and a VCSEL driver circuit. One array of VCSELs is driven by the 1st, 3rd, 5th ....(odd ) cells and the other VCSEL array is driven by the 2nd, 4th, 6th....(even) cells, as shown in the timing diagram of Fig. 3b.

It appears that interleaving the two VCSEL arrays is the optimum layout configuration since physically separating the arrays increases the length of the leads on the CMOS chip, thus increasing the chip area and the lead capacitance. The liquid crystal routing shutters must also be interleaved into two arrays in order to match the VCSEL arrays. Two shutter arrays are used so that while one shutter array is actively routing the signals from one of the VCSEL arrays, the second shutter array is being reconfigured. Figure 4 shows the optical layout of the demonstrator which utilizes an array of microlenses, 4f imaging optics and a cylindrical lens for fan in

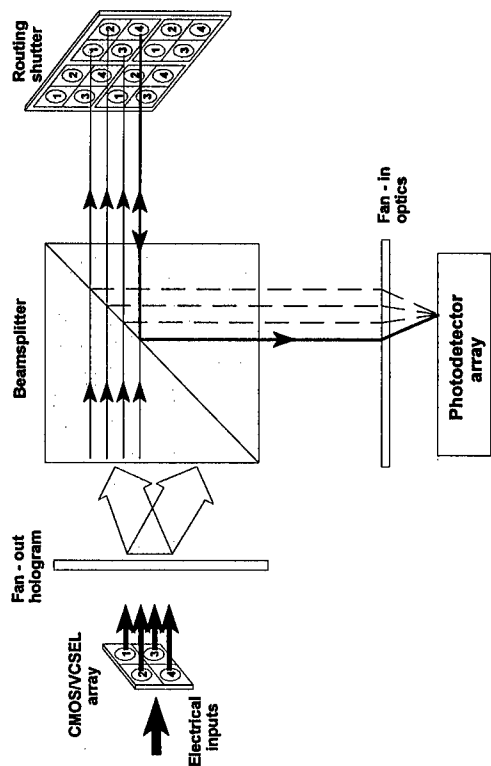


Fig 2. Layout of the VCSEL/liquid crystal cross point switch showing typical optical paths through the switch

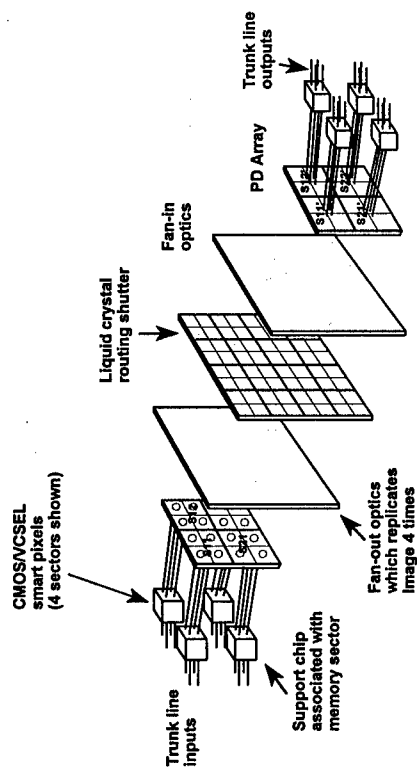


Fig 1. Conceptual illustration of the three stage ATM switch fabric

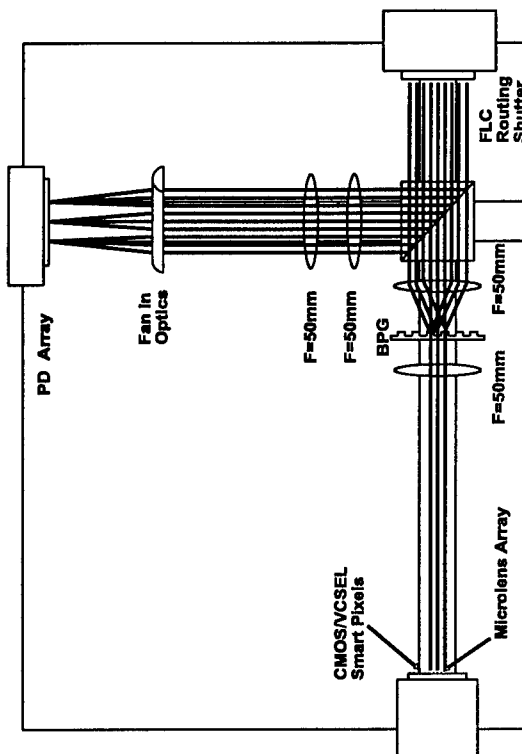


Fig 4. Optical layout of the demonstrator

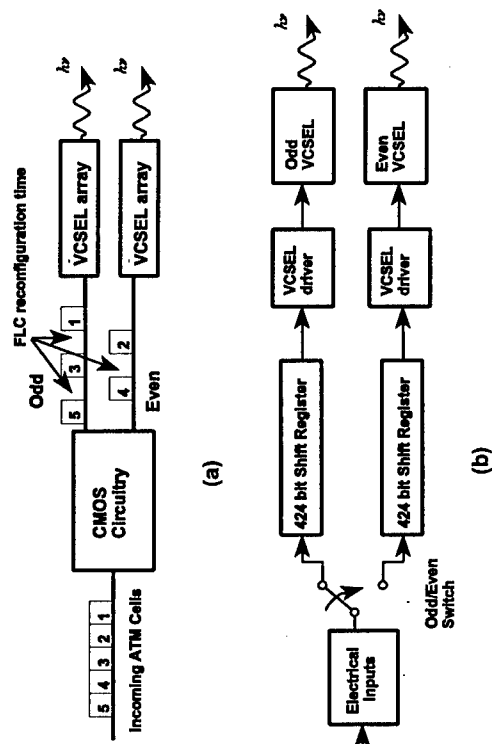


Fig 3. CMOS/VCSEL smart pixel (a) schematic timing diagram (b) block diagram

## **VERTICAL-CAVITY LASERS**

**Tuesday, 12 August 1997**

### ***Sessions:***

- TuA: Novel Material Technologies***
- TuB: Long Wavelength VCSELs***
- TuC: Postdeadline Session***



TuA1

8:30am - 8:45am

**Low-Threshold Continuous-Wave Operation of an Oxide-Confined Vertical-Cavity Surface-Emitting Laser Based on a Quantum Dot Active Region and Half-Wave Cavity**

D.L. Huffaker, L.A. Graham, M.R. McDaniel, and D.G. Deppe  
Microelectronics Research Center

Department of Electrical and Computer Engineering  
The University of Texas at Austin, Austin, Texas 78712-1084

Phone: (512) 232-1890, Fax: (512) 471-8575

email: dhuf@mail.utexas.edu

The use of quantum dot (QD) active regions can conceivably yield reduced threshold currents, increased differential gain, and reduced temperature sensitivity as compared to quantum wells (QWs), due to their atomic-like density of states. Although lasing has been recently reported using QD active regions [1-3], it is difficult to achieve from the lowest confined energy states, especially at room temperature [2,3]. To benefit from the QD density of states it is desirable to have a very low loss laser cavity with strong mode selectivity. In this talk, we describe the first room-temperature continuous-wave (CW) lasing characteristics of a QD active region placed in an oxide-confined half-wave vertical-cavity surface-emitting laser (VCSEL) structure. We have maintained nearly the same cavity design as used with an InGaAs QW [4] by choosing the active material as  $\text{In}_{0.50}\text{Ga}_{0.35}\text{Al}_{0.15}\text{As}$  to generate QD emission centered around  $0.97\mu\text{m}$ .

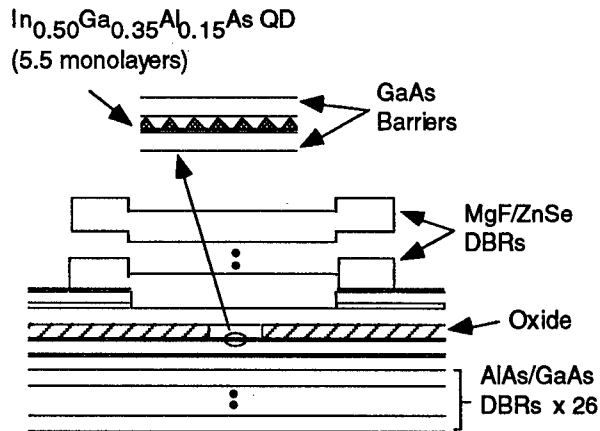


Figure 1: Cross-section schematic of oxide-confined  $\text{In}_{0.50}\text{Ga}_{0.35}\text{Al}_{0.15}\text{As}$  QD VCSEL.

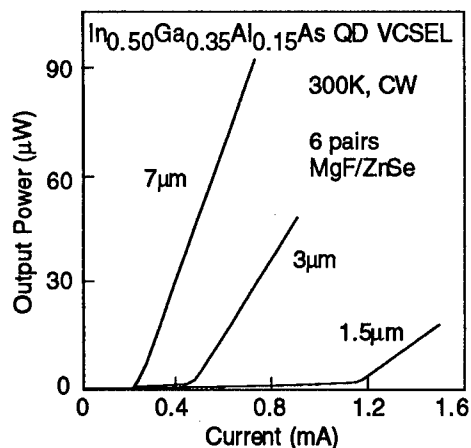


Figure 2: Light versus current curves for a  $7\mu\text{m}$ ,  $3\mu\text{m}$  and a  $1.5\mu\text{m}$  QD VCSEL. The low threshold device ( $7\mu\text{m}$ ) has a threshold current of  $235\mu\text{A}$  ( $480\text{A}/\text{cm}^2$ ).

Figure 1 shows a schematic cross-section of the structure with a single 5.5 monolayer  $\text{In}_{0.50}\text{Ga}_{0.35}\text{Al}_{0.15}\text{As}$  QD active region formed on an undoped  $100\text{\AA}$  GaAs layer at the center of the  $\text{Al}_{0.99}\text{Ga}_{0.01}\text{As}$  half-wave cavity spacer, at a substrate temperature of  $\sim 510^\circ\text{C}$ . Atomic force microscopy photographs show an average dot size of  $220\text{\AA}$  and a dot density of  $\sim 10^{11}/\text{cm}^2$ . The lower distributed Bragg reflector (DBR) consists of 26 n-type pairs of AlAs/GaAs and the upper DBR consists of a single quarter-wave layer of p-type GaAs followed by a MgF/ZnSe 6 pair DBR. Figure 2 shows light versus current curves for a

7 $\mu\text{m}$ , a 3 $\mu\text{m}$  and a 1.5 $\mu\text{m}$  square QD VCSEL, CW at room-temperature. The lowest threshold current is 235 $\mu\text{A}$  for the 7 $\mu\text{m}$  device which yields a threshold current density of  $\sim 480\text{A}/\text{cm}^2$ . This is lower than for QD room-temperature lasers reported elsewhere [1-3]. The 3 $\mu\text{m}$  and 1.5 $\mu\text{m}$  have increasingly higher thresholds of 435 $\mu\text{A}$  and 1.14mA. Figure 3(a) shows the electroluminescence from a 7 $\mu\text{m}$  VCSEL device before the deposition of any upper MgF/ZnSe pairs with the lasing spectra from the 7 $\mu\text{m}$  VCSEL of Fig.2 overlaid in Fig.3(b). In curve (a), the strong emission peak at 9350 $\text{\AA}$  and the shoulder at 9520 $\text{\AA}$  seem to be correlated to the wetting layer and to the cavity-modified QD emission, respectively. The lasing wavelength in Fig.3(b) is 9515 $\text{\AA}$ .

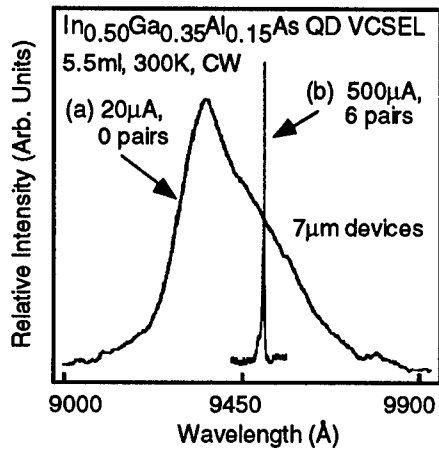


Figure 3: Spectral data showing (a) 7 $\mu\text{m}$  device with zero pairs MgF/ZnSe and (b) lasing spectrum for the 7 $\mu\text{m}$  device shown in Fig.2.

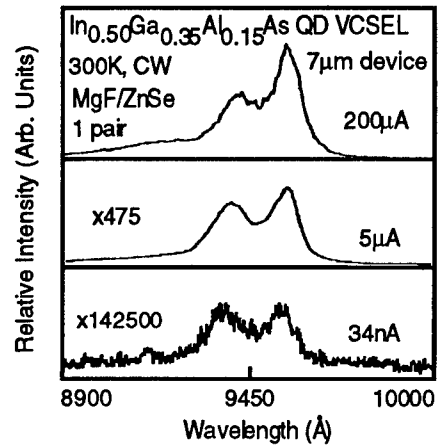


Figure 4: Spectral data at several bias currents from a 7 $\mu\text{m}$  device with one pair MgF/ZnSe DBRs.

To identify the lasing states with respect to the QD ground states, we have studied several other device structures. A six monolayer  $\text{In}_{0.50}\text{Ga}_{0.35}\text{Al}_{0.15}\text{As}$  QD active region with no mirrors (data not shown) at 300K has a QD emission peak at 9686 $\text{\AA}$  with full-width at half-maximum (FWHM) of 616 $\text{\AA}$  and wetting layer peak emission at 9249 $\text{\AA}$ . At 80K, the QD emission peak has shifted to 9119 $\text{\AA}$  with a FWHM of  $\sim 420\text{\AA}$ . The broad linewidths are indicative of the inhomogeneous broadening typical of QD active regions [1-3]. Occupation of the electronic states which participate in lasing seems to occur due to bandfilling at room temperature. An effect of this is seen in Fig.4 in electroluminescence at several bias currents for a 7 $\mu\text{m}$  VCSEL device after deposition of one pair MgF/ZnSe DBRs. The intensity of the long wavelength peak (9550 $\text{\AA}$ ) grows nonlinearly with respect to the short wavelength emission (9330 $\text{\AA}$ ) with increasing bias current. Such behavior is discerned from saturation of non-radiative defects using time-resolved and spectrally-resolved photoluminescence from a VCSEL structure at 300K and 80K and will be discussed further in the talk.

- [1] Kirkstaedter, N., Ledentsov, N., Grundmann, M., Bimberg, D., Ustinov, V., Ruvimov, S., Maximov, M., Kop'ev, P., Alferov, Zh., *Electron. Lett.*, 1994, **30**, pp. 1416-1417
- [2] Kamath, K., Bhattacharya, P., Sosnowski, T., Norris, T., and Phillips, J., *Electron. Lett.*, 1996, **32**, pp. 1374-1375
- [3] Saito, H., Nishi, K., Ogura, I., Sugov, S., and Sugimoto, Y., *Appl. Phys. Lett.*, 1996, **69**, pp. 3140-3142
- [4] Huffaker, D.L., Graham, L.A., Deng, H., and Deppe, D.G., *IEEE Phot. Tech. Lett.*, 1996, **8**, pp. 974-976



TuA2

8:45am - 9:00am

## Dynamically Stable Polarization Characteristics of Oxide-Confinement Vertical-Cavity Surface-Emitting Lasers Grown on GaAs(311)A Substrate

M. Takahashi and N. Egami

ATR Adaptive Communications Research Laboratories  
2-2 Hikaridai, Seika-cho, Soraku-gun, Kyoto, 619-02 Japan  
TEL:+81-774-95-1501 FAX:+81-774-95-1508

A. Mizutani, A. Matsutani, F. Koyama, and K. Iga  
Tokyo Institute of Technology, Precision and Intelligence Laboratory  
4259 Nagatsuta, Midori-ku, Yokohama, 226 Japan

Vertical-cavity surface-emitting lasers (VCSELs) have been developed as two-dimensional (2D) light sources for optical interconnects and parallel optical communications [1]. A conventional VCSEL grown on a (100)-oriented substrate exhibits unstable and random polarization states in plane because of an extremely small polarization selectivity. Polarization control of VCSELs has therefore been of great interest, especially for polarization sensitive applications. Polarization control is also important for low noise applications, because polarization fluctuations cause excess intensity noise even under fundamental transverse mode operations [2]. Several polarization control methods have been reported [3]-[4]. There have also been some interesting findings. Recently, for instance, it was theoretically predicted that strained-layer quantum wells (SL-QWs) grown on non-(100) substrates have an anisotropic optical gain distribution [5]. For our part, we experimentally demonstrated that the polarization mode of a VCSEL can be well controlled even under direct modulation by using the optical anisotropy of (n11)-oriented QWs.

Figure 1 shows a schematic diagram of a (311)A-oriented VCSEL with an oxide confinement structure. The epitaxial layer was grown on a GaAs(311)A substrate by molecular beam epitaxy. The active region consists of  $\text{In}_{0.2}\text{Ga}_{0.8}\text{As}$  double quantum wells centered in a single-wavelength-thick  $\text{Al}_{0.5}\text{Ga}_{0.5}\text{As}$  cavity. The upper and bottom DBR mirrors consist of a 25- and 22.5-pair AlAs/GaAs quarter-wave stack, respectively. A mesa with a 15  $\mu\text{m}$  square active region was formed by reactive ion beam etching (RIBE). After the etching, AlAs layers in the p-DBR were selectively oxidized in an  $\text{N}_2/\text{H}_2\text{O}$  atmosphere at 400 °C. Note that oxidization reduces the active region to 9  $\mu\text{m}$  square. An antireflection coating of SiN was deposited on the backside of the GaAs substrate.

Figure 2 shows a typical L-I characteristic under continuous wave (CW) operation at 25 °C. The threshold current is 1.0 mA, and the lasing wavelength is around 990 nm. Figure 3 shows a typical L-I characteristic resolved in two orthogonal polarization modes at 25 °C. In Fig. 3, curves calculated by two-mode rate equations are also plotted for various gain differences between two polarization states. The polarization mode with the maximum optical intensity is aligned along the  $[233]$  crystallographic direction, which corresponds to the maximum gain direction exhibited in the (311)A-oriented QWs. The orthogonal polarization mode ( $[01\bar{1}]$  polarization) was fully suppressed. A suppression ratio of 22.5 dB between these two polarization modes was obtained at 1.5 times the threshold. By comparing the experimental results with the theoretical curves, the net gain difference between the two orthogonal polarization modes was estimated to be as large as 20% of the threshold gain.

The dynamical stability of the polarization mode was also examined. The VCSEL was directly modulated with a NRZ 2<sup>7</sup>-1 PRBS pattern for 400 Mbps transmission. The data signal was measured at the InGaAs p-i-n photodiode, directly and through the polarizer, respectively. Figures 4 and 5 show bit error rate curves and eye diagrams in the case of receiving the total optical power and the resolved  $[233]$  polarization mode, respectively. No power penalty was observed even when the data resolved in the  $[233]$  polarization mode was received. These results indicate that (311)A-oriented VCSELs stably operate in the  $[233]$  polarization mode even under high frequency modulation.

### References

- [1] K. Iga, F. Koyama, and S. Kinoshita, IEEE J. Quantum Electron., 24 (1988) 1845.
- [2] T. Mukaiharu, N. Hayashi, N. Hatori, F. Koyama, and K. Iga, IEEE Photon. Technol. Lett., 7 (1995) 1113.
- [3] K. D. Choquette and R. E. Leibenguth, IEEE Photon. Tech. Lett., 6, (1994) 40.
- [4] T. Mukaiharu, N. Ohnoki, Y. Hayashi, F. Koyama, and K. Iga, Jpn. J. Appl. Phys., 33, (1994) L227.
- [5] T. Ohtoshi, T. Kuroda, A. Niwa, and S. Tsuji, Appl. Phys. Lett., 65 (1994) 1886.

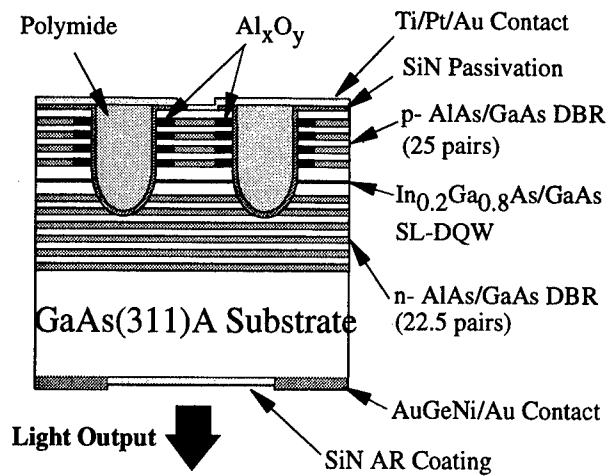


Fig. 1 Schematic of a (311)-oriented VCSEL.

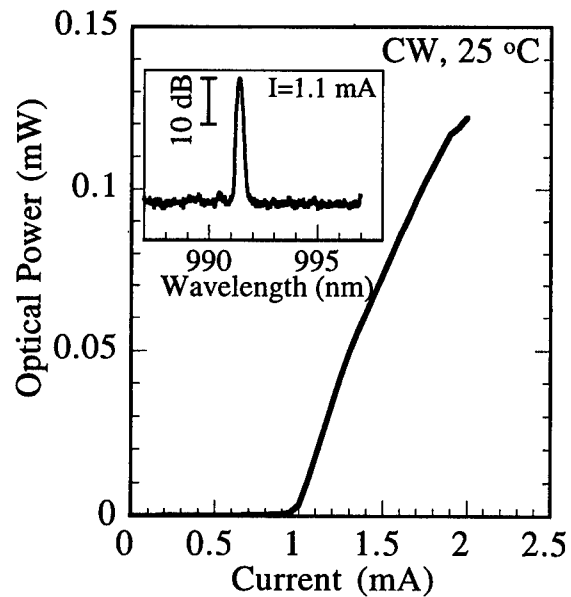


Fig. 2 L-I characteristic and lasing spectrum.

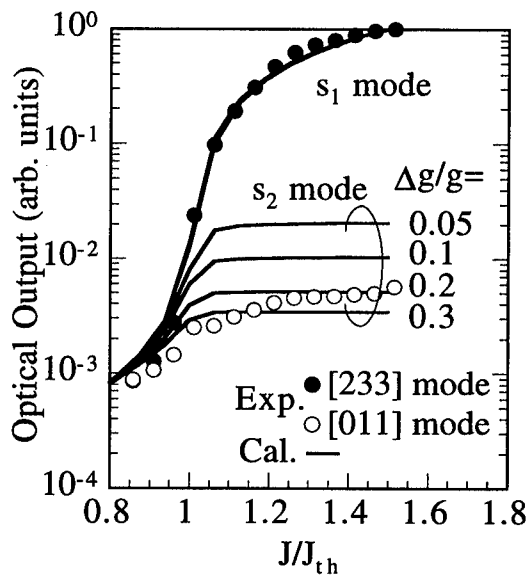


Fig. 3 L-I characteristics resolved in two orthogonal polarization modes.

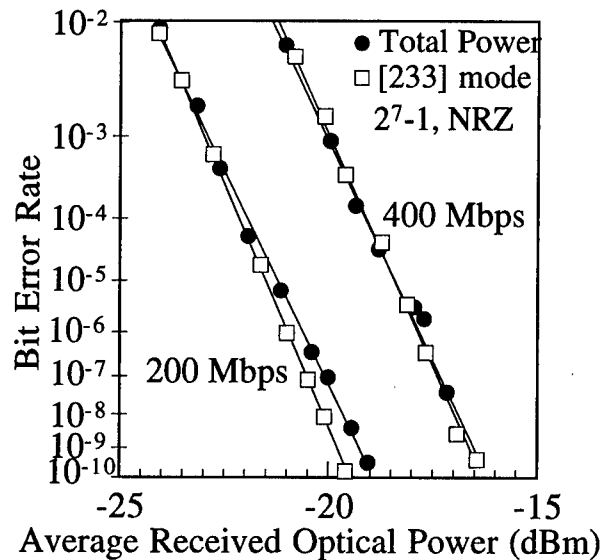
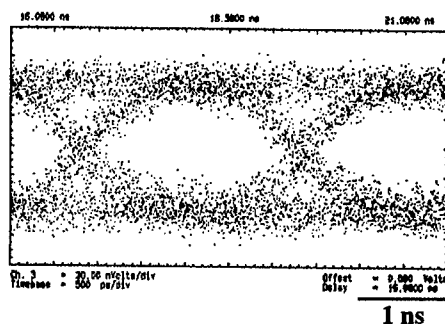
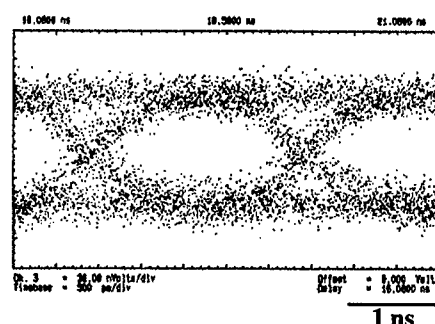


Fig. 4 Measured bit error rate for 200 Mbps and 400 Mbps transmission in receiving the total optical power and the resolved [233] polarization mode.



(a) Total optical power



(b) Resolved [233] polarization mode

Fig. 5 Eye diagram in receiving (a) the total optical power and (b) the resolved [233] polarization mode for 2<sup>7</sup>-1 PRBS at 400 Mbps.

**TuA3 (Invited)**  
**9:00am - 9:30am**

### **Multiple-Wavelength VCSEL Arrays on Patterned Substrates**

Wupen Yuen, Gabriel S. Li, Connie J. Chang-Hasnain  
EECS Department, University of California at Berkeley, Berkeley, CA 94720

Vertical-cavity surface-emitting lasers (VCSELs) are highly promising for overcoming the electronic bottleneck in local area networks and computer interconnects. The advantages of VCSELs include the surface-normal topology which facilitates integration of 1-D and 2-D arrays, the circular output beam which eases coupling of light into optical fibers, and the potential low fabrication cost due to the availability of wafer-scale processing and testing. Multiple-wavelength VCSEL (MW-VCSEL) arrays, with all the advantages of VCSELs and the extra flexibility of wavelength variation, allow various network functionalities and larger system capacities to be implemented. However, whether MW-VCSELs can become an *inexpensive* upgrade of VCSEL-based LANs and interconnects depends on the cost and performance of the transceivers. Low cost can be achieved by adopting widely spaced wavelengths which reduce the complexity of the MUX/DEMUX, and by increasing the MW-VCSEL yield. Therefore,  $\lambda$  spacing, yield and performance are the most important criteria for MW-VCSELs.

The lasing wavelength of a VCSEL is primarily determined by the effective cavity thickness which can be varied by changing the thickness of the  $\lambda$ -spacer or the DBR layers. There have been many efforts in making MW-VCSEL arrays, where different methods of varying the effective cavity thickness were explored. These methods include using the beam nonuniformity in an MBE system [1], varying the GaAs growth rate spatially by growing on a backside-patterned substrate [2], employing a nonplanar MOCVD growth technique [3], using post-growth processing [4] and shadow-masked MBE growth [5]. Among all these methods, patterned-substrate MBE growth presents a very attractive approach since only a *single* growth is necessary and wide and accurate wavelength spans can be achieved with in-situ monitoring. In this paper, we review two patterned-substrate methods. Both lead to simultaneous achievements of wide  $\lambda$  spacing, high yield and high performance. The comparison between the two methods will be discussed in the presentation.

Fig. 1 shows the schematic of the patterned-substrate growth. The basic principle of the patterned-substrate growth is to utilize the dependence of the Ga desorption rate on the surface temperature,  $T_s$ , in an MBE system. An intentionally created substrate surface temperature profile can be translated into a GaAs layer thickness profile and thereby the desired lasing wavelength variation. Using this basic principle, we in-situ calibrate the growth rates using a laser reflectometer in both high- and low- $T_s$  regions to control the wavelength span in the first method, as shown in Fig. 2(a). In the second method, we thermally desorb a GaAs  $\lambda$ -shifting layer in the high- $T_s$  region but not in the low- $T_s$  region and use a laser reflectometer to monitor the desorption process, as shown in Fig. 2(b). Fig. 3 shows the pulsed  $\lambda$  vs. position for 15 MW-VCSEL arrays grown using the first method. The lasing wavelength spans 62.7nm, which is thus far the largest for any MW laser array. High wafer reproducibility is achieved using the second method where most of the wafers have  $\lambda$  span accurate to within 1~2nm from the designed value. The uniformity of arrays is shown in Fig. 4 where nearly identical  $\lambda$  distributions are obtained for all arrays. With improved epitaxial design, threshold current as low as 450 $\mu$ A, output power as high as 8mW, and wall-plug efficiencies as high as 16% are obtained. Therefore all three criteria of MW-VCSELs are well satisfied. With these desirable properties, MW-VCSELs fabricated using these methods should have great potential in cost-effective WDM applications.

#### **References**

- [1] C. J. Chang-Hasnain et al., *IEEE J. Quantum Electron.*, vol. 27, pp. 1368-1376, 1991.
- [2] W. Yuen et al., *IEEE Photon. Technol. Lett.*, vol. 8, pp. 4-6, 1996.
- [3] F. Koyama et al., *Electron. Lett.*, vol. 30, pp. 1947-1948, 1994.
- [4] T. Wipiejewski et al., *IEEE Photon. Technol. Lett.*, vol. 7, pp. 727-729, 1995.
- [5] H. Saito et al., *Appl. Phys. Lett.*, vol. 66, pp. 2466-2468, 1995.

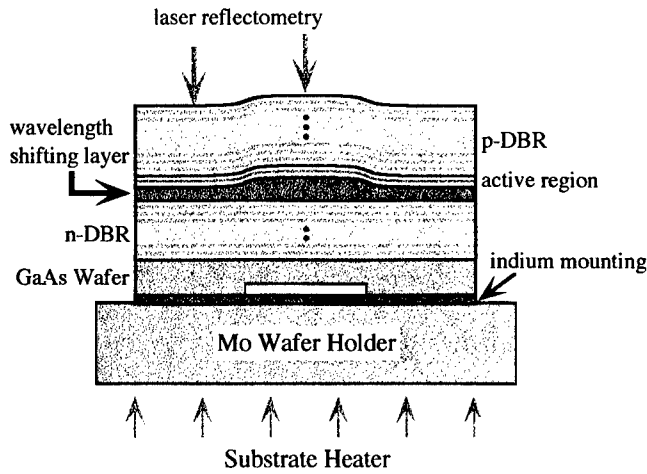


Fig. 1 Schematic of the patterned-substrate MBE growth

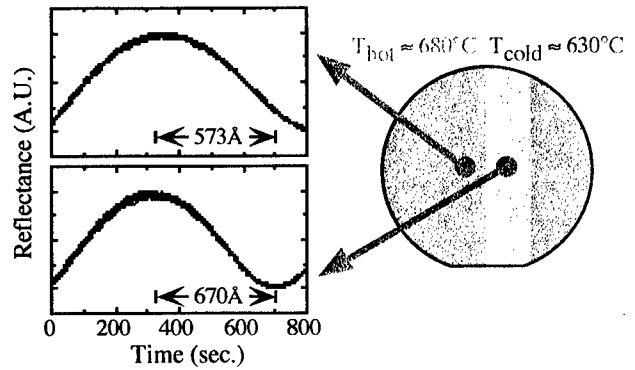


Fig. 2(a) Schematic of the patterned-substrate growth with location-resolvable in-situ pre-growth calibration.

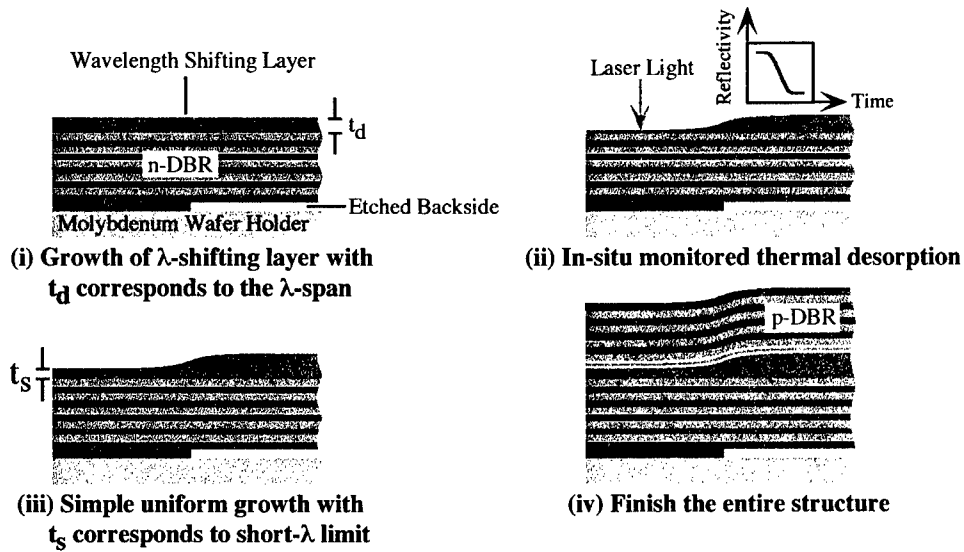


Fig. 2(b) Schematic of the patterned-substrate growth with in-situ monitored thermal redeposition.

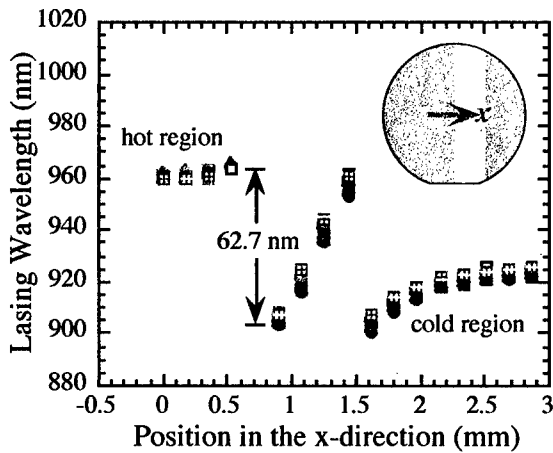


Fig. 3 Pulsed lasing wavelength of  $15 \times 16$  arrays with 62.7nm span.

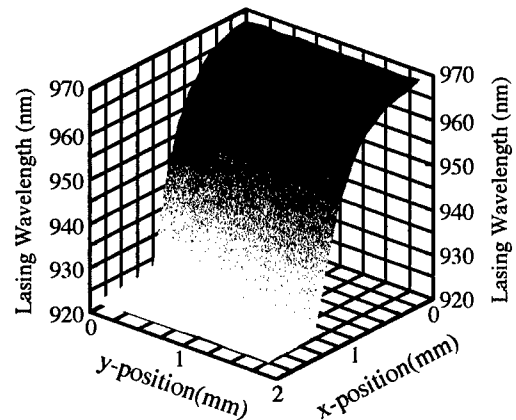


Fig. 4 Wavelength distribution of an  $11 \times 14$  2-D array.

TuA4

9:30am - 9:45am

# P-type Modulation Carbon-Doping to InGaAs/AlGaAs Quantum Wells by MOCVD Auto-doping for Surface-Emitting Lasers

N. Hatori, A. Mizutani, N. Nishiyama, F. Koyama and K. Iga

Tokyo Institute of Technology, Precision and Intelligence Laboratory,  
4259 Nagatsuta, Midoriku, Yokohama 226, Japan

InGaAs/AlGaAs quantum well (QW) vertical-cavity surface-emitting lasers (VCSELs) have been studied for optical interconnection due to their ultra low power consumption [1, 2]. In order to achieve its further reduction, modulation doped QWs [3] are attractive, and p-type and n-type modulation doped QWs lasers have been investigated. [3, 4] Especially, p-type modulation doped QW lasers have larger gain and larger differential gain than conventional undoped QW lasers, which cause lower threshold operation and higher resonant frequency. Furthermore, it has been examined that the carrier lifetime is also reduced.

In this report, we propose a novel p-type modulation doping to InGaAs/AlGaAs QWs for low threshold VCSELs, and have demonstrated the threshold reduction in edge emitting lasers employing p-type modulation doped InGaAs/AlGaAs QWs. We obtained a threshold current density of  $160\text{A/cm}^2$  for  $1 \times 10^{19}\text{cm}^{-3}$  modulation doped three QWs edge-emitting lasers.

Figure 1 schematically shows the proposed structure. The active region consists of three  $\text{In}_{0.2}\text{Ga}_{0.8}\text{As}$  QWs of  $80\text{\AA}$  thickness,

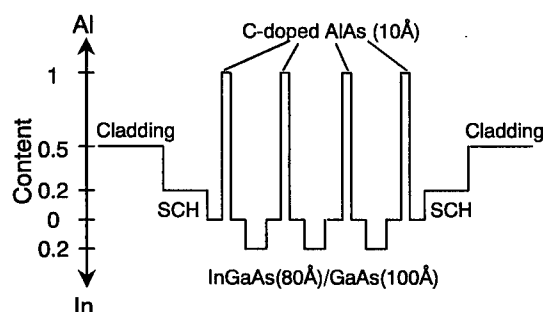


Fig. 1. A schematic band structure of active region employing p-type modulation doping AlAs layers (not a scale).

separated by GaAs barriers of  $100\text{\AA}$  thickness. The carbon-doped p-type AlAs ( $10\text{\AA}$ ) region is located only around the center of the barriers.

We grew carbon-doped AlAs layers by low-pressure metal organic chemical vapor deposition (LP-MOCVD). The growth temperature was  $700^\circ\text{C}$  and the growth pressure was 76 Torr. Trimethylaluminum (TMAI) were used as metal organic source for all the epi-layer growths, and arsine ( $\text{AsH}_3$ ) was employed as the As source. Figure 2 shows the net hole concentrations of AlAs layers grown on GaAs (100) substrates versus V/III ratio. The hole concentrations were measured by a standard capacitance-voltage (C-V) method. Hole concentration was over  $1 \times 10^{19}\text{cm}^{-3}$  at  $\text{V/III}=5$  and was controlled in the range of  $10^{16}\text{-}10^{19}\text{cm}^{-3}$ .

We fabricated edge emitting lasers using the grown wafers which have the active region as mentioned in the above and their cleaved facets are uncoated. The devices were tested at room temperature under pulsed condition. Figure 3 shows the threshold current density ( $J_{\text{th}}$ ) against the cavity length.

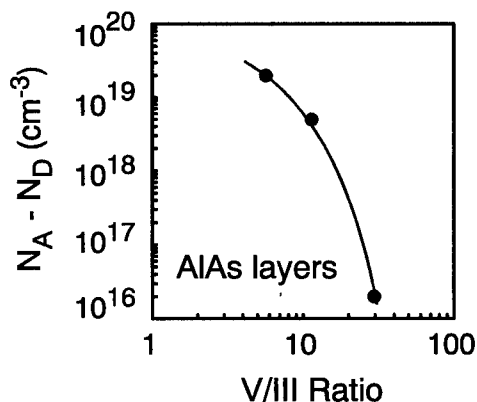


Fig. 2. The net hole concentration in AlAs layers using carbon auto doping against V/III ratio.

The minimum values of  $J_{th}$  were  $160\text{A/cm}^2$ , i.e.  $54\text{A/cm}^2$  per well. The lowest  $J_{th}$  with p-type doping decreases by 50% compared with that of the lasers without doping.

In Fig. 4, we show the calculated threshold current density of VCSELs against the impurity concentration, where we have assumed the threshold gain to be  $500\text{cm}^{-1}$ . The linear gain was calculated by using density matrix method.[5] In a p-type doped QW laser, the transparent current density is larger than that of n-type doped QW laser. However, the differential gain is larger, resulting in achieving the threshold condition earlier. In actual devices for both p-type and n-type QWs, the excess loss due to free carrier absorption should be considered.

In summary, we have proposed a novel structure of p-type modulation doped QWs using carbon auto doping method, and demonstrated carbon auto doping into AlAs layers by LP-MOCVD. We grew p-type modulation doped InGaAs/AlGaAs QWs, and fabricated edge emitting lasers using the QWs and achieved the reduction of the threshold current density for the first time. We estimated threshold current density of p-type modulation doped QW VCSEL, and showed the threshold reduction compared with undoped and n-type modulation QW VCSELs. The obtained result shows that the p-type modulation doping could improve the laser performance in terms of reduction of turn-on delay time, resulting in the possibility of future parallel optical transmission system.

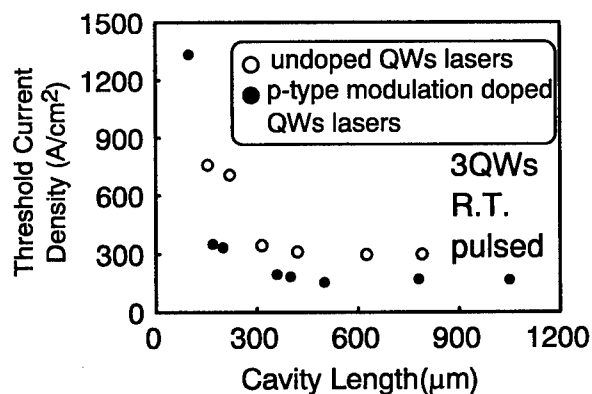


Fig. 3 Characteristics of threshold current density versus cavity length.

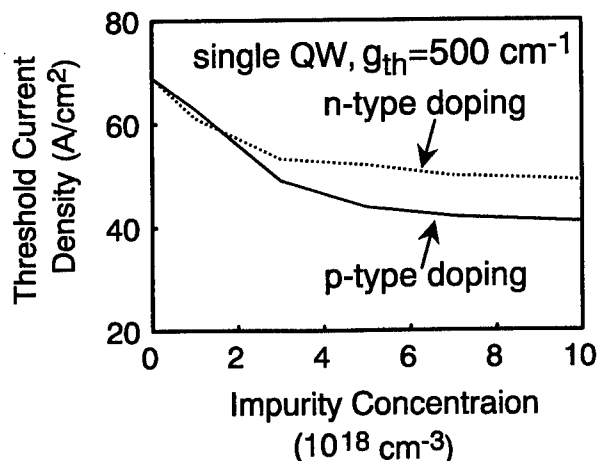


Fig. 4. Calculation of p-type and n-type modulation doped QW VCSELs.

This study was supported by Grant-in-Aid for COE Program from the Ministry of Education, Science, Sports and Culture (#07CE2003, "Ultra-parallel Optoelectronics").

#### References

- [1] Y. Hayashi *et. al.*, *Electron. Lett.*, **31**, pp. 560-562, (1995).
- [2] G. M. Yang *et al.*, Digest of CLEO '95, CPD4-1 (1995).
- [3] K. Uomi, *Jpn J. Appl. Phys.*, **29**, pp. 81-87, (1990).
- [4] N. Hatori, *et. al.*, Digest of CLEO'96, JTh5C, (1996).
- [5] M. Asada, *et. al.*, *J. Quant. Electron.*, QE-20, pp. 745-753, (1984).

TuA5

9:45am - 10:00am

*AlGaAsSb/AlAsSb Bragg Mirrors on InP for 1.3 and 1.55  $\mu\text{m}$  Vertical Cavity Surface Emitting Lasers*

Guilhem ALMUNEAU, Frédéric GENTY\*, Laurent CHUSSEAU,  
Serge GAILLARD, Nicolas BERTRU

CEM2, UMR 5507 CNRS-MEN, Université de Montpellier II,  
34095 Montpellier, France

Joel JACQUET

\*Alcatel-Alsthom-Recherche, Route de Nozay, 91460 Marcoussis, France

III-V antimonide materials are very attractive for a number of optoelectronic applications [1, 2, 3]. In particular, alloys as AlAsSb and AlGaAsSb exhibit a large index difference ( $\Delta n \approx 0.6$ ) allowing the fabrication of very high reflective Distributed Bragg Reflectors (DBR) centered at 1.3 and 1.55  $\mu\text{m}$  on InP. At these wavelengths, DBRs are usually grown lattice-matched to InP using quaternary and ternary phosphide alloys in spite of the low refractive index difference that implies a huge number of layers ( $\geq 40$  periods) [4]. To the contrary mirrors composed of arsenide-antimonide materials can reach reflectivities upper to 99% using only twenty periods in the stack.

In a first step, an index difference as large as possible was planned so a quaternary alloy containing only 4% of Aluminium has been elaborated. Corresponding gap was estimated to be 1.51  $\mu\text{m}$ . This is slightly lower than the 1.55  $\mu\text{m}$  mirror center wavelength. A measured peak reflectivity exceeding 96% at 1.6  $\mu\text{m}$  was obtained with such a DBR having 15.5 pairs whereas a 99% value has been calculated. Discrepancy between calculation and measurement occurs because of an important bandtail absorption below band gap in AlGaAsSb. This has not been considered neither in DBR design or in calculations and appears as the fundamental phenomenon limiting the DBR reflectivity. As a major conclusion more Al rate has to be incorporated in the quaternary in order to sufficiently increase its bandgap energy.

In a second step, a quaternary alloy containing about 20% of Aluminium has been elaborated. Its gap energy was measured by electroreflection (ER) and was found to be equal to 0.96 eV (1.29  $\mu\text{m}$ ) at 300 K, much higher than 0.8 eV (1.55  $\mu\text{m}$ ). Very efficient DBRs have been grown using this alloy. Thus, maximum reflectivities as high as 96%, 98.4% and 99.2% were measured around 1.55  $\mu\text{m}$  with stacks containing respectively 11.5, 15.5 and 19.5 pairs of layers. This shows that no residual absorption occurs with this Aluminium rate. Refractive indices were estimated using the Afromowitz formalism including an excitonic broadening to eliminate the singularity occurring at bandgap. Values of 3.57 for AlGaAsSb and 3.11 for AlAsSb were obtained within this framework. Measured and calculated reflectivity spectra of the 19.5 periods mirror are represented in figure 1. As seen they are in very good agreement thereby validating the refractive index model.

In a third step, mirrors based on arsenide-antimonide materials were designed to operate at 1.3  $\mu\text{m}$ . According to previous results DBR operation at 1.3  $\mu\text{m}$  requires a quaternary having a relatively high Aluminium concentration to significantly thrust the operating wavelength away from the material band-gap. The  $\text{Al}_{0.3}\text{Ga}_{0.7}\text{As}_{0.53}\text{Sb}_{0.47}$  composition was thus chosen as the high index medium,  $\text{AlAs}_{0.56}\text{Sb}_{0.44}$  being always the low index one. The quaternary gap energy was measured at 1.135 eV (1.09  $\mu\text{m}$ ) at 300 K by ER. Two structures respectively composed of 15.5 and 20.5 periods of AlGaAsSb/AlAsSb were grown. Maximum reflectivities of 97.7% and 98.8% were measured at 1.28  $\mu\text{m}$  and 1.3  $\mu\text{m}$  respectively. Measured and calculated reflectivity spectra of the 20.5 pairs device are given in figure 2. These results are demonstrated for the first time at such wavelength with the arsenide-antimonide system. Moreover strong

oscillation amplitudes in shorter wavelength reflectivity sidelobes are evident in fig. 2. It suggests that semiconductor materials grown in the stack (especially AlGaAsSb) effectively work in the transparent wavelength region down to  $\approx 1.1 \mu\text{m}$ . This validates our Al mole fraction choice for the quaternary. Within the framework of this model, the calculated reflectance spectrum well agrees with experiment. Stopband, absorption occurring at short wavelengths as well as refractive index dispersions that are responsible of long wavelength reflectance oscillations are correctly reproduced. Refractive indices were estimated at 3.6 for  $\text{Al}_{0.3}\text{Ga}_{0.7}\text{As}_{0.53}\text{Sb}_{0.47}$  and 3.15 for  $\text{AlAs}_{0.56}\text{Sb}_{0.44}$  at  $1.3 \mu\text{m}$  within our formalism framework. Furthermore the maximum reflectivity is calculated to be 99.2% at  $1.3 \mu\text{m}$  close to experiment. It induces us to believe that optical absorption is very low in the real device since calculation does not account for it. By increasing the number of layer periods beyond 22, reflectivities exceeding 99.5 % are then to be expected in agreement with the  $\Delta n=0.45$  refractive index difference between the two alloys.

In conclusion the AlGaAsSb system appears very suitable to elaborate high reflective DBRs with a low number of pairs operating at wavelengths of interest for telecommunications ( $1.3$  and  $1.55 \mu\text{m}$ ). Very high reflectivities of 99.2% at  $1.56 \mu\text{m}$  and for the first time 98.8% at  $1.3 \mu\text{m}$  have been obtained. We are now investigating this antimonide approach for fabricating monolithic VCSELs. Thus the elaboration of an active layer composed of InGaAs wells encapsulated within AlGaInAs barriers is under evaluation.

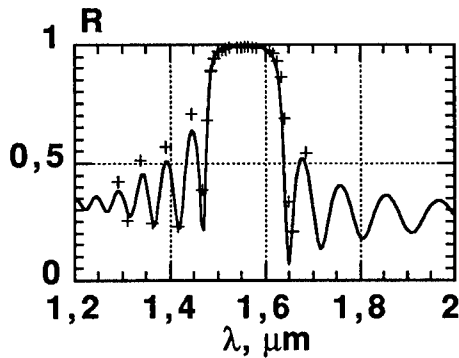


**Figure 1**

Measured (crosses) and calculated (solid line) reflectivity spectra of the 19.5 periods  $\text{Al}_{0.2}\text{Ga}_{0.8}\text{As}_{0.53}\text{Sb}_{0.47}/\text{AlAs}_{0.56}\text{Sb}_{0.44}$  DBR

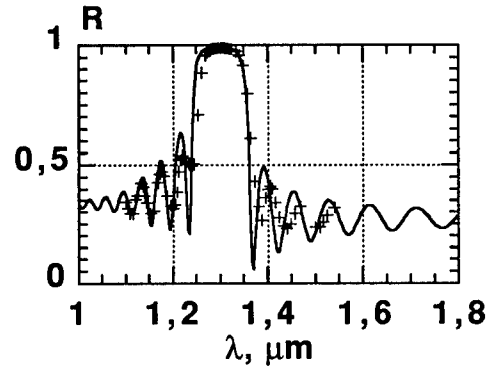


**Figure 2**

Measured (crosses) and calculated (solid line) reflectivity spectra of the 20.5 periods  $\text{Al}_{0.3}\text{Ga}_{0.7}\text{As}_{0.53}\text{Sb}_{0.47}/\text{AlAs}_{0.56}\text{Sb}_{0.44}$  DBR

- 1 B. Lambert, Y. Toudic, Y. Rouillard, M. Gauneau, M. Baudet, F. Alard, I. Valiente and J. C. Simon, *Appl. Phys. Lett.*, 66, 442 (1995)
- 2 J. C. Harmand, F. Jeannès, G. Le Roux and M. Juhel, *Electron. Lett.*, 33, 1689 (1995)
- 3 F. Genty, G. Almuneau, L. Chusseau, G. Boissier, J.-P. Malzac, P. Salet and J. Jacquet, *Electron. Lett.*, 33, 140 (1997)
- 4 P. Salet, C. Starck, A. Plais, J.-L. Lafragette, F. Gaborit, E. Derouin, F. Brillouin and J. Jacquet, *CLEO'96 (Anaheim)*, Paper CThK39, 421 (1996)



TuB1 (Invited)  
10:30am - 11:00am

## 120 °C pulsed operation from a 1.55 $\mu\text{m}$ vertical-cavity laser

### *Invited Paper*

Near Margalit, Yijen Chiu, Eric Hegblom, Patrick Abraham,  
Alexis Black, Jon Wesselmann, John E. Bowers, Evelyn L. Hu

Dept. of Electrical and Comp. Engineering  
University of California at Santa Barbara  
Santa Barbara, CA 93106

Klaus Streubel  
Royal Institute of Technology, Stockholm, Sweden

Vertical cavity lasers are potentially low cost sources for fiber optic communication. GaAs based VCLs have made great strides in performance over the last few years, but their wavelength of operation (0.6-1.1  $\mu\text{m}$ ) is not well suited for long distance, high speed fiber transmission. 1.3  $\mu\text{m}$  and 1.55  $\mu\text{m}$  sources are better matched to the loss dispersion and loss minimums of standard glass fiber. This can clearly be seen by a recent demonstration of a 200 km transmission experiment at 2.5 Gb/s using a 1.5  $\mu\text{m}$  VCL[1]. The problem with InP based VCLs, emitting at the communication wavelengths, has traditionally been their poor high temperature operation. Indeed in-plane lasers at these wavelength had suffered from similar problems, but proper design has allowed for commercial devices that operate well over the desire range of temperatures(-40°C to 85°C).

In this presentation we will focus on the design of vertical cavity lasers to achieve such high temperature operation. We have concluded that the key to such design is the reduction of round trip cavity loss. Figure 1 shows the low loss double-fused laterally oxidized structure used in our work. This structure allows for high mirror reflectivities using GaAs based mirrors reducing the necessary gain at threshold. This low loss allows for high temperature operation by reducing the necessary gain at threshold. The gain available from the InP/InGaAsP MQW at higher temperatures is greatly reduced due to Auger recombination and carrier overflow. Figure 2 shows the pulsed operation of a 20- $\mu\text{m}$  diameter device up to 120°C. Higher temperature operation was not tested due to thermo-electric cooler limitations(failure). The room temperature threshold currents of these devices were about 5 mA with a threshold voltage of 3 Volts. At 120°C the pulsed threshold currents increased by nearly a order of magnitude(40 mA), demonstrating the need for low, submilliamp, room temperature thresholds currents. Figure 3 shows the characteristic temperature of several loss mechanisms contributing to this increase in threshold. It can be inferred from this figure that Auger recombination is the dominant mechanism of increased threshold in that temperature range(10-65°C). Present devices operate cw up to 64°C where the active region temperature is much higher due to joule heating[2]. In order to achieve high temperature cw operation smaller diameter devices must be fabricated with lower threshold currents, while maintaining the low round trip loss. This high temperature pulsed result demonstrates that there is no inherent reason why VCLs should not operate cw over the -40°C to 85 °C temperature range.

### References

- [1] S. Z. Zhang, N. M. Margalit, T. E. Reynolds, and J. E. Bowers, *IEEE Photon. Technol. Lett.*, vol. 9, pp. 374-6, 1997.
- [2] N. M. Margalit, D. I. Babic, K. Streubel, R. P. Mirin, R. L. Naone, J. E. Bowers, and E. L. Hu, *Electr. Lett.*, vol. 32, pp.1675-6, 1996.

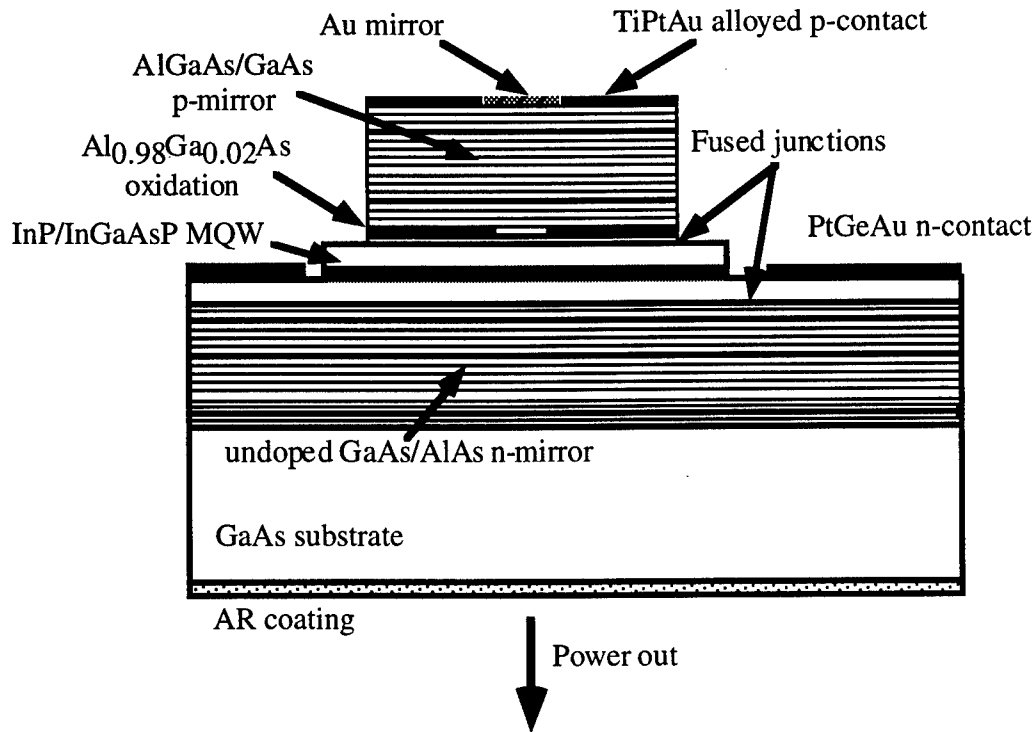


Figure 1 - Device schematic of double-fused laterally oxidized 1.55  $\mu\text{m}$  vertical-cavity laser.

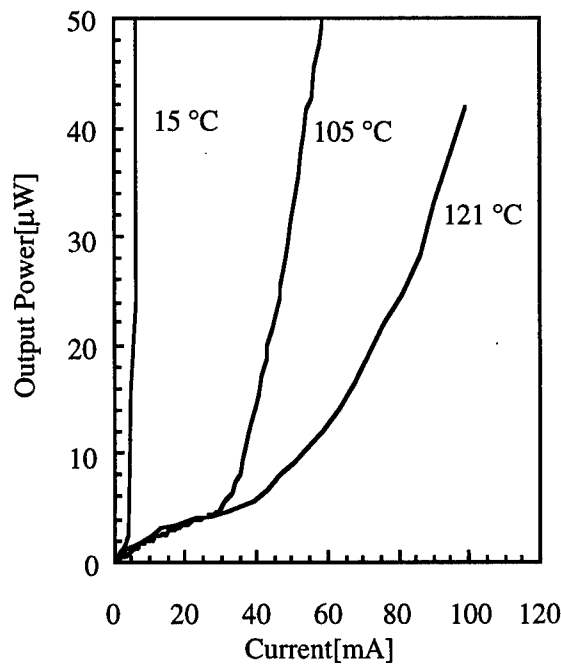


Figure 2 - Pulsed LI curves showing operation past 120°C.

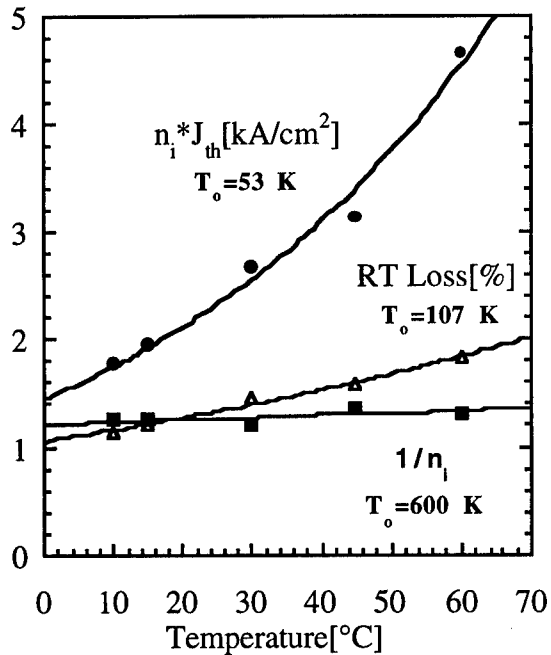


Figure 3 - Characteristic temperatures for several loss mechanisms, including gain reduction (Auger recombination), increased round trip loss, and reduced injection efficiency.

# High Performance 1.3 $\mu\text{m}$ Vertical-Cavity Surface-Emitting Lasers with Oxygen-Implanted Confinement Regions and Wafer-Bonded Mirrors

Y. Qian<sup>1</sup>, Z.H. Zhu<sup>1\*</sup>, Y.H. Lo<sup>1</sup>, D. L. Huffaker<sup>2</sup>, D. G. Deppe<sup>2</sup>, H. Q. Hou<sup>3</sup>, B.E. Hammons<sup>3</sup>, W. Lin<sup>4</sup>, and Y.K. Yu<sup>4</sup>

<sup>1</sup> School of Electrical Engineering, Cornell University, Phillips Hall, Ithaca, NY 14853

<sup>\*</sup> On leave from Zhejiang University, Hangzhou, China 310008

<sup>2</sup> Department of Semiconductor Materials, Sandia National Laboratories, Albuquerque, NM 87185

<sup>3</sup> Microelectronics Research Center, Department of Electrical and Computer Engineering, The University of Texas at Austin, Austin, TX 78712-1084

<sup>4</sup> Telecommunication Laboratories, Chunghwa Telecom Co., Taiwan

## Summary

Long wavelength (1.3  $\mu\text{m}$  and 1.55  $\mu\text{m}$ ) vertical-cavity surface-emitting lasers (VCSELs) are promising candidates for low cost, high performance light sources for optical communications and data links. We recently demonstrated a new structure for long wavelength VCSELs [1] where oxygen ions were implanted into a GaAs/AlGaAs mirror to form current confinement regions before wafer-bonding the GaAs/AlGaAs mirror with the AlGaInAs/InP cavity layers. This structure is easy to fabricate and a very low threshold current and threshold current density has been achieved for continuous-wave (cw) operation at 20°C [1]. Based on a similar design, we now obtain a record low pulsed threshold current density less than 500 A/cm<sup>2</sup> and a pulsed threshold current of 0.83 mA at 20°. The devices can operate up to 40°C under cw condition and above 100°C under pulsed condition.

Fig. 1 shows schematically the oxygen-implanted VCSELs. The devices consist of an oxygen-implanted p-GaAs/AlGaAs (28 pairs) mirror, AlGaInAs/InP strain-compensated multiple quantum well (SC-MQW) cavity layers, and a top ZnSe/MgF (6 pairs) dielectric mirror. The fabrication process is the same as in Ref. 1. The AlGaInAs SC-MQWs consist of nine 53 Å wells and ten 87 Å strain compensated barriers. Oxygen-implantation was performed to form current blocking regions in the p-GaAs/AlGaAs mirror before the p-mirror was wafer-bonded to the p-InP spacer of the cavity layers. After removal of the InP substrate and the InGaAs etch stop layer, metal ohmic contacts were made and then the ZnSe/MgF dielectric top mirror was formed by E-beam evaporation and lift-off process.

The devices were tested on a copper stage without heat sink. The output light was collected from the top dielectric mirror. Fig. 2 shows the dependence of threshold current density on device dimension under pulsed operation at 20°C. The lowest threshold current density of 454 A/cm<sup>2</sup> was detected on a 41  $\mu\text{m}$  diameter device, which is the best result for long wavelength VCSELs. The lowest threshold current is 0.83 mA measured from a 5  $\mu\text{m}$  diameter device, which is the smallest size in our design. As a comparison, in a similar structure but using proton-implantation through the quantum wells into the p-GaAs/AlGaAs bottom mirror, the lowest pulsed threshold current (2 mA) was found on a 15  $\mu\text{m}$  diameter device [2]. This indicates that oxygen-implantation gives rise to lower optical loss so works better for smaller devices. However, the thermal effect prevents the 5  $\mu\text{m}$  device from cw operation at room temperature, and the lowest room temperature cw threshold current of 1 mA was realized on a 9  $\mu\text{m}$  diameter device [1]. The devices also achieved excellent temperature characteristics as shown in Fig.3. The devices can operate up to 110°C under pulsed condition. It is noteworthy that the variation of the threshold currents from 15°C to 60° is smaller than 1 mA. However, junction heating has limited the maximum cw operation temperature to 40°C. With a reduced threshold voltage and resistance in the GaAs/AlGaAs mirror and a better alignment between the cavity mode and the quantum well gain peak, cw operation at a much higher temperature should be achievable.

[1] Y. Qian, Z.H. Zhu, Y.H. Lo, H.Q. Hou, B.E. Hammons, D.L. Huffaker, D.G. Deppe, W. Lin, and Y.K. Tu, Conference Digest of OFC'97, Postdeadline Paper, PD-14, Dallas, February 1997.

[2] Y. Qian, Z.H. Zhu, Y.H. Lo, D.L. Huffaker, D.G. Deppe, H.Q. Hou, B.E. Hammons, W. Lin, and Y.K. Tu, IEEE Photon. Tech. Lett. (to be published).

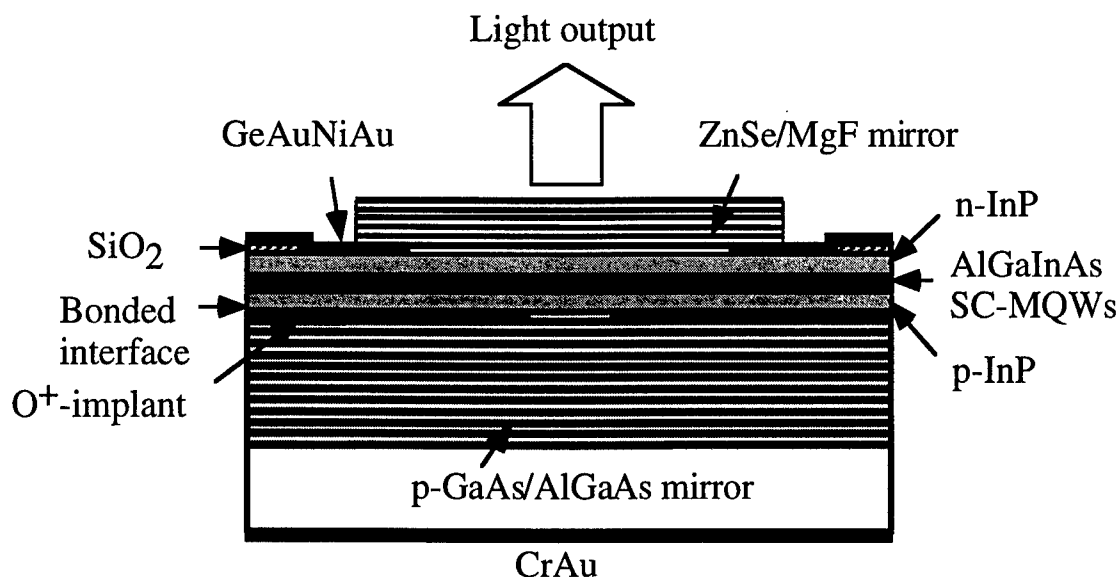


Fig. 1. Schematic cross-section of a single-bonded VCSEL with oxygen-implanted current confinement. The oxygen implantation was performed directly in the p-GaAs/AlGaAs mirror before wafer bonding.

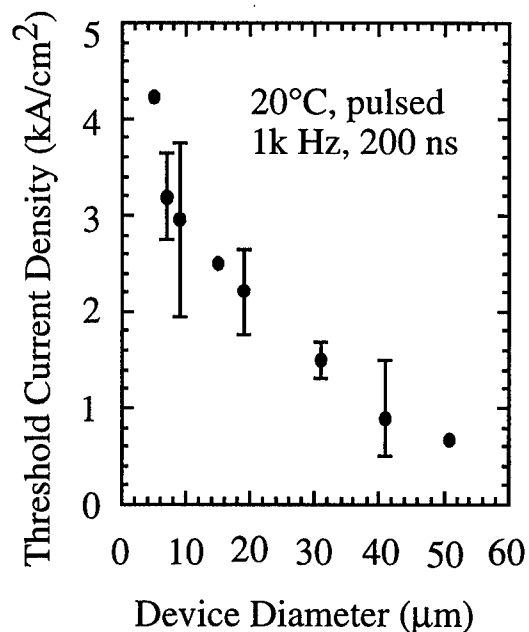


Fig. 2. Device diameter dependence of pulsed threshold current density at room temperature. The lowest threshold current density is  $454 \text{ A}/\text{cm}^2$  on a  $41 \mu\text{m}$  diameter device.

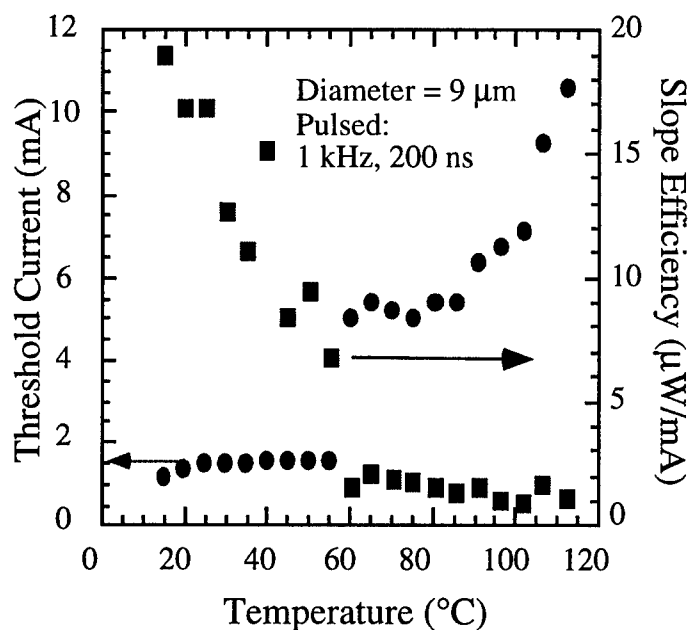


Fig. 3. Temperature dependence of pulsed threshold current and slope efficiency of a  $9 \mu\text{m}$  diameter device. The device can operate above  $100^{\circ}\text{C}$ .

**TuB3 (Invited)**  
**11:15am - 11:45am**

## **Long wavelength VCSELs with Monolithic Integrated GaInAsP/InP mirror**

Klaus Streubel

Department of Electronics, Royal Institute of Technology,  
Electrum 229, S-164 41 Kista, Sweden

Vertical cavity surface emitting lasers (VCSELs) are of potential importance in fiber communication and optical interconnects because of their single longitudinal operation, high fiber coupling efficiency and large lateral packing densities. The vertical laser cavity is formed by an active region incorporated between two multi-layer Bragg reflector stacks. To provide a sufficiently high optical gain the devices require two highly reflective DBRs which are made up of alternative layers of high and low refractive index material. The mirror reflectivity as well as the reflection bandwidth are dependent on the refractive index difference between the layers and the number of periods used. Using DBRs fabricated from III-V lattice matched materials allows the monolithic integration of the mirrors with the active region, hence simplifying processing and device design. Electrically conductive p- or n-doped mirrors allow current injection right through the mirrors providing laterally homogeneous current distribution across the active region. Furthermore buried VCSEL structures can be realized using epitaxial regrowth around all-semiconductor mesas improving the electrical and optical confinement in the lasers as well as the dissipation of excessive heat.

Available non-absorbing material combinations lattice matched to InP substrates are GaInAsP/InP and AlGaInAs/InP which both offer an index contrast of about 0.3 at 1.55 $\mu$ m wavelength. Reflector stacks of 40-50 layer pairs give a peak reflectivity above 99% and a reflection bandwidth of about 100nm. However, the reflectivity of a planar mirror in a laterally structured VCSEL cavity is significantly reduced by diffraction loss<sup>1</sup>, which together with the extreme device height has inhibited the fabrication of VCSEL with two lattice matched DBRs. Consequently one of the DBRs, preferably the p-side mirror, has to be replaced by either a dielectric or a GaAs/Al(Ga)As mirror. Dielectric mirrors offer a very high index contrast, but are electrical and thermally isolating. The combination of AlAs and GaAs is very suitable for Bragg reflectors due to their high index contrast and thermal conductivity as well as the possibility of forming oxidized Al-oxide apertures inside the cavity. Al(Ga)As/GaAs mirrors are either wafer-fused<sup>2,3,4,5</sup> or deposited by metamorphic growth. Cw operation up to 63°C and sub-miliampere threshold at room temperature have been demonstrated with 1.55 $\mu$ m VCSELs employing two GaAs-based mirrors wafer fused to a GaInAsP-quantum well active region. However, the impact of the GaAs/InP interface on the device reliability as well as suitability of double-fusion for a wafer scale production process are still open questions.

A promising VCSEL structure for 1.55 $\mu$ m operation is a monolithic GaInAsP/InP structure for n-side mirror and active layer together with a dielectric p-side DBR. The conductive mirror helps to flatten the carrier profile and to dissipate the generated heat. Mesas can be etched either above or through the active region for electrical and optical confinement. The first VCSEL with a monolithic GaInAsP/InP mirror operated pulsed at 77K with a threshold current of 120mA<sup>6</sup>. With the maturing epitaxial techniques such as MOVPE or MBE, high quality GaInAsP/InP DBRs became available<sup>7,8,9</sup> and were applied for the fabrication of 1.55 $\mu$ m VCSELs<sup>10,11,12,13,14</sup>. Electrically pulsed operation up to 40°C and a threshold current of 30mA corresponding to a threshold current density of 13kA/cm<sup>2</sup> at RT was demonstrated with

a VCSEL that employed a 50 period DBR together with a strain-compensated quantum well active region and a Si/SiO<sub>2</sub> top reflector<sup>15</sup>. The same laser operated cw up to -20°C. CW-operation at RT was achieved by Ohiso et. al.<sup>16</sup> by incorporating 9 compressively strained quantum wells between two 10 and 7 period GaInAsP/InP mirrors. The structure was completed by a wafer fused AlAs/GaAs DBR and an 15 period TiO<sub>2</sub>/SiO<sub>2</sub> mirror on the n- and p-side respectively. Those lasers exhibited a threshold current of 8.8mA and a threshold current density of 1.6kA/cm<sup>2</sup> at RT. Babic et. al.<sup>17</sup> reported on an optically pumped 1.55µm VCSEL that employed a wafer fused AlAs/GaAs DBR on top of a monolithic GaInAsP/InP structure. Such an all-epitaxial structure with two conductive mirrors could be an attractive alternative to devices with dielectric DBR and is investigated by several groups in Europe<sup>18</sup>.

The potential of 1.55µm VCSELs with a monolithically integrated GaInAsP/InP DBR has not been fully exploited yet. Considerable improvements are expected from an efficient electrical confinement using a selectively underetched contact layer<sup>19</sup> or a selectively oxidized AlInAs-layer<sup>20</sup> within the p-cladding region. Semi-insulating regrowth around tall etched mesas<sup>21</sup> will help to increase the thermal conductivity of the structure as well as to reduce the large diffraction losses in the GaInAsP/InP mirror.

## Acknowledgement

The financial support of the European ACTS/VERTICAL program is acknowledged

## References

- <sup>1</sup> D.I.Babic, S.W.Corzine, IEEE J. Quantum Electron., 28 (1992) 514
- <sup>2</sup> Z.L.Liau and D.E.Mull, Appl. Phys. Lett. 56 (1990) 737
- <sup>3</sup> Y.H.Lo, R.Bhat, D.M.Hwang, M.A.Koza and T.P.Lee, Appl.Phys.Lett. 62 (1991) 1961
- <sup>4</sup> J.J.Dudley, M.Ishikawa, D.I.Babic, R.Mirin, W.B.Jiang, J.E.Bowers, E.L.Hu, Appl. Phys. Lett. 61 (1992) 3095
- <sup>5</sup> N.M.Margalit, D.I.Babic, K.Streubel, R.P.Mirin, R.L.Naone, J.E.Bowers, E.L.Hu, Electr. Lett. (1996)
- <sup>6</sup> A.Chailertvanitkul, K.Iga and K.Moriki, Electron. Lett. 21 (1985) 303
- <sup>7</sup> F.S.Choa, K.Tai, W.T.Tsang, S.N.G.Chu, Appl. Phys. Lett., 59 (1991) 2820
- <sup>8</sup> K.Streubel, J.Wallin, L.Zhu, G.Landgren and I.Queisser, Mat. Sci. Eng. B28 (1994) 285
- <sup>9</sup> Y.Imajo, A.Kauskawa, S.Kashiwa, H.Okamoto, Jap. J. Appl. Phys., 29 (1990) L1130
- <sup>10</sup> K.Tai, F.S.Choa, W.T.Tsang, S.N.G.Chu, J.D.Wynn and A.M.Sergent, Electron. Lett. 27 (1991) 1540
- <sup>11</sup> R.Tadokoro, H.Okamoto, Y.Komama, T.Kawakami and T.Kurokawa, IEEE Photon. Techn. Lett. 4 (1992) 409
- <sup>12</sup> M.A.Fischer, A.J.Dann, D.A.O.Davies, D.J.Elton, M.J.Harlow, C.B.Hatch, S.D.Perrin, J.Reed, I.Reid and M.J.Adams, Electron. Lett. 29 (1993) 1548
- <sup>13</sup> K.Streubel, J.André, J.Wallin and G.Landgren, J. Mat. Sci. Eng. B28 (1994) 289
- <sup>14</sup> M.A.Fisher, Y.-Z.Huang, A.J.Dann, D.J.Elton, M.J.Harlow, S.D.Perrin, J.Reed, I.Reid and M.J.Adams, IEEE Photon. Tech. Lett. 7 (1995) 608
- <sup>15</sup> K.Streubel, S.Rapp, J.André, J.Wallin, IEEE Photon.Tech.Lett, 8 (1996) 1121
- <sup>16</sup> Y.Ohiso, C.Amano, Y.Itoh, K.Tateno, T.Tadokoro, H.Takenouchi, T.Kurokawa, Electron. Lett., 32 (1996) 1483
- <sup>17</sup> D.I.Babic, J.J.Dudley, K.Streubel, R.P.Mirin, E.L.Hu, J.E.Bowers, Electron. Lett., 30 (1994) 704
- <sup>18</sup> European ACTS program 'Vertical cavity laser Technology for InterConnection and Access Links' (VERTICAL)
- <sup>19</sup> J.J.Dudley, D.I.Babic, R.Mirin, L.Yang, B.I.Miller, R.J.Ram, T.Reynolds, E.L.Hu and J.E.Bowers, Appl. Phys. Lett. 64 (1994) 1463
- <sup>20</sup> S.J.Caracci, M.R.Krames, N.Holonyak Jr., N.J.Ludowise and A.Fischer-Colbrie, J. Appl. Phys. 75 (1994) 2706
- <sup>21</sup> S.Lourdudos, K.Streubel, J.Wallin, J.André, O.Kjebon and G.Landgren, IPRM'94, Santa Barbara, USA, (1994) paper ThF5

**TuB4**

**11:45am - 12:00noon**

**Metamorphic GaAs/AlAs Bragg mirrors deposited on InP for  
1,3/1,55 $\mu$ m vertical cavity lasers**

L.Goldstein, C.Fortin, P.Salet, A.Plais, J.Jacquet, A.Rocher\*, C.Poussou\*

Alcatel Alsthom Recherche

Route de Nozay 91460, Marcoussis, France

\*Centre d'Elaboration des Matériaux et d'Etudes Structurales (CEMES/CNRS)

BP 4347, 31055 Toulouse CEDEX, France

Long wavelength (1,3/1,5 $\mu$ m) Vertical Cavity Surface Emitting Laser (VCSEL) with Bragg mirror (GaAs/AlAs) wafer fused on InP substrate exhibits low threshold current and cw operation at room temperature (1, 2). However the wafer fusion technique requires additional substrate, epitaxy and technological steps. Furthermore the wafer fusion is difficult to achieve on a full 2 inches substrate. A new approach is proposed which consists in the metamorphic growth of GaAs/AlAs Bragg mirrors on InP by Gas Source Molecular Beam Epitaxy. The dislocations which are associated to the metamorphic growth process have low influence on refractive index and conductivity. So, it is expected that high quality Bragg mirror can be obtained even with layers having large mismatch differences with the substrate. However it is very important to prevent propagation's of dislocations from the Bragg structure to InP to avoid non radiative recombinaison into the active layer.

The growth sequence consists in the deposition on 2 inches substrate of the active layer ( $\lambda=1,3\mu\text{m}$ ) bulk material, InP (p) (0,3 $\mu\text{m}$ ), and 29,5 pairs of GaAs/Ga<sub>0,1</sub>Al<sub>0,9</sub>As layers. The substrate temperature is fixed at 450°C during the deposition of the metamorphic layers. This procedure results in smooth surface of the Bragg structure.

The double diffraction spectra exhibits relatively narrow linewidth of 350". Both p and n type Bragg mirror have been grown on InP. I-V curves show ohmic behaviour between InP(n)/GaAs(n). As shown on a InP(n)/InP(p)/GaAs(p) diode homojunction (figure 1), the transition between InP(p) and GaAs(p) do not introduce additional voltage as observed in the wafer fusion process. The reflectivity spectra for the Bragg structure designed at 1,3 $\mu\text{m}$  shows very high reflectivity in excess of 99,7% (Figure 2). The photoluminescence intensity has been determined from the back side

of the substrate. No degradation of the photoluminescence intensity has been observed. This demonstrates that the dislocations of the mirror do not propagate into the InP and active layer. This observation has been confirmed by Transmission Electron Microscopy experiments. In conclusion we have demonstrated that metamorphic growth structure is particularly well adapted to the realization of top Bragg mirror for long wavelength VCSEL's.

This work has been done within the frame work of VERTICAL (ACTS European program)

**References:**

- (1) D.I.Babic, K.Streubel, R.P.Mirin, N.M.Margalit, J.E.Bowers, E.L.Hu, D.E.Mars, L.Yang, K.Carey, IEEE Photonics Technology Letters, Vol 7, N°11 Nov 1995
- (2) N.M.Margalit, D.I.Babic, K.Streubel, R.P.Mirin, J.E. Bowers, E.L.Hu

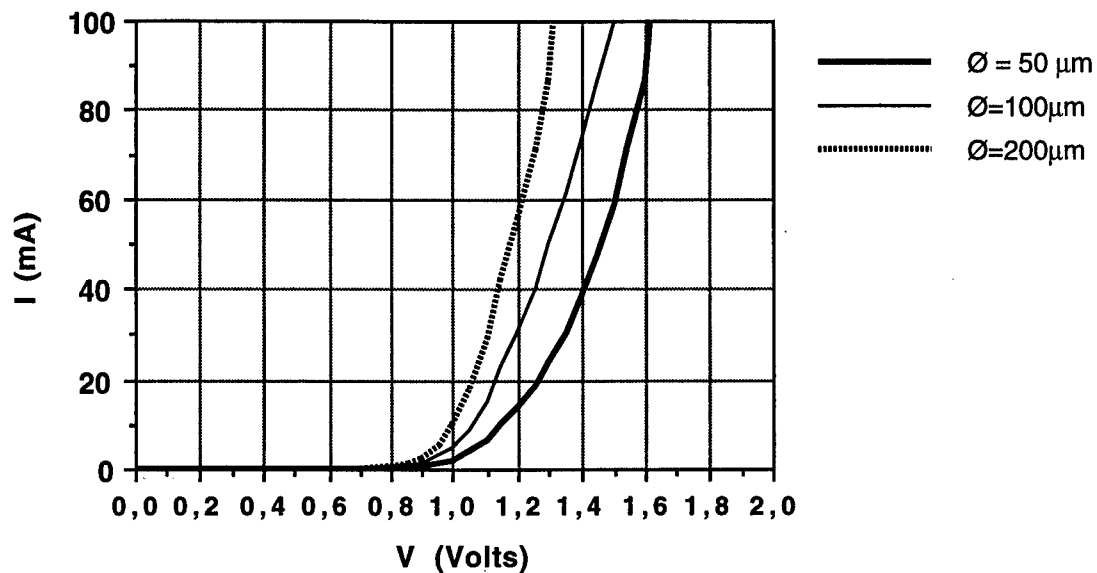


Figure 1: I-V characteristics of InP(n)/InP(p) homojunction with a top GaAs (p) layer.

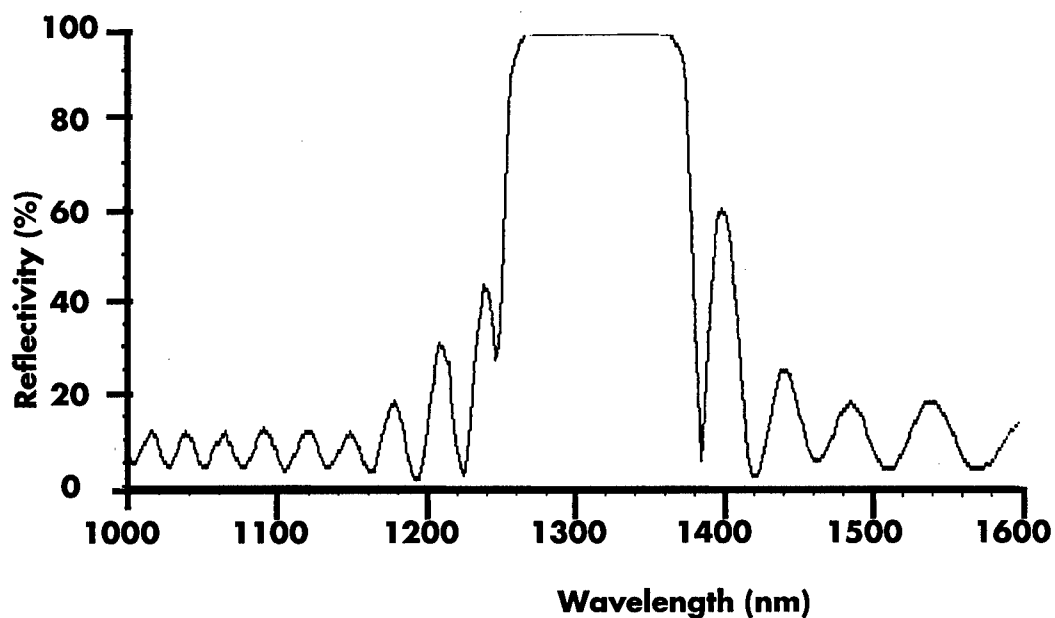


Figure 2: Reflectivity of a metamorphic GaAs/AlAs Bragg mirror



## **VERTICAL-CAVITY LASERS**

**Wednesday, 13 August 1997**

### **Sessions:**

- WA:    *High Speed Devices and Data Links***
- WB:    *Structures and Analysis***
- WC:    *Single Mode Applications and  
          Characterization***



WA1 (Invited)  
8:30am - 9:00am

### High-Speed Vertical Cavity Surface Emitting Lasers

K. L. Lear, M. Ochiai, V. M. Hietala, H. Q. Hou,  
B. E. Hammons, J. J. Banas, and J. A. Nevers

Sandia National Laboratories  
MS 0603 / PO Box 5800 / Albuquerque, NM 87185-0603  
E-mail: kllear@sandia.gov

We have previously demonstrated record modulation bandwidths for oxide-confined vertical cavity surface emitting lasers (VCSELs) based on strained InGaAs/GaAs quantum wells[1]. The monolithic oxide-confined structure[2] provides good optical confinement, low thresholds, efficient operation, and acceptable thermal resistance; these qualities promote high speed operation. Here we report work on nominally 850 nm wavelength oxide-confined VCSELs with modulation bandwidths in excess of 20 GHz.

High modulation bandwidths were achieved with an oxide confined VCSEL structure modified to decrease parasitic circuit elements. Figure 1 shows a schematic cross section of the VCSEL with a corresponding small signal equivalent circuit. Coplanar waveguide pads designed for on wafer probing were placed on a 5  $\mu\text{m}$  thick polyimide to reduce the capacitance between the pad and the conducting substrate to approximately 50 fF. The device capacitance was further reduced by implanting the mesa area lying outside the active region. This was necessary due to the high capacitance of the thin oxide layer. The non-radiative recombination associated with the deep implant damage may also reduce the charge storage associated with diffusion underneath the oxide region. Finally, the sheet resistance of the upper mirror layer was reduced to  $\sim 30\Omega/\text{square}$  by making it n-type instead of the conventional p-up structure.

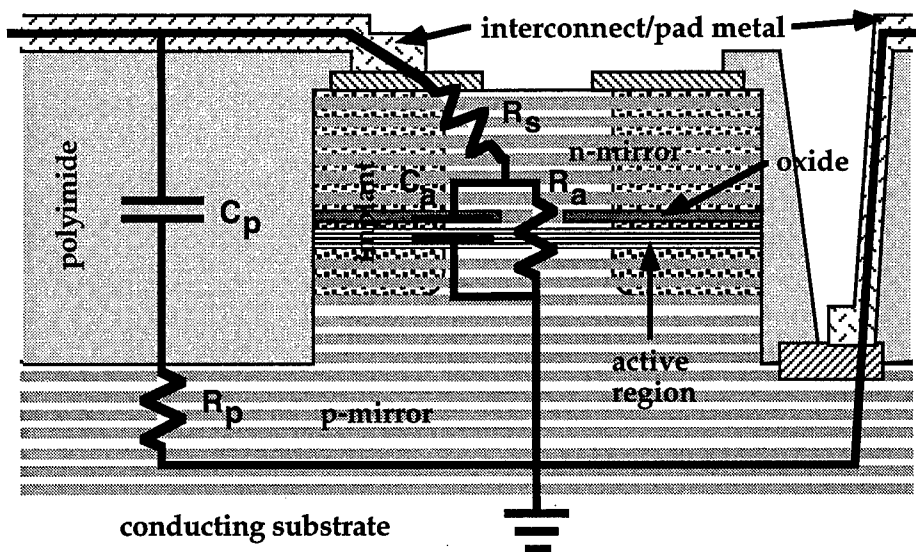


Figure 1. Schematic cross section of high speed VCSEL structure with superposed equivalent circuit.

The small signal response of VCSELs as a function of bias current was measured using a calibrated vector network analyzer with on wafer probing and a 30 GHz photodetector connected through approximately 2 m of the multimode fiber. Figure 2 shows the response of a single mode,  $\sim 4 \times 4 \mu\text{m}^2$  laser with a 0.5 mA threshold current. The modulation response at various bias currents was fit with a traditional damped resonator model to extract the resonant frequency and equivalent damping frequency ( $\gamma/2\pi$ ). These quantities for plotted in Figure 3 along with the -3dB

bandwidth. At low bias currents, the bandwidth and resonant frequency increase in proportion to the square root of the current above threshold as expected from the conventional rate equation analysis. The rate of increase in this region yields a modulation current efficiency factor (MCEF) of 14.2 GHz/ $\sqrt{\text{mA}}$  which is slightly lower than the highest value we previously reported for oxide confined VCSELs with InGaAs quantum wells[1]. The resonant frequency increases steadily to 15 GHz at 2.7 mA and then becomes nearly constant. The -3dB bandwidth is as high as 21.5 GHz.

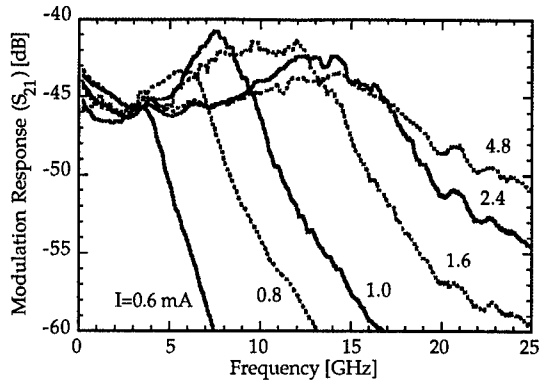


Figure 2. Frequency response of a VCSEL coupled to a high speed detector for various laser bias currents.

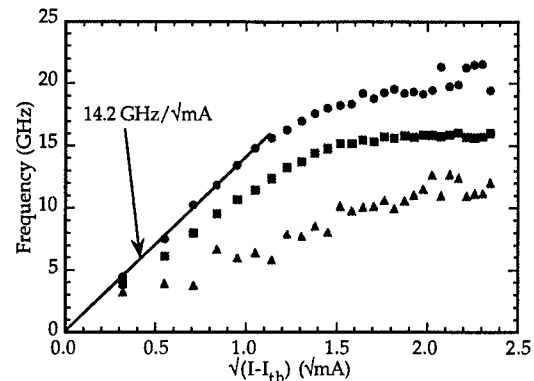


Figure 3. Resonance frequency (squares), -3dB frequency (circles), and equivalent damping frequency( $\gamma/2\pi$ ) (triangles) as a function of square root of current above threshold.

Large signal, digital modulation experiments were also performed. Figure 4a shows the eye diagram during a 6 Gb/s test using  $\sim 8 \times 8 \mu\text{m}^2$  multimode lasers with both drive levels above threshold. Bit error rates as low as  $10^{-13}$  were observed in preliminary investigations at a data rate of 12Gb/s. Reducing the "0" level slightly below threshold resulted in substantial, pattern dependent jitter as seen in Figure 4b. Results for turn on delay, jitter, and other pulsed excitation experiments now in progress will be presented.

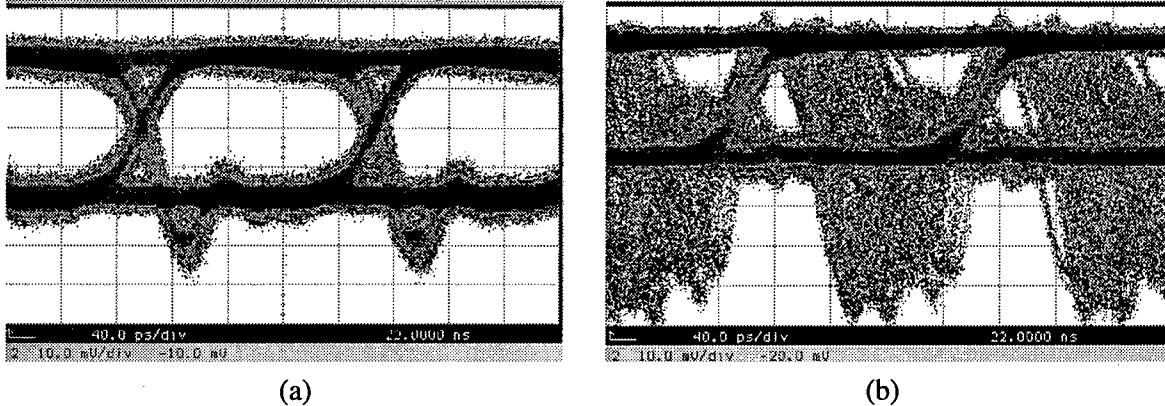


Figure 4. Eye diagrams generated by 6 Gb/s digital modulation of a multimode VCSEL at bias currents of (a) 7 mA and (b) 4 mA. In the latter case, the low drive level falls below threshold.

This work was supported by the United States Department of Energy under Contract DE-AC04-94AL85000. Sandia is a multiprogram laboratory operated by Sandia Corporation, a Lockheed Martin Company, for the United States Department of Energy.

[1] K. L. Lear et al., *Electron. Lett.* **32**(5), 457 (1996).

[2] K. D. Choquette et al., *Photon. Tech. Lett.*, **7**(11), 1237 (1995).

## Turn-on Jitter in Zero-Biased Single-Mode Vertical Cavity Surface Emitting Lasers

T. Czogalla and K. Petermann  
Technical University of Berlin,  
Fachgebiet Hochfrequenztechnik  
HFT 4, Einsteinufer 25  
10587 Berlin, Germany

### Abstract

An analytical expression and experimental results for the turn-on delay probability density function (PDF) of single mode vertical cavity surface emitting lasers (SM-VCSELs) are presented.

### Introduction

It is of great interest to operate VCSELs in optical interconnects with zero-bias since the laser driving circuit is simplified and power consumption can be reduced.

As a disadvantage this kind of operation increases the bit-error rate (BER) at gigabit data rates which is due to bit pattern effects and turn-on-jitter [1].

This paper deals with the turn-on-jitter due to fluctuations of the photon number at the laser bias point.

### Theory

An analytical expression to describe the probability density function (PDF) for the turn-on delay for a single-mode edge emitting laser was given in [2].

In contrast to the single TE-polarization state in edge emitting lasers usually two orthogonal polarizations contribute to the emitted light of SM-VCSELs. The PDF for the turn-on delay of a transversal single mode VCSEL with two orthogonal polarizations can be derived in a similar way as shown in [2].

In Fig. 1 a turn-on event is shown, where at  $t=0$

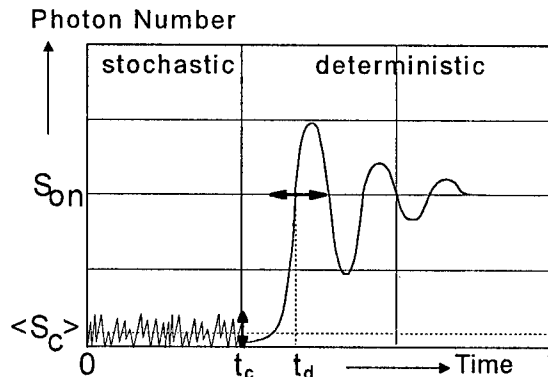


Fig.1: Turn-on event [2]

the laser drive current is switched from  $I_{off}$  below the threshold current  $I_{th}$  to  $I_{on}$  above threshold.

At the crossing time  $t_c$ , the carrier density in the active layer of the VCSEL reaches the threshold carrier density  $n_{th}$ . The crossing time  $t_c$  depends only on the ratio  $I_{on} / I_{off}$  and is therefore known.

The time  $t_{on}$  during which the photon number grows from the laser threshold ( $S_c$ ) to the "on"-state ( $S_{on}$ ) is given by [3]

$$t_{on} = \frac{1}{2\pi \cdot f_r} \sqrt{2 \cdot \ln\left(\frac{S_{on}}{S_c}\right)} \quad (1)$$

where  $f_r$  denotes the relaxation resonance frequency. Obviously  $t_{on}$  fluctuates with fluctuations of  $S_c$  leading to the turn-on-jitter.

In order to evaluate the turn-on-jitter, the dynamics of the photon number  $S(t)$  is divided into a stochastic ( $t < t_c$ ) and a deterministic region ( $t > t_c$ ). In the statistic region the photon number exhibits very strong fluctuations, since the spontaneous emission is dominant. The PDF of the photon number in each polarization  $i = 1, 2$  of the TSM-VCSEL is given by

$$p(S_{c,i}) = \frac{1}{\langle S_{c,i} \rangle} \cdot \exp\left(-\frac{S_{c,i}}{\langle S_{c,i} \rangle}\right), \quad i = 1, 2 \quad (2)$$

At the crossing time  $t_c$ ,  $S_{c,i}$  and  $\langle S_{c,i} \rangle$  denote the photon number and its mean value in the considered polarizations.

In the case of the SM-VCSEL both polarizations contribute to the total photon number  $S_c = S_{c,1} + S_{c,2}$  and its mean value  $\langle S_c \rangle = \langle S_{c,1} \rangle + \langle S_{c,2} \rangle$ . The PDF of  $S_c$  is given by the convolution of the PDFs of both polarizations yielding

$$p(S_c) = 4 \frac{S_c}{\langle S_c \rangle^2} \cdot e^{-\frac{2S_c}{\langle S_c \rangle}} \quad (3)$$

where  $\langle S_{c,1} \rangle = \langle S_{c,2} \rangle = \langle S_c \rangle / 2$  was assumed. In the deterministic region  $t_{on}$  is given by eq. 1 for a known  $S_c$ .

The PDF for the photon number  $S_c$  can be transformed into a PDF for the turn-on delay using the relation  $p(t_{on}) dt = p(S_c) dS_c$  yielding

$$p(t_{on}) = 4\omega_r^2 t_{on} \frac{S_{on}^2}{\langle S_c \rangle^2} \times \exp\left[-(\omega_r t_{on})^2\right] \exp\left[\frac{2S_{on}}{\langle S_c \rangle} \exp\left[-\frac{(\omega_r t_{on})^2}{2}\right]\right] \quad (4)$$

where  $\omega_r = 2\pi f_r$ . The turn-on-jitter is given by the standard deviation of eq. (4).

### Measurements

In order to examine eq. (4), some jitter measurements were carried out.

A proton implanted VCSEL with  $I_{th} = 1.3$  mA, an operating wavelength of  $\lambda = 870$  nm, an active diameter of  $10\mu\text{m}$  and an aperture diameter of  $6\mu\text{m}$  was used in the experimental setup. It was driven with square pulses, delivered by a pulse generator with a risetime of  $<100$  ps and a jitter of  $<2.5$  ps. By choosing different pulse amplitudes while keeping the zero-bias condition, the relaxation resonance frequency could be varied. The output light of the VCSEL was collimated and focused onto an avalanche photo diode whose electric signal was monitored with a sampling oscilloscope.

The relaxation resonance frequency was evaluated from the time interval between two successive peaks of the relaxation oscillation in the "on"-state.

The probability distribution of the turn-on delay was recorded using the horizontal histogram function of the sampling oscilloscope. The turn-on jitter was then calculated while the jitter of the pulse generator was taken into account.

### Measurement Results and Conclusion

A good qualitative agreement between the measured and the theoretical PDF (4) can be seen in Fig. 2.

Neglecting one of the polarizations would lead to a significant disagreement between the theoretical and the measured PDF, which can also be seen in Fig. 2 showing the best fit of experimental data with the previous theory [2].

The measured rms turn-on jitter versus relaxation resonance frequency is presented in Fig. 3. The turn-on-jitter decreases with increasing  $f_r$ .

As can be seen in Fig. 3 the average photon number  $\langle S_c \rangle$  decreases with increasing pulse amplitude. This effect is not quite clear yet, but at least to some extent can be explained theoretically from the laser rate equations.

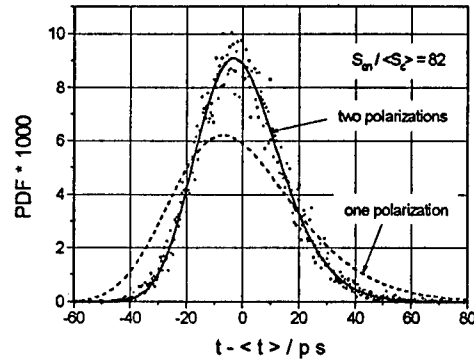


Fig. 2: PDF of the turn-on delay for  $f_r = 2.87$  GHz. The solid curve was calculated using eq. (4), the dots are the measured values, the dashed curve is the PDF of the turn-on delay with only one polarization being taken into account [2].

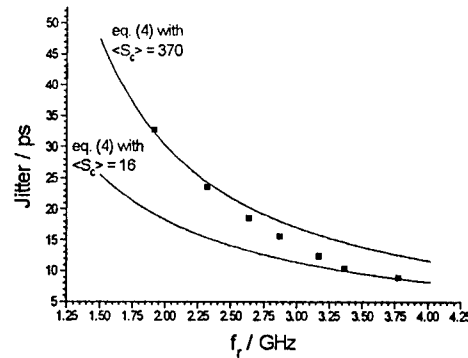


Fig. 3: Turn-on jitter versus relaxation resonance frequency. The solid curves are calculated according to eq. (4), the squares are the measured values.

### Acknowledgements

The author wish to thank Dr. P. Claisse, Motorola Corp., USA for providing the investigated VCSEL samples and Mr. Ziegler from the Heinrich-Hertz-Institut für Nachrichtentechnik, Berlin, for bonding the VCSELs.

### References

- [1] D. M. Cutrer and K. Y. Lau, "Ultralow Power Optical Interconnect with Zero-Biased, Ultralow Threshold Laser - How Low a Threshold is Low Enough?", *Photon. Technol. Lett.*, vol. 7, pp. 4-6, 1995.
- [2] K. Obermann, S. Kindt and K. Petermann, "Turn-On Jitter in Zero-Biased Single-Mode Semiconductor Lasers", *Photon. Technol. Lett.*, vol. 8, pp. 31-33, 1996.
- [3] R. S. Tucker, "High-speed modulation of semiconductor lasers", *J. Lightwave Technol.*, vol. 3, pp. 1180-1192, 1985.

**WA3 (Invited)**  
**9:15am - 9:45am**

**Vertical Cavity Lasers for Datalinks**

Steve Joiner  
Hewlett-Packard CSSD  
370 W. Trimble Road  
San Jose, CA 95131

**Abstract:**

The commercialization of Vertical Cavity Lasers (VCSELs) forces rethinking the optimum choice of wavelength and sources for data link market segments. These choices will be reviewed.

**Paper:**

The fiber optic data communication industry is in the midst of its third phase of technology evolution for local communication.

850 nm LED sources used with large numerical aperture glass fibers constituted the first phase and thus the beginning of fiber optic local communication ( $\leq 2$  kilometers). In this period the typical signaling rate was 20 Mega-Baud (MBd).

The second phase was led by the development of the Fiber Distributed Data Interface (FDDI) standard operating at 125 MBd. During this period 1300 nm LED based links were developed in order to achieve the required link distances of 2 km. Also during this period, 62.5  $\mu$ m multi-mode fiber became the prevalent fiber for intra-building fiber wiring.

The Fibre Channel standards effort initiated the third phase characterized by gigabit communication rates. Fibre Channel's data rate of 1062.5 MBd and need for local communication and low cost forced the evaluation of low cost laser solutions. Due to the popularity of compact disks (CDs), edge emitting 780 nm lasers became inexpensive and reliable. These lasers were written into the Fibre Channel specification at 266, 531 and 1063 MBd. Both the 622 Mb/s ATM standard and the 1250 MBd Gigabit Ethernet standard were developed from the basic Fibre Channel specification.

During the first half 1995, the ATM Forum hosted a series of meetings to choose the best solution for local communication at 622 MBd. These meetings became the coming out party for vertical cavity lasers

The three technology solutions considered for the 622 MBd ATM standard were 850 nm VCSELs, 980 nm VCSELs, and 1300 nm LEDs. The ATM forum ultimately chose both the 850 nm VCSEL solution and the 1300 nm LED solution.

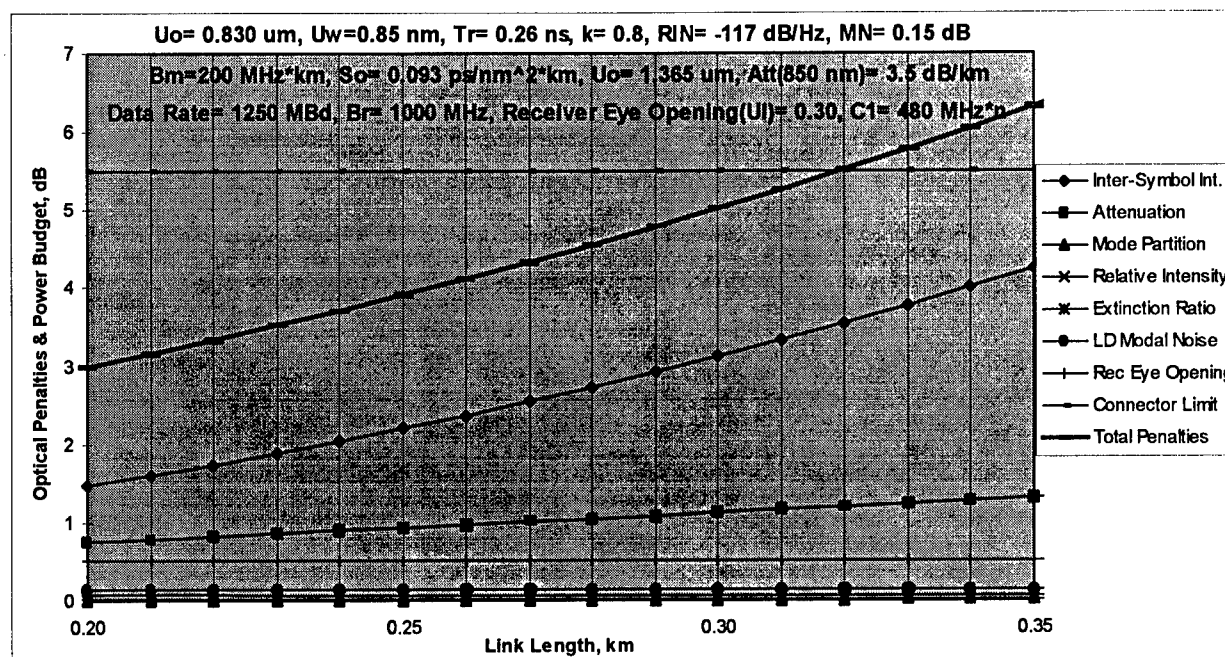
In this paper I would like to make a few comments about the 850 versus 980 nm VCSEL choice. Within the standard's decision process all major arguments are based on

technical criteria but decisions are not entirely made based on technical merits. Companies participating in the standards process realize the commercial benefit of a standard but also realize that each company is maneuvering the decisions to enhance its ability to compete.

Technically the 850 nm and 980 nm solutions were very close in performance with an edge to the 980 nm solution because the fiber had lower attenuation and higher modal bandwidth. The advantage of the 980 nm solution was the ability to develop links which were interoperable with 1300 nm solutions. The primary advantage of the 850 nm solution was a greater number of potential vendors and the existence of 780 nm compatible CD lasers while VCSELs matured. An additional selling point for the 850 nm solution was the perception of lower cost detectors which has not been realized in the market. The ATM forum chose the 850 nm VCSEL and the industry embraced the choice.

This third phase will continue for at least two more years while posturing for the fourth phase is just beginning. What shift in technology will dominate and drive the fourth phase? Three possible candidates are 1300 nm VCSELs, 1300 nm single mode solutions at multimode prices, and high density parallel optics.

A link model for a 1250 Mb/s 850 nm VCSEL link over 62.5  $\mu$ m MM fiber is shown below. Link models for other wavelengths will be shown during the presentation. This link model was developed by Del Hanson and David Cunningham of Hewlett-Packard in conjunction with the IEEE 802.3z Gigabit Ethernet physical layer standards committee.





WA4

9:45am - 10:00am

## Using VCSELs and Multicore Fiber for Multi-channel Transmission

Bogdan ROSINSKI, Jacques CHI, Philippe GROSSO\*, and Jean LE BIHAN

Ecole Nationale d'Ingénieurs de Brest, Laboratoire RESO

C.P. 15, 29608 BREST Cedex, France

\* CNET LAB/FCM, 22307, Lannion Cedex, France

Vertical Cavity Surface Emitting Lasers (VCSELs) show many interesting features such as low threshold current, high speed modulation, low divergence and symmetric beam, and low cost. Moreover, room-temperature CW-operation VCSELs have been obtained recently at  $\lambda=1.3$  and  $1.55 \mu\text{m}$  [1], [2]. These VCSELs may therefore be used as light sources in fiber networks.

To our knowledge, however, the possibility of using fiber arrays to take the advantage of VCSELs' 2D geometry has not been studied. It is evident that a combination of pitch-matched VCSELs and fiber arrays can multiply the transmission capacity of a conventional fiber, and may offer an alternative method to wavelength-division-multiplexing (WDM). In this paper we present our experimental results about a link using direct coupling between a GaAs/GaAlAs VCSELs and a novel  $2 \times 2$  core optical fiber. We demonstrate a two-channel simultaneous transmission with this fiber array.

A commercially available  $1 \times 8$  array of VCSELs emitting at  $\lambda=0.85 \mu\text{m}$  is used as light source in our experiments. The emitting surface of each laser diode has a diameter of  $10 \mu\text{m}$ , separated by a distance of  $62.5 \mu\text{m}$  from each other. To match this VCSEL array, we used a  $2 \times 2$  core fiber. The fabrication process is as follows : four conventional and identical preforms are cutted mechanically and then thermally fused together to obtain a 4-core preform, which results in the  $2 \times 2$  multicore fiber (Fig.1). The diameter of each core is  $10 \mu\text{m}$ , the same as that of the emitting surfaces. The distance between two diagonally separated cores is exactly  $62.5 \mu\text{m}$  in order to match the VCSEL array. Direct coupling between two lasers in the VCSEL array and two cores in the multicore fiber is therefore possible. The overall diameter of this multicore fiber is  $125 \mu\text{m}$ , in agreement with the actual standard.

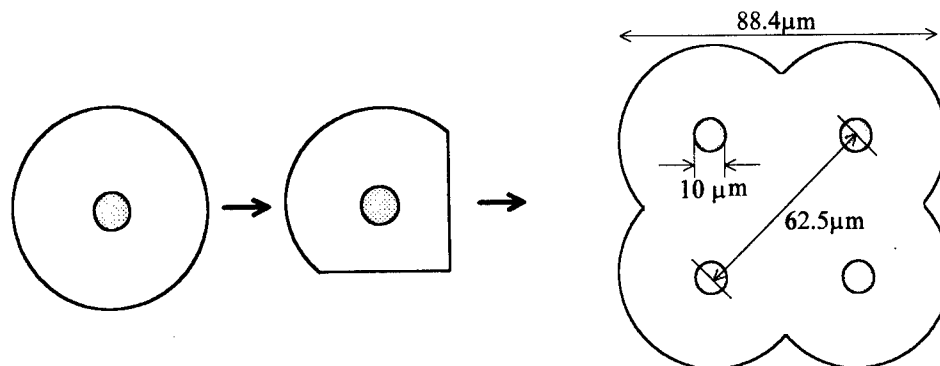


Fig.1 Fabrication of a  $2 \times 2$  multicore fiber

The  $1 \times 8$  VCSEL array is then directly coupled with the multicore fiber, as shown in Fig. 2a. Two independent channels are then formed. The power coupling efficiency can be as high as 70% (Fig. 2b), thanks to the low divergence and symmetric beams from VCSELs. The mechanical tolerance is good enough for the same reason. These results could be qualitatively extended to 1.33 and 1.55  $\mu\text{m}$  VCSELs, since their beams have nearly the same geometrical characteristics. Note that the 10  $\mu\text{m}$ -core fiber is multimode at  $\lambda=0.85 \mu\text{m}$  and monomode at 1.3 and 1.55  $\mu\text{m}$ . The transmission characteristics are similar to that of conventional fibers.

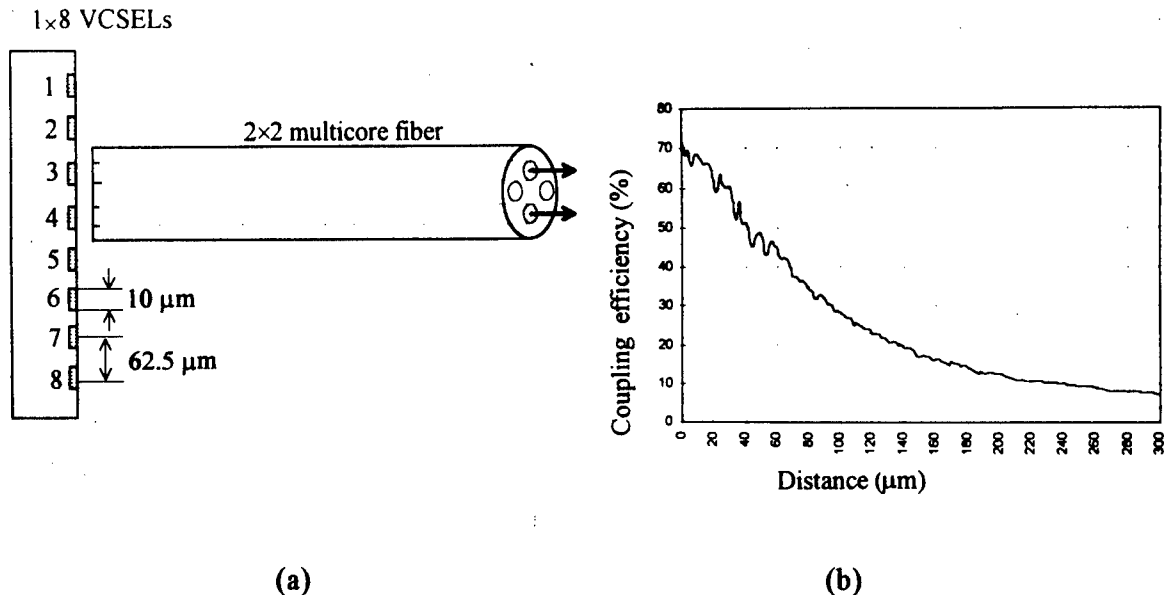


Fig. 2 Direct coupling of a  $1 \times 8$  VCSEL array with a  $2 \times 2$  multicore fiber

Inter-channel crosstalk is an important issue for such a system. We have measured the crosstalk power level (CPL) at  $\lambda=0.85$  and 1.55  $\mu\text{m}$  by injecting a laser beam into one core, and then detecting the power output levels from other cores for the fiber lengths from several meters up to 1 km. In all cases  $\text{CPL} < -40 \text{ dB}$  is obtained. Such a low level is due to tiny but intrinsic fiber parameter fluctuations, which results in different propagating constants for different cores at a given wavelength. Inter-channel crosstalk is thus negligible in practice. It is noticeable that VCSELs can also be used as narrow-band photodetectors [3], implying therefore a highly efficient, bi-directional VCSEL-multicore fiber-VCSEL transmission system.

In conclusion, two channel simultaneous transmission is realized using direct coupling between pitch-matched VCSEL array and multicore fiber. The transmission capacity can be upgraded by using specifically designed VCSELs and fibers (e.g.  $3 \times 3$  or  $4 \times 4$  arrays) or possibly by 1.3–1.6  $\mu\text{m}$  light sources. These results show that the combination of VCSELs and multicore fiber may be a promising candidate in local network applications.

#### References

- [1] Dubravko et al., «Room-temperature continuous-wave operation of 1.54- $\mu\text{m}$  vertical-cavity lasers», *IEEE Photonics Technology Lett.* Vol. 7, No. 11, pp. 1225-1227, 1995
- [2] Y. Qian et al., «1.3- $\mu\text{m}$  vertical-cavity surface-emitting lasers with double-bonded GaAs-AlAs Bragg mirrors», *IEEE Photonics Technology Lett.* Vol. 9, No. 1, pp. 8-10, 1997
- [3] B. Rosinski, J. Chi and J. Le Bihan, «A nouvel transceiver based on VCSELs », submitted to *IEEE Photonics Technology Letters*.

## Diode Cascade Quantum Well VCSEL

K. J. Ebeling, M. Grabherr, R. Jäger, R. Michalzik

Department of Optoelectronics, University of Ulm,

Albert-Einstein-Allee 45, D-89069 Ulm, Germany, Fax: +49-731-502-6049

Vertical cavity surface emitting laser diodes (VCSELs) of low threshold current below 100  $\mu\text{A}$  or high wallplug efficiency above 50% [1] have become available. A distinct disadvantage of VCSELs for many applications is their extremely low roundtrip gain resulting in the requirement of high reflectivity mirrors for achieving reasonably low threshold currents. Periodic gain structures [2] or lasers with two active layers [3] were proposed to increase the gain. In the present study we investigate diode cascade structures containing two active quantum well layers connected by a modulation doped backward tunnel diode. This approach of applying several diodes in series may potentially lead to a threshold current close to the transparency current and provide high differential gain but requires an enlarged operating voltage depending on the number of pn-junctions employed.

Fig. 1 shows a schematic of the MBE grown diode cascade VCSEL studied. P- and n-type mirrors consist of conventional epitaxial AlGaAs-GaAs Bragg reflectors. The active section contains two pn-junctions in series, each of which comprises three undoped 8 nm thick  $\text{In}_{0.2}\text{Ga}_{0.8}\text{As}$  quantum wells separated by 10 nm thick GaAs barriers and embedded in  $\text{Al}_{0.4}\text{Ga}_{0.6}\text{As}$  claddings as indicated in the schematic energy band diagram in Fig. 2. The  $\text{Al}_{0.4}\text{Ga}_{0.6}\text{As}$  cladding layer separating the two groups of InGaAs quantum wells contains a highly doped tunneling junction driven in backward direction. Modulation doping with 10 nm thick layers of  $n = 5 \cdot 10^{18}\text{cm}^{-3}$  Si doped and  $p = 5 \cdot 10^{19}\text{cm}^{-3}$  C doped layers is applied to obtain reasonably low breakdown voltages of the  $\text{Al}_{0.4}\text{Ga}_{0.6}\text{As}$  diode operated in backward direction. The active quantum wells are placed in antinodes and the reverse biased junction is placed in a node of the standing wave pattern. Current confinement is achieved by wet chemical mesa etching and subsequent selective oxidation of a 30 nm thin AlAs layer located in the first Bragg pair above the active region. Ring contacts deposited on the mesa allow for top surface emission.

Fig. 3 and Fig. 4 show output power and current voltage characteristics for devices of 4  $\mu\text{m}$  and 16  $\mu\text{m}$  diameter, respectively, for 100 ns pulsed excitation. Maximum output power is 80 mW for the 16  $\mu\text{m}$  device and 8 mW for the 4  $\mu\text{m}$  device. Threshold currents are 4 mA for the smaller and 20 mA for the larger device. Threshold voltages of about 7 V for both cases are still large compared to twice the bandgap voltage and are to be attributed to the non-negligible breakdown voltage of the backward driven tunnel diode. Obviously, current spreading at the reverse driven diode results in slightly inhomogeneous pumping of the two active segments and saturable absorption is considered responsible for the strong increase of output power observed slightly above threshold. Far above threshold, from the slope of the output characteristics the differential quantum efficiency is 66%. Output spectra in the insets of Figs. 3 and 4 show single transverse mode emission in both devices for the 100 ns excitation studied.

In conclusion, we have fabricated diode cascade quantum well VCSELs and demonstrated high power, high efficiency pulsed operation at room temperature.

[1] R. Jäger et al., *Electron. Lett.* **33** (1997) 330–331.

[2] S.W. Corzine et al., *IEEE J.QE* **25** (1989) 1513–1523.

[3] Y. Kotaki et al., 16th Int. Conf. Sol. State Devices and Materials, Kobe, 1984, pp. 133–136.

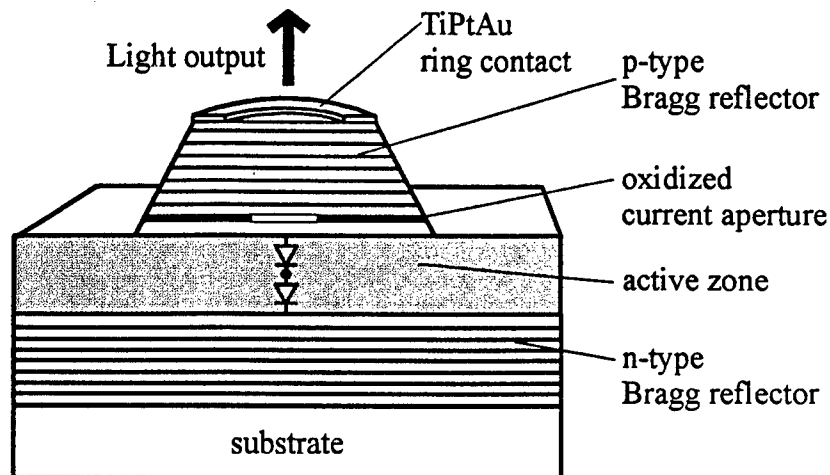


Fig. 1. Schematic of top emitting oxide confined diode cascade VCSEL.

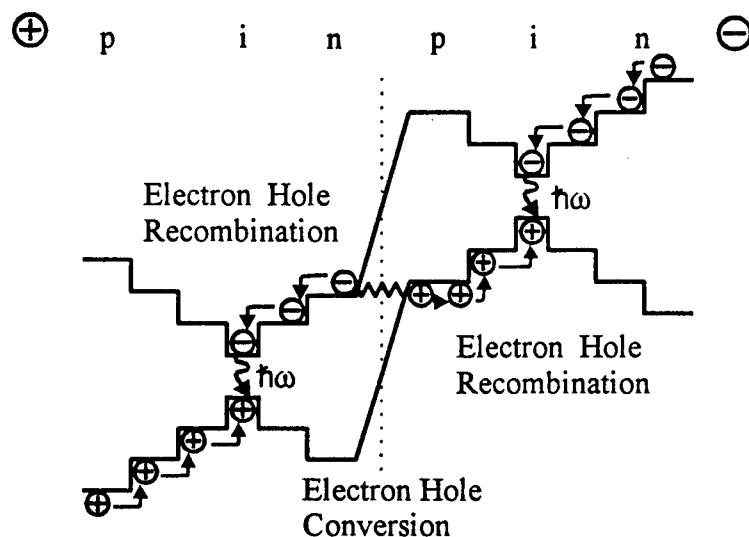


Fig. 2. Schematic band diagram of the active region with cascaded pn-junctions.

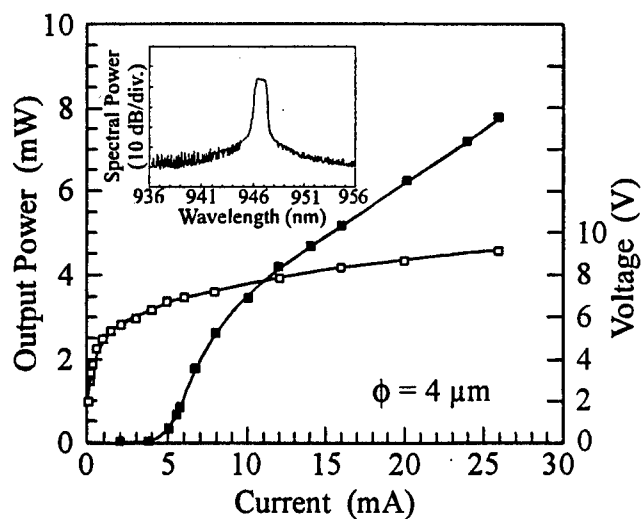


Fig. 3. Output characteristics of 4  $\mu\text{m}$  diameter diode cascade VCSEL.

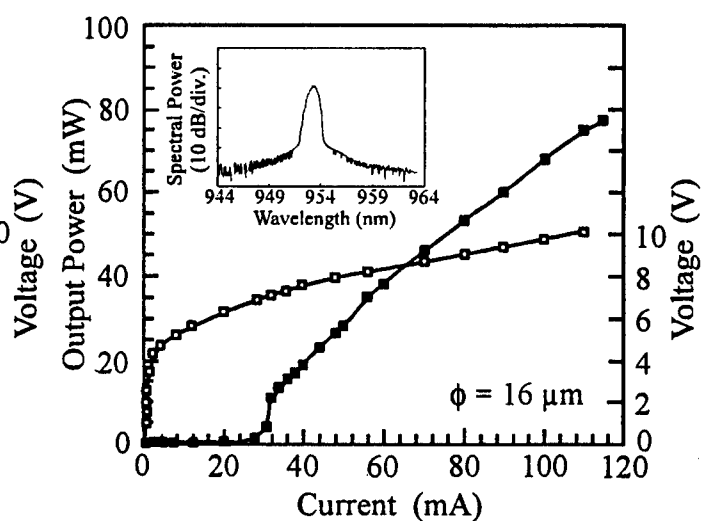


Fig. 4. Output characteristics of 16  $\mu\text{m}$  diameter diode cascade VCSEL.

# A High Performance Continuously Tunable Top-Emitting VCSEL

M.Y. Li\*, W. Yuen\*, G.S. Li\*, and C. J. Chang-Hasnain

211-56 Cory Hall, EECS Department, University of California, Berkeley, CA 94720, U.S.A.

\*Also affiliated with Stanford University, Stanford, CA 94305, U.S.A.

Tunable sources are important for WDM applications. The desirable features include wide and continuous tuning range, low threshold, high power, low tuning power, and single-fundamental mode emission for ease of coupling into fibers. Tunable vertical cavity surface emitting lasers (VCSELs) have the advantage that adjacent Fabry-Perot modes are spaced far apart that the limited gain bandwidth suppresses discontinuous hops during tuning. We recently reported micromechanical tunable VCSELs with a cantilever design that achieved a tuning range of 19.1nm centered at 965nm with threshold  $>3\text{mA}$  and peak power  $<0.2\text{mW}$ .<sup>1</sup> Using a deformable membrane as the top mirror, Sugihwo et al.<sup>2</sup> have demonstrated another tunable VCSEL with 0.34mA threshold but  $\mu\text{W}$  range power. Both are bottom-emitting devices. A top-emitting structure is more desirable especially for packaging and integration considerations. Packaging bottom-emitting lasers usually requires flip-chip bonding which is not feasible for this tunable structure. In this paper, we present the first top-emitting tunable VCSEL with 20nm tuning, low threshold and mW range output throughout the entire tuning range. Furthermore, this device has  $<1\text{mA}$  threshold and  $\sim 1\text{mW}$  power over 11nm of the tuning range.

A schematic of the device is shown in figure 1. The n-p-n structure is grown on an n+ substrate by molecular beam epitaxy. The n-doped bottom distributed bragg reflector (DBR) consists of 33.5 pairs of AlAs/GaAs  $\lambda/4$  layers. The active region is a one  $\lambda$ -Al<sub>0.5</sub>Ga<sub>0.5</sub>As spacer sandwiching 3-80Å In<sub>0.15</sub>Ga<sub>0.85</sub>As quantum wells which are separated by 100Å GaAs barriers. The p-DBR consists of 4 mirror pairs of Al<sub>0.5</sub>Ga<sub>0.5</sub>As/Al<sub>0.1</sub>Ga<sub>0.9</sub>As layers with the last Al<sub>0.1</sub>Ga<sub>0.9</sub>As layer being  $3/4 \lambda$ -thick and doped p+ for contacting. For current confinement, a 300Å thick AlAs layer is grown at the Al<sub>0.5</sub>Ga<sub>0.5</sub>As/Al<sub>0.1</sub>Ga<sub>0.9</sub>As interface closest to the active region. A 1.41 $\mu\text{m}$  undoped GaAs sacrificial layer is grown above the p+ layer, followed by 20.5 pairs of ungraded Al<sub>0.1</sub>Ga<sub>0.9</sub>As/Al<sub>0.9</sub>Ga<sub>0.1</sub>As n-DBR.

This structure can be seen as two coupled cavities. Wavelength tuning is achieved electrostatically by reverse-biasing the air gap cavity. As the reverse bias increases, the cantilever is attracted towards the p+ contact, changing the coupling in the air gap through a phase shift and thus the Fabry-Perot wavelength of the structure.

The sample is measured at room temperature (22°C) with the substrate in contact with a heat sink. Figure 2 shows the tuning spectra for one device (2 $\mu\text{m}$  wide by 100 $\mu\text{m}$  long by 3 $\mu\text{m}$  thick cantilever, 8 $\mu\text{m}$  current aperture), when the active region is pumped at 2.5mA. The strong transverse oxide modes at the long wavelength end are due to the gain peak at 930nm. (Note that the threshold current in this wavelength range is  $<0.8\text{mA}$ .) As the tuning voltage increases and the lasing wavelength decreases past the gain peak, these higher order modes are suppressed. A continuous tuning range of 20.0nm (935.8nm- $\rightarrow$ 915.8nm) is achieved for tuning voltages between 0V and 16.8V. When the tuning voltage is increased further, the lasing spectrum contains multiple transverse modes with the fundamental mode at 942nm. As designed, the lasing mode is expected to be at 956nm. This discrepancy is due to the blue-shifted gain by 20nm. Figure 3 shows the threshold current and peak output power as a function of the lasing wavelength. The LI- and IV-characteristics of the laser at the opposite ends of the tuning range are shown in figure 4. The kinks in the 16.8V LI-curve indicate multiple transverse modes appearing.

In conclusion, we report the first high performance, micromechanical tunable top-emitting VCSEL that continuously tunes over 20nm, has threshold current between 0.76mA - 1.9mA and output power 0.92 mW - 1.9mW throughout the entire tuning range. Such a top-emitting tunable structure is highly desirable for easy optical and electrical packaging and for integration with other devices. The achieved high performance of low threshold and high power renders its practical implementation extremely feasible.

The authors gratefully acknowledge E.C.Vail for his helpful comments and the staff at the Microfabrication Laboratory at UC Berkeley. This work was supported by DARPA Ultra contract #N00014-96-1-1267.

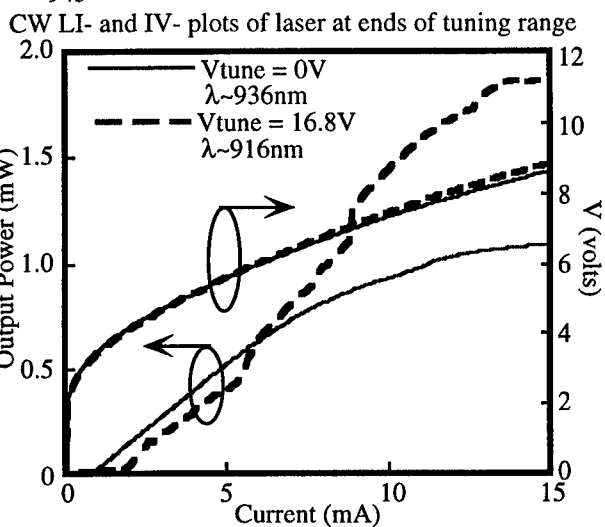
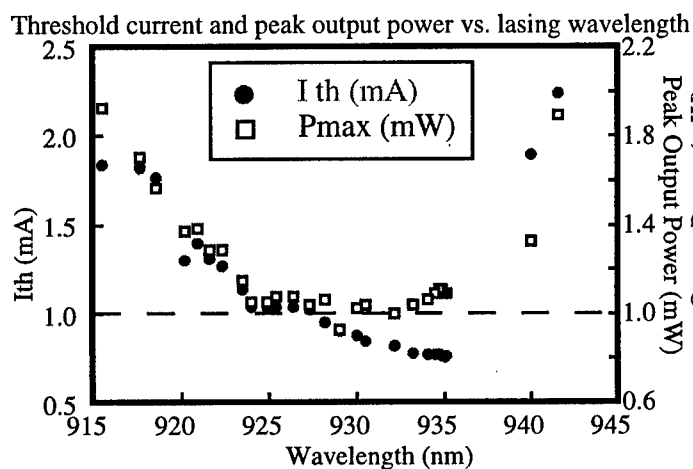
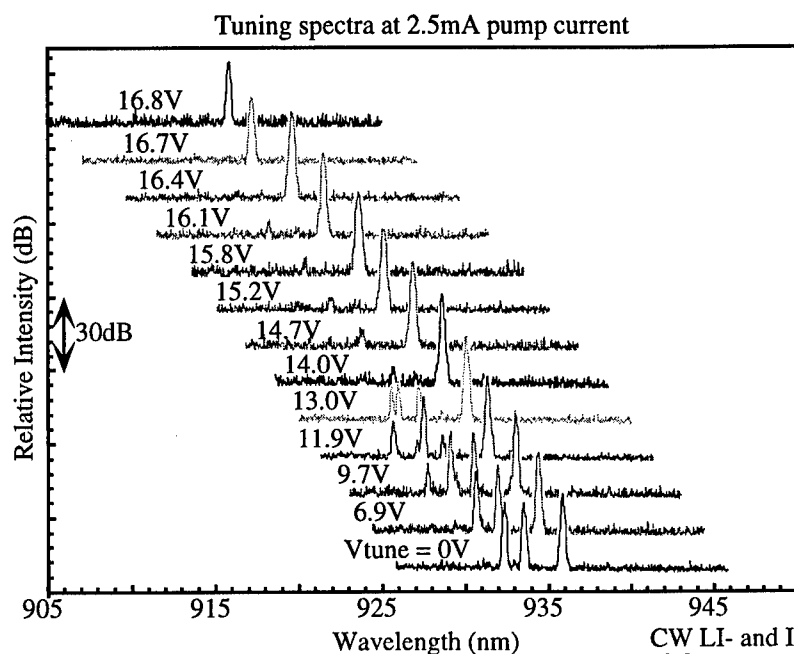
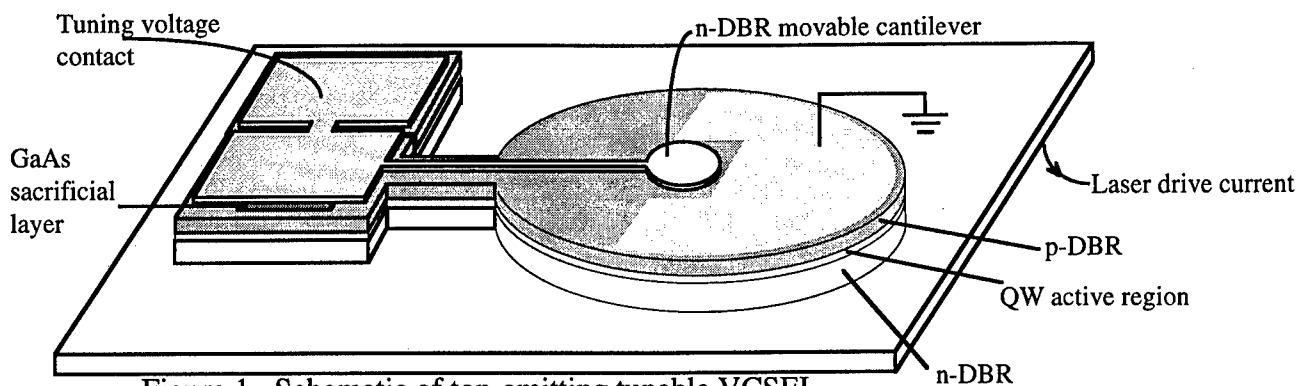


Figure 3. Threshold current and peak output power as a function of lasing wavelength at threshold

#### References

1. E.C. Vail, G.S. Li, W. Yuen, and C. J. Chang-Hasnain, Elec. Lett., 32, 1888 (1996).
2. F. Sugihwo, M.C. Larson, and J.S. Harris, Appl. Phys. Lett., 70, 547 (1997).

## Diffraction Loss of Confined Modes in Microcavities

G. R. Hadley and K. L. Lear

MS/0603

Sandia National Laboratories

Albuquerque, New Mexico 87185-5800

## SUMMARY

The recent performance improvements by selectively-oxidized vertical-cavity lasers has led to a number of investigations into the relevant physics of these devices, particularly with regard to their optical confinement and loss mechanisms. Qualitative explanations for the dominant loss mechanism have been reported that include scattering by the oxide aperture<sup>1</sup> and diffraction loss resulting from coupling by the oxide layer to lossy parasitic modes of the cavity<sup>2</sup>. However, systematic quantitative theoretical investigations of the excess lateral losses of microcavities such as those of an oxidized VCSEL have not been reported thus far.

In this paper, the loss of a simplified cavity is studied using an accurate numerical model that solves the scalar Helmholtz Equation at each point in the cavity. The idealized cavity geometry consists of two perfect mirrors as shown in the inset in Fig. 1. The upper mirror is offset inward at some radius as shown, so that the cavity is laterally index-guided. A  $10\lambda$  cavity length was chosen to mimic (approximately) the number of standing waves in a VCSEL cavity, including the distributed Bragg mirrors. The use of the idealized cavity shown was selected for study because of its simplicity together with the fact that there is no internal element to generate scattering loss. Thus, all losses in this cavity must be of a diffractive nature and occur as a radiative loss through the right problem boundary.

The solution of the Helmholtz Equation was obtained by direct band matrix inversion and determinant computation together with a complex root finder to determine the eigenvalue. The offset in the upper mirror was treated by the introduction of a region interior to the problem in which the field was set to zero (shown as a darkened rectangle near the upper boundary in Fig. 2). The fundamental cavity mode was then determined numerically for a variety of offsets and radii as shown in Fig. 1. For the two smallest values of the mirror offset, calculations are not shown for the smaller radii because loss of confinement caused the field to overlap the absorption region and thus give artificially high losses.

Before discussing the quantitative results, the qualitative appearance of the modes in all cases resembles the amplitude contours shown in Fig. 2 for the specific case of 40 nm offset and 2  $\mu\text{m}$  radius. The presence of the offset does indeed confine the mode as expected from the effective index model<sup>3</sup>, since the shorter cavity appears to the mode as a region of depressed refractive index. However, as is the case with confinement by an oxide layer inserted into the cavity, optical losses occur that cannot be explained by this model. In fact, it has been noticed that calculations performed using oxide confinement with an equivalent index step result in comparable losses to those calculated for offset cavities. For the latter case, however, the origin of the loss cannot be scattering (since there is no scattering medium) and evidently results from the tilt in the wavefronts caused by the shortened cavity as shown in the figure. Such tilt will be present to some degree any time a lumped low-index element is introduced into such a cavity<sup>1</sup>. It thus appears that the excess loss seen in selectively-oxidized lasers results (at least for thin oxide layers) not from scattering but from diffraction loss resulting from the phase mismatch introduced by the oxide layer. This picture is consistent with the diffraction loss model previously published by Deppe et. al<sup>2</sup>.

Quantitatively, it is seen in Fig. 1 that the magnitude of the loss increases with increasing offset (or index step). In the figure the loss is normalized by an approximate (but somewhat arbitrary) value representing total 1D losses in a typical VCSEL. It is thus clear from the figure that if diffraction losses in small radius cavities are to be kept well below the level normally associated with VCSEL operation, effective index values should be kept below about 0.01. This may be compared with typical values of 0.06 that result from oxidation of a quarter-wave mirror layer. Thus the present calculations confirm recent experimental findings that thinner oxide layers provide lower loss devices<sup>4</sup>. Generally, the diffraction loss is also seen to decrease with increasing radius, but resonance behavior is observed that causes a

departure from this trend at certain radii. Whether such resonances can be used to advantage in device design is yet to be determined.

1. K. L. Lear, K. D. Choquette, R. P. Schneider, Jr. and S. P. Kilcoyne, Appl. Phys. Lett. 66,2616(1995).
2. D. G. Deppe, T.-H. Oh, and D. L. Huffaker, to be published in Phot. Tech. Lett.
3. G. R. Hadley, Opt. Lett. 20,1483(1995).
4. K. D. Choquette, W. W. Chow, G. R. Hadley, H. Q. Hou, and K. M. Geib, Appl. Phys. Lett. 70,823(1997).

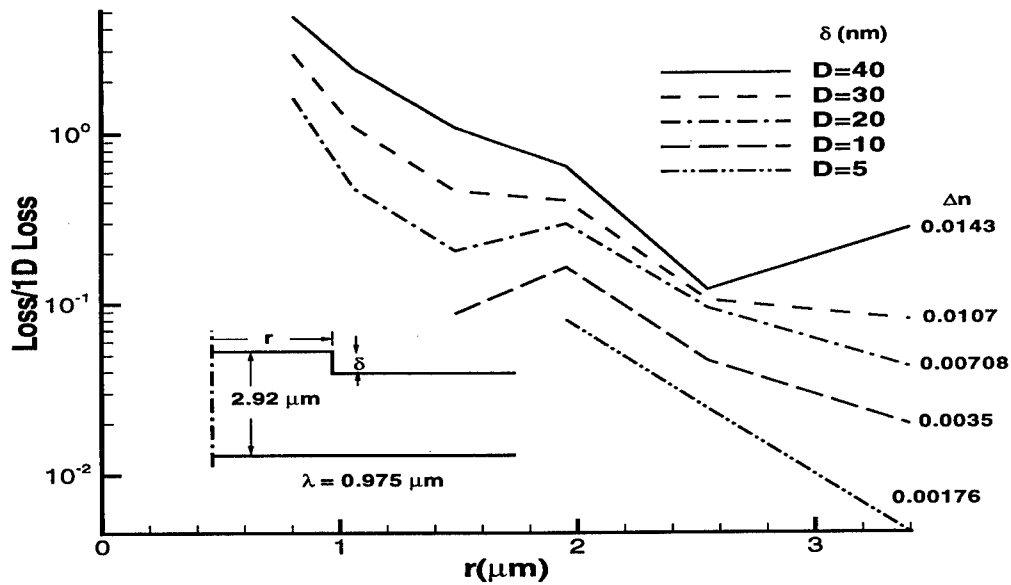


Figure 1

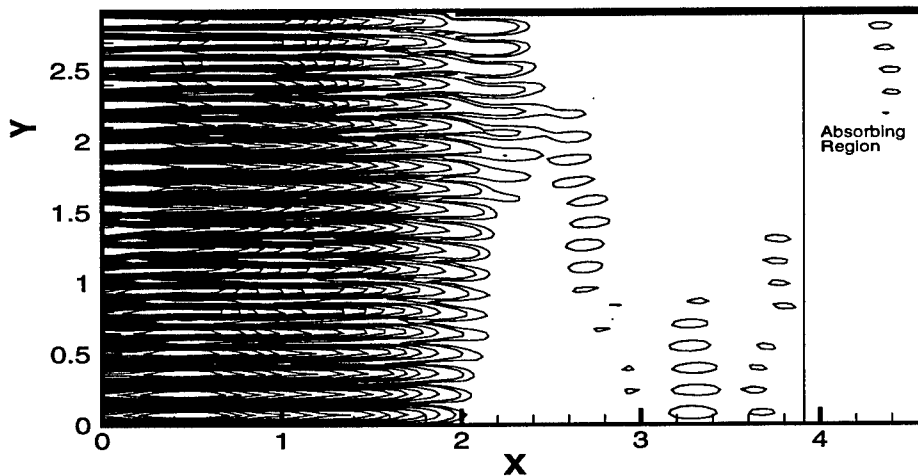


Figure 2



# Analysis of three dimensionally confined microcavity surface emitting lasers using vector finite elements

Michael J. Noble<sup>†</sup>, James A. Lott<sup>†</sup>, John P. Loehr<sup>§</sup>, and Paul Sotirelis<sup>¶</sup>

<sup>†</sup>Department of Electrical and Computer Engineering,  
Air Force Institute of Technology (AFIT/ENG),  
2950 P Street, Bldg 640, Wright-Patterson Air Force Base, Ohio 45433-7765

<sup>§</sup>Heterojunction Physics Branch, Avionics Directorate (WL/AADP),  
Wright-Patterson Air Force Base, Ohio 45433-7765

<sup>¶</sup>Aeronautical Systems Center (ASC/MSRC),  
2435 5th Street, Bldg 676, Wright-Patterson Air Force Base, Ohio 45433-7765

Added design flexibility resulting in the improved performance of vertical cavity surface emitting lasers (VCSELs) can be largely attributed to the advent of native oxides. Conventional VCSEL designs include native oxide apertures surrounding active optical cavities for the purpose of current confinement, with the added potential benefit of optical mode control. Multiple oxide layers are envisioned within the VCSEL's distributed Bragg reflectors, each with variable open area profiles to form a designer waveguide. These waveguides are expected to provide higher-order mode suppression, lensing, or other useful diffractive effects. The physics becomes increasingly interesting as the VCSEL's radial dimension is reduced to or below the lasing wavelength. Such microcavity SELs cannot be accurately modeled as one-dimensional Fabry-Perot resonators.

Recent models which incorporate the higher dimensional field effects include for example a beam propagation model developed at UC Santa Barbara<sup>1</sup> and a finite difference model created at Sandia National Laboratories.<sup>2</sup> These models solve the scalar Helmholtz equation via a two dimensional approach. We present a new model which solves the vector wave equation in the variational sense using Galerkin's form of the finite element method. This model allows for calculation of general three dimensional cavity modes including for example hybrid-electric-magnetic (HEM) modes<sup>3</sup> not found in previous models. The finite element approach should offer more accurate results especially in the case of radially small and complex geometry (ex. multiple oxide regions) devices.

The finite element method is used to solve a variational form of Maxwell's equations,<sup>4</sup>

$$\int_{\Omega} \left[ \frac{1}{\mu_r} (\nabla \times \vec{E}) \cdot (\nabla \times \vec{W}^*) - k_0^2 \epsilon_r \vec{E} \cdot \vec{W}^* \right] dv - \oint_{\Gamma} \frac{1}{\mu_r} (\vec{W}^* \times \nabla \times \vec{E}) \cdot \hat{n} ds = -i\omega\mu_0 \int_{\Omega} \vec{J}_s \cdot \vec{W}^* dv, \quad (1)$$

where  $\vec{E}$  and  $\vec{W}$  are the electric field and testing field of frequency  $\omega$ ,  $\vec{J}_s$  is a source current,  $\Omega$  is the volumetric domain of the calculation, and  $\Gamma$  is the surface boundary of the domain. The  $\vec{E}$  field is expanded over a piece-wise linear basis on a two dimensional mesh formed over the  $\rho - z$  half-plane cross-section of the VCSEL geometry. For Galerkin's method the testing field  $\vec{W}$  is expanded over the same basis set. A perfectly matched absorbing layer<sup>5</sup> is included on the periphery of the VCSEL to facilitate truncation of the finite element mesh/basis.

VCSEL eigenmodes are found by recasting Eqn 1 in the form of a generalized eigenvalue problem

$$A\vec{x} = \lambda B\vec{x}; \quad (2)$$

where the eigenvalue  $\lambda = k_0^2$  gives the eigenmode frequency,  $\vec{x}$  is the vector of  $\vec{E}$  field basis expansion coefficients, and A and B are matrices given by the integral operators applied to  $\vec{E}$  and each testing function  $\vec{W}_i$  in the testing field expansion set. The source term  $\vec{J}_s \equiv 0$  for the eigenmode solution.

A sample calculation was performed on an etched-post 980 nm VCSEL. The device structure and estimated field intensity are shown in Fig. 1. The mode shown is the first higher order lasing mode,  $TM_{01}$ .

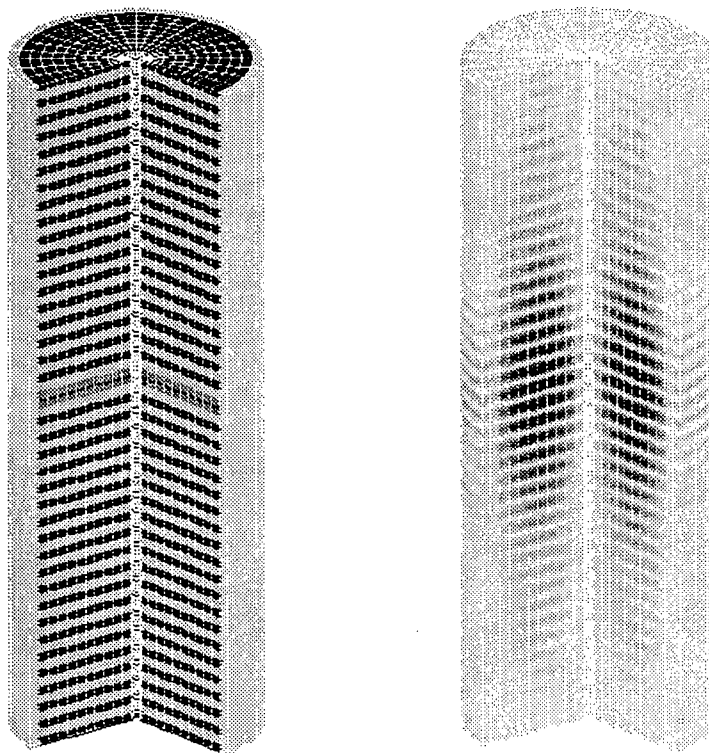


Figure 1. Etched-post VCSEL structure and  $TM_{01}$  field intensity

This new finite element method model is expected to be valuable for the design of microcavity devices. It can be used to optimize optical mode control by examining changes of size, shape, number, and location of native oxide layers. It may also be combined with semiconductor gain calculations to determine the higher order mode suppression level for various microcavity SEL designs. Finally, it may be used to analyze VCSEL lasing and spontaneous emission near-field structure. This information is of considerable importance in the design of optical interconnect and communication systems.

### ACKNOWLEDGEMENTS

We wish to thank our sponsor organization, USAF Wright Laboratories Avionics Directorate. This work was accomplished as part of AFOSR initiative 2305DW.

### REFERENCES

1. E. Hegblom, D. Babić, B. Thibeault, and L. Coldren, "Estimation of scattering losses in dielectrically apertured vertical cavity lasers," *Applied Physics Letters* **68**, pp. 1757-1759, Mar. 1996.
2. G. Hadley, K. Lear, M. Warren, K. Choquette, J. Scott, and S. Corzine, "Comprehensive numerical modeling of vertical-cavity surface-emitting lasers," *IEEE Journal of Quantum Electronics* **32**, pp. 607-616, Apr. 1996.
3. M. Noble, J. Loehr, and J. Lott, "Calculation of microcavity vcsel field modes using a doubly iterative weighted index method," in *Proceedings of the SPIE*, vol. 2994, 1997.
4. J. Jin, *The Finite Element Method in Electromagnetics*, John Wiley and Sons, Inc., 1993.
5. Z. Sacks, D. Kingsland, R. Lee, and J. Lee, "A perfectly matched anisotropic absorber for use as an absorbing boundary condition," *IEEE Transactions on Antennas and Propagation* **43**, pp. 1460-1463, 1995.

**WB5**

**11:30am - 11:45am**

**Microcavity LEDs with an overall efficiency of 4 % into a numerical aperture of 0.5**

R. Bockstaele, C. Sys, J. Blondelle, H. De Neve, F. Goussaert, B. Dhoedt, I. Moerman, P. Van Daele  
and R. Baets

University of Gent - IMEC , INTEC-departement  
Sint Pietersnieuwstraat 41 B- 9000 Gent, Belgium  
tel : secr. ++32 9 264 3316 , fax : ++32 9 264 3593  
e-mail : ronny.bockstaele@intec.rug.ac.be

**Abstract** Microcavity LEDs were optimised for optical interconnect requirements. Overall quantum efficiency of upto 4.3 % into a numerical aperture of 0.5 and a FWHM beam divergence angle of 105 degrees at a drive current of 1 mA was achieved.

**Introduction** Conventional planar LEDs have a low external quantum efficiency due to total internal reflection at the semiconductor - air boundary. For a semiconductor refractive index of 3.5 only 2 % of the emitted light escapes to the  $2\pi$  solid angle into air. Furthermore only 25 % of this externally emitted light falls within a numerical aperture of 0.5. The methods used in display LEDs to enhance this efficiency are not applicable in dense parallel optical interconnect applications. In recent years it has been demonstrated that the microcavity effect allows to enhance the efficiency by more than a factor 10 [1]. A record efficiency of 22.8 % has been obtained in a large area  $\lambda$ -cavity with 3 InGaAs quantum wells [2]. However these microcavity LEDs (MCLEDs) exhibit a large beam divergence and only a small fraction of the power can be coupled into a lens or waveguide with a limited numerical aperture. In this paper we present theoretical and experimental results on the optimisation of microcavity LEDs for small beam divergence and high efficiency into a limited NA of 0.5.

**Simulation and design.** We consider a MCLED structure as shown in fig 1 consisting of 3 InGaAs quantum wells positioned at the antinode position of a cavity with a gold mirror on one side and a GaAs/AlAs DBR at the other side. The cavity is (approximately) one wavelength long. Using a dedicated MCLED model [3] that takes into account the microcavity effect, guided modes and the finite spectral width of the spontaneous emission, simulations were done to study the effect of the cavity parameters on the beam divergence and the efficiency. The results are shown in fig 2 and 3. One can see that it is not possible to achieve both low beam divergence and high efficiency into an NA of 0.5 for the same design. The best efficiency values are around 8 % assuming a 100 % internal quantum efficiency and the corresponding FWHM beam divergence angle is 80 to 90 °

**Experiment** Devices as shown in fig 1 were fabricated with a 6-pair DBR and two values for the thickness of the GaAs-layer, 120 nm and 108 nm respectively, thereby varying the cavity length. The layer structure was grown on GaAs in a MOCVD reactor. After growth gold mirrors, also serving as p-contact, with a diameter of 50  $\mu$ m were deposited. The substrate was thinned to 250  $\mu$ m to reduce substrate absorption and an anti-reflective coating was deposited on the back surface.

**Measurements** Fig 4 and 5 show the P/I curves and radiation pattern for the two devices. The efficiency values at 1 mA and divergence angles are summarised in Table 1. For comparison, an ideal non-microcavity LED and performances of earlier MCLEDs [2], not optimised for low beam divergence, have been added. From this table, it can be concluded that devices offering efficiencies of about 4 % in a numerical aperture of 0.5 can be realised. In order to facilitate comparison, experimental values for structures A and B were extrapolated for a substrate thickness of 90  $\mu$ m (actual substrate thickness is 200  $\mu$ m). Tuning the cavity can achieve a severe reduction of the light emitted outside the NA of 0.5, thereby reducing stray light and associated cross talk.

**Conclusion** Microcavity LEDs with one gold and one GaAs/AlAs DBR-mirror have been optimized for efficiency into a limited NA of 0.5. Simulations indicate that an efficiency of 8 % can be achieved. Experimental devices give a best value of 3.7 %.

**Acknowledgements** The authors acknowledge partial support from the European Commission through the ESPRIT-IV MEL-ARI project OIIC 22641 as well as from the Belgian DWTC through the IUAP-13 project. R. Bockstaele, J. Blondelle, H. De Neve, B. Dhoedt, F. Goussaert and C. Sys, acknowledge support from the Flemish IWT.

## References

- [1] D. L. Huffaker et al, Appl.Phys.Lett, 66(23) pp 3096-3098 (1995)  
 [2] H. De Neve et al, Appl.Phys.Lett., 70(7), 1997.  
 [3] H. De Neve et al., IEEE Phot.Techn.Lett., Vol. 7, no 3, pp 287-2890

	FWHM divergence angle	total external efficiency	fraction to NA = 0.5	efficiency to NA=0.5
A. 108 nm MC-LED	85 °	7.2 % [7.8 %] *	41 %	3.0 % [3.2 %] *
B. 120 nm MC-LED	105 °	11.4 % [12.3 %] *	34 %	3.9 % [4.2 %] *
C. high efficiency MC-LED	120 °	17.2 %	26 %	4.3 %
D. ideal non MC-LED	120°	2 %	25 %	0.5 %

Table 1 : Comparison of different MCLEDs. \* Calculated values for substrate thinned to 90  $\mu\text{m}$ .

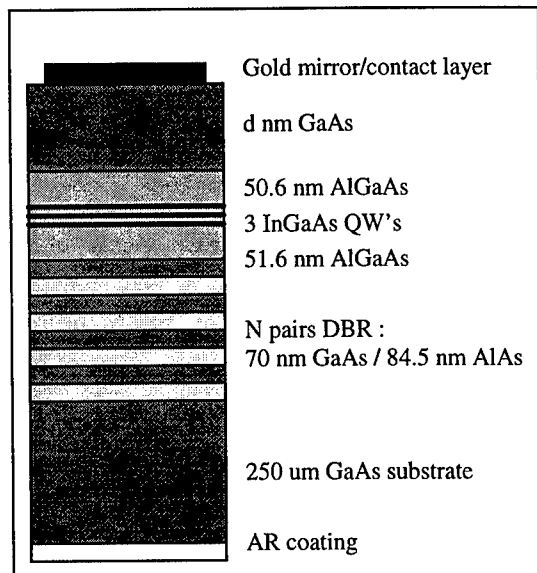


Fig 1 : structure of MCLED.

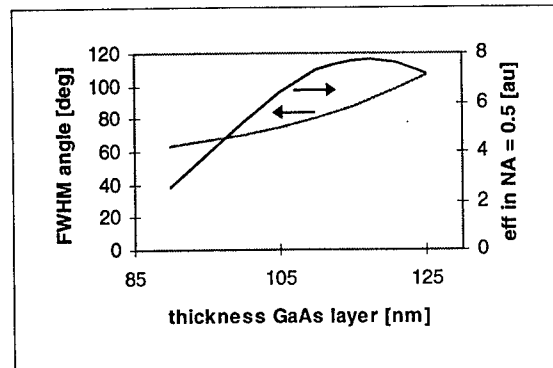


Fig 2 : FWHM angle and efficiency as a function of thickness cavity ( $N=7$ ).

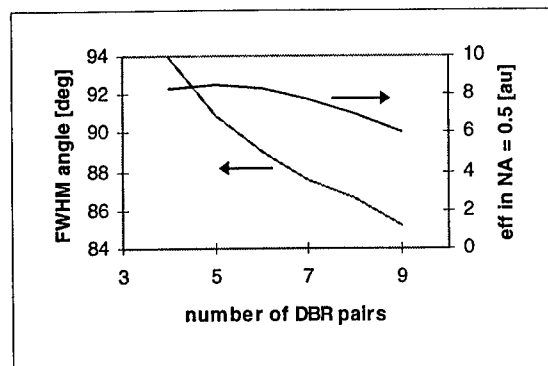


Fig 3 : FWHM angle and efficiency as a function of DBR pairs ( $d=115\text{nm}$ ).

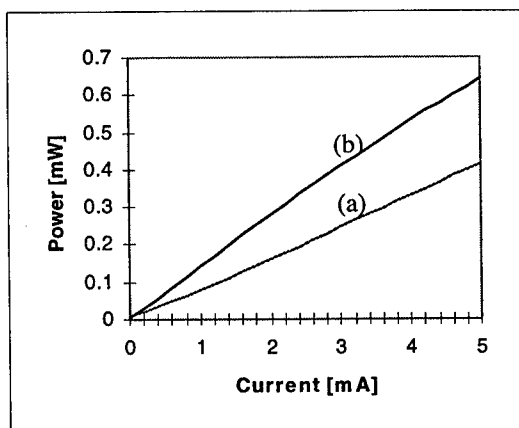


Fig 4 : P,I characteristic of (a) 108 nm MCLED and (b) 120 nm MCLED.

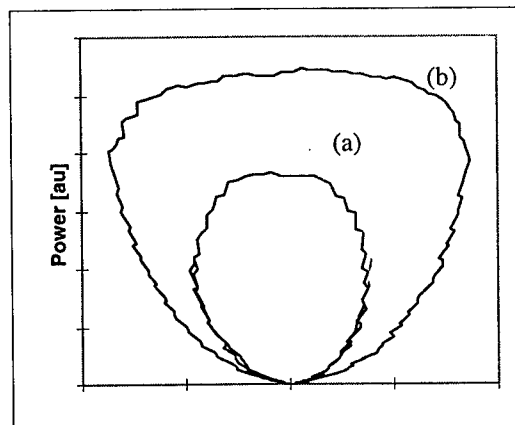
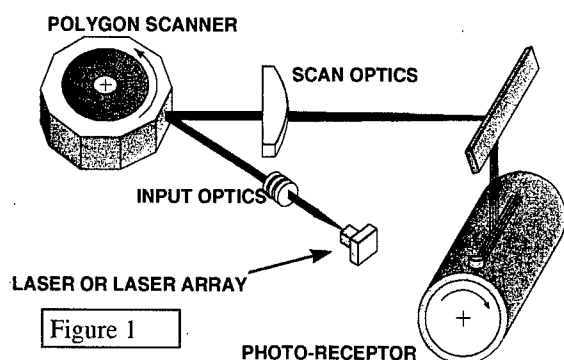


Fig 5 : far field plot of (a) 108 nm MCLED and (b) 120 nm MCLED.

## Vertical Cavity Lasers for Printing

Robert L. Thornton  
Xerox Palo Alto Research Center  
3333 Coyote Hill Road  
Palo Alto, CA 94304  
<http://www.parc.xerox.com/thornton>

The laser printer, depicted in Figure 1, uses a rotating polygon mirror to scan a modulated laser beam across a photoconductive material, writing a latent image as an electrostatic charge pattern. This electrostatic charge pattern attracts toner particles which are then transferred to paper. Semiconductor lasers have been a key enabler in the

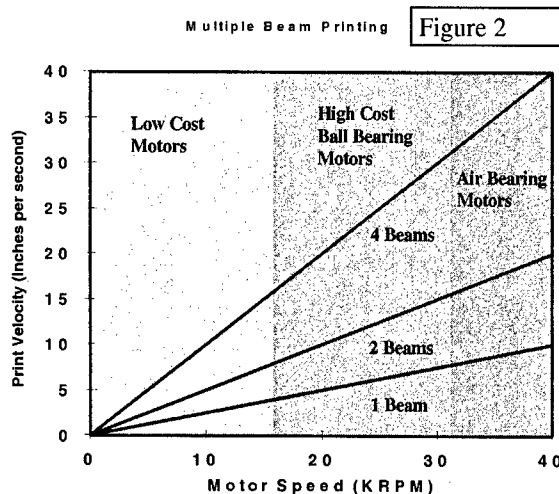


development of small and low cost desktop laser printers. These devices, operating in the 5-20 page per minute (ppm) print speed range, have become nearly ubiquitous for low print volume applications at moderate print resolutions up to 600 spots per inch (spi).

When one looks at networked environments or long print run applications, desired print speeds increase rapidly from several tens to well in excess of 100 pages per minute. As one attempts to access these much higher performance printing models, the rotation speed of the polygon becomes prohibitive. In Figure 2 we show, for a given print resolution, the achievable throughput in inches per second as a function of the polygon rotation speed.

Writing multiple scan lines simultaneously using multiple lasers in parallel is a highly leveraged strategy for overcoming the problem of high polygon rotation speed. Figure 2 shows this for the case of 2 or 4 beam laser arrays. Edge emitting lasers are making inroads into this area. However, considering the further evolution of this strategy, the advantages of the VCSEL architecture are revealed. The VCSEL device largely circumvents array size issues, providing a robust, high yield process by which large arrays of lasers can be realized.

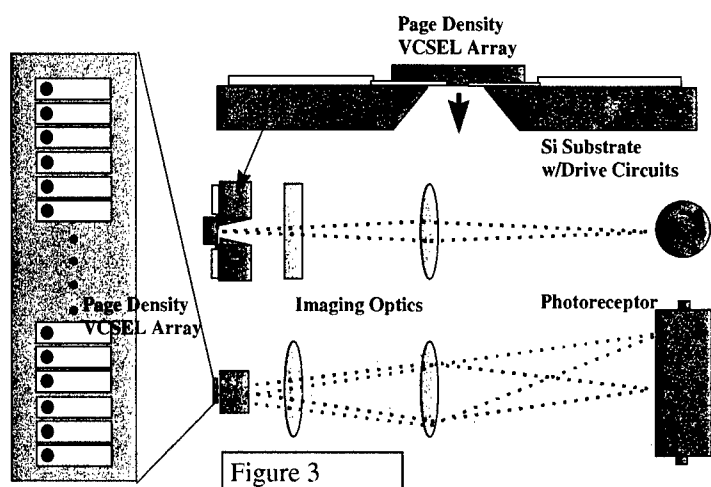
A further evolution of the use of VCSELs for laser printing would involve the complete elimination of the polygon with a linear high density light source array with one element per



pixel across the full width of the printed page. The resulting device, depicted schematically in Figure 3, would be very much akin to the LED printbar that has found its way into some printing applications. The introduction of a VCSEL device into this architecture, however, offers some powerful advantages.

LED Printbars are full page width devices with several thousand top surface emitting LEDs in a linear array. Multiple chips are fabricated and precision mounted on a substrate. Both the electrical conversion and the optical collection efficiencies of the LEDs is low, resulting in a relatively expensive system with high dissipative power.

With the advent of ultra-low threshold current VCSELs with very high conversion efficiencies<sup>2</sup>, one is able to consider the fabrication of a high density VCSEL array, also



with several thousand emitters, but with the important distinction that the entire array is of a length short enough to enable several arrays to be fabricated on a single GaAs wafer in a monolithic fashion. The array would then be magnified to full page width using commonly available optics. A potential increase in system throughput (electrical power in to optical power delivered to the photoreceptor)

of more than two orders of magnitude could be realized. In addition, flip chip bonding or monolithic integration techniques can be used to eliminate the multiple die attach and wirebonding steps associated with the LED printbar. Recognizing the numerous technical challenges associated with the implementation of such an architecture, the fundamental device performance necessary for this application has nevertheless already been established.

At this time, there is still considerable uncertainty as to exactly how the future of VCSELs in the world of laser printing will unfold. However, with a wealth of potential applications and performance enhancements, the likelihood is quite high that these devices will have a substantial impact on the future of laser printing.

1. Guerin, J-M, "Dual-beam modulation subsystem for high speed digital copier", Proceedings of the SPIE, Volume 1987 pp341-353, 1993
2. Lear, K.L., Choquette, K.D., Schneider, R.P. Jr., Kilcoyne, S.P., Geib, K.M.; "Selectively oxidized vertical cavity surface emitting lasers with 50% power conversion efficiency," Electron. Lett., Vol. 31, pp. 208-209, 1995

**High Power Single Transverse Mode Selectively Oxidized VCSELs**

Kent D. Choquette, H. Q. Hou, G. R. Hadley, K. M. Geib, D. Mathes,\* and Robert Hull\*

Center for Compound Semiconductor Technology  
Sandia National Laboratories  
Albuquerque, NM 87185  
kdchoqu@sandia.gov

Buried oxide apertures within VCSELs<sup>1,2</sup> transversely confine both charge carriers and photons.<sup>3,4</sup> Decoupling the electrical and optical confinement arising from the oxide apertures will allow tailoring specific VCSEL performance. For example by reducing the transverse optical confinement while maintaining a small current injection aperture, VCSELs which promote a single transverse mode can be fabricated. In addition to confinement, the optical loss for small oxide confined VCSELs is influenced by the thickness, tapering, and position of the apertures.<sup>5-7</sup> We report the high single mode output from selectively oxidized monolithic VCSELs using  $3/4\lambda$  thick buried oxide layers which have been designed for minimal optical confinement and optical loss.

Selectively oxidized top emitting monolithic VCSELs with various oxide aperture configurations are grown by MOVPE and fabricated as described previously.<sup>2</sup> Surrounding the  $1\lambda$  thick optical cavity we introduce  $3/4\lambda$  thick low index layers of  $\text{Al}_{0.92}\text{Ga}_{0.08}\text{As}$  in which a thin (8 or 14 nm thick)  $\text{Al}_{0.98}\text{Ga}_{0.02}\text{As}$  layer is embedded, as shown in Fig. 1. This allows insertion of oxide apertures within the laser cavity to overlap either field nulls or antinodes without complication from the compositional grading between the high and low index DBR layers. Fig. 2 indicates the selective oxidation of the thin high Al-content layer forms the tip of a thicker tapered oxide. Thus the more rapid lateral oxidation of the thin  $\text{Al}_{0.98}\text{Ga}_{0.02}\text{As}$  layer<sup>2</sup> "drags" along the oxidation of the thicker surrounding  $\text{Al}_{0.92}\text{Ga}_{0.08}\text{As}$  layers. The result is the oxidation rate of the  $\text{Al}_{0.98}\text{Ga}_{0.02}\text{As}$  ( $\text{Al}_{0.92}\text{Ga}_{0.08}\text{As}$ ) layer is decreased (increased) by a factor of 1.5 (3.0) relative to a bulk layer. This produces the tapered oxide profile in the thick oxides apparent in Fig. 2, similar to thin tapered oxides reported in Ref. 8. VCSEL samples with 20 top DBR periods and oxide apertures overlapping field null(s) or antinode(s) on one side (single aperture) or both sides (double aperture) of the optical cavity are compared in the following.

Selectively oxidized VCSELs with tapered  $3/4\lambda$  thick apertures and cross section area  $< 4 \times 4 \mu\text{m}$  ( $4.5 \mu\text{m}$  dia.) emit a single transverse mode over their entire operation for single or double apertures overlapping field null(s) or antinode(s). By contrast, VCSELs with a single nontapered 30 nm thick oxide aperture operate single mode only  $\leq 3 \mu\text{m}$  dia. ( $2.6 \times 2.6 \mu\text{m}$ ) VCSELs.<sup>9</sup> Moreover, multimode VCSEL emission is obtained for all laser sizes using double  $1/4\lambda$  thick oxide apertures due to much greater optical confinement.<sup>7</sup> Hence the tapered oxides produce reduced optical confinement, in spite of their larger thickness. In Fig. 3 we present typical single mode output powers from VCSELs with  $3.5 \times 3.5 \mu\text{m}$  apertures. The maximum single mode power is consistently found to be greatest for a single, tapered oxide with a thin tip located at a field null due to the minimum concomitant optical loss from the aperture. The loss is expected to be less for reduced number of apertures and thinner oxides.<sup>7</sup> In addition oxides which overlap field nulls, which minimally perturb the longitudinal fields, also exhibit reduced loss. To the best of our knowledge, the 3.5 mW fundamental mode power shown is the highest reported to date for GaAs quantum well VCSELs, and is of interest for applications requiring high single mode output.

In summary, a tapered oxide layer positioned at a field null produces reduced optical confinement and optical loss, in spite of large thickness, and maintains efficient electrical confinement. In this manner the optical and electrical confinement derived from the buried oxide can be decoupled for design of specific VCSEL performance, such as enabling high single transverse mode output power. Sandia is a multiprogram laboratory operated by Sandia Corporation, a Lockheed Martin Company, for the United States Department of Energy under contract No. DE-AC04-94AL85000.

## References

\*Dept. of Materials Science, University of Virginia, Charlottesville, VA 22903

- <sup>1</sup>D. L. Huffaker, *et al.*, Appl. Phys. Lett. **65**, 97 (1994).
- <sup>2</sup>K. D. Choquette, *et al.*, Electron. Lett. **30**, 2043 (1994).
- <sup>3</sup>K. D. Choquette, *et al.*, Appl. Phys. Lett. **66**, 3413 (1995).
- <sup>4</sup>K. L. Lear, *et al.*, Appl. Phys. Lett. **66**, 2616 (1995).
- <sup>5</sup>E. R. Hegbloom, *et al.*, Appl. Phys. Lett. **68**, 1757 (1996).
- <sup>6</sup>T. H. Oh, *et al.*, Appl. Phys. Lett. **69**, 3152 (1996).
- <sup>7</sup>K. D. Choquette, *et al.*, Appl. Phys. Lett. **70**, 823 (1997).
- <sup>8</sup>R. L. Naone, *et al.*, Electron. Lett. **33**, 300 (1997).
- <sup>9</sup>B. Weigl, *et al.*, Photon. Tech. Lett. **8**, 971 (1996).

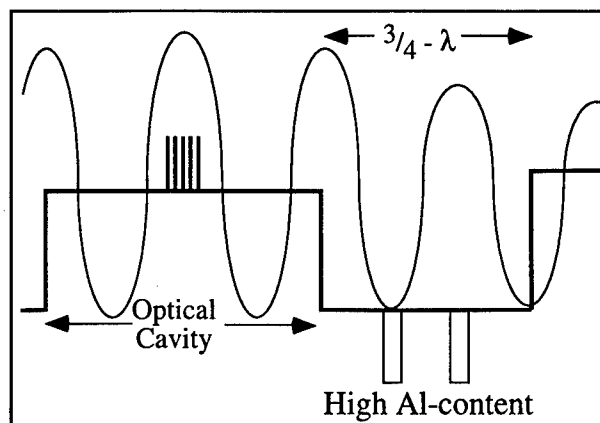


Fig. 1. Index and field intensity within a VCSEL with high Al-content layer at field null or antinode.

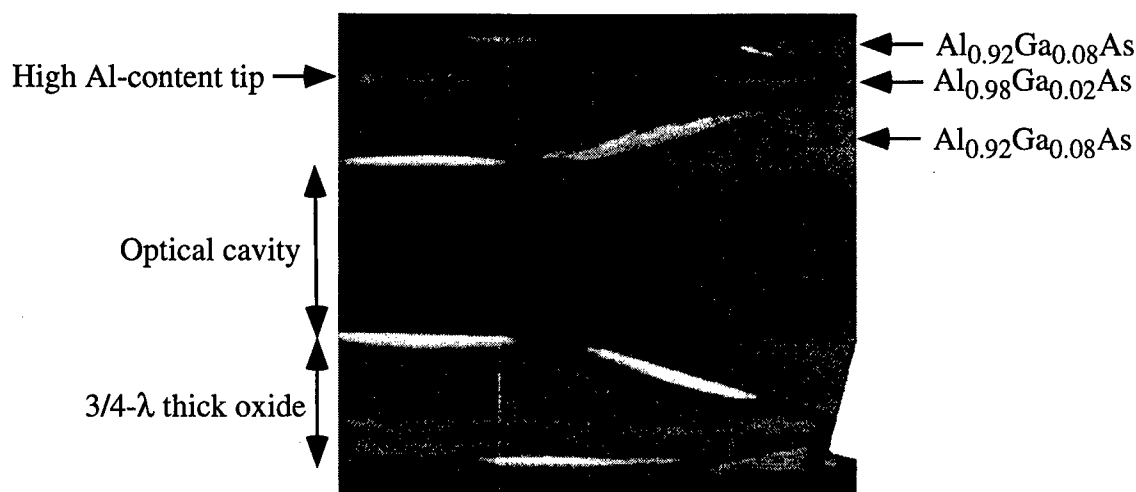


Figure 2. TEM cross section of  $3/4-\lambda$  thick buried oxide layers on each side of optical cavity showing oxide layer tips positioned  $1/2-\lambda$  from edge of cavity overlapping field antinode.

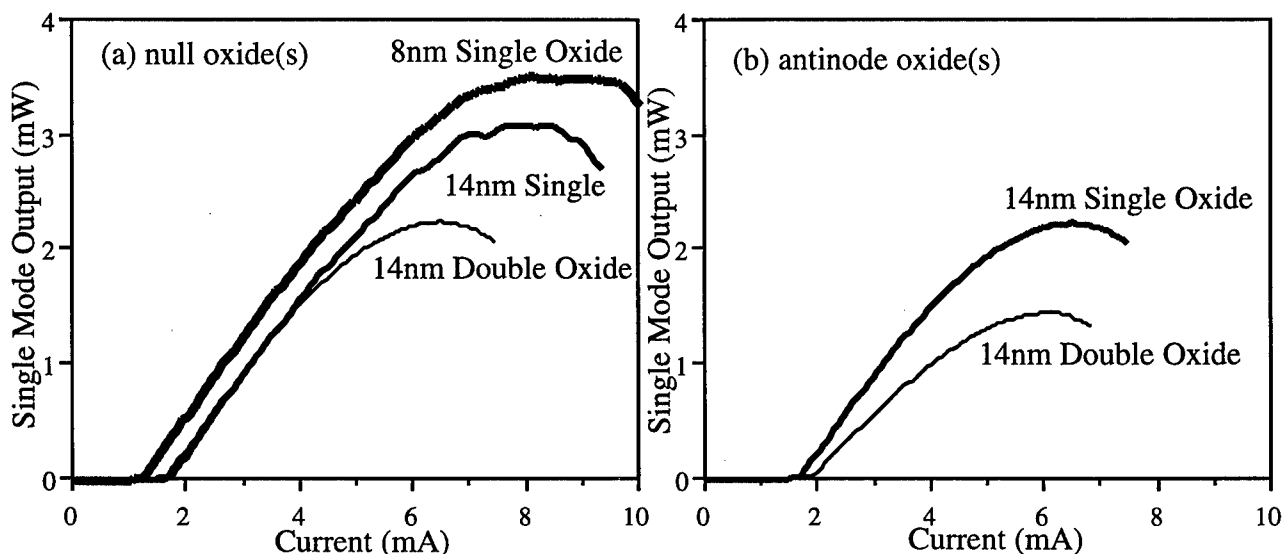


Figure 3. Single mode power from  $3.5 \times 3.5 \mu\text{m}$  VCSELs with oxide(s) at field: (a) null(s) or (b) antinodes (see Fig.2) on one or both sides of cavity with varying tip thickness (8 or 14 nm).



# Single-mode Vertical-Cavity Surface-Emitting Laser With Cavity Induced Antiguiding

T.-H. Oh, D.L. Huffaker, M.R. MacDaniel, and D.G. Deppe

Microelectronics Research Center

Department of Electrical and Computer Engineering

The University of Texas at Austin, Austin, Texas 78712-1084

e-mail : tchoh@mail.utexas.edu

Single-mode operation of vertical-cavity surface-emitting lasers (VCSELs) over a wide dynamic range is difficult to achieve with present device structures due to effects such as spatial hole burning and thermal lensing. This makes the introduction of antiguiding into the laser cavity of interest to increase the threshold discrimination between the lowest and higher order lasing modes. Elsewhere it has been suggested that a novel form of antiguiding may be possible in the VCSEL due to the high Q cavity by introducing a resonance red-shift in the cavity region outside the lasing area [1]. To our knowledge, the effect has not yet been clearly demonstrated experimentally in a VCSEL. Here we demonstrate a single-mode VCSEL structure based on the cavity induced antiguiding. The basic device structure may be suitable for many single mode applications, and potentially lead to the implementation of high power single mode VCSELs.

The schematic of the MBE-grown VCSEL structure is shown in Fig.1. On top of the 26 pairs of n-type AlAs/GaAs DBR are grown three 60Å thick In<sub>0.2</sub>Ga<sub>0.8</sub>As QWs inside a full-wave spacer. The antiguiding is accomplished through the introduction of a single, quarter-wave oxide layer into the upper DBR in the pumped region that blue-shifts the cavity resonance away from the as-grown structure. The quarter-wave oxide layer has a 10µm diameter and is formed by surface oxidation of 90% AlGaAs at the center of a 30µm diameter mesa. The use of a ring pattern in lithography ensures correct centering of the oxide mirror. The area under this oxide layer forms a high-Q cavity with its top mirror consisting of three pairs of GaAs/AlGaAs quarter-wave stacks, the quarter-wave oxide layer, and 4.5 pairs of ZnSe/MgF DBR. The oxide scheme maintains optical integrity (low scattering) between the lasing and antiguiding regions. Carrier confinement to the lasing region is accomplished by introducing a thin oxide layer (186Å) formed by lateral oxidation simultaneously with the quarter-wave mirror oxide layer to provide current funneling. The aperture formed by the thin oxide is slightly smaller (7 to 9µm) than the oxide mirror. In order to reduce its effect on the optical field, the thin oxide layer is placed at a node of the standing wave formed inside the cavity.

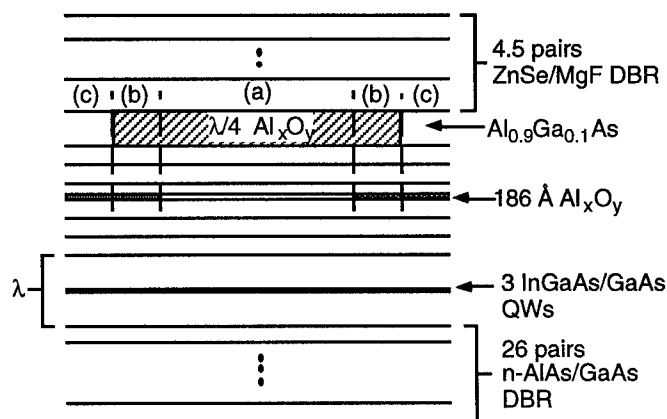


Fig.1: Schematic of the single-mode oxide-antiguided VCSEL

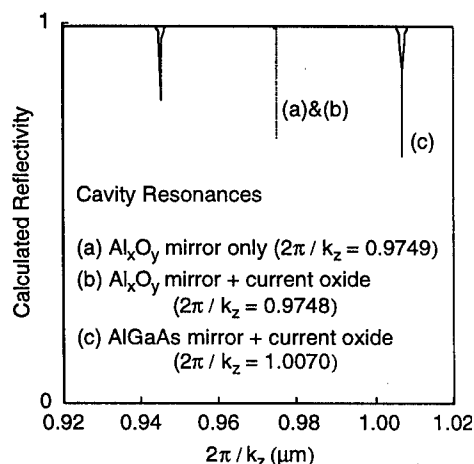


Fig.2 : Calculated cavity resonances at three different regions

There are three regions of interest for understanding the behavior of the device. Each region denoted by (a), (b), and (c) in Fig.1 forms separate resonant cavities with different oxide configurations. The calculated field amplitudes to determine the resonant vertical wavevectors,  $k_z$  (into cavity normals), versus wavelength for each cavity are shown in Fig.2, and determines the effect of the oxide layers on the eigenmode of the device [2]. The cavity in (a) has the quarter-wave oxide mirror layer only and becomes the lasing region. The cavity in (b) has the thin current confining oxide layer in addition to the quarter-wave oxide mirror layer. The cavity in (c) has the thin oxide only. Figure 2 shows almost no vertical resonance shift between regions (a) and (b) with the thin oxide placed at a node, with the vertical resonance occurring at  $2\pi/k_z \approx 0.975\mu\text{m}$ . However, between these regions and region (c) occurs a significant red-shift in the vertical resonance to the value of  $2\pi/k_z \approx 1.007\mu\text{m}$ , and that provides the cavity induced antiguiding. The vertical resonance at  $2\pi/k_z \approx 0.945\mu\text{m}$  is due to a higher order longitudinal mode of the cavity region (c).

Figure 3 shows the light versus current characteristics and far-field radiation patterns at three different current levels for a device with a  $10\mu\text{m}$  diameter for region (a). Although the operating range of this device is limited, from examining the near field we observe a significant antiguiding effect on the lasing mode in comparison to our more standard oxide-confined VCSELs. The threshold current is  $3.4\text{mA}$  with a differential quantum efficiency of 14%. We believe the relatively high threshold current and low slope efficiency are in large part due to an unintentional blue shift of the cavity resonances with respect to the gain peak that yields a lasing wavelength of  $\sim 940\text{nm}$ . A large electrical resistance limits the continuous wave (CW) operation beyond  $10\text{mA}$ . However this limitation is not simply due to device heating, since pulsed operation also shows a saturation of the light output at about  $10\text{mA}$ . We believe the limitation is due to leakage current turning on through the thin oxide region. At  $10\text{mA}$  the forward voltage is  $\sim 10\text{V}$ . Measurement of the far-field pattern shows lowest order mode operation throughout the operating regime, but with a slight broadening at higher currents. As with other VCSELs, thermal lensing will compete with the antiguiding to provide mode confinement. The near-field of the VCSEL is rather striking, with a near-field spot size of  $\sim 10\mu\text{m}$  diameter. The near-field remains stable and uniform throughout the operating range. Compared to a Gaussian approximation from the far-field radiation pattern, it appears that the antiguiding results in non ideal Gaussian mode behavior.

In summary, we present a device design that incorporates to our knowledge the first cavity induced antiguiding on the lasing mode. Compared to other oxide confined VCSELs of this size, the antiguided device shows a large area stable near-field of  $10\mu\text{m}$  diameter. We expect that once the resistance is reduced, the structure will show lowest order mode operation over a wide dynamic range. This work is supported by the Joint Services Electronics Program under contract No.F49620-95-C-0045.

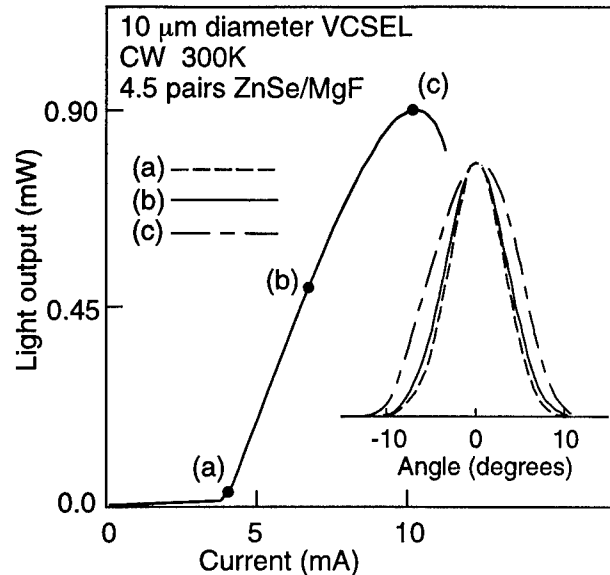


Fig.3 : Light versus current characteristics and far-field radiation patterns

- [1] G.R. Hadley, "Effective index model for vertical-cavity surface-emitting lasers," *Opt. Lett.*, vol. 20, pp. 1483-1485, 1995.
- [2] D.G. Deppe, T.-H. Oh, and D.L. Huffaker, "Eigenmode confinement in the dielectrically apertured Fabry-Perot microcavity," *IEEE Phot. Tech. Lett.*, vol. 9, (June, 1997).

WC4

2:30pm - 2:45pm

### Failure analysis of 850 nm proton-implanted VCSELs

Robert W. Herrick<sup>a)</sup>, Y. Michael Cheng<sup>b)</sup>, and Pierre M. Petroff<sup>c,a)</sup>

a) Dept. of Electrical and Computer Engineering, Univ. of Calif. Santa Barbara

b) Dr. Cheng was with the University of California. He now is with M/A COM.

c) Dept. of Materials, University of California, Santa Barbara, CA 93106

VCSELs are increasingly being adopted for use in data communications products, with numerous other applications being explored. Their low threshold current, circular beam, and excellent temperature stability are advantageous for many applications. While excellent lifetimes have been reported [1,2], lower early failure rates at high temperatures and high powers would be desirable, so we seek to better understand the aging process.

Our past work has shown that dislocations grow not only in the active region (as expected) but also in the p-DBR. This has been shown by cross-sectional TEM in totally degraded (non-lasing) VCSELs [3]. TEM on partially-degraded VCSELs showed no detectable dislocation networks. We have proposed that high-energy spontaneous emission from the active region (which is above the bandgap of the p-Al<sub>0.16</sub>Ga<sub>0.84</sub>As DBR layers) is a driving force for degradation in the p-mirror layers. In the past year, we have been concentrating on developing new techniques to allow us to examine the VCSELs in plan view, and explore the radial extent of the degradation.

These techniques have shown some surprising findings, with different analytical techniques giving very different results. Electroluminescence data has been taken, both from cross-sectioned VCSELs, as well as from VCSELs with a transparent contact, and shows (as expected) a dark area in the center, where the aging rate is highest due to high carrier densities during device operation. The contrast observed between the electroluminescence efficiency of the undegraded periphery and the degraded core is very high, as seen in Fig. 1. The square outer boundary seen in the plan-view image is determined by the deep isolation implant; the dark inner circle's size is determined by the (shallower) current confinement implant, which forces operating current through the center of the device, as shown in Fig. 2.

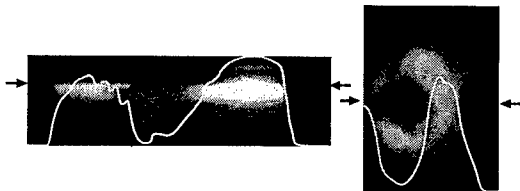


Fig. 1: Electroluminescence images from degraded VCSELs in cross section (left) and in plan view with a transparent contact (right). Line scans superimposed show intensity across line indicated by arrows.

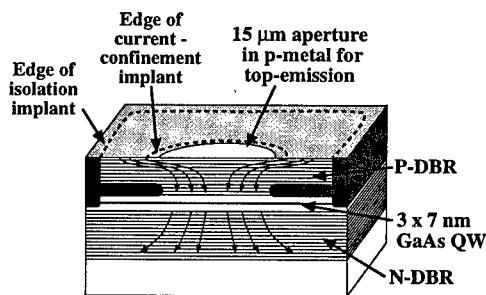


Fig. 2: Schematic of 850 nm proton-implanted VCSEL studied. Internal arrows depict current flow through the device.

Recently, we have studied degraded arrays of VCSELs in plan view by cathodoluminescence (CL). After rapidly aging different elements of the array by varying amounts using extreme currents (~80 mA), we polish off the substrate and most n-DBR layers. The remaining active region and p-DBR layers are then inspected by CL. Results were expected to be very similar to those shown in Fig. 1, which was degraded under

nearly identical conditions, but instead are dramatically different, as seen in Fig. 3. Virtually no difference could be detected between the luminescence of degraded and undegraded devices, either through monochromatic imaging, monochromatic linescans, or careful spectral comparisons. The inconsistencies between the EL and CL results are difficult, but not impossible, to reconcile. While the EL is affected by a number of different factors, including available current paths in the device, the CL measurement *directly injects* carriers into the active region, and is thus able to measure luminescence efficiency of the quantum wells directly, without being influenced by other factors. We are currently exploring the theory that dopant passivation in DBR layers near the lower central part of the p-DBR may be shunting current around the active region of our degraded devices [4]. Even without any degradation of the active region itself, substantially lower electroluminescence would still be observed in the center, as current was forced off to the sides. It is believed that if the devices were aged even further, formation of dislocation networks in the active region would eventually create a dark area in the middle. However, the results presented address the critical early part of the device failure process. Further experiments with scanning capacitance microscopy are planned to explore changes in the dopant profile as the device ages.

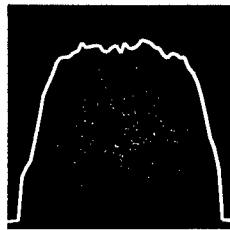


Fig. 3: Low-temperature cathodoluminescence image of deeply degraded VCSEL active region, taken at 825 nm. Note uniform luminescence, with no dark central area.

#### References:

- [1] J. K. Guenter, R. A. Hawthorne, D. N. Granville, M. K. Hibbs-Brenner, and R. A. Morgan, Proc. of SPIE (Fabrication, Testing, and Reliability of Semiconductor Lasers) **2683**, 102-13 (1996).
- [2] R. A. Hawthorne, III, J. K. Guenter, D. N. Granville, M. K. Hibbs-Brenner, and R. A. Morgan, 34th Annual Proceedings of International Reliability Physics Symposium, 203-10 (1996).
- [3] Y.M. Cheng, R.W. Herrick, P.M. Petroff, M. K. Hibbs-Brenner, and R. A. Morgan, 34th Annual Proceedings of International Reliability Physics Symposium, 211-13 (1996).
- [4] Personal Communication with James Guenter of Honeywell MICRO-SWITCH

WC5

2:45pm - 3:00pm

## Structural Dependence of the Thermal Resistance of Vertical Cavity Surface Emitting Lasers

K. M. Lascola, W. Yuen\*, and C.J. Chang-Hasnain

211-165 Cory Hall, EECS Department, University of California, Berkeley, CA 94720, USA

**Abstract** - Thermal effects are well known to limit peak output power and efficiency of vertical cavity surface emitting lasers (VCSELs)[1-3]. However, they are often disregarded in VCSEL design. In this work, using a simple thermal model, we consider the effect of device structure (both geometry and layer composition) on the thermal properties of VCSELs and verify the validity of the model by comparing with experimental results.

**Model** - The thermal model is implemented by modeling the time-independent heat equation (Poisson's equation) using finite difference techniques. In all cases, the VCSEL structure is assumed to be cylindrically symmetric. In order to simplify the calculations, individual VCSEL layers are not included in the model, but are replaced with an effective anisotropic thermal conductivity[1]. The substrate is assumed to be GaAs, 100  $\mu\text{m}$  thick, and 500  $\mu\text{m}$  in diameter. The bottom of the substrate is held at 300 K to simulate a heat sink and thermal radiation at the top surface of the device is also included. Three heat sources were assumed: one plane source in the active region, and one uniformly distributed source in each of the two DBRs. The relative distribution between the active region and the two DBRs varies depending on the cases simulated.

**Results** - Fig.1 shows a typical L-I, V-I measurement of a 950nm, 5  $\mu\text{m}$  oxide confined VCSEL under room temperature, CW operation. These lasers have  $\text{Al}_x\text{Ga}_{1-x}\text{As}/\text{GaAs}$  p-DBRs and  $\text{AlAs}/\text{GaAs}$  n-DBRs, and typically have  $R_d \sim 150 \Omega$  and a wallplug efficiency of  $\sim 15\%$ .

To verify the accuracy of the thermal model, pulsed lasing wavelengths were recorded as a function of heat sink temperature. The observed wavelength shift for these lasers was in the range .96-1.03  $\text{\AA}/\text{K}$ . The wavelength shift for different CW pump levels was then measured and used as an indicator of average temperature rise in the lasers. Fig. 2 (symbols) shows the measured temperature rise as a function of heating power for five typical lasers. The total heating power is taken as the input electrical power minus the output optical power. From this data, thermal resistances of 1211-1505 K/W were calculated. From the L-I, V-I trace the heat distribution between the active region and DBRs can be extracted. Further, assuming  $R_p = 3R_n$ , an average temperature is calculated using our model (Fig.2 - solid line). The calculated thermal resistance of 1174 K/W agrees well with the experimental results.

The effect of device geometry was next considered. Using the same layer structure as above, the post diameter was varied to simulate air-post (A-P), oxide-confined (O-C), and proton-implanted (P-I) VCSELs. The diameter of the post was assumed to be 5  $\mu\text{m}$  (the same as the heat source diameter), 90  $\mu\text{m}$ , and 500  $\mu\text{m}$ , respectively. An input heating power of 30 mW with a similar distribution to that of Fig. 2 was used. Posts were assumed to be etched just past the active region. Results are shown in Fig. 3. The air-post design is found to be much hotter than the oxide-confined and proton-implanted designs, due to the difficulty of lateral heat flow out of the post. Also, note the degeneracy of the curves for the proton-implanted and oxide-confined cases: although the oxide-confined laser also has a post, this post can be made large enough that its effect on the laser temperature is insignificant. Calculated thermal resistances were 2021 K/W and 1174 K/W for the air-post and oxide-confined/proton-implanted devices, respectively.

Lastly, the effect of layer composition was considered. Two 950nm devices with identical mirror reflectivities were modeled: one with  $\text{AlAs}/\text{GaAs}$  mirrors, and another with  $\text{Al}_{0.9}\text{Ga}_{0.1}\text{As}/\text{Al}_{0.15}\text{Ga}_{0.85}\text{As}$  mirrors. One 30 mW heat source is assumed to be present and confined entirely to the active region. Electrical resistance of the mirrors is neglected so that only differences in the thermal properties of these two structures are analyzed. Temperature profiles in the active region plane are shown in Fig. 4. Calculated thermal resistances were 1023 K/W and 1873 K/W for the binary and alloy mirrored structures, respectively. The increased thermal resistance of the alloy mirrored structure is due to the low thermal conductivity of  $\text{AlGaAs}$  alloys when compared to  $\text{GaAs}$  and  $\text{AlAs}$ . [4] This illustrates the dramatic effect that even a small amount of alloy can have.

\*also affiliated with Stanford University, Stanford, CA 94305, USA

- [1] M. Osinski and W. Nakwaski, *Int'l J. of High Speed Electronics and Systems*, vol. 5, pp.667-730.
- [2] T. Wipiejewski et al, *IEEE Photon Technology Letters*, vol. 8, pp.980-982.
- [3] G. Hadley et al, *IEEE J. of Quantum Electronics*, vol. 32, pp. 607-616.
- [4] M. Afromowitz, *J. Appl. Phys.*, vol. 44, pp.1292-1294.

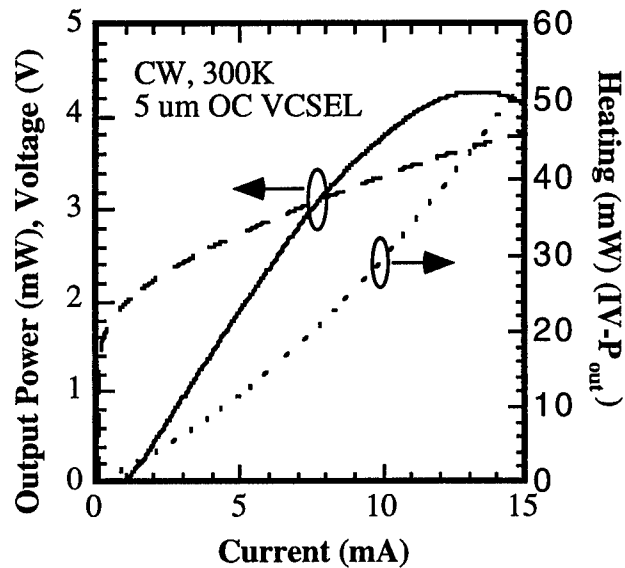


**Figure 1** - Measured L-I, V-I and heating power for a typical 950nm oxide confined VCSEL

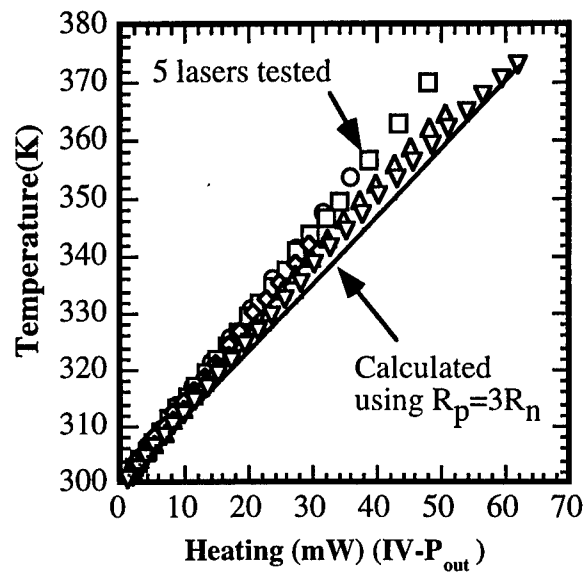


**Figure 2** - Observed (symbols) and calculated (solid line) average temperature rise for 950 nm oxide confined VCSELs.

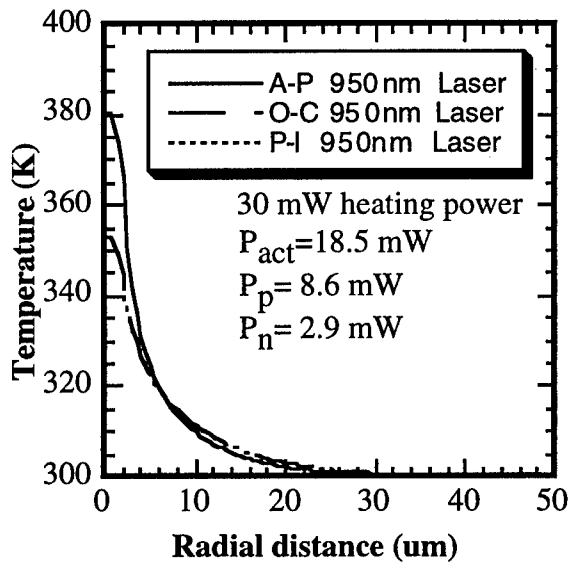


**Figure 3** - Temperature rise for air-post (A-P), oxide-confined (O-C), and proton implanted (P-I) VCSELs.

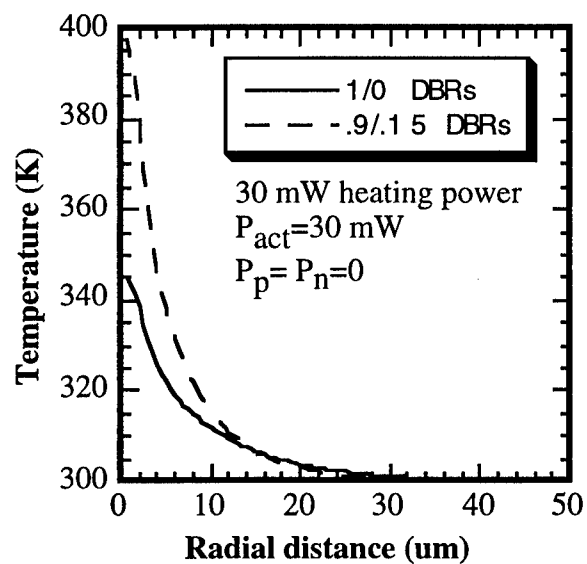


**Figure 4** - Temperature rise for two equivalent proton implanted VCSELs with different mirror compositions.

## AUTHOR INDEX

# AUTHOR INDEX

## **P**

Petermann, K.	WA2
Petroff, P.M.	WC4
Plais, A.	TuB4
Poussou, C.	TuB4
Pu, R.	MD2

## **Q**

Qian, Y.	TuB2
----------	------

## **R**

Rajkumar, N.	MD3
Reiner, G.	MB3
Rocher, A.	TuB4
Rosinski, B.	WA4

## **S**

Salet, P.	TuB4
Scott, J.	MD1
Shin, H.K.	MC2
Sotirelis, P.	WB4
Streubel, K.	TuB1, TuB3
Sugimoto, Y.	MA3
Swirhun, S.	MD1
Sys, C.	WB5

## **T**

Takahashi, M.	TuA2
Thibeault, B.J.	MB1
Thornton, R.L.	WC1

## **V**

Van Daele, P.	WB5
---------------	-----

## **W**

Wasserbauer, J.	MD1
Weigl, B.	MB3
Wesselmann, J.	TuB1
Wilmsen, C.W.	MD2, MD4

## **Y**

Yu, Y.K.	TuB2
Yuen, W.	MC3,
	TuA3, WB2, WC5

## **Z**

Zhu, Z.H.	TuB2
-----------	------



**1997 DIGEST  
of the IEEE/LEOS  
Summer Topical Meetings  
11-12 August 1997**

**Technologies For A Global  
Information Infrastructure**

**at  
*THE QUEEN ELIZABETH HOTEL  
MONTREAL, QUEBEC, CANADA***

**IEEE Catalog Number: 97TH8276  
Library of Congress: 97-70754**

The papers in this book make up the digest of the meeting mentioned on the cover and title page. They reflect the authors' opinions and are published as presented and without change in the interest of timely dissemination. Their inclusion in this publication does not necessarily constitute endorsement by the editors, the Institute of Electrical and Electronics Engineers, Inc.

Copyright and reprint permissions: Abstracting is permitted with credit to the source. Libraries are permitted to photocopy beyond the limits of U.S. copyright law for private use of patrons those articles in this volume that carry a code at the bottom of the first page, provided the per-copy fee indicated in the code is paid through the Copyright Clearance Center, 222 Rosewood Drive, Danvers MA 01923. Instructors are permitted to photocopy isolated articles for noncommercial classroom use without fee. For other copying, reprint or republication permission, write to IEEE Copyrights Manager, IEEE Service Center, 445 Hoes Lane, P.O. Box 1331, Piscataway NJ 08855-1331.

© 1997 by The Institute of Electrical and Electronics Engineers, Inc. All right reserved.

IEEE Catalog Number: 97TH8276

ISBN:	0-7803-3891-X	Softbound Edition
	0-7803-3892-8	Microfiche Edition

Library of Congress: 97-70754

Additional copies can be ordered from:

IEEE Service Center  
445 Hoes Lane  
P.O. Box 1331  
Piscataway, NJ 08855-1331  
Tel: (732) 981-1393  
Fax: (732) 981-9667



# **TECHNOLOGIES FOR A GLOBAL INFORMATION INFRASTRUCTURE**

## **Co-Chairs:**

Rod Alferness, *Bell Laboratories Lucent Technologies, Holmdel, NJ*

Peter Kaiser, *Consultant, Rumson, NJ*

Stephen B. Weinstein, *NEC C&C Research Center, Princeton, NJ*

Alan E. Willner, *University of Southern California, Los Angeles, CA*

## **Program Committee:**

Steve Finn, *MIT Lincoln Laboratories, Cambridge, MA*

Del Hanson, *Hewlett-Packard, San Jose, CA*

Manfred Huber, *Siemens AG, Munich, Germany*

Bertram Hui, *DARPA, Arlington, VA*

Paul Lagasse, *University of Gent, Gent, Belgium*

Yukuo Mochida, *Fujitsu Laboratories, Kawasaki, Japan*

Neal Ransom, *Bellsouth, Atlanta, GA*

Adel Saleh, *AT&T Laboratories/Research, Holmdel, NJ*

Kenichi Sato, *NTT Optical Network Systems Laboratories, Yokosuka, Japan*

Lawrence Seidman, *Hughes, Los Angeles, CA*

David Smith, *British Telecom, Great Britain, UK*

Gert Van der Plas, *Alcatel Telecom, Antwerp, Belgium*

# TABLE OF CONTENTS

## Monday, 11 August 1997

### **Session MA: Applications Drivers**

- MA1 The Internet: An Application Driver ..... (paper withdrawn)  
 MA2 Residential Broadband Internet Service Architecture ..... 3

### **Session MB: Network Strategies**

- MB1 The Impact of Gb/s Ethernet and ATM LANs in the Premises Network  
 Evolution ..... (paper not available)  
 MB2 Multimedia Communication and its Impact on Photonic Networking ..... 5

### **Session MC: Access Networks**

- MC1 Broadband Access Network Technologies and Strategies ..... 7  
 MC2 New Cable TV Network Strategies and Implementation Scenarios .. (paper not available)

### **Session MD: Switching Technologies**

- MD1 Digitally Programmable Wavelength-Switching Technology ..... 9  
 MD2 Counter-Mixing Mode Integrated Heterodyne Transceivers ..... 11  
 MD3 A Dynamic Dense WDM Network ..... 13

## Tuesday, 12 August 1997

### **Session TuA: Hybrid Systems**

- TuA1 Satellites in the World of Fiber Optics ..... 17  
 TuA2 Terabit Switching and Security Enhancement in a WDM/TDM Hybrid System ..... 20  
 TuA3 Integration of All-Optical Components for "Off ramp" Demonstration in 100 Gbit/s  
 TDM Access Node ..... 22

### **Session TuB: Optical Networking I**

- TuB1 Directions for High Capacity Optical Backbone Networks ..... 24  
 TuB2 Just-Enough-Time (JET): A High Speed Protocol for Bursty Traffic in  
 Optical Networks ..... 26  
 TuB3 Configuration and Performance for a WDM NAM Network ..... 28

### **Session TuC: Optical Networking II**

- TuC1 Issues in the Deployment of Optical Networks ..... 30  
 TuC2 Influence of Crosstalk on the Scalability of Optical Multi-Wavelength Switching  
 Networks ..... 32  
 TuC3 Performance of Wavelength Translation in All-Optical Cross-connected Networks ... 34

### **Session TuD: Transport**

- TuD1 Undersea Lightwave Networks ..... (paper not available)  
 TuD2 Effects of Optical Filter Drifts in Wavelength Division Multiplexing System with  
 Cascaded Optical Amplifiers ..... 36

# **TECHNOLOGIES FOR A GLOBAL INFORMATION INFRASTRUCTURE**

**Monday, 11 August 1997**

## **Sessions:**

- MA: Applications Drivers**
- MB: Network Strategies**
- MC: Access Networks**
- MD: Switching Technologies**

## **Monday Papers Not Available**

- MB1      “The Impact of Gb/s Ethernet and ATM LANs in the Premises Network Evolution”, *Nathan Walker, CISCO Systems, San Jose, CA*
- MC2      “New Cable TV Network Strategies and Implementation Scenarios”, *A.T. Futro, Futro Consulting Group, Golden, CO*
- 

## **Monday Withdrawn Papers**

- MA1      “The Internet an Application Driver”, *Don Heath, Internet Society, Reston, VA*

## Residential Broadband Internet Service Architecture

Timothy C. Kwok

Microsoft Corporation

*One Microsoft Way  
Redmond, WA 98052  
(206) 936-6755  
timkwok@microsoft.com*

### *Summary*

In 1995, while the much-hyped Interactive TV (ITV) market has faded, the Internet "phenomenon" suddenly took most people by surprise. Consumer interest in Internet access for browsing the World Wide Web has exploded. However, the current narrowband residential infrastructure using dialup (either POTS or ISDN) is slow, which led to the term "World Wide Wait." There is a clear pent-up demand for bandwidth to get much better user satisfaction. Proving high-speed Internet access has become the new driving force for deploying residential broadband (RBB) networks [1], which were originally envisioned for ITV.

Also, the circuit switched-based PSTN is very unsuitable for supporting the Internet access, which is a packet-based service. It is not atypical for online subscribers to tie up the telephone circuits for hours. By using packet-switched-based RBB networks, the PSTN infrastructure can be bypassed, which avoids a costly upgrade to circuit switching capacity to support the online dial-up access. Furthermore, such RBB networks can provide an always-on experience to the user, which has not been possible in the circuit-switched network (without adding significant capacity).

In this talk, I will present an end-to-end broadband Internet service architecture to enable a variety of new services for public network operators [2]. This broadband service architecture provides tremendous new business opportunities for public network operators, such as Web hosting, business solution providers and MIS outsourcing.

The residential broadband service model is based on a PPP over ATM architecture between the home or small business and the destination networks, which can be an ISP for Internet access or a corporate network for telecommuting. This also allows simultaneous access to both the corporate network and the Internet by having multiple VCs connecting to different networks. Moreover, it can provide quality of service guarantees and support multicast traffic by utilizing the ATM service capabilities. Furthermore, in addition to supporting TCP/IP, this also allows supporting other protocols such as IPX or Appletalk for accessing corporate network, because PPP support protocol negotiation between the home client and the destination network on a per PPP session basis. Finally, since many homes (especially those with online services) and small businesses have more than one PC and such ratio continues to increase, I will also explore the home network architectures to support multiple PCs.

## Reference

---

- [1] T. Kwok, "A Vision for Residential Broadband Services: ATM-to-the-Home," IEEE Network, Sept/Oct, 1995, pp. 14-28.
- [2] T. Kwok, *ATM: A New Paradigm for Internet, Intranets and Residential Broadband Services and Applications*, Prentice Hall, 1997.



## **Multimedia Communication and its Impact on Photonic Networking**

Ken-ichi Sato

NTT Optical Network Systems Laboratories

1-1 Hikari-no-oka, Yokosuka

Kanagawa, 239 Japan

Telephone: +81 468 59 3432, Fax: +81 468 55 1282

e-mail: kenichi@exa.onlab.ntt.co.jp

The recent explosion in Internet traffic implies the dawn of the multimedia age. Not only has the traffic volume of data communication increased, but also requirements for new service attributes are becoming more tangible.

One important attribute that any future broadband multimedia network must possess is flexibility. It can be realized by the logical realization of various transport functions. The key technology to enable this has been developed -- ATM. With ATM technologies, traffic with diverse bit rates, ranging from a few Kb/s to several Mb/s, and with diverse burstiness can be effectively processed in the network.

Another important attribute that must be developed is cost effective, bandwidth-abundant physical transport capability. The desire for quick content transmission, say one megabyte per mouse click, and for very cost effective transmission of MPEG 2 level data streams are but two examples. The first attribute urges the development of new transfer mechanisms. Cut-through transfer technology realized as direct connections among routers with virtual paths accompanied with a new addressing scheme that uses address servers in the network is one solution. This incurs at the expense of less efficient use of path capacity or decreased link utilization. To make future broadband multimedia services as ubiquitous as existing telephone services, an enhancement of the transport network capability is, therefore, necessary. In other words, broadband multimedia services will fully penetrate our society only after the desired attributes are completely realized.

The TDM point-to-point transmission capacity has been increased by more than one order of magnitude in this decade, and has recently reached 10 Gb/s for commercial use. The current progress in LSI performance does not suggest that the past trend in optical transmission speed increases can be extrapolated because the electrical bottleneck seems to be insurmountable above several Gb/s. Furthermore, traffic requirements between two nodes in a network are not always large enough to justify the introduction of the largest capacity transmission systems directly between the nodes. To maximally exploit this large transmission capacity, the accompanying development of cost effective access mechanism to the transmission system (called trans-access, hereafter), and effective grooming capability at nodes is indispensable to effectively share the large capacity.

What is happening in transport node technologies? ATM hardware can be realized with existing, or reasonable enhancements of existing silicon-based electrical technologies. This, however, makes the increases in transport node throughput (cross-connect/ADM) dependent on advances in semiconductor process technology, which cannot achieve the leaps in transport capability needed to create the cost-effective large-capacity networks mentioned above. Furthermore, the technology is not effective in providing large-capacity paths (trans-access paths) between arbitrary node pairs, since ATM cross-connection entails cell-by-cell switching at every cross-connect.

The optical path concept was proposed to resolve these problems. It offers quantum leaps in both transmission capacity and cross-connect throughput simultaneously by exploiting WDM transmission and the wavelength routing capabilities of paths. The transmission capacity expansion due to WDM and the commensurate increase in cross-connect throughput possible with wavelength routing enable flexible and cost-effective broadband networking.

The optical paths can be developed using the recent advances in photonic device technologies such as wavelength multi-/demultiplexers and space switches. For example, silica glass arrayed waveguide grating multiplexers, thermo-optic switches, and other functional devices have been demonstrated to offer excellent characteristics such as low loss, low cross-talk, and high reliability. A recently developed 8x16 delivery-and-coupling type matrix switch exhibited fiber-to-fiber average loss and crosstalk of 12.8 dB and 58.4 dB, respectively (the average loss includes the 8 x 1 coupling loss; the theoretical minimum is 9 dB). These devices have been utilized to create large-scale optical path cross-connect/ADM systems, and a 320 Gb/s throughput cross-connect system demonstrator has been successfully developed.

To develop robust and efficient networks utilizing these new technologies, new network architecture and network operation systems need to be developed. Graceful network introduction is also an important point to be considered. Therefore, a maximum commonality with already established SDH networks should be retained, and the techniques must be fully applied. As a result, optical paths should accommodate Virtual Containers (VC-4-16c, etc.), because this scheme enables very efficient and robust networking in terms of providing the networks with QoS monitoring capability of the optical layer and exploiting overhead processing LSI's already developed for SDH. New photonic network-node interfaces need to be created and standardized. Transparency is one of the important potential benefits of photonic networks, but it will not always be necessary. This is because more transparency lowers the robustness of the network since only rather limited performance measurement/monitoring capabilities such as optical power level measurements can be realized in a transparent network. Thus, the important thing is that different adaptation functions need to be developed in accordance with the client signals of the optical paths, or depending on the transparency required for the optical path, and choices should be available in network development.

Photonic network technologies will enable a network paradigm shift to bandwidth-abundant and ubiquitous multimedia networks. In order to accelerate their achievement, NTT will develop testbeds and perform field tests from 1998 to 2000.

## BROADBAND ACCESS NETWORK TECHNOLOGIES AND STRATEGIES

Gert Van der Plas

Alcatel Telecom, Research Division

Francis Wellesplein 1, B-2018 Antwerp, Belgium

Phone: +32 3 240 8923, Fax: +32 3 240 9932, E-mail: plasg@btmaa.bel.alcatel.be

Access networks have since the origins of the telephone, consisted of copper pairs designed for transmission of analogue voice signals. More recently, CATV operators have been installing coaxial cable networks, providing broadband unidirectional transmission of analog TV channels. Providing access to the 'information superhighway' for residential customers requires new technologies capable of improving the performance and capacity of these access networks.

Taking into account the broad range of network and service requirements, the broadband access network will develop via alternative paths during the following years. No single access network solution will fulfill the requirements from the various operators and a large portfolio of access network alternatives will be needed: optical systems (FTTC, FTTB, FTTH), twisted pair systems (ADSL, VDSL), Hybrid Fiber Coax systems and radio systems (e.g. LMDS, Hybrid Fiber Radio). Since the requirements for the upgrading of the access network are different for the various types of operators, alternative evolution scenarios can be outlined along three main paths. Each of these are characterised by a gradual penetration of optical fibre in the local loop. It is clear however that, unless major breakthroughs in the realisation of low cost OE components, full fibre penetration (FTTH) is not for the next 15 years.

### *1. Upgrade of twisted pair network*

The network upgrade scenario for twisted pair will be realised in several steps, where the penetration of optical fibre in the access network is increased and DSL modem technology is introduced:

- *ADSL: Asymmetric Digital Subscriber Line* is a first step towards the introduction of interactive broadband services for residential subscribers. Upgrading the network only requires the installation of ADSL modem equipment at both ends of the subscriber line. The bit rates considered are up to 6 Mbit/s downstream and up to 640 kbit/s upstream.
- *long-range VDSL (Very high speed Digital Subscriber Line)*: a next step in the evolution of the twisted pair access network is the introduction of optical fibre in the feeder part of the network, in order to reduce the range of the copper drop to 1 - 1.5 km (FTTSA - Fibre To The Serving Area). As a result, the transmission capacity can be increased up to 25 Mbit/s downstream and up to 3 Mbit/s upstream.
- *short-range VDSL*: a natural evolutionary step is bringing the optical fibre further to the subscriber, as a result of increased penetration and bandwidth requirements for broadband services (FTTC - Fibre To The Curb, FTTB - Fibre To The Building). Only the

final copper drop (last 300 m) is reused for transporting the broadband services into the customer premises.

- finally the last copper drop can be replaced with optical fibre, resulting in FTTH. This step can only be motivated by a reduction of the operations cost of the network.

## *2. Upgrade of CATV network*

New digital interactive services can be introduced on CATV networks either by fitting in between analog channels in accordance with the existing raster system or by occupying a number of analog channels, dependent of the selected modulation format and bit rate. As a CATV network is distributive, all channels will be broadcasted to all the customers connected to the network, which leads to a demand for a conditional access system (both for up- and downstream signals).

Large CATV networks will have to be broken up in smaller parts. The size of these is determined by the number of available digital channels in relation to the number of active customers of interactive services sharing the same part of the CATV network. The size of each sector of a CATV network must be reduced as the number of connected customers increases. Therefore optical fibre is introduced in the feeder part of the network, resulting in the construction of Hybrid Fibre-Coax (HFC) networks. Depending on the penetration of the optical fibre, different alternative configurations are possible: FTTSA (Serving Area) with an active coax drop network (range 500m - 1000m, 500 - 1000 homes passed) or FTTLA (Last Amplifier) with a passive drop network (range 200m - 300m, 20 - 120 homes passed). FTTH can be reached in the end, if it can be motivated by a reduction of the operations cost of the local loop.

## *3. Fast deployment with Wireless Local Loop*

Wireless access has gained wide acceptance for narrowband telephony services in recent years as a rapid deployment technology in emerging economies or rural areas. The use of wireless for delivery of broadband services has been limited up to now to terrestrial broadcasting (e.g. MMDS in 2 Ghz band) . New WLL systems operating at mm-wave frequencies will provide the required capacity for interactive broadband applications.

The range limitation inherent in millimetre-band propagation leads to a cellular distribution concept for these WLL systems. Similar to an HFC architecture using fibre optic trunks for data transmission down to the last amplifiers in the coax network and coaxial distribution beyond that point, a Hybrid Fibre-Radio (HFR) architecture can be considered that combines the advantages of both technologies. A fibre optic supertrunk running from the network head-end supplies the WLL distribution bases which provide broadband service delivery to the subscriber's home. Limited transmitter power is required and frequency reuse between cells is easier due to faster attenuation at higher frequencies. Optical millimetre-wave transmission is used on the fibre optic trunk, resulting in a simple and transparent ONU.

## Digitally Programmable Wavelength-Switching Technology

Jian-Yu Liu and Kuang-Yi Wu  
Macro-Vision Communications, LLC.  
5490 Conestoga Court, Boulder, CO 80301  
TEL: 303-939-0027, Fax: 303-413-9177

### Summary:

As the information flow in the fiber rapidly increased, dense wavelength-division-multiplexing (DWDM) technology becomes the ultimate solution in meeting the challenge of huge bandwidth demand. In this paper, we introduce a novel wavelength slicing concept that results a digitally programmable wavelength switch for the DWDM networks. The wavelength switch demonstrated not only achieves wavelength filtering and signal routing operations in one single compact device, but also provides superior performance based on its innovative architecture. Moreover, this concept provides a scale factor of  $\log_2 N$  for the controlling management, as the number of optical channel  $N$  is increased. This unique logarithm scaling relation will greatly simplify the hardware complexity to implement large-size WDM interconnection networks.

The conceptual device is shown in Figure 1, where a three-staged wavelength router is illustrated. The output spectra at each output ports are shown in the table I, with its corresponding control state. By simply control the three digital signal,  $C_0$ ,  $C_1$  and  $C_2$ , the eight output optical spectra are permuted as indicated.

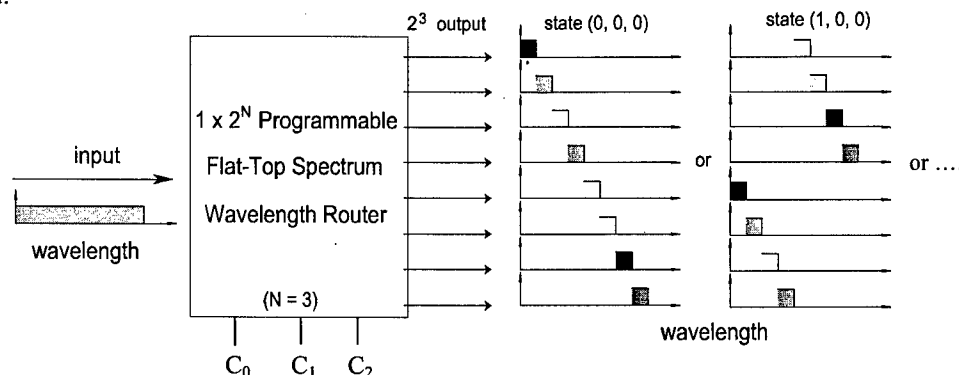


Figure 1. Diagram of the  $1 \times 2^N$  digitally programmable wavelength router.

Table I. Digitally Programmable Wavelength Switch Output

control state ( $C_0, C_1, C_2$ )	spectral response at ports (1, 2, 3, 4, 5, 6, 7, 8)	control state ( $C_0, C_1, C_2$ )	spectral response at ports (1, 2, 3, 4, 5, 6, 7, 8)
(0,0,0)	(1, 2, 3, 4, 5, 6, 7, 8)*	(1,0,0)	(5, 6, 7, 8, 1, 2, 3, 4)
(0,0,1)	(2, 1, 4, 3, 6, 5, 8, 7)	(1,0,1)	(6, 5, 8, 7, 2, 1, 4, 3)
(0,1,0)	(3, 4, 1, 2, 7, 8, 5, 6)	(1,1,0)	(7, 8, 5, 6, 3, 4, 1, 2)
(0,1,1)	(4, 3, 2, 1, 8, 7, 6, 5)	(1,1,1)	(8, 7, 6, 5, 4, 3, 2, 1)

\* The numbers are the optical channels appearing at that specific port.

In developing this wavelength router, we started with a simple concept that if an optical spectrum can be sliced into roughly equal amount of sub-spectra and be spatially separated, a function similar to a grating, it then forms the basic wavelength filtering with spatial separation. (Figure 2) If we now add some kind of controlling elements that can "move" these sub-spectra in between the output ports, then a "wavelength router" can be built. The word of "move" used here is to distinguish from the simple on/off

switch, because this then adds the new dimension of moving the spectra in space, instead of just turning on/off the spectrum at a fixed space position.

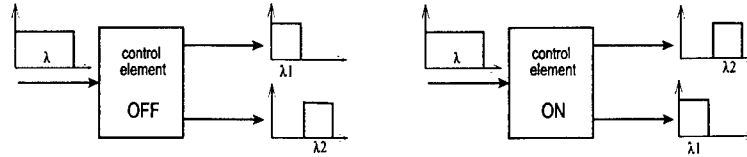


Figure 2. Block diagram shows the basic concept of wavelength slicing in space domain.

Based on this basic wavelength routing element, a second stage with narrower spectra can be cascaded in series to form a wavelength switch with an even narrower spectral response. In Figure 3, the spectra of a two-stage wavelength router is presented to illustrate this concept. From the divided four groups, it can be seen that with each controlling stage ON or OFF, the corresponding wavelength band are moved in between the output ports and permuted according to the control signals.

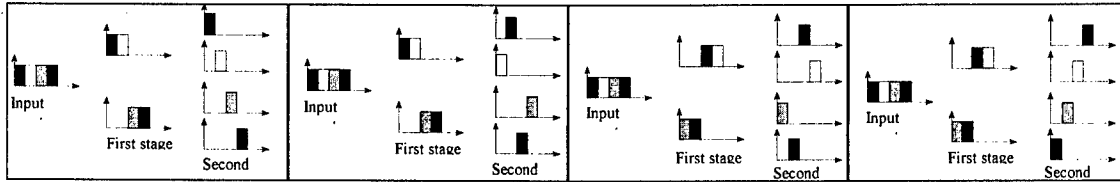


Figure 3. Spectral slicing of a two staged programmable wavelength router. With each of the controlling signal turns on and off, the spectra are moved from one to the other at the output ports.

The wavelength switch illustrated above is based on the cascading 1 x 2 structure. We have also developed a series of wavelength switches that can perform N x M reconfiguration. One of examples that performs the 4 x 10 wavelength switching is illustrated in Figure 4, where a 4 x 5 and a 5 x 10 wavelength switches are cascaded. In such as case, a simple two-digit control can route the desired wavelengths from one WDM network to the other or distributed as indicated.

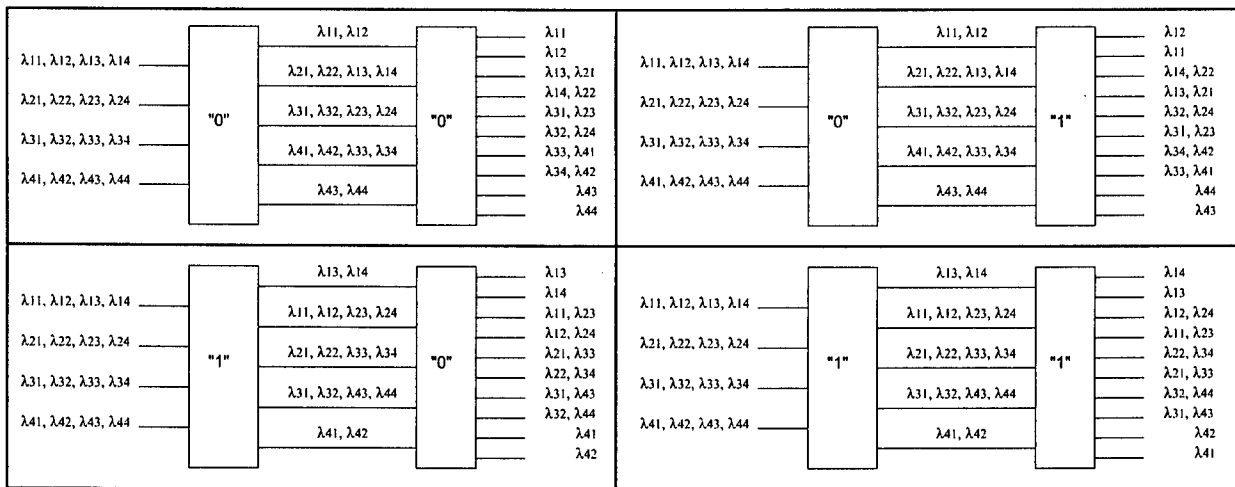


Figure 4. A 4 x 10 wavelength switch is illustrated with their wavelength distributions controlled by two simple control bit.

In the presentation, we will show the detailed experimental results. Currently, all the wavelength switches achieved have channel isolation of < -30 dB, insertion loss of < -3 dB, and switching times of 30 msec to 100 msec.

### Counter-Mixing Mode Integrated Heterodyne Transceivers

L.M. Wang, J.H.Chen, M.H.Shih, F.S.Choa

Department of Computer Science And Electrical Engineering

University of Maryland at Baltimore County

1000 Hilltop Circle, Baltimore, MD21228

e-mail: Liwang@engr.umbc.edu

T.Tanbun-Ek, P.wisk, W.T.Tsang, and C.A.Burrus\*

Lucent Technologies, Murray Hill, NJ 07974; \* Lucent Technologies, Holmdel. NJ 07733

The excellent receiving sensitivity, very high wavelength granularity and extremely flexible system reconfiguration capacity are unique advantages of coherent optical communications. Many works have been done in coherent optical communication systems with focuses on the designs of laser sources, receivers, frequency stabilization and implementation of distribution systems. However, to allow coherent optical communications technology for real applications, the integration of transmitters and receivers for full-duplex operations are worth of serious considerations.<sup>[1][2]</sup>

The structure and performance of this integrated transceiver and its multichannel operation characteristics were previously reported.<sup>[3][4]</sup> Basically, it is a 4-section device [gain(G), phase(P), grating(A) and detection(D)] with the Multi-Quantum-Well (MQW) active material. Figure 1 shows the detection schemes with signal and local laser output co-incident and counter-incident into the detector. In the co-incident case (Fig.1(a)), input signal passes through the local laser cavity and mixes with local beam in the detection section. Good mixing efficiency is expected in this way. However, the local laser is subject to the influence of the input signals. The laser cavity have to be specially designed to allow only one single below threshold mode<sup>[3]</sup> and to avoid side mode excitation by the incident multichannel signals. In the counter-incident (counter-mixing) case (Fig.1(b)), the input signal is coupled to the detector from the other side. The mixing efficiency is reduced. However, it is possible to relax the cavity design requirement of the local oscillator to obtain higher power and wider tunability.

Furthermore, it is much more convenient to achieve full-duplex operations with the counter-mixing scheme. For example, we can use FSK format for downstream and FSK or ASK/DPSK for upstream. In the FSK-FSK scheme, the upstream signal is modulated via the grating section of the transceiver while the downstream signal is demodulated with a frequency discriminator. The upstream signal is expected to be at much lower bit rate, so that it can be eliminated from the downstream signal by using a high pass filter. In the FSK-ASK/DPSK scheme, the upstream signal is modulated by a ASK/DPSK modulator which could be an integrated or external one. In this scheme the upstream signal is, in principal, totally independent of the downstream and they can use different bit rates. In both schemes the upstream and downstream channels are isolated from each other and the intrinsic 22 dB power penalty of full-duplex operation in reference [2] is avoided.

Two devices with detector lengths of 150  $\mu\text{m}$  and 80  $\mu\text{m}$  were tested in our experiment. The Bit-Error-Rate (BER) results are shown in Fig.2. A BER of  $10^{-9}$  with the shorter detector is obtained with received optical power of -32 dBm for 100 Mb/s with  $2^{15}$ -1 pseudo-random pattern with an estimated coupling loss around 5 dB. Compared with the co-

incident case, sensitivity degradation of 11 dB and 15 dB is measured with the shorter detector and longer detector, respectively. A simple model of the mixing efficiency based on exponential distributions of light intensity in the detection section is illustrated in Fig.3. The minimum sensitivity degradation is calculated to be only 2.7 dB for an optimized detector length at 40  $\mu\text{m}$  if we assume the quantum absorption coefficient of the MQW is 500  $\text{cm}^{-1}$ . The sensitivity degradation of devices used in our experiment is calculated to be 5.4 dB and 14 dB for detector lengths of 80  $\mu\text{m}$  and 150  $\mu\text{m}$ , respectively

In conclusion, a new detection scheme using integrated heterodyne transceiver with counter-mixing operation was experimentally investigated. A received power sensitivity of -32 dBm at 100 Mb/s was obtained. A simple theoretical model to optimize the receiver sensitivity was developed. Different full-duplex operation schemes were discussed. The counter-mixing mode heterodyne receivers could be a good candidate for broadband coherent access networks.

The authors acknowledge support from DARPA/AFOSR under grants F49620-96-1-0230 and F49620-95-1-0446.

- [1] T.L.Koch, F.S.Choa, *et. al.*, *IEEE Photon. Tech. Lett.*, vol.2, pp577-580, 1990;
- [2] R.A.Linke, K.C.Reichmann, *et. al.*, *IEEE Photon. Tech. Lett.*, vol.1, pp278-280, 1989
- [3] M.H.Shih, F.S.Choa, *et. al.* *LEOS'96*, TuS4, Boston, MA, Nov. 1996;
- [4] M.H.Shih, L.M.Wang, *et. al.*, *CLEO'97*, CWJ5, Baltimore, MD, May, 1997;

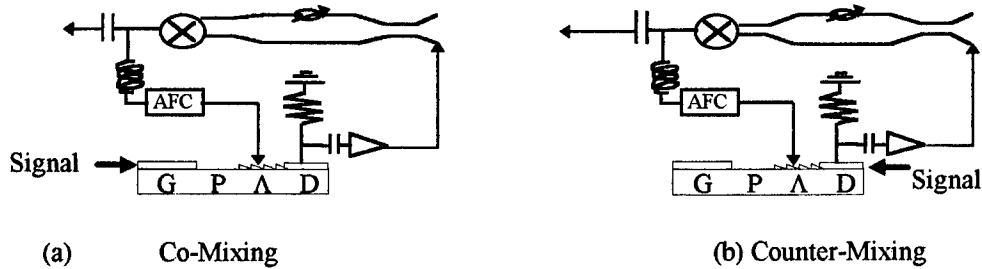


Fig.1 Heterodyne Detection Schemes with Signal Forward-Incident and Reversibly-Incident

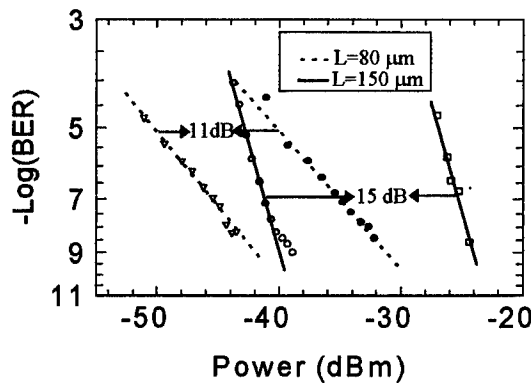


Fig.2 BER Comparison Between the Co-Mixing Scheme and Counter-Mixing for detectors with Lengths of 80  $\mu\text{m}$  and 150  $\mu\text{m}$ , respectively.

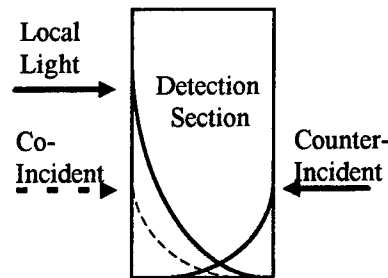


Fig.3 The Model of Light Distributions in the Detection Section



## A Dynamic Dense WDM Network <sup>1</sup>

*H. Jonathan Chao <sup>1</sup>, Fow-Sen Choa <sup>2</sup>, Mei-Hao Shih <sup>2</sup>, and Ti-Shiang Wang <sup>1</sup>*

Polytechnic University <sup>1</sup>, Department of Electrical Engineering

6 Metrotech Center, Brooklyn, New York 11201.

University of Maryland Baltimore County <sup>2</sup>

Department of Computer Science and Electrical Engineering

1000 Hilltop Circle, Baltimore, MD 21250

Multiwavelength optical networks using wavelengths routing have been recognized to be very attractive for the future B-ISDN and can potentially be used for the next-generation Internet to meet the demands for quality of service and bandwidth configurability. Wavelength conversion provides flexibility and reduces the blocking probability in the circuit-switched networks [1]. As a set of precious resources, wavelengths are used as carriers of information and have to be assigned properly to prevent two same wavelengths in the same fiber link.

Figure 1 shows a dense WDM network consisting of edge switches and backbone switches. The edge switch receives traffic from users, e.g., IP packets or ATM cells; the backbone switch performs the routing function through the wide area network. The interconnection of edge switches are made through the backbone switches via multiple virtual paths (VPs). Each VP is assigned a wavelength to carry the traffic between the edge switches. By using the coherent receiver [2], there can be up to 128 wavelengths on each fiber link; each carries 155 Mb/s bandwidth. The edge switches interface with user's various traffic and aggregate them into a number of VPs. Buffers are required at the edge switches to resolve contention among multiple connections in the same virtual path. When there is more traffic than the allocated bandwidth, the buffer will build up, which may trigger the edge switch to request more VPs to the destination edge switch. One should note that VPs can be allocated dynamically, depending on the traffic demand. The VPs allocation and their routing is performed in a distributed manner by the routing controllers in the backbone switches. The communications between different routing controllers is made through by a designated wavelength among the 128 wavelengths.

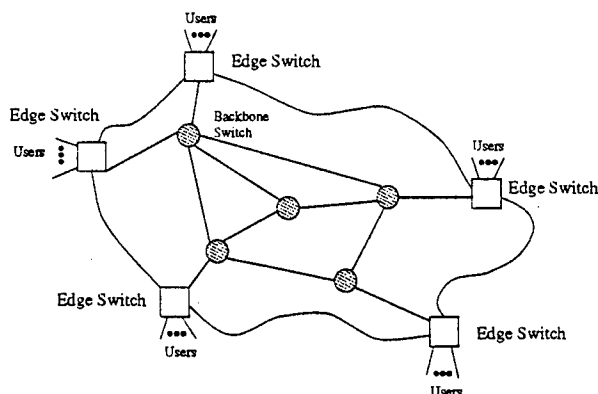


Figure 1: A dense WDM Network

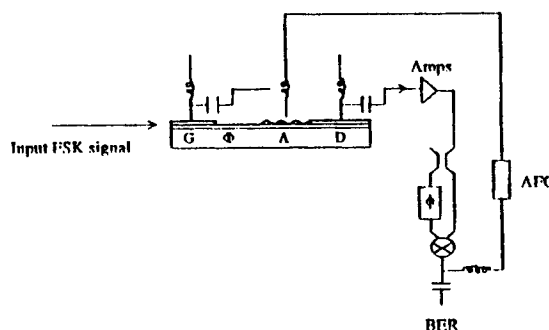


Figure 2: Integrated coherent receiver

Several different approaches of performing wavelength conversion function have been described in [3]. In this paper, the backbone switch performs the VP switching and the wavelength conversion in electronic domain. The backbone switch consists of wavelength demux/mux in line interface cards and a Clos-type circuit switch. The mux/demux function is implemented by using our recently developed low cost integrated coherent receivers [2]. As shown in Figure 2, the device has a very simple structure. The first three sections (gain, phase, and grating) form a tunable laser and an optical mixer. The mixed signal is extracted from the detector and sent to the following RF circuits, which can be mounted on a small circuit board. This integrated coherent receiver has a very high

<sup>1</sup>This research is supported by DARPA/AFOSR under grants F49620-96-1-0230 and F49620-95-1-0466.

receiving sensitivity of  $-43.4\text{dBm}$  when operating at 108 Mb/s. Multichannel experiment results show that a minimum spacing of 3 GHz per channel for 155 Mb/s bit-rate can be achieved with our devices [4]. By increasing the channel spacing to 5 GHz, we can operate more than five hundreds 155 Mb/s channels within the Er amplification band. The polarization issue is resolved by using a miniaturized in-line polarization combiner that includes a polarization splitter, a polarization rotator, and a combiner. It can eliminate the polarization drift noise at a price of  $\sim 3\text{dB}$  insertion loss which is acceptable with our high sensitivity receiver used in the system.

There are several advantages for the proposed dense WDM network. First, because of the fine granularity of each VP (155 Mbit/s), the bandwidth allocation can be more flexible and the optical link can have a higher utilization. It has been shown that the blocking probability in the WDM network reduces significantly as the number of wavelength increases [1]. For instance, the blocking probability can be as low as  $10^{-11}$  with expected number of hops of 20, the number of wavelengths of 128 and a traffic load of 0.8. Second, the proposed switching node provides data transparent. That is because the wavelength routing and conversion are implemented by using space-division switch and no clock recovery. As long as the bit rate is less than the speed that the electronic switch can handle, the data stream of each VP will be transparently routed to a different output link with a different wavelength. Therefore, the backbone switch doesn't need to know the bit rate, or the format of the data stream, which can be SONET, IP, ATM, or custom-designed transmission format. Third, the switch can be implemented with low cost by using newly developed coherent technology and electronic circuit switch. The switch fabric can easily be implemented with commercially available crosspoint chips ( $64 \times 64$ ) operating at 200 Mbit/s per port. A  $1024 \times 1024$  nonblocking switch network can be implemented with 128 such chips with a cost less than \$100,000. Since there is no clock recovery circuit, no synchronization among the incoming streams as SONET requires, nor detection of ATM cells or IP packets, the hardware complexity of the line interface card can be very low and thus the whole system's cost is low.

Since at the each backbone switch, there is no clock recovery and no data regeneration, the jitter may be accumulated along the path through multiple backbone switch. It is necessary to investigate how many backbone switches can be cascaded before the regeneration function is required. Note that the optical signal is converted to electronic and then converted to optical again. Its amplitude is amplified through the double conversions.

## References

- [1] R. A. Barry and P. A. Humblet, "Models of blocking probability in all-optical networks with and without wavelength changers," *IEEE JSAC*, Vol. 14, No. 5, pp. 858-867, June 1996.
- [2] M. H. Shih *et al*, "A very simple integrated coherent receiver with record high sensitivity," *IEEE Summer Topical Meeting, Broadband Optical Networks-Enabling Technologies and Applications*, Vol. , paper. MC4, pp. 28-29, 1996.
- [3] M. Kovacevic and A. S. Acampora, "Benefits of wavelength translation in all-optical clear-channel networks," *IEEE JSAC* , Vol. 14, No. 6, pp. 868-880, June 1996.
- [4] M. H. Shih *et al*, "Multichannel operating characteristics of integrated coherent receivers for optical networks ," *CLEO'97* , Vol. , paper. CWJ5, pp. , 1997.

# **TECHNOLOGIES FOR A GLOBAL INFORMATION INFRASTRUCTURE**

**Tuesday, 12 August 1997**

## **Sessions:**

- TuA:    *Hybrid Systems***
- TuB:    *Optical Networking I***
- TuC:    *Optical Networking II***
- TuD:    *Transport***

## **Monday Papers Not Available**

TuD1      “Undersea Lightwave Networks”, *Peter Runge, AT&T, Holmdel, NJ*

## **Satellites in the World of Fiber Optics**

**Wilbur Pritchard (Life Fellow IEEE)**  
**W.L. Pritchard & Co., Inc.**  
**7315 Wisconsin Ave**  
**Bethesda, MD 20814**

The telecommunications world is flourishing to an extent unanticipated even a decade ago. The proliferation of personal services, wide band distribution, video and audio broadcast, and just plain old telephone service has created demands on our transmission means, both quantitative and topological that we don't know how to meet.

We are familiar with the unique geometric advantages of satellites in providing mobile, broadcast and small terminal wide band services but we focus here on the advantages derivable from the constructive symbiosis of the two major means of electrical communications: satellites and optical fiber cables. Although these two altogether diverse technologies have been regarded as fiercely competitive developments in satellites systems and in particular the results gathered from theoretical and experimental work at Ka band and V band indicate that the situation has matured to where much can be gained by combining the two technologies operationally.

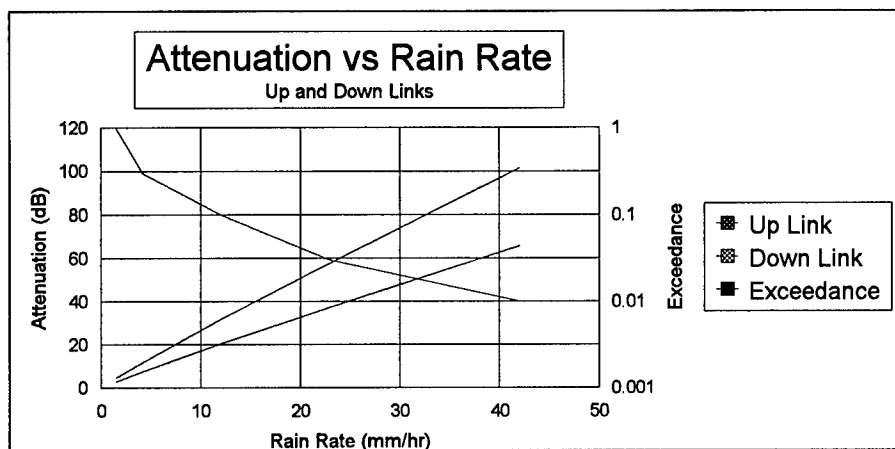
The importance of frequency bands higher than C and Ku bands for satellite communications had been identified back in the early seventies. The availability at the Ka and V bands (20/30 and 38/48 GHz) of wide spectrum allocation, the possibility of high gain antennas on board of modest size and the possible use of multiple hopping beams are attractive elements to the designers of future satellite. In addition it is clear that future satellites will be no longer simple transparent repeaters but rather repeaters with switching capabilities at R.F. as well as base band. There is still the problem of having to deal with rain induced attenuation. The experiments carried out in the United States with near Ka beacons on commercial domestic satellites, in Italy with the SIRIO satellite and with ACTS have been helpful in acquiring useful information about rain attenuation and techniques for counteracting it. The ACTS satellite has been unique, owing to its four 800 MHz wide transponders and its steerable. Compensation of fades due to rain have been effected by the combined use of convolutional coding, power margins of 6 and 15 dB respectively for the down and up links and adaptive data rate reduction. Efforts to use it in conjunction with Synchronous Optical Networks (SONETs) operating in the Asynchronous Transfer Mode (ATM) have been directed to developing equipment, algorithms, and protocols possible the seamless operation of satellites and optical cables.

It is entirely possible to design a satellite as an interconnecting facility among fiber terminals. Even the extremely high frequencies, with their rain attenuation can be used with very narrow beam antennas and high, but quite practical powers, to provide channel capacities adequate for fiber interconnection.

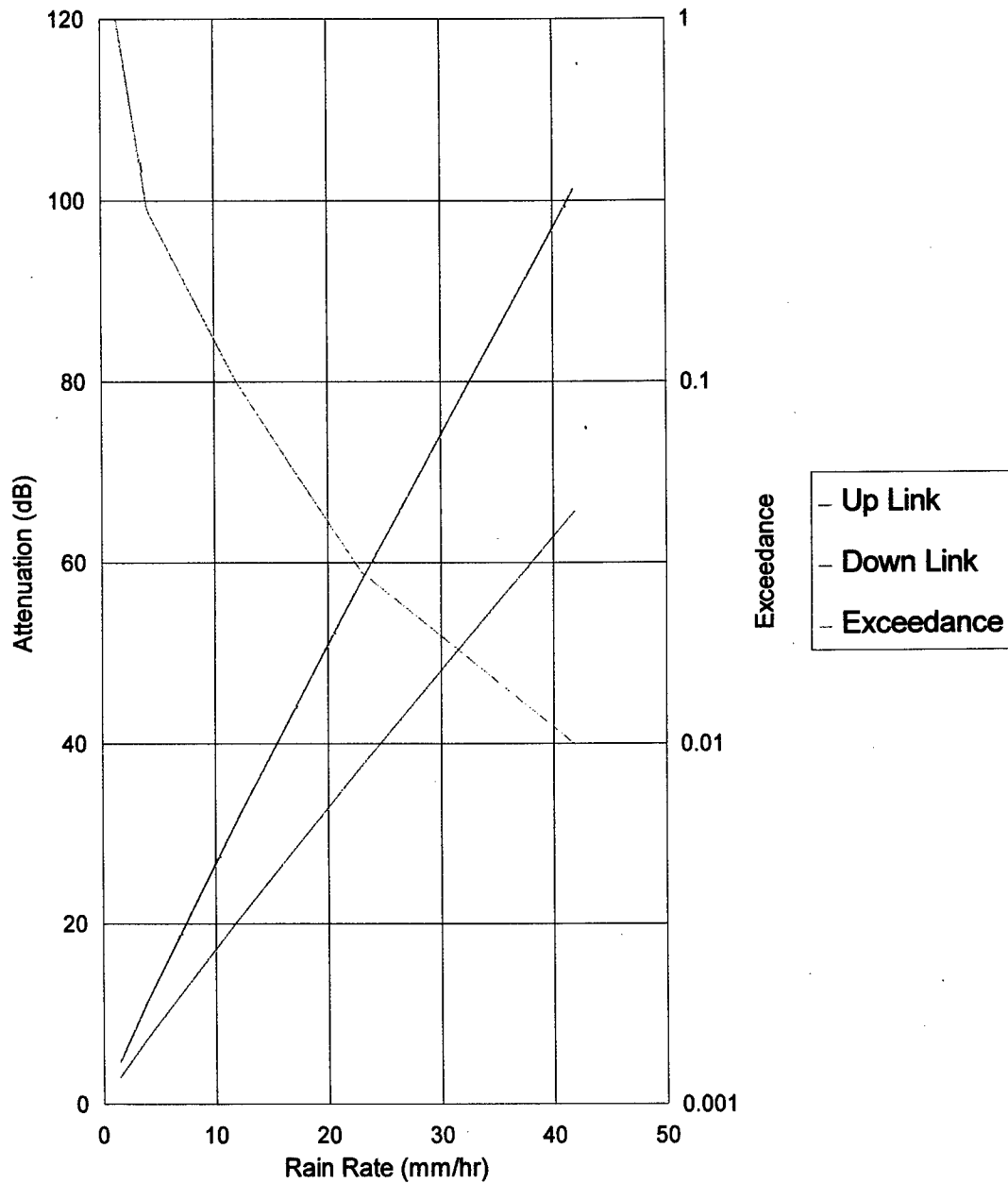
The sample link calculation shows a system at 48 GHz up and 38.5 GHz down with adequate margin for rain as plotted in the graph. Note that grades of service of 99.9 % are achievable.

## Ku Band

<b>TRANSMIT EARTH STATION</b>	Uplink Freq.(GHz)	48.50	48.50
	Trans. Antenna Diam.(m)	6.00	6.00
	Trans. Power (watts)	1000.00	1000.00
	Info Bit rate (Mb/s)	155.52	466.56
	Total QPSK Bandwidth (MHz)	186.62	559.87
<b>SATELLITE</b>	Antenna Size (m)	2.00	2.00
	Rec. Noise Figure	3.00	3.00
	G/T (dB/K)	30.65	30.65
	Uplink (C/N) dB	23.52	18.75
	Downlink Freq.(GHz)	38.50	38.50
	Trans.Power (watts)	200.00	200.00
	EIRP per channel	65.02	65.02
<b>RECEIVE EARTH STATION</b>	Receive Ant. Diam.(m)	6.00	6.00
	G(dBi)	65.81	65.81
	System Temp T(K)	423.67	423.67
	G/T (dB/K)	39.54	39.54
	Downlink (C/N) dB	14.12	9.35
	Uplink (C/N) dB	23.52	18.75
	Intermod (C/I)(dBHz)	40.00	40.00
	Composite (C/N) (dB)	13.64	8.87
	Info Bit rate (Mb/s)	155.52	466.56
	Misc Margin for clouds, gases, et	6.93	2.16



# Attenuation vs Rain Rate Up and Down Links



## Terabit Switching and Security Enhancement in a WDM/TDM Hybrid System

Cedric F. Lam and Eli Yablonovitch  
 UCLA Electrical Engineering Department  
 405 Hilgard Ave., Los Angeles, CA 90095-1594

### Summary

Development in the WDM technologies has made multi-wavelength optical sources and components available [1-3]. By combining WDM mux-demux and fast electro-optic switches, a fast configurable WDM add-drop filter can be obtained. This enables using WDM with TDM in a way that each TDM time slot is also wavelength multiplexed. Hence introducing a second dimension for switching in addition to the time dimension. This also alleviates the demanding requirement on TDM as the switching throughput increases.

The number of channels that can be supported in a WDM/TDM hybrid switching system is the product of the number of time slots and the number of available wavelengths. We have done preliminary analysis on the system throughput. It shows that switching with tera-bit throughput and capable of supporting ten thousands of channels at more than 100 megabit per channel bandwidth is possible. This will be important for supporting future bandwidth-hungry applications such as video on demand.

Using fast configurable wavelength add/drop filters, we can also design a spectrally encoded code division multiple access (CDMA) system [4] in which each channel transmits on a combination of different wavelengths to enhance the security. Encryption has been conventionally used to for secure communications. However, in time critical applications such as voice and video transmissions where the tolerance to delay is low, encoding method at the physical level is necessary to ensure the throughput and delay requirement.

Another possibility offered by fast configurable WDM add/drop filters is a fast wavelength hopped system. In stead of coding in the spectral domain only as in spectrally encoded CDMA, each user hops its wavelength from time to time to make eavesdropping of the signal difficult. As in conventional fast radio frequency hopped CDMA systems [5], each bit is divided into many chips and a different wavelength is used for each chip. Bit symbols of different channels are multiplexed using appropriate wavelength hopping patterns to minimize crosstalk. An example is the prime codes. In order to reconstruct the signal bits, the receiver hops in synchronous with the transmitter. By combining the wavelength dimension and time dimension coding, the security of the system can be made very high [6]. In addition, because of the use of multiple wavelengths in the system, the throughput will be much better than pure time-hopped CDMA systems.

We will present implementation considerations of the above described systems and give the comparison on the throughput and security sides.



## References

1. C. Dragone, "An  $N \times N$  Optical Multiplexer Using a Planar Arrangement of Two Star Couplers", IEEE Photonics Tech. Let., Vol. 3, no. 9, pp812-815, Sep. 1991.
2. "WDM and Optical Networking Mature", Optics and Photonics News, pp52, Dec. 1996.
3. I.P. Kaminow, et. al, "A Wideband All-Optical WDM Network", IEEE J. Sel. Areas Comm., Vol. 14, No. 15, June 1996.
4. D. Zacarrin and M. Kavehrad, "An Optical CDMA System Based on Spectral Encoding of LED", IEEE Photonics Tech. Let., Vol. 4, No. 4, pp479-482, Apr. 1993.
5. R.L. Peterson et. al, "Introduction to Spread Spectrum Communications", Prentice-Hall, New Jersey, 1995
6. L. Tancevski et. al, "Massive Optical LAN's Using Wavelength Hopping/Time Spreading with Increased Security", IEEE Photonics Tech. Let., Vol. 8, No. 7, July 1996.

## Integration of All-optical Components for "Off-ramp" Demonstration in 100Gb/s TDM Access Node

Y. Liang, T. J. Xia, K. H. Ahn, X. D. Cao, J. W. Lou, O. Boyraz, Y-H. Kao, S. Chaikamnerd  
and M. N. Islam

Department of Electrical Engineering and Computer Science  
The University of Michigan  
1301 Beal Avenue  
Ann Arbor, Michigan 48109-2122

We experimentally demonstrate the "off ramp" or drop function in a 100Gb/s TDM access node by integrating synchronized short pulse lasers, fixed word encoders, all-optical logic gates, demultiplexers and 2x2 packet routing switches. Our demonstration shows the inter-compatibility of the various optical components as well as the network functionalities of all-optical header processing and demultiplexing. Using an 8-bit, 100Gb/s word, we achieve a 10:1 contrast ratio from the header processor and demultiplexer and 17:1 contrast ratio from the packet routing.

A block diagram of the access node "off-ramp" is shown in Fig.1. An 8-bit packet (3 bit header '101', 5 bit payload '10100') is generated by the transmitter and sent to the node. The all-optical header processor selects the address and checks to see if the packet is empty (with INVERTER gate) or if it matches the local address (with XOR gate). If the address matches, a lithium-niobate ( $\text{LiNbO}_3$ ) switch routes the packet to the demultiplexer. The header processor and demultiplexer are powered by a local laser synchronized to the transmitter.

The components developed for the demonstration are as follows. Both lasers are passively mode locked, Er/Yb co-doped fiber lasers (EDFL's) producing 1.5ps pulses at 1535nm wavelength. A novel acoustic optical modulator (AOM)/grating scheme and a phase lock loop are used to synchronize the local laser to the incoming packet with a timing jitter of less than 1ps.[1] The cascaded, Boolean complete, all-optical logic gates are low-birefringent nonlinear optical loop mirrors (low-bi-NOLM)[2] with switching energies of 10pJ, timing windows of 5ps and nonlinear transmissions of 50%. The terahertz optical asymmetric demultiplexer (TOAD)[3] bit-rate down-converts the payload into individual bits with a switching energy of 1pJ and timing windows of 8ps. A commercial 2x2  $\text{LiNbO}_3$  modulator is used as the packet routing switch, and Nx1 couplers and delay lines are used to encode the fixed words.

The header processor output is detailed in Fig.2. The header is given in Fig.2a, while the INVERTER output is given in Fig.2b. The XOR gate output when the header matches (no match) the local address is given in Fig.2c (2d), which is detected and used to drive the packet router. The on-off contrast ratio after the cascaded gate is 10:1, which is limited by pulse distortion from erbium-doped fiber amplifiers (EDFA's) that lead to incomplete switching through degradation of the polarization extinction ratio.

The payload is routed to the demultiplexer for the match case of Fig.2c. The demultiplexed output for each channel is shown in Fig.3. For channels (1-4), the clock pulse is delayed to select the appropriate bit. Again, the contrast ratio is 10:1. The residual signals in the '0' bits indicates pump leakage and the energy tails from the adjacent '1' bit of the payload.

The output returning to the network from the  $\text{LiNbO}_3$  modulator is illustrated in Fig.4. When the header does not match the local address, the packet is routed undistorted. The contrast ratio compared with when the packet is sent to the demultiplexer is 17:1, which is limited by the electro-optic switch extinction.

These preliminary results show inter-compatibility of the all-optical components towards a TDM access node. The major challenges are in power budget, pulse distortion from EDFA's and long-term timing jitters. Our results prove that the timing window for the logic gates are wide enough to handle inter-laser jitter. For the 1.5 ps pulses used, however, dispersion and nonlinearity must be carefully checked.

In summary, all-optical processing is used experimentally for the 100Gb/s "off-ramp" part of a TDM network access node. The two cascaded low-bi-NOLMs have a switching energies of 10pJ and contrast ratio of 10:1 for the header processor, while the demultiplexer has a switching energy of 1pJ and contrast ratio of 10:1. The packet is routed with a contrast ratio of 17:1, which should prevent cross-talk with adjacent nodes.

This work is sponsored by DOD and DARPA.

## References

1. M.Jiang, et al., Opt. Lett., **21**, 1996, pp.809-811
2. X.D.Cao, et al., Opt. Lett., **21**, 1996, pp.1211-1213
3. J.P. Sokoloff, et al., IEEE Photon. Tech. Lett., **5**, 1993, pp.787-789

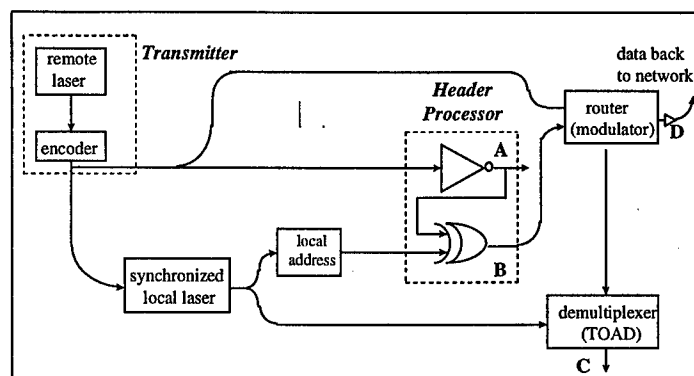


Fig.1 The "off-ramp" part in an access node consists of synchronized laser sources (EDFL's) with encoder and local address generators, the header processor (cascaded low-bi-NOLM logic gates), a router (LiNbO<sub>3</sub> modulator) and a demultiplexer (TOAD)

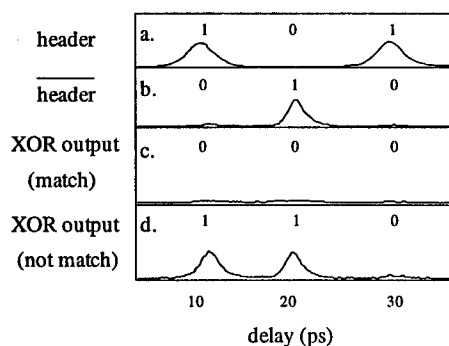


Fig.2 The results of the header processor. (a) the header (b) inverted header at point A in Fig.1. XOR output at point B in Fig.1 when (c) local address matches and (d) does not match with the inverted header.

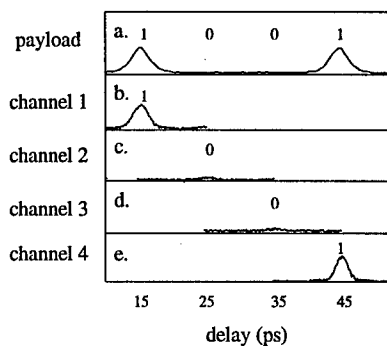


Fig.3 Demultiplexed output of TOAD with the payload shown in (a) and individual bits (b-e) from channel 1 to channel 4 at point C

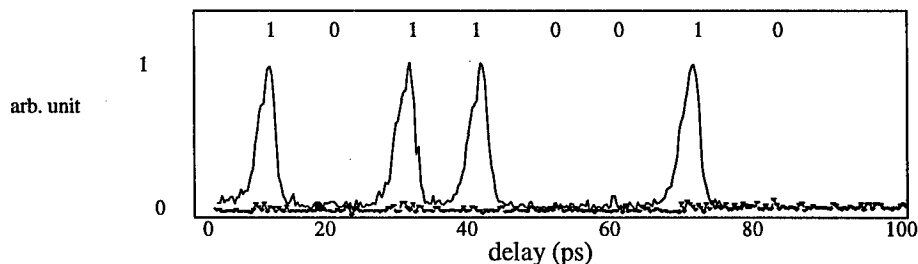


Fig.4 Output after packet router at point D in Fig.1. Dashed line: header matches local address (packet sent to demultiplexer), solid line: header does not match local address (packet back to network).

**Directions for High Capacity Optical Backbone Networks**

Joseph E. Berthold  
CIENA Corporation

The past year has been one of major change for the long-distance telecommunications infrastructure of the United States. Traffic demand has increased substantially, somewhat unexpectedly, prompting carriers to add capacity quickly and in the most cost-effective way possible. This growth in end-user demand is not driven by telephony, which continues to grow at several percent each year. In fact telephony network growth is inflated beyond the growth of voice because of the use of the telephony infrastructure for traffic which will soon migrate to the Internet, such as Fax. There is no sign that this increase is an anomaly, and both traffic and backbone capacity are likely to continue a rapid increase into the foreseeable future.

Traffic demand has increased primarily among business users who find data networking and information systems essential to the operation of a modern business. Information is increasingly composed of rich media, while it was dominated by text in the past. Internet technology enables a business to provide access to information to its employees and customers. There is a large growth in the bandwidth of private networks (Intranets), as well as the public Internet. Large business customers are increasingly requesting high bandwidth circuits, at rates of 155 Mbit/sec and 622 Mbit/sec where several years ago rates of 1.5 Mbit/sec and 45 Mbit/sec would have been adequate for their needs.

The growth of the capacity of public Internet backbones is driven in large part by the popularity of the World Wide Web. Internet backbone capacity is doubling every three to four months, resulting in a factor of 10 increase annually. At the time of this conference a typical Internet backbone link rate is likely to be 622 Mbit/sec. Six months later, in early 1998, it will be 2.5 Gbit/sec. While a few years ago the Internet was considered unimportant from the perspective of the total network traffic it generated, the day will soon arrive where it will be the dominant source of traffic for our communications infrastructure.

The change in the fundamental character of backbone network traffic will change the type of network equipment that supports the backbone in the future. The leaders of the data communications industry are not the same companies that lead the marketplace today in sales of telecommunications equipment, so one cannot extrapolate to the future by simply assuming the network element types deployed today will increase in speed and number to meet the capacity growth required in the future.

The two protocols which will dominate the backbone in the future are IP, the Internet Protocol, and ATM, Asynchronous Transfer Mode. While there is much speculation about which of these two protocols will dominate, it is likely that both will be important, and fill complimentary roles. Both IP and ATM equipment have made a great deal of progress in the total data throughput and port speeds. Both types of equipment are currently available with multiple 622 Mbit/sec ports, and are expected to be capable of

supporting 2.5 Gbit/sec port speeds in 1998. Aggregate throughput of commonly deployed IP routers today is 1 Gbit/sec, but a new generation of routers which exploit parallelism and incorporate switching technology will push their capacity by a factor of 20 to 40. ATM switches are commonly available with throughput of 5-10 Gbit/sec, and their throughput will increase to 100 Gbit/sec within the next few years.

In a data-centric network of the future it will be most efficient to aggregate and switch traffic in ATM switches and IP routers than it will be to aggregate and switch in telephony oriented equipment which was optimized for manipulation of signals at the lowest levels of the digital signal hierarchy, at 64 Kbit/sec, 1.5 Mbit/sec or 2.0 Mbit/sec. With data networking equipment capable of aggregating and grooming traffic to fill links that are already at speeds of typical fiber systems, there will soon be many situations where further circuit oriented multiplexing is not necessary to make efficient use of backbone transmission facilities.

What types of transport systems can best interconnect a network of IP routers and ATM switches with port speeds of 2.5 Gbit/sec? Three choices are multiple fibers, time division multiplexing and dense wavelength division multiplexing. The best choice will be dependent on the distances involved, the availability of additional fibers, and the suitability of the fiber for transmission of either high-speed or multiple wavelength signals.

What role will optical switching play? That of course depends on what optical switching can deliver, and at what price. One valuable role for an optical switch would be a fiber channel cross connect. To make it attractive to a network operator it would need to terminate a large fraction of the optical channels entering a network node. In the future even a relatively modest node could have several tens of fibers, each capable of carrying 40 wavelengths. Thus a capacity goal for an optical cross connect might be a thousand transport channels. If we assume a common channel bit rate is 2.5 Gbit/sec, this yields a switch fabric with a capacity of several Terabits/sec. This size is far beyond what appears to be technically feasible today.

## Just-Enough-Time (JET) : A High Speed Protocol for Bursty Traffic in Optical Networks

Myungsik Yoo & Chunming Qiao  
Department of Electrical and Computer Engineering  
State University of New York at Buffalo  
Buffalo, New York 14260  
{myoo,qiao}@eng.buffalo.edu

### 1. Introduction

As the bandwidth-distance product gets higher and higher in high-speed multi-gigabit networks, two issues, namely reducing latency and increasing link utilization, become increasingly important. In an all-optical network, once data enters the network, it is desirable to keep the data in the optical domain until it is delivered to its destination. With current optical technology, data cannot be buffered for an indefinite period without having to go through optical-to-electronic (O/E) and electronic-to-optical (E/O) conversions. A tell-and-go (TAG) [1, 2] protocol can reduce the pre-transmission delay associated with end-to-end reservations (e.g. in circuit switching), but if intermediate nodes do not buffer data, blocked data bursts are dropped, leading to a potentially high retransmission overhead when lossless communication is required. Deflection routing [2, 3] has been proposed as a way to reduce the retransmission overhead, but a data burst may have to be sent in several packets (or cells). It may also result in a low degree of data transparency (in terms of bit-rate, coding format etc.).

In this study, we investigate a high speed protocol called Just-Enough-Time (JET) based on TAG. It is suitable for bursty traffic where the duration of each burst is neither long enough to warrant circuit switching nor short enough to fit in a packet. The proposed JET protocol can efficiently utilize the bandwidth, reduce the latency and provide data transparency.

### 2. The Just-Enough-Time (JET) protocol

In a TAG protocol, a source node sends a control packet to set up a path. Instead of waiting for an acknowledgement from the destination, the data burst follows the control packet after an *offset-time*,  $T$ , and cuts through the intermediate nodes along the path [4]. For simplicity, let  $\delta$  be the processing delay of the control packet at each node, then  $T$  should be equal to (or larger than)  $\delta * H$ , where  $H$  is the total number of hops along the path. Assuming no blocking at any intermediate node, the latency may be roughly calculated as  $(t + p) \cdot H + T + d$ , where  $t$  is the transmission time of the control packet (which is negligible),  $p$  is the one-hop propagation delay, and  $d$  is the transmission time of the data burst. This latency is roughly  $2 \cdot p \cdot H$  shorter than that in circuit switching. It will be increased if there is a blocking and retransmission.

The proposed JET protocol has two features. One is *delayed reservation*, which reserves the bandwidth on each link just for the data burst duration. For example, let  $t_0$  be the time when the control packet, after being processed, tries to reserve the bandwidth at a node that is  $h$  hops away from the destination. Normally, the bandwidth is reserved from  $t_0$ . With delayed reservation, the bandwidth is reserved from  $t'_0 = t_0 + T$ , which is the time data burst arrives at this node, to  $t'_0 + d$ . This increases bandwidth utilization and helps reduce retransmissions.

Retransmissions can be further reduced by *postponing the arrival of the data burst*, which is the second feature of JET. Specifically, the control packet (and data burst) will be blocked if the bandwidth on the link, being occupied by another data burst, is not available until  $t_1 > t'_0$ . In JET, the control packet determines whether the local node can provide a delay of  $l$  to the data burst, which is at least  $t_1 - t'_0$ . If so, the bandwidth will be reserved from  $t'_1 = t'_0 + l$  ( $\geq t_1$ ) to  $t'_1 + d$ . Note that such delay of the data burst does not waste the link bandwidth, it only increases the latency, which may still be less than the latency involved in dropping and retransmitting the data burst. Thus, JET takes advantage of the optical delay lines, which are well suited for use as FIFO buffers in optical networks to provide limited delay to data bursts.

### 3. Simulation Results

We compare the performance of the JET protocol with the performance of the following TAG-based protocols: protocol 1 does not use delayed reservation but uses delay lines, protocol 2 does not use delay

lines but uses delayed reservation, and protocol 3 (conventional TAG) use neither delayed reservation nor delay lines. In addition, a protocol based on deflection routing, in which an entire data burst is deflected as if it is a super packet (but without pre-empting existing data burst), is also evaluated. We refer to this protocol as protocol 4, which may be considered as a variation of protocol 3 since it uses adaptive routing while all the other protocols use deterministic routing. These protocols are simulated by assuming a  $4 \times 4$  mesh where each link is 10 Gbps (there is no multiplexed channels on each link). It is also assumed that the duration of each data burst has an exponential distribution with an average of  $d$ , and the total delay available at each node is  $4d$ . Figure 1 shows the throughput versus latency for each protocol, where throughput is of each node.

As can be seen from the Figure 1, the maximum throughput of JET is about twice of that of protocol 3 (conventional TAG), and JET achieves a much lower latency for the same throughput than other protocols. The results also show that using either delay lines (protocol 1) or delayed reservation (protocol 2) alone does not lead to significant performance improvements. In addition, although protocol 4 performs better than protocol 3 under light traffic, its performance deteriorates as the traffic becomes heavy. This is because a deflected data burst causes other data bursts to be dropped, and wastes the bandwidth when itself is dropped eventually.

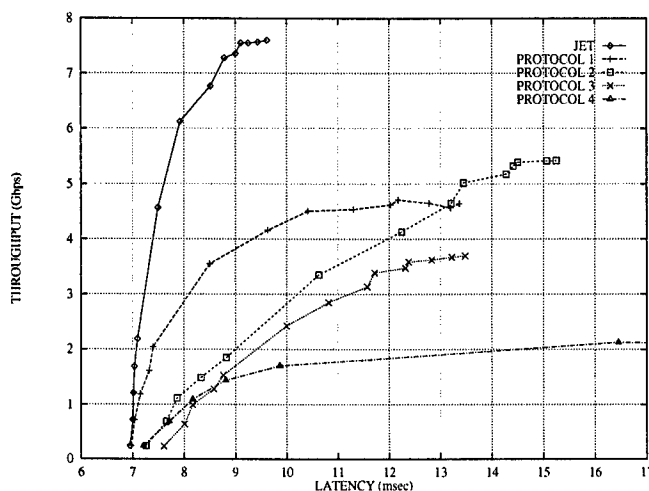


Figure 1: Throughput versus latency when  $d$  is  $0.25\text{msec}$ ,  $\delta$  is  $10\mu\text{sec}$ , and  $p$  is  $2.5\text{msec}$ .

#### 4. Conclusion and Further work

The proposed JET protocol results in a short latency and a high throughput for bursty traffic and is suitable for use as a high speed protocol in optical networks under distributed control. It improves traditional TAG-based protocol in two aspects : delayed reservation increases bandwidth utilization, and optical delay lines help reduce retransmissions. The effect of applying deflection routing and congestion control mechanisms to JET will be investigated in the future.

#### References

- [1] G. C. Hudek and D. J. Muder, "Signaling analysis for a multi-switch all-optical network," *1995 IEEE international conference in communications*, pp. 1206-1210, June 1995.
- [2] E. Varvarigos and J. P. Lang, "A novel virtual circuit deflection protocol for multigigabit networks and its performance for the MS topology," tech. rep., ECE Dept., UC Santa Barbara, Feb. 1996.
- [3] A. G. Greenberg and J. Goodman, "Sharp approximate models of deflection routing in mesh networks," *IEEE Transactions on Communications*, vol. 41, pp. 210-223, Jan. 1993.
- [4] P. Kermani and L. Kleinrock, "Virtual cut-through : A new computer communication switching technique," *Computer Networks*, vol. 3, pp. 267-286, 1979.

# Configuration and Performance for a WDM NAM Network

Adrian Grah  
Communications Research Centre  
Ottawa, Ontario K2H 8S2  
adrian.grah@crc.doc.ca

## Abstract

At the Communications Research Centre, in collaboration with Nortel and the National Research Council, an eight wavelength Network Access Module (NAM) is currently under development. Such devices can be deployed so as to form an opto-electronic, regenerative, broadband ring backbone network for ATM traffic. This paper reports on the impact of wavelength assignment on the number of add/drop lines required at each NAM when configured in a ring topology. Additionally, system performance in the absence of adequate media access control on the ring is examined.

## 1 Introduction

Once a subject solely of academic interest, Wavelength Division Multiplexing (WDM) is now becoming a commercially viable and anticipated technology for data communications. Point-to-point links, followed by Metropolitan and Wide Area Networks (MANs and WANs) will be among the first to benefit from the potentially enormous amount of bandwidth available in optical fiber. It is expected that the technologies enabled from such pursuits will eventually filter into the local area, bringing high bandwidth fiber to the desktop.

In the meantime it is necessary to develop high bandwidth WDM systems which efficiently allocate bandwidth where and when needed. Often addressed as a Routing and Wavelength Assignment problem (RWA), optimal solutions have been shown to be computationally demanding under a Lightpath continuity constraint [1]. The removal of the Lightpath continuity constraint greatly simplifies the problem which can be easily solved using banal algorithms.

NAMs are connected to one-another and utilize WDM to transmit independent bit streams, each over a specified wavelength. Each NAM provides a protocol independent "clear" channel, capable of transferring digital information at SONET rates up to OC-48. An interesting feature of these devices is their "transparency" to bit rates and protocol. At the heart of the box is a digital cross-point switch al-

lowing the connection of each output wavelength and drop line to any of the input wavelengths or add lines. Control is asserted by a host computer, possibly running a SNMP (Simple Network Management Protocol) agent, which connects to a NAM.

It is envisioned that NAMs will form a broadband backbone for use in an ATM environment. Figure 1 illustrates the use of NAMs as a backbone for an ATM network. Wavelength access can be configured on a per link, circuit switched basis, or on a shared, broadcast and select basis. The determination of network configuration involves a trade-off between bandwidth efficiency, fairness, add/drop line requirements, and the number of required wavelengths.

For the purposes of this paper, a Lightpath is defined to be a required connection between a source and destination. A link consists of a single wavelength on a physical fiber connecting adjacent NAMs in the ring. Each Lightpath is thus composed of one or more WDM links between a source and destination.  $L$  is the set of all Lightpath in the system. Each Lightpath configuration is a result of a solution for the RWA problem for this system and can be solved by the following simple graph coloring algorithm.

```

for each path,  $l$ , in  $L$ 
  for each link,  $k$ , in  $l$ 
    assign an unused wavelength,  $w$  on link  $k$  to
    path  $l$ 
    mark wavelength  $w$  on link  $k$  as used
  end
end

```

The simplicity of the above algorithm is a direct consequence of the availability of wavelength conversions at each NAM. It has been shown that the absence of wavelength conversions causes this problem to become NP-complete [1]. It is now a simple matter of translating the wavelength assignments into switch settings. In configuration A, full uniform connectivity is generated between four ATM switches configured in a ring topology by the above algorithm.

Two other configurations, B and C, which reduce the required number of drop lines through the use of a broadcast-and-select configuration, were also investigated for the same physical topology used in A.



Conf.	$a$	$d$	$W$	Cap.
A	3	3	6	12
B	1	3	4	4
C	2	3	4	8

Table 1: Network Configuration Summary

The idea is to exploit some degree of multicasting on selected Lightpaths. Since only cells with an appropriate VCI (Virtual Circuit Identifier) would be processed by any of the intermediate ATM switches, a single path can serve a number of connections which are sourced from the same node. The result is a reduction in the required number of wavelengths and add lines over that achieved in A. Table 1 summarizes the requirements of the three cases where  $a$  and  $d$  denote the number of add and drop lines utilized at a NAM and  $W$  is the total number of wavelengths required.

## 2 Performance

Computer simulations performed on the above configurations indicate results as expected. The first result is that network capacity is a strong function of the virtual topology and the degree of wavelength reuse achieved. For configuration A, an overall capacity of 12 times the bit-rate was found. With a constant backlog of packets for each destination ATM switch, configurations B and C result in a total capacity of 4 and 8 respectively.

Another measure of performance is mean delay which usually refers to the difference in time between the generation of a cell at a source, and its reception at a destination. For each of the proposed variations, queuing delay at an ATM switch can be represented as a simple M/D/1 system [2], scaled to account for a given amount of wavelength reuse. Results shown in Figure 2 depict the expected queuing delay at each ATM switch for the above configurations. Simulation

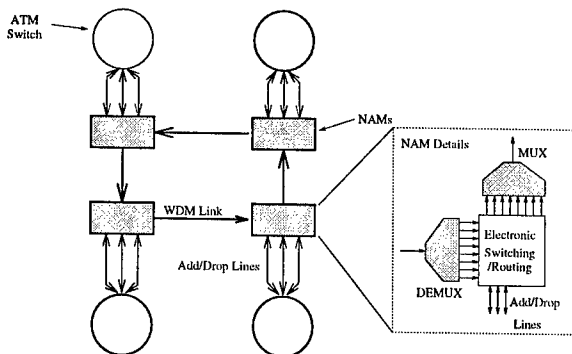


Figure 1: NAM/ATM Network Topology

results are indicated by discrete points. The results clearly show a marked capacity performance difference between the different configurations. Configuration C is particularly interesting from a hardware requirement/performance standpoint, and two scenarios were investigated. The first scenario was for a uniform traffic case and the second was for a skewed traffic case where an increased proportion of traffic was generated to stations immediately downstream of the transmitting station. These results thus give an indication of the traffic pattern dependency that various configurations will exhibit and their respective hardware requirements.

## 3 Conclusions

This paper examined the use of Network Access Modules building blocks for WDM backbone ring network for ATM. Three WDM network configurations were proposed requiring varying levels of hardware support. Results indicate that overall system performance will be limited not only by physical constraints, but on topological design.

The NAMs are currently in the assembly stage with 4 units expected shortly. Future generations of this NAM are expected to provide bi-directional links, improved performance monitoring, and diagnostics. Scalability of NAM networks will inevitably require a larger number of wavelengths or the implementation of some media access strategy to share in the available channel pool.

## References

- [1] Imrich Chlamtac, Aura Ganz, and Gadi Karmi. Lightpath communications: An approach to high bandwidth optical WAN's. *IEEE Transactions On Communications*, 40(7):1171-1182, July 1992.
- [2] Jermiah F. Hayes. *Modeling and Analysis of Computer Communications Networks*. Plenum Press, New York, 1984.

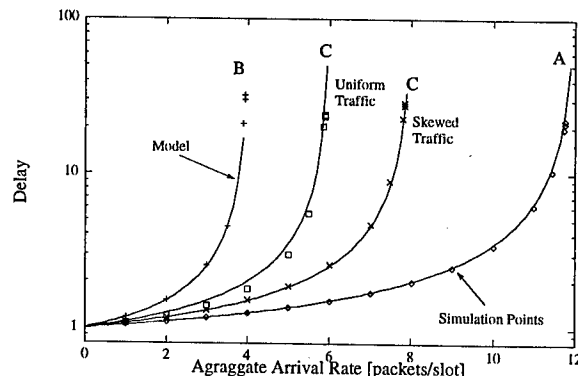


Figure 2: Queuing Delay Results: Cell Size 53 Bytes

## TuC1 (Invited)

1:30pm - 2:15pm

### IEEE Summer Topical Meeting: Technologies for a Global Information Infrastructure

Title: Issues in the Deployment of Optical Networks

Authors: Goff Hill, Alan McGuire and Ewart Lowe

Speaker: Goff Hill

#### Abstract:

WDM systems can be used to minimise the need for expensive cable and duct installations, to reduce transmission system costs and improve network resilience. However a number of compatibility issues need to be resolved before widespread deployment is possible.

#### Summary

European Telcos are designing broadband networks to deliver interactive multimedia services to business and residential customers and this is increasing traffic levels in core networks. Modern installations to date have used SDH transmission with single wavelength working, coupled with digital routing to provide a transmission layer able to support various switched platforms such as ATM, SMDS, Frame Relay etc. This is leading to increased pressure on cable and transmission resources and now more efficient utilisation strategies are needed if transmission costs are to be held down and broadband growth continue. Moves to meet this challenge by the use of high capacity WDM transmission systems and an optical network layer are now well under way in Europe.

In comparison, WDM is already a widely used technology in USA long haul networks where the cost benefits of cable resource sharing and of using a single optical amplifier to regenerate many transmission streams have revolutionised transmission technology. The majority of systems carried here on long haul routes are SONET OC-48 (2.4Gb/s) and soon OC192 (10 Gb/s), with little legacy PDH (or asynchronous) systems being carried. The unrelenting pressure to move to higher bit rates has produced a situation where the legacy PDH systems are not considered for transport over the WDM systems. In Europe, where the implementation of SDH has lagged behind the USA, a high proportion of the revenue generating traffic is still carried over PDH systems and will continue to do so into the next millennium. More significantly, the PDH platform does not have the inherent resilience features of SDH and is more vulnerable to cable outages. In these circumstances an underlying WDM platform with optical protection offers distinct benefits.

Looking to the future an optical network layer can also offer opportunities for network restructuring through its ability to provide very high capacity pipes between consolidated network nodes. For example, ATM signals are currently carried over either a PDH or an SDH transmission platform which could in turn be carried over WDM. Increasing traffic levels are leading to increased sizes of ATM switch. In turn this is likely to lead to the implementation of higher order STM interfaces which in principle could be supported directly over an optical channel. This immediately raises the question: is a separate SDH equipment platform needed in such a scenario? If the SDH platform was omitted, what additional functionality would be needed in the ATM platform to compensate for the loss of functionality provided by the SDH transport infrastructure? How would protection be implemented in such a new structure? By analogy IP routers could also offer optical channel interfaces.

How should an optical network platform be designed to enable the shorter term needs for more capacity to be met at an economical cost whilst still allowing a smooth progression to longer term network structures and technologies? One possible approach to WDM implementation suggests that WDM optical interfaces should be incorporated into SONET/SDH equipment (with wavelength specified transmitters to provide terminal WDM). This approach would involve close linkage of the WDM and SDH management layers and would not necessarily map in with the possible need to support PDH or for the possible future requirement to support other clients. A feature of optical networks that has often been discussed is their ability to offer transparency to signal format and bit rate (within some design limits). This flexibility can be exploited in optical network developments by treating optical elements as a separately managed network platform that is able to support different types of client such as PDH or SDH.

Many architectural variants become possible and a precise methodical description is needed. ITU-T Recommendation G.805 provides a suitable framework and its architectural principles show how a transport network can be decomposed into layer networks. The framework allows relationships between layers to be described and a set of functionalities to be associated with each layer. The approach has been applied to a number of technologies including PDH, SDH and ATM in ETSI and BT has developed a model for optical networks that is now the basis for much of the material in ITU-T draft Recommendation G.806. Three optical network layers are anticipated, (reflecting the 3 layers of

SDH networks). They include an optical channel layer which represents individual channel connections from transmitter to receiver, an optical multiplex section layer representing a multiplex of channels and an optical transmission layer which conditions the signal for transmission and defines the network node interface. This Recommendation, when completed, will be a key factor in shaping future optical networks.

In the UK, BT plans two pilot deployments of WDM with ranges 200km and 350km. In terms of UK geography, these represent long distance routes. The systems will support both existing SDH and PDH systems. They will be installed over diverse cable routes, feature 16 wavelengths and will include 1+1 optical protection switching. The WDM network will be managed by a standalone system which will provide optical channel and multiplex characteristics, performance management including thresholding, configuration management and event management, including alarm and status events. A key advantage of the approach taken is that no modifications are required to the existing PDH or SDH transmission equipment.

### **Conclusion**

WDM transmission is an attractive technology for medium to long haul, high capacity transmission systems. The addition of optical switching will improve network restoration capability following major cable outage and avoid the need to reconfigure large numbers of SDH and PDH tributaries, thus reducing the impact of a major incident. The pilot deployments being undertaken will help to build confidence and operational expertise in WDM technology.

### **Acknowledgments**

The authors would like to thank Jim Jackson, Dave Austin, John Wright and Ian Hawker for their support in producing this paper.

# Influence of crosstalk on the scalability of optical multi-wavelength switching networks

Lars Gillner, Claus Popp Larsen<sup>(\*)</sup>, and Mats Gustavsson

Ericsson Components AB, Fiber Optics Research Center, S-164 81 Stockholm, Sweden

(<sup>\*</sup>) also with L. M. Ericsson A/S, Denmark, and EMI at the Technical University of Denmark

**Abstract:** Regarding accumulation of interferometric crosstalk and noise, large all-optical networks (>10 nodes in diameter with 32 inputs/outputs per node and 32 wavelengths per fibre) should be feasible, given component crosstalk of about -30 dB.

**Introduction:** Optical networks are presently the subject of intense research, because it is anticipated that the use of wavelength division multiplexing (WDM) together with optical amplifiers and switches will provide networks with large data capacity, efficient traffic rearrangement possibilities, and relaxed network management requirements. One important aspect of optical networks is scalability, by which here is meant the changing of one or several of the network parameters, e.g., the number of WDM channels per fibre, and the resulting number of optical nodes that can be reached.

Serious restrictions on the size of meshed optical networks may be imposed by accumulation of interferometric crosstalk, see [1, 2, 3, 4]. In order to find the restrictions on network scalability set by crosstalk, this paper combines power budget calculations [5], the number of first and second order crosstalk contributions in an optical cross-connect (OXC) [3, 4], and a statistical model for interferometric crosstalk [4] to obtain the crosstalk requirements on optical space switches, multiplexers (MUXs), and demultiplexers (DMUXs). The crosstalk in all of these devices are assumed to be the same.

**Optical node architectures:** Fig. 1 shows an OXC node architecture for a meshed all-optical multi-wavelength switching network [3, 4, 5, 6]. The number of input or output connections to the node is  $N_f$  and the number of wavelength channels per fibre is  $N_\lambda$ . The OXC needs  $N_\lambda$  number of  $N_f \times N_f$  space division switches. From now on,  $N_f = N_\lambda = N$ , where  $N$  is referred to as the node size. This OXC can be configured in two fundamentally different ways [2, 3, 4]: Each switch routes channels of the same wavelength (configuration 1), or each switch routes channels of different wavelengths (configuration 2). Both configurations can be divided into two subcases: Either the signals are combined at the switch output using conventional power combiners, or wavelength multiplexers are employed. In [2], similar OXCs were analysed; however, only first order crosstalk

	Configuration 1		Configuration 2	
	First order	Second order	First order	Second order
PC	$2(N-1)$	$5(N-1)^2$	$2(N-1)$	$5(N-1)^2$
$\lambda$	$N-1$	$N(N-1)$	0	$3(N-1)$

Table 1: Total number of first and second order crosstalk contributions (suppressed once and twice, respectively) per node at the same wavelength as the main signal for different values of  $N$ . PC = power combiner,  $\lambda$  = wavelength MUX. From [3] for the special case  $N_\lambda = N_f = N$ .

was treated and second order crosstalk was ignored.

**First and second order crosstalk contributions:** The main result of [3] is shown in Table 1. Particularly interesting is configuration 2 with MUXs, because it completely lacks first order crosstalk, which is a very desirable OXC property. This is a consequence of the double filtering—by DMUXs and MUXs—in the node and the absence of two or more main signals of the same nominal wavelength in each space switch. In order for this architecture not to lose flexibility, the (D)MUXs have to be tunable; such devices have been demonstrated [7].

**Scalability calculations:** Starting from the power budget calculations in [5] in the absence of crosstalk to obtain the amplified spontaneous emission accumulation from the optical amplifiers, the statistical crosstalk model of [4] will be applied to the number of crosstalk contributions per node shown in Table 1 to give the total number of traversable nodes. The results will be for a bit error rate (BER) of  $10^{-12}$ . The statistical treatment of crosstalk introduces the (small) probability  $p$  that the BER is larger than a certain value, i.e., with this probability, the network will have worse BER than  $10^{-12}$ . Here,  $p = 10^{-5}$  which corresponds to failure times of 5 minutes per year.

For the power combiner architecture (configuration 1 or 2), the number of first order crosstalk contributions per node is  $2(N-1)$ , cf. Table 1, i.e., for  $N = 4, 8, 16, 32$ , the number of crosstalk contributions per node becomes 6, 14, 30, 62, respectively. This corresponds to the dashed lines in Fig. 2. The first thing to note is the very low required component crosstalk (below -40 dB). The second is how quickly the required component crosstalk decreases when the node size increases. Here, the number of traversable

nodes  $N_n = 10$  or 40 and the received average power of the main signal  $\bar{P}_0 = -10$  or 0 dBm. As it is difficult to experimentally reach below  $-40$  dB component crosstalk, this type of OXC node architecture will limit the all-optical network to only a few nodes in diameter.

For configuration 2 with wavelength MUXs, there are no first order contributions thanks to the double filtering at the node inputs and outputs, cf. Table 1, which will give much better transmission characteristics. The solid lines in Fig. 2 show how this network scales with node size. Both the required crosstalk and the scaling with node size is significantly better for this architecture. Here, the requirements are not unrealistic to fulfil (between  $-20$  and  $-33$  dB depending on node size, number of nodes, and signal power), which shows that this node architecture is scalable in the presence of interferometric crosstalk. If  $p$  is decreased from  $10^{-5}$  to  $10^{-15}$  (not shown), which corresponds to failure times of 32 ns/year, the crosstalk requirement is aggravated with less than 3 dB. Component crosstalk suppression below  $-30$  dB has been reported both for space switches with integrated semiconductor optical amplifier gates [8] and for arrayed-waveguide grating (D)MUXs [9]. Note that the calculations in this paper assume that, e.g., fibre dispersion and non-linearities do not limit the networks, which is seldom true in a real system.

**Conclusions:** The influence of interferometric crosstalk on the scaling properties of meshed optical WDM networks has been examined. It was shown that optical cross-connect node architectures, which suppress all first order crosstalk contributions, were necessary in order to give crosstalk requirements on multiplexers and space switches that are realistic to fulfil given current state of the art devices. From the interferometric crosstalk point of view it should be possible to construct a fairly large all-optical network (more than 10 nodes in diameter with 32 inputs/outputs per node and 32 wavelengths per fibre) if the component crosstalk [switches and (D)MUXs] is about  $-30$  dB.

This work was partly supported by the ACTS project METON (AC073).

## References

- [1] C. P. Larsen, L. Gillner, M. Gustavsson, *Photonics in Switching*, paper PMB4, Sendai, Japan, April 1996.
- [2] J. Zhou, R. Cadeddu, E. Casaccia, C. Cavazzoni, M. J. O'Mahony, *J. Lightwave Technol.*, vol. 14, pp. 1423–1435, June 1996.
- [3] C. P. Larsen, L. Gillner, M. Gustavsson, *Photonics in Switching*, paper PWA4, Stockholm, Sweden, April 1997.
- [4] M. Gustavsson, L. Gillner, C. P. Larsen, *Photonics in Switching and Europ. Conf. Integr. Opt.*, plenary paper JWA4, Stockholm, Sweden, April 1997.
- [5] L. Gillner, M. Gustavsson, *IEEE J. Select. Areas Commun.*, vol. 14, no. 5, pp. 952–961, June 1996.

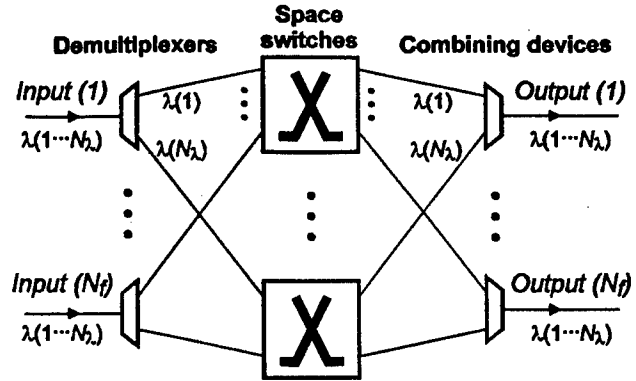


Figure 1: Schematic representation of an OXC node for a meshed multi-wavelength network [6].

- [6] G. R. Hill et al., *IEEE J. Lightwave Technol.*, vol. 11, no. 5/6, pp. 667–679, May/June 1993.
- [7] J.-P. Weber, B. Stoltz, O. Öberg, *Europ. Conf. Integr. Opt.*, paper EThE5, Stockholm, Sweden, April 1997.
- [8] C. P. Larsen, M. Gustavsson, *Optical Fiber Communication*, paper TuC2, Dallas, TX, USA, February 1997.
- [9] K. Takada, H. Yamada, Y. Inoue, *Electron. Lett.*, vol. 31, no. 14, pp. 1176–1177, July 1995.

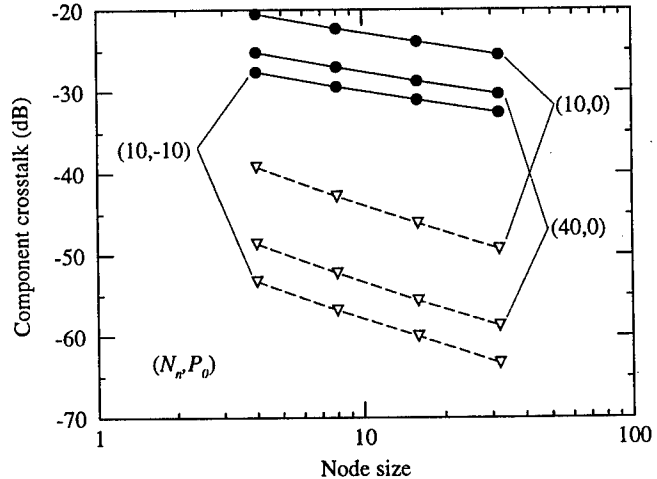


Figure 2: Calculated required component crosstalk as function of node size,  $N$ , with number of traversable nodes,  $N_n$ , and received signal power,  $\bar{P}_0$ , (in dBm) as parameters at 10 Gb/s.

*Dashed lines:* Configuration 1 or 2 with power combiners, i.e.,  $2(N - 1)$  first order crosstalk contributions per node. *Solid lines:* Configuration 2 with wavelength MUXs, i.e.,  $3(N - 1)$  second order crosstalk contributions per node.

# Performance of Wavelength Translation in All-Optical Cross-connected Networks

G. A. Castanon, O. K. Tonguz and A. Bononi<sup>1</sup>.

**Abstract**— The teletraffic performance of regular two connected multi-hop datagram optical networks in uniform traffic under a combination of wavelength translation routing and hot-potato routing is presented. Manhattan Street (MS) Network and ShuffleNet (SN) are compared in terms of average propagation delay and throughput.

## I. INTRODUCTION

This paper analyzes the steady-state behavior of two connected mesh *packet-switched* optical networks under wavelength translation. We present the limit of operation based on a uniform traffic scenario. We introduce an optimized wavelength translation routing algorithm that minimizes the probability of packet deflection. We analyze wavelength translation assuming that packets in transit have translation priority over new locally generated packets. Packets are wavelength translated in the case of local conflict to an available slot in an output wavelength to avoid deflection, otherwise packets will transparently traverse the node. In case of local conflict, but no available alternative slots, one packet is randomly chosen for deflection instead of being dropped.

The teletraffic performance of *circuit-switched* all optical [1], [2] and electronic (regenerative) [3] wavelength translation has recently been reported. However, the teletraffic performance of *packet-switched* wavelength translation with deflection routing has not been reported yet.

## II. NODE STRUCTURE

The node is composed of a stack of submodules, one per wavelength. Fig. 1 shows the architecture of the wavelength translation node. All the submodules are interconnected and there is a central control unit which decides absorption, translation, injection of a new packet, and routing operations. The wavelengths from the input fibers are spatially demultiplexed and sent to the appropriate submodule. Packets from the submodules are finally re-multiplexed onto the output fibers. The logical flow of submodule operations is *absorption*, *translation* to a receiving wavelength, *electronic translation/injection* of a new generated packet, and *routing*.

<sup>1</sup>G. A. Castanon, O. K. Tonguz are with the Photonics Research Laboratory, Department of Electrical and Computer Engineering, State University of New York at Buffalo, Buffalo, NY 14260, USA  
A. Bononi is with Dipartimento di Ingegneria dell'Informazione Università di Parma, I-43100 Parma ITALY

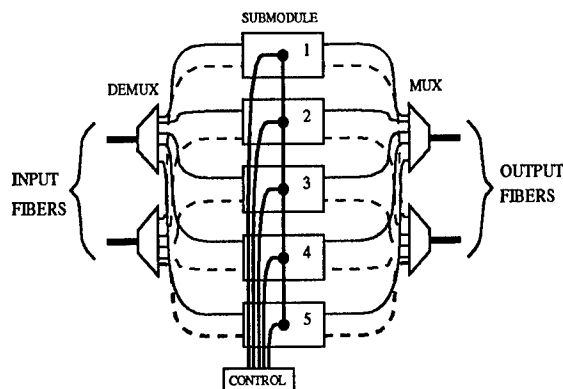


Figure 1: Architecture of the wavelength translation node. All the submodules are interconnected and there is a central control unit which decides transmission operations.

## III. RESULTS

Fig. 2 shows propagation delay  $H$  in number of hops versus number of channels  $n$  for ShuffleNet (SN) and Manhattan Street (MS) networks with 64 nodes. Observe that propagation delay for hot-potato, single-buffer [4], and ideal store-and-forward (S&F [5]) keep constant because channels are independent of each other whereas propagation delay for wavelength translation routing improves with the number of channels. The reason for this is that packets in conflict have the possibility of being translated to an available non-conflictive slot. The probability of deflection then decreases and the propagation delay improves. Simulations use uniform traffic conditions for each channel. Full load (probability of packet generation  $g = 1$ ) is used for each channel in the network, corresponding to the case of a saturated infinite shared input queue at the transmitters ( $TX$ 's) [6]. SN64 network performs better than MS64 due to the fact that SN has less traffic congestion because the link load is lower and the packet absorption probability is higher. Simulation statistics were collected for 30,000 clock cycles, after discarding 10,000 initial cycles to allow for transients to die out. Observe the good match between an approximate analytical model and the simulation results in Fig. 2 for MS (at  $g=1, 0.5$ ) and for SN (at  $g=1$ ). The discrepancies in results for MS and SN between theory and simulation are in the range of 0 to 0.08.

Figs. 3a and 4a show results (for MS and SN respectively) of the average propagation delay  $H$  ver-

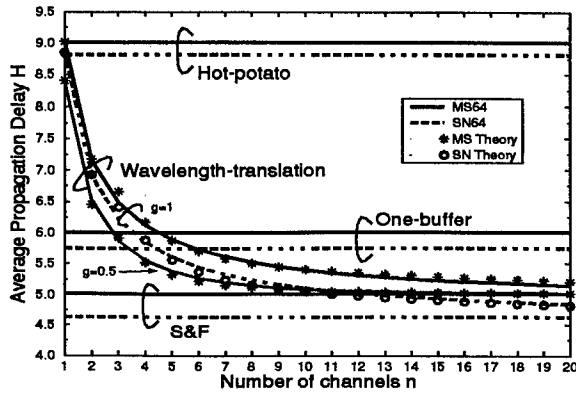


Figure 2: Results of average propagation delay  $H$  in number of hops versus number of channels  $n$  for hot-potato, single-buffer, store-and-forward (S&F) and wavelength translation at  $g=1$ . Results are for ShuffleNet (SN64) and Manhattan Street (MS64) networks with 64 nodes.

throughput per channel  $S$ . Where throughput is the average number of packets inserted/absorbed per slot. Observe that the throughput and propagation delay improve depending on the number of channels used. As a measure of the benefit of wavelength translation for packet switching, define the *Gain* as the increase in throughput for the same average propagation delay. Then *Gain* is

$$Gain = \left| \frac{S(n > 1)}{S(n = 1)} \right|_{H, g > 0} \quad (1)$$

where  $S(n = 1)$  represent the throughput per channel of a network without wavelength translation, and  $S(n > 1)$  represent the throughput per channel of a network with wavelength translation. Figs. 3b and 4b show curves of *Gain* for fixed values of  $H = 5.2, 5.3, 5.5, 6.0$  for MS, and  $H = 4.7, 4.9, 5.0, 5.8$  for SN. As  $H$  decreases the *Gain* increases depending on the number of channels used, however this *Gain* comes at the expense of increased hardware.

In summary, the benefits of wavelength translation for two-connected packet switching networks increase with the number of wavelengths used due to the fact that the probability of deflection decreases, therefore average propagation delay decreases, throughput per channel increases, and thus *Gain* increases.

#### IV. CONCLUSIONS

Wavelength translation in *packet switching* networks with deflection routing has the feature of decreasing the probability of deflection, i.e. improving the throughput and propagation delay depending on the number of channels used in the network. In this paper an optimized wavelength translation routing algorithm has been used that minimizes the probability of packet deflection. The results show that, on the

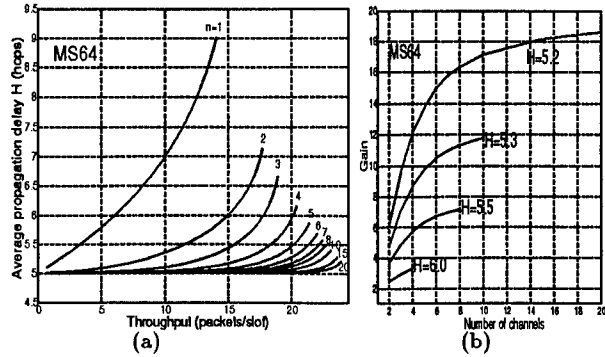


Figure 3: a) Results of average propagation delay  $H$  versus throughput for MS b) Results of *Gain* versus number of channels  $n$  for values of  $H=5.2, 5.3, 5.5, 6.0$

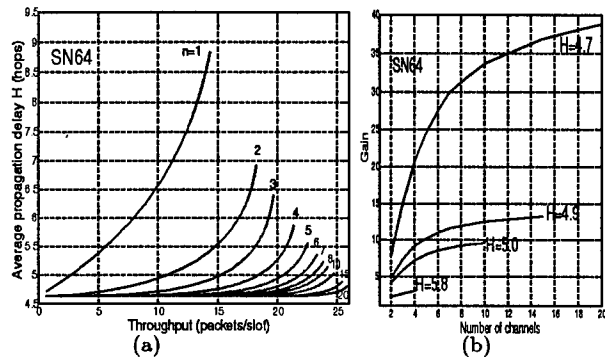


Figure 4: a) Results of average propagation delay  $H$  versus throughput for SN b) Results of *Gain* versus number of channels  $n$  for values of  $H=4.7, 4.9, 5.0, 5.8$

average, SN has higher throughput and lower propagation delay than MS when wavelength translation is used due to the fact that SN has less traffic congestion. The effectiveness of wavelength translation is quantified. It is verified that under uniform traffic, the use of wavelength translation recovers more than 60% of the propagation delay loss of hot-potato with respect to store-and-forward when five or more channels are used in the network.

#### References

- [1] R. A. Barry and P. A. Humblet, *IEEE J. Select. Areas Commun.*, vol. 14, no. 5, pp. 858–867, June 1996.
- [2] M. Kovacevic and A. Acampora, *IEEE J. Select. Areas Commun.*, vol. 14, no. 5, pp. 868–880, June 1996.
- [3] M. Kovacevic and A. Acampora, *J. Lightwave Technol.*, vol. 14, no. 6, pp. 1161–1169, June 1996.
- [4] F. Forghieri, A. Bononi, and P. Prucnal, *IEEE Trans. on Commun.*, vol. 43, no. 1, pp. 88–98, January 1995.
- [5] G. A. Castanon, O. K. Tonguz, and A. Bononi, *IEEE J. Lightwave Technol.*, submitted for publication, 1996.
- [6] A. Bononi and P. Prucnal, *IEEE/ACM Transactions on Networking*, vol. 4, no. 5, pp. 726–730, October 1996.

## Effects of Optical Filter Drifts in Wavelength Division Multiplexing System with Cascaded Optical Amplifiers

Y. Chai, F. S. Choa

Department of Computer Science and Electrical Engineering  
University of Maryland Baltimore County, Baltimore, MD 21250

Wavelength-Division-Multiplexing (WDM) systems can provide ultrahigh transmission capacity. Erbium Doped Fiber Amplifier EDFA[1] is widely employed in WDM system to achieve long distance and high performance transmission. In an optically amplified WDM system, many optical components, such as multi/demultiplexers, optical signal add/droppers, noise-limiting filters, will perform as optical filters. Filter frequency drifts can induce Signal-to-Noise Ratio (SNR) degradation at a receiver. In previous works, Willner[2] considered crosstalk and filtering effects with perfectly aligned laser and filter frequencies for Fabry-Perot type filters. Khrais[3] considered a system with 30 misaligned (de)multiplexers, but without any optical amplifier in the system. In a real system there exist many amplifiers and filters to enhance system performance.

In this presentation, we report the analysis and results on an optically amplified WDM system with cascade of optical amplifier-filter pairs. System performance is described by receiver electrical SNR(SNR<sub>e</sub>).

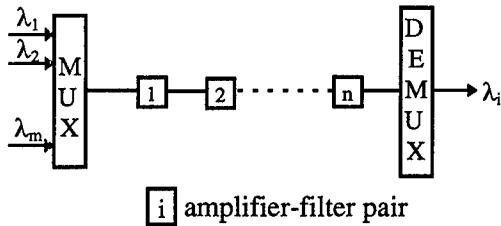


Fig.1. Configuration of optically amplified WDM system with amplifier-filter pairs

The WDM system consists of  $m$  equally spaced optical channels and  $n$  stages of amplifier-filter pairs, as shown in Fig. 1. For ideal situation, each filter frequency are

perfectly aligned with laser frequency. EDFA is assumed to operate with constant total output power model, thus we have [1]:

$$P_{out,i} = L_i \cdot G_i \cdot P_{out,i-1} + P_{ase,i} \quad (1)$$

$$P_{ase,i} = F \cdot (G_i - 1) \cdot h\nu \cdot B_o \quad (2)$$

where  $P_{out,i}$ ,  $G_i$ ,  $L_i$ ,  $P_{ase,i}$  are the output power, gain, path loss between adjacent EDFAs and ASE power for  $i$ th EDFA, respectively.  $F$ ,  $h\nu$ ,  $B_o$  are EDFA noise figure, photon energy and optical filter bandwidth, respectively. SNR<sub>e</sub> at receiver can be written as [2]:

$$SNR_e = \frac{(P_{out,n} - \sum_{i=1}^n P_{ase,i} - C)^2}{\sigma^2} \quad (3)$$

where  $C$  is the optical power due to crosstalk from all the rejected channels,  $\sigma^2$  is the total noise power including the receiver circuit noise, the spontaneous-spontaneous beat noise, and the signal-spontaneous beat noise.

If one of the optical filters has a frequency drift of  $\Delta f$  with respect to the laser frequency, the loss of that path will increase, and the input to next stage EDFA will be reduced. The saturated EDFA will provide more gain to keep its output power constant. The noise power  $P_{ase}$  from that EDFA will increase because of higher gain  $G_i$ . At the receiver, the SNR<sub>e</sub> will degrade because of more ASE noise accumulation when there is a filter drift. The SNR<sub>e</sub> will further degrade due to the crosstalk induced by filter frequency drift.

Two cases are considered here. One is the "worst case" where all filters have a drift of  $\Delta f$ , the other is the "best" case where only one filter suffers a drift of  $\Delta f$ . For both cases, the system analyzed has eight 2.5Gb/s



equally spaced channels with 200 GHz spacing, 10 stage EDFAs (with noise figure 5dB and saturation power 6 dBm), 25dB fiber loss between adjacent EDFAs and 3dB optical filter bandwidth of 100 GHz. We calculated the  $SNR_e$  at the receiver for three types of filters: Fabry-Perot, Gaussian and 3rd order Butterworth.

For the "worst" case, The relation between  $SNR_e$  degradation and filter frequency drift is given in Fig.2. It is shown that the filter drift for 1dB receiver  $SNR_e$  degradation are 8GHz, 10GHz and 28GHz for Fabry-Perot, Gaussian and 3rd order Butterworth filters, respectively. It is easy to understand that the 3rd order Butterworth filter has the maximum tolerance to filter drift because of its flat-top passband.

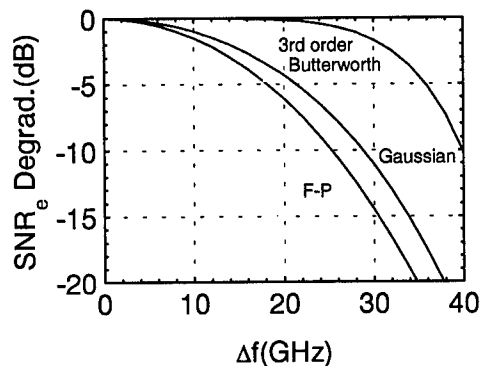


Fig.2.  $SNR_e$  degradation caused by frequency drift of three types optical filters.

For the "best" case, the obtained  $SNR_e$  degradation and filter frequency drift is shown in Fig.3 for different stage with same frequency drift of 30GHz. We can see that if only one filter has drift, the ASE increased from one EDFA is very small compared with the "worst" case where the ASE increased at every EDFA stage. The result also shows that the  $SNR_e$  degradation is smaller if the drift occurs at stage nearer to the transmitter. It is because that the reduced optical signal can be well recovered if the filter drift happens at an earlier stage.

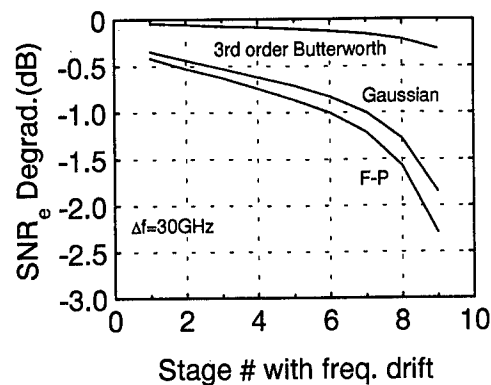


Fig. 3.  $SNR_e$  degradation for different stage if only one filter has frequency drift.

The analysis also shows that the receiver  $SNR_e$  degradation weakly depends on the number of amplifier-filter pairs because saturated EDFA can compensate the excess optical power loss caused by optical filter drift. The  $SNR_e$  degradation also weakly depends on bit rate, but strongly depends on filter type and bandwidth. Larger optical filter bandwidth can provide more tolerance to filter drift.

In conclusion, the  $SNR_e$  degradation due to the filter frequency drift in an optically amplified WDM system is analyzed. In such a system, the excess loss caused by optical filter drift can be recovered by EDFAs operated under saturation condition. However, the signal power recovery is accompanied by a  $SNR$  degradation. We have studied the system performance of the "worst" and "best" cases for different filters.

The authors acknowledge support from DARPA/AFOSR under grants F49620-96-1-0230 and F49620-95-1-0446.

#### References:

- [1] C.R. Giles, et al, J. Lightwave Tech., vol.9, no.2, 1991, pp147-154
- [2] A.E. Willner, IEEE Photonics Tech. Lett., vol.4, no.2, 1992, pp186-189
- [3] N.N. Khrais, et al, IEEE Photonics Tech. Lett., vol.7, no.11, 1995, pp1348-1350

# AUTHOR INDEX

<b>A</b>					
Ahn, K.H.	TuA3				
<b>B</b>					
Berthold, J.	TuB1				
Bononi, A.	TuC3				
Boyras, O.	TuA3				
Burrus, C.A.	MD2				
<b>C</b>					
Cao, X.D.	TuA3				
Castanon, G.A.	TuC3				
Chai, Y.	TuD2				
Chaikamnerd, S.	TuA3				
Chao, H.J.	MD3				
Chen, J.H.	MD2				
Choa, F.S.	MD2,MD3, TuD2				
<b>F</b>					
Futro, A.T.	MC2				
<b>G</b>					
Gillner, L.	TuC2				
Grah, A.	TuB3				
Gustavsson, M.	TuC2				
<b>H</b>					
Heath, D.	MA1				
Hill, G.	TuC1				
<b>I</b>					
Islam, M.N.	TuA3				
<b>K</b>					
Kao, Y.H.	TuA3				
Kwok, T.C.	MA2				
<b>L</b>					
Lam, C.F.	TuA2				
Larsen, C.P.	TuC2				
Liang, Y.	TuA3				
Liu, J.-Y.	MD1				
Lou, J.W.	TuA3				
<b>P</b>					
Pritchard, W.	TuA1				
<b>Q</b>					
Qiao, C.	TuB2				
<b>R</b>					
Runge, P.	TuD1				
<b>S</b>					
Sato, K.	MB2				
Shih, M.H.	MD2, MD3				
<b>T</b>					
Tanbun-Ek, T.	MD2				
Tonguz, O.K.	TuC3				
Tsang, W.T.	MD2				
<b>V</b>					
Van der Plas, G.	MC1				
<b>W</b>					
Walker, N.	MB1				
Wang, L.M.	MD2				
Wang, T.S.	MD3				
Wisk, P.	MD2				
Wu, K.Y.	MD1				
<b>X</b>					
Xia, T.J.	TuA3				
<b>Y</b>					
Yablonovitch, E.	TuA2				
Yoo, M.	TuB2				

**1997 DIGEST  
of the IEEE/LEOS  
Summer Topical Meetings  
13-15 August 1997**

**WDM Components Technology**

**at  
*THE QUEEN ELIZABETH HOTEL  
MONTREAL, QUEBEC, CANADA***

**IEEE Catalog Number: 97TH8276  
Library of Congress: 97-70754**

The papers in this book make up the digest of the meeting mentioned on the cover and title page. They reflect the authors' opinions and are published as presented and without change in the interest of timely dissemination. Their inclusion in this publication does not necessarily constitute endorsement by the editors, the Institute of Electrical and Electronics Engineers, Inc.

Copyright and reprint permissions: Abstracting is permitted with credit to the source. Libraries are permitted to photocopy beyond the limits of U.S. copyright law for private use of patrons those articles in this volume that carry a code at the bottom of the first page, provided the per-copy fee indicated in the code is paid through the Copyright Clearance Center, 222 Rosewood Drive, Danvers MA 01923. Instructors are permitted to photocopy isolated articles for noncommercial classroom use without fee. For other copying, reprint or republication permission, write to IEEE Copyrights Manager, IEEE Service Center, 445 Hoes Lane, P.O. Box 1331, Piscataway NJ 08855-1331.

© 1997 by The Institute of Electrical and Electronics Engineers, Inc. All right reserved.

IEEE Catalog Number: 97TH8276

ISBN:	0-7803-3891-X	Softbound Edition
	0-7803-3892-8	Microfiche Edition

Library of Congress: 97-70754

Additional copies can be ordered from:

IEEE Service Center

445 Hoes Lane

P.O. Box 1331

Piscataway, NJ 08855-1331

Tel: (732) 981-1393

Fax: (732) 981-9667



# **WDM COMPONENTS TECHNOLOGY**

## **Co-Chairs:**

Mario Dagenais, University of Maryland, College Park, MD  
Tien P. Lee, Bellcore, Red Bank, NJ  
Thomas Koch, Bell Laboratories Lucent Technologies, Holmdel, NJ  
Louis Lome, BMDO/TRI, Washington, DC

## **Program Committee:**

Philip J. Anthony, Bell Laboratories Lucent Technologies, Murray Hill, NJ  
Dan Blumenthal, Georgia Institute of Technology, Atlanta, GA  
Marko Erman, Alcatel, Marcoussis, France  
Wagiush S. Ishak, Hewlett-Packard Laboratories, Palo Alto, CA  
Robert F. Leheny, DARPA, Arlington, VA  
Ikuko Mito, NEC Corporation, Tsukuba, Japan  
William W. Morey, 3M Bragg Grating Technologies, Bloomfield, CT  
Richard Normandin, National Research Council of Canada, Ottawa, Canada  
Katsunari Okamoto, NTT Optoelectronics Labs, Ibaraki, Japan  
Gen Ribakovs, Nortel Technology, Ottawa, Canada  
Kristian E. Stubkjaer, Technical University of Denmark, Lyngby, Denmark  
Michel Tetu, Laval University, Quebec, Canada  
B.H. Verbeek, Philips Optoelectronics Centet, Eindhoven, The Netherlands  
John Zyskind, Bell Laboratories Lucent Technologies, Holmdel, NJ

# TABLE OF CONTENTS

## Wednesday, 13 August 1997

### **Session WA: Network Technologies I**

- WA1 WDM Networking Technology: Opportunities and Challenges . . . . . (paper not available)  
 WA2 Impact of WDM Network Management on Optical Component Functionalities . . . . . 3

### **Session WB: WDM Network Technologies II**

- WB1 Systems Issues for WDM Components . . . . . 5  
 WB2 Mutliwavelength Network Access Technologies . . . . . 7  
 WB3 Monolithic Array Photoreceivers for Multichannel WDM Application . . . . . 9

### **Session WC: Datacom and Access**

- WC1 Are WDM Component Needs for Datacom Different than for Telecom? . . . . . 11  
 WC2 Hybrid and Monolithic Integrated Optical Devices for WDM Subscriber Systems . . . . 13  
 WC3 Low-Cost Multimode WDM for the Local Area Network . . . . . 15

### **Session WD: Wavelength Control**

- WD1 Selectable Wavelength Laser Arrays for WDM Applications . . . . . 17  
 WD2 A Compact Wavelength Stabilization Scheme for Telecommunication Transmitters . . 19  
 WD3 An Absolute Frequency Reference at 1556 nm for WDM Communication Systems . . 21  
 WD4 Wavelength-Controlled DFB Lds for WDM Systems . . . . . 23

## Thursday, 14 August 1997

### **Session ThA: Wavelength Routing/Conversion I**

- ThA1 Applications of Integrated Optic Switches in WDM Networks . . . . . 27  
 ThA2 An Integrated Optical Add/Drop Multiplexer In InP Based on Elliptic Couplers and  
 Bragg Grating Reflector . . . . . 28  
 ThA3 Self-Routing Wavelength Switches . . . . . 30  
 ThA4 Injection-Locking For Coherent Detection of Multi-Wavelength Systems . . . . . 32  
 ThA5 Electronically Switchable Waveguide Bragg Gratings for WDM Routing . . . . . 34

### **Session ThB: Wavelength Routing/Conversion II**

- ThB1 Progress in Wavelength Conversion by Difference-Frequency-Generation in AlGaAs  
 Waveguides . . . . . 36  
 ThB2 A Reconfigurable Optoelectronic Wavelength Converter Based on an Integrated  
 Electroabsorption Modulated Laser Array . . . . . 38  
 ThB3 Improved Frequency Response of A Semiconductor-optical-amplifier Wavelength  
 Converter Using A Fiber Bragg Grating. . . . . 40  
 ThB4 Wavelength Conversion Techniques in Optical Networks . . . . . 42

# TABLE OF CONTENTS

## Session ThC: Filters I

ThC1	Tunable Acousto-Optical Filters, Multiplexers and Lasers in LiNbO <sub>3</sub> .....	44
ThC2	Dynamic Holographic Eight-Channel Spectral Equalizer for WDM .....	46
ThC3	WDM Channel Monitoring and Signal Power Control/Equalization Using Integrated Tunable Active Filters .....	48
ThC4	Monolithic Integration of WDM Components Using QW Shape Modification .....	50

## Session ThD: Filters II

ThD1	Wafer Scale Integration of WDM Wavelength Routers and Cross-connect Switches for Dynamic Network Control .....	(paper not available)
ThD2	Demultiplexer With 90 channels and 0.3 nm Channel Spacing .....	52
ThD3	High Performance Metal-Coated Multimode Interference (MMI) Devices for WDM Applications .....	54
ThD4	An Asymmetric Dielectric-Strip Loaded Y-Junction Wavelength Demultiplexer by K <sup>+</sup> -Na <sup>+</sup> Ion Exchange in Glass .....	56

## Friday, 15 August 1997

## Session FA: Laser Arrays

FA1	Multiwavelength DFB Laser Arrays for WDM Lightwave Communication Systems (not available)	
FA2	5-Wavelength Surface Emitting Laser Diode Array Based on Post Growth Adjustment of Surface Mode Emission .....	60
FA3	Improved Crosstalk Performance in a 10-Wavelength 25 Gbps Multichannel Laser Array Transmitter Module .....	63
FA4	Design of a 40Gbps WDM Laser Module .....	65
FA5	Mode-Locked Laser Arrays for WDM Applications .....	67

## Session FB: Optical Amplifiers

FB1	Broadband WDM Amplifiers: From Research to Field Deployment. . . (paper withdrawn)	
FB2	EDFA Chain Control: A Comparison of Two All-Optical Approaches .....	69
FB3	A Simplifying Model of Fiber Amplifiers For The Design of Cascaded WDM-Systems .....	71
FB4	Optical Amplifiers for Optical Networks .....	73

## Session FC: Filters III

FC1	Fibre Gratings for WDM Systems .....	(Paper not available)
FC2	Apodized Fiber Gratings for DWDM Using Variable Efficiency Phase Masks .....	75
FC3	A Configurable Wavelength Demultiplexer Using Periodic Filter Chains .....	77
FC4	Fiber Grating Devices for WDM Systems .....	(paper not available)

# TABLE OF CONTENTS

## Session ThC: Filters I

ThC1	Tunable Acousto-Optical Filters, Multiplexers and Lasers in LiNbO <sub>3</sub> .....	44
ThC2	Dynamic Holographic Eight-Channel Spectral Equalizer for WDM .....	46
ThC3	WDM Channel Monitoring and Signal Power Control/Equalization Using Integrated Tunable Active Filters .....	48
ThC4	Monolithic Integration of WDM Components Using QW Shape Modification .....	50

## Session ThD: Filters II

ThD1	Wafer Scale Integration of WDM Wavelength Routers and Cross-connect Switches for Dynamic Network Control .....	(paper not available)
ThD2	Demultiplexer With 90 channels and 0.3 nm Channel Spacing .....	52
ThD3	High Performance Metal-Coated Multimode Interference (MMI) Devices for WDM Applications .....	54
ThD4	An Asymmetric Dielectric-Strip Loaded Y-Junction Wavelength Demultiplexer by K <sup>+</sup> -Na <sup>+</sup> Ion Exchange in Glass .....	56

## Friday, 15 August 1997

## Session FA: Laser Arrays

FA1	Multiwavelength DFB Laser Arrays for WDM Lightwave Communication Systems (not available)	
FA2	5-Wavelength Surface Emitting Laser Diode Array Based on Post Growth Adjustment of Surface Mode Emission .....	61
FA3	Improved Crosstalk Performance in a 10-Wavelength 25 Gbps Multichannel Laser Array Transmitter Module .....	64
FA4	Design of a 40Gbps WDM Laser Module .....	66
FA5	Mode-Locked Laser Arrays for WDM Applications .....	68

## Session FB: Optical Amplifiers

FB1	Broadband WDM Amplifiers: From Research to Field Deployment. . . (paper withdrawn)	
FB2	EDFA Chain Control: A Comparison of Two All-Optical Approaches .....	70
FB3	A Simplifying Model of Fiber Amplifiers For The Design of Cascaded WDM-Systems .....	72
FB4	Optical Amplifiers for Optical Networks .....	74

## Session FC: Filters III

FC1	Fibre Gratings for WDM Systems .....	(Paper not available)
FC2	Apoized Fiber Gratings for DWDM Using Variable Efficiency Phase Masks .....	76
FC3	A Configurable Wavelength Demultiplexer Using Periodic Filter Chains .....	78
FC4	Fiber Grating Devices for WDM Systems .....	(paper not available)



## **TABLE OF CONTENTS**

### **Session FD: Filters IV**

FD1	Arrayed-Waveguide Gratings for Dense-WDM Systems .....	80
FD2	Using A Retro-Reflecting Echelle Grating to Improve WDM Demux Efficiency .....	82
FD3	High-Performance Optical Polymers for Low-Cost High-Port-Count Planar Wavelength-Division-Multiplexing Devices .....	84
FD4	PHASAR-based PICs for WDM-applications .....	86



## **WDM COMPONENTS TECHNOLOGY**

**Wednesday, 13 August 1997**

### **Sessions:**

- WA:    *Network Technologies I***
- WB:    *WDM Network Technologies II***
- WC:    *Datacom and Access***
- WD:    *Wavelength Control***
- WE:    *Post-Deadline/Rump Session***

## **Wednesday Papers Not Available**

WA1      “WDM Networking Technology: Opportunitites and  
Challenges”, *R.C. Alferness, Bell Laboratories Lucent  
Technologies, Holmdel, NJ*

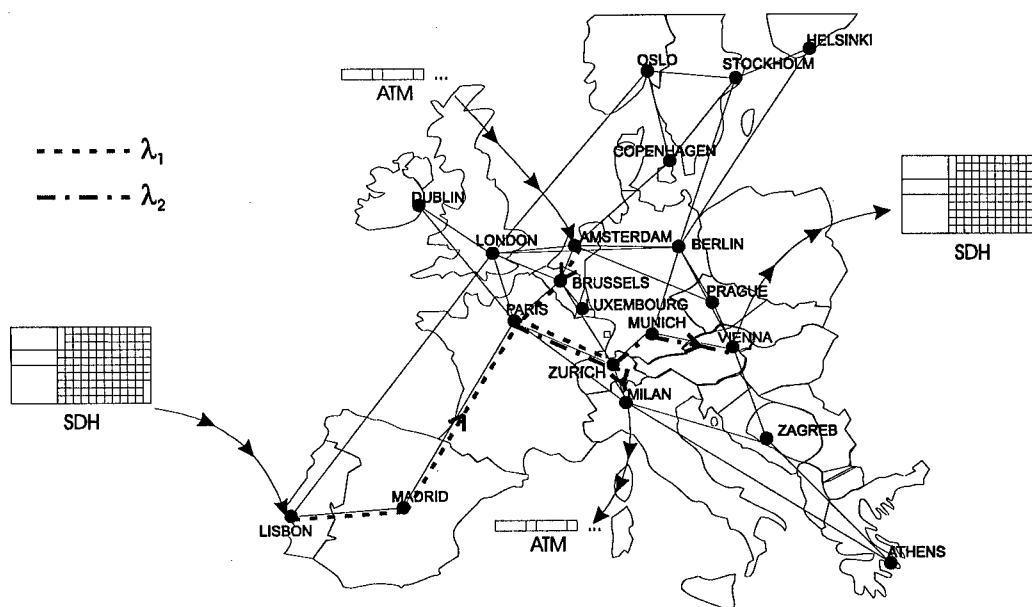
**WA2 (Invited)**  
**9:30am - 10:00am**

### **Impact of WDM network management on optical component functionalities**

Piet Demeester, Lode Vandendriessche, Bart Van Caenegem, Wim Van Parys  
IMEC-University of Gent  
Department of Information Technology (INTEC)  
Sint-Pietersnieuwstraat, 41  
B-9000, Gent, Belgium  
tel.: +32-9-264 33 34  
fax : +32-9-264 35 93  
e-mail : [demeester@intec.rug.ac.be](mailto:demeester@intec.rug.ac.be)

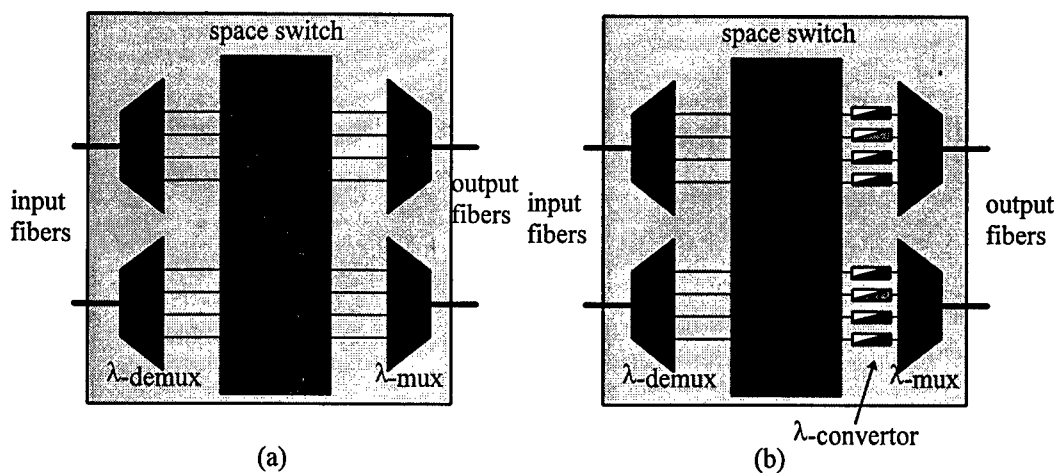
WDM transport networks are moving fast from the laboratory and field trial environment to deployment in operational networks. One of the key issues is the management of these transparent networks and the impact on the required component functionalities. This paper will address these issues in more detail.

A typical WDM transport network will be composed of optical network elements (WDM terminal multiplexers, optical add-drop multiplexers and optical cross-connects) and wavelength multiplexed links in between. An example of a Pan-European network is shown in the figure.



**Example of a Pan-European photonic transport network carrying SDH and ATM traffic and using wavelength conversion**

The basic architecture of an optical cross connect is shown in the figure below. The optical components typically used, are : wavelength multiplexer/demultiplexer, optical filter, wavelength converter, space switch, optical amplifier, etc. At the two end-points of an optical path, tunable transmitters and receivers are also required. The two major classes of optical cross-connects (OXC) are wavelength routing and wavelength translating OXC's (also shown on the figure).



**Difference between a wavelength routing OXC (a) and a wavelength translating OXC (b)**

In this presentation we will first describe the functionality of a WDM transport network and the functionality of the network elements. A second part will make a comparison between the current SDH signaling and monitoring capabilities and the requirements in a WDM network. This will take into account that a WDM network is more behaving like an analogue transmission network and not a digital transmission network. A last part will discuss the impact on the optical components.

Acknowledgment : Bart Van Caenegem thanks the Fund for Scientific Research - Flanders (FWO-V) for financial support. Part of the work has been supported by the ACTS projects Photon and Open.

WB1 (Invited)  
10:30am - 11:00am

Invited Paper

## SYSTEM ISSUES FOR WDM COMPONENTS

Alan E. Willner

Dept. of Electrical Engineering - Systems  
University of Southern California  
Los Angeles, California 90089-2565  
(213) 740-4664, FAX: (213) 740-8729, E-mail: willner@solar.usc.edu

Two major advantages of wavelength-division-multiplexing (WDM) [1] are: (i) added capacity when transmitting several wavelengths on the same fiber simultaneously, and (ii) added throughput and flexibility in a network when routing of data is based on the wavelength of the signal. This paper will describe some of the limitations which WDM devices place on optical system and network performance and, conversely, some of the specifications which systems require of WDM devices. Some of the issues specified below will serve as a starting point for the paper to be presented.

**Transparency and Reconfigurability:** There are certain throughput benefits of ensuring an all-optical data path from source to destination [2], but the additional cost and complexity may be the key stumbling blocks to widespread implementation. A straightforward method of providing transparency in a dynamically reconfigurable WDM network is to use passive wavelength routers and active crossbar switches [1]. Another technique of providing transparency is all-optical wavelength shifting of data [3,4], which would typically be performed using semiconductor optical amplifiers at switching nodes. However, all wavelength shifting methods can have one or more of the following deleterious effects: reduced output contrast ratio, low conversion efficiency, additive noise, induced chirp, unstable power and bias operating point, wavelength dependence, data-format dependence, low fabrication yield, and polarization dependence. These issues, along with robustness and generic crosstalk problems in all WDM components, must be dealt with in a reasonable manner.

The optical devices in the WDM switching nodes must not significantly degrade the SNR of the packet. This is critical for a network in which data will traverse several switching nodes from source to destination. A real network must ensure that the output SNR will not be dependent on the particular path through the network, including variations in network topologies, traffic patterns, and wavelength assignment algorithms.

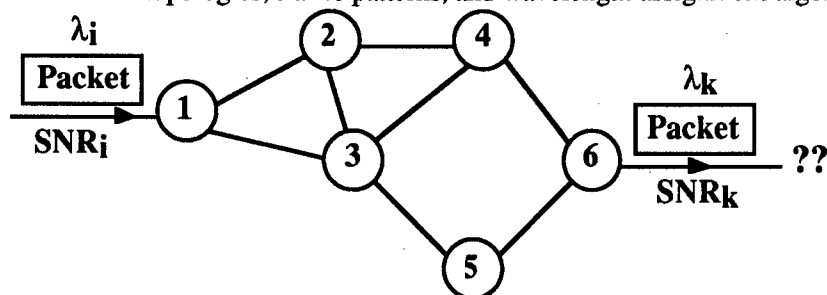


Fig. 1. The output SNR of a data packet may change depending on the path it takes through a network, in which each node may slightly degrade the signal recoverability.

The concept of reconfigurability brings to mind the desired transformation speed of such a dynamic process. Circuit-switched networks require reconfigurability on the order of ms, whereas future WDM packet-switched networks will require much faster reconfiguration times. Over the coming years, there will be some growth from circuit switching into high-performance packet switching, and it may behoove systems designers to install where feasible hardware which can be upgraded later to faster reconfiguration times.

**Compatibility:** The optical communications community has historically thought of systems as either point-to-point transmission links or point-to-multipoint networks. This definition has enabled point-to-point systems to act somewhat independently in terms of standardization (e.g., undersea cable systems). However, future systems will probably not be divided into these neat categories. Points A and B in a single link will most likely also be optical gateways into other parts of a larger network. This may especially be true when using WDM and wavelength routers (e.g., integrated wavelength routers [5]), in which some wavelengths can easily propagate beyond point B to other destinations thereby reducing delay and increasing throughput. Therefore, even point-

to-point systems must be compatible in terms of wavelengths and fiber types with the outside networks in order to anticipate the future upgrading of all systems.

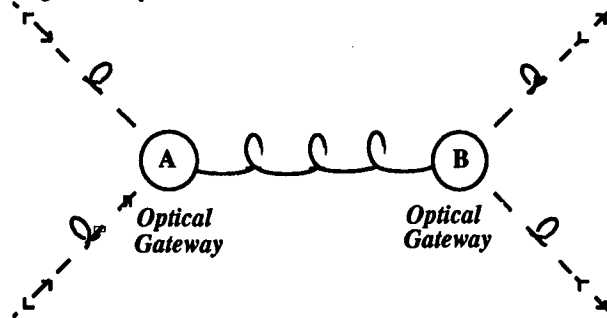


Fig. 2. Point-to-point optical systems will eventually be upgraded such that points A and B will be optical gateways into the larger network, thereby requiring compatibility.

**Wavelength Range:** An issue directly related to compatibility is the wavelength range which will be used for WDM systems. Since almost all fiber-based systems will incorporate Erbium-doped fiber amplifiers (EDFAs), it is the conventional wisdom that the EDFA will define and limit the usable wavelength range of transmitted channels. The wavelength range of commercially available EDFAs is, approximately: (i) <30 nm for a single EDFA, spanning 1530-1560 nm, and (ii) <10 nm for a long cascade of EDFAs, spanning 1550-1560 nm. The International Telecommunications Union is finalizing a frequency standard for WDM systems in which all channels must lie along a grid of 100-GHz (0.8-nm) spacing and the reference wavelength is 1552.5 nm; channel spacing will be a multiple of this 100-GHz spacing. Therefore, given the EDFA bandwidth, channel spacings of 3.2 nm may only be able to accommodate very few channels, whereas 0.8 nm spacings can accommodate a more significant number of channels. There is a concerted effort to extend this EDFA-based wavelength range limitation by several possible means: (i) passive fiber-Bragg-grating filters to equalize the gain peak of the EDFA [6], (ii) power balancing of the WDM input channels [7], and (iii) power equalization modules using acousto-optic techniques [8]. A potentially more dramatic range extender is the introduction of new co-dopants, such as Tellurite, which may extend the bandwidth to >1600 nm and more than double the usable range [9].

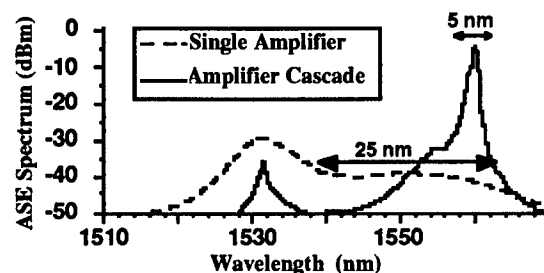


Fig. 3. Amplified-spontaneous-emission (i.e., gain) spectrum for a single EDFA and for an EDFA cascade.

### References

1. *IEEE/OSA J. Lightwave Technol.*, Special Issue on Multiple Wavelengths Technologies and Networks, vol. 14, no. 6, 1996.
2. R.A. Barry, "WDM and TDM All-Optical Network Architectures," OSA Annual Meeting '96, Rochester, NY.
3. J.M. Wiesenfeld, J.S. Perino, A.S. Gnauck and B. Glance, *Electron. Lett.*, vol.30, pp. 720-721, 1994.
4. W. Shieh and A.E. Willner, "Demonstration of Output-Port Contention Resolution in a 2X2 WDM Switching Node Based on All-Optical Wavelength Shifting and Subcarrier-Multiplexed Routing-Control Headers," OFC '96, paper PD-36 (OSA, Washington D.C., 1996).
5. C. Dragone, *IEEE Photon. Technol. Lett.*, 3, 812-815, 1991.
6. P. Wysocki, et. al., "Erbium-doped fiber amplifier flattened Beyond 40 nm Using Long-Period Gratings," OFC '97, Post-Deadline paper PD-2 (OSA, Washington D.C., 1997).
7. A.K. Srivastava, et. al., "32 X 10 Gb/s WDM Transmission over 640 km using Broadband, Gain-Flattened Erbium-Doped Fiber Amplifiers," OFC '97, Post-Deadline paper PD-18 (OSA, Washington D.C., 1997).
8. J.-X. Cai, K.-M. Feng, X.P. Chen, A. E. Willner, D. A. Smith, C.-H. Lee and Y.-J. Chen, *IEEE Photonics Technology Letters*, vol. 9, pp. 678-680, 1997.
9. A. Mori, et. al., "1.5  $\mu$ m Broadband Amplification by Tellurite-Based EDFAs," OFC '97, Post-Deadline paper PD-1 (OSA, Washington D.C., 1997).



**WB2 (Invited)**

**11:00am - 11:30am**

## **MULTIWAVELENGTH NETWORK ACCESS TECHNOLOGIES**

**Cecile Dreze  
Nortel Technology  
P.O.Box 3511, Station C  
Ottawa, Ontario K1Y 4H7  
e-mail: cecile@nortel.ca**

### **INTRODUCTION**

Increased bandwidth and functionality will be offered by WDM networks compared to single wavelength ones, with applications ranging from straightforward capacity enhancement through to switched virtual dark fiber carrying disparate traffic to customers' premises. However, their implementation depends on their capability of offering the users cost effective solutions. This means that WDM equipment must be built small, rugged with low power consumption and high functional density. The Network Access Module (NAM) developed at Nortel as part of the Optical Networks Technology Consortium illustrates such integration.

### **THE NETWORK ACCESS MODULE**

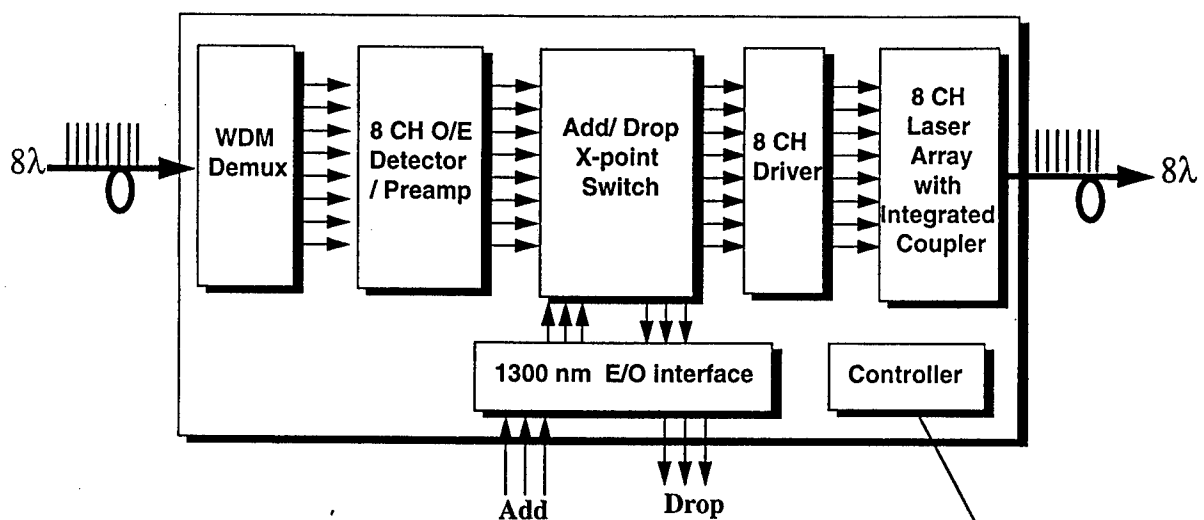
The Network Access Module (NAM) was developed as part of the ONTC investigation and demonstration of WDM optical networks and their technology. The NAM is able to transmit, receive and dynamically switch digital signals at 2.5 Gb/s across 8 different wavelengths on a single optical fiber. In an optical network, the NAM acts as a repeater and a wavelength translator, receiving a signal at one wavelength and retransmitting it on another. The crosspoint switch placed between the multiwavelength receiver and transmitter allows rapid reconfiguration of the optical network by changing the wavelength mapping. It also adds flexibility in routing locally dropped signals to the appropriate peripherals, and assigning added signals to the correct wavelengths. A functional diagram of the NAM is shown in the attached figure.

### **MULTIWAVELENGTH TECHNOLOGY APPLICATIONS**

The NAM constitutes a flexible building block which will help network designers to take full advantage of the multiwavelength technology. Some of these well recognized benefits are:

- increase capacity without additional fiber requirement
- overlay services - digital format transparency and no grooming required
- wavelength bypass where data travelling on specific wavelength pass unchanged through specific network nodes
- reconfigurable adding/dropping specific traffic at specific nodes within the network
- wavelength translation which allows wavelength re-use throughout the optical network

## ***WDM Network Access Module (NAM)***



- Target performance
- 8 wavelengths of 1546 -1560 nm spaced @  $2 \pm 0.25$  nm
  - -25 dBm receiver sensitivity
  - -17 dBm launch power
  - 2.5 GBit/s data rate / channel



**WB3 (Invited)**  
**11:30am - 12:00noon**

### **Monolithic Array Photoreceivers for Multichannel WDM Application**

**S.Chandrasekhar**

**Bell Laboratories, Lucent Technologies  
Crawford Hill Laboratory, Holmdel, NJ 07733**

The past few years has seen the rapid progress of optical communication systems employing wavelength division multiplexing (WDM) architectures in order to exploit the enormous bandwidth offered by the optical fiber. There has been concurrent activities in the photonic component arena to find viable solutions for realizing such WDM architectures requiring multichannel transmitters and receivers. One such area where research has been focused is in array technologies. Monolithic integration has progressed sufficiently that arrays of lasers and photodetectors are being envisioned as key device components which enable novel architectures. In particular, optoelectronic integrated circuit (OEIC) photoreceiver arrays have been actively researched worldwide for such applications. Arrays of p-i-n photodetectors have been monolithically integrated with a variety of field effect transistors (FETs) and heterojunction bipolar transistors (HBTs) [1]. The number of channels reported on a single semiconductor chip has been from two to sixteen [2-7], with aggregate throughput between 20 Gb/s and 160 Gb/s.

The merits of monolithic integration lies in the uniform performance of the individual channels in the array. Several of the results reported in literature demonstrated this feature in the small signal bandwidth, the transimpedance, sensitivity, and the photodetector responsivity. Channel to channel variations of less than 10% have been routinely observed while variations of less than 5% have been seen when the process technology is carefully controlled. The usefulness of the receiver array technology can only be appreciated if the yield of fully functional chips is reasonable. The fabrication technology has to be suitably modified to achieve high process yield and this is greatly simplified if the technology requires fewer lithographic steps. The receiver arrays in which the p-i-n photodetectors have been fabricated from the base-collector junction of the HBT have been able to demonstrate all the above attributes of monolithic integration [6,7].

An important consideration for all monolithic array photoreceivers is crosstalk between adjacent channels under simultaneous multichannel operation. Usually optical crosstalk, arising from light exiting from one fiber leaking into adjacent photodiodes, is negligible since the photodiodes are atleast 250 microns away from each other. Numbers as low as -50 dB have been measured [8]. The dominant crosstalk is electrical in nature, and is fundamentally due to inadequate grounding of the high frequency signals on all the dc power supply lines. The rf signals from adjacent channels appear as crosstalk signal at the output of the central channel and degrade its performance. The level of crosstalk depends on the signal power being received by the adjacent channels and increases as the number of channels under simultaneous operation increases. Proper chip and package design should minimize crosstalk to levels which are acceptable for system performance, as demonstrated by the excellent performance of an eight channel p-i-n/HBT receiver array in an eight-wavelength WDM transmission experiment over 720 km of standard fiber at 2.5 Gb/s per channel [8].

An area that is receiving increased attention now is in the integration of guided-wave devices with photoreceivers for realizing a "spectrometer-on-a-chip". The monolithic chip is a wavelength demultiplexed receiver capable of resolving the wavelength channels, detecting and amplifying the signals. Present WDM architectures require such demultiplexed receivers not only at the end of a link, but also in wavelength adaptors and wavelength add-drop multiplexers. Currently, hybrid modules have been put together in which a silica WGR module is interfaced with an array of photodetector module. Monolithic integration offers all the advantages of compactness, simplified packaging, versatility, and scalability. There have been several demonstrations of monolithic demultiplexed receivers, in which an etched Rowland grating [9] or a waveguide grating router (WGR) have been integrated with p-i-n photodetectors [10]. Channel spacings as narrow as 0.8 nm and number of channels as large as 65 have been demonstrated. The issues that have to be taken into consideration for such monolithic implementations are insertion loss, polarization sensitivity, input optical coupling efficiency, waveguide-to-photodiode coupling efficiency, chip size, channel pass band shape, number of channels, whether there are out-of-band passbands, and finally complexity of multi-step epitaxy and its influence on the WGR properties. The devices reported so far have to be optimized further for any practical application. If the silica WGR is to be used as a benchmark device, then the semiconductor equivalent should have insertion losses between 5 dB and 8 dB and a polarization sensitivity of less than 0.1 nm. These are challenging targets and research worldwide is in progress to realize viable solutions.

The quick maturity of monolithic array photoreceivers have made them key enablers in multichannel WDM applications and one expects the trend to continue towards larger array size and towards higher speed on each channel. There is, however, a need for a concurrent development of array technologies for some of the electronic signal processing functions that need to be done following the front end, and presently there is minimal effort at speeds of 2.5 Gb/s and higher. It is expected that the advancement of WDM optical technology will spur the IC technologies for the realization of arrays of electronic functions. Nevertheless, OEIC array photoreceivers have demonstrated excellent potential in system experiments and hopefully will continued to be used in novel architectures.

## REFERENCES

1. S.Chandrasekhar and M.A.Pollack, "Optoelectronic and Photonic Integrated Circuits", Ch. 4 in *Perspectives in Optoelectronics*, ed. By Sudhanshu S. Jha, World Scientific, Singapore, 1995.
2. K.Takahata et al., *IEEE Photon. Technol. Lett.*, vol.8, pp. 563-565, 1996.
3. W.S.Lee et al., *Electron. Lett.*, vol. 28, pp.612-614, 1992.
4. K.Aga et al., *Tech. Dig., Optical Fiber Commun. Conf. OFC'91*, San Diego, CA. Feb. 1991, paper TuB2.
5. R.H.Walden et al., *Tech. Dig., LEOS Sum. Top. Meet., ICs for New Age Lightwave Commun.*, Keystone, CO, Aug. 1995, paper FC1.
6. S.Chandrasekhar et al., *IEEE Photon. Technol. Lett.*, vol. 8, pp.682-684, 1996.
7. K.C.Sayo et. al., *Tech. Dig., Optical Fiber Commun. Conf. OFC'97*, Dallas, TX, Feb. 1997, paper TuD5.
8. L.D.Garrett et al., *IEEE Photon. Technol. Lett.*, vol. 9, pp.235-237, 1997.
9. J.B.Sooile et al., *Electron. Lett.*, vol.29, pp.558-559, 1993.
10. S.Chandrasekhar et al., *IEEE Photon. Technol. Lett.*, vol. 7, pp.1342-1345, 1995.

**WC1 (Invited)**  
**2:00pm - 2:30pm**

**Are WDM Component Needs for Datacom Different Than for Telecom?**

Karen Liu,  
Tellabs Optical Networking Group  
30 Saw Mill River Road  
Hawthorne, NY 10532  
914-784-7378  
914-784-6225 Fax

In the last few years, wavelength division multiplexing has successfully penetrated the long-haul telephony infrastructure to the degree that some general agreement exists as to the associated component requirements. Although manufacturers still make primarily custom devices, these custom designs resemble each other more than they differ. As a result, manufacturers have been able to make the commitments that allow their technology to develop which, in turn, enable faster maturing of WDM systems. In this, the work on standardization has been quite helpful even though the stated purpose of ensuring interoperability of systems is far from realized. Now, the research community's attention is beginning to turn to new WDM markets, primarily access telephony, but also high-end datacom. The purpose of this paper is to discuss some early ideas on how component requirements might differ for these new markets. Of course, there has been much discussion about the general trends towards a blurring between datacom and telecom as Internet traffic becomes a significant fraction of the telephony load, and as voice/video real-time applications are of increasing interest for Internet and Web applications. However, these trends are likely to result in changes at higher layers than the physical layer so it is impossible to account for them except to note that perhaps WDM offers some flexibility to meet changing resource allocation needs in the future.

In some regards, high-end datacom requirements look a bit more like access telephony than long-haul telephony. The distances are those for metropolitan area networks, or even local-area networks. The assumption is that communications over longer distances will be carried over telephony as a payload. As a result, it is not a foregone conclusion that optical amplifiers will be used. There is strong pressure on link budgets since there is a step-function in cost once an amplifier is required no matter how low the gain. At the same time, datacom equipment may reside in a less protected environment than telephony equipment. The safety limits for such equipment are typically Class 1, not Class 3a, so it is unlikely the link budget can be stretched using higher power transmitters. These factors together create a demand for more sensitive receivers.

Since most datacom applications today are 1 Gb/s and below, it is technically possible to make sensitive receivers. However, over the last few years more sensitive low-speed receivers have been taken off the market in favor of SONET-standard sensitivities. Even for access telephony where SONET may be used, the restriction of these components

makes implementation of WDM difficult. Consider a fiber link that currently meets the SONET requirement for intermediate-reach by having 12 dB link loss. If WDM components are now introduced to the link, the additional loss of mux/demux, and perhaps monitoring functions, may mean the intermediate reach transmitters and receivers are no longer sufficient. Thus, having very low loss mux/demux and slightly more sensitive receivers could keep the component costs more reasonable than making the jump to long-haul receivers requiring APDs or even EDFAs.

In long-haul systems, the cost of the link with its associated EDFAs dominates over the terminal equipment. This is no longer the case in either access or datacom. Hence, it is essential that cost and ease of use of terminal equipment improve. Ease of use includes such factors as adjustment-free manufacturing, automatic configuration on installation, and automatic identification of WDM channels. Depending on whether the enterprise owning the datacom equipment owns the entire fiber or is sharing it with other WDM users, there may also be a security issue. For example, the automatic identification of the WDM channels may require some sort of proof of valid ownership of that wavelength to avoid the possibility of tapping into someone else's wavelength channel. Or, the hardware may somehow be structured to preclude access to the wrong channel.

A major issue for all WDM systems is wavelength accuracy budget. Current laser and mux/demux wavelength accuracies at manufacture are only tolerable; aging projections make open-loop operation of systems problematic. The product lifetimes of datacom products is more likely to be 10 years compared with 25 years for telecom, which provides a certain degree of relief. Also, datacom is more permissive of scheduled outages during which maintenance can occur. On the other hand, the pressures on terminal equipment cost argue against stabilization schemes if they cost too much. Also, if the WDM equipment is owned by the datacom end-user (rather than leased from a large service provider), the end-user is unlikely to have enough WDM installations to amortize the cost of WDM specific test equipment and skilled technician training. It is also unlikely that such an end-user will be willing to inventory many spare parts. Thus strategies for maintenance are likely to differ for datacom, telecom, and for datacom leased from provider.

Datacom is fortunate in having relatively benign environmental requirements. If the WDM equipment is integrated or lives close to the data source, it may be in an office or computer room with controlled indoor climate. The opposite is true for telecom access where the equipment may be outdoors. The mechanical design of datacom products is similarly not so regulated as in telecom. The easier environment, shorter product life, lower bit rates can hopefully be translated into component cost reductions that will in turn enable WDM to migrate down from the high-end toward low-end datacom.

WC2 (Invited)  
2:30pm - 3:00pm

## Hybrid and Monolithic Integrated Optical Devices for WDM Subscriber Systems

Junichi YOSHIDA, Yasuhiro SUZUKI, and Hiroshi TAKAHASHI\*

NTT Opto-electronics Laboratories

3-1 Morinosato-Wakamiya, Atsugi-shi, 243-01, Japan

\* 162 Shirakata-Shitrane, Tokai, Naka-Gun, Ibaraki, Japan

Optical access networks, FTTx ( $x = \text{Cab/C/B/H}$ ), have become strategic targets for telecommunication operators to satisfy the future demands for high-speed, high-quality information networks. Generally, FTTx systems should provide WDM functions for both 1.3- $\mu\text{m}$  and 1.5- $\mu\text{m}$  wavelengths, or D-WDM transmission capabilities for future upgrades of the system. Optical devices or modules for these systems are expected to be of high-performance and high-reliability, while the cost being low.

Figure 1 shows a 1.3- $\mu\text{m}$  /1.5- $\mu\text{m}$  WDM optical transceiver[1] for an FTTH system[2] which enables 1.3- $\mu\text{m}$  bi-directional TCM transmissions for POTS and N-ISDN services and a simultaneous transmission of 1.5- $\mu\text{m}$  video distribution signals. This transceiver contains the following innovative component technologies to achieve the low-cost target;

- Planar-lightwave-circuit(PLC) platform[3],
- Lensless coupling and passive alignment with PLC and a spot-size-converter-integrated laser diode (SS-LD) and two waveguide photodiodes (WG-PD),
- SC-compatible simplified optical connectors (receptacle)[4].

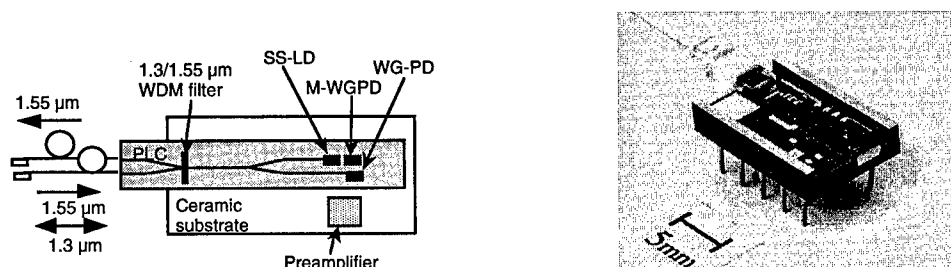


Fig. 1. Optical hybrid integrated module for FTTH systems <sup>[1]</sup>

Although the configuration of the transceiver in Fig. 1 is designed for simultaneous transmission of 50 Mb/s burst-mode digital signals and video distribution signals, the same technologies are applicable to the transceivers for other access network configurations such as FTTB or FTTC/Cab, even at higher bit rates.

The monolithically integrated spot-size converter waveguide has become widely recognized as a powerful tool in solving the coupling problem in semiconductor waveguide devices. F-P laser diodes with an integrated spot-size converter (SS-LD)[5] are good examples, and they have shown wide variety of integrated components by combining with the PLC platform technology. Figure 2 shows a promising low-cost 4-wavelengths-light-source for WDM networks composed of 4 SS-LDs mounted on a PLC platform with waveguide gratings.

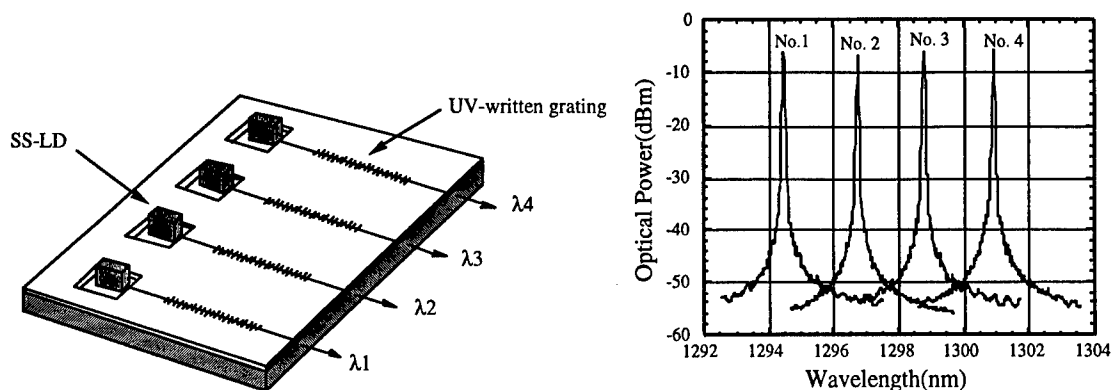


Fig. 2. Multi-wavelengths light source composed of SS-LDs and PLC platform with waveguide gratings

For semiconductor optical devices, such as lasers, wavelength filters and AWGs, not only polarization sensitivity but also temperature sensitivity are critical. Recently, however, novel structures for temperature insensitive operation of optical filters were proposed, and the most temperature independent characteristics have been reported in the semiconductor M-Z filter[6] and the AWG[7]. Concerning these progress in the integration technology, integrated optoelectronic components, such as spot-size converter waveguide integrated lasers (SS-LDs) and AWGs, and the PLC optical hybrid integrated devices will lead the way toward low-cost components for WDM access networks.

#### References:

- [1] N. Uchida, et al., "Low-cost and high-performance hybrid WDM module on a PLC platform for fiber-to-the-home", ECOC'96, Oslo, Norway, Sept. 1996, paper TuC3.1.
- [2] I. Yamashita et al., "Fiber optic subscriber network field trial", NTT Review, Vol.4, No.2, pp.16-12, 1992
- [3] Y. Yamada et al., "Hybrid integrated optical WDM transmitter/receiver module for optical subscriber systems utilizing planar lightwave circuit platform", Proc. OFC'95, San Diego, USA, Feb. 1995, paper PD12.
- [4] R. Nagase et al., "Simplified SC-type receptacles for optical subscriber systems", Proc. ECOC'95, Brussels, Belgium, Sept. 1995, paper Tu. P.12.
- [5] Y. Tohmori et al., "High temperature operation with low-loss coupling to fiber for narrow-beam 1.3  $\mu\text{m}$  lasers with butt-jointed selective grown spot-size converter", Electron. Lett., Vol.31, pp.1838-1840, 1995.
- [6] H. Tanobe et al., "A Temperature insensitive InGaAsP/InP wavelength filter", Tech. Digest, Integrated Photonics Research, Boston, 1996, paper IME3-1.
- [7] H. Tanobe et al., "Temperature insensitive arrayed waveguide grating on InP substrates", OFC'97, Dallas, USA, 1997, to be presented



**WC3 (Invited)**  
**3:00pm - 3:30pm**

### **Low-Cost Multimode WDM for the Local Area Network**

Brian Lemoff, Lewis B. Aronson, Lisa A. Buckman, and David W. Dolfi  
Hewlett-Packard Laboratories, 3500 Deer Creek Road MS26M9, Palo Alto, California, 94304 USA

For some time now, fiber optic links have played an important role in local area networks. The initial use of fiber-optic links has been for 10 Mbit/s Ethernet extensions and 100 Mbit/s FDDI loops. These links are predominately based on 62.5/125 graded-index multimode fiber (62MMF) and LED sources. Recently, there has been an explosion of demand for much faster links. Components for 622 Mb/s ATM, 1.06 Gb/s Fiber Channel and Gigabit Ethernet (1.25 Gb/s signaling rate) are now available.<sup>1</sup> These higher data rates have forced a transition from the use of LEDs to CD lasers and vertical cavity surface emitting lasers (VCSELs). As data rates approach and exceed 1 Gb/s, modal dispersion begins to severely limit link length. For 622 Mb/s, the maximum link length for short-wavelength (~850 nm) sources is about 500 - 600m. At Gigabit Ethernet rates, the maximum link length is less than 300m, the minimum practical length for backbone links. One way to go beyond these limits is to use 1300 nm Fabry-Perot lasers. These devices are generally more expensive than short-wavelength sources and will only provide about a factor of three in improvement. Another possible, but expensive, solution is to install single mode or higher bandwidth multimode fiber in the building infrastructure. We believe that the best solution may be the use of low cost, multimode wavelength division multiplexing. WDM is scalable to 4 - 16 times the bandwidth of conventional links and is compatible with low cost 1300 nm lasers when they become available. This paper describes a compact transceiver module that achieves an aggregate data rate of 2.5 Gb/s over 500m and 4 Gb/s over 300m of 62MMF using 4 wavelength channels each running at 622 Mb/s and 1 Gb/s respectively.

Figure 1 shows the key components of our WDM transceiver module. Currently, all of the optoelectronic and integrated circuits are contained on a ceramic module that is approximately 40 x 40 mm<sup>2</sup>. Four VCSELs, with wavelengths of 820, 835, 850, and 865 nm, are driven by a silicon bipolar laser driver array. The light from the VCSELs is combined in a polymer waveguide (Polyguide™<sup>2</sup>) 4-to-1 combiner, which is coupled to an outgoing fiber. Incoming light passes from the fiber through a Polyguide™ wavelength demultiplexer. The light is detected on an array of GaAs MSM photodiodes, and silicon bipolar receiver electronics convert the signal to a digital electronic output. Many of the packaging and electronic technologies used were originally developed as part of a parallel optical link project.<sup>3</sup>

In the Polyguide™ combiner, four input waveguides merge into one output waveguide. The light emitted from the lasers is coupled into the waveguides through reflection off of a 45° mirror cut into the edge of the waveguides. By choosing the width of the input waveguides to be smaller than the width of the output waveguide, loss due to the combining process can be minimized. All of the devices built to date have been pigtailed. We have observed total insertion losses, from VCSEL to fiber, of 2.1 dB in the combiner. It should be noted that a 4-to-1 combiner using single mode waveguides would have a minimum loss of 6 dB. It is the multimode nature of our combiner that allows much lower loss.

We have been investigating a number of techniques for demultiplexing. The simplest technique and the one used in this work, shown in Figures 2 and 3, is to use a polymer waveguide 1-to-4 splitter to divide each wavelength equally among the four outputs. A tiny dielectric interference filter is then attached at each output. The filters are made by depositing a multilayer dielectric stack onto a fused quartz substrate using a PECVD process. The advantage of such a device is its simplicity and ease of fabrication. Splitting the light before filtering, however, introduces a fundamental 6 dB loss for a four-channel system. The filter functions of each output are shown in Figure 4, which shows a usable channel width of nearly 8 nm for our 15 nm channel spacing.

Figure 5 shows the optical spectrum in the multimode fiber when all VCSELs are turned on. Independent data sources were used to drive each laser at 622Mb/s or 1 Gb/s with 2<sup>23</sup>-1 PRBS patterns. Figure 6 shows the output of the receiver IC for the two data rates through 500m of 62MMF. The marginal quality of the 1 Gb/s/channel output is due to operating beyond the normal modal dispersion limits.

In conclusion we have demonstrated 2.5 and 4 Gb/s data transmission through 500m of 62MMF using four channel WDM. We believe that the types of components used can be inexpensive enough for practical use in local area networks.

<sup>1</sup> See for example: "Hewlett-Packard Fiber Optic Components Selection Guide", 1996.

<sup>2</sup> Booth, B. L., "Low Loss Channel Waveguides in Polymers", IEEE J. Lightwave Tech. **LT7**, 1445-1453 (1989).

<sup>3</sup> Hahn, K.H. et al., "Gigabyte/s Data Communications with the POLO Parallel Optical Link", Proc. 46<sup>th</sup> ECTC, 1996 pp. 301-307.

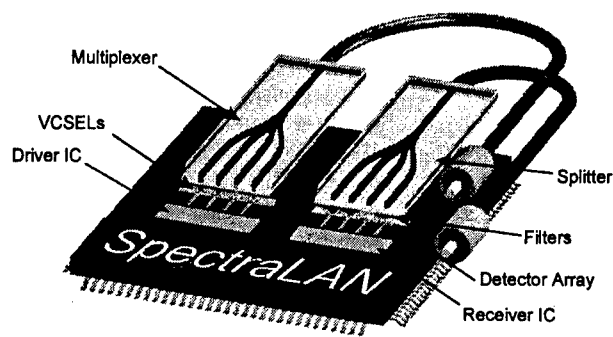


Fig. 1 Transceiver module components

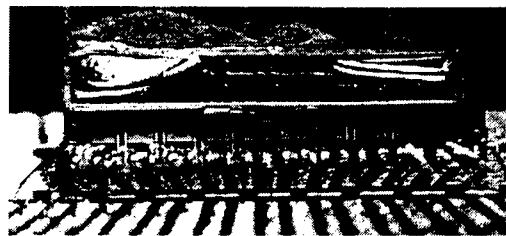


Fig. 2 Demultiplexer with filters over MSM Detector Array

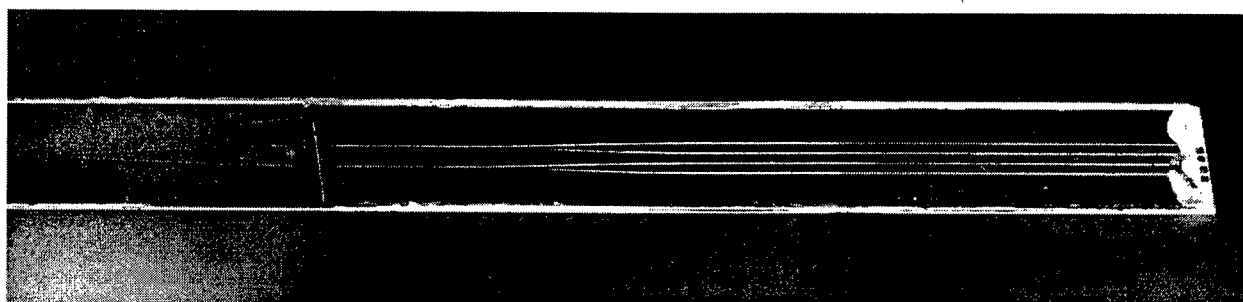


Fig. 3 Splitter demultiplexer with filters at far right

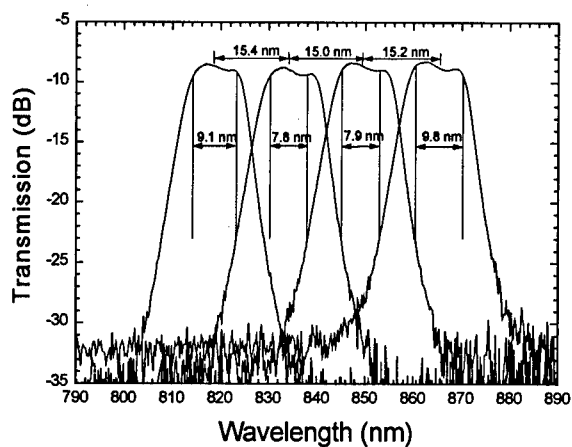


Fig. 4 Filter functions of the splitter demultiplexer channels.

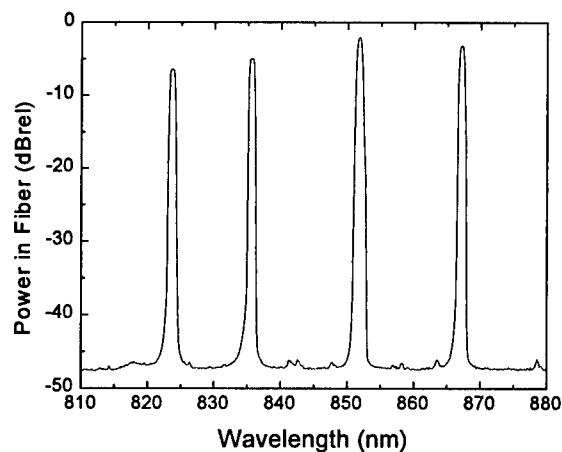


Fig. 5 Spectrum of the optical signal launched in the fiber

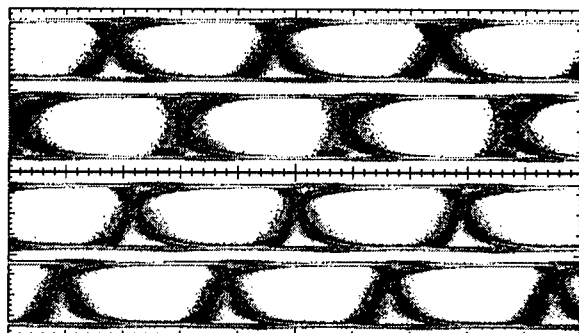


Fig. 6 Eye Diagrams of received signals through 500m of 6.5/125 MMF. (Left) 622 Mb/s/channel. (Right) 1 Gb/s/channel.

**WD1 (Invited)**  
**4:00pm - 4:30pm**

## **Selectable wavelength laser arrays for WDM applications**

U. Koren, Bell Laboratories, Lucent Technologies, Holmdel N.J. 07733

As WDM systems are becoming an increasingly important factor in optical telecommunications, there is a strong need for practical and inexpensive WDM sources. Such sources will enable spreading WDM technology to metropolitan area networks and local access markets, as well as for long distance transmission and networking. In current WDM systems, the most commonly used sources are single wavelength DFB lasers. These lasers are selected from different wavelength "bins" to cover all the system channels, with relatively relaxed tolerances, as each DFB laser can be temperature tuned over a spectral bandwidth (typically 1-2 nm) that is comparable to the current system channel spacing. These lasers are widely available and have about 0.1 nm long term wavelength stability. This good wavelength stability can be improved even further with a feedback control loop. In the near future, the next generation WDM sources will have a similar footprint to DFB lasers in terms of size and cost, but with improved functionality that is already apparent in the available rapidly growing WDM systems.

Functionally, the next generation WDM sources can be differentiated as two general classes. The first is wavelength selectable laser sources (WSL's), that can operate at one wavelength at a time but can be remotely programmed to switch wavelengths. Another class of devices are laser arrays or multi-frequency lasers which are used as Simultaneously Modulated multi channel Sources (SMS's). These general classes can be subdivided further. For the WSL device, an important parameter is the reconfiguration time. Many system architectures require only a relatively slow (0.05 - 1 second) wavelength switching time, but some architectures are using package switching and require fast (10 nsec) wavelength switching times. An example is the all optical network (AON) testbed deployed in the Boston metropolitan area [1] which is employing DBR tunable lasers for rapidly switched WSL sources. For this application DBR lasers present a very attractive and simple solution. Reliability and wavelength stability have been improving, as recent reports by F. Delorme et al [2] have demonstrated. However these devices are still limited in tuning range, as typically the fast tuning capability is well below 15 nm, and simultaneous operation of several channels cannot be obtained.

In the present talk will review some of the ongoing work considering DFB arrays for WSL and SMS applications. To ensure output power levels and chirp performance similar to current DFB lasers with integrated electroabsorption (EA) modulators, a semiconductor optical amplifier (SOA) and an EA modulator are sometimes integrated with these arrays [3]. We review the available data on uniformity, chirp and wavelength precision of these arrays, as well as the packaging requirements. An approach that separates a tunable wavelength source and the amplifier-modulator part into two different packages have also been suggested [4]. For an SMS source, simultaneously modulated channels create significant cross talk penalties when propagating through a common SOA [5]. However, without an SOA, a laser array with six directly modulated DFB lasers combined into a single output fiber, has been demonstrated.

Wavelength converters will be an essential part in future WDM networks. At present it is possible to use single DFB lasers for a fixed output - variable input wavelength converters [6]. However, in the near future, WSL devices will enable the emergence of programmable wavelength converters where the output wavelength can be remotely switched to any of the system channels.

#### REFERENCES:

1. B.R. Hemenway et al, "Performance of a wavelength routed all optical network at over 100 Gb/sec" IEEE-LEOS optical networks summer topical Keystone CO. (1996).
2. F. Delorme et al, "Reliability study of 1.55 micron DBR lasers grown in three MOVPE steps" OFC - 97 paper FC2, Dallas Texas, (1997).
3. M.G. Young et al
4. R.E. Behringer et al "Integrated EA modulator/SOA for 2.5 Gb/sec modulation with fiber to fiber gain" OFC - 97 paper WG1, Dallas Texas, (1997).
5. G. Raybon et al "1.7 Gb/sec transmission over 217 km using a 16X1 PIC transmitter" Electronics Lett. 29, 1295, (1993).
6. L Spiekman et al. "All optical Mach Zender wavelength converter monolithically integrated with a  $\lambda/4$  wavelength shifted DFB source" OFC - 97 paper PD10-1, Dallas Texas, (1997).

# A Compact Wavelength Stabilization Scheme for Telecommunication Transmitters

B. Villeneuve, H. B. Kim, M. Cyr and D. Gariépy

Nortel Technology, P.O. Box 3511, Station C, Ottawa, Ontario, Canada K1Y 4H7

With the 100/200 GHz channel spacing of current commercial DWDM systems, severe restrictions are imposed on transmitter wavelengths in order to meet crosstalk specifications and ensure reliable operation of the system in all conditions of its 25 years lifetime. While very stable in the short-term, free-running DFB laser transmitters are expected to exhibit long-term wavelength drifts exceeding these requirements [1], leading to a need for practical wavelength monitoring and control. In this paper we describe a compact dither-free wavelength stabilization method based on a Fabry-Perot (FP) filter. While the concept can be implemented in a stand-alone unit, its small footprint allows its incorporation into existing laser modules without increasing either real estate or dissipated power.

The basic principle of operation relies on the well-known angular behavior of FP filters, for which the peak wavelengths corresponding to each order vary as the cosine of the internal tilt angle. As represented in Fig. 1, a slightly diverging beam of light transmitted through an FP is detected by two closely spaced photodetectors  $P_1$  and  $P_2$  acting as apertures. Each captures a different portion of the total solid angle emitted by the divergent source. Thus, two different spectral responses, offset in wavelength according to their angular difference, are produced. Since  $P_2$  captures

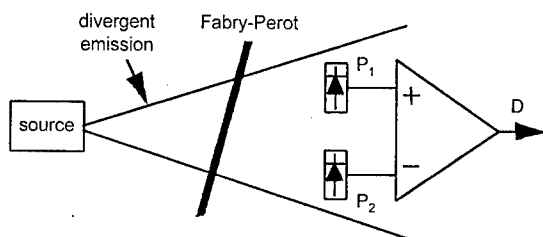


Fig. 1: wavelength discrimination arrangement

a portion of the emitted light which traversed the FP at a lower tilt angle than that captured by  $P_1$ , its response will peak at a slightly higher wavelength than  $P_1$ , a situation which is reproduced for every FP order. Fig. 2 shows the result for one particular FP order, in the preferred case where the different FP and alignment parameters are chosen so that the wavelength offset between the two responses is roughly equal to their effective bandwidths. Common locking techniques can then use the discrimination signal  $D$  (Fig. 1) to maintain  $\lambda = \lambda_0$ , either through current or temperature feedback,

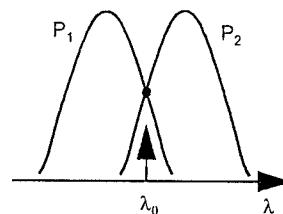


Fig. 2: photodetector signals

without the need for wavelength dithering. Note that, by selecting a  $P_1 / P_2$  gain ratio different than one, a stable locking point can be obtained anywhere in the wavelength region around  $\lambda_0$  where the two slopes are roughly linear. This feature can be useful for initial trimming. A wide range of discrimination slopes and locking ranges can be accommodated by selecting an appropriate intrinsic FP filter bandwidth.

The diverging emission source can for example be a singlemode fiber or a laser, usually combined in practice with a lens for adjusting the divergence. This adjustment allows more latitude in the choice of photodetector size and placement, increases detected power and helps in reducing source to detector distance. Lens choice is not critical, and various aspheric and spherical lenses have been used successfully. The photodetectors are ideally placed on a single chip, easily obtained by cleaving together a matched pair of adjacent devices. Two basic types of Fabry-Perot filters have been used. First is the solid etalon variety, where high-reflectivity coatings are deposited on both sides of a glass spacer. With an appropriately chosen thickness, the arrangement described above will then produce simultaneous dither-free locking points for each channel on the ITU grid (or any other regular frequency grid). The second filter type is the single-cavity multilayer dielectric filter, giving a single well-defined locking position. In both cases, high deposition energy coatings are preferably used for optimal environmental and long-term stability.

A number of prototypes of stand-alone reference were assembled in standard 10-pin butterfly packages with singlemode fiber input and various combinations of aspheric or ball lenses, fused silica solid FPs or multilayer dielectric filters, and pairs of small (25  $\mu\text{m}$ ) or large (350  $\mu\text{m}$ ) photodiodes. In one example, reliable wavelength locking was achieved with less than -20 dBm signal input and 5 pm polarization sensitivity.

While the results on stand-alone references were promising, it was decided to concentrate our efforts toward integrating this concept into existing laser modules, taking advantage of its compact footprint.

A current implementation uses the laser's back-facet emission. All the necessary optical elements are secured to the existing 4.5x8 mm<sup>2</sup> laser carrier. A ball lens ground to height is used for divergence adjustment. The FP filter element is placed next, standing on its edge. Two photodetectors, cleaved as one chip and vertically bonded to a carrier, complete the optical assembly. A thermistor is used to monitor and control carrier temperature. In order to obtain required long-term reliability characteristics, the lens and filter are secured to the carrier with a thin layer of thermally-cured epoxy, their large contact surfaces giving adequate mechanical stability. The finished carrier can then be assembled into existing laser modules with minor modifications and, significantly, without additional space or power dissipation on the transmitter board. This has been demonstrated with both CW laser modules and modules containing laser/external modulator assemblies. We present now some performance characteristics for ten CW laser module prototypes incorporating wavelength-stabilized carriers with standard front-end optics.

Multilayer dielectric filters fabricated by a high-energy ion-plating deposition technique [2], and obtained from the National Research Council in Ottawa, Canada, were used. A  $\pm 20$  pm initial tolerance from target was achieved for the finished modules. Fig. 3 shows a comparison of wavelength variations observed for a single module in both free-running and locked laser operation, as a function of carrier temperature. Here, 30°C is taken as the reference temperature. The average coefficient for all modules was about 4 pm/°C, corresponding to the dielectric filter characteristics. Placing the same module in an oven cycled 3 times from 0 to 75°C (5 hour cycles) while monitoring the locked wavelength gives the result presented in Fig. 4.

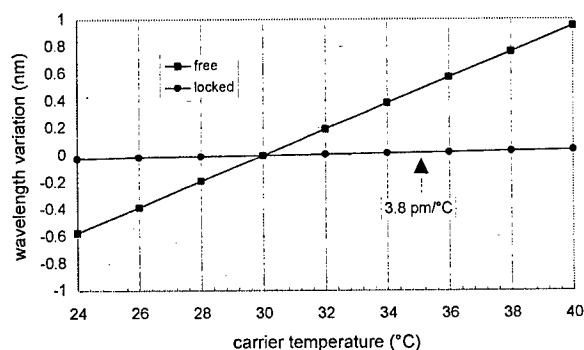


Fig. 3: wavelength dependence on carrier temperature

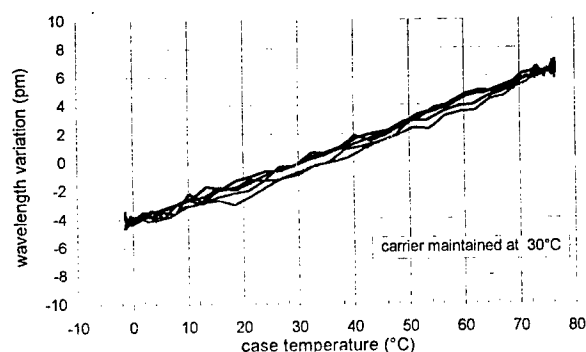


Fig. 4: wavelength dependence on case temperature

A similar hysteresis-free 0.16 pm/°C average coefficient was observed for all modules, and this wavelength dependence is likely due to a slight variation in actual filter temperature. Since filters with an order of magnitude reduction in temperature dependence are now available, the measured carrier and case temperature coefficients are expected to be reduced similarly in future implementations.

In order to test the mechanical stability, two units were submitted to 500 cycles of rapid -40 to +85°C change, with 1-2 pm resulting variation in locking wavelength. Regarding long-term characteristics, two different units were stored at 80°C for an extended period of time: -14 and -18 pm shifts were observed after 2000 hours, with 75% of the shifts occurring in the first 500 hours. Less than 2 pm further change was observed after 5000 hours. Characteristics of these shifts suggest that the initial stabilization period can be burned-in, thus reducing actual operational lifetime variations. After 5000 hours at 80°C, one of these two units was monitored in normal operation at room temperature: a locked wavelength stability better than  $\pm 0.2$  pm was then observed over a one week period. We are presently investigating the long-term stability characteristics of various filter types.

In conclusion, we have demonstrated a novel, compact dither-free wavelength stabilization scheme suitable for incorporation into existing laser modules with minimal increase in real estate or dissipated power.

## References

- [1] R.S. Vodhanel, M. Krain, R.E. Wagner and W.B. Sessa, "Long-term wavelength drift of the order of -0.01 nm/yr for 15 free-running DFB laser modules", OFC'94, San Jose, CA, Feb 1994, paper WG5.
- [2] A.J. Waldorf, J.A. Dobrowolski, B.T. Sullivan and L.M. Plante, "Optical coatings deposited by reactive ion plating", Applied Optics, 1 Oct. 1993, Vol. 32, No 28, pp. 5583-5593.

## An absolute frequency reference at 1556 nm for WDM communication systems

M. Poulin, C. Latrasse, N. Cyr and M. Têtu

*Centre d'Optique, Photonique et Laser**Département de Génie Electrique et de Génie Informatique, Université LAVAL**Ste-Foy, Qc, G1K 7P4, Canada*

Standardization of channel frequency allocation and calibration of the frequency scale at  $1.55 \mu\text{m}$  will require some frequency standards in this range. A promising avenue consists of making use of the two-photon transitions of rubidium at 778 nm to frequency-lock a 1556 nm laser. These lines have been recently measured by direct comparison to the Cs frequency standard with an uncertainty of 2 kHz [1]. The method which we develop consists in using the second harmonic of the 1556 nm laser to injection-lock a low-cost laser diode operating at 778 nm which is then used to observe the transitions in rubidium.

*Second harmonic generation and linewidth reduction of the 1556 nm laser*

In order to be able to injection-lock the Fabry-Pérot laser at 778 nm, a second harmonic power of at least a few microwatts must be generated. This is done by placing a nonlinear crystal of  $\text{KNbO}_3$  in a resonant ring cavity similar to that described in ref 2. The crystal, cut to allow critical phase-matching at 1560 nm, can also be used efficiently at 1556 nm with a slightly different angle. The experimental setup is shown on figure 1. With 43.1 mW of 1556 nm laser power impinging on the cavity input mirror, a power of about  $15 \mu\text{W}$  is generated at 778 nm.

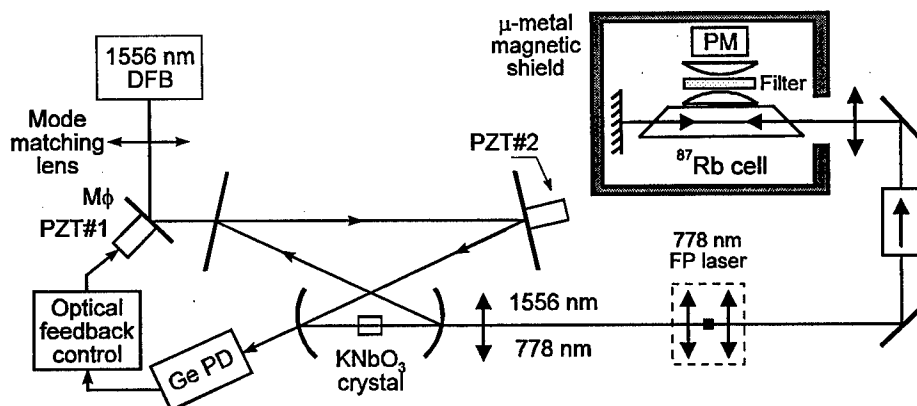


Figure 1: Experimental setup.

Also, as the natural width of the two-photon transition in rubidium is only of 300 kHz [3], the linewidth of the 1556 nm laser has to be reduced. This is realized by using optical feedback from the resonant cavity. On resonance, scattering on the crystal facets excites the counter-propagating mode which is fed back into the DFB laser [4]. As the stabilization is dependent on the phase of the feedback light, we use a piezo-mounted mirror ( $M\phi$ ) to control the length between the laser and the cavity input mirror. The position of mirror  $M\phi$  is modulated at 3 kHz and the fundamental transmitted power, detected with a Ge photodiode, is sent to a lock-in amplifier. A correction is applied to the piezo element PZT#1 to maintain locking to the top of the transmission curve. In this way, the linewidth of the 1556 nm DFB laser is reduced from 3.5 MHz to a few tens of kilohertz. The modulation of the position of mirror  $M\phi$  also leads to a modulation of the laser frequency which is used subsequently.

### Injection-locking of the 778 nm laser and rubidium spectroscopy

The second harmonic signal is focused on the rear facet of a low cost quasi-monomode Fabry-Pérot laser (Mitsubishi ML4402) operating at 778 nm. The front facet output of this laser (about 5 mW) is sent into a  $^{87}\text{Rb}$  cell heated to about 75°C. A  $f = 30$  cm lens and a plane mirror are used as a cat-eye to obtain two counterpropagating beams inside the Rb cell. A photomultiplier (PM) is used to detect the fluorescence at 420 nm due to the radiative cascade  $5D-6P-5S$ . The Rb cell, the mirror and the detection apparatus are all placed inside a  $\mu$ -metal magnetic shield. A two-photon absorption spectrum, obtained by scanning the resonant cavity length is shown on figure 2. The voltage applied to the photomultiplier is 800 V. Four lines, corresponding to the transitions  $5S_{1/2} (F_g = 2) \rightarrow 5D_{5/2} (F_e = 4, 3, 2, 1)$  can be seen. The strongest line exhibits a linewidth of about 640 kHz. To obtain a discrimination pattern as the one shown in figure 3, we take advantage of the 1556 nm laser frequency modulation that is caused by the modulation of the position of mirror  $M\phi$ . The photomultiplier output is sent in a lock-in amplifier and demodulated at 3 kHz. The error signal is fed to PZT#2 in order to lock the cavity resonant frequency, and thus the 1556 nm laser frequency, to the strongest observed line.

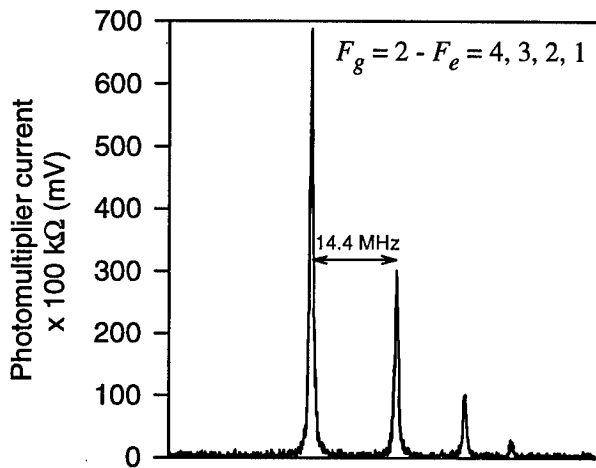


Fig. 2: Two-photon absorption spectrum of  $^{87}\text{Rb}$ .

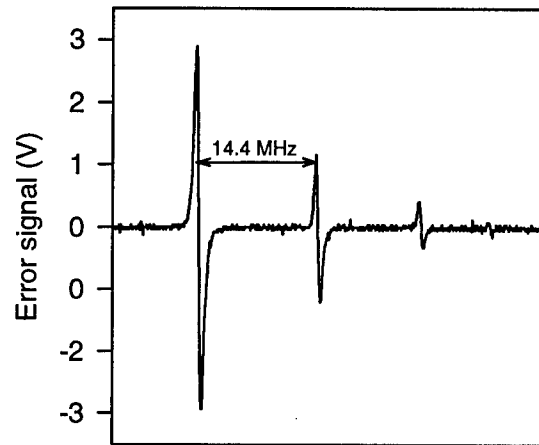


Fig. 3: Discrimination pattern.

### Conclusion

We have demonstrated efficient second harmonic generation of a 1556 nm DFB laser using a nonlinear crystal of  $\text{KNbO}_3$  placed in a resonant cavity. Optical feedback from this cavity is used to reduce the laser linewidth to a few tens of kilohertz. The second harmonic of the 1556 nm laser is used to injection-lock a 778 nm laser which is used to observe the two-photon lines of  $^{87}\text{Rb}$  at 778 nm and frequency-lock the 1556 nm laser to the  $5S_{1/2} (F_g = 2) \rightarrow 5D_{5/2} (F_e = 4)$  transition. This laser could be used as an absolute frequency reference for multiwavelength communication systems.

### References

- [1] D. Touahri *et al.*, *Opt. Commun.*, Vol. 133, pp. 471-478, 1 January 1997.
- [2] M. Poulin *et al.*, *IEEE Trans. Instrum. Meas.*, Vol. 46, No. 2, pp. 1-5, April 1997.
- [3] F. Nez *et al.*, *Opt. Commun.*, Vol. 102, Nos. 5-6, pp. 432-438, 15 October 1993.
- [4] A. Hemmerich *et al.*, *Opt. Lett.*, Vol. 15, No. 7, pp. 372-374, 1 April 1990.



### Wavelength-controlled DFB LDs for WDM systems

M. Yamaguchi, K. Kudo, H. Yamazaki, T. Sasaki

Opto-electronics Research laboratories, NEC corporation

34 Miyukigaoka, Tsukuba, 305 JAPAN

**Introduction** Wavelength division multiplexed (WDM) lightwave systems are expected to use many wavelength-controlled light sources. The simultaneous fabrication of different wavelength laser diodes (LDs) on a wafer is therefore an important technology which would allow WDM light sources to be prepared at low cost. The lasing wavelengths of these LDs must be precisely controlled to coincide with pre-assigned wavelength grids for WDM systems. Each LD with different wavelength should have uniform lasing characteristics even if the lasing wavelengths are distributed over a wide range, for example an Erbium-doped fiber amplifier (EDFA) gain band (1530 nm-1560 nm) or more. We developed a new type of wavelength controlled distributed feedback (DFB) LD. Electron-beam (EB) direct writing for grating formation [1] was combined with selective MOVPE growth technology for active layer bandgap energy control [2]. Uniform lasing characteristics were demonstrated for 40-channel different wavelength DFB LDs fabricated on one wafer, over a 75nm-wide wavelength range.

**Device fabrication** To control the wavelength of DFB LDs almost arbitrarily, the grating pitch controllability needs to be less than 0.01 nm. However, the minimum drawing step of a conventional EB machine is 2.5 nm. To reduce this value, we introduced a field size variation technique as shown in Fig. 2 [3]. The field size can be changed by 0.05% allowing fine pitch control of a 0.0012 nm step. Forty-channel different pitch gratings ( $\lambda/4$ -shift) from  $\Lambda_1=235.98$  nm to  $\Lambda_{40}=247.68$  nm by a 0.3 nm step were successfully formed on an n-InP wafer, as shown in Fig. 1.

DFB LD lasing characteristics will deteriorate if the lasing wavelength deviates greatly from the active layer gain peak wavelength. Therefore we used the selective MOVPE growth to adjust gain peak wavelength to the lasing wavelengths, to obtain uniform LD performance for all channels [4]. As shown in Fig. 1, 40 different pairs of SiO<sub>2</sub> masks with 1.5  $\mu$ m-wide stripe windows between them were formed on the grating wafer. The mask width varied from  $Wm_1=24.0$   $\mu$ m to  $Wm_{40}=35.7$   $\mu$ m by a 0.3  $\mu$ m step, depending on the grating pitch. An InGaAsP/InGaAsP compressive strain MQW active layer was then grown by a 1st selective MOVPE and buried with a p-InP cladding layer by a 2nd MOVPE. LD chips were cleaved into a 300  $\mu$ m-long cavity and anti-reflection-coated on both end facets.

**Characteristics** Figure 3 shows the measured lasing wavelengths and gain peak wavelengths for all channels. Stable single frequency operations with more than a 35-dB side mode suppression ratio were obtained over a wide wavelength range from 1518.2-nm to 1593.2- nm (75-nm wide). The average channel spacing was 1.95-nm which agreed well with the calculated value of 1.93-nm. The standard deviation for lasing wavelength was estimated to be 0.62-nm. The gain peak wavelengths were well-controlled within  $\pm 10$ -nm of the lasing wavelengths. This result is reflected in the uniform lasing characteristics shown in Fig. 4. Low threshold current operations of less than 12.0mA (8.9mA in average) were obtained for all channels

and lasing wavelength dependence was not clearly observed.

**Summary** We demonstrated for the first time over 75-nm-wide different wavelength DFB LDs with uniform characteristics in a wafer. The wavelength range was sufficiently wide compared with present EDFA gain bandwidth. We believe the fine pitch control of grating by EB lithography combined with the bandgap energy control by selective MOVPE are promising technologies to reduce the cost of WDM light sources.

## References

- [1] M. Suehiro et al, J. Quantum. Electron., vol. 29, p. 2081 (1993)
- [2] T. Sasaki et al, J. Crystal Growth, vol. 132, p. 435 (1993)
- [3] H. Yamazaki et al, OECC '96, PD2-1(1996), Makuhari Messe
- [4] K. Kudo et al, to be published in proc. IEICE General conf., (1997)

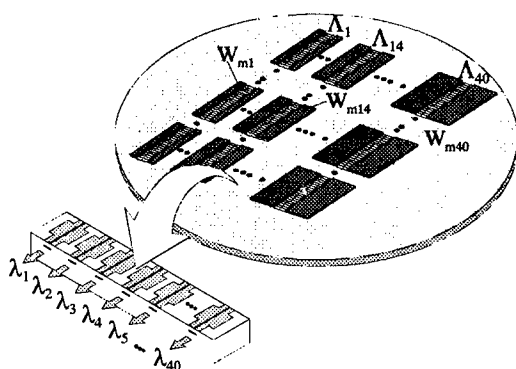


Fig. 1 Wavelength controlled DFB LDs fabricated on a wafer

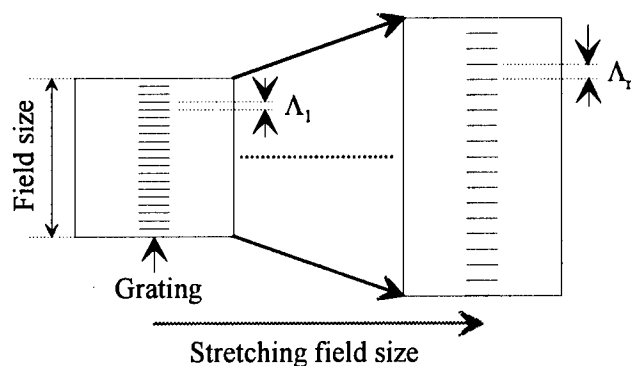


Fig. 2 Grating fine pitch control using field size variations by EB lithography

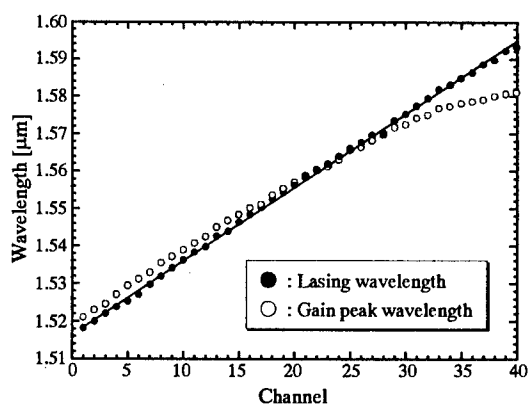


Fig. 3 Lasing and gain peak wavelength distributions

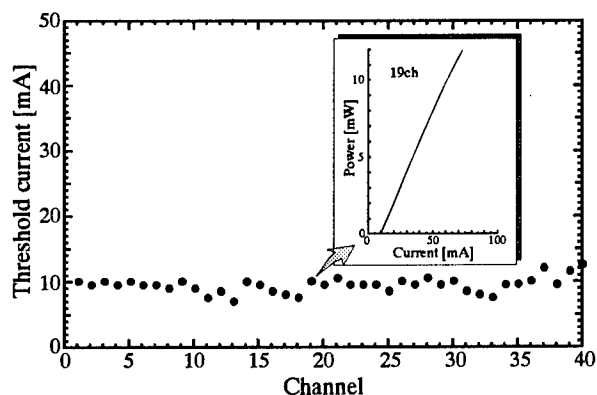


Fig. 4 Threshold current distributions  
Inset shows L-I characteristics

## **WDM COMPONENTS TECHNOLOGY**

**Thursday, 14 August 1997**

### **Sessions:**

- ThA: Wavelength Routing/Conversion I**
- ThB: Wavelength Routing/Conversion II**
- ThC: Filters I**
- ThD: Filters II**

## **Thursday Papers Not Available**

ThD1      “Wafer Scale Integration of WDM Wavelength Routets and  
Cross-connect Switches for Dynamic Network Control”, *Y. Chen,*  
*University of Maryland, Baltimore, MD*

**ThA1 (Invited)**  
**8:30am - 9:00am**

## **Applications of Integrated Optic Switches in WDM Networks**

Edmond J. Murphy  
Bell Laboratories  
Lucent Technologies  
Breinigsville, PA 18031  
edmond@lucent.com

Guided wave switch arrays are currently being utilized in WDM network experiments. The combination of switching and WDM technologies in optical networks allow new system capabilities such as rapid restoration and wavelength provisioning. In this paper, we will review the attributes of polarization independent switches in lithium niobate and describe recent devices that have been developed for use in experimental switching networks.

Guided wave switches based on Y-shaped or "digital" optical switch elements offer many advantages for WDM networks. First, the saturating characteristic of the optical transfer curve allows polarization independent operation by suppressing crosstalk associated with the secondary maxima of more conventional switch designs. This flattened response also reduces the sensitivity to control voltages, allowing operation of all devices with a single, uniform voltage. Secondly, the broad optical passband, which easily exceeds 100 nanometers, eliminates the need for any wavelength selection or tuning. Thirdly, the high speed of the electro-optic effect allows switching speeds several orders of magnitude faster than mechanical or thermo-optic devices - far exceeding the microsecond switching time needed for these networks. Finally the low polarization-independent crosstalk and the high yield attainable for these switch elements allow the fabrication of switch modules with extremely low levels of system level crosstalk.

We have fabricated highly integrated arrays of switches using the Y-switch as the basic switch element (1). The devices will be described in greater detail at the conference. Each array is comprised of 8 passive splitters and 88 active switches integrated on a single substrate. The elements are interconnected to form two 'enhanced' 4x4 switch arrays. Each 4x4 is strictly non-blocking and includes bridging (power splitting), disconnect switches (for terminating signal paths in the switch), and crosstalk reduction switch stages. Twenty of these modules have been built. Typical insertion loss is 10 dB (including 3 dB passive splitting), typical crosstalk per switch element is -18 dB. Further details of the measurements will be given at the conference.

This work is partially supported by DARPA as part of the MONET Consortium.

Reference: (1) E.J. Murphy, T.O. Murphy, R.W. Irvin, R. Grencavich, G.W. Davis, G.W. Richards, "Enhanced Performance Switch Arrays for Optical Switching Networks", European Conference on Integrated Optics, Stockholm, April 2-4, 1997.

ThA2

9:00am - 9:15am

## AN INTEGRATED OPTICAL ADD/DROP MULTIPLEXER IN InP BASED ON ELLIPTIC COUPLERS AND BRAGG GRATING REFLECTOR

C. Wei<sup>1</sup>, D. Van Thourhout, I. Moerman, S. Goeman, K. Vandeputte, R. Baets  
Univ. Gent-IMEC, INTEC-dept., ST-Pietersnieuwstraat 41, B-9000 Gent, Belgium

F. Groen, Y. Zhu  
Technical Univ. Delft, Dept of Physics, The Netherlands

### INTRODUCTION

The wavelength add/drop multiplexer (ADM) is one of the key components for dense wavelength division multiplexing (DWDM) systems. To realise this function, a number of schemes have been proposed and tested based on planar waveguide circuits or optical fibers, such as the planar waveguide based grating-folded directional coupler ADM [1], fiber based ADM's using Mach-Zehnder Interferometer structure and photoimprinted Bragg gratings [2] and so on. We proposed a new add/drop scheme based on elliptic beam collimators [3] and Bragg gratings realised in InP. In this paper, we will report the device design, fabrication and the preliminary experimental results.

### ANALYSIS AND DESIGN

The proposed configuration is shown in Fig. 1. The structure consists of four elliptic beam collimators, a Bragg grating on top of a slab guiding layer and four connecting channel waveguides. The light signals ( $\lambda_1, \lambda_2, \dots, \lambda_n$ ) are launched from guide 1. The guided beam is expanded and collimated by elliptic coupler 1. For the unresonant wavelengths, the collimated waves go through the slab region as if there is no grating existing, and are re-focussed onto waveguide 3. For the grating resonant wavelength (e.g.  $\lambda_i$ ) the collimated beam is reflected by the grating and is re-focussed by coupler 2 onto guide 2, forming the dropping channel. Because of the symmetrical nature of the structure, the  $\lambda_i$  channel can be added again into guide 3 from port 4.

The waveguide structure is formed by a 600 nm thick quaternary InGaAsP guiding layer is embedded in InP. A thin top quaternary layer (60 nm) is added for etching the grating. The design method of the elliptic beam collimators has been described in reference [4]. In the present design we selected the long and the short half axis of the elliptic section to be  $a=1000 \mu\text{m}$  and  $b=18 \mu\text{m}$  respectively and all the four couplers have the same geometry. The length of the slab free space is  $1000 \mu\text{m}$  and the length of the grating region is  $800 \mu\text{m}$ . The collimator structure has been experimentally investigated [3].

The depth of the grating, formed in the top quaternary layer, is designed to be 60 nm which corresponds to TE mode coupling coefficient of  $0.0025/\mu\text{m}$ . Hence the  $\kappa L$ -product of the grating is designed to be 2.0. The grating period is 234.5 nm for a Bragg wavelength of 1550 nm. Based on those parameters, the calculated FWHM bandwidth of the reflected spectrum is 0.8 nm.

### DEVICE FABRICATION AND EXPERIMENTAL RESULTS

The undoped waveguide layers were grown on a Si-InP substrate with MOCVD. The bandgap wavelength of the quaternary layer is  $1.3 \mu\text{m}$ . A 50 nm thick SiN<sub>4</sub> was sputtered on the layered sample surface to serve as mask. The grating pattern is formed by holographic exposure and etched to the top quaternary layer by RIE. The device processing use two contacting e-beam written chromium masks on quartz glass. One is for defining the grating windows and the other is for defining the waveguide structure.

To characterise the device spectrum responses, a tunable laser and a polariser controller was used. TE polarised light was launched into port 1, the transmitted and reflected spectrums were measured from port 3 and port 2. For the channel adding function, light (TE) was launched from port 4 and detected from port 3. The measurement results are shown in Fig. 2. From the transmitted and reflected spectrum curves one can see that the FWHM bandwidth is about 0.7 nm which is narrower than the designed value. No sidelobes were observed. The dip appearing in the transmission spectrum is not as deep as designed. This is due to a insufficient coupling coefficient

<sup>1</sup> Present address: QPS Technology, 2270 ST-Francois Road, Dorval, QC H9P 1K2, Canada

in the realised device-the etching depth turned out to be less than  $60\text{ }\mu\text{m}$  and can be strengthened by a deeper etching. Of the diffracted power at the Bragg wavelength, 20% comes out from the output waveguide of port 2. There are three possible reasons for the losses: the grating may be angularly misaligned, the beam collimation and refocussing of the elliptic couplers may be imperfect and the use of sharp bends may induce losses. The first and the third loss sources can be controlled within a minimum value by accurately define the grating direction and choosing a larger bend radius. The second loss source can be further optimised through design.

## CONCLUSIONS

A new add/drop multiplexer structure has been designed based on elliptic beam collimators and Bragg gratings. The device is fabrication tolerant (apart from the grating fabrication), narrow bandwidth is readily achievable, compact and has a potentially low loss. A testing sample has been fabricated and the preliminary results show that the device concept works.

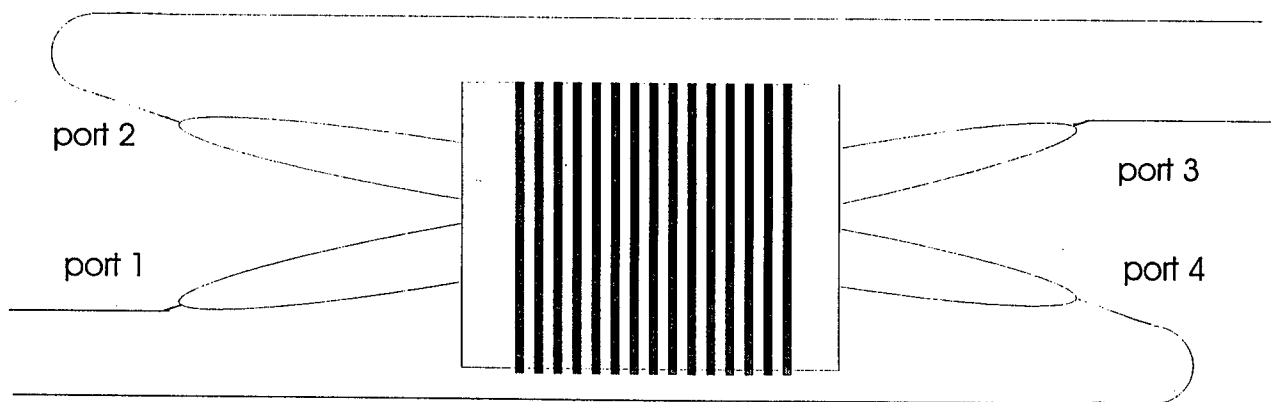


Fig.1. Schematic configuration of the proposed add/drop multiplexer.

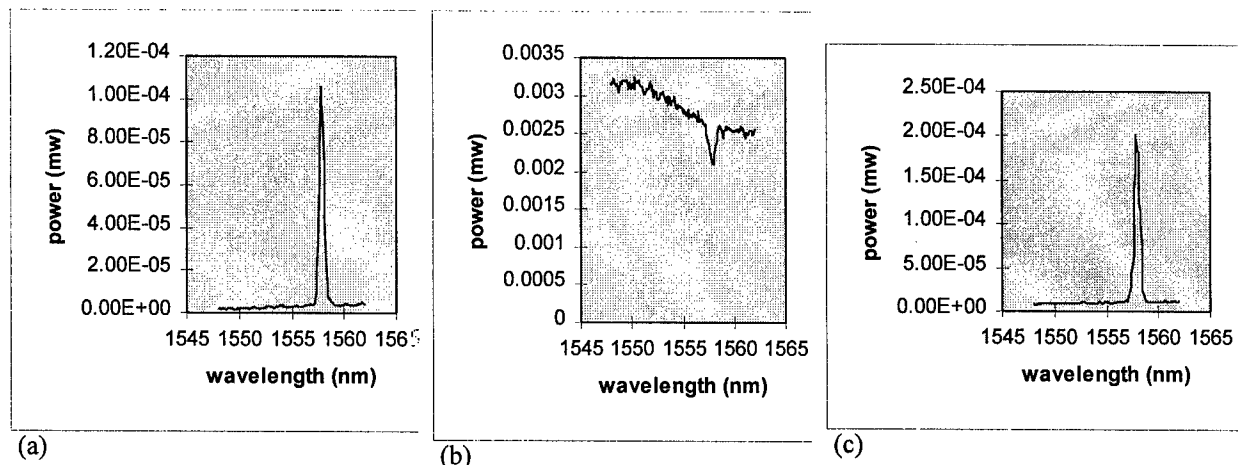


Fig. 2. Measurement results of (a) reflection (b) transmission and (c) the channel adding spectrum.

## References

- [1] Y. Shibata, et al., *IEEE Photonics Technology Letters*, Vol. 8, No. 1, Jan. 1996, pp87-89.
- [2] F. Bilodeau, et al., *IEEE Photonics Technology Letters*, Vol. 7, No. 4, Apr. 1995, pp388-40.
- [3] C. Wei, et al., *Electronics letters*, Vol. 32, No. 16, 1<sup>st</sup> Aug. 1996, pp1480-81.
- [4] C. Wei, et al., *IEEE J. Lightwave Technology*, Vol. 15, No. 5, May 1997.

**ThA3**  
**9:15am - 9:30am**

## **Self-Routing Wavelength Switches**

Kuang-Yi Wu and Jian-Yu Liu

Macro-Vision Communications, LLC  
5490 Conestoga CT, Boulder CO 80301  
TEL (303) 939-0027, FAX (303) 413-9177

### **Introduction**

A wavelength routing switch structure for applications of dense wavelength-division-multiplexing (DWDM) network is proposed and experimentally demonstrated. This innovative structure integrates both wavelength filtering and spatial routing functions into a compact device. The versatile filter design provides a prescribed wavelength transmission function and maintains low optical channel crosstalks. Liquid crystal technology is implemented in the device to perform the spatial routing function.

Several these DWDM routing switches have been constructed. The insertion loss of  $< -3$  dB and channel crosstalks of  $< -30$  dB are achieved for all these switches. A two-channel self-routing DWDM system based on these wavelength switches has been demonstrated. In this optical self-routing demonstration, the data signals are carried by 1533 nm and 1549 nm optical channels and the routing information is coded at 1310 nm wavelength.

### **Wavelength Routing Switch**

The proposed wavelength routing switch is a three-terminal device. DWDM signals incident onto the switch is first split into two sub-spectral components and then guided to the two output ports. The two sub-spectra are complementary to each other. They exchange position once the control signal reversed. Figure 1 illustrates the experimental result of a wavelength switch that has a 16-nm channel spacing and a passband width of 8 nm.

Figure 2 depicts a dual-stage four-channel reconfigurable DWDM demultiplexed circuit consisting of three liquid-crystal wavelength routers. The first wavelength router decomposes the incoming spectrum into two main groups. Each of them is sent to a following wavelength router which has a finer spectral width to further slice the spectra. By controlling the states of these routers, four demultiplexed spectra can be permuted among output ports.

### **DWDM Self-Routing Switching Demonstration**

Based on this wavelength switch, we demonstrated a dual-channel WDM self-routing switching network. In this demonstration, the payloads are encoded within two optical channels at 1533 nm and 1549 nm, whereas the control signal is coded at 1310 nm wavelength. These two signals are combined through an 1310/1550 filter and sent down to the fiber line. On the receiving end, the 1310 nm control signal is first stripped off from the incoming light signal. It then converted into an electronic format such that the routing control signal can be decoded. The rest of the optical energy which contains both data signals at 1533 and 1549 nm are incident onto the wavelength switch. According to the decoded routing signal, the wavelength switch determines the transmission function



of the output ports and directs the corresponding wavelength channels to the desired outputs.

Figure 3a shows the filtered spectrum of one output port of the wavelength switch in the self-routing network. The incident power of both payload wavelengths are -17 dBm. On state A operation, the 1549 nm DFB line is selected to output port #1 at an insertion loss of -3 dB, while the 1533 nm channel is suppressed by more than a 30 dB loss. Figure 3b records the dynamic switching function of the self-routing WDM network. Two wavelength channels are exchanged when the decoded 1310nm routing signal (top trace) is reverted.

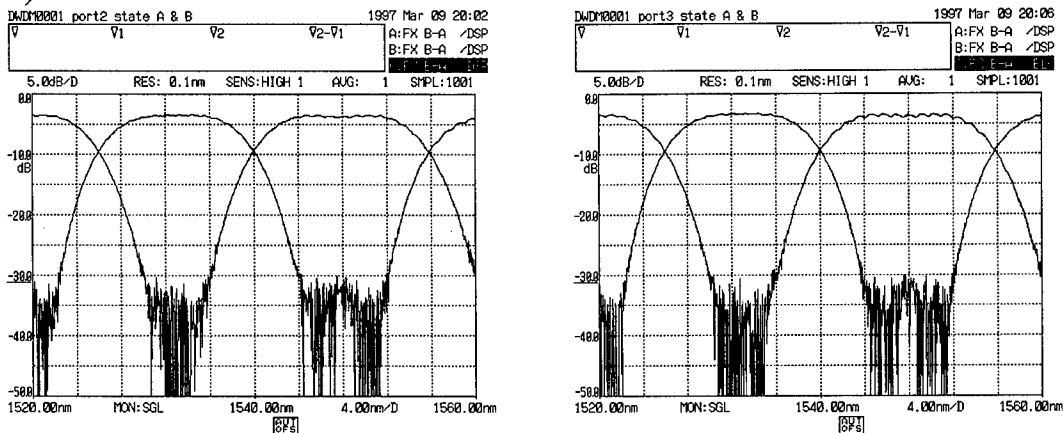


Figure 1. Transmission spectra of a 16-nm wavelength routing switch at its two operating states.

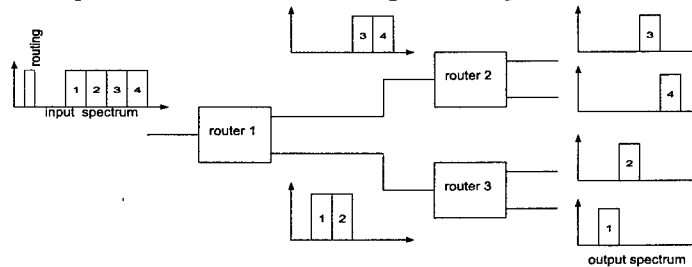


Figure 2. Spectral slicing of the two-stage four-channel programmable wavelength router. By rearranging the operating states of individual routers, four output spectra can be permuted.

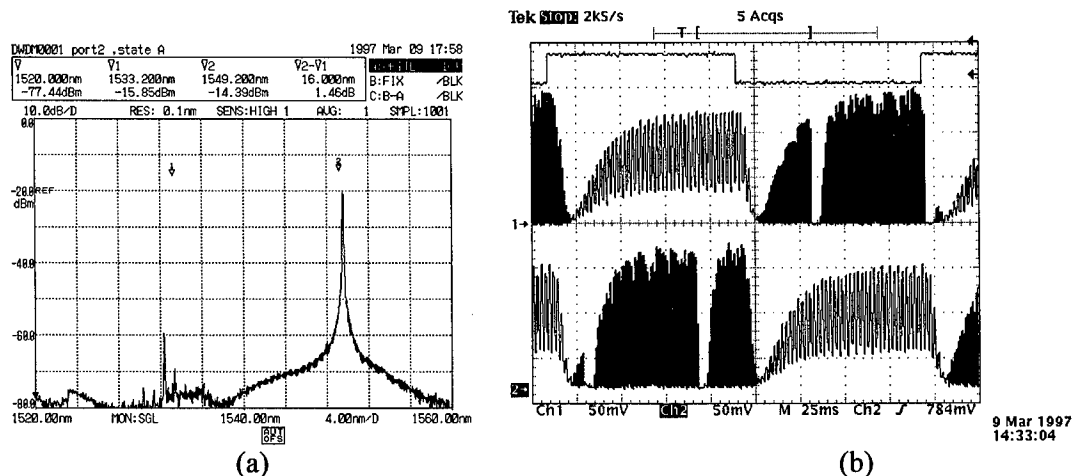


Figure 2. (a) The output spectra of port #2 of the liquid-crystal wavelength router on self-routing network. (b) Dynamic operation of self-routing switching.

## Injection-locking for Coherent Detection of Multi-wavelength Systems

Christine Latrasse, Bernard Ruchet, Leslie Ann Rusch, Michel Têtu  
*Centre d'Optique, Photonique et Lasers (COPL)*  
 Département de Génie Electrique et de Génie Informatique  
 Université Laval, Québec, Canada, G1K 7P4  
 Phone: (418) 656-2131, ext 8099, Fax: (418) 656-3159  
 (<http://www.gel.ulaval.ca/~cogel>)

Multi-wavelength transmission has become the accepted solution to enhancing the capacity of optical communications systems. The use of coherent detection in multi-wavelength systems offers improved receiver sensitivity and wavelength selectivity. In addition to these fundamental advantages, coherent detection also allows the direct application of sophisticated multiple access protocols such as CDMA (code division multiple access) which are common in radio frequency communications. For instance, the capacity of a high-bandwidth local area network can be enhanced by employing a hybrid CDMA/WDMA protocol [1].

### Description of the multi-wavelength coherent system

Techniques developed for radio frequency multiple access often use phase modulation with coherent detection. In optical systems, the laser phase noise can be considerable when using inexpensive distributed feedback (DFB) lasers. We propose the use of a set of centralized narrow linewidth, highly stable reference sources which are circulated through the network, thus amortizing their cost among the base of network subscribers. Individual users would employ these reference signals to injection-lock their DFB lasers for either transmission or reception. Although the reference signals are attenuated by distance, the output of the injection-locked laser will be on the order of a few milliwatts. Wavelength selection is provided by activating one of the user's bank of DFB lasers with nominal center frequency on the desired wavelength. Injection-locking leads to the DFB laser adopting the absolute frequency and frequency purity of the reference source. The use of injection-locking therefore provides many benefits such as power amplification, wavelength selection and transfer of spectral purity and stability.

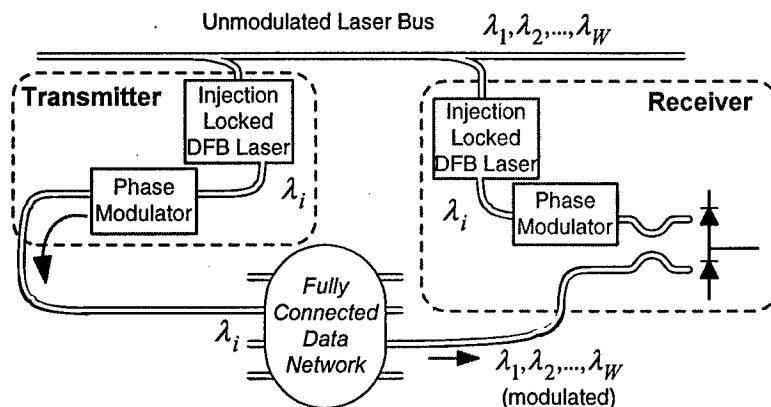


Figure 1: Injection-locking in a WDMA coherent system

Either homodyne coherent detection (using an injection-locked DFB laser as the local oscillator) or direct detection can be used. Figure 1 illustrates how data is transferred from one user to another. The first user activates the DFB laser with nominal center frequency  $\lambda_i$ , locking it to the signal from the reference bus. The output of the DFB laser is modulated externally by the data and sent to all users via the data network. The second user demodulates his message by also injection-locking to  $\lambda_i$ .

### Injection-locking experiments

As the information is coded onto the phase of the signal, sources with narrow linewidth are required [2]. We have built an extended-cavity laser (ECL) to be used as a narrow linewidth wavelength reference in our system. The source is made of an AR coated semiconductor laser, a collimating lens and a Littrow-mounted diffraction grating. We measured the linewidth of the ECL using a self-heterodyne technique and found it to be on the order of 190 kHz, which meets the requirements of our application. The wavelength of the laser is set at 1558.17 nm (192.4 THz), and the optical useful power is on the order of a few mW.

This ECL is used to injection-lock [3] a standard DFB laser as shown in Figure 2. The DFB laser has a free-running linewidth on the order of 10 MHz and its front facet optical power is about a few mW in an optical fiber. The beam of the master laser is focused on the rear facet of the slave laser, so that the power exiting the slave laser from the front facet is available for the user. The master laser beam is also sent in an acousto-optic modulator (AOM) to shift its frequency by 80 MHz. This beam is combined with the slave laser beam to obtain a beat note between the two lasers on a fast photodiode.

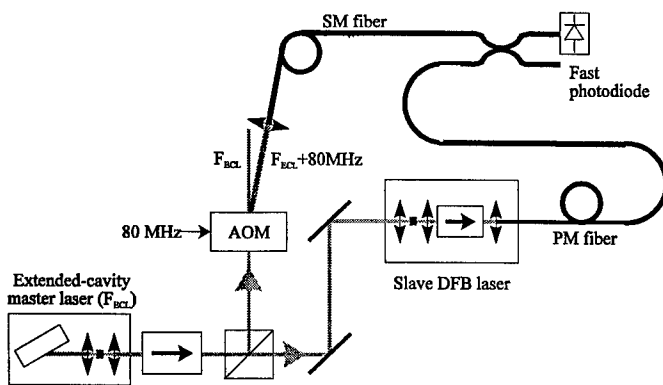


Figure 2: Experimental setup for the optical injection-locking of the slave DFB laser by the narrow linewidth extended-cavity laser.

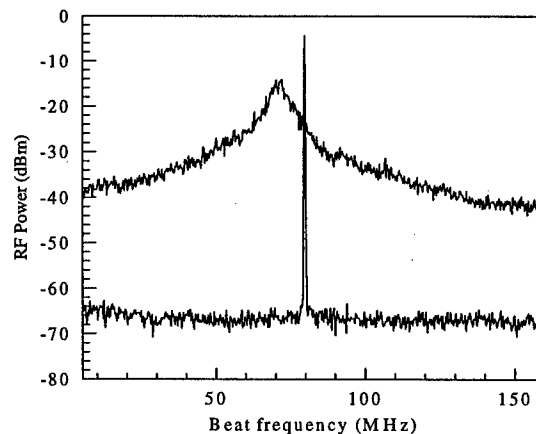


Figure 3: Beat frequency between the master and slave lasers without injection-locking (upper trace) and with injection-locking (lower trace).

When the slave is not injection-locked, the beat note presents a Lorentzian lineshape (Fig. 3, upper trace) with a linewidth of about 9 MHz, mainly due to the slave DFB laser. When injection-locking is achieved, the beat note becomes very narrow (Fig. 3, lower trace) and its frequency position is exactly 80 MHz, due to the shift of the master laser in the AOM. The frequency position indicates that the slave laser has the same frequency as the master laser and the narrow linewidth shows that they are highly correlated under injection-locking. The slave laser linewidth was measured to be around 190 kHz from the beat note between it and the master laser decorrelated in 25 km of fiber. The input power used to achieve injection-locking is on the order of a few hundreds of microwatts. The locking range was measured to be several GHz. Therefore, we can conclude that injection-locking provide wavelength selectivity and spectral purity transfer. The DFB laser can be used to provide power amplification for transmission as well as for a local oscillator at the receptor.

A similar experiment was conducted with pigtailed DFB lasers. The injected DFB laser was used as a pigtailed master laser to injection-lock another DFB laser. This one was pigtailed on both sides, with isolators allowing the injection-locking at the rear facet, and the output power to exit from the front facet. We also observed the second DFB laser adopted the frequency and narrow linewidth of its master, with master optical power as low as 10  $\mu$ W.

As our system will use several wavelength references, the wavelength spacing should be chosen judiciously. Wavelengths should be placed far enough apart to accommodate high bit rate modulation and the locking range of the slave lasers. In our system, we plan to use a 100 GHz scale for the reference frequencies [4]. We have used the first injection-lock DFB laser described above and a second ECL to simulate two reference master lasers at respectively 1558.17 nm and 1557.36 nm. We have injected both of them in the second DFB laser set at 1558.17 nm. We observed that the slave locked to the first master, and that the second one was transmitted through the slave without controlling it, because it was not in its locking range. Therefore, the 100 GHz scale is adequate for our network where bit rates will be on the order of 10 Gb/s. By using this injection-locking method, we have avoided the expense of tunable optical filters for wavelength selection, and the crosstalk induced by the non-zero sidelobes of such filters.

## Conclusion

We have proposed a multi-user, multi-wavelength high-bandwidth local area network using coherent detection. An ensemble of reference narrow linewidth lasers are used to perform injection-locking of users local DFB lasers. This method allows power amplification, wavelength selection and spectral purity transfer. This novel use of injection-locking makes wavelength multiplexing, phase modulation and coherent detection more attractive.

## References

1. F. Ayadi and L. A. Rusch, *IEEE Commun. Lett.*, Vol. 1, No. 1, pp. 28-30, January 1997.
2. L. A. Rusch et H. V. Poor, *IEEE J. on Selected Areas in Communications*, special issue on *High Speed Point-to-Point Optical Communications Systems*, Vol. 13, No. 3, April 1995.
3. R. Hui, A. D'Ottavi, A. Mecozzi, P. Spano, *IEEE J. Quantum Electron*, Vol. 27, No. 6, pp. 1688-1695, 1991.
4. C. Gamache, M. Têtu, C. Latrasse, N. Cyr, M.A. Duguay, B. Villeneuve, *IEEE Photon. Technol. Lett.*, Vol. 8, No. 2, pp. 290-292, February 1996.

ThA5

9:45am - 10:00am

## Electronically switchable waveguide Bragg gratings for WDM routing

Lawrence H. Domash, Yong-Ming Chen, Paul Haugsjaa and Moshe Oren

Foster-Miller, Inc., Photonics Division  
195 Bear Hill Road, Waltham MA 02154  
voice 617+684+4164, email: ldomash@worldnet.att.net

Just as Bragg gratings are a favored technique for wavelength-selective filtering in optical waveguide systems, switchable Bragg gratings are theoretically an optimum active WDM switching mechanism. To date however, few practical methods for switchable waveguide Bragg gratings are available that combine large dynamic range, index compatibility, good optical quality, and ease of fabrication. Recently, Sutherland and coworkers demonstrated a holographic polymerization process in a polymer-dispersed liquid crystal composite that results in efficient electronically switchable Bragg gratings (ESBG) with low scattering (1-3). We report the first waveguide WDM applications.

Holographic polymerization as illustrated in Figure 1 means that a solution containing a prepolymer, a nematic liquid crystal such as Merck E7, photoinitiators and other ingredients is captured in a liquid film layer 2-25  $\mu\text{m}$  thick and then exposed to interfering 488 nm laser beams to record a volume grating. This results in the formation of very small, 30-100 nm microdroplets of liquid crystal distributed spatially into Bragg planes. By chemical composition the magnitude of the index modulation can be varied from  $>4\%$  (desirable for short pathlength spatial transmission gratings) to  $<1\%$  for longer path, narrow band Bragg filters. Application of an electric field causes index matching and the grating vanishes. Diffraction efficiencies may be modulated from  $>99\%$  to  $<0.1\%$  by application of electric fields on the order of 2-5 V/ $\mu\text{m}$ , for dynamic ranges approaching 40 dB. Due to microencapsulation, ESBG switching speeds are also much faster (10-50  $\mu\text{s}$ ) than for the same nematic liquid crystals in bulk.

A variety of photonic switching elements are under development (4-5). Figure 2 indicates the recording process of a transmission grating for a space switch in a silicon microbench waveguide. Figure 3 shows an experimental switchable Bragg filter ESBG film on a polished half-coupler containing a single mode fiber; indium tin oxide electrodes have been deposited on the upper and lower substrates. Using a broadband LED with 100 nm bandwidth at 1550 nm, we have demonstrated a single-channel drop switch and will present experimental results including spectral width, extinction ratio, switching dynamic range, insertion loss and speed. Figure 4 shows a wavelength selective 2X2 switch in the form of a switchable grating-frustrated coupler (6) using an ESBG film fabricated between two half-couplers.

1. R.L. Sutherland, L.V. Natarajan, V.P. Tondiglia, T.J. Bunning, Chem. of Materials, 1993, 5, 1533-38.
2. V. P. Tondiglia, L. V. Natarajan, R. L. Sutherland, T. J. Bunning and W.W. Adams, Opt. Lett. v. 20, p. 1325, 1995.
3. R. Sutherland, L. Natarajan, V. Tondiglia, T. Bunning, Proc. SPIE Vol. 3010, Diffractive and Holographic Device Technologies and Applications IV, 1997.
4. L. Domash, C. Gozewski, A. Nelson, J. Schwartz, Proc. SPIE Vol. 2026c, Very Large Optical Memories, Ed. S. Kowel, 1993.
5. L. Domash, Y.M. Chen, B. Gomatam and C. Gozewski, Proc. SPIE Vol. 2689, Diffractive and holographic optics technology III, 1996.
6. J.L. Archambault, St. J. Russell, S. Barcelos, P. Hua, and L. Reekie, Opt. Lett. V.19, p. 180, 1994.

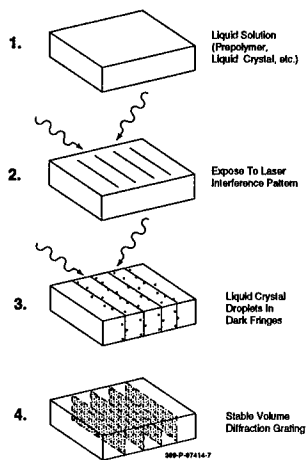


Figure 1. Holographic polymerization

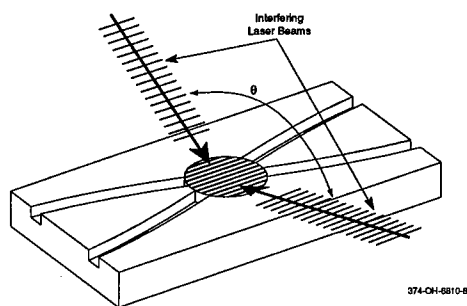


Fig. 2. 2X2 space switch

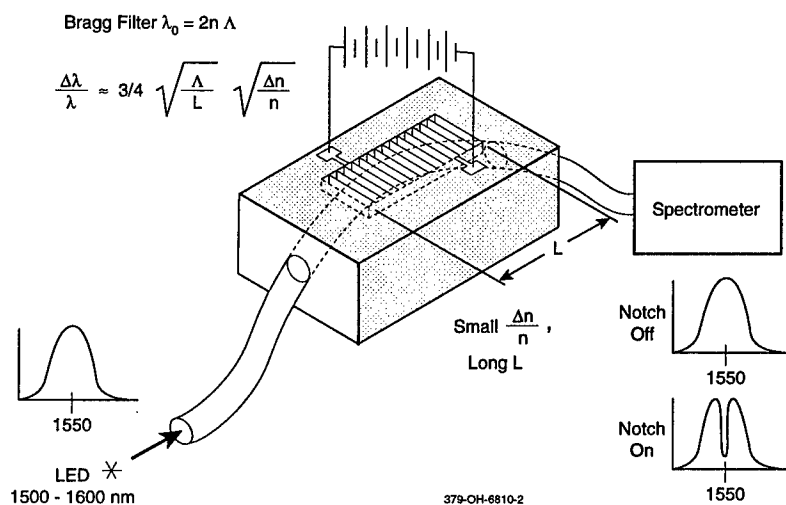


Figure 3. Experimental channel drop switch

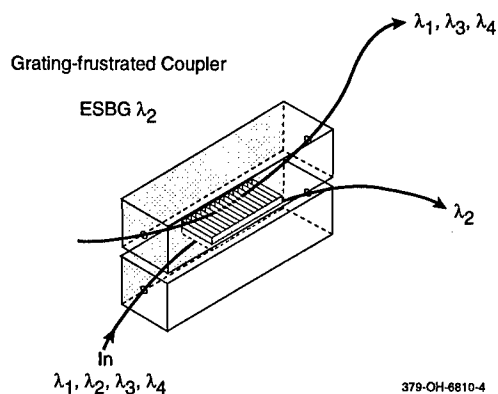


Figure 4. Wavelength selective space switch

## Progress in Wavelength Conversion by Difference-Frequency-Generation in AlGaAs Waveguides

S. J. B. Yoo, C. Caneau, R. Bhat, M. A. Koza, A. Rajhel, J. Ringo  
*Bellcore*  
331 Newman Springs Road, Red Bank, NJ 07701

Significant technological progress in wavelength conversion by difference-frequency-generation (DFG) has taken place since its conception for wavelength-division-multiplexing (WDM) network applications in 1991 [1]. The first implementation was in periodically poled LiNbO<sub>3</sub> waveguides [2, 3], and subsequent demonstrations in periodically domain inverted AlGaAs waveguides [4] showed a number of promising properties including multi-channel wavelength conversion, polarization independent wavelength conversion, and polarization diversified operation [5, 6, 7]. The fabrication technique for realizing such AlGaAs waveguides included wafer-bonding and OMCVD regrowth[8]. A number of new techniques are currently being investigated by a number of groups to achieve phasematched interactions in semiconductor waveguides: type-I quantum well waveguides with patterned disordering [9], strain-compensated type-II quantum well waveguides with patterned disordering[10], and AlGaAs waveguides with selective oxidation for formed birefringence phasematching[11]. This paper reviews progress in wavelength conversion by DFG in AlGaAs waveguides and discusses its implications for WDM network applications.

Numerous wavelength conversion methods have been proposed and demonstrated for WDM network applications. DFG wavelength conversion offers a number of unique advantages not readily available in other techniques. It offers a full range of transparency without adding excess noise to the signal. Its multi-channel conversion capability also allows the cross-connect architecture to be scalable and modular. Realization of DFG wavelength converters with zinc-blende semiconductors gives two significant impacts. First, the unique nonlinear tensor symmetry in this material system allows a Type-II interaction wherein the TE component of the input signal is converted to a TM output wave and the TM component is converted to TE. These two interactions are symmetric, equal in strength, and follow the identical phasematching condition. Consequently, although the conversion process alters the state of polarization during the conversion process, it offers polarization insensitive conversion efficiency in terms of optical power. It is also possible to filter input signals at the output of the wavelength converter by using a polarization diversified configuration.

Figure 1 shows measured conversion efficiency vs. the input wavelength for two input polarizations. The figure demonstrates extremely broad tuning curve with ~90 nm bandwidth and polarization independent conversion process. Figure 2 shows simultaneous conversion of 17 channels. Here, arbitrary input polarizations were used, and each channel achieves identical conversion efficiency. One of the important considerations for network applications is a requirement for an effective means to filter unwanted channels. One such method is based on polarization diversity, and Figure 3 shows the measured spectrum exploiting the unique polarization characteristics of the conversion process in an AlGaAs waveguide. Such a multichannel filtering scheme is an essential building block in realizing a scalable and modular wavelength-interchanging cross-connect (WIXC) to be utilized in WDM networks. DFG wavelength conversion also demonstrated excellent systems performance. Figure 4 shows 10 Gb/s wavelength conversion result. The conversion penalties are approximately 1.1 dB for 10 Gb/s, and, as the baseline in the figure indicates, the majority of the penalty rises from the noise added from optical fiber amplifiers. Lastly, the ultimate performance of DFG wavelength converter is expected in a wavelength converter with an integrated pump laser source. We report completion of the first fabrication run and discuss the future direction.

## REFERENCES

1. S. J. B. Yoo, *Bellcore Internal Memorandum* (1991), also in *U. S. Patent 5,434,700* (1993).
2. C. Q. Xu, H. Okayama, and M. Kawahara, *Appl. Phys. Lett.* **63**, 3559 (1993).
3. M. L. Bortz, D. Serkland, M. M. Fejer, and S. J. B. Yoo, *CLEO'94*, paper CTHD6 (1994).
4. S. J. B. Yoo, C. Caneau, R. Bhat, M. A. Koza, *OFC '95* paper PD-13 (1995).
5. S. J. B. Yoo, C. Caneau, R. Bhat, M. A. Koza, A. Rajhel, N. Antoniadis, *Appl. Phys. Lett.* **68**, p. 2609, (1996).
6. S. J. B. Yoo, C. Caneau, R. Bhat, M. A. Koza, A. Rajhel, N. Antoniadis, *CLEO'96*, paper JTUE1. (1996)
7. S. J. B. Yoo, R. Bhat, C. Caneau, A. Rajhel, M. A. Koza, *CLEO'97*, paper CMF3. (1997).
8. S. J. B. Yoo, R. Bhat, C. Caneau, M. A. Koza, *Appl. Phys. Lett.*, **66**, 3410 (1995).
9. M. W. Street, N. D. Whitbread, C. J. Hamilton, B. Voge, C. R. Stanley, D. C. Hutchings, J. H. Marsh, J. S. Atchinson, G. T. Kennedy, W. Sibbett, *Appl. Phys. Lett.*, **70**, 2804 (1997).
10. S. J. B. Yoo, R. Bhat, M. A. Koza, C. Caneau, *QELS'95*, paper QWJ3. (1995).
11. A. Fiore, V. Berger, E. Rosencher, N. Laurent, S. Theilmann, N. Vodjdani, J. Nagle, *Appl. Phys. Lett.*, **68**, 1320 (1996).

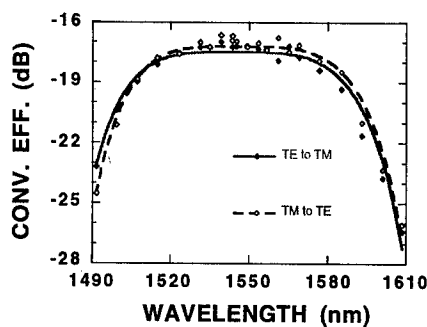


Figure 1. Measured conversion efficiency as a function of the input wavelength for two input signal polarization states. Both sets of data points are curve fit to according to theory.

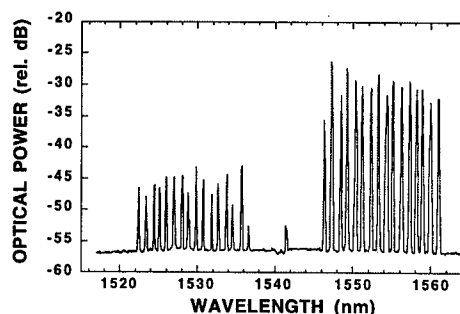


Figure 2. Simultaneous conversion of 17 input wavelengths in the 1545-1561 nm range to a set of 17 output wavelengths in the 1523-1539 nm range. The structure at 1542 nm is a second-order spectrometer response of the pump wave at 771 nm.

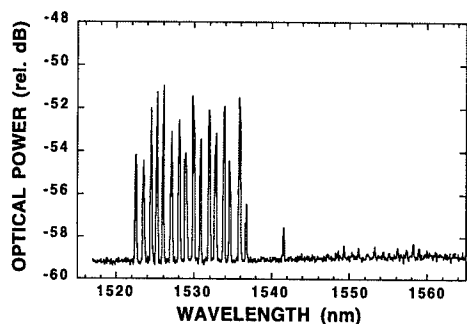


Figure 3. Same as in Figure 2, except all input waves are in TE polarization and resulting converted waves are in TM polarization. Using a polarizer, only the converted waves are collected.

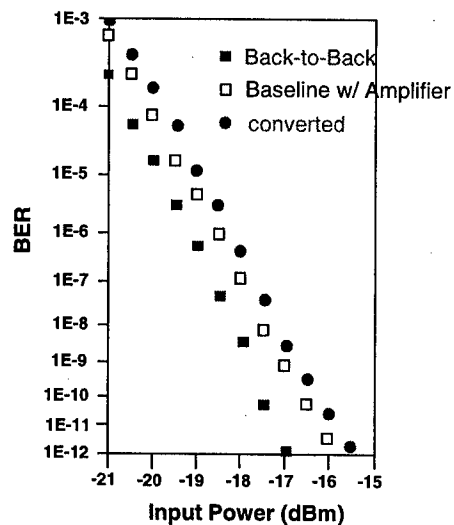


Figure 4. BER curves for 10 Gb/s wavelength conversion

ThB2

11:00am - 11:15am

**A Reconfigurable Optoelectronic Wavelength Converter based on an Integrated Electroabsorption Modulated Laser Array**

G. Raybon, U. Koren, B. I. Miller, M. Chien, K. Dreyer,  
R. E. Behringer, D. M. Tennant, K. Feder and M. R. Cheyne\*  
Lucent Technologies,  
791 Holmdel-Keyport Rd, Holmdel, NJ 07733  
\*Colgate University, Hamilton, NY

Optical wavelength conversion or wavelength adaptation is a desired functionality for evolving WDM network architectures [1]. The ability to perform routing and switching as a function of wavelength in a network can be achieved through wavelength conversion. Many types of wavelength converters, all-optical and optoelectronic, have been previously reported. A comparison of the various conversion techniques reveals that there are trade-offs in performance and feasibility [2]. The one feature necessary for all wavelength converters however, is the ability to provide a new wavelength which complies with the specified wavelengths in the system. A multiwavelength or tunable laser source can provide the compliant wavelength in both optoelectronic or all-optical techniques. Here we describe an optoelectronic wavelength converter in which the new wavelength is provided by an integrated electroabsorption modulated laser (EML) array suitable for low-chirp long haul transmission [3]. The transmitter can be configured to provide either selected fixed wavelength output or to switch between output wavelengths as determined by network control. In this paper we demonstrate the operation of the wavelength converter at 2.5 Gbits/s. The output wavelength is switched between compliant wavelengths spaced by 200 GHz through software control and bit-error-rate (BER) performance is measured.

The optoelectronic wavelength converter, shown schematically in Fig.1, consists of a photodiode which converts the input optical signal to an electrical signal. This signal is amplified to drive an electroabsorption (EA) modulator which is integrated with a DFB laser array, passive optical power combiner and optical amplifier. Each laser in the array has a different grating and thus lases at a different wavelength in the 1550-1560 nm region. The wavelength separation between adjacent lasers is 200 GHz and channel selection is achieved by simply activating the appropriate laser. Without temperature tuning, the measured standard deviation from uniform wavelength-spacing is  $\pm 0.09$  nm. Typically, temperature compensation is required to strictly comply with system wavelengths specifications. In this design, the temperature and bias conditions which correspond to a given wavelength are predetermined and subsequently accessed by a software routine controlling the laser array. If the system needs to be reconfigured, the user simply selects a new wavelength using a graphical interface on standard PC which controls the instruments via GPIB commands. Reconfiguration time is on the order of a 2 to 3 seconds which is presently limited mostly by GPIB commands. The time required to change the temperature of the laser to fine tune the wavelength has been reduced to less than 1 second for small temperature changes by mounting the array on a silicon submount on a thermoelectric cooler. If the array wavelengths are accurately registered at the same temperature, then only the laser currents need to be switched. We have measured less than 10 ms switching time using software controlled mechanical relays connected to a common current supply.

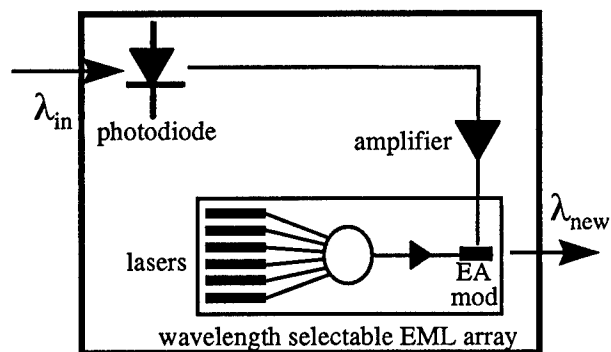


Fig.1: Schematic of optoelectronic wavelength converter based on laser array transmitter.



Figure 2 shows the output optical wavelength achieved by selecting each of the six lasers in the array and appropriately selecting the temperature to obtain the desired wavelength. The lasers were configured to meet the standard wavelengths as defined by the MONET consortium [1]. The deviation from the MONET specification is shown on the right side of Fig. 2 as measured on an HP optical spectrum analyzer with a sampling error of 0.02 nm. Only channel 3 deviates by more than the sampling error. The input data to the wavelength converter was derived from a tunable external cavity laser (ECL) followed by a LiNbO<sub>3</sub> modulator driven with 2.5 Gbit/s, 2<sup>23</sup>-1 pseudorandom data. This signal is received using an HP O/E converter, amplified to a peak-to-peak voltage of 2.5 V and applied to the EA modulator which is reversed biased with -1.5 V. The data on the new wavelength is received using a 2.5 Gbit/s regenerator and the BER is measured as a function of received optical power. Figure. 3 shows the BER measurements for each wavelength converted channel compared to two baseline measurements. All six converted wavelengths show similar performance with measured receiver sensitivity near -32.6 dBm. The filled circles correspond to the LiNbO<sub>3</sub> modulator sensitivity and the filled squares correspond to the laser array optimized as a transmitter driven directly by the pseudorandom pattern generator (CH 4 selected). The BER penalty due to wavelength conversion is 1.6 dB at a BER = 1x10<sup>-9</sup>. This penalty is mostly due to the degraded characteristics of the electrical drive to the EA modulator in the wavelength converted case. The measured Q factor of the different electrical data signals applied to the modulator for the baseline and wavelength converted cases is 16.7 dB and 11.2 dB respectively.

In summary, we have demonstrated reconfigurable optoelectronic wavelength conversion to system compliant wavelengths using an integrated EML array transmitter at 2.5 Gbit/s. Selecting an array technology with high precision wavelength accuracy can enable rapid reconfiguration of wavelengths with low system penalty.

#### References

1. R. E. Wagner, et. al., "MONET: Multiwavelength Optical Networking," *Journ. of Lightwave Technol.*, vol. 14, pp. 1349-1355, 1996.
2. S. J. B. Yoo, "Wavelength Conversion Technologies for WDM Network Applications," *Journ. of Lightwave Technol.*, vol. 14, no. 6, pp. 955-966, 1996.
3. B. I. Miller et.al., "Low Chirp Wavelength Selectable 1x6 Laser Arrays Suitable for WDM Applications," 15<sup>th</sup> IEEE Int. Semicon. Laser Conf., 1996.

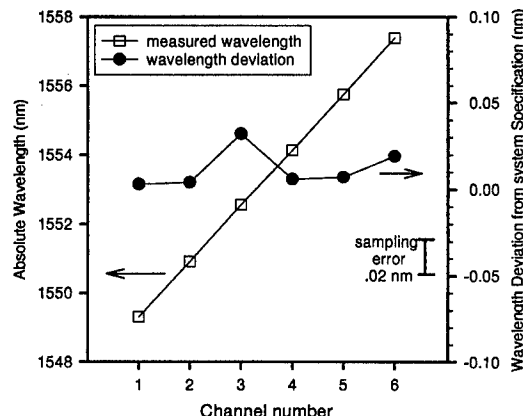


Fig. 2: Wavelength vs. channel number and wavelength deviation from system specification.

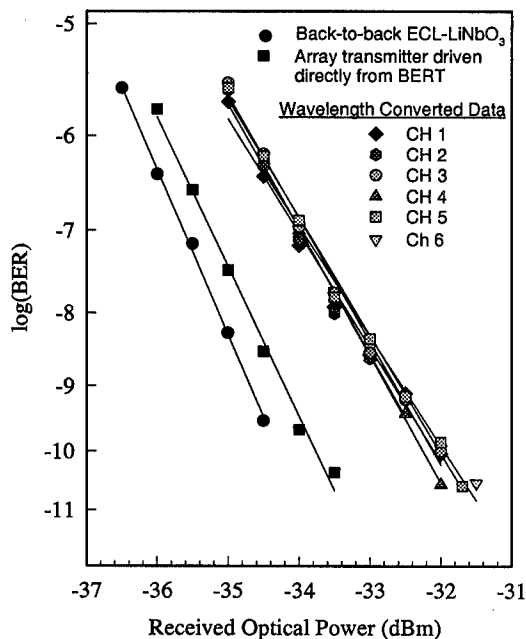


Fig. 3: BER vs. received optical power for six output channels of the wavelength converter.

ThB3

11:15am - 11:30am

### Improved frequency response of a semiconductor-optical-amplifier wavelength converter using a fiber Bragg grating

Hsiao-Yun Yu, Daniel Mahgerefteh, Pak Cho, Julius Goldhar, Geoffrey L. Burdge,  
University of Maryland, College Park, MD

Semiconductor-optical-amplifier (SOA) based wavelength converters are becoming attractive because of their small size, integrability, and low latency for operation up to 40 Gb/s. The bit-rate limitation is primarily caused by the SOA gain recovery rate which can be improved at the expense of higher input optical powers. High speed wavelength conversion can be achieved either by cross gain or cross phase modulation in one or two amplifiers placed in an interferometer.<sup>1</sup> The cross phase modulation technique is favored because of its efficiency and that it requires lower optical power. However, it also requires integrating the amplifiers in an interferometer which is complex.<sup>1</sup> Alternatively, the interferometer can be formed externally to the amplifier with a birefringent fiber.<sup>2</sup>

We demonstrated a novel SOA-fiber-grating wavelength converter for RZ data that has a better frequency response than a single SOA wavelength converter at the same optical power level. The SOA-fiber-grating wavelength converter uses a single amplifier and requires *no* interferometers. The principle of this device is described as follows: Consider an input pump beam at  $\lambda_1$  and a CW probing signal at  $\lambda_2$  coincident in the amplifier (Fig. 1). The pump beam partially depletes the gain of the amplifier. This rapidly increases the refractive index of the semiconductor and chirps the CW signal at  $\lambda_1$  towards the red. There is a smaller, blue chirp associated with the slower recovery of the amplifier's gain. The probing signal's wavelength,  $\lambda_2$ , is adjusted such that the fiber grating passes the red chirped portion of the CW signal and blocks its unchanged spectral components. The concept used here has been demonstrated by D. M. Patrick and R. J. Manning<sup>3</sup> using a sinusoidal birefringent filter. Also, L. Noel *et al.* used a similar device for NRZ to RZ conversion.<sup>4</sup> Here we use a more compact, fiber grating step filter which selects the phase modulated portions of the probing signal more effectively.

We characterized the frequency response of our SOA-fiber grating wavelength converter. We found an increase in modulation bandwidth by a factor of 10 with the fiber grating compared to wavelength conversion without the fiber grating. Figure 1 shows the experimental setup. The modulated pump beam was from a CW tunable semiconductor laser sinusoidally modulated from 20 MHz to 17.5 GHz using a LiNbO<sub>3</sub> intensity modulator. The pump beam was operated at 1539 nm. The modulated pump signal was amplified and launched into a SOA through a 3-dB fiber coupler. The modulation depth of the pump beam was 33.4%. The input average pump power was 5.8 dBm. The probing signal was the CW output of a tunable semiconductor laser at 1535 nm which was injected into the SOA counter-propagating to the pump pulses. The input probe had an average power of 3 dBm. After the SOA, the probing signal passed through an isolator and a step fiber Bragg grating. An additional 2 nm wide band-pass filter rejected any residual pump light. The isolator was necessary to prevent the reflected portion of the probing signal from coupling back into the SOA.

We used a commercially available, fiber-pigtailed semiconductor optical amplifier with a chip length of 700  $\mu\text{m}$  and a fiber-to-fiber gain of 10 dB. The fiber coupling loss of the SOA was  $\sim 3$  dB/facet. The fiber Bragg grating was 0.49 nm wide, and had a -27.3 dB transmission at its center wavelength of 1535.18 nm. The probing signal was carefully tuned in order to filter out most of the CW and blue chirp components of the converted signal. The converted output probe peak power,  $p_2(\nu)$ , at modulation frequency,  $\nu$ , and the output probe average power,  $P_2$ , was measured using a lightwave RF spectrum analyzer. In order to obtain the normalized conversion efficiency, the ratio of the input pump peak power,  $p_1$ , and the average power,  $P_1$ , was measured and kept constant at 33.4% from 20 MHz to 17.5 GHz.

Figure 2 shows the normalized conversion efficiency (defined as  $\eta = (p_2/P_2)/(p_1/P_1)$ ) versus pump modulation frequency with and without the fiber Bragg grating. In the absence of the fiber grating, wavelength conversion is achieved by cross gain modulation and the modulation bandwidth is predominantly determined by carrier lifetime and stimulated emission rates. From Figure 2, the 3-dB bandwidth is approximately 6.5 GHz without the fiber grating. When the fiber

grating is in place, the converter frequency response is significantly enhanced with an extrapolated 3-dB bandwidth of more than 65 GHz (see Figure 2).

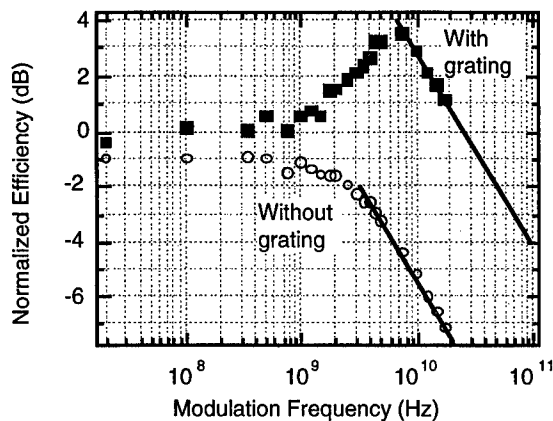
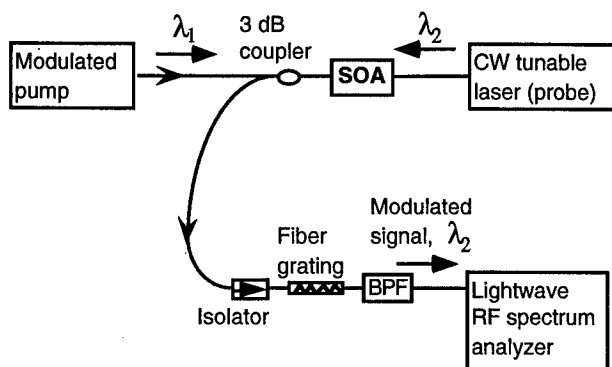


**Figure 1: Setup for SOA-fiber grating hybrid wavelength converter. BPF: band-pass filter.** **Figure 2: Normalized wavelength conversion efficiency ( $\eta$ ) versus modulation frequency ( $\nu$ ).**

The improvement observed here is the result of the large linewidth enhancement factor of the semiconductor optical amplifier. This leads to very efficient cross phase modulation at a relatively small pump-induced change in gain of the SOA. The fiber grating uses the cross phase modulation by converting the phase to amplitude modulation. At low modulation frequencies ( $< 1$  GHz), there is no significant difference in conversion efficiency with and without the fiber grating. This is because the modulation sidebands created by both cross gain and phase modulations are too close together for the fiber grating to discriminate since it is not an ideal step filter. Therefore, the modulation is primarily from cross gain compression. At high frequencies ( $> 1$  GHz), however, the modulation sidebands are far enough apart for the fiber grating to discriminate efficiently. Thus, for this frequency regime, conversion of phase to amplitude modulation by the fiber grating is extremely effective. This compensates for the gradual decrease of the amplitude modulation sidebands caused by the roll off of the cross gain modulation response at high frequencies. At approximately 6.5 GHz,  $\eta$  for both cases drops rapidly, clearly showing the finite gain recovery time. Note that the peak of response with the fiber grating coincides with the 3-dB bandwidth of response without the fiber grating at 6.5 GHz. Theoretical investigations and modelling of the frequency response are being carried out.

The observed enhanced frequency response of the wavelength converter implies reduced pattern dependent effects which results in lower power penalty. To demonstrate power penalty reduction, wavelength conversion was performed using RZ data as input pump. Bit-error-rate (BER) measurements were performed at 5.3 Gb/s using a  $2^{31}-1$  bit long pseudo-random sequence. The power penalty was significantly reduced from 14 dB at  $10^{-12}$  BER without the fiber grating to 5 dB with the fiber grating. Details of the BER measurements will be presented.

## References

1. T. Durhuus *et al.*, *J. Lightwave Technol.* **14**, 942 (1996).
2. N. S. Patel *et al.*, *IEEE Photon. Technol. Lett.* **8**, 1695 (1996).
3. D. M. Patrick and R. J. Manning, *Electron. Lett.* **30**, 252 (1994).
4. L. Noel, X. Shan and A. D. Ellis, *Electron. Lett.*, **31**, 277 (1995).

ThB4 (Invited)  
11:30am - 12:00noon

## Wavelength Conversion Techniques in Optical Networks

*J. M. Wiesenfeld*  
*AT&T Laboratories-Research*  
*Crawford Hill Laboratory, Holmdel, NJ 07733*

Wavelength interchange will become an important function in optical networks. The most fully equipped nodes in future optical networks will include spatial switching and wavelength conversion to ensure the largest degree of flexibility and best performance with regard to blocking of paths in the network. One of the major benefits of optical networks will be their ability to support a variety of optical signal wavelengths and formats and, therefore, a high degree of "transparency" will be required for the wavelength interchange function. The wavelength conversion device which performs the function of wavelength interchange may impose the most significant limitation on the transparency of the network because of the degradation caused in optical signal quality. In particular, the wavelength converter may limit the data format and bit-rate allowed on the network, as well as the allowed all-optical signal propagation distances on the network.

All-optical wavelength conversion techniques based on semiconductor optical amplifiers (SOA's) are most promising candidates for the function of wavelength conversion [1-3]. In particular, nonlinearities in SOA's applied to wavelength conversion are cross-gain modulation (XGM), cross-phase modulation (XPM) and four-wave mixing (FWM). Cross-gain modulation and cross-phase modulation rely on carrier density dynamics within the SOA, while FWM relies on carrier intraband dynamics for the wavelength conversion range of interest for optical networks.

The simplest technique is XGM, in which a signal at  $\lambda_1$  reduces the carrier density within the SOA by stimulated emission, thereby imposing a gain modulation on a second, independently tunable, cw input at  $\lambda_2$  to the amplifier (the probe), which becomes the wavelength-converted output [4-6]. Using XGM, wavelength conversion has been demonstrated for signals at bit rates up to 40 Gb/s.[7] Two problems associated with XGM are extinction ratio degradation [8] and chirp, produced by the phase modulation that necessarily accompanies gain modulation in a SOA [9]. This technique requires only a single SOA, is bit-rate transparent up to at least 40 Gb/s, and is effective only for intensity modulated formats.

In a second technique, the phase modulation caused by the signal-induced carrier depletion by  $\lambda_1$  in the SOA is used to advantage. To use this cross-phase modulation (XPM) to produce intensity modulation on the probe at  $\lambda_2$  requires an interferometric configuration, in which one or two SOA's is placed inside a Michelson or Mach-Zehnder interferometer. [10, 11] Dramatic recent progress has been achieved because of the fabrication of monolithically integrated SOA interferometers, of both the Michelson [12] and Mach-Zehnder configurations [13-15]. With these devices the extinction ratio can be enhanced by the interferometric transfer function [14], the chirp is controlled, so that transmission over dispersive fiber at high bit rate is possible [12-14], and the nonlinearity of the transfer function may lead to some noise reduction[16]. Wavelength conversion by XPM in a Michelson configuration has been reported for data at 40 Gb/s [17] but, as with XGM, functions only for intensity-modulated formats. Recently, a DFB laser probe source has been integrated monolithically with a Mach-Zehnder wavelength converter, to provide an increased level of device functionality [18].

Cross-gain and cross-phase modulation techniques operate only on intensity-modulated signals, both digital and analog [19]. Coherent wave-mixing techniques, such as four-wave mixing (FWM) in SOA's [20] or difference-frequency generation in quasi-phase matched waveguides [21] allow for greater

transparency because they can convert frequency and intensity-modulated signals. For FWM in SOA's, polarization-sensitivity, the wavelength dependence of the conversion efficiency, ASE noise from the SOA, and complicated optical arrangements are issues. Nevertheless, wavelength conversion over a significant range has been reported for data at rates up to 10 Gb/s [22,23] and with minimal polarization sensitivity [24, 25]. For this technique, however, signal-to-noise ratio issues and power requirements [26] remain significant.

Alternatively, wavelength conversion for intensity-modulated signals could be performed optoelectronically, which consists of a photodiode to detect the input signal at  $\lambda_1$ , followed by electronic amplification, followed by remodulation of a cw laser at  $\lambda_2$ . For incorporation in future optical networks, the all-optical wavelength conversion techniques must offer advantages above the optoelectronic method.

This work is supported, in part, by ARPA via the MONET program.

1. J. M. Wiesenfeld, *Int. J. High Speed Electronics and Systems*, 7, 179 (1996).
2. T. Durhuus, et al., *J. Lightwave Tech.*, 14, 942 (1996).
3. S. J. B. Yoo, *J. Lightwave Tech.*, 14, 955 (1996).
4. M. Koga, N. Tokura, and K. Nawata, *Appl. Opt.*, 27, 3964 (1988).
5. B. Glance, et al., *Electron. Lett.*, 28, 1714 (1992).
6. C. Joergensen, et al., *IEEE Photonics Tech. Lett.*, 5, 657 (1993).
7. C. Joergensen, et al., *Electron. Lett.*, 32, 367 (1996).
8. J. M. Wiesenfeld, B. Glance, J. S. Perino, and A. H. Gnauck, *IEEE Photonics Tech. Lett.*, 5, 1300 (1993).
9. J. S. Perino, J. M. Wiesenfeld, and B. Glance, *Electron. Lett.*, 30, 256 (1994).
10. B. Mikkelsen, et al., *Electron. Lett.*, 30, 260 (1994).
11. T. Durhuus, et al., *IEEE Photonics Tech. Lett.*, 6, 53 (1994).
12. B. Mikkelsen, et al., *Proc. 20th Eur. Conf. Opt. Comm.*, Vol 4, p. 67, post-deadline (1994).
13. F. Ratovelomanana, et al., *IEEE Photonics Tech. Lett.*, 7, 992 (1995).
14. W. Idler, et al., *Electron. Lett.*, 31, 454 (1995).
15. X. Pan, et al., *IEEE Photonics Tech. Lett.*, 7, 995 (1995).
16. B. Mikkelsen, et al., *Electron. Lett.*, 32, 566 (1996).
17. C. Joergensen, et al., *Conf. Optical Fiber Commun.*, Paper Tu-O1, p. 72 (1997).
18. L. H. Spiekman, et al., *Conf. Optical Fiber Commun.*, Post-deadline paper PD10 (1997).
19. J. S. Perino and J. M. Wiesenfeld, *Conf. Lasers and Electro-Optics*, paper CThE1 (1994).
20. L. Tiejmeijer, *Appl. Phys. Lett.*, 59, 499 (1991).
21. S. J. B. Yoo, C. Caneau, R. Bhat, M. A. Koza, A. Rajhel, N. Antoniadis, *Appl. Phys. Lett.*, 68, 2609 (1996).
22. R. Ludwig and G. Raybon, *Electron. Lett.*, 30, 338 (1994).
23. D. F. Geraghty, et al., *IEEE Photonics Tech. Lett.*, 9, 452 (1997).
24. R. M. Jopson and R. E. Tench, *Electron. Lett.*, 29, 2216 (1993).
25. G. Hunziker, et al., *IEEE Photonics Tech. Lett.*, 8, 1633 (1996).
26. M. S. Summerfield and R. S. Tucker, *IEEE Photonics Tech. Lett.*, 8, 1316 (1996).

## Tunable Acousto-Optical Filters, Multiplexers and Lasers in LiNbO<sub>3</sub>

W. Sohler, H. Herrmann, and K. Schäfer

Universität-GH Paderborn, Angewandte Physik  
D-33095 Paderborn, Germany  
Phone: +49 5251 602712 Fax: +49 5251 603422  
e-mail: sohler@physik.uni-paderborn.de

By combining acousto-optical polarization converters and passive polarization splitters in various ways on a single (X-cut) LiNbO<sub>3</sub> substrate a whole family of tunable integrated optical WDM-devices has been developed. Among them are wavelength filters, wavelength-selective switches and add-drop multiplexers[1]. They offer fast and broad tunability. Due to their unique multi-wavelength operation capability simplified architectures of optical cross-connects and add-drop nodes can be realized. By fabricating these devices in erbium-diffusion doped LiNbO<sub>3</sub> internal amplification can be added by optical pumping. Moreover, by optical feedback in a cavity even lasing can be achieved with a tunable emission wavelength. In this contribution, the current state-of-the-art of tunable, acousto-optical devices in LiNbO<sub>3</sub> is reviewed, illustrated by a number of selected examples.

The best known acousto-optical devices are tunable filters. They have been demonstrated as polarization-dependent and -independent devices, as single- and double-stage filters with and without polarizers or polarization splitters integrated on the same substrate. The most advanced design for polarization-independent double-stage operation is shown in Fig. 1[2]. It consists of four integrated polarization splitters and two acousto-optical polarization converters embedded in one arm of an acoustical directional coupler for guided surface acoustic waves yielding a weighted acousto-optical coupling. With a fiber-pigtailed and packaged device high sidelobe suppression ( $> 30$  dB), low insertion loss ( $< 5$  dB), small polarization dependence ( $< 0.5$  dB), and a wide tuning range ( $> 80$  nm) have been achieved.

The latest add-drop-multiplexer [1] is shown in Fig. 2; it has four passive polarization splitters and four acousto-optical polarization converters monolithically integrated on the same chip. Two of them only serve as frequency shifters to compensate the shift induced by the two acousto-optical switches. Good results have been obtained: the extinction of the dropped wavelength channel is  $> 25$  dB due to the double-stage filtering. The sidelobe suppression of the dropped channel is  $> 15$  dB and there is practically no crosstalk from the add-channel to the dropped signal due to the spatial separation of the add-and drop sections.

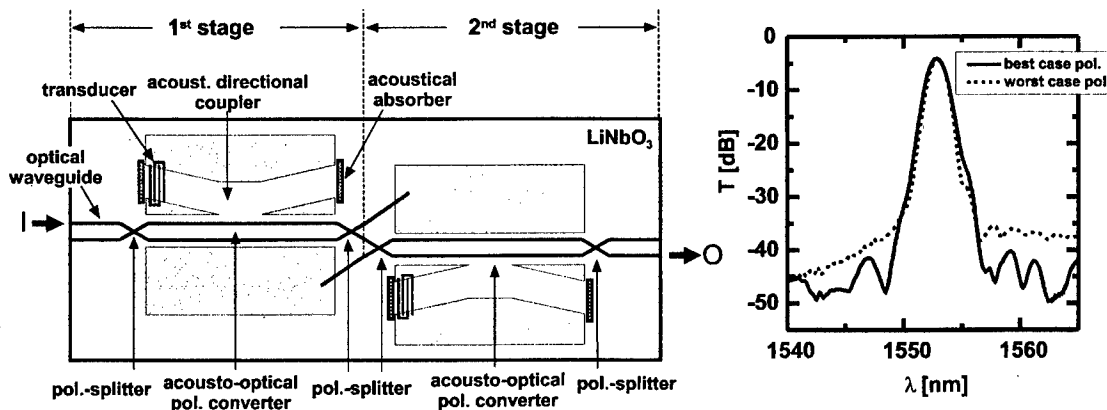


Fig. 1: Polarization independent, double-stage wavelength filter

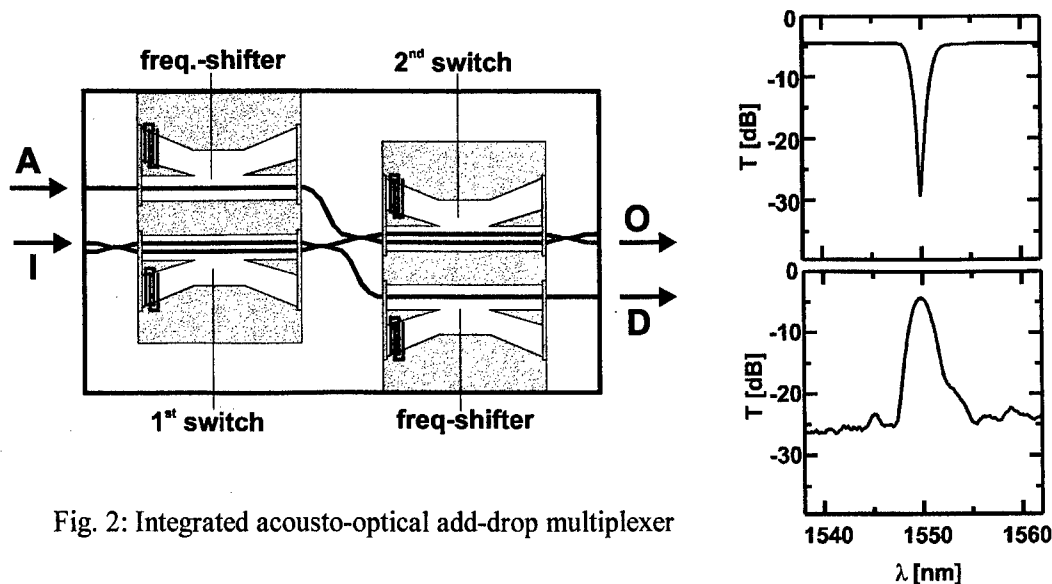


Fig. 2: Integrated acousto-optical add-drop multiplexer

A special combination of polarization-dependent, single-stage filter and frequency shifter has been fabricated in an erbium-diffusion doped substrate to develop a tunable laser [3]. One polarization splitter serves as coupler for the  $\lambda = 1480$  nm pump. A gold and a dielectric endface mirror form the waveguide laser cavity. Threshold is achieved if the internal optical gain compensates the round-trip losses. As the gain is wavelength-dependent and due to a nonideal cavity lasing is not yet observed in the whole "erbium-window"  $1530 \text{ nm} < \lambda < 1610 \text{ nm}$ . The tuning characteristics of the fiber-pigtailed, packaged and laser-diode pumped device is shown in Fig.3.

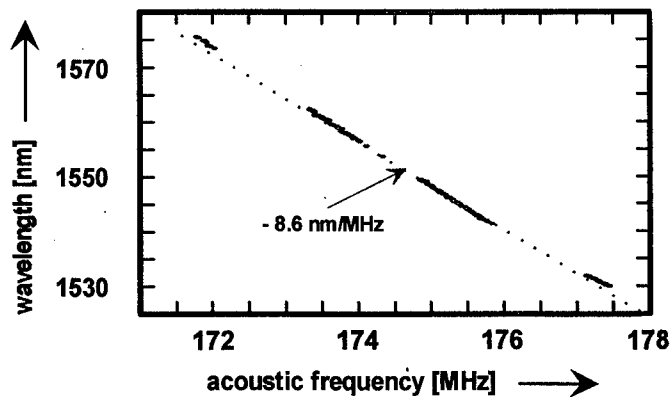


Fig. 3: Tuning characteristics of the integrated acousto optical laser

In conclusion, a variety of attractive monolithically integrated, acousto-optical devices has been developed in  $\text{LiNbO}_3$ . Due to their tunability they are ideal candidates for the construction of flexible, reconfigurable WDM-networks.

#### References:

- [1] H. Herrmann, A. Modlich, Th. Müller, W. Sohler, F. Wehrmann: "Advanced integrated acousto-optical switches, add-drop multiplexer and WDM cross-connects", Proc. European Conference on Integrated Optics (ECIO'97), Stockholm, pp. 578-581 (1997)
- [2] H. Herrmann, K. Schäfer, Ch. Schmidt: "Low loss, tunable integrated acousto-optical wavelength filters with strong sidelobe suppression", submitted to IEEE Photonics Technology Letters
- [3] K. Schäfer, I. Baumann, W. Sohler, H. Suche, S. Westenhöfer: "Diode-pumped and packaged, acousto-optically tunable  $\text{Ti:Er:LiNbO}_3$ -waveguide laser of wide tuning range", submitted to IEEE J. Quantum Electronics

ThC2

2:30pm - 2:45pm

## Dynamic Holographic Eight-channel Spectral Equaliser for WDM

A.D. Cohen and R.J. Mears

Cambridge University Engineering Department, Trumpington St., Cambridge, CB2 1PZ, UK.

Tel. +44 1223 339762 Fax +44 1223 330264

### Abstract

We report equalisation of eight 3-4nm-spaced WDM channels amplified by a non-gain-flattened EDFA. The 9.5dB spectral gain range is reduced to 0.75dB. Flattening of the filter passband has been experimentally demonstrated.

### Introduction

WDM optical telecommunications networks require components that satisfy, amongst others, the following criteria: polarisation-insensitivity, optical transparency, low crosstalk, low insertion loss, fast high resolution tuning, compact, robust and low power operation. The dynamic holographic technology is based on a 128 x 128 pixellated FLC SLM (ferroelectric liquid crystal spatial light modulator) displaying 1-D binary-phase holograms, in combination with a fixed binary-phase grating, both aligned within a 4-*f* free-space lensing system. The technology has the potential to meet all the aforementioned criteria, although there are fundamental limits to FLC switching speed ( $\sim 20\mu\text{s}$  [1]) and insertion loss (5-6dB), the latter a consequence of the optical power lost to the zero order and symmetrical first order of the SLM replay field.

The application of this holographic filtering technique to digitally tunable filters and fibre lasers with 1.3nm tuning resolution has recently been demonstrated [2]. We have recently demonstrated the expansion of the dynamic digitally tunable filter to a multiple passband device with variable passband amplitudes, i.e. a spectral power equaliser suitable for compensation of signal and amplifier gain variation in a dynamic WDM network. A recent experiment combining an alumino-germanosilicate EDFA with a dynamic Mach-Zehnder filter [3] provides active control of the amplifier gain to compensate fluctuations with dynamic input load, however the need for more flexible dynamic spectral equalisation remains, since individual signal powers will be prone to variation in a dynamic wavelength-switched network. Papers scheduled for publication describe in greater detail the design of the dynamic filter and holograms. Results have demonstrated the ability to dynamically equalise four [4] and six [5] amplified WDM channels having a separation of approximately 4nm. The holographic filter reduced a spectral EDFA gain variation of  $\sim 6\text{dB}$  and an input signal variation of  $\sim 8.5\text{dB}$  to less than 0.4dB for the four channel experiment, and to less than 0.6dB for six-channel equalisation.

### Results

*Eight Channel Equalisation.* Figure 1 shows results for the equalisation of eight WDM channels spanning the spectral range 1538-1565nm, representing a mean channel spacing of 3.85nm and corresponding to an EDFA gain range of approximately 9.5dB. Input signals varied from -39.6 to -38.8dBm over the 27nm range. The variations in both input signals and EDFA gain have been reduced to less than 0.75dB. The net loss through the system of  $\sim 11\text{dB}$ , representing a filter loss of  $\sim 41\text{dB}$ , is consistent with predicted performance; a slight net improvement would have been achieved had lower input signal powers been used to obtain the maximum small-signal gain from the EDFA. Key areas to be addressed to reduce losses include the use of a blazed grating in place of the fixed binary-phase grating, and the employment of a high tilt-angle FLC material in the SLM. Elimination of other sundry filter losses by the use of antireflection coatings and so on would lead to a basic filter loss of  $\sim 5\text{-}6\text{dB}$  plus a fan-out loss of  $-10\log_{10}C$ , where  $C$  is the number of channels, and a channel-dependent term accounting for equalisation down to the level of the weakest channel.

*Spectral Shaping of Passband.* The spectral form of the filter passband is of key importance for WDM systems application. An ideal filter passband would be centred on an ITU-specified frequency, have a -3dB-width of  $\pm 20\%$  of channel spacing commensurate with the emerging ITU recommendations for source tolerances, and have a -25dB-width equal to the channel spacing. For a channel spacing of 100GHz, this corresponds to -3dB and -25dB-widths of 0.32nm and 0.8nm respectively, a form ratio of  $\sim 2.5$ . Figure 2 demonstrates that the holographic filter can produce a passband of such form by overlap of three adjacent passbands. The -3dB and -25dB widths are 4.0nm and 10.3nm respectively, a form ratio of 2.57, representing a significant improvement on the near-Gaussian characteristic of a single passband. The 3dB-width of the filter response, approximately 2nm for a single passband in the current configuration, is related to the finite range of filtered wavelengths that couple into the core of the output fibre, and can be shown to be given approximately by [6]



$$\Delta\lambda_{-3dB} \approx 1.07 \frac{\varphi_{core} d}{f}$$

where  $\varphi_{core}$  is the core diameter of the output fibre,  $d$  the line-pair width of the fixed grating and  $f$  the lens focal length. Assuming that the composite response of three overlapping passbands scales linearly with the form of a single passband, the result shown in Fig. 2 should scale down to -3dB and -25dB widths of 0.9nm and 2.3nm respectively by replacing the current grating of  $d = 18\mu\text{m}$  with one of  $d = 4\mu\text{m}$ . Further scaling down to the desired 0.32 and 0.8nm would require an increase in the lens focal length or the use of a tapered output fibre, or a combination of the two. This passband engineering can be expanded for multichannel filtering and equalisation. Suitable choice of filter design parameters [4] will ensure that individual passband centres conform to ITU standards.

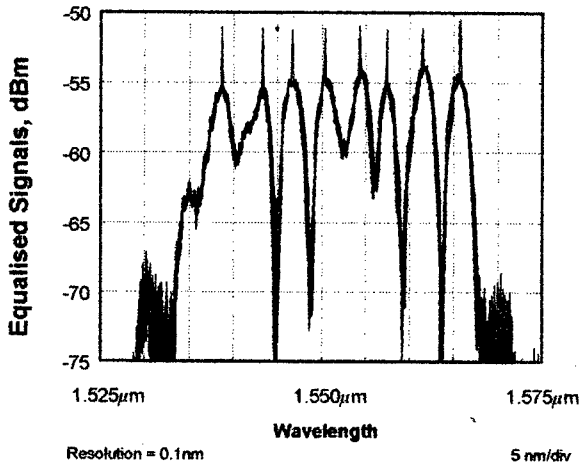


Figure 1. Equalisation of eight WDM channels

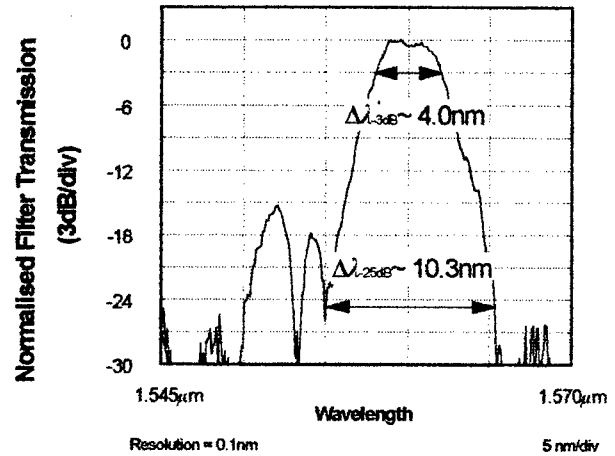


Figure 2. Flattening of filter passband

### Conclusions

The technique of dynamic holographic filtering has successfully equalised eight amplified WDM channels with a mean spacing of 3.85nm, reducing the EDFA spectral gain variation from 9.5dB to 0.75dB. A -25dB:-3dB filter passband form ratio of 2.57 has been achieved by overlap of three adjacent near-Gaussian passbands.

### References

1. H.J. White *et al.*, "The OCPM demonstrator system," in Technical Digest of Topical Meeting on "Photonics in Switching" (Optical Society of America, Salt Lake City, 1995), Paper PPd1.
2. M.C. Parker and R.J. Mears, "Digitally tunable wavelength filter and laser," *Photon. Tech. Lett.* **8**(8) pp. 1007-1008 (1996).
3. M.C. Parker, A.D. Cohen and R.J. Mears, "Dynamic Holographic Spectral Equalisation for WDM," *Photon. Tech. Lett.*, *Scheduled for publication* (April 1997).
4. A.D. Cohen, M.C. Parker and R.J. Mears, "Active Holographic Spectral Equalisation and Channel Management for WDM," *OSA Topics in Optics and Photonics Series*, *Scheduled for Publication* (July 1997).
5. Y.W. Lee, J. Nilsson, S.T. Hwang and S.J. Kim, "Experimental characterization of a dynamically gain-flattened erbium-doped fiber amplifier," *Photon. Tech. Lett.* **8**(12) pp. 1612-1614 (1996).
6. M.C. Parker, "Dynamic Holograms for WDM," PhD Thesis (University of Cambridge, 1996).

## WDM Channel Monitoring and Signal Power Control/Equalization Using Integrated Tunable Active Filters

J. H. Chen, Y. Chai, J. Y. Fan, F. S. Choa

Department of Computer Science and Electrical Engineering  
University of Maryland Baltimore County, Baltimore, MD 21250

T. Tanbun-Ek, R. A. Logan, W. T. Tsang, C. A. Burrus<sup>a)</sup>

Lucent Technologies, Murray Hill, NJ 07974, a) Lucent Technologies, Holmdel, NJ 07733

To manage a WDM network, the signal at each wavelength channel must be constantly monitored, and the power of each channel should be individually controlled to provide a reliable, user friendly system. Although terminal devices (such as detectors) can monitor, an optical in-line device that can perform both the monitoring and controlling function, would be optimal. In this paper, we present the experimental results of using an integrated tunable active filter as just such a useful device.

The tunable active filter we used is an integrated 4-section InGaAs/InGaAsP distributed-Bragg-reflector (DBR) laser biased below threshold. By controlling cavity length and the coupling constant of the grating, the device allows only a single below-threshold Fabry-Perot (FP) mode in the cavity<sup>1</sup>. Since no other side modes will be excited by incoming signals, such an active filter can truly be utilized in WDM systems.

The experimental setup is illustrated in Fig. 1. The DBR laser is composed of gain, phase, grating, and post-filter gain sections. Error signals for wavelength control and

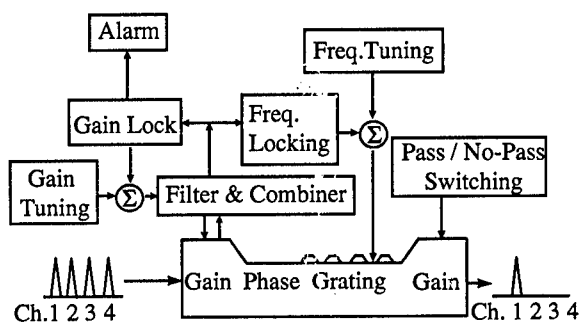


**Fig.1 System setup of DBR active filter**

dynamic gain control are extracted from the gain section and feedback to the grating section and the gain section, respectively. The post-filter gain section can be used to switch the output on or off. An alarm will be triggered if the signal level in the channel is lower than a preset level. As shown in Fig.2, such active filters can be applied to a multichannel system for channel selection, signal monitoring and equalization.

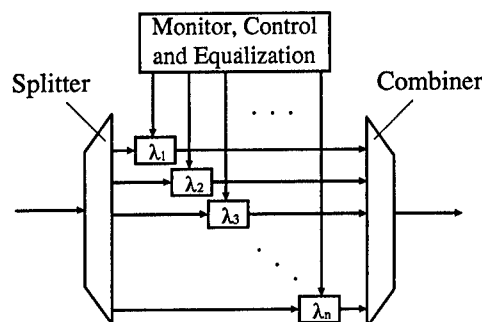


**Fig.2 Multichannel application of active filters**

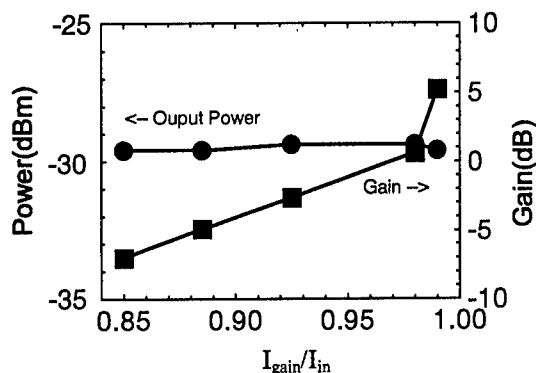


**Fig.3 Dynamic gain control by active filter**

Fig. 3 shows the dynamic-gain-control operation of the active filter. When the optical signal intensity is varying, we can keep the optical output constantly stay at a preset level. The DC bias current, provided by the feedback control circuits through a bias-T, correspondingly varies with the input level. A dynamic gain control range of 12dB and an output power fluctuation of less than 0.5dB were achieved. With this device, dynamic gain equalization of WDM channels<sup>2</sup> can be easily achieved. With the capability of tuning, locking (the input can be locked at different positions with respect to the filter center wavelength), and gain control, it is also possible to eliminate the problem of the band-narrowing effect caused by cascading misaligned passive optical (de)multiplexers in all optical networks<sup>3</sup>.

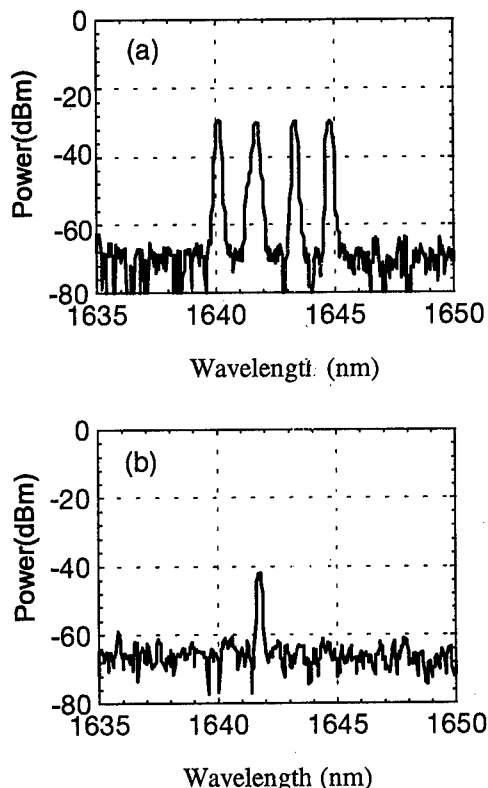


Fig.4 Optical spectrum of transmission  
(a) before active filter, (b) after active filter

The central wavelength of the DBR filter can be easily tuned and locked to a desired channel by changing the grating bias current. As shown in Fig. 4, 4-channel WDM signals

with 1.6nm (200GHz) spacing were coupled into the DBR gain section. A channel extinction ratio of 20dB was achieved when the average input power of each channel was at -30dBm. The extinction ratio reduced to 12dB when the signal level was increased to -18dBm, due to the gain saturation of the active filter.

When a transmitter was directly modulated at 1.24Gb/s, a penalty of less than 2dB at  $10^{-9}$  BER was observed for transmission with and without the active filter. We think this penalty is caused by the spontaneous noise generated in the active filter.

In conclusion, we have demonstrated that an integrated tunable active filter can be a simple and useful device to provide the functions of channel filtering, monitoring, and gain control/equalization to facilitate the WDM network control and management. With this simple and integrated structure, the cost to implement a WDM network monitoring and control system can be greatly reduced.

The authors acknowledge support from DARPA/AFOSR under grants F49620-96-1-0230 and F49620-95-1-0446.

#### References:

1. M. H. Shih, et al., "High performance integrated coherent transceivers for optical access networks", IEEE LEOS Annual Meeting, paper TuS4, (1996).
2. S. H. Huang, et al., "Experimental demonstration of dynamic equalization of three 2.5Gbit/s WDM channels over 1000km using acousto-optic tunable filters", OFC, paper WM6, (1996).
3. N. N. Khrais, et al., "Performance of cascaded misaligned optical (de)multiplexers in multiwavelength optical networks", IEEE Photon. Technol. Lett., **8**, 1073, (1996).

ThC4 (Invited)  
3:00pm - 3:30pm

## Monolithic Integration of WDM Components Using QW Shape Modification

Emil S. Koteles  
Institute for Microstructural Sciences  
National Research Council of Canada  
Ottawa, Ontario, Canada K1A 0R6

The ultimate goal of optoelectronics research is the realization of an inexpensive, reliable technique for monolithically integrating optoelectronic devices of differing functionalities, such as lasers, detectors, modulators, transparent waveguides, etc. Such a technology would make practical many of the components required to implement the information superhighway, optical computation, optical interconnects, etc.<sup>1</sup> Spatially selective quantum well (QW) shape modification, which increases QW bandgap energies in a simple, controllable manner, is a promising candidate. It utilizes no special epitaxial growth procedures, has no detrimental effect on active devices, and, in fact, can enhance device performance by, for example, eliminating the polarization sensitivity of QW optical devices, such as amplifiers, photodetectors, and modulators.<sup>2</sup>

To be practical, any monolithic fabrication technique for photonic integrated circuits (PICs) must fulfill certain requirements: 1) there must be large, precisely controllable bandgap energy differences between the various devices in the PIC - (Fig. 1 illustrates the decrease in bandgap wavelength (increase in bandgap energy) as a function of two implantation parameters) for two types of QW waveguides; 2) loss in the integrated waveguide devices must be comparable to or lower than that present in the "normal" as-grown (i.e., unmodified) structure - (Fig. 2 demonstrates that losses in intermixed QW waveguides are comparable to those in as-grown QW waveguides); 3) the electrical properties of the various devices must suffer insignificant deterioration due to the processing technique - (Fig. 3 and 4 illustrate that the quantum confined Stark effect (reverse bias) and lasing action in diodes (forward bias) are unaffected by QW intermixing); 4) there should be no adverse effects on the lifetimes of the various devices in the PIC after processing - (Accelerated lifetime testing of QW intermixed laser diodes indicate no significant adverse effects.<sup>3</sup>), 5) any other process-dependent changes in the properties of the devices must be either performance neutral or advantageous to the PIC - (Fig. 5 demonstrates the polarization insensitive operation of a QW intermixed optical amplifier). We have demonstrated that spatially selective QW bandgap energy shifting due to QW shape modification fulfills all of these requirements.

Further, Fig. 6 illustrates the performance of an actual WDM PIC, a two-wavelength, waveguide demultiplexer, fabricated using QW intermixing.

<sup>1</sup> For a review of monolithic integration techniques, see, for example, Emil S. Koteles, **Applications of Photonic Technology**, edited by G.A. Lampropoulos, J. Chrostowski, and R.M. Measures (Plenum Press, New York, N.Y. 1995), page 413 (1995).

<sup>2</sup> For a review presenting more details on the results summarized below, please see "Photonic Integration Using Quantum Well Shape Modification" by Emil S. Koteles, S. Charbonneau, P. Poole, J.J. He, M. Davies, M. Dion, G. Aers, Y. Feng, I.V. Mitchell, and R.D. Goldberg, *Physics in Canada*, **52**, 251(1996).

<sup>3</sup> J.P. Noël, D. Melville, T. Jones, F.R. Shepherd, C.J. Miner, N. Puetz, K. Fox, P.J. Poole, Y. Feng, E.S. Koteles, S. Charbonneau, R.D. Goldberg, and I.V. Mitchell, *Appl. Phys. Lett.* **69**, 3516(1996).

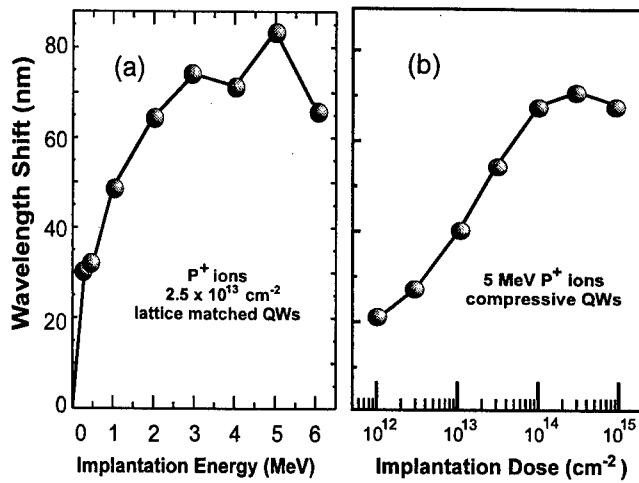


Figure 1: QW PL peak wavelength changes as a function of (a) ion implantation energy for a lattice matched InP-based 6-nm-wide QW; (b) ion implantation dose for a compressively strained InP-based 5-nm-wide QW.

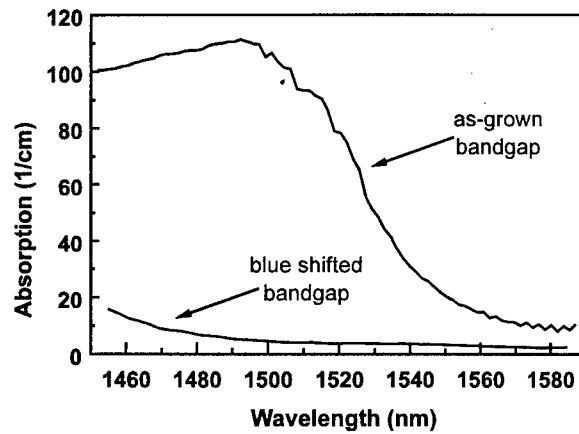


Figure 2: Waveguide absorption spectra of as-grown and QW intermixed InGaAs/InGaAsP QW waveguides. Note the shift of the bandgap of the intermixed QW to lower wavelengths (higher energies) and the absence of any increase in waveguide loss.

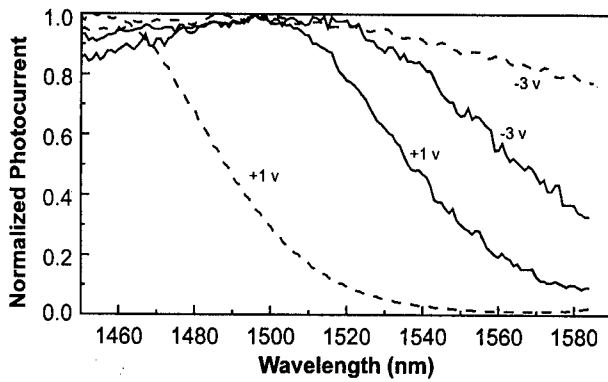


Figure 3: Quantum confined Stark effect in as-grown (solid lines) and QW intermixed (dashed lines) waveguides. Only the effects of two voltages (+1 volt cancels the built-in electric field and produces zero internal electric field and -3 volts generates an inverse electric field of about 110 kV/cm) are shown.

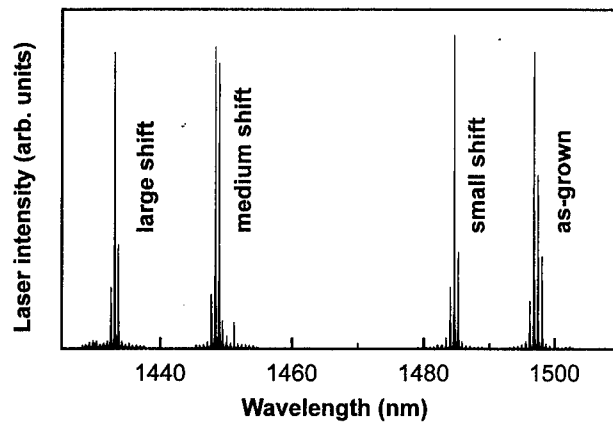


Figure 4: QW intermixed laser diode emission spectra. These Fabry-Perot lasers were from a single wafer bar and shifted different amounts using ion implantation through a mask of varying thickness.

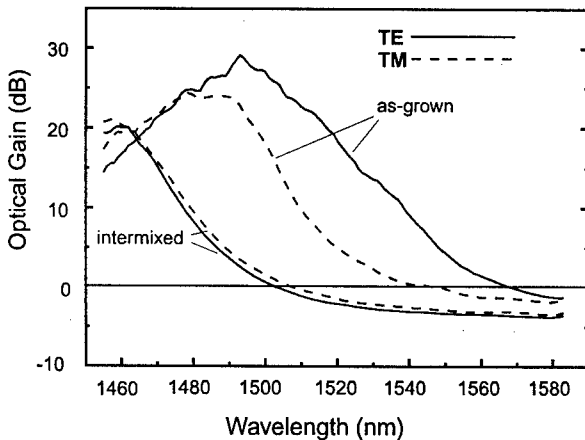


Figure 5: Optical amplification as a function of wavelength in as-grown and QW intermixed waveguides for both TE (solid lines) and TM (dashed lines) polarizations.

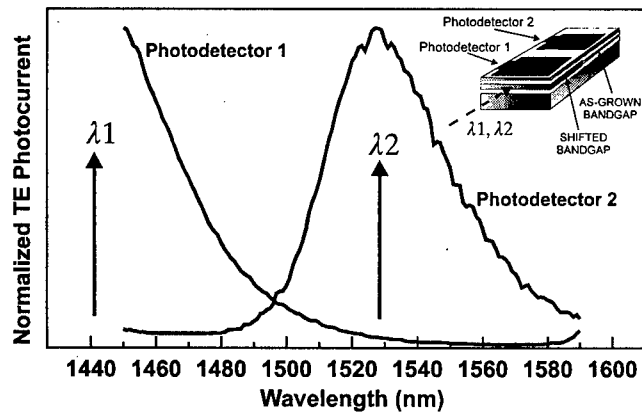


Figure 6: Normalized room temperature TE photocurrent spectra of as-grown and intermixed regions of the two wavelength WDM demultiplexer shown schematically in the insert.

ThD2

4:30pm - 4:45pm

## Demultiplexer with 90 channels and 0.3 nm channel spacing

Z.J.Sun<sup>(1,2)</sup>, K.A.McGreer<sup>(1,2)</sup> and J.N.Broughton<sup>(3)</sup>

<sup>(1)</sup>TRLabs, 10-75 Scurfield Blvd., Winnipeg, MB, Canada, R3Y 1P6

<sup>(2)</sup>Dept. of Physics, University of Manitoba, Winnipeg, MB, Canada, R3T 2N2

<sup>(3)</sup>Alberta Microelectronic Centre, Edmonton, AB, Canada, T6G 2C2

Wavelength division multiplexing (WDM) is a useful technology for increasing the information capacity of optical systems. Multiplexers and demultiplexers are key elements in WDM systems. Planar integrated demultiplexers based on concave gratings[1,] and arrayed waveguide gratings[2] are attractive both for mass production and the ability to support large number of channels. Here, we report our preliminary results on concave grating demultiplexer with 90 channels and 0.3 nm channel spacing.

The device was fabricated at the Alberta Microelectronic Centre facility from a single mode planar glass waveguide composed of a 2 $\mu$ m SiON waveguide core with a refractive index of 1.492, a 0.5  $\mu$ m SiO<sub>2</sub> upper cladding and 5  $\mu$ m SiO<sub>2</sub> lower cladding with refractive index of 1.45. The layers were deposited onto a silicon substrate using plasma enhanced chemical vapor deposition(PECVD) with silane, ammonia, nitrous oxide, helium, and nitrogen. The device reported here was not annealed. The propagation loss for slab waveguide is 2.0 dB/cm and 2.8 dB/cm for a ridge waveguide. A single reactive ion etch(RIE) was used to simultaneously fabricate 14 input ridge waveguides, 90 output ridge waveguides and a concave diffraction grating with diffraction order 20. The final chip size is 8 $\times$ 34 mm<sup>2</sup>. The RIE had a 2.6  $\mu$ m depth and yielded nearly perpendicular sidewalls (89.4°). The grating was designed using a method described elsewhere[3]. Devices were diced from the wafer using a wafer saw leaving rough input and output waveguide surfaces. The wavelength dependence of the optical transmission from an input waveguide to each output waveguide was measured with a tunable external cavity laser which has a wavelength range from 1520 nm to 1575 nm. The light from the laser was coupled into a single mode, polarization maintaining fiber. This fiber was butt-coupled to an input waveguide. A multimode fiber was butt-coupled to an output waveguide. Index matching fluid was used to enhance the device/fiber coupling at the input and output. The output light from the multimode fiber was measured with a germanium diode and a lock-in amplifier. To characterize one peak in the spectral response, the tunable laser was fine tuned with 0.01nm steps over 0.28nm tuning range. To characterize the adjacent channel, coarse tuning the laser was required before a fine tune scan was initiated.

Fig.1 shows the measured transmission signals versus wavelength for two adjacent channels. The spectral response consists of central lobe and some side lobes. The peak of the first side lobe is typically 17 to 20

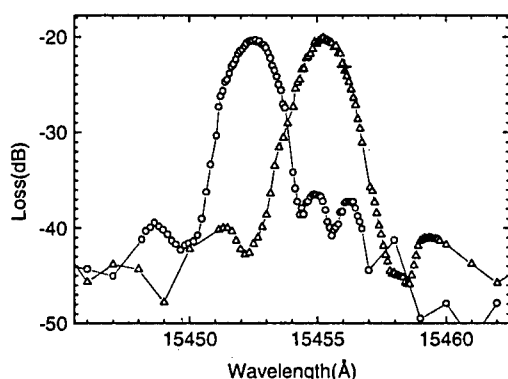


Fig.1 Transmission loss against wavelength for channel 32 and 33. The light was in TM mode and applied to input no.1 waveguide

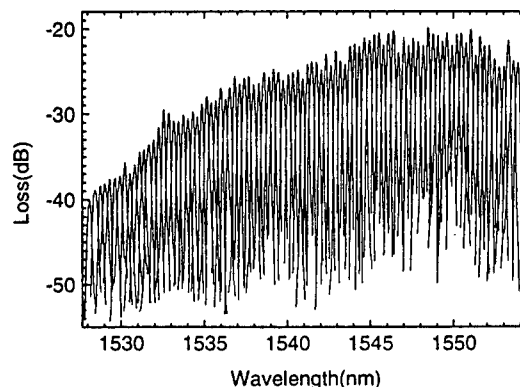


Fig.2 Transmission loss against wavelength from output of channels 1 to 90. The light was in TM mode and applied to input no.1 waveguide

dB below the peak of the main lobe. The full width at half maximum for those two channels is 0.16 nm. The average spectral width for all 90 channels is 0.18 nm. The cross talk between these two channels is 9 dB, i.e. the curves cross at 9 dB below the peak. Fig.2 shows the main lobes of 90 channels where light was launched into the demultiplexer through the no.1 input waveguide. Fig.3 is the signals from six adjacent channels. The average channel spacing for all 90 channels is 0.29 nm while our designed value is 0.3 nm. Fig.3 suggests that the channel spacing in this device is not very evenly spaced, and we think this is because during coarse tuning the laser, the measurement uncertainty in the spectral peak locations is 0.1nm. The fiber to fiber loss ranges from -19.9 dB to -40 dB for channel 1 to channel 90, which includes fiber-waveguide coupling loss, slab-ridge waveguide coupling loss, waveguide propagation loss and grating loss.

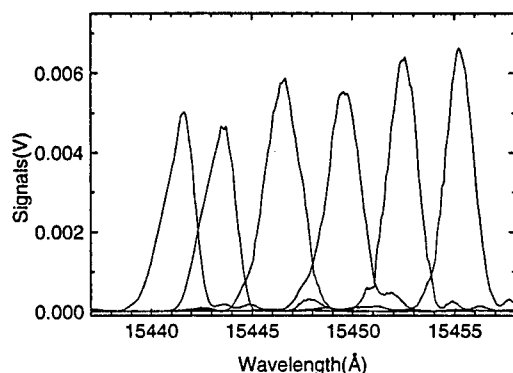


Fig.3 Signals from six adjacent channels when TM light was launched into the device through no.1 input waveguide

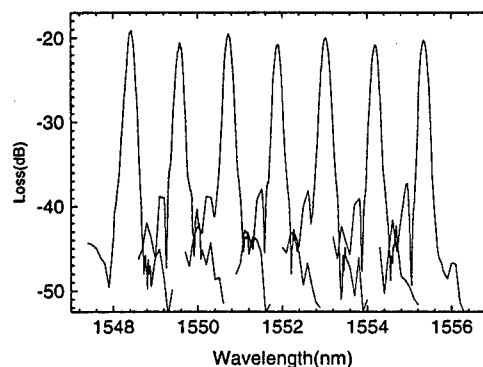


Fig.4 Transmission loss against wavelength for output from channel 20. The light was in TM mode, and applied to input no.1 to input no.7 waveguides respectively

The long wavelength channels have shorter output waveguides, thus have lower waveguide propagation loss. Also, the long wavelength channels collect light at points that are closer to the input point, so have lower diffraction loss since the blaze is optimized to the input point. If we use the no.2 input waveguide, the wavelength from all channels will increase by 1.2 nm, and will increase further by 1.2nm if no.3 input waveguide was used, and so on. Fig.4 gives the transmission loss against wavelength for output from channel 20 where the light was applied to no.1 to no.7 input waveguides respectively. The birefringence of the demultiplexer is  $B = n_{TE} - n_{TM} = 1.15 \times 10^{-3}$ , which includes stress birefringence caused by stress exerted by the silicon substrate, and waveguide birefringence due to large waveguide core and cladding refractive index difference 0.041.

*Acknowledgments:* This work was supported in part by NSERC and HyPIC.

## Reference:

- 1) F.TONG, C.S.LI, A.E. STEVENS, and Y.H.HKWARK: 'Characterization of 16-channel optical/electronic selector for fast packet-switched WDMA networks', IEEE Photonics letters, 1994,6(8),pp.971-974
- 2) K.OKAMOTO, K.SYUTO, H. TAKAHASHI and Y.OHMORI : 'Fabrication of 128-channel arrayed-waveguide grating multiplexer with 25ghz channel spacing', 'Electron.Lett.', 1996,32(16), pp.474-475
- 3) K.A.MCGREER : 'Theory of concave gratings based on a recursive definition of facet positions', Applied Optics, 1996, 35,(30), pp. 5904-5910

ThD3

4:45pm - 5:00pm

### High Performance Metal-Coated Multimode Interference (MMI) Devices for WDM Applications

*J. Z. Huang, M. H. Hu, J. Fujita, R. Scarmozzino, R. M. Osgood, Jr.  
Microelectronics Sciences Laboratories, Columbia University  
New York, NY 10027  
Tel. (212) 854-8042 Fax (212) 860-6182*

#### ABSTRACT

A metal-coated MMI device is proposed and analyzed. Simulations show that due to its ideal mode spectrum and resulting enhanced imaging performance, the device has applications to low index contrast polymer waveguides.

#### SUMMARY

MMI couplers can implement several optical signal routing and processing functions for WDM systems. Their low excess loss, high extinction ratio, small size, and low sensitivity to fabrication tolerances and polarization meet the needs for large-scale production of PICs.

The imaging principle of MMI devices is based upon a specific integral relationship of the propagation constant differences between the modes [1]. However, for dielectric waveguides, this ideal mode spectrum is only an approximation, especially in the case of weakly confined structures. This restricts the application of MMIs in low index contrast materials, such as silica on silicon or polymers, which are being used increasingly in PICs. Even for high contrast structures, the mode deviation also degrades the device performance when the splitting number is large or multiple imaging lengths are necessary. In this paper, we propose MMI devices with metal-coated side walls, which allow an ideal mode spectrum even in low contrast systems.

For dielectric waveguides, the ideal mode spectrum, upon which the imaging is based, is given by:  $\beta_0 - \beta_m = m(m+2)\pi / 3L_\pi$  (1), with  $L_\pi = 4n_r W_e^2 / 3\lambda_0$ , and is obtained under the approximation  $K_{ym} \approx (m+1)\pi / W_e$ . Here,  $\beta_m$  and  $K_{ym}$  are the propagation constant and the lateral wave number for mode  $m$ , respectively, and  $W_e$  is the effective width for  $m=0$  [2]. The approximation for  $K_{ym}$  only holds for high index contrast. On the other hand, with a perfect conductor coating the waveguide, the boundary conditions require  $E_x = 0$  for TE modes, which makes the expression for  $K_{ym}$  exact, with  $W_e = W$ , the width of the waveguide. This leads to the ideal mode spectrum desired, independent of index contrast.

We now demonstrate that even for a non-ideal conductor the above conclusion is highly accurate. A 2D geometry for 2x2 couplers is shown in Fig.1 (a), and a cross section of a 3D structure, realizable in polymers, is illustrated in Fig.1 (b). The waveguide core and cladding are polymers with  $\Delta n / n = 0.008/1.49$  or  $0.02/1.49$ , and the metal coating is Al with  $n=1.44-j16$ . The beam propagation method (BPM) was used to determine the mode spectrum for this device, with and without Al coating, and the results are shown in Fig. 2, along with a line indicating the ideal behavior of Eq. (1). Clearly, the metal-coated MMI has an almost ideal mode spectrum, while the standard devices show significant deviation.

The improvement in mode spectrum leads directly to enhanced imaging quality for the metal-coated device. Fig.3 shows BPM simulations for the MMI with and without metal and



plots power coupled into the output waveguides as a function of MMI length. The imaging performance of the metal-coated devices is nearly perfect, while the non metal-coated one has a poor overlap at the 3dB point and degrades with distance. The above concept demonstrated in 2D can be realized in 3D with typical polymer waveguide processing as shown in Fig.1 (b). A 3D vectorial BPM analysis of the device shows the same superior performance as illustrated in Fig.3.

In summary, metal-coating can significantly enhance the performance of MMI devices for low index-contrast materials. We demonstrate its feasibility by the design and simulation of a polymer channel waveguide MMI coated with Al. Experimental demonstration and application will be the next step for this design concept.

This work was supported by DARPA/AFOSR and NCIPT.

## REFERENCES

- [1] R. Ulrich and T. Kamiya, J. Opt. Soc. Am., **68**, 583, 1978
- [2] L. B. Soldano and E. C. M. Pennings, J. Lightwave Technol., **13**, 615, 1995.

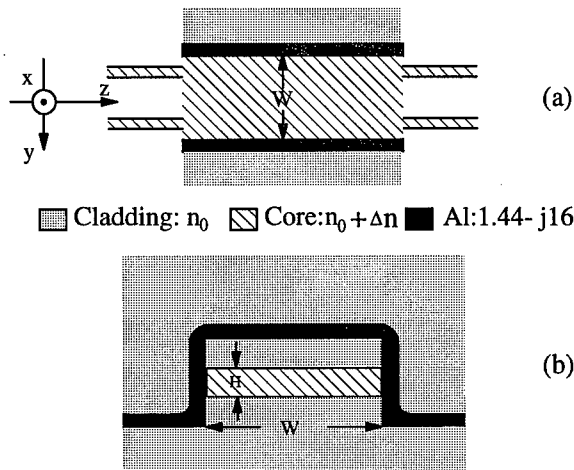


Fig.1 (a) 2-D structure for metal-coated MMI. (b) 3-D polymer channel waveguide MMI cross section. ( $n_0 = 1.49$ ,  $\Delta n = 0.008, 0.02$ ,  $W=36\mu\text{m}$ ,  $H=5\mu\text{m}$ )

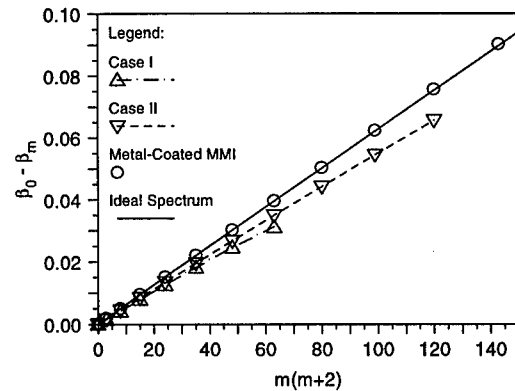


Fig. 2 Mode spectrum analysis for MMI without metal-coating (Case I:  $\Delta n = 0.008$ , Case II:  $\Delta n=0.02$ ), and with an Al metal coating. ( $\lambda_0=1.55\mu\text{m}$ )

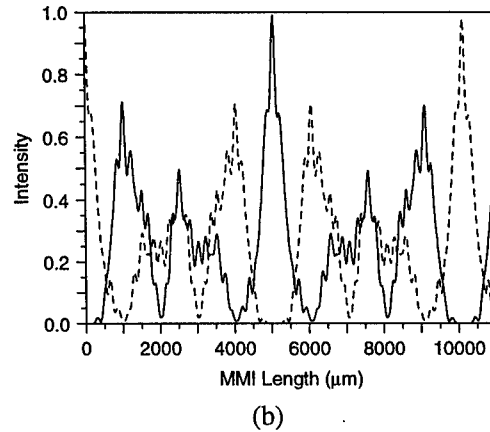
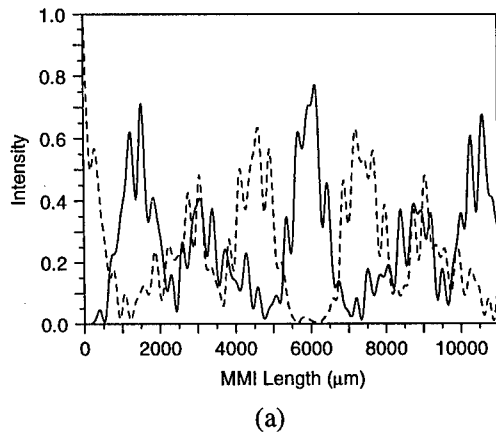


Fig. 3dB MMI coupler output intensities of TE polarization as a function of coupling Length. (a) MMI without metal coating, for Case I. (b) metal-coated MMI. ( $\lambda_0=1.55\mu\text{m}$ )

ThD4

5:00pm - 5:15pm

**An Asymmetric Dielectric-strip Loaded Y-junction Wavelength  
Demultiplexer by  $K^+$  -  $Na^+$  Ion Exchange in Glass**

F. Xiang and G.L. Yip

Guided-Wave Photonics Laboratory

Department of Electrical Engineering, McGill University

3480 University Street, Montreal, P.Q., Canada H3A 2A7

There has been growing interest in glass waveguide wavelength demultiplexers for applications in optical fiber communication systems. The device to be presented is shown in Fig.1. Its two waveguide branches are made by  $K^+$  -  $Na^+$  ion exchange with its arm 2 cladded by an  $Al_2O_3$  layer. The demultiplexing is based on the difference in the dispersion characteristics of the two asymmetric branches. A study of this device concept was performed [1]. Although its feasibility was established, the measured extinction ratios (ER), defined as the ratio of the output powers from the two arms, were below 10 dB for both  $1.3\mu m$  and  $1.55\mu m$ . The difficulties were mainly with the deposition of a reliable  $Al_2O_3$  layer. In this paper, we will present the much improved BPM design simulations, fabrication techniques and performance figures of this device.

Due to the geometrical and refractive index differences in the two branches, their respective dispersion curves will intersect at a certain wavelength, according to our design, between the two wavelengths to be demultiplexed as shown in Fig. 2. It can be seen that the effective index of arm 1 is higher than that of arm 2 at  $\lambda_1 = 1.55\mu m$ , but the reverse at  $\lambda_2 = 1.31\mu m$ , hence the demultiplexing and separation of the waves at  $\lambda_1$  and  $\lambda_2$  into arm 1 and arm 2, respectively. An  $Al_2O_3$  cladding on arm 2 enhances the asymmetry between the two arms, permitting high ER's to be obtained.

To reduce scattering loss in arm 2 due to the  $Al_2O_3$  strip, the strip width is made twice that of arm 2. Other measures need also be taken to protect the deposited  $Al_2O_3$  strip during various fabrication processes. Optimized device parameters for high ER's can be obtained through BPM design simulations. Fig. 3 shows the BPM simulations for the TM modes at  $1.55\mu m$  and  $1.31\mu m$ , employing a set of optimized parameters, yielding the corresponding ER at 32 dB and 29 dB, respectively. Due to the difficulties in controlling the precise device parameters during fabrication, the measured parameters of the implemented device deviate somewhat from the design-optimized values. Fig. 4 shows the near-field output spots of a fabricated device. For the set of device parameters  $W_0 = W_1 = 5.32 \pm 0.4\mu m$ ,  $W_2 = 5.02 \pm 0.4\mu m$ ,  $D_1 = 5.0 \pm 0.1\mu m$ ,  $D_2 = 1.5 \pm 0.1\mu m$ ,  $f = 0.56 \pm 0.02\mu m$ ,  $\theta_1 = 0.005$  rad and  $\theta_2 = 0^\circ$ , the ER values at  $1.55\mu m$  and  $1.31\mu m$  are 26 dB and 24 dB, respectively, by BPM calculations and 25dB and 20 dB, respectively, by measurements. The design and measured ER's are, therefore, in good agreements. More details will be presented at the meeting.

**Reference**

1. N. Goto and G.L. Yip, Electronics Letters, 26, No.2,102(1990)

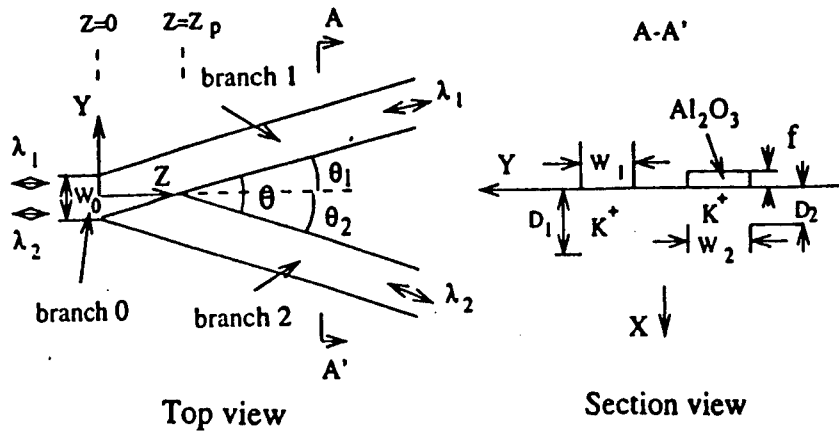


Fig. 1 : The configuration of a Y-junction demultiplexer  $\lambda_1 = 1.55 \mu\text{m}$   $\lambda_2 = 1.31 \mu\text{m}$ .

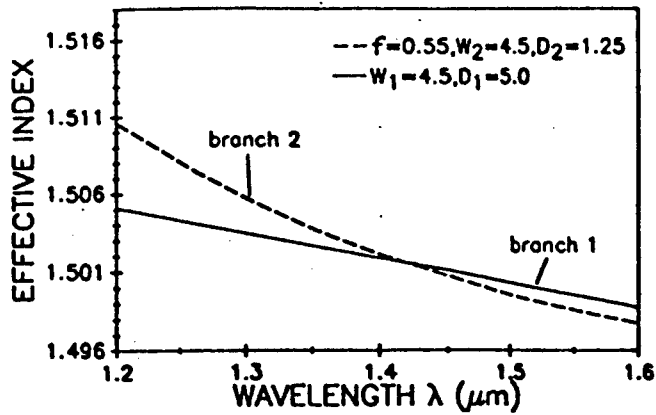


Fig. 2 : Dispersion curves of TM mode in isolated branch 1 and branch 2. The parameters are in  $\mu\text{m}$ .

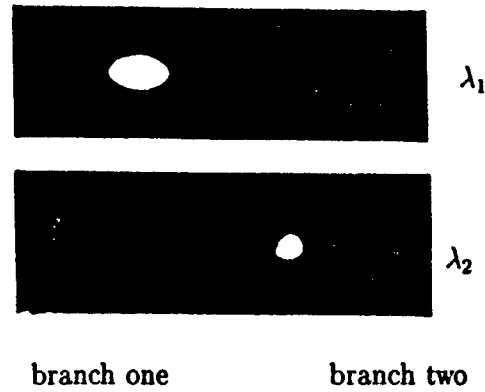
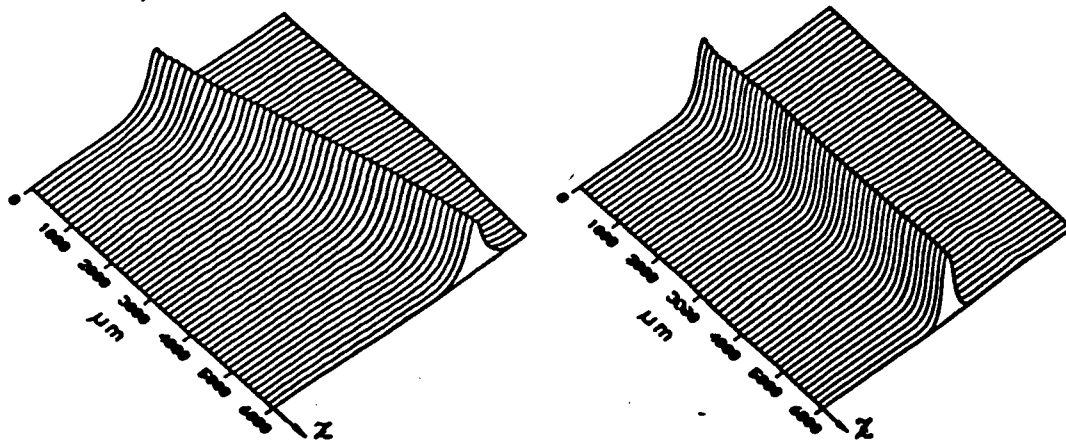


Fig. 4 : Output spots at the device's end facet



(a)  $\lambda_1 = 1.55 \mu\text{m}$ , ER = 32dB and device loss -0.18dB

(b)  $\lambda_2 = 1.31 \mu\text{m}$ , ER = 29dB and device loss -0.17dB

Fig. 3 : BPM simulations(TM) for the device with  $\theta_1 = 0.005 \text{ rad}$ ,  $\theta_2 = 0^\circ$ ,  $W_0 = W_1 = W_2 = 4.5 \mu\text{m}$ ,  $D_1 = 5.0 \mu\text{m}$ ,  $D_2 = 1.25 \mu\text{m}$ , and  $f = 0.55 \mu\text{m}$ .



## **WDM COMPONENTS TECHNOLOGY**

**Friday, 15 August 1997**

### **Sessions:**

**FA: Laser Arrays**  
**FB: Optical Amplifiers**  
**FC: Filters III**  
**FD: Filters IV**

## **Friday Papers Not Available**

- FA1      “Multiwavelength DFB Laser Arrays for WDM Lightwave Communication Systems”, *C.E. Zah, P.S.D. Lin, N.C. Andreadakis, M.R. Amersfoort, B. Pathak, F. Favire, A. Rajihel, R.Bhat, C. Caneau, M.A. Koza, K.-P. Ho, and T.P. Lee, Bellcore, Red Bank, NJ*
- FC1      “Fibre Gratings for WDM Systems”, *R.I. Laming, Southampton University, Southampton, UK*
- FC4      “Fiber Gratings Devices for WDM Systems”, *S. Poole, Index Pty Ltd., Sydney, Australia*
- 

## **Friday Withdrawn Papers**

- FB1      “Broadband WDM Amplifiers: From Research to Field Deployment”, *B. Clesca, Alcatel Telecom, France*

## 5-Wavelength Surface Emitting Laser Diode Array Based on Post Growth Adjustment of Surface Mode Emission

*A. Golshani, P. O. Kellermann, A. Köck and E. Gornik*

*Institute of Solid State Electronics, Vienna University of Tech., Floragasse 7, A-1040 Vienna, Austria*

Tel. (+43-1) 504 55 25-15; Fax: (+43-1) 504 55 25-9 email: amir@fkeserver.fke.tuwien.ac.at

*L. Korte*

*Siemens AG, Otto Hahn Ring 6, D-81730 Munich, Germany*

The Multi-wavelength Optical Networking (MONET) is the ultimate solution for future optical communication systems serving both commercial and specialized communication applications. Wavelength division multiplexing (WDM) schemes have been developed to fully utilize the bandwidth of optical fibers. Multi-wavelength semiconductor laser diode (LD) arrays are considered as a compact choice for WDM sources due to their capability of simultaneous transmission of several channels into an optical fiber from a single structure. This increases the total system speed and resolution without significantly increasing system size or costs. Efforts on LD arrays for WDM applications focus on LDs such as DFB/DBR and VCSEL and.

Several attempts on fabrication of DFB laser arrays are reported so far. Electron beam lithography has been used to fabricate multi-pitched gratings for WDM DFB laser arrays. Wavelength spacing of 2 nm with a deviation of  $\pm 0.2 \text{ nm}^1$  and spacing of  $\sim 1.5 \text{ nm}$  in DFB lasers with 30 dB SMSR have been reported<sup>1,2</sup>.

We have demonstrated recently that the emission wavelength of the surface mode emission (SME) based laser diodes can be adjusted by adapting the surface waveguide thickness on top of the laser structure<sup>3</sup>. This can be considered as an alternative approach with high flexibility to fabricate single mode multi-wavelength arrays for WDM systems

We report on the fabrication of the first 5-wavelength surface emitting SME LD array by post growth adjustment of the emission wavelength. The array consists of 21 LDs, each separated from the adjacent LDs by  $250 \mu\text{m}$ . Every 3 SME LDs form a group on the array and are assigned to operate at the same wavelength. The array consists of 5 groups (15 LDs) and the groups are separated by a reference LD without surface structure. Each group emits at a different wavelength by adjusting the surface waveguide for each group individually. The structure of the array is schematically sketched in fig. 1.

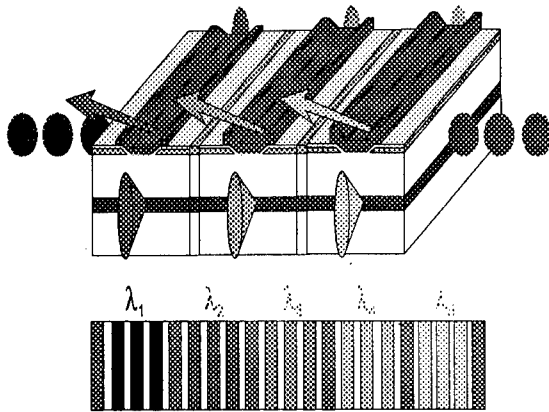
Conventional AlGaAs/GaAs double heterostructure diode lasers have been

grown by MOVPE. The undoped GaAs active layer is cladded by  $\text{Al}_{0.35}\text{Ga}_{0.65}\text{As}$  layers and is 550 nm below the surface. A grating with a period of 415 nm is exposed holographically on the surface of the samples and is etched to a depth of about 100 nm into the top

cladding layer by ion milling. Laser stripes are semitransparent Au films (30 nm thick, 12 nm wide) and are spin coated with photo resist (Hoechst AZ 6615), which serves as the surface waveguide.

The SME surface emission is based on the coupling between the laser

Figure 1: Schematic structure of the SME diode laser array. The Thickness of the surface waveguide is slightly different on each LD group, which leads to emission at different wavelengths.



modes in the active region and the  $TE_0$  surface mode in the surface waveguide. The  $TE_0$  surface mode is excited by the laser mode via one grating vector. The excited  $TE_0$  mode couples either back into the laser structure through the grating and provides an active feedback leading to the single mode emission or decays via one grating vector into the air as the surface emission.

Figure 2 shows the spectra of the LD groups (different layers) with respect to their position on the laser bar. The surface waveguide thickness' of all LDs are adjusted (255 nm) in the first step for emission around 867 nm and then the waveguide of each individual LD group is thinned by low power plasma etching to a different thickness. A waveguide thickness variation of 9 nm is achieved, which resulted in a wavelength shift of 4.78 nm over the laser array. The average wavelength spacing between the LD groups is 1.1 nm with a wavelength adjustment precision of 0.13 nm in average. The samples are AC driven with the same current and duty cycle (pulse width = 0.5  $\mu$ s and frequency = 30 kHz). The typical threshold current density is  $1.8 \pm 6\%$  kA/cm<sup>2</sup>. Every LD on the sample shows single mode emission with an average FWHM of 0.08 nm. SMSR is about 20 dB in the best case. Single mode emission is achieved at a current of  $1.1 I_{th}$  which retains up to  $1.4 I_{th}$ . At  $1.8 I_{th}$  the FWHM is 0.22 nm and the SMSR is less than 10 dB. The total array yield per wavelength is about 100 mW, where 20 % of the power is radiated via the surface.



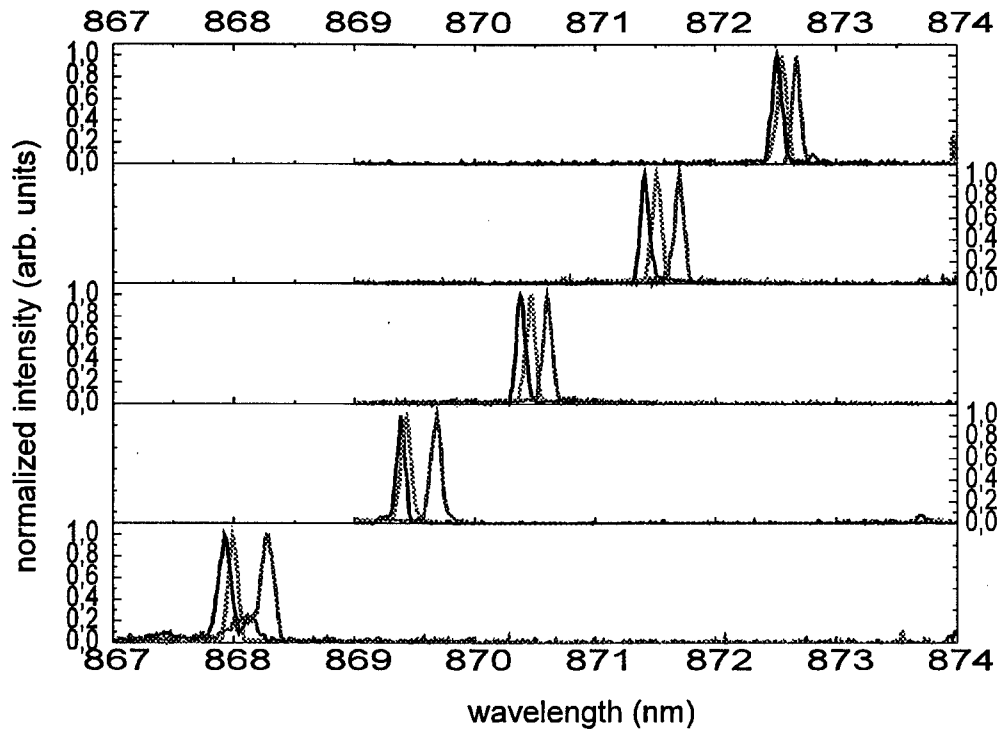


Figure 2: Spectra of the array elements. Each layer in figure refers to spectra of one LD group. The average FWHM is 0.08 nm. Wavelength spacing is 1.1 ( $\pm 0.13$ ) nm.

The main advantage of the SME laser diodes in comparison to DFB/DBR laser diodes is their simple and flexible fabrication process, which does not require any regrowth. Due to the flexible SME technique the emission wavelength of each array element can be controlled by simply adjusting the waveguide thickness. We demonstrate here the high potential of this type of laser diodes to be employed in WDM systems.

#### References

1. C. E. Zah et. al.; Jour. Optoelectr. Devices and Tech., **9**, 153 (1994)
2. L. S. Lome; Proceedings of Photonic West'96, SPIE 2690, p. 2 (1996)
3. A. Golshani, A. Köck, S. Freisleben, C. Gmachl, E. Gornik, L. Korte; *Appl. Phys. Lett.* **69** (16), 2312-4 (1996)

## Improved Crosstalk Performance in a 10-Wavelength 25 Gbps Multichannel Laser Array Transmitter Module

M. Shell and D. J. Blumenthal  
Optical Communications and Photonic Networks Laboratory  
School of Electrical and Computer Engineering  
Georgia Institute of Technology, Atlanta, GA 30332-0259

### Introduction

Multiwavelength laser arrays are an important component for future wavelength division multiplexed (WDM) links and networks [1,2]. The ability to modulate multiple wavelengths simultaneously from a single transmitter provides increased capacity in multichannel links and supports network functions like multicasting, multichannel add/drop, and optoelectronic wavelength conversion. Fully functional transmitters must integrate laser drivers, the laser array, temperature control, DC power distribution and high-speed electronic signal distribution. A critical issue for multiwavelength transmission is electronic, thermal and optical crosstalk within the laser array transmitter [2,3]. In this paper we demonstrate a 10-wavelength multiwavelength transmitter with improved electrical and optical crosstalk performance. Simultaneous modulation of 10 lasers at 2.5 Gbps per channel is demonstrated with low crosstalk resulting in a 25 Gbps data rate into the fiber. The transmitter utilizes the laser array reported in [4] and the laser array driver reported in [5]. Electronic crosstalk is reduced through capacitive decoupling techniques and proper voltage balancing of the laser array common cathode.

### Transmitter Configuration

The Bellcore laser array is mounted on a copper submount that is thermally and electrically isolated from the driver structure as shown in Figure 1a. The laser ground pads were wire bonded to the laser submount. The laser submount is cooled with a TEC to the copper block heat sink. Two Rockwell 1x8 laser driver arrays are mounted on copper pedestals thermally connected to the primary heat sink but isolated electrically from the laser array.

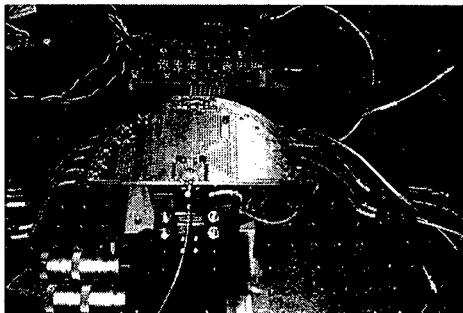


Figure 1a

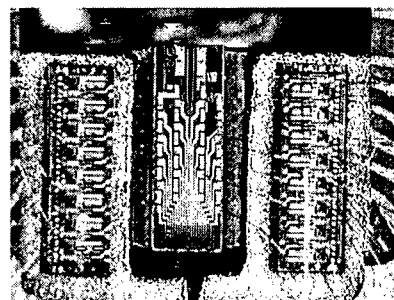


Figure 1b

### Results and Summary

The eye diagram for each wavelength is shown with all 10 lasers modulated at 2.5 Gbps  $2^{31}-1$  PRBS. Channels were detected using a fiber Fabry-Perot and fiber amplifier. The optical spectra shows uniform channel power in Figure 3. The SNR of each eye is limited by our 8 channel source data generator rise time. Figure 4 illustrates that we are not crosstalk limited by showing four channels driven in parallel using a high speed HP 12.5 Gbps BERT. The improved digital signal results in higher SNR and it is expected that driving all 10 channels with these signals

will improve the eyes in Figure 2. The effect 9 2.5 Gbps channels on a CW channel is shown in Figure 5, illustrating negligible crosstalk.

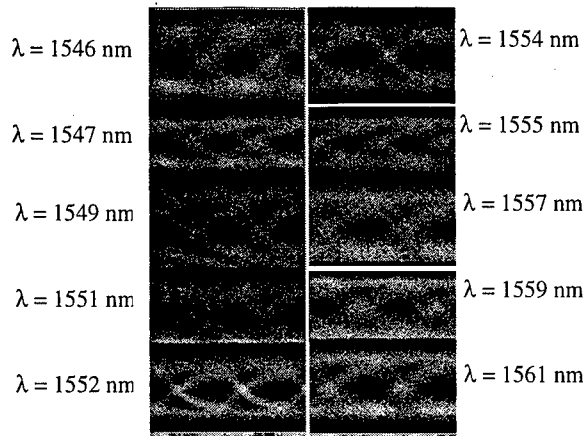


Figure 2

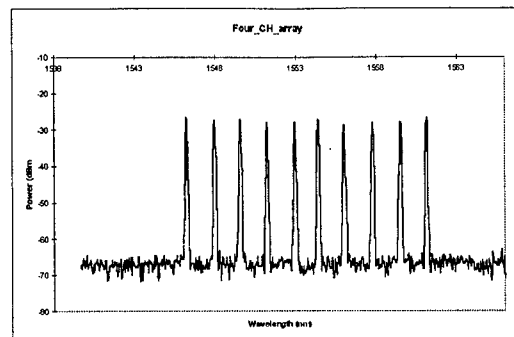


Figure 3

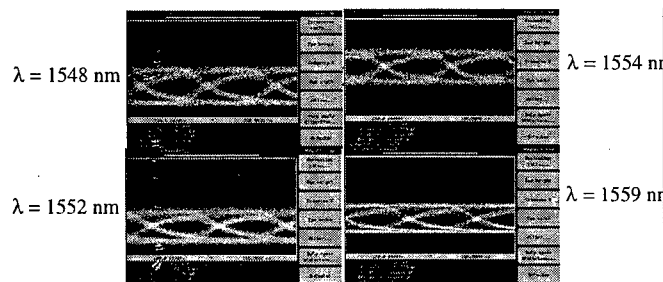


Figure 4

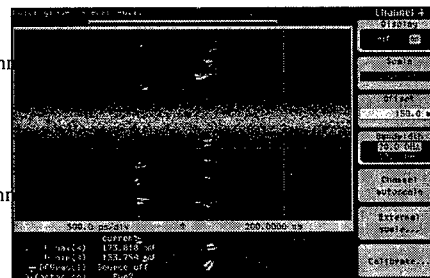


Figure 5

### Acknowledgments

The authors wish to thank K. Pedrotti and K.C. Wang of Rockwell, T.P Lee and C. E. Zah of Bellcore, and C. Dreze and C. Rolland of Nortel for their valuable support and experience. This work was sponsored by funding from an NSF National Young Investigator Award, a Georgia Research Alliance (GRA) award, support from Nortel, and a DARPA DURIP award. We also thank Stan Halpern and Bob House for their invaluable help with wire bonding and circuit board fabrication.

### References

- [1] T. P. Lee et. al, "Multiwavelength DFB laser array transmitters for ONTC reconfigurable optical network testbed," *J Lightwave Technol*, v 14, pp. 967-976, Jun 1996.
- [2] S. Hanatani et. al., "10 channel fully-integrated high-speed optical transmitter module with a throughput larger than 8 Gbit/s," *European Conference on Optical Communication (ECOC)*, vol. 2, pp. 875-878, 1995.
- [3] T. Hayashi, et. al, "Reducing electrical crosstalk in laser-diode array modules by using a film-carrier interconnection," *J Lightwave Technol*, vol. 13, pp. 1885-1891 Sep 1995.
- [4] C. E. Zah et. al, "Monolithic integration of multiwavelength compressive-strained multiquantum-well distributed-feedback laser array with star coupler and optical amplifiers," *Electron Lett.*, vol. 28, p 2361-2362, Dec., 1992.
- [5] K. Pedrotti et. al, "HBT transmitter and data regenerator arrays for WDM optical communications application," *GaAs IC Symposium*.

FA4

9:30am - 9:45am

## Design of a 40 Gbps WDM Laser Module

D. J. Copeland, S.A. Tabatabaei, S.A. Merritt, S. Didde, M. Dagenais, Y.J. Chen, D. Stone, A. Springthorpe<sup>†</sup>

Department of Electrical Engineering, University of Maryland  
and Laboratory for Physical Sciences, 8050 Greenmead Drive, College Park, Maryland, 20740

<sup>†</sup> Nortel Technology, Advanced Technology Laboratory  
Ottawa, Ontario, Canada, K1Y 4H7

We report on the development of a 4 channel, 10 Gbps / channel WDM laser transmitter module. The module includes four DFB MQW lasers operating in the 1550 nm fiber window. The small-signal characteristics of the DFB laser was measured from 50 MHz to 18 GHz, and a small-signal bias-dependent model was implemented using EEsof Libra software. This model was used with measured characteristics of the driver to analyze their interaction and predict the combined response. The drivers employ a commercially available HBT-based monolithic amplifier. The electrical cross-talk of the drivers is presented. 10 Gbps waveforms are presented for the drive output and the optical signal.

The lasers used in this effort have a typical threshold current of 16 mA and produce 5 mW at 40 mA. The lasers were packaged on a copper carrier with a ceramic bond post. The laser model incorporates an RLC model of the active region with the laser parasitic elements and physical models of the package parasitic elements. Parameters for the active region were determined by matching the measured response to a simple model yielding the relaxation oscillation frequency  $\omega$ , and damping factor  $\gamma$  as functions of bias current, and values for the RLC network were then calculated for each bias point from  $\omega$ , and  $\gamma$  [1],[2]. The diode resistance was modeled as a linear function of bias current - this relationship provided a good fit to the measured DC V-I characteristic of the diode. The device capacitance was extracted from impedance measurements. The bond wire and bonding post were modeled using physical dimensions; the bonding post was modeled as a microstrip transmission line, which was quarter-wave resonant at approximately 9 GHz. The parasitic elements were optimized to fit impedance and frequency response data. Figure 1 shows the measured and modeled frequency response.

The WDM module is shown in figure 2. The driver circuit was designed using the Mini-Circuits ERA-1 monolithic amplifier. Two bias tees per section provide power to the amplifier and laser bias. Each driver can source up to 48 mA modulation current, and has a bandwidth of 7.4 GHz. The four driver sections were constructed on a 20 mil thick Teflon microwave substrate, bonded to a copper carrier. The channels of the WDM module are spaced 0.5" apart.

Each driver connects to its respective laser through a short length of microstrip line and a 45  $\Omega$  thin-film resistor. The lasers and the interconnecting components mount on a separate carrier. The return loss at the laser is severely degraded by the package parasitic elements, which tend to transform the low impedance of the laser towards a high impedance at 9 GHz. This mismatch, in combination with mismatch at the driver output, introduces a ripple in the frequency response, and can degrade the eye pattern. Measured s-parameters of the driver circuit were used with the laser model to minimize this effect in the design.

Electrical cross-talk was measured between driver sections from 50 MHz to 18 GHz. The worst-case crosstalk between adjacent channels was -28 dB, occurring at 2.5 GHz. Typically, the cross-talk was less than -32 dB in the measured frequency range.

Figure 3 shows a typical driver output for a 10 Gbps, 2<sup>31</sup>-1 PN code. The output drive level is 40.4 mA p-p. The optical output of a single-channel prototype appears in figure 4. As shown, an open eye pattern is obtained. Subsequent tests with a bit error rate test set verified that the bit error rate was less than  $1 \times 10^{-15}$ .

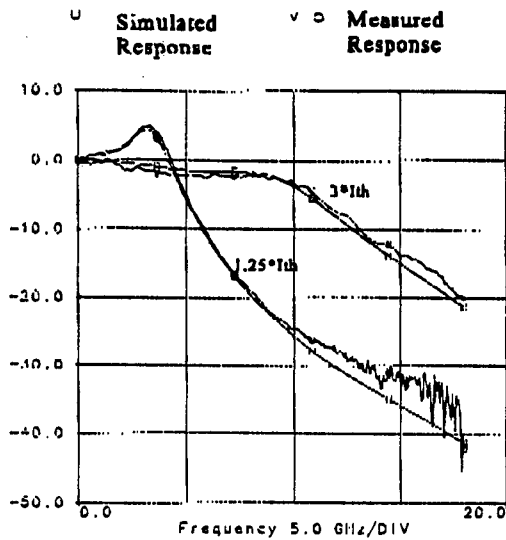


Figure 1 - Laser Frequency Response

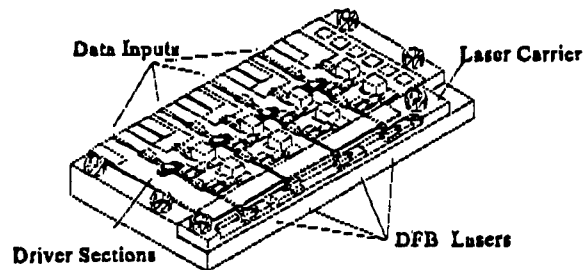


Figure 2 - WDM Laser Module

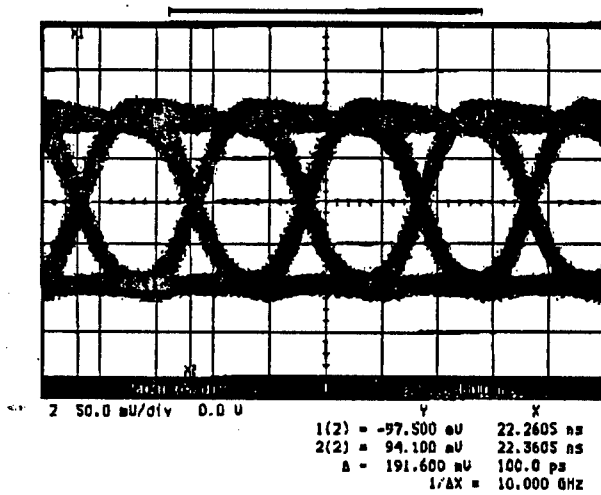


Figure 3 - Driver Output into 50 Ω, 10 Gbps

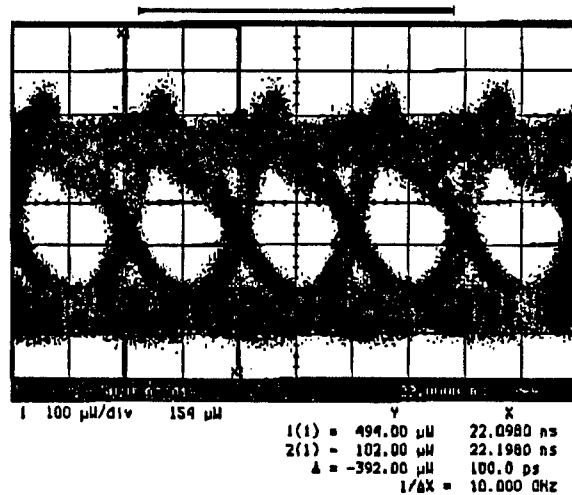


Figure 4 - Optical Waveform, 10 Gbps

## REFERENCES:

- [1] Tucker, R.S., Pope, D.J., "Microwave Circuit Models of Semiconductor Injection Lasers", *IEEE Transactions on Microwave Theory and Techniques*, vol. MTT-31, no.3, March 1983, pp. 289-294.
- [2] Nagarajan, R., Tauber, D., Bowers, J.E., "High-Speed Semiconductor Lasers", *International Journal of High-Speed Electronics and Systems*, vol. 5, no.1, January 1994, p. 1-44.

FA5

9:45am - 10:00am

### Mode-Locked Laser Arrays for WDM Applications

L. Davis, M.G. Young, S. Forouhar  
Center for Space Microelectronics  
Jet Propulsion Laboratory  
California Institute of Technology  
4800 Oak Grove Drive  
Pasadena, CA 91109

#### Summary

High bandwidth mode-locked laser arrays are being developed for a bit-parallel wavelength (BPW) link for high performance computer networks[1]. The system design requires a 10 element WDM transmitter with an aggregate bandwidth in the 100-800 Gb/s range.

The devices employ a colliding pulse mode-locked (CPM) cavity consisting of a 5 section, 3 contact symmetric cavity: a saturable absorber at the center of the cavity, 2 gain sections and 2 grating sections. The devices can operate as passively mode-locked lasers; however, in order to reduce the noise in the mode-locked laser and to synchronize the signals from all the lasers in the array, the contact to the saturable absorber section is designed for a G-S-G probe for application of a synchronizing RF signal. The grating operates in two capacities: to determine the center wavelength and trim the excess spectral bandwidth. The devices are 3.5 micron ridge waveguide lasers, and the top InGaAs contact is etched to isolate the different sections (1-2 k $\Omega$  between contacts). The repetition rate in a CPM laser is twice the fundamental mode spacing of the cleaved cavity; for 20 GHz operation, the cavity length is  $\sim$  4.3 mm. When the devices are operated as Fabry-Perot mode-locked lasers (no gratings), typical threshold currents are  $I_{th} = 150$  mA (best = 120 mA), and external differential efficiency of  $\sim$  10%. Significant reduction of the phase noise can be achieved in these devices with as little as -20 dBm RF power, with the best mode-locking results occurring for 10 dBm. Reverse bias to the saturable absorber is typically -1.0 to -2.0V. Mode-locking occurs up to approximately 1-2 mW output power/facet.

Development of the grating-based devices required optimization of the grating strength (length and etch depth). An additional constraint is added by presence of gain material in the grating section in these initial devices. The best results were obtained by shorting the grating section, and by using a high  $\kappa$  grating with very short length (75  $\mu$ m at each end).

The initial WDM array devices incorporating gratings were designed for 3.3 nm spacing between channels, with all the wavelengths occurring in the EDFA gain bandwidth. The repetition rate is 18.2 GHz. The spectrum of the five channel array is shown in Fig. 1. An interferometric scan of a single mode-locked spectrum shows a FWHM of 85 GHz (Fig. 2) and a complete suppression of the cavity fundamental frequency of 9.1 GHz. The RF frequency response shows this as well (Fig. 3), with a 10 dB enhancement of the mode-locked peak over the resonance frequency peak. The measurement of the temporal width has been instrument-limited to  $\sim$  20 ps; autocorrelation measurements of the pulses will be performed.

Reduction of the threshold current and removal of the gain from the grating section is being pursued through the development of BH structures and active/passive transitions within the device cavity. Packaging of the devices, including the synchronous RF feeding of the lasers, is presently being addressed.

[1] L. Bergman, L. Lome, A. Mendez, "Bit Parallel Wavelength Links for High Performance Computer Networks," *SPIE Critical Review*, CR62, Jan. 96, 210.

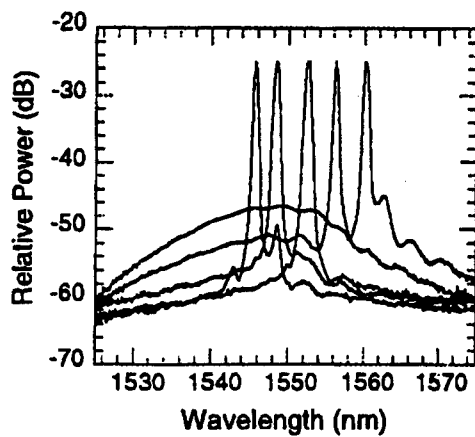


Fig. 1 Optical spectrum of the 5 element mode-locked laser array.

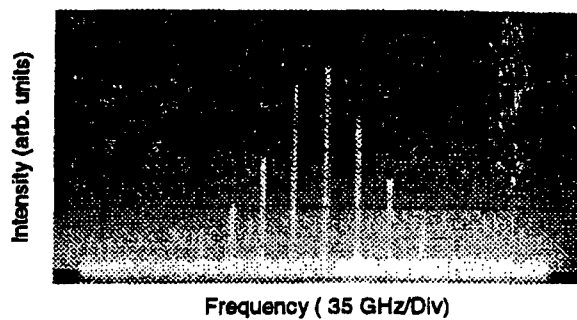


Fig. 2 Interferometric scan of the mode-locked spectrum (center wavelength ~ 1546 nm). The mode spacing is 18.2 Ghz.

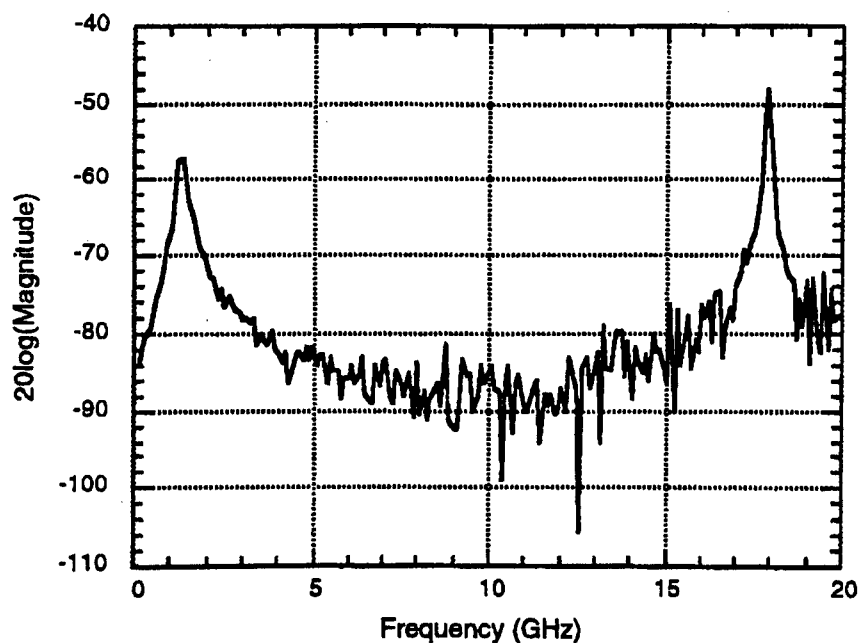


Fig. 3 The RF frequency response of a typical mode-locked laser.

## EDFA chain control: A comparison of two all-optical approaches

Dwight H. Richards and M. Ali, CUNY, New York, NY and Janet L. Jackel, Bellcore, Red Bank, NJ

EDFA's are a key technology enabler for multiwavelength optical communications, but despite their usefulness, a number of significant technological challenges remain. One which can have a large impact, particularly on wavelength routed networks, is cross saturation, i.e. the dependence of the gain in any one channel on the total input power in all channels. When the number of wavelength channels in a saturated EDFA changes, the gain in the remaining channels also changes. The resulting power excursions in the surviving channels can degrade the system performance.

Among the variety of methods used to prevent this problem is all-optical gain clamping.<sup>1,2</sup> In this paper we present the results of a time- and spectrally-resolved simulation of two version of this all-optical stabilization method to examine some of the limitations of these techniques. The model assumes a completely homogeneous gain medium and a commercially-available alumino-silicate fiber pumped at 1480 nm. We assume 2 input channels for the results presented here, and we drop and add one of them. The numerical results presented here are not necessarily optimized, but can be used to develop a quantitative understanding of the behavior of these amplifier chains.

The two approaches to chain stabilization are shown in Fig. 1. In Type 1 stabilization, the ring laser acts both to clamp the gain and to generate a compensating signal at wavelength  $\lambda_C$  which takes the place of the dropped channels  $\lambda_D$  in the subsequent EDFA's. Type 2 is the conceptually simpler method of gain clamping each of the EDFA's individually. As we will see, each of these methods creates demands on the EDFA's or on the chain as a whole. For Type 1, the gain flatness of the individual amplifiers is critical, but the loss budget of the chain as a whole is less important. For Type 2 stabilization, the gain flatness of the amplifiers is of little importance, but the output of a chain is highly dependent on the loss between amplifiers.

Fig. 2 shows the output of the surviving channel,  $\lambda_S$ , in a six-EDFA chain using Type 1 stabilization. The wavelength of the compensating signal is 1545, and the loss between EDFA's has been adjusted to give constant output power. We see that the steady-state output of the chain does not change, but that the transients at the time of channel drop/add become larger as the length of the chain increases. If the loss between EDFA's is held constant, the power in  $\lambda_S$  increases because of the non-

flat gain in the EDFA. ( $\lambda_S$  has higher gain than  $\lambda_D$ .) However, the variation in output power grows only slowly, as Fig. 3 shows for chains of 1, 6, and 20 EDFA's. Fig. 2 and 3 show results when the compensating channel has nearly the same gain as the dropped channel; Fig. 4 shows the effect of placing the compensating signal out of the region of maximum gain flatness. In Fig. 4,  $\lambda_C$  is 1530 nm and has greater gain than  $\lambda_D$ . Thus,  $\lambda_C$  grows at the expense of the surviving signal, and the output at  $\lambda_S$  becomes lower at every EDFA, when  $\lambda_C$  is present.

The dependence on gain flatness disappears when each EDFA is gain clamped individually. Fig. 5 shows the output of EDFA 1, 3, and 6 for Type 2 stabilization. Here each EDFA uses a different lasing wavelength. These results are only subtly different when the same  $\lambda_C$  is used at each EDFA. Comparison of Fig. 2 and 5 show that the transients die down somewhat faster for Type 2 stabilization. This comparison seems to show that Type 2 stabilization is preferable to Type 1. However, Fig. 6 shows that Type 2 stabilization is more sensitive to changes in the loss between EDFA's than is Type 1. When the loss between the first and second amplifiers of a 6-EDFA chain is increased by 3 dB, the output of a Type 1 chain is only minimally affected, while that of the Type 2 chain is reduced by 3 dB.

These results help us compare the two types of chain stabilization. Type 1 is less expensive to implement, since it requires modification of only the first EDFA, but it is sensitive to deviations from gain flatness. For short EDFA chains, where changes due to the different gains of the signal and compensating channels have no chance to accumulate, Type 1 stabilization appears to have an advantage. For long chains, we will need either to control the gain flatness very accurately, accept some signal level variation due to non-flat gain, or to control the gain at every EDFA, as is done in Type 2. In this case, we see that it is necessary to control the loss budget of the chain more accurately than is necessary when using Type 1 stabilization. Thus, both of these techniques can be used to compensate for changing numbers of WDM channels, but the demands they place on the EDFA chain are different.

<sup>1</sup> J. F. Massicott, S. D. Willson, R. Wyatt, J. R. Armitage, R. Kashyap, D. Williams, and R. A. Lobbett, "1480 nm pumped erbium doped fibre amplifier with all optical automatic gain control," *Electron. Lett.*, **30**, 962-964 (1994).

<sup>2</sup> J. L. Jackel and D. Richards, "All-optical stabilization multi-wavelength EDFA chains: a network-level approach," in *Proceedings of LEOS'96* (IEEE Lasers and Electro-Optics Society) postdeadline paper.



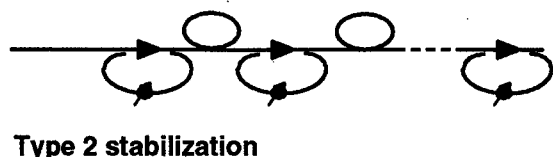
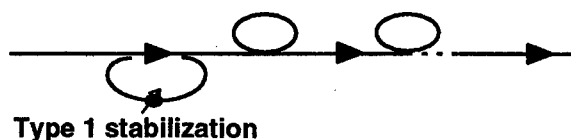


**Fig. 1** In Type 1 stabilization, the ring laser has a wavelength insensitive coupler at the output, so that  $\lambda_c$  is coupled out and passed to the remaining EDFA's in the chain. In Type 2, the output coupler is wavelength selective, and  $\lambda_c$  is not transmitted. Each subsequent EDFA is stabilized in the same way.

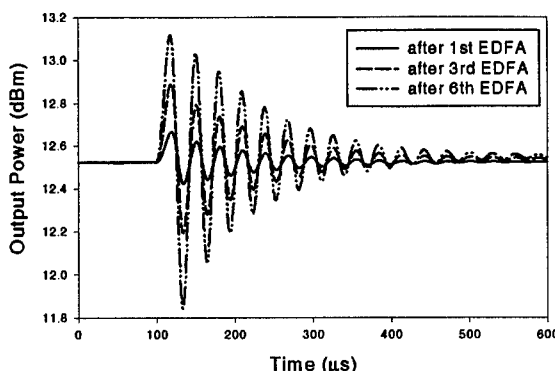


**Fig. 2** Type 1 stabilization, for 1, 3, and 6 EDFA's, with  $\lambda_c = 1545$  nm, in the flat gain region. Output power has been equalized at each stage.

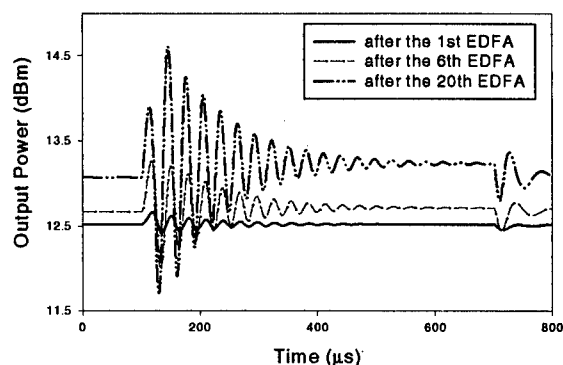


**Fig. 3** Type 1 stabilization, for 1, 6, and 20 EDFA's, with  $\lambda_c = 1545$  nm, in the flat gain region. Losses are the same between each stage.

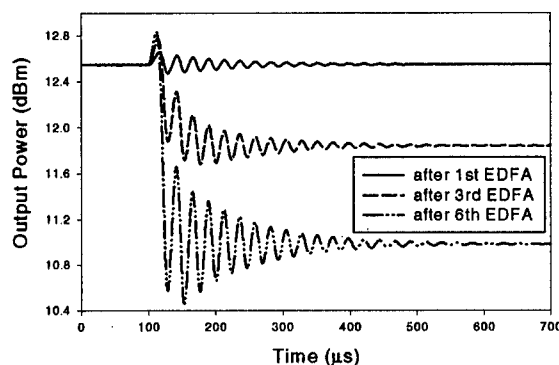


**Fig. 4** Type 1 stabilization, for 1, 3, and 6 EDFA's, with  $\lambda_c = 1530$  nm, i.e. with greater gain than dropped and surviving signals. Compare with Fig. 2.

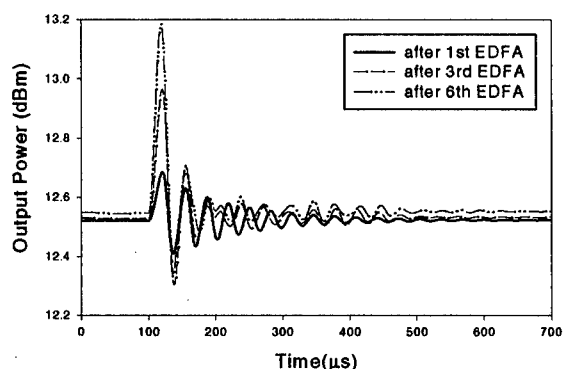


**Fig. 5** Type 2 stabilization, with different  $\lambda_c$  at each EDFA, for 1, 3, and 6 EDFA's. Note that transients die down more rapidly than in Fig. 2.

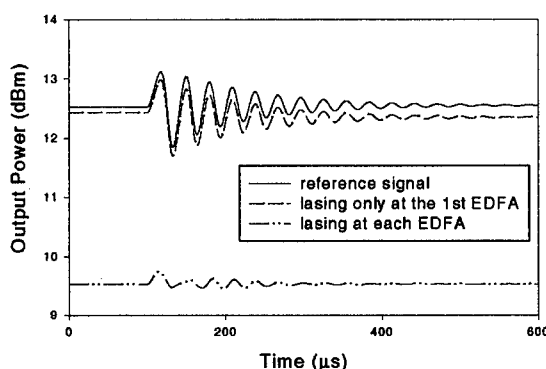


**Fig. 6** Comparison of Type 1 and Type 2 stabilization, after 6 EDFA's, when and excess 3 dB loss is inserted between the first and second EDFA's. Output power is recovered in Type 1, but not in Type 2.

FB3

11:15am - 11:30am

## A Simplifying Model of Fiber Amplifiers for the Design of Cascaded WDM-systems

J. Burgmeier, B. Stummer, Siemens AG, ÖN TR, D-81359 München  
R. März, Siemens AG, Research Laboratories, D-81739 München  
A. Cords, C. Schäffer, FH Lüneburg FB ET, Stephensonstr. 3, D-23562 Lüneburg  
FAX: +49-451-500 5236, e-mail: schaeffer@fh-luebeck.de

### Summary

In optical WDM-systems fiber optical line amplifiers are installed to compensate the fiber loss. The bit error rate performance of such a system is mainly determined by the optical signal-to-noise ratio and the eye degradation due to fiber dispersion. For the system design it is therefore necessary to evaluate the propagation of signal and noise power along the WDM-system for all operation modes [1]. A simple model of an EDFA, allowing fast and efficient calculation of the noise limits of an optical line amplifier system will be very helpful even for the design of the fiber amplifiers.

In this paper a simple scheme for the calculation of the spectral gain and noise of a given EDFA is presented. The parameters of the model can be derived from measured data or from data supplied by the manufacturer. Measurements of the spectral gain at average inversions and ASE power densities provide enough information to describe an optical amplifier with sufficient accuracy [2]. The measurements are carried out for two types of optical amplifiers, one pumped at  $\lambda=1480$  nm and the other was pumped at  $\lambda=980$  nm.

One advantage of the model is that the system designer is independent of the fiber manufacturer, who may supply detailed data about his fiber or not.

Within the specified limits (input power, WDM-window) the entire spectral gain behaviour of the fiber amplifier can be approximated by only two characteristic curves, the spectral gain  $G(\lambda, I)$  for a constant average inversion  $I_0$  and the spectral gain tilt  $T(\lambda)$ . The gain tilt can be written as a ratio in terms of the material absorption  $\alpha(\lambda)$  and the emission cross section  $g(\lambda)$ . The gain tilt is only dependant on the fiber type.

$$T_{\lambda_0}(\lambda) = \frac{dG/d\lambda}{dG/d\lambda|_{\lambda=\lambda_0}} = \frac{\alpha(\lambda) + g(\lambda)}{\alpha(\lambda_0) + g(\lambda_0)} \quad (1)$$

With a reference gain  $G_0$  at a reference wavelength  $\lambda_0$  and an average inversion  $I_0$  the gain of an EDFA is given by

$$G(\lambda, I) = G(\lambda, I_0) + T_{\lambda_0}(\lambda) \{G(\lambda_0, I) - G_0\} \quad (2)$$

with  $G$  in dB and  $T$  in dB/dB.

In practice a good choice for the reference wavelength  $\lambda_0$  is a value at the short wave side of the EDFAs gain window ( $\lambda_0 = 1530$ nm) because there the influence of the inversion on the gain is stronger. The higher the value of the differential gain, the lower is the influence of

measurement errors on the accuracy of the EDFA-model [3]. Fig. 1 shows the tilt difference  $\Delta T$  between the tilt calculated from the amplifier parameters supplied by the manufacturer and the tilt calculated from measured data with eq. (1). The reference wavelength is  $1.551\mu\text{m}$ . In the WDM-window (1548-1562nm) the tilt difference is always less than  $\pm 0.15$  dB/dB.

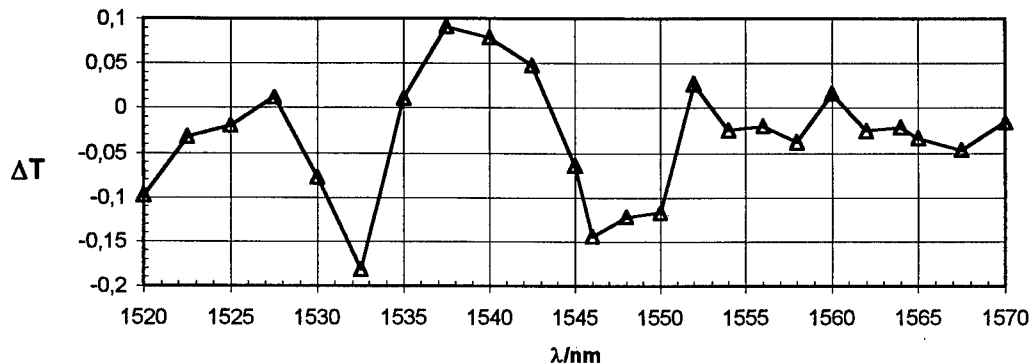


Fig. 1. Tilt difference between measured and calculated tilt for an EDFA ( $\lambda_{\text{pump}}=1.48\mu\text{m}$ ).

The differential gain equation (2), derived from a homogeneous gain model, predicts the nonuniform gain behaviour of erbium-doped fiber amplifiers very well [3].

With help of equation (2) the propagation of the signal power through the amplifier stages of a WDM-system can be calculated. Multiwavelength operation of the system can be simulated as well.

The spectral power density of the amplified spontaneous emission  $S_{\text{out}}(\lambda)$  at the output of the fiber amplifier is proportional to  $S_{\text{eq}}(\lambda) \cdot G(\lambda, l)$ , where  $S_{\text{eq}}$  is the equivalent input spectral noise density of the fiber amplifier.  $S_{\text{eq}}(\lambda)$  is measured or calculated. With eq. (2) the propagation of the ASE power and the optical signal-to-noise ratio in the WDM-system and at the output can be computed. If the eye degradation due to the total dispersion is taken into account by a dispersion loss, both main contributions determining the bit error rate performance of the WDM-system are considered. An investigation of the system performance as a function of span loss, number of spans, number of channels etc. is possible in a very efficient way because of the simple amplifier model based on measured data. The operation of the WDM-system in a constant signal power or constant total power mode can be compared easily.

Part of the work was supported by the European Union under the „ACTS PHOTON“ and „ACTS BLISS“ grants.

## References

- [1] M. Ali, A. Elfrefaie, R. Wagner, F. Mendez, J. Pan, S. Ahmed: Optimized Performance of Erbium-Doped Fiber Amplifiers in Multiwavelength Lightwave Systems, IEEE Photon. Technol. Lett., vol. 6, pp. 1039-1042, 1994
- [2] Desurvire, E.: Erbium-Doped Fiber Amplifiers, J. Wiley, New York, 1994
- [3] Burgmeier, J., Cords, A., März, R., Schäffer, C., Stummer, B.: A Black-Box Model of EDFAs Operating in WDM Systems; submitted for publication to IEEE Journal of Lightwave Technology

FB4

11:30am - 12:00noon

## Optical Amplifiers for Optical Networks

A. K. Srivastava and Y. Sun

Crawford Hill Laboratory, Bell Laboratories, Lucent Technologies  
Holmdel, NJ07733, USA

The Erbium Doped Fiber Amplifier (EDFA) is a key enabler of WDM transmission systems and wavelength routed optical networks. EDFA's are well suited to compensate the optical loss of network elements and transmission spans. Although the EDFA's are almost ideal in their characteristics, they are not quite perfect. Two effects which are critical in WDM networks and transmission systems are spectral gain non-uniformity and channel cross saturation in EDFA's.

The growing need for higher capacity WDM networks will require EDFA's having broader spectral bandwidth to support larger numbers of signal channels without sacrificing signal to noise ratio. Commercial silica based EDFA's currently offer up to 12nm of optical bandwidth. Greater optical bandwidth has been reported using fluoride based EDFA's, which have an optical bandwidth of about 24nm.<sup>1</sup> In a recent report<sup>2</sup> silica based EDFA's having 35nm bandwidth (Fig.1) were used to demonstrate error free transmission of 32 WDM channels over 640kms at 10Gb/s. The end of system power variation (Fig.2) was 4.9dB which is 3.5% of the total gain in the transmission system. In addition to broad bandwidth, the amplifiers also had wide dynamic range, which is essential to accommodate various span losses seen in real systems. The EDFA's were operated with flat gain characteristics by changing the attenuator loss in the mid section when the span loss varied by 6dB.

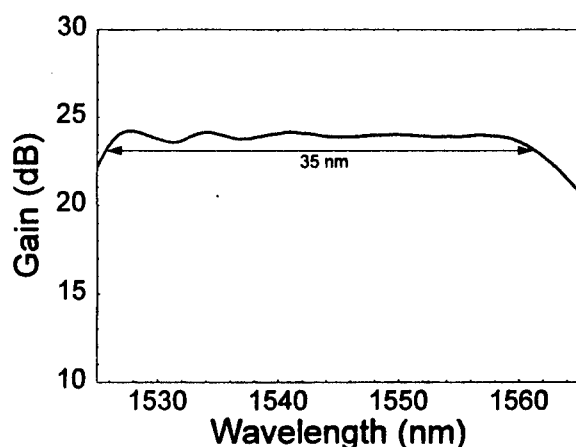


Fig.1. Gain Spectrum of broadband silica EDFA<sup>2</sup>.

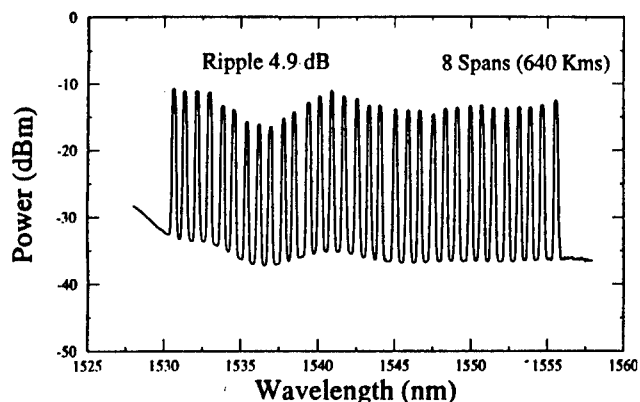


Fig.2. End of system spectrum after transmission over 640km and 8 broadband EDFA's<sup>2</sup>.

In WDM networks containing chains of EDFA's, network reconfiguration or failures can change the number of propagating channels in an amplifier. It has been reported<sup>3,4</sup> recently that even though the characteristic times of gain saturation and recovery effects are long (0.1-10ms), the power transients (Fig.3) experienced by surviving channels traversing a chain of EDFA's can be very fast ( $<1 \mu s$  for a 10 EDFA chain). Loss of channels can create error bursts since the power of surviving channels may

surpass the threshold for nonlinear effects. Insertion of channels can cause errors by depressing the power of the surviving channels below the receiver sensitivity. In order to prevent the degradation of surviving channels under these situations, it is necessary to restore their power levels on a short time scale, which poses a major challenge for the design of optical networks containing add/drop nodes.

Recently several schemes for fast gain control in EDFA's have been reported to mitigate the effects of fast power transients. One of them is automatic pump control in each EDFA on  $\mu\text{s}$  time scale to limit<sup>5</sup> the surviving channel power excursions for a single EDFA to less than 0.5dB. Another technique is *link control*<sup>6</sup>, which protects surviving channels on a link by link basis. The power of a control channel inserted before the first EDFA in the chain forming the link is adjusted using a fast feed back control circuit to hold constant the total power of signal channels and the control channel at the input of the first EDFA. Without control, the data transmission suffers from a power penalty of 3dB and an error floor at the end of a 560km transmission link with 8 EDFA's when part of the WDM channels are cut. With a feedback circuit that limits the power increase after 4  $\mu\text{s}$  (Fig.4), penalties are reduced to a few tenths of a dB, and the error floor disappears. A new scheme based on laser automatic gain control (AGC) was demonstrated recently, where a compensating signal in the first EDFA is generated using an all-optical laser feedback loop and then propagated down the link.<sup>7</sup> Stabilization was reached in a few tens of microseconds and output power excursion after a chain of 6 EDFA's was reduced by more than a few tenths of a dB. Another report pointed out the importance of inhomogeneity<sup>8</sup> in the EDFA gain spectrum for laser AGC. The spectral hole burning at the control signal should be small for both link and laser control schemes to be effective.

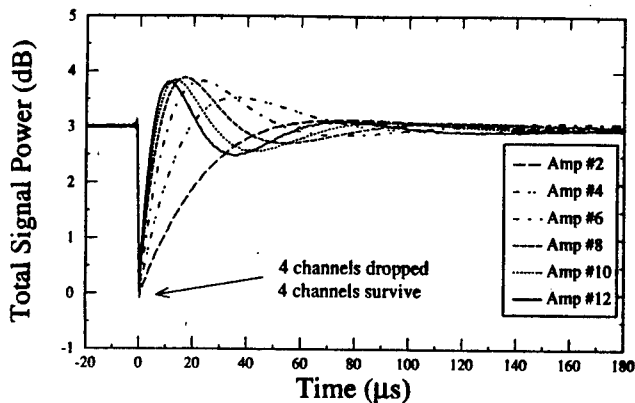


Fig.3. Output power transients after 2, 4, 6, 8, 10 and 12 EDFA's.<sup>3,4</sup>

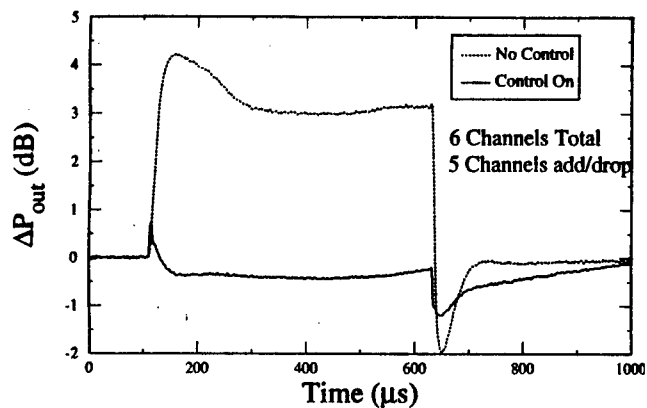


Fig.4. End of system power excursions for a surviving channel when 5 out of 6 channels are dropped/added.<sup>6</sup>

The authors are grateful to J. L. Zyskind for his foresight and leadership. They thank J. W. Sulhoff, C. Wolf R. Tkach and many other colleagues in Bell Labs., AT&T Labs, and MONET Consortium for their help and discussions. This project is supported by the MONET Consortium, partially funded by DARPA under agreement MDA972-95-3-0027.

<sup>1</sup>S. Artigaud *et al.*, Proc.OFC, PD27,1996 and M. Fukutoku *et al.*, Proc.OAA, FA4,1996.

<sup>2</sup>A. K. Srivastava *et al.*, Proc. OFC, PD18, 1997.

<sup>3</sup>J. L. Zyskind *et al.*, Proc. OFC, PD31, 1996.

<sup>4</sup>Y. Sun *et al.*, Electron. Lett. 33 (p. 313), 1997.

<sup>5</sup>A. K. Srivastava *et al.*, Proc. OAA, PDP4, 1996.

<sup>6</sup>J. L. Zyskind *et al.*, Proc. ECOC, Post Deadline Paper ThC.3.6, 1996.

<sup>7</sup>J. L. Jackel *et al.*, Proc. OFC, p. 84, 1997.

<sup>8</sup>G. Luo *et al.*, Proc. OFC, p. 130, 1997.

**FC2**

**2:30pm - 2:45pm**

## **Apodized Fiber Gratings for DWDM Using Variable Efficiency Phase Masks**

Harmeet Singh and William W. Morey

3M Bragg Grating Technologies

206 W. Newberry Road, Bloomfield, CT 06002

860-243-8822, hsingh@connix.com, wmorey@connix.com

### Introduction

Of the various applications of Fiber Bragg gratings, their use as spectral filter is perhaps the most common. Fiber gratings have come to replace other technologies such as thin film filters, arrayed waveguides, and other interference filters for many filtering applications. While the most important reasons why Bragg gratings are preferred over interference filters are cited as low insertion loss and polarization insensitivity, an often overlooked, but very important feature of Bragg gratings is the control over filter profile. Bragg gratings can easily be designed to have high or low reflectance, narrow or wide bandwidth, and none or any chirp. All these features make Bragg gratings a very attractive filter for DWDM applications such as channel multiplexing/demultiplexing or channel add/drop. While most requirements for DWDM applications such as low PDL, low insertion loss, low PMD are usually met by Bragg gratings, high channel isolation due to narrow bandwidth gratings is still a topic of investigation. The lower limit on the bandwidth is usually imposed by the existence of side lobes found in any grating filter. While it is well known that narrow bandwidth gratings can be achieved simply by apodizing the grating, a simple apodization yields a self induced chirp [Morey et. al.] leading to resonance on the blue side of the filter. Strasser et. al. reported that such effects can be eliminated by raising the average index of the grating such that it is constant along the grating. This phenomenon is illustrated in Figs. 1 and 2 using simulation tools. Figure 1 represents three apodization profiles with grating envelope denoted by dark shading, and average index by the white line through the shading. In Fig. 1a, the grating exposure is spatially constant, as is the average index. The resulting grating is shown in Fig. 2 with solid lines at the top, and is seen to have most side-lobes. Fig. 1b represents Gaussian apodization with a Gaussian envelope, and a Gaussian average index. The corresponding grating structure (dotted line in Fig. 2) has much reduced side-lobes, but has strong Fabry Perot resonance on the short wavelength side. These Fabry-Perot resonance occur because of self induced chirp caused by non-uniform index along the grating length. Finally, the raised Gaussian apodization denoted by Fig. 1c is seen to yield a grating (Fig. 2) with highly suppressed side-lobes, and at the same time devoid of short wavelength resonances. In all these examples the gratings were designed to have maximum isolation of 30dB.

### Apodization Techniques

There have been two reported methods of achieving the modulation of Fig. 1c. The first method demonstrated by Erickson et. al., used focussed ion beam implantation and wet etching technique to apodize the mask efficiency profile. An alternate apodizing scheme was demonstrated by Strasser et. al. where the desired apodization was achieved by scanning a UV beam across the phase mask, and dithering the phase mask as the scanning beam departs from the center of the beam. The amplitude of the dither is controlled such that the fringe contrast is somewhat Gaussian. Since the average intensity is constant throughout the scan, the average index remains constant giving the desired effect. In this paper we have used an alternate approach which relies on affecting only the groove depth of phase mask to control its diffraction efficiency. These variable groove depth phase masks developed and fabricated at Lasiris Inc., in St Laurent, Quebec, Canada are made by a process that combines holographic recording, selective etching and thin film technology. The mask fabricated by this process has a rectangular surface relief grating leading to optimized efficiency, and spatially varying relief depth. For the results presented in the following section, the efficiency was a Gaussian function of position.

## Experimental Results

Figure 3 shows the efficiency of the first and zeroth order beams. It is seen that the power in the zero order beam is minimum at the center of the mask, where the power in the first (and negative first) order beam is maximum. As the distance from the center increases, the power in the zero order beam increases, and the power in the first order beams decreases. The fringe contrast resulting from this mask is somewhat similar to that of Fig. 1c, and would be expected to form an ideally apodized grating. This hypothesis is proved from Fig. 4 where the experimental spectra from an unapodized and an apodized gratings are compared. Due to the exposure techniques, the grating marked unapodized is partially apodized, and the side lobes are better than expected. It is seen that the bandwidth of the apodized grating is much reduced compared to the bandwidth of the unapodized grating for the same maximum reflection of 99.9% (30dB). However, it is noticed that the floor of broadband reflection for both gratings is roughly -35dB. This is seen to be caused by the backreflection in the mechanical splices used to connect the grating to the measurement setup. This ideally apodized grating shown here is very useful for DWDM applications because it allows for a channel spacing of 0.8nm with 30-40dB channel isolation. Other profile designs provide the option of further compressing the bandwidth of the filter, opening the door for a narrower channel spacing and higher isolation.

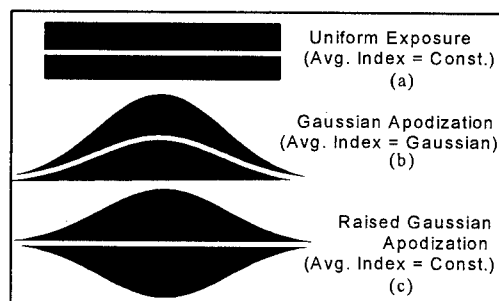


Fig. 1 Fringe envelopes for different apodizations

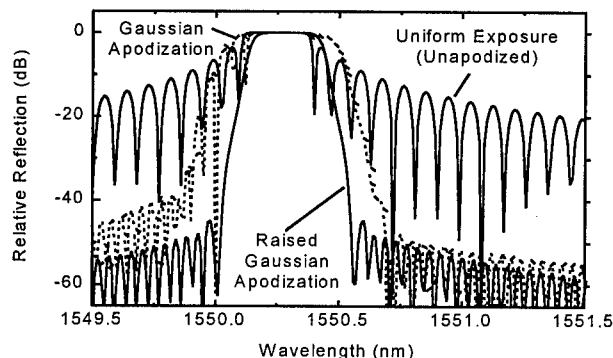


Fig. 2 Simulated grating profiles for apodizations of Fig. 1.

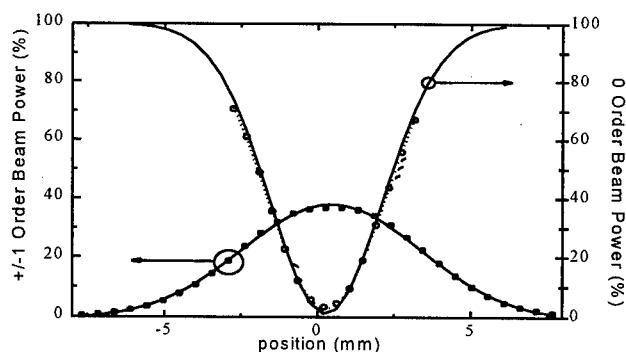


Fig. 3 Efficiency profiles of first (+/-) and 0 order beams.

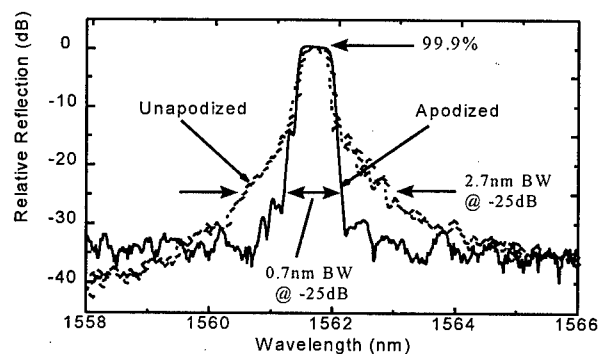


Fig. 4 Apodized and unapodized gratings.

## References

- Erickson, L.E. et. al., "Fabrication of a Variable Diffraction Efficiency Phase Mask by Multiple Dose Ion Implantation," J. Of Vac. Sci. Tech. B 13(6), pp.2940-2943, Nov/Dec 1995.
- Morey, W.W. et. al., "In Fiber Bragg Gratings," 17<sup>th</sup> Australian Conf. on Opt. Fiber Tech., pp 162-169, 1992
- Strasser, T.A. et. al., "UV-Induced Fiber Grating OADM Devices for Efficient Bandwidth Utilization," Post Deadline Paper, Part A, Paper PD8, OFC'96, San Jose, CA 1996.

**A Configurable Wavelength Demultiplexer Using Periodic Filter Chains**

Cedric F. Lam and Eli Yablonovitch  
UCLA, Electrical Engineering Department  
405 Hilgard Ave., Los Angeles, CA 90025-1594

**Summary**

The ability to select an arbitrary wavelength out of a large set of wavelengths is important for future dense wavelength division multiple access (DWDM) systems. Current approaches use a spectrometer to demultiplex the wavelengths and use a switch at each wavelength to select or deselect that particular wavelength at the output [1]. In a DWDM system with  $N$  wavelengths,  $N$  number of switches at each receiver need to be employed in order to select an arbitrary wavelength using the conventional approach. Since switches are active components, this is undesirable when  $N$  is large.

A better scaling can be achieved if we can arrange a series of configurable filters in a way that half of the spectral energy is filtered out when the input spectrum is passed through each successive stage of the filter. So the first stage filters out half of the spectrum. The second stage filters out another half of the spectrum that is left from the output of the first stage, etc. Figure 1(a) shows the spectrum of an eight-wavelength WDM signal. Figure 1(b) shows the filter function of each stage in a three-stage cascaded filter which is able to select any one wavelength in the signal spectrum shown in Figure 1(a). The solid lines represent the normal filter output transmission and the dotted lines represent the complimentary filter output. Optical filters are usually interferometric devices which generate periodic complementary outputs at the same time. An example is a Mach-Zehnder interferometer (MZI) [2]. A switch in series with each filter stage is used to select either one of the two complementary spectra as the input to the next stage (Figure 2). The period of the next filter is twice that of the previous filter. Any wavelength can be selected by properly setting the switches at each stage to select the appropriate normal transmission spectrum or complementary transmission spectrum. Scaling then becomes  $\log_2 N$  instead of  $N$  which is much more favorable. To select one wavelength out of 1000, only ten switches are needed.

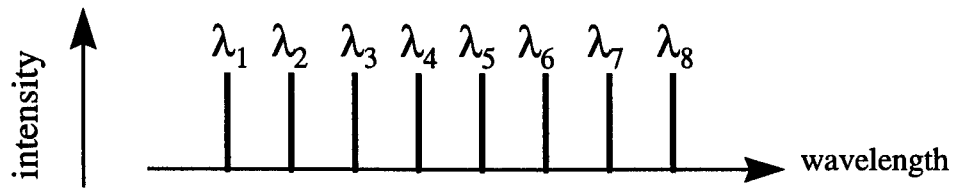
The filters used at different stages could be MZI's for which the periodicity is controlled by varying the optical path differences between the two arms of the MZI. To generate more square like transmission functions, a periodic cavity structure in the form similar to a one-dimensional photonic crystal [3] may be used. More detailed design considerations and analysis will be presented in the conference.

**References**

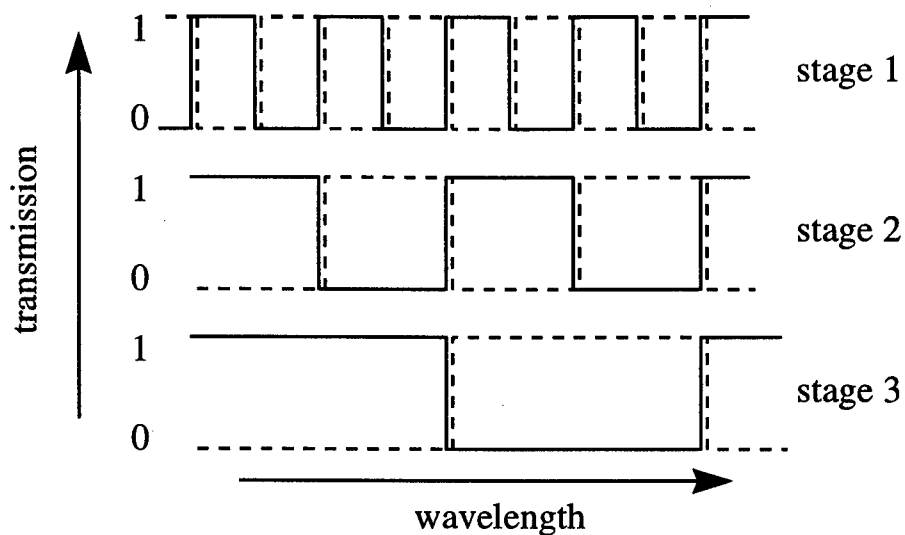
1. R.T. Hofmeister et. al, "Project LEARN - Light Exchangeable, Add/Drop Ring Network", OFC 97 post deadline paper, IEEE
2. P. E. Green, "Fiber Optics Networks", Prentice-Hall, 1993



3. E. Yablonovitch, J. Opt. Soc. Am. B, Vol. 10, No. 2, Feb. 1993



(a) Wavelength Multiplexed Signals



(b) Transmission Functions of Successive Stages

Figure 1. An example of a 3-stage WDM demultiplexer with the ability to isolate an arbitrary wavelength out of the eight multiplexed wavelengths.

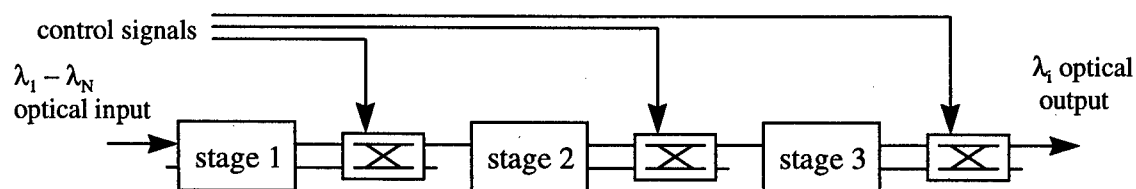


Figure 2. The schematic diagram of an eight-wavelength demultiplexer using three cascaded filter stages.

**FD1 (Invited)**  
**4:00pm - 4:30pm**

## **Arrayed-Waveguide Gratings for Dense-WDM Systems**

**Senichi Suzuki**

NTT Opto-Electronics Laboratories, 162 Shirakata, Tokai, Naka, Ibaraki 319-11 Japan  
Tel: +81 29 287 7405, Fax: +81 29 287 7881, e-mail: ssuzuki@iba.iecl.ntt.co.jp

Optical dense wavelength division multiplexing (WDM) systems have been investigated in order to enlarge transmission capacity [1] and improve network flexibility [2]. Arrayed-waveguide grating (AWG) multiplexers [3] are key components in such systems because they can process plural wavelengths simultaneously. This paper reviews recent work on AWGs based on silica-based planar lightwave circuits and their applications to dense-WDM systems.

An AWG consists of plural input/output waveguides, two focal slab waveguides and a waveguide array with an optical path difference of  $\Delta L$ , as shown in Fig. 1. The input signal light excites the arrayed waveguides as it radiates in the first slab waveguide. After propagating through the arrayed waveguides, the light is focused at the output waveguides which correspond to the wavelength as a result of interference in the second slab waveguide. A thin polyimide half wavelength plate is inserted at the mid point of the arrayed waveguides to eliminate polarization dependence. By designing the  $\Delta L$  value, AWGs with a desired channel spacing and channel number can be achieved. Table I shows the range of AWG fabricated in NTT laboratories.

One of the most important advantages of the AWG is the flexibility of its channel number. The channel number was increased to  $64 \times 64$  for a 100 GHz spacing and a low crosstalk of  $< -29$  dB and a low loss of 2.8 dB were obtained [4]. In terms of achieving larger scale AWGs with a narrow channel spacing, the phase error in arrayed waveguides, caused by fabrication errors, is a serious problem because of the resulting crosstalk degradation [5], [6]. Therefore, phase error limits the AWG channel number. Recently, a  $128 \times 128$  AWG with a 25 GHz-spacing was reported. In this AWG, a crosstalk of -16 dB was obtained by improving the fabrication process to reduce the phase error [7]. Further phase error control is needed to improve the performance.

For practical WDM systems, flat and wide-band characteristics are required in order to suppress the loss deviation due to the wavelength drift of the light sources and AWGs. To achieve such characteristics, a rectangular optical field had to be generated at a connection point between slab and input or output waveguides. Many kinds of method, including the Y-branch [8], sinc-functional field [9], multimode interference [10] and two focal point method [11] have been proposed. NTT laboratories have developed the flatband AWG using parabolic tapers [12]. The wavelength response is shown in Fig. 2. The 1-dB, 3-dB and 20-dB bandwidths were 98 GHz, 124 GHz and 196 GHz, respectively, for a 200 GHz channel spacing. The crosstalk to neighboring ports was  $< -27$  dB and the chip insertion loss was 6.1 dB.

AWGs integrated with other circuits are being actively proposed in order to achieve new functional devices. Optical add/drop multiplexers [13] and wavelength selective switches [14], [15] incorporating AWGs and space division switches have been reported. Figure 3 shows a  $2 \times 2$  wavelength selective switch for four wavelengths. One AWG and a four-array thermo-optic switch and loop-back paths were integrated on one Si chip. A desired wavelength  $\lambda_i$  can be switched between two lines by operating  $SW_i$ , that is the  $2 \times 2$  switch corresponding to  $\lambda_i$ . Also, novel AWG configurations were proposed to achieve a dual functions of wavelength routers and splitters [16], [17] and applied to an individual attenuation measurement for a passive branched optical network [18].

Several AWG applications to WDM systems have been investigated. These include optical add/drop multiplexers, wavelength routers and multi-channel light sources. An AWG with unequal spacing was used to suppress a four-wave mixing generation, and this enabled a 12 channel  $\times$  2.5 Gbit/s WDM transmission to be achieved over a 540-km dispersion shifted fiber [19]. A photonic ATM switch has been proposed using an AWG as the wavelength router. Recently a rack-mounted prototype was developed with a speed of 2.5 Gbit/s and  $16 \times 16$  switch size [20]. Multi-channel light sources using the AWG have also been investigated.

A 16 wavelength light source has been achieved using an AWG and a 200 nm boarded supercontinuum [21].

In summary, recent progress on the arrayed waveguide grating and its applications has been reviewed. The AWG has great potential for dense-WDM system applications because of its design flexibility and unique functions and it will enable novel functional WDM systems to be realized.

## References

- [1] Y. Yano, T. Ono, K. Fukuchi, T. Ito, H. Yamazaki, M. Yamaguchi and K. Emura, ECOC'96, ThB.3.1, 1996.
- [2] M. Koga, Y. Hamazumi, A. Watanabe, S. Okamoto, H. Obara, K. Sato, M. Okuno and S. Suzuki, IEEE J. Lightwave Technol., **14**, 6, p. 1106, 1996.
- [3] H. Takahashi, S. Suzuki and I. Nishi, IEEE J. Lightwave Technol., **12**, 6, p. 989, 1994.
- [4] K. Okamoto, ECOC'95, Mo.B.4.1, 1995.
- [5] S. Day, J. Stagg, D. Moule, S. Clements, C. Rogers, S. Ojha, T. Clapp, J. Brook and J. Morley, IPR'96, IMC5-1, 1996.
- [6] T. Goh, S. Suzuki and A. Sugita, To be submitted to IEEE J. Lightwave Technol.
- [7] K. Okamoto, K. Shuto, H. Takahashi and Y. Ohmori, Electron. Lett., **32**, 16, p. 1474, 1996.
- [8] C. Dragone: US patent No. 5412744, also T.L. Koch, Proc. 21st Eur. Conf. on Opt. Comm., 4, Mo.B.T.2, 1995.
- [9] K. Okamoto and H. Yamada, Optics Lett., **20**, 1, p. 43, 1995.
- [10] J.B.D. Soole, M.R. Amersfoort, H.P. LeBlanc, N.C. Andreadakis, A. Rajhel, C. Caneau, R. Bhat, M.A. Koza, C. Youtsey and I. Adesida, IEEE Photonic Technol. Lett., **8**, 10, p. 1340, 1996.
- [11] D. Trouchet, A. Beguen, C. Prel, C. Lermiaux, H. Boek and R.O. Maschmeyer, OFC'97, ThM7, 1997.
- [12] K. Okamoto and A. Sugita, Electron. Lett., **32**, 18, p. 1661, 1996.
- [13] K. Okamoto, K. Takiguchi and Y. Ohmori, Electron. Lett., **31**, 9, p. 723, 1995.
- [14] S. Suzuki, A. Himeno, Y. Tachikawa and Y. Yamada, Electron. Lett., **30**, 13, p. 1091, 1994.
- [15] S. Suzuki, A. Himeno and M. Ishii, To be submitted to IEEE J. Lightwave Technol.
- [16] Y. Inoue, A. Himeno, K. Moriwaki and M. Kawachi, Electron. Lett., **31**, 9, p. 726, 1995.
- [17] Yuan P. Li, L.G. Cohen, C.H. Henry, E.J. Laskowski and M.A. Cappuzzo, ECOC'96, TuC.3.4, 1996.
- [18] K. Tanaka, M. Tateda and Y. Inoue, IEEE Photonics Technol. Lett., **8**, 7, p. 915, 1996.
- [19] M. Fukui, M. Fukutoku, T. Sakamoto, K. Shimano, K. Okamoto, M. Yamada, K. Oda and H. Toba, ECOC'96, ThD.1.1, 1996.
- [20] K. Habara, Y. Yamada, A. Misawa, K. Sasayama, M. Tsukada, T. Matsunaga and K. Yukimatsu, ECOC'96, ThC.3.4, 1996.
- [21] T. Morioka, K. Uchiyama, S. Kawanishi, S. Suzuki and M. Saruwatari, Electron. Lett., **31**, 13, p. 1064, 1995.

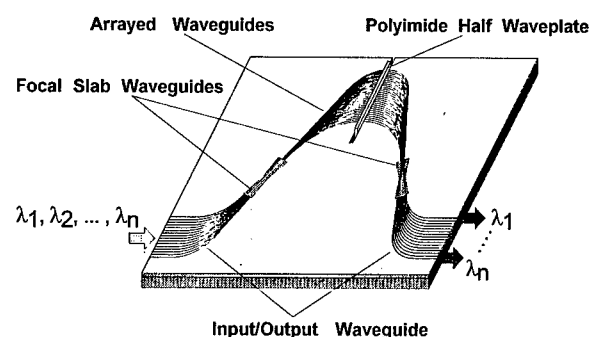


Fig. 1 Schematic configuration of arrayed-waveguide grating multiplexer.

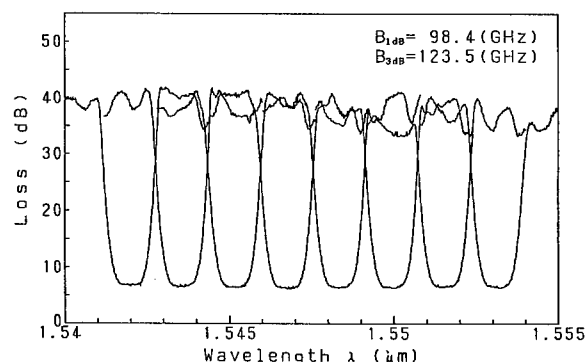


Fig. 2 Wavelength response of fabricated  $8 \times 8$  AWG with a flat and wide passband.

Table I Fabricated arrayed-waveguide gratings.

Parameters	Experimental results					
Channel spacing $\Delta\lambda$	15 nm	1.6 nm (200 GHz)	0.8 nm (100 GHz)		0.2 nm (25 GHz)	Unequal (0.8/0.48 nm)
Number of channels N	8	8	32	64	128	16
Path difference $\Delta L$	12.8 $\mu\text{m}$	84.0 $\mu\text{m}$	63.0 $\mu\text{m}$	30.9 $\mu\text{m}$	63.0 $\mu\text{m}$	79.21 $\mu\text{m}$
Focal length F	2.38 mm	11.35 mm	11.35 mm	18.50 mm	36.30 mm	14.42 mm
Diffraction order m	12	79	59	29	59	74
On-chip loss	2.4 dB	6.1 dB	2.1 dB	2.8 dB	3.5 dB	2.8 dB
3-dB passband FWHM (FWHM/ $\Delta\lambda$ )	6.3 nm (42 %)	124 GHz (62 %)	40 GHz (40 %)	44 GHz (44 %)	11 GHz (44 %)	30.2 GHz
Channel crosstalk	< -28 dB	< -27 dB	< -28 dB	< -29 dB	< -16 dB	< -25 dB

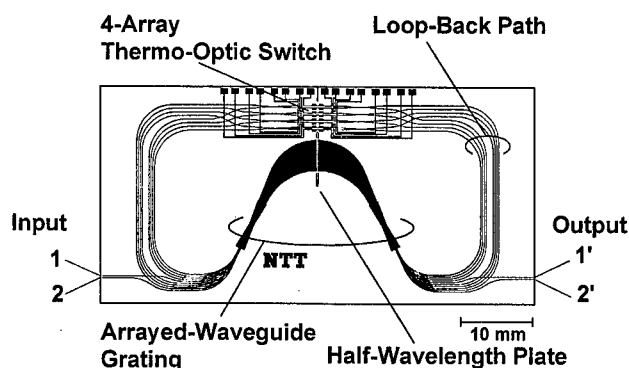


Fig. 3 Circuit layout of monolithically integrated  $2 \times 2$  wavelength selective switch.

## Using a retro-reflecting echelle grating to improve WDM demux efficiency

Lynden Erickson, Boris Lamontagne, J. J He, André Delâge, Mike Davies and Emil Koteles  
Institute for Microstructural Sciences, National Research Council  
Ottawa, Ontario, Canada, K1A 0R8

The use of uncoated facets on the echelle grating in a monolithic InP WDM demux leads to a reflection loss of 5.65 db for an index of refraction  $\approx 3.18$ . This loss can be largely eliminated by coating the out of plane facet with gold, but it involves another processing step. An alternative is to use total internal reflecting (retro-reflecting) facets<sup>1</sup>. We have fabricated a WDM demux in InP for use at 1550 nm using an echelle with retro-reflecting facets and have compared its performance to another demux on the same wafer using an echelle with flat facets.

The Rowland<sup>2</sup> configured demux shown in Fig. 1 consists of a single mode input guide (3um wide ridge) and eleven multi-mode output guides (13 um wide ridges), and a concave echelle. The echelle facets, both flat and retro-reflecting, are tilted so that they are always normal to the line joining the input guide to minimize the optical path difference across their full width, thereby maximizing their efficiencies. A section of the front face of the echelle with retro-reflecting facets is shown schematically in Fig. 2. Each facet is a 90 degree corner reflector.

The demux, less grating, was patterned using optical lithography and then processed to define the waveguide structures. The two echelles were then patterned in PMMA using focused ion beam lithography. The pixel size was 25 nm. Reactive ion etching (RIE) was used to etch a SiO<sub>2</sub> mask on the InP, and a chemically assisted ion beam etching (CAIBE) process was used to etch the InP. Nearly vertical walls were achieved.

The spectral response of the devices were measured by coupling light from a single frequency tunable diode laser into the input guide and measuring the light intensity as a function of wavelength for each output guide. The results for a typical channel are shown in Fig. 3. The upper curve is the spectral response of one channel for the demux with the retro-reflecting facets. The lower curve is for the demux with flat facets. The optical transmission of the demux is increased by 4 db with retro-reflecting facets slightly less than the 5.65 db expected if all of the light is reflected from the retro-reflectors compared to the 27% reflectivity of flat facets. This may be due to scattering from the rough reflecting surfaces (two surfaces for the retro-reflectors vs. one for the flat facets) and the corners of the retro-reflectors because of slight rounding.

We have shown that the use of a retro-reflecting echelle in a WDM demux improves its efficiency compared to an uncoated flat faceted echelle by 4 db.

---

<sup>1</sup>K. A. McGreer, J. N. Broughton, H. J. Hnatiuk, Z. J. Sun, and R. Cameron, Proc. SPIE 2918, 92 (1996).

<sup>2</sup>H. A. Rowland, Phil. Mag., 16, 197 (1883).

Fig. 1. The spectral response of the echelles were measured using this WDM demux structure. The straight waveguides are the single-mode input guides. The curved structures are multi-mode output guides. The center of the front face of echelle and the right-hand end of the waveguides are on a 9 mm dia. Rowland circle.

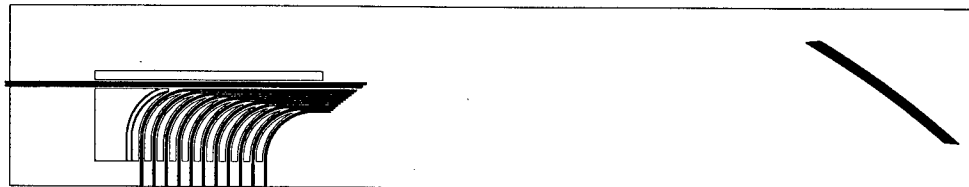


Fig. 2. A section of the front face of the echelle showing the retro-reflecting facets. The shaded area is etched well below the optical confinement layer in the InP wafer. The arrow shows the direction of the incident light.

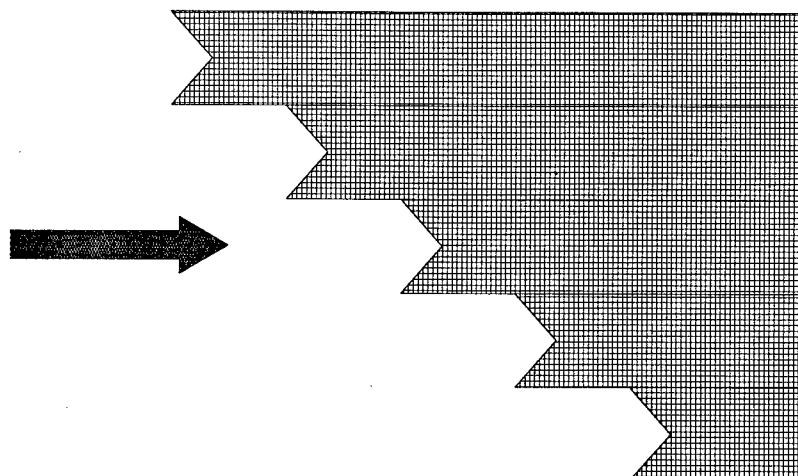
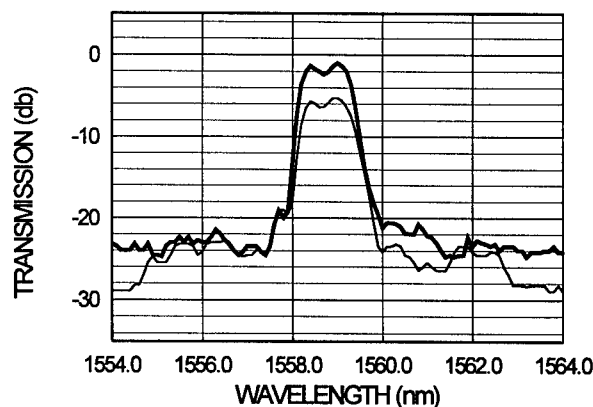


Fig. 3. The spectral response of a 24th order retro-reflecting echelle (top curve) and a 12th order flat-faceted echelle. The transmission of the retro-reflecting echelle is 4 db higher than that of the flat faceted echelle. The background and the crosstalk at a channel 2 nm away are the same for both devices. The transmission scale is offset by -9 db due to coupling losses.



## High-Performance Optical Polymers for Low-Cost High-Port-Count Planar Wavelength-Division-Multiplexing Devices

Louay Eldada, Lawrence W. Shacklette, Robert A. Norwood, and James T. Yardley  
AlliedSignal Inc., Electronic & Optical Materials Division, 101 Columbia Road, Morristown, NJ 07962  
Telephone: (201) 455-3069, Facsimile: (201) 455-3008, e-mail: eldada@research.allied.com

### I. INTRODUCTION

**W**AVELENGTH division multiplexing (WDM) offers an attractive means to increase the capacity of installed optical fiber to address the ever-increasing demand for more bandwidth. Although glass optical fibers provide a very convenient means for carrying optical information over long distances, they are very inconvenient for complex high-density circuitry. High-port-count WDM devices produced in glass optical fibers are difficult to fabricate, and as a result are quite expensive. Polymeric materials, on the other hand, offer the potential to create low-cost highly-complex optical interconnection circuitry on a planar substrate. In addition, they provide the possibility for a much higher degree of ruggedness and hermeticity. We have developed in detail one technology for polymeric optical interconnection which addresses the needs of the telecom industry. Our polymeric waveguiding structures are very low loss (0.06 dB/cm at 1550 nm), temperature resistant (they can endure more than 65 years at 100°C before a loss of 0.1 dB/cm is thermally induced), humidity resistant (no humidity effects on bare device after 600 hours at 85°C 85% RH), and exhibit low dispersion and low birefringence.

### II. MATERIALS

We have developed a wide variety of photochemically-set optically transparent polymers which are based on combinations of multifunctional acrylate monomers/oligomers and various additives. Upon photochemical exposure, these monomer systems form highly crosslinked networks which exhibit low intrinsic absorption in the wavelength range extending from 400 to 1600 nm. By blending and copolymerizing selected miscible monomers, the synthetic scheme allows for tailoring of the refractive index continuously from 1.30 to 1.60 with 0.0001 accuracy. This control of refractive index allows us to fabricate step-index optical waveguide structures with well-defined numerical apertures (NA's). At the same time, other physical properties of the materials such as flexibility and toughness as well as such important properties as surface energy and adhesion can be tailored to meet the needs of specific applications. Thin films of optical quality from 1 to 500  $\mu\text{m}$  have been prepared by spin casting or slot coating then photo-exposing at room temperature. Waveguide structures have been fabricated by either mask photolithography or direct laser writing.

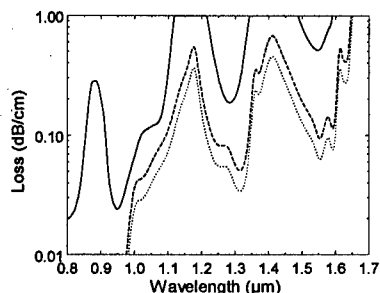


Fig. 1. Absorption losses for three AlliedSignal polymer systems. Acrylic with full CH content is solid line. Dashed line is for material with 30% CH content; dotted line is for material with 20% CH content.

The results of a waveguide spectrometry study<sup>1</sup> performed in our standard acrylates are shown in Fig. 1. Notable features are the region of transparency in the visible range and toward the telecom/computing wavelength of 840 nm, the C-H vibrational

overtone in the infrared (IR), and the IR windows of transparency near 1.3 and 1.55  $\mu\text{m}$ , the wavelengths of interest for telecom. Substitution of fluorine for hydrogen in a C-H bond has the effect of greatly increasing the reduced mass, thereby lowering the energy of the fundamental bond vibration and its overtones and virtually eliminating absorption from 1 to 2  $\mu\text{m}$ . The solid line in this figure represents the loss of our standard acrylates; these materials exhibit loss values of 0.02, 0.15, and 0.45 dB/cm at 840, 1300, and 1550 nm, respectively. The dashed and dotted lines show the results of partial fluorination (70% and 80%, respectively). This partial fluorination makes the losses as low as 0.001, 0.03, and 0.06 dB/cm at 840, 1300, and 1550 nm, respectively. In waveguide spectrometry studies, absorption was measured on slab waveguides where fabrication imperfections are easily avoidable. However, we also performed loss measurements on channel waveguides using the cleave-back method and found that, remarkably, the loss in these guides was absorption-limited.

Our polymers were subjected to humidity cycling tests. The test guides were pigtailed but not packaged or protected in any way. A thin cladding was printed around the core layer to give a short path for the diffusion of water. The sample was cycled between rigorously dry and humid (85°C 85% RH) conditions for 600 hours. Transmission measurements were performed at 1550 nm. The results are shown in Fig. 2 and they reveal that no increase in loss was observable. The fact that humidity has very little effect on our polymers was expected. When fully cured, these materials have a very high level of crosslinking, resulting in a tightly bound network with a low level of voids, leaving little space for water to be absorbed. The present observations also give no evidence of mechanical failure of devices due to water incursion, such as delamination or loss of integrity at the interface with the glass fibers.

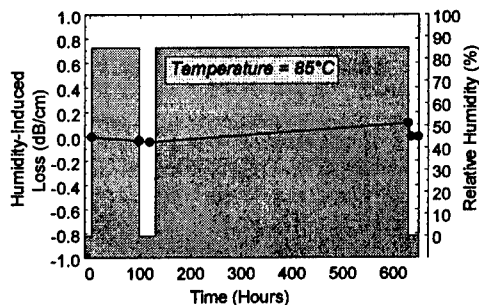


Fig. 2. Results of humidity cycling experiment showing no humidity-induced loss after 600 hours

A key characteristic for practical applications is thermal stability of optical properties since organic materials may be subject to yellowing upon thermal aging. Because of their highly crosslinked nature, these polymers are quite stable thermally. Thermal stability of the waveguide materials was studied by a variety of techniques including TGA (Thermal Gravimetric Analysis), spectrophotometry, and in-situ optical loss measurement. The thermal decomposition temperature, defined as the 5% weight loss temperature at a heating rate of 10°C/min., is 415°C, making our polymers the only acrylates reported to have a decomposition temperature above 400°C. However, much more important is the retention of high optical transmission upon thermal aging. In order to investigate this phenomenon, we carried out loss measurements on

5-cm-long fiber-pigtailed straight waveguides. These data show conclusively that the thermal stability of these polymer waveguides is excellent, with practical stabilities (time for thermally inducing 0.1 dB/cm loss) at 840 nm of about 65 years at 100°C, 10 years at 120°C, one year at 150°C, two weeks at 200°C, and one day at 250°C. The experiments suggest that thermal stability at longer wavelengths will be even greater. It has also been observed that these polymeric devices are mechanically robust; no mechanical failure such as cracking or delamination occurs after extended treatment at 250°C.

Since most WDM systems rely on controllable optical phase delays or gratings, the refractive indices of the waveguide materials and their sensitivity to temperature and wavelength changes are of considerable importance. Below their glass transition temperature, glassy polymers generally have a  $dn/dT$  of  $10^{-4}/^{\circ}\text{C}$ , which may be unacceptably large for some applications. For our highly cross-linked acrylate systems,  $dn/dT$  is as low as  $5 \times 10^{-6}/^{\circ}\text{C}$ . As for  $d\Delta n/dT$  for a core/cladding polymer pair, it is essentially zero. The lower  $dn/dT$  and  $d\Delta n/dT$  can be made, the fewer measures are necessary to control temperature, thus reducing the overall cost of a system.

Many WDM schemes rely on having no wavelength-dependent optical effects other than those geometrically designed into the system. Therefore, material dispersion is generally to be avoided. We have measured  $dn/d\lambda$  in our polymers at several wavelength ranges of interest. The values obtained at 1300 and 1550 nm are  $-4 \times 10^{-6}$  and  $-2 \times 10^{-6} \text{ nm}^{-1}$ , respectively. These values are comparable to those for  $\text{SiO}_2$  and are much lower than those for semiconductors and doped glasses.

A key material property impacting polarization transparency is the birefringence and its dispersion. We have measured the TE and TM indices for our standard polymers. The birefringence was measured to be  $\Delta n = n_{\text{TE}} - n_{\text{TM}} = -0.0008$  at 543.5 nm. This value decreases for longer wavelengths and varies with processing conditions.

### III. WDM DEVICE FABRICATION

Polymeric optical waveguide devices may be fabricated in many ways. For the materials described above, a photolithographic fabrication scheme is most appropriate. Within our approach, photosensitive polymerization initiators are added to the monomer mixtures to provide a means for photochemically initiating the polymerization. Device fabrication is achieved by either conventional mask photolithography or by laser direct-writing. These lithographic processes offer very high contrast responses allowing us to define polymeric features with dimensions ranging from a few microns to a few millimeters with a high degree of accuracy and process latitude.

Another useful aspect of these materials is that, owing to the nature of the lithographic process, selective undercutting can be performed to make structures that can grip optical fibers, resulting in a simple and inexpensive fiber pigtailed process.<sup>2</sup> Fibers can be "snapped in" to these grippers after development, when the crosslinked polymer is highly elastomeric.

By selecting an appropriate pair of acrylate mixtures as core and cladding materials, the NA of a waveguide as well as its mode profile can be very accurately controlled. For example, single-mode waveguides that match single-mode glass fibers have been produced.<sup>3</sup>

Beside having the intrinsic material properties required in a WDM device, AlliedSignal optical polymers lend themselves easily to the fabrication of WDM components. WDM devices typically utilize either gratings or phased arrays to separate wavelength channels. Our materials have the contrast needed to produce both types of elements. Gratings can easily be fabricated in our polymers using one of many techniques including replication, embossing, phase-mask lithography, two laser beam interference, and e-beam writing. Figs. 3 and 4 depict gratings fabricated in AlliedSignal single-mode polymeric waveguides by replication.

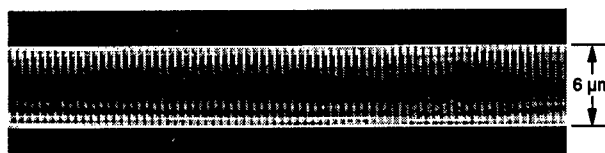


Fig. 3. Laser scanning micrograph of a grating replicated in a single-mode waveguide



Fig. 4. Scanning electron micrograph of a grating replicated in polymer

The other elements commonly used to demultiplex channels are phased-array waveguides in waveguide grating routers.<sup>4</sup> A typical design is shown in Fig. 5. These structures require patterning varying-density single-mode waveguides. The 6-μm guides are close together around the free-space region (about 3 μm apart) and are furthest apart at the ends where they mate with glass fibers (250 μm pitch).

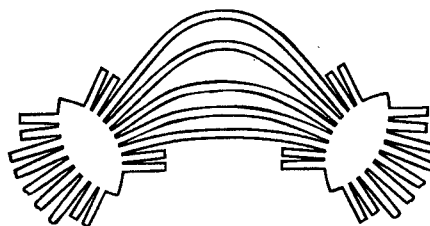


Fig. 5. Schematic diagram of a waveguide grating router

In order to pattern such an optical circuit photolithographically, the material has to have high contrast, in that polymerization in dark areas must be highly inhibited while it is locally allowed in light areas. Our polymers exhibit the high level of contrast needed. Fig. 6 shows segments of a waveguide grating router that was exposed through a photomask, and it reveals good contrast and resolution in areas of widely different waveguide densities.

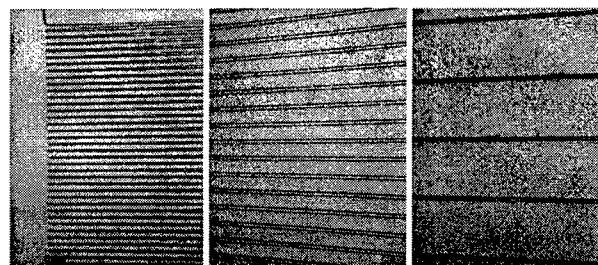


Fig. 6 Segments of waveguide grating router produced in polymers revealing good contrast at different waveguide densities

### IV. CONCLUSION

We have extensively verified the technical and commercial viability of an advanced polymer technology and have demonstrated the practical efficacy of our polymers for WDM components. As the WDM market matures and the demand for high-port-count components increases, we are confident that low-cost high-performance polymeric materials will play a key role in this market.

### V. REFERENCES

1. K.W. Beeson et al., *Nonlin. Opt.* **3**, 205 (1992).
2. L. Eldada et al., *Proc. SPIE* **3006**, 344 (1997).
3. L. Eldada et al., *J. Lightwave Technol.* **14**, 1704 (1996).
4. C. Dragone, *Photon. Technol. Lett.* **3**, 812 (1991).

**FD4 (Invited)**  
**5:00pm - 5:30pm**

**PHASAR-based PICs for WDM-applications**

**M.K. Smit**

**Delft University of Technology**  
**Department of Electrical Engineering, P.O. Box 5031, 2600 GA Delft,**  
**The Netherlands**  
**Tel: + 31-15-2782279, Fax: +31-15-2784046, E-mail: [smit@et.tudelft.nl](mailto:smit@et.tudelft.nl)**

**ABSTRACT**

*Wavelength multiplexers, demultiplexers and routers based on optical phased arrays play a key role in multi-wavelength telecommunication links and networks. Photonic integration of PHASARS with active components will provide the functionality required in tomorrows multi-wavelength networks.*

**SUMMARY**

Commercial interest in multi-wavelength components and systems is rapidly increasing. WDM provides a new dimension for solving capacity and flexibility problems in the telecommunication network. It offers a huge transmission capacity and allows for novel network architectures which offer much more flexibility than the current networks [1,2]. Multi-wavelength links and networks require optical components with an increased functionality, such as multi wavelength (MW) receivers, MW-sources, add-drop multiplexers and optical cross connects.

A key component in MW-devices and circuits is the wavelength (de)multiplexer. Phased array (PHASAR) demultiplexers have proven to be robust components [3] which are particularly suitable for integration with other components. Integration with detectors in MW-receivers [4,5], with optical amplifiers in MW-lasers [6,7] and with optical switches in MW-add-drop multiplexers [8,9] has been reported.

Photonic integration offers the potential to provide the functionality required in future MW-networks in a compact way. Performance and fabrication issues of integrated PHASAR-based devices will be discussed.



## References.

- [1] C.A. Brackett, "Dense wavelength division multiplexing networks: principles and applications", *IEEE J. Select. Areas Comm.*, Vol. 8, pp. 948-964, 1990.
- [2] C.A. Brackett, A.S. Acampora, J. Sweitzer, G. Tangonan, M.T. Smith, W. Lennon, K.C. Wang, R.H. Hobbs, "A scalable multiwavelength multihop optical network: A proposal for research on all-optical networks", *J. Lightw. Technol.*, 11 (5/6), pp. 736-753, May/June 1993.
- [3] M.K. Smit, PHASAR-based WDM devices: principles, design and applications, invited paper, *J. of Sel. Topics in Quantum. Electron.*, Vol. 2, No. 2, pp. 236-250, June 1996.
- [4] M. Zirngibl, C.H. Joyner and L.W. Stulz, "WDM receiver by monolithic integration of an optical preamplifier, waveguide grating router and photodiode array", *El. Lett.*, 31 (7), pp. 581-582, March 1995.
- [5] C.A.M. Steenbergen, C. van Dam, A. Looijen, C.G.P. Herben, M. de Kok, M.K. Smit, J.W. Pedersen, I. Moerman, R.G. Baets and B.H. Verbeek, "Compact low-loss 8x10 GHz Polarisation independent WDM Receiver", *Proc. 22nd Eur. Conf. on Opt. Comm. ECOC '96*, Oslo, Sept. 15-19, 1996, Vol.1, pp. 129-132.
- [6] M. Zirngibl, C.H. Joyner, C.R. Doerr, L.W. Stulz, H.M. Presby, "A 18 channel multi frequency laser", *Integrated Photonics Research 1996*, Boston, USA, April 29 - May 2, pp. 128-131, 1996.
- [7] A.A.M. Staring, L.H. Spiekman, J.J.M. Binsma, E.J. Jansen, T. van Dongen, P.J.A. Thijs, M.K. Smit, and B.H. Verbeek, "A compact 9 channel multiwavelength laser", *IEEE Photon. Technol. Lett.*, Vol. 8, nr. 9, pp. 1139-1141, Sept. 1996.
- [8] K. Okamoto, K. Takiguchi and Y. Ohmori, "16-channel add/drop multiplexer using silica-based arrayed-waveguide gratings", *El. Lett.*, 31 (9), pp. 723-724, April 1995.
- [9] C.G.M. Vreeburg, T. Uitterdijk, Y.S. Oei, M.K. Smit, F.H. Groen, E.G. Metaal, P. Demeester and H.J. Frankena, "First InP-based reconfigurable integrated add-drop multiplexer", *Photonic Technol. Lett.*, Vol. 9, No. 2, pp. 188-190, Feb. 1997

# AUTHOR INDEX

<b>A</b>		<b>E</b>			
Alferness, R.	WA1	Eldada, L.	FD3	Lemoff, B.	WC3
Ali, M.	FB2	Erickson, L.	FD2	Liu, K.	WC1
Aronson, L.B.	WC3			Liu, J.-Y.	ThA3
				Logan, R.A.	ThC3
<b>B</b>		<b>F</b>		<b>M</b>	
Baets, R.	ThA2	Fan, J.Y.	ThC3	Mahgerefteh, D.	ThB3
Behringer, R.E.	ThB2	Feder, K.	ThB2	Marz, R.	FB3
Bhat, R.	ThB1	Forouhar, S.	FA5	McGreer, K.A.	ThD2
Blumenthal, D.J.	FA3	Fujita, J.	ThD3	Mears, R.J.	ThC2
Broughton, J.N.	ThD2			Merritt, S.A.	FA4
Buckman, L.A.	WC3			Miller, B.I.	ThB2
Burdge, G.L.	ThB3	<b>G</b>		Moerman, I.	ThA2
Burgmeier, J.	FB3	Gariepy, D.	WD2	Morey, W.W.	FC2
Burrus, C.A.	ThC3	Goeman, S.	ThA2	Murphy, E.	ThA1
		Goldhar, J.	ThB3		
		Golshani, A.	FA2		
		Gornik, E.	FA2		
		Groen, F.	ThA2		
<b>C</b>				<b>N</b>	
Caneau, C.	ThB1			Norwood, R.A.	FD3
Chai, Y.	ThC3	<b>H</b>			
Chandrasekhar, S.	WB3	Haugsjaa, P.	ThA5		
Chen, Y.J.	FA4	He, J.J.	FD2	<b>O</b>	
Chen, Y.-M.	ThA5	Herrmann, H.	ThC1	Oren, M.	ThA5
Chen, J.H.	ThC3	Hu, M.H.	ThD3	Osgood Jr., R.M.	ThD3
Chen, Y.	ThD1	Huang, J.Z.	ThD3		
Cheyne, M.R.	ThB2			<b>P</b>	
Chien, M.	ThB2			Poole, S.	FC4
Cho, P.	ThB3	<b>J</b>		Poulin, M.	WD3
Choa, F.S.	ThC3	Jackel, J.L.	FB2		
Clesca, B.	FB1			<b>R</b>	
Cohen, A.D.	ThC2			Rajhel, A.	ThB1
Copeland, D.J.	FA4	<b>K</b>		Raybon, G.	ThB2
Cords, A.	FB3	Kellermann, P.O.	FA2	Richards, D.H.	FB2
Cyr, N.	WD2, WD3	Kim, H.B.	WD2	Ringo, J.	ThB1
		Kock, A.	FA2	Ruchet, B.	ThA4
<b>D</b>		Koren, U.	WD1, ThB2	Rusch, L.A.	ThA4
Dagenais, M.	FA4	Korte, L.	FA2		
Davies, M.	FD2	Koteles, E.	ThC4, FD2		
Davis, L.	FA5	Koza, M.A.	ThB1		
Delage, A.	FD2	Kudo, K.	WD4		
Demeester, P.	WA2			<b>S</b>	
Didde, S.	FA4	<b>L</b>		Sasaki, T.	WD4
Dolfi, D.W.	WC3	Lam, C.	FC3	Scarmozzino, R.	ThD3
Domash, L.H.	ThA5	Laming, R.	FC1	Schafer, K.	ThC1
Dreyer, K.	ThB2	Lamontagne, B.	FD2	Schaffer, C.	FB3
Dreze, C.	WB2	Latrasse, C.	WD3, ThA4	Shacklette, W.	FD3
				Shell, M.	FA3

# AUTHOR INDEX

Singh, H.	FC2	<b>Y</b>	
Smit, M.K.	FD4	Yablonovitch, E.	FC3
Sohler, W.	ThC1	Yamaguchi, M.	WD4
Springthorpe, A.	FA4	Yamazaki, H.	WD4
Srivastava, A.K.	FB4	Yardley, J.T.	FD3
Stone, D.	FA4	Yip, G.L.	ThD4
Stummer, B.	FB3	Yoo, S.J.B.	ThB1
Sun, Z.J.	ThD2	Yoshida, J.	WC2
Sun, Y.	FB4	Young, M.G.	FA5
Suzuki, S.	FD1	Yu, H.-Y.	ThB3
Suzuzki, Y.	WC2		

<b>T</b>		<b>Z</b>	
Tabatabaei, S.A.	FA4	Zah, C.E.	FA1
Takahashi, H.	WC2	Zhu, Y.	ThA2
Tanbun-Ek, T.	ThC3		
Tennant, D.M.	ThB2		
Tetu, M.	WD3, ThA4		
Tsang, W.T.	ThC3		

<b>V</b>	
Van Parys, W.	WA2
Van Caenegem, B.	WA2
Van Thourhout, D.	ThA2
Vandendriessche, L.	WA2
Vandeputte, K.	ThA2
Villeneuve, B.	WD2

<b>W</b>	
Wei, C.	ThA2
Wiesenfeld, J.M.	ThB4
Willner, A.	WB1
Wu, K.-Y.	ThA3

<b>X</b>	
Xiang, F.	ThD4

**1997 DIGEST  
of the IEEE/LEOS  
Summer Topical Meetings  
13-15 August 1997**

**Advanced Semiconductor Lasers  
and Applications**

TECHNICALLY CO-SPONSORED BY THE OPTICAL SOCIETY OF AMERICA

at  
***THE QUEEN ELIZABETH HOTEL  
MONTREAL, QUEBEC, CANADA***

**IEEE Catalog Number: 97TH8276  
Library of Congress: 97-70754**

The papers in this book make up the digest of the meeting mentioned on the cover and title page. They reflect the authors' opinions and are published as presented and without change in the interest of timely dissemination. Their inclusion in this publication does not necessarily constitute endorsement by the editors, the Institute of Electrical and Electronics Engineers, Inc.

Copyright and reprint permissions: Abstracting is permitted with credit to the source. Libraries are permitted to photocopy beyond the limits of U.S. copyright law for private use of patrons those articles in this volume that carry a code at the bottom of the first page, provided the per-copy fee indicated in the code is paid through the Copyright Clearance Center, 222 Rosewood Drive, Danvers MA 01923. Instructors are permitted to photocopy isolated articles for noncommercial classroom use without fee. For other copying, reprint or republication permission, write to IEEE Copyrights Manager, IEEE Service Center, 445 Hoes Lane, P.O. Box 1331, Piscataway NJ 08855-1331.

© 1997 by The Institute of Electrical and Electronics Engineers, Inc. All right reserved.

IEEE Catalog Number: 97TH8276

ISBN:	0-7803-3891-X	Softbound Edition
	0-7803-3892-8	Microfiche Edition

Library of Congress: 97-70754

Additional copies can be ordered from:

IEEE Service Center  
445 Hoes Lane  
P.O. Box 1331  
Piscataway, NJ 08855-1331  
Tel: (732) 981-1393  
Fax: (732) 981-9667



# **ADVANCED SEMICONDUCTOR LASERS AND APPLICATIONS**

## **Co-Chairs:**

David Welch, *SDL Inc., San Jose, CA*  
Peter Moulton, *Schwartz Electro-Optics Inc., Concord, MA*  
Kam Lau, *University of California, Berkeley, CA*  
Leo Holberg, *NIST, Boulder, CO*

## **Program Committee:**

Dan Botez, *University of Wisconsin, Madison, WI*  
Ross Bringans, *Xerox PARC, Palo Alto, CA*  
Hong Choi, *MIT Lincoln Laboratories, Cambridge, MA*  
James Coleman, *University of Illinois, Urbana, IL*  
Renny Fields, *Aerospace Corporation, El Segundo, CA*  
Randy Geels, *SDL Inc., San Jose, CA*  
Lew Goldberg, *Naval Research Laboratory, Washington, DC*  
Motoichi Ohtsu, *Tokyo Institute of Technology, Yokohama, Japan*  
Tirumala Ranganath, *Hewlett Packard, Palo Alto, CA*  
Michel Tetu, *Universite Laval, Quebec, Canada*  
Won-Tien Tsang, *Bell Laboratories Lucent Technologies, Murray Hill, NJ*  
Kerry Vahala, *CALTECH, Pasadena, CA*



# TABLE OF CONTENTS

## Wednesday, 13 August 1997

### **Session WA: Commercial Applications**

WA1	Current Status of ZnMgSSe-based Lds .....	3
WA2	Portable Semiconductor Laser System To Stop Internal Bleeding .....	5
WA3	Direct Diode Laser Marking and Micromaching. .... (paper not available)	

### **Session WB: Novel Devices I**

WB1	Beam Steering Laser Arrays & Applications in 2D Laser Scanning .....	7
WB2	Long Wavelength Triangular Shaped Waveguide Diode Ring Laser With Dry Etched Facets .....	9
WB3	Progress in AlGaInN Opto-electronic Devices. .... (paper not available)	
WB4	Improved Performance of Single-Mode Lasers by Using Native-Oxide Lateral-Confinement Layers .....	11

## Thursday, 14 August 1997

### **Session ThA: Microwave-Optical Systems**

ThA1	All-Optical Buffers for High-Speed Slotted TDM Networks .....	15
ThA2	Microwave Generation With Monolithic Dual-Wavelength DFB Lasers .....	17
ThA3	Application of a Novel Two-Longitudinal-Mode LD as a Source for CW Thz Wave Generation by Photomixing .....	19
ThA4	Optoelectronic Microwave Oscillators Using Diode Lasers .....	21

### **Session ThB: Novel Devices II**

ThB1	Super Wide Span Optical Frequency Comb Generation by Nonlinear Self-Phase-Modulation in an Optical Fiber .....	23
ThB2	Single-mode Operation and Switching of a Fabry-Perot Semiconductor Laser with Self-Seeding from an External Fiber Grating by Modulated Optical Injection ....	25
ThB3	Application of Semiconductor Lasers to Agile Optical Phased Arrays .....	27
ThB4	Compound Cavity Semiconductor Lasers (CCSL) .....	29
ThB5	A Diode Laser With An External High-Q Microcavity .....	31

### **Session ThC: Mid-IR Sources**

ThC1	Type-II Quantum Well and Interband Cascade Lasers for the Mid-IR .....	33
ThC2	Tunable Sources and Quantum Cascade Lasers in the Mid-IR .....	35
ThC3	Measurement of $^{13}\text{CH}_4/^{12}\text{CH}_4$ Ratios in Air Using Diode-Pumped $3.3\mu\text{m}$ Difference-Frequency Generation in PPLN .....	37
ThC4	Monitoring Trace Gases with Antimonide Diode Lasers .....	39



# TABLE OF CONTENTS

## **Session ThD: Spectroscopic Applications**

ThD1	Spectrochemical Applications of Semiconductor Lasers .....	41
ThD2	Compact, All Diode-Laser, Optical Frequency Reference Based on Laser-Trapped Atomic Calcium .....	42
ThD3	Coherent Transient Measurements With A Semiconductor Diode Lasers .....	44
ThD4	Monitoring of Molecular Species Using Near-Infrared Extended Cavity Diode Lasers. .	46
ThD5	The Applications of Diode Lasers to Frequency Standards and Optical Frequency Standards at CMS .....	48

## **Friday, 15 August 1997**

## **Session FA: Device Theory**

FA1	The Origins of Quantum Noise in Photonics .....	51
FA2	Classical Corpuscular Optical Theory of Squeezed States of Light .....	53
FA3	Fine-Scale Analysis of Gain-Coupled MQW DFB Lasers .....	55
FA4	A Quantum-Well Laser Model for SPICE-Like Simulators .....	57
FA5	Beam Propagation Modelling of Tapered Waveguide Lasers .....	59

## **Session FB: Device Characteristics**

FB1	Wide Temperature Range Operation of DFB Lasers at 1.3 $\mu$ m Wavelength .....	61
FB2	Longitudinal Effects on SMSR in Gain-Coupled DFB Lasers .....	62
FB3	Low Short Term Timing Jitter in an Integrated Monolithic Extended Cavity Semiconductor Mode-Locked Laser .....	64
FB4	Measurement of Self-Phase Modulation in a Semiconductor Optical Amplifier Using A Mach-Zehnder Interferometer .....	66
FB5	Novel Mechanism for Ultrafast Optical Nonlinearity in Semiconductor Laser Amplifier Using Assist Light .....	68

## **Session FC: High-Brightness Sources**

FC1	New Advances in High Power, High Brightness Diode Lasers .... (paper not available)	
FC2	Applications of Lasers for Printing .....	70
FC3	Narrow-Linewidth, High-Brightness Laser Diode Arrays .....	72
FC4	High-Power, Diffraction-Limited InGaAsP Flared Unstable Resonators at 840 nm ...	74

## **Session FD: High Power Sources**

FD1	High-Performance Al-free Diode Lasers .....	76
FD2	Laser Diode Bar Lifetime Testing: The User's Perspective ..... (paper not available)	
FD3	Performance Tests of Quasi-CW Laser Diode Pump Arrays Conducted or Sponsored by NASA Goddard Space Flight Center .....	78

# **ADVANCED SEMICONDUCTOR LASERS AND APPLICATIONS**

**Wednesday, 13 August 1997**

## **Sessions:**

**WA:    Commercial Applications**

**WB:    Novel Devices I**

## **Wednesday Papers Not Available**

- WA3      “Direct Diode Laser Marking and Micromaching”, *J. McKillop, Laser Fare, Inc., Warwick, RI*
- WB3      “Progress in AlGaInN Opto-electronic Devices”, *Richard Miles, SDL, Inc., San Jose, CA*

## Current Status of ZnMgSSe-based LDs

*Hiroyuki Okuyama and Akira Ishibashi*

*Sony Corporation Research Center, Fujitsuka 174, Hodogaya, Yokohama 240, Japan*

In recent years, short-wavelength semiconductor lasers have been well investigated. This is because a light source suitable for 10GB-class mass-storage optical-disk system has been anticipated, especially for RAM usage. The first laser operation at a wavelength shorter than 600nm was achieved in 1991 by Haase *et al.* [1] using ZnSe-based II-VI compounds with improvement of p-type doping techniques. A breakthrough which accelerated research on II-VI blue-green semiconductor lasers was the ZnMgSSe cladding layer, firstly reported by our group [2]. The use of Mg allowed the ZnCdSe to be electrically and optically confined while maintaining lattice-matching to the GaAs substrate. We demonstrated continuous wave (CW) laser operation at room temperature (RT) using the ZnMgSSe cladding layer in 1993 [3]. Since then, improvements in growth techniques have lengthened device lifetime. After announcement of one-hundred-hour CW operation at RT in 1996 [4], II-VI blue-green semiconductor lasers have been brought closer to commercialization, which requires further improvement of lifetime under severer conditions such as high power operation and high temperatures. In this paper, we report recent progress in ZnSe-based II-VI compound semiconductor lasers, particularly lasers using ZnMgSSe cladding layers.

### 1. Lasing Characteristic of II-VI Green Laser Diode

The epitaxial layers of the separate confinement heterostructure (SCH) of ZnMgSSe-based LDs are grown on n-type GaAs (001) substrate using molecular beam epitaxy (MBE) at a growth temperature of 280°C. The structure consists of a ZnTe:N / ZnSe:N, ZnTe:N superlattice layer / ZnSe:N / ZnSSe:N / ZnMgSSe:N cladding layer / ZnSSe:N guiding layer / ZnCdSe active layer / ZnSSe:Cl guiding layer / ZnMgSSe:Cl cladding layer / ZnSSe:Cl / ZnSe:Cl / GaAs:Si buffer layer / GaAs:Si substrate [4]. After a growth by MBE, the p-ZnSe top contact layer is chemically etched, leaving a 10μm-wide mesa stripe. An insulating layer is deposited to reduce leakage current, followed by the forming of a Au / Pt / Pd electrode. The wafers are cleaved into 600-μm-wide bars whose facets are coated 75% in the front and 90% in the rear to reduce the threshold current density. Typical threshold current  $I_{th}$  under CW conditions is 30mA, (threshold current density  $J_{th} = 500A/cm^2$ ) and the lasing wavelength is 515nm. Our LDs were tested under automatic power control setting at the light output power of 1mW. The longest lifetime of the II-VI laser diode is 101.5h, which is the longest ever reported for blue-green lasers.

For high power operation, it is necessary to reduce loss from the rear facet. The cleaved facets of the wafers described above were asymmetrically coated; the rear facet was prepared with high-reflectivity (HR) coating using dielectric stacks, while single-layer antireflection (AR) coating was employed at the front facet to reduce the reflectivity to 1%. The laser chip was mounted on the header with the epi-side down. The maximum output power at RT reached 87mW with no remarkable kink [5]. The slope efficiency below 60mW was about 1.9W/A, corresponding to an external differential

quantum efficiency of 80%. The laser generates 30mW light output even at 60°C with a slight increase of the slope efficiency. The characteristic temperatures of the operating current at 30mW are 236K (20-40°C) and 111K (50-60°C)

## 2. Degradation of II-VI Laser Diode

Degradation of the II-VI LD is related to pre-existing defects such as stacking faults [6]. From electroluminescence (EL) images of the active region through the transparent electrode, dark spots are observed as seeds of dark line defects propagating along the  $\langle 100 \rangle$  direction. From the transmission electron microscopy, these pre-existing defects are identified as stacking faults originating from the vicinity of the GaAs / ZnSe interface, and bounded by Frank partial dislocations with Burgers vector  $\mathbf{b} = a/3 \langle 111 \rangle$ . It is also found that the dark spots spread out, forming a triangular dark region composed of dislocation dipoles and loops. The dipoles are closely aligned to the  $\langle 110 \rangle$  lying in the  $\{111\}$  plane, with Burgers vector of the type  $a/2 \langle 011 \rangle$  inclined at  $45^\circ$  to the (001) junction plane. The mechanism of forming the degraded region is thought to be as follows: non-radiative recombination between electrons and holes, occurring at dangling bonds along the dislocation cores, creates thermal stress which dissociate Frank partial dislocation into  $60^\circ$  - type perfect dislocation dipoles. These dipoles form dislocation networks, expanding by glide and climb process. Such a degradation process is the so-called recombination enhanced defect reaction (REDR). S. L. Chuang *et al.* showed that his REDR model explained the time dependence of the EL aging from the early exponential decay to the  $1/t$  behavior [7]. And their theory can be applicable to both rapid degradation due to stacking faults and gradual degradation due to point defects, as long as the defect reactions are caused by the carrier-recombination-enhanced defect motion. To improve the device life time, we must reduce both the stacking fault density and the point defect density.

- [1] M. A. Haase, J. Qiu, J. M. DePuydt, and H. Cheng, Appl. Phys. Lett., **59**, 1272 (1991).
- [2] H. Okuyama, K. Nakano, T. Miyajima, and K. Akimoto, Jpn. J. Appl. Phys., **30**, L1620 (1991).
- [3] N. Nakayama, S. Itoh, T. Ohata, K. Nakano, H. Okuyama, M. Ozawa, A. Ishibashi, M. Ikeda, and Y. Mori, Electron. Lett., **29**, 1488 (1993).
- [4] S. Taniguchi, T. Hino, S. Itoh, N. Nakayama, A. Ishibashi, and M. Ikeda, Electron. Lett., **32**, 552 (1996).
- [5] N. Nakayama, S. Taniguchi, T. Hino, K. Nakano, and A. Ishibashi, 15th IEEE Int. Semiconductor Laser Conf., Haifa, Israel (1996).
- [6] S. Tomiya, E. Morita, M. Ukita, H. Okuyama, S. Itoh, K. Nakano, and A. Ishibashi, Appl. Phys. Lett., **66**, 1208 (1995).
- [7] S. L. Chuang, M. Ukita, S. Kijima, S. Taniguchi, and A. Ishibashi, Appl. Phys. Lett., **69**, 1588 (1996).

**WA2 (Invited)**  
**2:00pm - 2:30pm**

## **PORTABLE SEMICONDUCTOR LASER SYSTEM TO STOP INTERNAL BLEEDING**

**Frederic M. Durville, Robert R. Rediker, Georges Cho**  
Cynosure, Inc., 35 Wiggins Ave, Bedford, MA 01730  
**Raymond J. Connolly, Steven D. Schwaitzberg, John Lantis**  
New England Medical Center, Surgical Research Laboratory  
NEMC #37, 750 Washington St, Boston, MA 02111

Hemostasis, the stopping or prevention of blood loss, is a matter of urgent concern in many areas of clinical medicine including surgery, trauma and obstetrics. If not stopped in a timely manner, severe bleeding leads to certain death. Bleeding can be caused by accidental conditions during a trauma, or during surgery where tissue and vessels have to be cut to have access to the target site or to remove an organ or local tissue. Small bleeding can usually be stopped using simple means, but more intense bleeding is more difficult to stop. Intense bleeding is the prevalent cause of death following severe trauma such as bullets or stab wounds.

An electro-cautery device is usually used by doctors and surgeons during surgery to stop or prevent the bleeding, or they can also simply tie the blood vessel when the bleeding is too intense and the source can be localized. The electro-cautery device is based on the use of radio-frequency electrical current to cauterize the bleeding site. This implies the use of high voltage electrical energy, which can be sometimes more harmful than the bleeding itself when used in certain areas of the human body such as the brain or the heart. In such areas of the human body, the electro-cautery device can not be used to stop undesirable bleeding. The electro-cautery device is efficient only on small vessels of less than approximately 1.5 mm diameter, and is inefficient on intense bleeding typically found in severe trauma situations such as bullets or stab wounds. The electro-cautery equipment also requires the availability of a utility current source such as 110 or 220 VAC, and therefore is not portable and cannot be used outdoors.

We have developed a new technique using a small and portable semiconductor laser to stop or prevent the bleeding under any condition, including in proximity of the heart or the brain, or in absence of a utility electrical supply such as in outdoors environment. The medical procedure to stop bleeding using this invention is very similar to standard procedures commonly practiced by doctors and surgeons.

In this technique, a specifically designed medical forceps is combined with an efficient, self-contained and hand-held semiconductor laser to provide hemostasis. The laser energy is delivered through an optical fiber cable to the tip of a dedicated medical forceps to provide rapid local heating of the vessels and/or tissue contained between the jaws of the medical forceps, thereby cauterizing said bleeding vessel and/or tissue.

The cauterization mechanism being essentially thermal, the tip of the forceps is designed to minimize its thermal mass and minimize heat losses. The tip is also coated with a PFA Teflon coating to minimize the sticking of the cauterized tissue onto the tip.

The dedicated forceps is mounted on a small, battery operated semiconductor laser unit. The laser unit contains one fiber-coupled linear array of semiconductor lasers delivering 5 W of cw power at 980 nm through a 600  $\mu$ m diameter fiber. This array contains seven wide-stripe

emitters each individually coupled into a 150  $\mu\text{m}$  diameter fiber. The fiber-coupled laser package is mounted on a heat sink with small fins to dissipate the excess heat by natural convection of the air around the fins of the heat sink. The laser unit also contains an efficient current control circuit and a small disposable lithium battery to provide the necessary electrical current to the semiconductor lasers. A simple finger switch mounted on the dedicated medical forceps is used to activate the device. The complete system is designed and fabricated to be easily cleaned and sterilizable using the ETO gas sterilizing procedure.

When the finger-switch is depressed, the semiconductor lasers are activated and laser energy is delivered through the optical fiber to the tip of the medical forceps. This energy is sufficient to quickly heat up the blood vessels and/or tissue contained between the jaws of the forceps to cauterize and weld together body tissue, including blood vessels, clamped between the jaws of the medical forceps.

The device is used to provide hemostasis in the human body during surgical procedures or in severe trauma situations in a manner similar to a bi-polar electrocautery device. After visual location of the bleeding site or local vessel(s), the surrounding tissue is grabbed and clamped with the tips of the dedicated forceps. This provides temporary hemostasis at the targeted site. The device is then activated for a duration of typically 5 sec or until traditional visual clues such as local bubbling and popping indicate that the targeted site is effectively cauterized. When the device is activated, the clamped tissue and blood vessels contained between the tips of the forceps is quickly heated up by laser energy to such a temperature as to effectively cauterize and weld said clamped tissue and blood vessels, thus providing hemostasis at this site. The procedure can be repeated as many times as needed to provide hemostasis at all the desired sites. The procedure can also be repeated several times at the same site if necessary. The activation time can be increased or decreased to provide appropriate hemostasis at the targeted site. Larger vessels or more intense bleeding requires longer activation time.

Animal studies on live, anesthetized rabbits have demonstrated the efficacy and safety of the device and procedure. Various vessels in the mesentery tissue of the small intestine of the rabbits are quickly and effectively cauterized using this technique. The studies have also shown that this technique can effectively cauterize large vessels such as the Aorta of a rabbit, which could not be cauterized with the electro-cautery system.

We have developed a new technique to provide hemostasis using a small semiconductor laser. The device is battery operated, self-contained and can easily be hand-held. It can therefore be used in any environment or in places where no utility electrical source is available such as outdoors. This new technique is more effective than the standard electrocautery.

This work was supported by the USAF Phillips Laboratory, Kirtland AFB, NM 87117-6008 under contract #F29601-95-C-0050.

The animals involved in this study were procured, maintained, and used in accordance with the Federal Animal Welfare Act and the Guide for Care and Use of Laboratory Animal, prepared by the Institute of Laboratory Animal Resources - National Research Council.

## Beam Steering Laser Arrays & Applications in 2D Laser Scanning

D. A. Francis, C. J. Chang-Hasnain, M.-H. Kiang, K. Y. Lau, R. S. Muller

*EECS Department, University of California at Berkeley, Berkeley, CA 94720-1770*

*Tel: (510) 643-2330, Fax: (510) 643-1878, e-mail: dfrancis@diva.eecs.berkeley.edu*

Beam steering is very useful in many areas such as integrated optics, optical interconnects, optical computing, CD players<sup>1</sup> and laser printers.<sup>2,3</sup> A reliable beam steering laser has been sought by scientists for many years. Monolithic beam steering in semiconductor lasers has potential for high speed operation while being compact, low cost and mechanically stable.

Monolithic beam steering is limited in the total number of attainable resolvable spots by the diffraction from the total laser aperture. As such, it is unlikely that a monolithic laser beam steering device will compete with bulk optics beam steering techniques in total number of resolvable spots. However, monolithic beam steering sources can be used to increase the total throughput of an optical system by allowing parallel transmission of multiple channels of data, without significantly increasing the cost of the system.

The optics used in consumer applications are low cost and have limited numerical aperture (NA). In order to take advantage of the low cost optics, multi-beam sources must be designed to fit within a restricted field of view. In a laser printer, for example, the optics field of view is  $\sim 50 \mu\text{m}$  wide. The minimum allowable separation between lasers is limited by cross-talk. These competing constraints have limited the number of elements in individually addressable arrays to only 2 or 4.<sup>2</sup>

In this talk, we review the recent development of a novel individually addressable beam steering diode laser array; the fan laser array. We show that the fan laser array outperforms parallel laser arrays because it simultaneously reduces the effective aperture of the laser array and the cross-talk between array elements.

Using these devices we were able to attain beam steering over a total steering angle of  $80^\circ$  with 11 resolvable spots. Each spot can be individually addressed allowing for much greater data throughput by the optical system. The beam steering results achieved tripled all previous beam steering results in both total steering angle and in total number of resolvable spots. The results showed 50% improvement in thermal cross-talk performance without taking into account the effective reduction of aperture size. Because of the laser design, the actual effective minimum aperture is smaller than the physical aperture of the device. This effectively reduces the inter-element spacing without increasing cross-talk. Taking the effective aperture reduction into account, we decreased the inter-element cross-talk by over one order of magnitude.

Additionally, to demonstrate system feasibility of these devices, we built a 2D laser scanner using the fan laser array and a Si micromachined microscanner. The system is capable of read and write operations generating or detecting patterns with  $7 \times 10$  pixel resolution.<sup>4</sup> This is the first compact laser scanner of this sort built by integrating a microscanner with a beam steering source it shows promise for high speed operation and it demonstrates system viability of these novel devices.

Figure 1a shows a schematic of the fan laser array. Figure 1b shows the LI characteristics of one fan laser array. Figure 2a shows the far-field characteristics of a fan laser array, and figure 2b the comparison between cross-talk between parallel and angled etched facet lasers. Figure 4 shows the system performance of the 2D laser scanner. Further detailed characterization of the laser array as well as the 2D scanner system will be presented at the meeting.



References:

1. R. Arai et. al, *Japanese Journal of Applied Physics*, vol. **32**, Pt. 1, no. 11B, pp. 5411-5416, 1993.
2. M. Geslicki et. al, *Laser focus world*, **March**, pp. 167-169, 1996.
3. R. Thornton et. al, *Applied Physics Letters*, vol. **56**, pp. 1623-1625, 1990.
4. D.A. Francis et. al, *Proceedings of 9<sup>th</sup> annual meeting of the IEEE Lasers and Electro-Optics Society (LEOS)* '96, Boston, Massachusetts, paper (Post Deadline) P1.5 (1996).

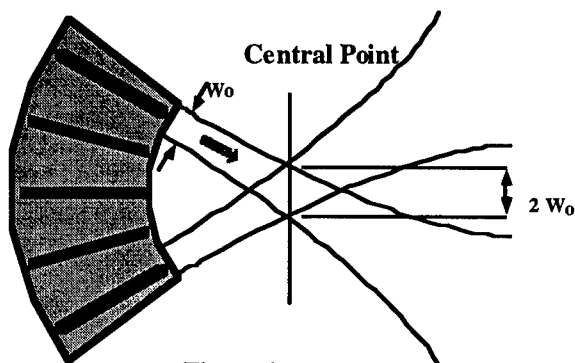


Figure 1a

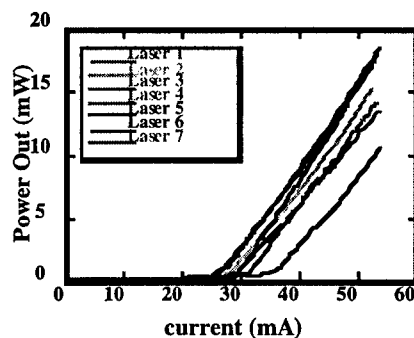


Figure 1b

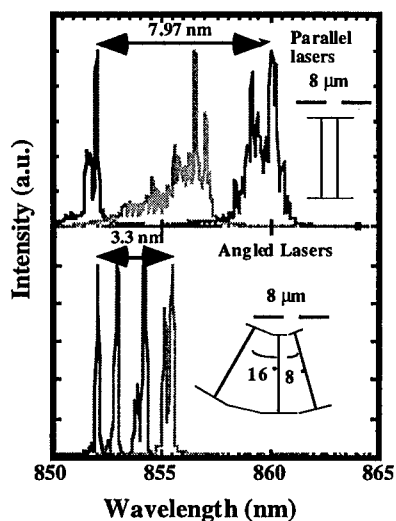


Figure 2a

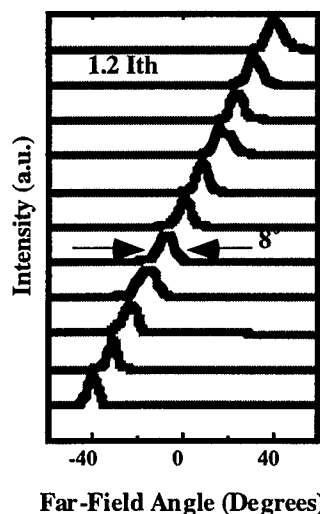


Figure 2b

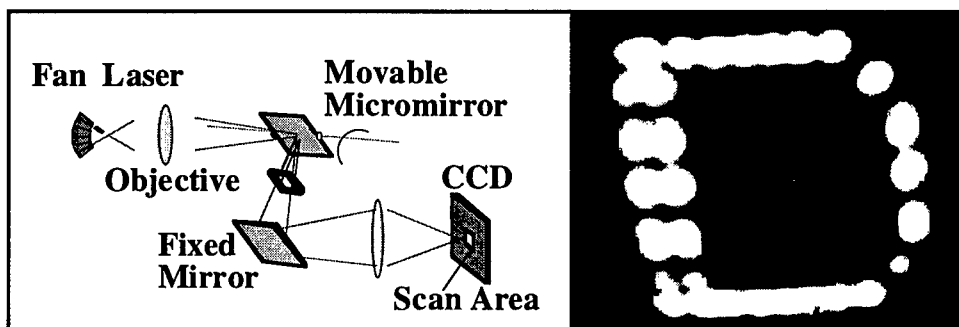


Figure 3

## Long Wavelength Triangular Shaped Waveguide Diode Ring Laser With Dry Etched Facets

Chen Ji and Joseph M. Ballantyne

School of Electrical Engineering, Cornell University, Phillips Hall, Ithaca, NY 14853

### Summary

High spectral purity and low noise are the principle requirements for semiconductor lasers serving as optical transmitters in modern optical communication systems. They should also operate in long wavelengths to take advantage of the minimal loss and dispersion points of silica fiber. DFB and VCSELs are good candidates, but they require costly layer structures or processing steps. Semiconductor ring lasers offer an alternative approach at lower cost. Semiconductor ring lasers in unidirectional operation set up a traveling wave inside the cavity, thus avoiding the standing wave spatial hole burning effects relevant in DFB and Fabry-Perot lasers. This results in high spectral purity<sup>1</sup>, and hence lowering intensity noise by reducing the mode partition noise. Among the triangular<sup>1,2,3</sup>, square and circular ring lasers reported, the first mentioned geometry is attractive because of its inherent output coupler and demonstrated power efficiency. We report record low threshold current and large side mode suppression ratio (SMSR) for long wavelength triangular ring lasers.

A SEM picture of the triangular shaped waveguide diode ring laser (WDRL) is shown in Fig. 1. The triangular shaped waveguide structure and the three facets are all dry etched using CAIBE for monolithic integration. A self aligned process is used for single lateral mode operation. The waveguide is shallow etched, stopping slightly above the active region, while the facets are deep etched through the active region. A traveling wave is set up in the triangular waveguide, with the left two facets designed to be nearly total internal reflection (TIR) mirrors, and the output light coupled out through the right facet. Threshold current and output power can be varied by adjusting the included structural angle between the waveguides at the output facet.

We used triple QW InGaAsP epitaxial material with InP cladding layers and InGaAs cap. The processing following the general approach described earlier<sup>2</sup>. Various modifications are made. A Cl<sub>2</sub>/Ar CAIBE recipe is developed to etch smooth and vertical facets in InP/InGaAsP at 200 C, 1 KV ion energy and  $1 \times 10^{-4}$  torr chamber pressure, as shown in Fig 2. 2000 Å of PECVD amorphous carbon is used for facet protection during the shallow ridge formation etch, which is also performed using CAIBE. The PECVD amorphous carbon is stripped in O<sub>2</sub> plasma to expose the facet position for deep facet etch. Compared with our previous results<sup>3</sup>, where the lasers operate gain guided, the current CAIBE etch recipe produces much smoother facets, together with greater control of etch depth. As a result, the current triangular ring lasers operate weakly index guided with single lateral mode, significantly improved SMSR and lower threshold current.

Triangular ring lasers of various structural angle and cavity lengths and corresponding Fabry-Perots are fabricated on the same chip. The devices are pulse tested at room temperature. A typical L-I of a 400 µm ring laser is shown in Fig. 3, the threshold current in this case is around 87mA, which is the best one so far for long wavelength WDRLs. A SMSR of 25.4 dB is obtained for a 400 µm ring (Fig. 4) laser. The triangle ring lasers show a much stronger tendency toward single mode operation compared to the Fabry-Perots under the same testing conditions. The latter have SMSR of no more than 10 dB. The background longitudinal mode spacing for a 400 µm ring laser is measured to be 10.34 Å, confirming that the lasing action indeed takes place over the full ring cavity. Noise measurements and works in further improving the SMSR of the triangular ring lasers are currently underway.

### References:

1. Behfar-Rad, A., Ballantyne, J. M., and Wong, S. S. Appl. Phys. Lett., 1992, **60**, (14), pp. 1658-1660
2. Liang, J. J., and Ballantyne J. M., J. Vac. Sci. Technol, 1994, **B12**, (5), pp. 2929-2932
3. Ji, C., Leary, M., and Ballantyne J. M., "Triangular Shaped Waveguide Diode Ring Laser Fabricated Using Cl<sub>2</sub> RIBE in InP/InGaAsP", Electron. Lett., 1997, Accepted for publication.

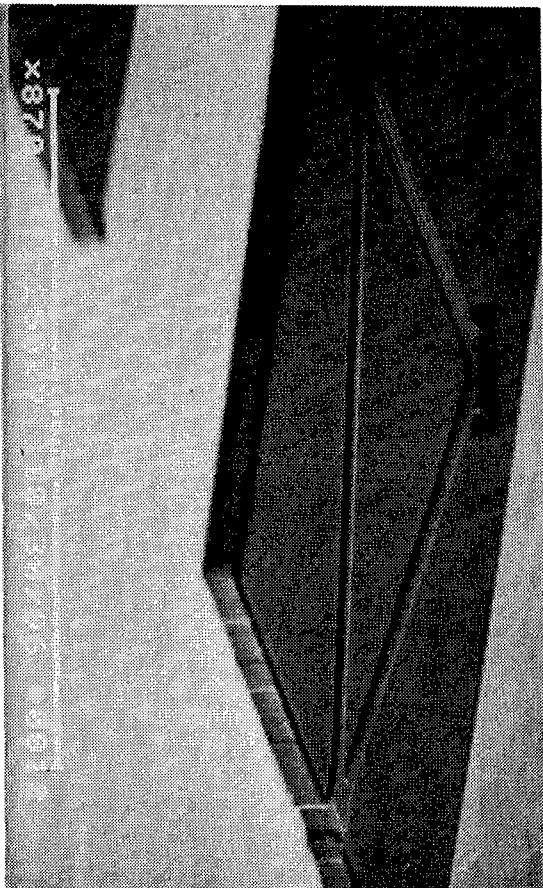


Figure 1. SEM of triangular waveguide diode ring laser (WDRL)

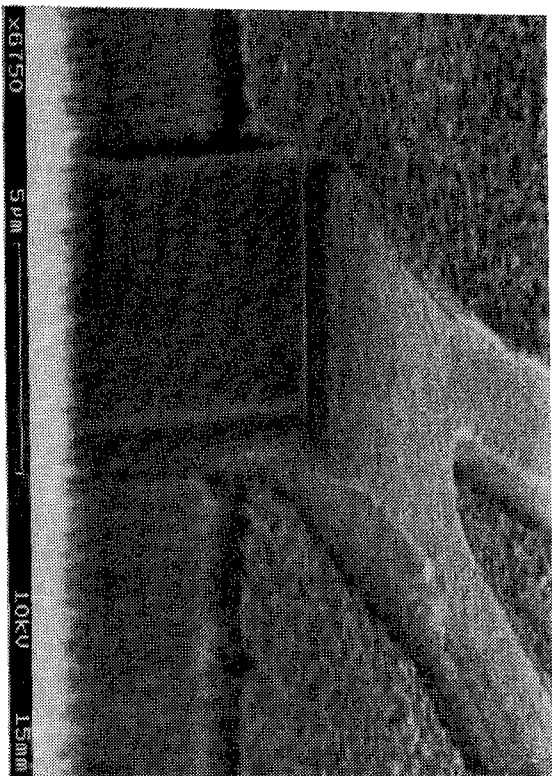


Figure 2. SEM of ring laser facet etched using CAIBE

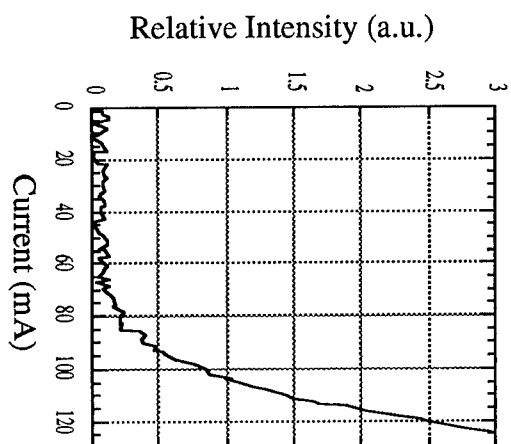


Figure 3. L-I curve of a triangular ring laser with cavity length 400  $\mu\text{m}$

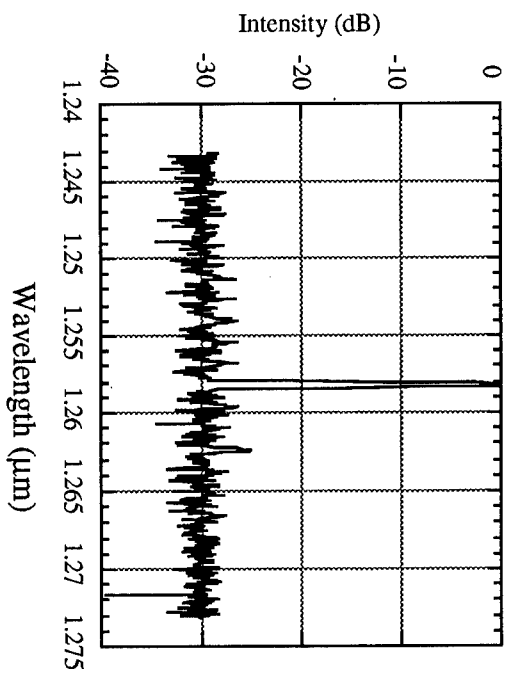


Figure 4. Pulsed spectrum of a triangular ring laser, cavity length 400  $\mu\text{m}$ , SMSR 25.4 dB.

# Improved Performance of Single-Mode Lasers by Using Native-Oxide Lateral-Confinement Layers

J. Heerlein, M. Grabherr, R. Jäger, and P. Unger

Department of Optoelectronics, University of Ulm, 89069 Ulm, Germany

Phone: +49(731)502-6046, Fax: +49(731)502-6049

**Abstract**— We report on results of wet oxidized narrow stripe laser diodes operating in single lateral and longitudinal mode around an emission wavelength of 850 nm. Devices with an active width of 3–11  $\mu\text{m}$  achieved single mode output powers of up to 240 mW in continuous wave operation at room temperature.

## I. INTRODUCTION

INDEX-GUIDED single-stripe laser diodes offer the advantages of single lateral and longitudinal mode operation, making them attractive for many applications. Such lasers have been fabricated with ridge waveguides or planar buried heterostructures [1], [2], [3]. Recent improvements in the performance of vertical-cavity surface-emitting lasers (VCSELs) have been achieved by using a selective wet oxidation process for injected current confinement and lateral index guiding. Wall-plug efficiencies and multi-mode output powers have been increased up to 57% and 180 mW, respectively [4], [5]. For stripe lasers, an oxidized layer also provides advantages for electrical and optical confinement.

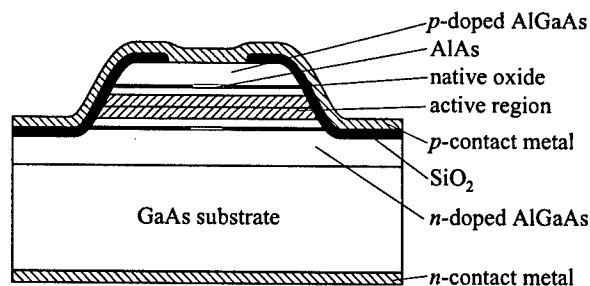


Fig. 1. Schematic drawing of a narrow-stripe laser with an oxidized AlAs layer above and below the active region.

Fig. 1 shows a schematic drawing of a native-oxide-confined narrow-stripe laser. A thin AlAs layer above and below the active region has been wet oxidized from the side walls. By using this technique, the refractive index of the AlAs layer is reduced to  $n \sim 1.6$  building a lateral index guiding. The effective index step can be adjusted exactly and reproducibly by the

thickness of the AlAs layer and its distance to the active region. The active lateral geometry is defined by the width of the oxidized AlAs layer. Furthermore, the isolating  $\text{Al}_x\text{O}_y$  layer provides an aperture for a homogeneous, non-dissipative current injection without surface recombinations. Compared to a ridge waveguide structure the  $p$ -side contact resistance is reduced due to a larger contact area. First Caracci et al. [6] presented encouraging results on native-oxide index-guided lasers. In this paper we present the results on GaAs quantum well lasers exhibiting maximum optical output powers of 240 mW with wall-plug efficiencies of nearly 40% as cleaved in continuous wave operation without mounting on subcarriers.

## II. DEVICE STRUCTURE

The epitaxial structures which are grown by molecular beam epitaxy (MBE) consist of a single GaAs quantum well surrounded by graded-index AlGaAs layers and  $\text{Al}_{0.5}\text{Ga}_{0.5}\text{As}$  cladding layers. The thin AlAs layers are positioned in a distance of 200 nm from the graded-index layers. After wet chemical mesa etching a selective oxidation of the 33-nm-thick AlAs layers above and below the active region is carried out. The oxidation width is around 8  $\mu\text{m}$ . Devices with an active lateral width of 3–11  $\mu\text{m}$  have been fabricated.

## III. DEVICE CHARACTERISTICS

For the characterization of the epitaxial laser structures, broad-area lasers have been fabricated. Internal efficiencies and intrinsic losses are 90% and  $4\text{ cm}^{-1}$ , respectively. Threshold current densities of  $130\text{ Acm}^{-2}$  for  $2\text{ mm} \times 100\text{ }\mu\text{m}$  large devices have been measured under pulsed conditions.

Single mode lasers with an oxide confinement have been fabricated from this epitaxial qualities. All devices are tested as cleaved at room temperature under continuous wave operation. Fig. 2 depicts the CW output characteristic of an oxide-confined laser with a cavity length of 500  $\mu\text{m}$  and an aperture width

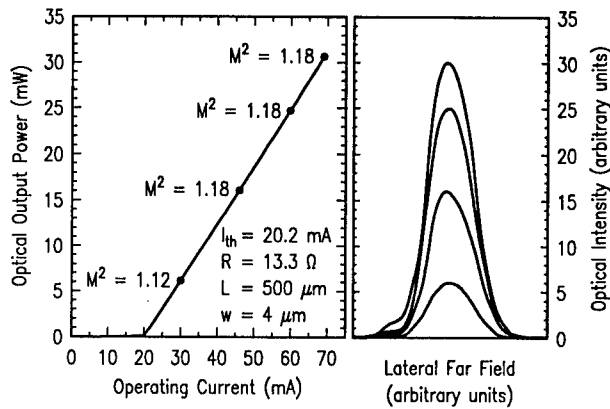


Fig. 2. Output characteristic of an oxidized laser with an active area of  $500 \cdot 4 \mu\text{m}^2$ . Beam quality factors  $M^2$  between 1.1 and 1.2 have been measured. The corresponding nearly gaussian far-field patterns are depicted on the right hand side.

of  $4 \mu\text{m}$ , where only the top AlAs layer is oxidized. The threshold current is 20 mA. On the right hand side, the far-field patterns at different pumping levels are shown. The intensity distribution is nearly gaussian. Beam quality measurements showed  $M^2$  values below 1.2.

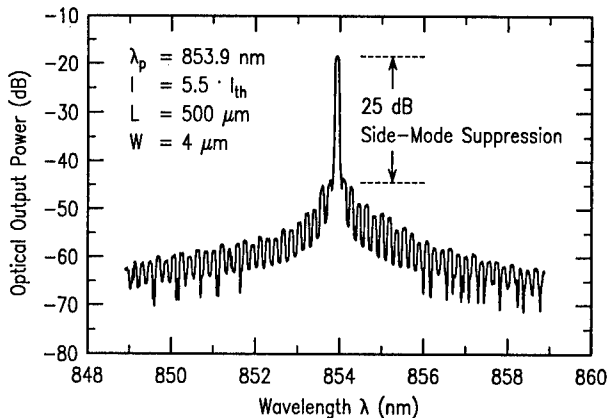


Fig. 3. The emission spectrum of an oxidized laser shows a side-mode suppression of 25 dB at an operating current of 5.5 times of the threshold value.

The optical emission spectrum at a current of 5.5 times of the threshold value is shown in Fig. 3 where the peak emission wavelength is 854 nm and the side mode suppression of the longitudinal modes is 25 dB. Considerable high, near single mode maximum total output powers of up to 240 mW have been achieved for laser diodes of  $750 \cdot 11 \mu\text{m}^2$  as depicted in Fig. 4. The series resistance is  $2.6 \Omega$ . Threshold current and differential quantum efficiencies are 31 mA and 60 %, respectively. The wall-plug efficiency stays nearly constant for a wide operation range with a maximum value of 38 %.

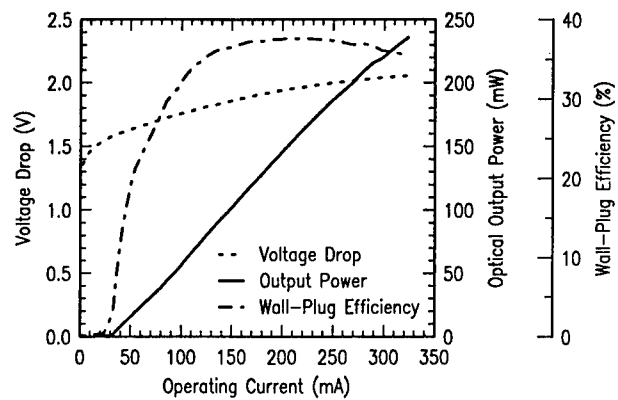


Fig. 4. The CW output characteristic of a  $750 \cdot 11 \mu\text{m}^2$  large oxidized laser shows a maximum output power of 240 mW.

#### ACKNOWLEDGMENTS

This work has been supported by the German Ministry of Education, Science, Research, and Technology (BMBF).

#### REFERENCES

- [1] A. Shima et al., "0.78- and 0.98- $\mu\text{m}$  ridge-waveguide lasers buried with AlGaAs confinement layer selectively grown by chloride-assisted MOCVD", IEEE J. Sel. Top. Quantum Electron., vol. 1, pp. 102-109, 1995.
- [2] B. Elman et al., "High power 980 nm ridge waveguide lasers with etch-stop layer", Electron. Lett., vol. 27, pp. 2032-2033, 1991.
- [3] S. S. Ou et al., "High performance InGaAs/GaAlAs laser diodes for electronic/photonic integrated circuit applications", Electron. Lett., vol. 29, pp. 542-544, 1993.
- [4] R. Jäger et al., "57 % Wallplug efficiency oxide-confined 850 nm wavelength GaAs VCSELs", Electron. Lett., vol. 33, pp. 330-331, 1997.
- [5] M. Grabherr et al., "High power top-surface emitting oxide confined vertical-cavity laser diodes", Electron. Lett., vol. 32, pp. 1723-1724, 1996.
- [6] S. J. Caracci et al., "High-performance planar native-oxide buried-mesa index-guided AlGaAs-GaAs quantum well heterostructure lasers", Appl. Phys. Lett., vol. 61, pp. 321-323, 1992.

# **ADVANCED SEMICONDUCTOR LASERS AND APPLICATIONS**

**Thursday, 14 August 1997**

## **Sessions:**

***ThA: Microwave-Optical Systems***

***ThB: Novel Devices II***

***ThC: Mid-IR Sources***

***ThD: Spectroscopic Applications***



## **All-Optical Buffers for High-Speed Slotted TDM Networks**

K.L. Hall, MIT Lincoln Laboratory, C-237, 244 Wood Street, Lexington, MA 02173,  
tel: (617) 981-0229, fax (617) 981-4129, khall@ll.mit.edu

The development of system technologies for ultra-high speed, time division multiplexed (TDM) packet-switched local area networks is an area of active research [1,2]. Because bandwidth-on-demand represents an important network service, and because all users may not generate or accept data at the ultrafast optical bus rate, optical buffers operating at the network data rate are key components. To date, a variety of optical storage elements have been demonstrated. Short term pulse pattern storage has been demonstrated in recirculating loop experiments [3-8]. In general, these loops can not be applied to TDM network applications because they require sliding guiding filters to suppress continuum and reduce timing jitter and are not compact single-wavelength, single-packet buffers [3,4]. Compact passive loop buffers have limited application because the demonstrated storage times (tens of circulations) are too short for certain network configurations [6-8]. Longer term storage has been demonstrated in regenerative loops employing optical fiber logic gates operating at 50 MHz [9-11] and semiconductor amplifier logic gates at 1.5 Gb/s [12]. Also, long term storage at ultrafast data rates has been demonstrated in active fiber loop buffers [13-19]. These active fiber loop buffers and regenerative buffers are attractive from a network standpoint because they can be designed to store a single packet at a single wavelength for hundreds of circulations.

Much of the recent work on optical buffers has centered on techniques to extend the attainable data rates. In active loop buffers using electro-optic (EO) modulators to provide the data timing stability, the data rate (determined by the RF driving frequency) can be multiplied by factors of 2 or 3 by overdriving the (EO) modulator [16,20]. Utilizing semiconductor optical amplifiers (SOA's) as the modulator in the cavity is another way to extend the buffer operation to high data rates. In this scheme, the gain of an SOA is modulated by an external sinusoidal or pulsed optical source. Through cross gain saturation, this external control signal provides gain modulation for data pulses in the optical buffer [15]. Figure 1 shows a schematic of the all-optical fiber loop buffer. Data is coupled in and out of the buffer by a 90/10 coupler. The erbium doped fiber amplifier provides gain and the isolator forces unidirectional operation. Cross gain saturation in the SOA provides gain modulation at the data rate. In this example, the cross-saturating signal is a sinusoidally modulated optical beam at 1480 nm. This optical control beam is coupled into the storage loop via a polarization beam splitting cube and out of the loop by a WDM coupler. Approximately 1 mW of power is required in the optical control beam. The data rate in the loop will be limited by the nonlinear response time of the SOA and not by the electrical parasitics in the biasing circuit or the SOA.

In this presentation we will give an overview of the recent advances in fiber optic buffer design and describe how these buffers might be used in ultrafast TDM networks. In particular, we will describe buffers that rely on semiconductor optical amplifiers as the switching and timing elements. Recent experimental results will be described



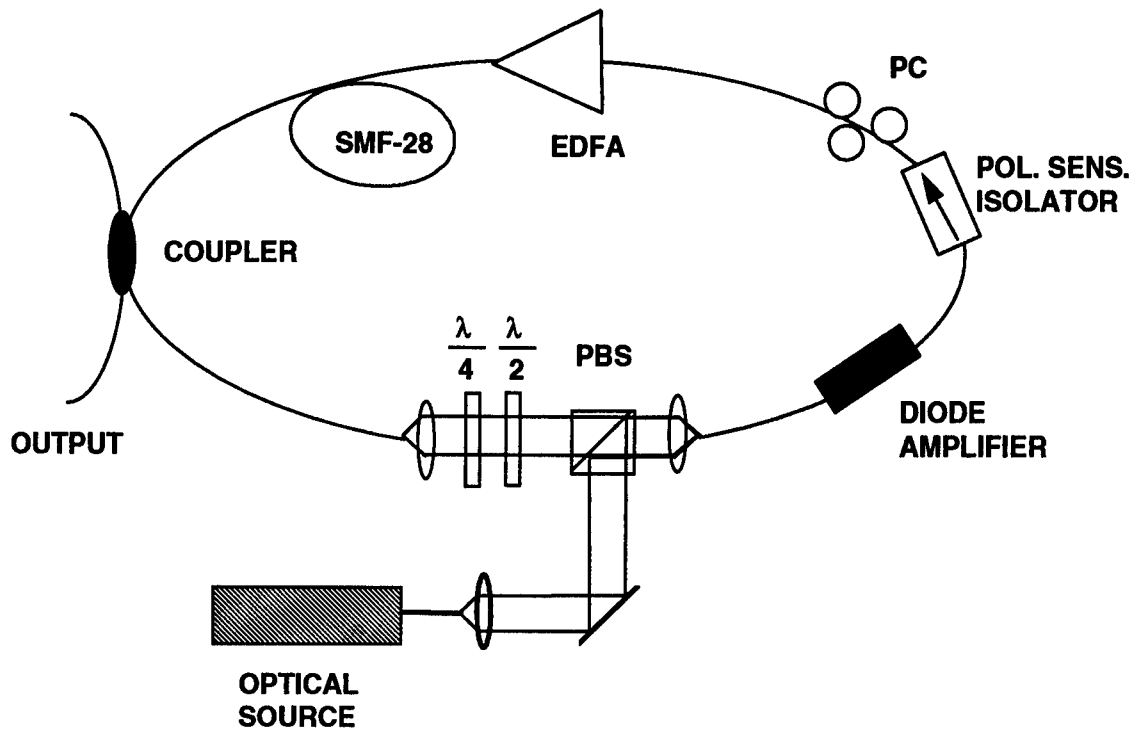


Figure 1: Schematic of the all-optical fiber loop buffer.

## REFERENCES

- [1] S.G. Finn and R.A. Barry, *IEEE Network Magazine*, November/December, (1996).
- [2] R.A. Barry et al., *JLT/IEEE JSAC*, **14**, no. 5, p. 999, (1996).
- [3] L.F. Mollenauer et al., *Electron. Lett.*, **28**, no. 8, p. 792, (1992).
- [4] M. Nakazawa et al., *Electron. Lett.*, **28**, no. 12, p. 1099, (1992).
- [5] W. Pieper et al., *Electron. Lett.*, **30**, no. 5, p. 435, (1994).
- [6] Y. Yamada et al., *OFC '95 Tech. Dig.*, **8**, p. 140, (1995).
- [7] G. Bendelli et al., *OFC '95 Tech. Dig.*, **8**, p. 141, (1995).
- [8] R. Langenhorst et al., *J. Lightwave Technol.*, **14**, no. 3, p. 324, (1996).
- [9] V.I. Belotitskii et al., *Electron. Lett.*, **29**, no. 1, p. 49, (1993).
- [10] H. Avamopoulos and N. Whitaker, *Opt. Lett.*, **18**, no. 1, p. 22, (1993).
- [11] N.A. Whitaker et al., *Opt. Lett.*, **16**, no. 24, p. 1999, (1991).
- [12] A.J. Poustie, *Electron. Lett.*, **32**, no. 13, p. 1215 (1996).
- [13] C.R. Doerr et al., *Opt. Lett.*, **19**, no. 21, p. 1747, (1994).
- [14] J.D. Moores et al., *IEEE Photon. Technol. Lett.*, **7**, no. 9, p. 1096, (1995).
- [15] K.L. Hall et al., *IEEE Photon. Technol. Lett.*, **7**, no. 9, p. 1093, (1995).
- [16] J.D. Moores et al., *Opt. Lett.*, **20**, no. 24, p. 2547, (1995).
- [17] K.L. Hall and K.A. Rauschenbach, *IEEE/LEOS Summer Top. Mtg. Tech. Dig., Broadband Optical Networks*, MB2, p. 16, (1996).
- [18] J.D. Moores, *OFC '97 Tech. Dig.*, **6**, p. 88, (1997).
- [19] K.L. Hall, *OFC '97 Tech. Dig.*, **6**, p. 251, (1997).
- [20] N. Onodera et al., *Appl. Phys. Lett.*, **62**, no. 12, p. 1329, (1993).

# Microwave Generation with Monolithic Dual-Wavelength DFB Lasers

C. Laperle, M. Svilans<sup>†</sup>, M. Poirier, and M. Têtu

<sup>†</sup>Nortel Technology, P.O. Box 3511, Station C, Ottawa, Ontario K1Y 4H7 Canada

Elect. Eng. Dept., Université Laval, Sainte-Foy, Québec G1K 7P4 Canada

## ABSTRACT

Microwave beat signals were generated from a novel dual-wavelength DFB laser integrated with an active Y-junction coupler. This compact laser device is highly manufacturable due to its simple design which uses only the standard DFB process.

## INTRODUCTION

Electrical microwave frequencies can be generated within a square-law photodetector by illuminating it with the outputs of two optical sources with a highly stable optical frequency difference. Integrating both sources into the same device improves temperature tracking, ensuring that effects of ambient fluctuations are minimized.

To combine the two laser outputs into a single fiber, the lasers need to be integrated with an optical combiner. So far, most of the multi-wavelength laser sources have used a passive coupler integrated with DFB lasers [1] and DBR lasers [2-3]. However, this has generally required substantial additional crystal growth and processing.

In this work, we demonstrate the generation of heterodyne microwave signals using a monolithic dual-wavelength DFB laser with an active Y-coupler. As this is fabricated using the standard DFB process, the resulting structure can be made very compact.

## DESIGN AND FABRICATION

As shown in Fig. 1, the devices consist of two DFB lasers whose ridges are tilted such that their outputs combine into a Y-coupler. Since the coupler shares the same layer structure as the lasers, it can be electrically pumped to make it transparent or even give it net optical gain.

The DFB lasers are 1.55  $\mu\text{m}$  InGaAsP-InP strained-layer GRINSCH-MQW devices, grown by a standard two-step MOCVD process with uniform, holographically generated gratings. The ridge width is 2  $\mu\text{m}$  and the total device length is 500  $\mu\text{m}$ . The ridge tilt of each laser is 2° and the minimum radius of curvature of the bends in the Y-coupler is about 1 mm.

A total of three electrodes are used for current injection in each laser separately as well as in the coupler. Fi-

nally, the output facet at the coupler end of the device is anti-reflection coated.

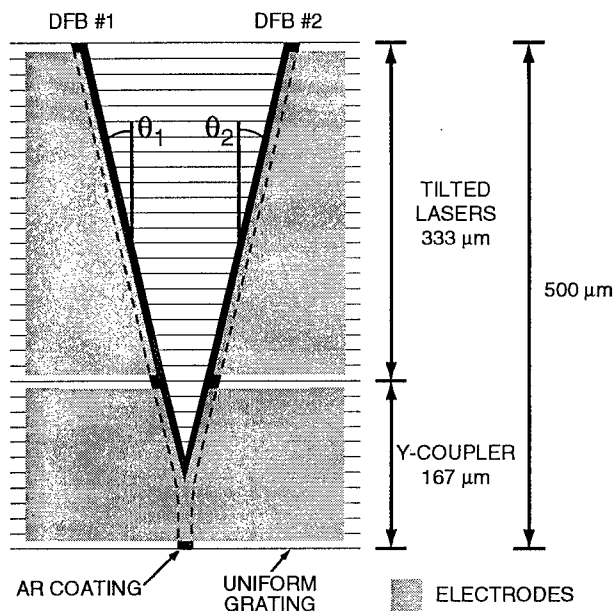


Fig. 1 – Schematic diagram of dual-wavelength DFB laser structure with a uniform grating.

## RESULTS AND DISCUSSION

The optical output of the energized device was coupled through a microlensed single-mode fiber and isolator into an HP71400 Lightwave Signal Analyzer. The resulting microwave frequency could be tuned simply by varying one laser injection current relative to the other. In our device, the losses normally associated with passive combiners could be overcome by applying a small forward bias to the Y-coupler. Moreover, with an increased biasing gain could be achieved.

Fig. 2 shows how the beat signal frequency can be controlled by varying one laser injection current while keeping the other laser current fixed. The two different curves shown are for the Y-coupler section in an unbiased state (quasi passive), and with a nominal bias. The frequency variation is slightly parabolic when the Y-coupler is unbiased while it is practically linear when it is biased above 0 mA.

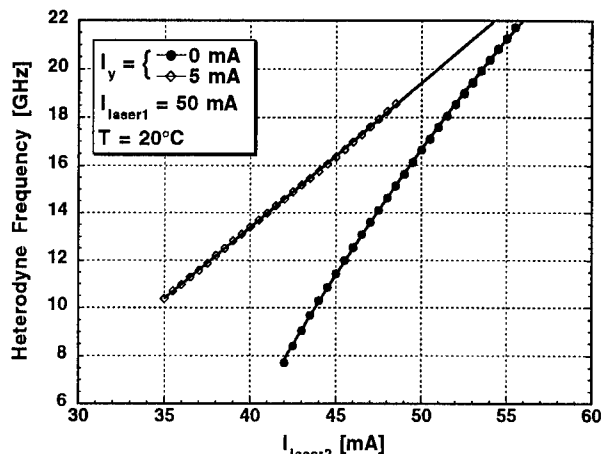


Fig. 2 – Heterodyne frequency for two Y-coupler currents as a function of one laser current while the other laser current is kept at a fixed value.

As Fig. 2 indicates, the beat frequency cannot be controlled properly below about 8–10 GHz. This is due to one laser injection locking onto the other. The locking bandwidth of DFB lasers increases with injected optical power and can reach values as high as 20 GHz [4]. In this structure each laser has a fraction of its output power reflected back into the other laser by the grating in the coupler region. As expected, the injection level is higher when the coupler is biased to transparency giving the wider locking bandwidth.

We propose the use of this property to even further improve the heterodyne frequency stability by the following method. Optical sidebands are generated in one of the lasers by applying a suitable modulation, so that the other laser can be locked on one of them.

The spectrum of the heterodyne signal at 15.187 GHz is shown in Fig. 3 with a linewidth of 10.7 MHz (FWHM). The two lasers were in a “free-running” mode. The linewidths of the separate lasers were measured by the standard self-heterodyne method and compared to that of the heterodyne signal shown in Fig. 3. Good consistency with the Lorentzian sum was observed.

To generate higher heterodyne frequencies, one of the ridge waveguide branches can be tilted more than the other, thereby increasing the relative detuning of the two lasers [5].

## CONCLUSIONS

DFB lasers and a coupler were fabricated on the same device using the same process technology. No adverse effects due to the grating in the coupler section could be observed. The heterodyne signal tuning range was limited by injection locking at the low end and by measuring instrumentation at the high end.

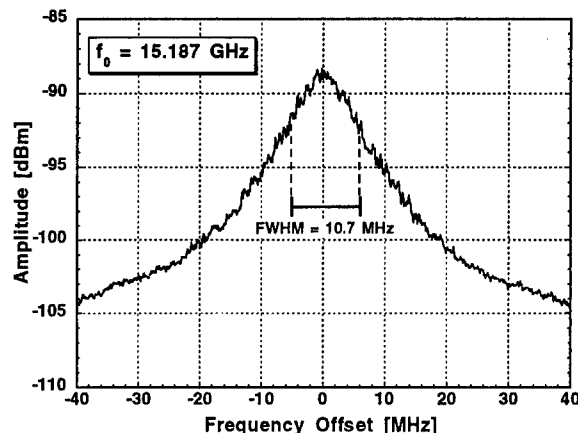


Fig. 3 – Linewidth of heterodyne beat note at -3 dB (FWHM). [ $I_y = 20$  mA,  $I_{laser1} = 124.9$  mA,  $I_{laser2} = 100$  mA, and  $T = 20$  °C.]

## ACKNOWLEDGMENTS

C. Laperle acknowledges the financial support of the Fonds pour la Formation de Chercheurs et l'Aide à la recherche (FCAR) and of Nortel Technology. The authors greatly acknowledge the assistance of N. Puetz, C. Blaauw, B. Benyon, F. Shepherd, R. Rousina-Webb, J. Marks, T. Jones, and Z. Husain.

## REFERENCES

- [1] K. Aiki *et al.*, “A frequency-multiplexing light source with monolithically integrated distributed-feedback diode lasers,” *IEEE J. Quantum Electron.*, vol. QE-13, no. 4, pp. 220–223, Apr. 1977.
- [2] M. Maeda *et al.*, “Photonic integrated circuit combining two GaAs distributed Bragg reflector laser diodes for generation of the beat signal,” *Jpn. J. Appl. Phys.*, Part 2, vol. 31, no. 2B, pp. L183–L185, 15 Feb. 1992.
- [3] H. Okamoto *et al.*, “A wavelength-tunable duplex integrated light source for fast wavelength switching,” *J. Lightwave Technol.*, vol. 14, no. 6, pp. 1033–1041, June 1996.
- [4] R. Hui *et al.*, “Injection locking in distributed feedback semiconductor lasers,” *IEEE J. Quantum Electron.*, vol. 27, no. 6, pp. 1688–1695, June 1991.
- [5] W.T. Tsang *et al.*, “Control of lasing wavelength in distributed feedback lasers by angling the active stripe with respect to the grating,” *IEEE Photon. Technol. Lett.*, vol. 5, no. 9, pp. 978–980, Sept. 1993.

## Application of a Novel Two-Longitudinal-Mode LD as a Source for CW THz Wave Generation by Photomixing

Takehiko Hidaka<sup>1</sup>, and  
Shuji Matsuura<sup>2\*</sup>, Masahiko Tani<sup>2</sup> and Kiyomi Sakai<sup>2</sup>

<sup>1</sup> Department of Electrical Engineering, Shonan-Institute of Technology, Fujisawa 251 Japan, E-Mail: hidaka@elec.shonan-it.ac.jp.

<sup>2</sup> Kansai Advanced Research Center, CRL, MTP, Kobe 651-24, Japan

<sup>2\*</sup> E-Mail: matsuura@crl.go.jp

Generation of cw THz electromagnetic waves by photomixing of two lights from independent two lasers[1], [2] had been attracted a great deal of attention for the fields of far infrared spectroscopy, radio astronomy and optical communications. However, each laser in the system should be stabilized separately, and a perfect spatial mode matching was required for efficient THz generation. Optical-alignment procedure is troublesome in practical uses. Two LD lights (joined by a fiber coupler) pumped photomixing method[3] is very interesting by means of the reduction of cost and optical alignment-procedure. We need, however, two LDs with two drivers, two frequency stabilizers and a multiplexer as the pumping source in the system. It is strongly desired a much simpler pumping source for an practical application of THz waves. We here report a novel cw THz wave generation system using a two-longitudinal-mode LD[4] in place of those complex or expensive light sources so far used.

The two-longitudinal-mode LD used here radiated two coherent lights with their separation about 0.9THz, simultaneously from a single stripe[4]. The essential structure of the DBR part of the laser is shown in Fig.1. The bi-periodic binary grating reflects two frequencies, simultaneously, within the gain bandwidth of the LD. There is a lot of side lobes in the reflection spectrum as shown in the Fig.1(c). However, for multi-mode oscillation, each product of the reflectance and the gain for each mode should be equal; only the strongest two modes with the same reflectances of the grating in Fig.1(b) oscillate under a critical condition. An example of output-wavelength characteristics vs. temperature and injection current is shown in Fig.2. The *difference (or ratio)* between two oscillation wavelengths is determined essentially by the DBR structure, not by temperature nor refractive index of the DBR part. Those situations, two lights radiated from a single stripe and the stability of the difference frequency between two laser lights, will be very promising to use a local oscillator in THz radiometer.

The experimental setup to generate cw THz wave is shown in Fig.3. One of the experimental result (sub THz radiation power vs. input power) is shown in Fig.4(a). We have not a spectrum analyzer for the range of the expected radiation frequency; therefore we could not confirm if the measured radiation from the photomixing material was surely the expected 0.9THz radiation or not. However, we can see, from Fig.4(a), that the output is almost proportional to the square of the input power (sum of two lights). Fig.4(b) shows polarization characteristics of the output which was in agreement with the expected one. These data show the validity of the two-longitudinal mode LD as a source for cw THz wave radiation by photomixing. The authors are grateful to T. Sawada and T. Sakamaki of technical assistance in experiments.

[1] E.R. Brown et.al., *Appl. Phys. Lett.*, 64, 3311 (1994).

[2] E.R. Brown et.al., *Appl. Phys. Lett.*, 65, 285 (1995).

[3] Matsuura et al. *Appl. Phys. Lett.*, 70, 559 (1997).

[4] S.Iio et.al., *IEEE Photonics Tech. Lett.*, 7, pp959-961 (1995).

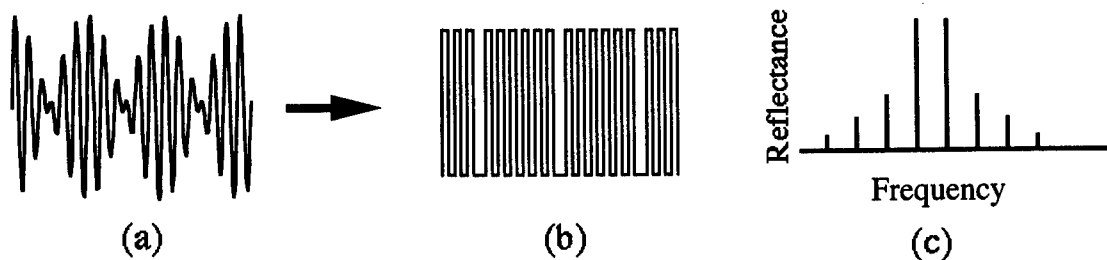


Fig.1.(a) Bi-periodic grating with the profile  $\sin(x/\Lambda_1) + \sin(x/\Lambda_2)$ . (b) Bi-periodic binary grating as an altanate of  $\sin(x/\Lambda_1) + \sin(x/\Lambda_2)$ . (c) Reflectance of the bi-periodic binary grating.

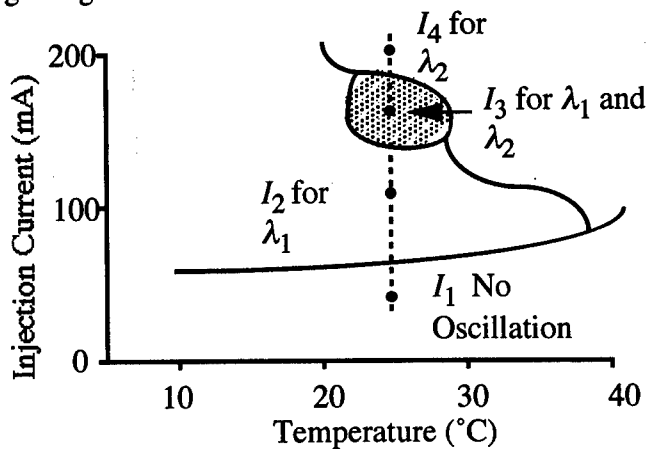


Fig.2. An example of the oscillation frequency vs temperature and injection current. Shaded area is that of two-mode oscillation. Lot. No. 509 B5B6.

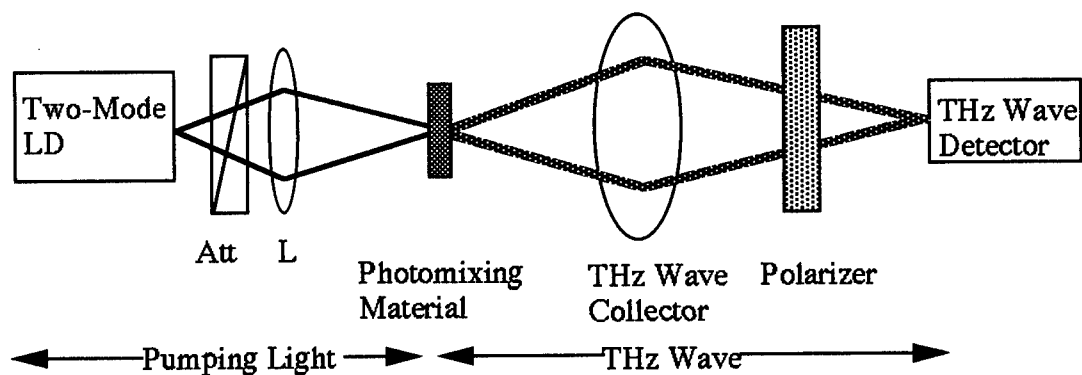


Fig.3. Experimental setup for THz Wave Generation by Photomixing.

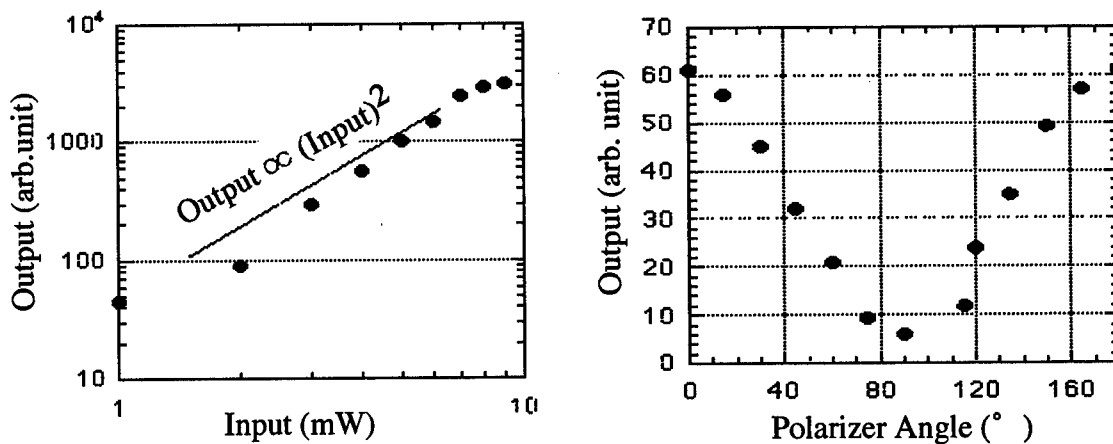


Fig.4(a) THz wave intensity vs pumping-light power, and (b) polarization characteristics of THz wave.

## Optoelectronic Microwave Oscillators Using Diode Lasers

J. Kitching, E. Ferre-Pikal, L. Hollberg and F. Walls

Time and Frequency Division,  
National Institute of Standards and Technology,  
325 Broadway, Boulder, CO 80303

Diode lasers and fiber optics are increasingly finding application in solutions to a variety of technological problems. Optical communication systems, fiber sensors and medical uses are but three examples. One idea proposed recently<sup>1</sup> is to use optoelectronic components to generate extremely stable microwave signals at frequencies near 10 GHz. Although still in the early stages of development, these oscillators have the potential to compete with state-of-the art dielectric resonator oscillators in terms of phase stability while offering a number of desirable features including tunability, low cost and easy integration with optical systems. These optoelectronic oscillators (OEOs) have potential applications in atomic frequency standards, photonic microwave systems and optical communications.

The unique feature of this type of oscillator is the use of optical fiber rather than microwave waveguide or a dielectric resonator in the oscillator loop in order to achieve long delay times with small RF power loss. As shown in Figure 1, a microwave signal is encoded as amplitude modulation on laser light either by direct modulation of the diode laser injection current or by external electrooptic modulation. The light is then sent through the fiber and detected in a high-speed photodiode which recovers the original microwave signal with a small amount of added noise associated with the light. The

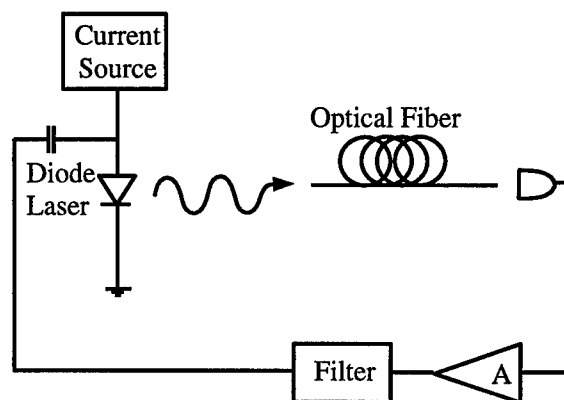


Figure 1 A typical optoelectronic oscillator

photodetector output is then amplified, filtered and sent back into the light modulator forming a closed feedback loop. When the RF amplification exceeds the RF loss in the rest of the loop, oscillation occurs at a frequency determined by the roundtrip phase condition and filter center frequency. Since extremely long delays (many kilometers) with very low loss ( $\sim 0.3$  dB/km at a laser wavelength of  $1.3 \mu\text{m}$ ) are attainable using commercial optical fiber, the oscillator phase stability can be exceptional. The RF spectrum of the oscillator is given by an expression similar to the Schawlow-Townes formula for the optical spectrum of a laser oscillator. Far from the RF carrier, the phase noise is found to be proportional to the RF noise-to-signal ratio at the detector output under open loop conditions and inversely proportional to the square of the delay time<sup>1</sup>. The noise sources which are important in this oscillator include shot noise, excess laser noise and thermal noise at the RF amplifier input, although several other, more technical, noise processes appear also to be important. The long delays made possible by the use of optical fiber can result in very low phase noise: For reasonable operating conditions of 50 mW of optical power, 50% amplitude modulation index, shot noise limited detection and a fiber length of 10 km the SSB phase noise is of order -150 dB with respect to the carrier in a 1 Hz bandwidth (dBc/Hz) at a

frequency offset of 1 kHz. In addition, the phase noise of the OEO is in principal independent of oscillation frequency, although a realistic upper limit of about 20 GHz is imposed primarily by how fast the optical field can be efficiently amplitude modulated and subsequently detected.

We have constructed two such oscillators at NIST, operating at frequencies between one and five gigahertz. The first uses an 850 nm distributed Bragg reflector (DBR) diode laser and 1 km of single-mode fiber. The oscillation frequency was 1.00 GHz and side-modes (due to the time delay in 1 km of fiber) spaced by 200 kHz were suppressed by over 50 dB below the main mode. The noise in this system has been fairly well characterized and, for the most part, understood. A single sideband (SSB) phase noise of -138 dBc/Hz was measured at a frequency 20 kHz from the carrier. In this frequency region, the oscillator spectrum appears to be dominated by interferometric noise generated through double-Rayleigh scattering of the light in the optical fiber<sup>2</sup>. Although some reduction of this interferometric noise was achieved through phase modulation techniques<sup>3</sup>, this source still dominated at Fourier frequencies between 1 kHz and 100 kHz. On longer time scales, temperature fluctuations dominated the phase noise spectrum. The thermal coefficient of delay for standard optical fiber is about  $10^{-5}$  per degree Celsius. Uncontrolled environmental fluctuations in the fiber temperature therefore result in changes in the oscillation frequency by several kHz.

In order to obtain improved performance, a second oscillator using 1.3  $\mu\text{m}$  optics has been constructed. The longer wavelength offers a number of advantages: The fiber loss is significantly lower, the Rayleigh scattering is less and finally it is possible to buy specialized single-mode fiber at this wavelength which has a substantially reduced thermal coefficient of delay. With these improvements, some modest thermal and mechanical stabilization of the fiber and higher speed optical components, we hope to achieve oscillation above 10 GHz with a SSB phase noise of -70 dBc/Hz at 1 Hz resulting in an Allan variance of about  $10^{-14}$  at 1 sec.

Using direct current modulation of the laser, oscillation frequencies as high as 4.3 GHz have been achieved with this 1.3  $\mu\text{m}$  system. However, poor modulation efficiency of the laser limited the signal at the detector and therefore the phase noise performance and side mode suppression was not particularly good. For operation at even higher frequencies, external modulation appears to be the most promising route: Optical power levels as high as 100 mW can be modulated efficiently at frequencies up to 20 GHz using commercial Lithium Niobate modulators whereas high-speed diode lasers typically produce output powers on the order of several mW.

We will present the latest experimental results obtained with this 1.3  $\mu\text{m}$  oscillator in addition to low frequency measurements of the phase noise of the 850 nm system. A configuration using two fiber loops used to further suppress the side modes<sup>1</sup> will also be described.

1. X. S. Yao and L. Maleki, J. Opt. Soc. Am. B, **13**, 1725 (1996); X. S. Yao and L. Maleki, Opt. Lett., **21**, 483 (1996); X. S. Yao and L. Maleki, IEEE J. Quantum Electron., **32**, 1141 (1996).

2. S. Wu, A. Yariv, H. Blauvelt and N. Kwong, Appl. Phys. Lett., **59**, 1156 (1991).

3. A. Yariv, H. Blauvelt and S. Wu, J. Lightwave Tech., **10**, 978 (1992).

## Super wide span Optical Frequency Comb generation by nonlinear self-phase-modulation in an optical fiber

M. Kourogi<sup>1,2</sup>, K. Imai<sup>1</sup>, B. Widiatmoko<sup>1</sup> and M. Ohtsu<sup>1,2</sup>

1)Tokyo Institute of Technology, Midori-ku, Yokohama 226 Japan

2)Kanagawa Academy of Science & Technology, Takatsu-ku, Kawasaki Kanagawa 213 Japan.

An optical frequency comb (OFC) generator<sup>1,2</sup>, which is based on an Electro-Optic modulator enclosed in a high finesse optical cavity<sup>6</sup> driven by microwave with a constant frequency, generates more than one thousand of equally spaced sidebands on large frequency span as wide as several THz from a cw laser light. Those sidebands are called as an OFC. When frequency of one of the sideband-components in the OFC is compared with the other laser by using photodetectors, the difference frequency between the laser and the carrier frequency of the OFC can be determined with an accuracy as high as that of the microwave frequency, and frequency and phase of lasers can be controlled very precisely within the span of the OFC. The OFC generator is a suitable device for frequency measurement of widely wavelength-tunable lasers such as semiconductor lasers used in optical communication networks. An optical frequency atlas of semiconductor lasers locked to 1.5 $\mu$ m bands acetylene lines have been made by using an OFC generator<sup>7</sup>. Therefore, there has been a heightened interest in expanding OFC generation.

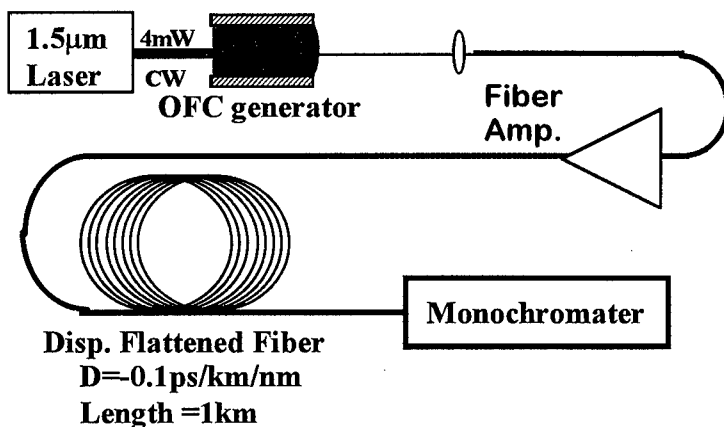


Fig.1 Experimental setup.

In order to expand the frequency span of an OFC much more, we applied nonlinear self-phase-modulation (SPM) technique<sup>8</sup> to output of an OFC generator. Since, additionally generated sidebands by SPM is also equally spaced, SPM can be applied for expansion of OFC span.

The experimental configuration is shown in Fig.1. The laser beam (4mW) from an 1.54 $\mu$ m semiconductor laser was introduced into a coupled-cavity monolithic OFC generator<sup>2</sup>. Then the output of the OFC generator was introduced into a dispersion-flattened-fiber<sup>9</sup> (DFF) via an optical fiber amplifier. The modulation frequency of the

OFC generator and the efficiency of OFC generation were 6GHz and 25%, respectively. The output of the OFC forms a train of short optical pulses. The width of optical pulse have been measured as 1ps. The dispersion of DFF was -0.12ps/km/nm at 1.54 $\mu$ m wavelength. The optical fiber amplifier, connected before the DFF, amplified the average OFC power to 40mW which corresponds to peak power of pulses as high as 2W.

The spectral envelopes of OFC's are shown in Fig.2. Where curves **a**, **b** and **c** are the spectral envelopes of the original OFC, the amplified OFC, and the OFC after passing through the DFF, respectively. Though the gain curve of the fiber amplifier affected the shape of the OFC envelope as shown in curve **b**, the curve **c** shows that the envelope was extended to a span as large as 47THz with power larger than 1nW. This value corresponds to 8000 sidebands generation, and is about 7 times larger than the span of OFC obtained without DFF (curve **a**).



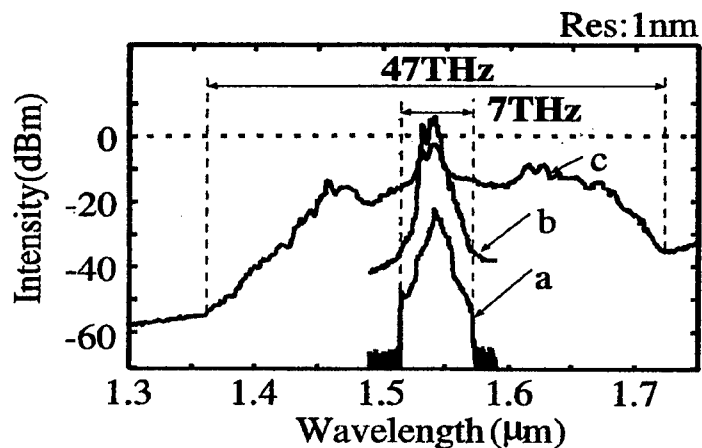
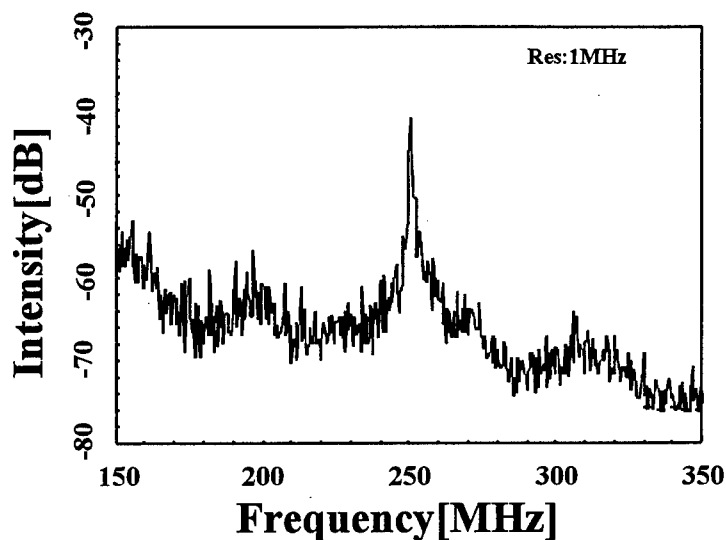


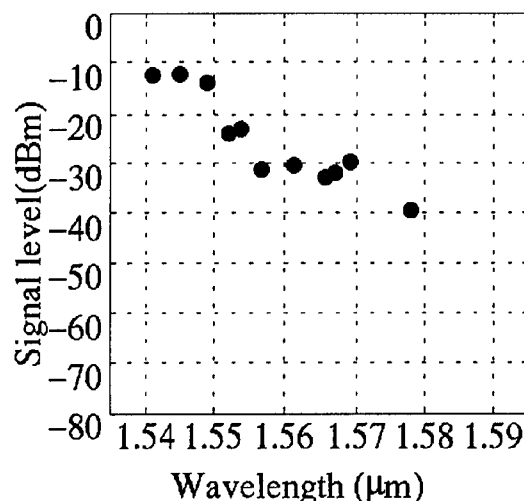
Fig.2  $\text{\AA}$  Spectral envelopes of OFC.  
a: original OFC.  
b: amplified OFC.  
c: OFC after passing through the DFF.

In order to confirm that the newly generated sideband can be used as a member of OFC, we tried to measure the beat signal between the sideband generated by SPM and a reference semiconductor laser. The narrow linewidth beat signal was successfully obtained as shown in Fig.3. In Fig.3(a), the difference frequency between the carrier frequency of the OFC and the reference laser was 4THz (This is the limit of the reference laser.), which is larger than the half span of the original OFC (i.e., 3.5THz) shown in curve a in Fig.2.

In summary, expansion of the OFC span was realized by applying self-phase-modulation, and the resulted span of the OFC was 47THz.



(a)



(b)

Fig.3  $\text{\AA}$  Beat signal. (a) Spectrum of the beat signal. (b) Signal level of the beat signal as a function of the wavelength of the reference laser.

The authors would like to thank Mr.M.Onishi, Sumitomo Electric Industries for the helpful discussions about optical fibers.

- [1] M.Kourogi, et.al. IEEE J.Quantum Electron., vol.29, pp.2693--2701, (1993).
- [2] M. Kourogi, et.al., IEEE Photon. Technol.Lett., in press, (1996).
- [3] T.Saitoh, et.al., IEEE Photon. Technol.Lett., vol.8, pp.1379--1381, (1996).
- [4] L.R.Brothers, et.al., Opt.Lett., vol.19, pp.245--247, (1994).
- [5] A.S.Bell, et.al., Opt. Lett., vol.20, pp.1435--1439, (1995).
- [6] T.Kobayashi, et.al., Appl. Phys. Lett., vol.21, pp.341--343, (1972).
- [7] K.Nakagawa, et.al., J.Opt. Soc. AAm. B, vol.13, pp.2708--2714, (1996).
- [8] T.Morioka, et.al., Electron. Lett., vol.30, pp.790--791, (1994).
- [9] Y.Kubo, et.al., ECOC, vol.21, pp.505--508, (1990).

# Single-mode operation and switching of a Fabry-Perot semiconductor laser with self-seeding from an external fiber grating by modulated optical injection

Shenping Li and Kam Tai Chan

Department of Electronic Engineering, The Chinese University of Hong Kong, New Territories, Hong Kong  
Tel: 852-26098457, Fax: 852-26035558, E-mail: spli@ee.cuhk.edu.hk.

Hao Ding

Shanghai Institute of Optics and Fine Mechanics, CAS, P. R. China.

The generation of single-mode short pulses is of great interest for many applications such as optical clock and wavelength sensitive sensors. A simple way to generate such pulses is self-seeding of gain-switched Fabry-Perot (FP) laser diodes (LD)[1-3], in which the gain switching is achieved by applying a RF electrical signal to the laser diode. However, in some applications such as sensors where any detrimental RF electromagnetic interference is forbidden, it is desirable that the high-frequency electrical signal source used for the gain switching can be located at some place far away from the optical source and the detector heads. Therefore, a remote modulation and switching scheme is preferred. In this work, we propose and demonstrate such a scheme in which a laser diode self-seeded by a fiber Bragg grating is gain-switched by a RF modulated optical injection through its pigtailed fiber.

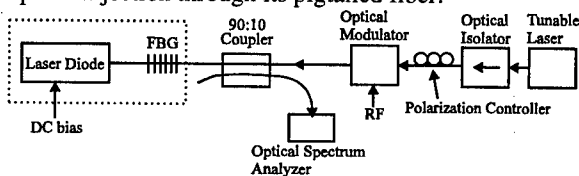


Fig.1. Experimental setup. FGB: fiber Bragg grating.

The experimental setup is shown in Fig.1. A modulated light generated by a continuous wavelength tunable laser and a LiNbO<sub>3</sub> modulator was injected into the cavity of a commercial FP LD with a cavity mode spacing of 1.5 nm through a 90:10 fiber coupler and a fiber Bragg grating (FBG). The Bragg wavelength of the grating is 3 nm shorter than the peak emission line ( $\lambda=1552$  nm) of the solitary LD. The center of the FBG was positioned about 3.57 m from the LD to give a fundamental cavity frequency of around 28.8 MHz. The wavelength of the injection light was detuned from the Bragg wavelength of the fiber grating so that it could pass through the grating with very small loss. The insertion loss of the modulator was minimized to about 5 dB by proper adjustment of its input polarization state. The output power of the tunable laser was set at 5 mw.

As shown in Fig.2(a), when the LD was DC biased above the threshold of the LD with the external grating (the threshold of the solitary LD is ~37 mA),

because the effective loss of the LD emission wavelength that falls inside the reflection band of the grating was reduced, this emission line became the dominant lasing mode. When a CW optical signal was injected into the LD, the intensities of all the emission

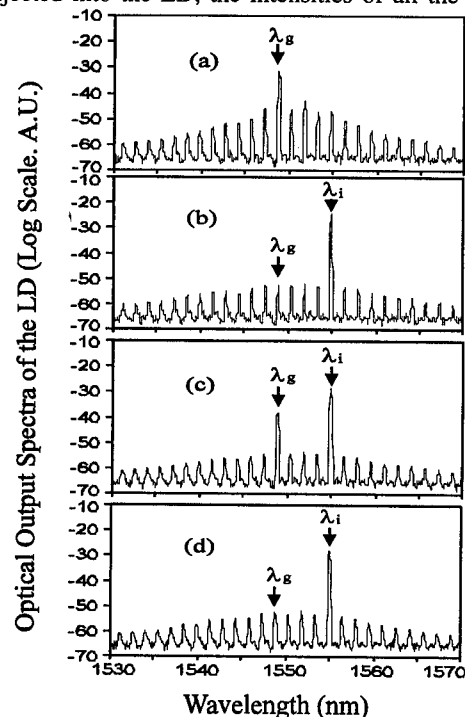


Fig.2. Emission spectra of the laser with an external fiber grating (a) without optical injection; (b) with CW optical injection; (c) with modulated optical injection at one of the harmonic frequencies ( $f=1271.33$  MHz) of the external cavity; (d) with modulated optical injection at a detuned frequency ( $f=1276$  MHz). The LD was biased at 37.4 mA.  $\lambda_g$  is the Bragg wavelength,  $\lambda_i$  is the injected wavelength.

lines decreased due to carrier depletion [4] as illustrated in Fig.2(b). If instead of CW injection, a sinusoidal modulating light with the same wavelength was injected into the LD, the gain of the LD would be modulated at the same frequency of the injected light but with a 180° phase shift due to carrier depletion. When the modulating frequency approached the fundamental or

any one of the harmonic frequencies of the external cavity, the feedback from the grating would be in phase and an enhanced self-seeding occurred. Therefore, as shown in Fig.2(c), the emission line closest to the Bragg wavelength was enhanced while the other emission lines were suppressed due to carrier depletion. When the modulation frequency was detuned from the fundamental or harmonic frequencies, all emission lines were suppressed as illustrated in Fig.2(d). Thus, this LD can be remotely switched by changing the repetition rate of the injection light pulses.

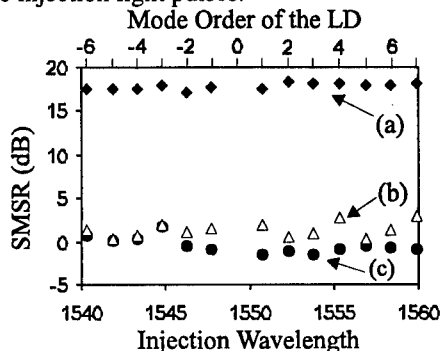


Fig.3. Sidemode suppression ratio as a function of the injection light wavelength, which was chosen to coincide with the center of the laser diode emission lines denoted by the mode order in the figure. The injected optical signal was modulated at (a) the 44th harmonic frequency (1271.33 MHz); (b) 5 MHz above the 44th harmonic frequency; (c) 5 MHz below the 44th harmonic frequency.

Fig.3 shows the sidemode suppression ratio (SMSR) as a function of the injection light wavelength which was exactly tuned to the emission lines of the LD Fabry-Perot modes. SMSR better than 17 dB have been achieved in the range from 1540.35 nm to 1559.9 nm, covering 13 mode spacings of the LD, when the injection light was modulated at the 44th harmonic frequency. After detuning the modulation frequency by  $\pm 5$  MHz, the SMSR decreased to below 5 dB due to the reduction of the dominant mode intensity and spectra resembling that of Fig.2(d) were observed. Similar results were also observed when the modulation frequency was varied from the 4th up to 110th harmonic frequencies. Fig.4 shows the effect of wavelength detuning on the resonance(on)/detuning(off) power ratio of the dominant mode. It was found that when the injection wavelength was detuned within  $\pm 0.6$  nm from the emission lines, switching and self-seeding could still be achieved with a power ratio better than 10 dB. It is believed that with an increase of the injected light power the wavelength detuning range for switching and self-seeding could be enhanced. The effect of detuning the modulation frequency on SMSR is illustrated in Fig.5. It was found an enhanced self-seeding range of about 3 MHz with SMSRs better than 15 dB could be achieved.

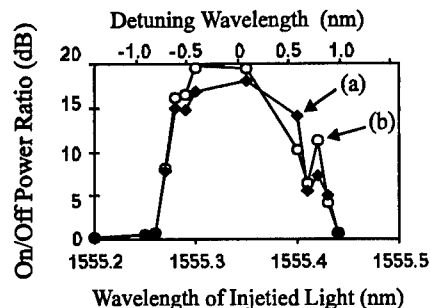


Fig.4. Power ratio of the dominant mode between resonance (ON state, 44th harmonic at 1271.33 MHz) and the detuned (OFF) state as a function of the wavelength of the injected light. (a) 5 MHz above resonance; (b) 5 MHz below resonance.

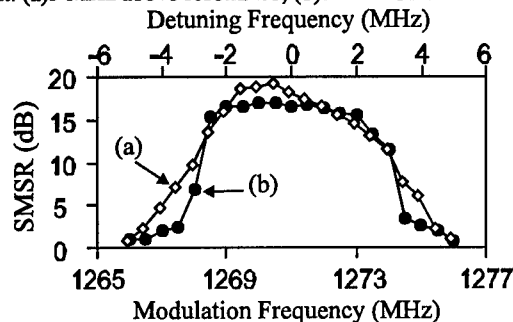


Fig.5. Sidemode suppression ratio as a function of the detuning frequency when the modulation frequency was around the 44th harmonic of the external cavity frequency and the wavelength of the injection light coincided with (a) the 4th order emission line ( $\lambda=1555.3$  nm); (b) the -4th order emission line ( $\lambda=1543.3$  nm).

In conclusion, we have demonstrated a remote scheme for achieving single-mode operation and switching in a gain-switched LD with self-seeding from an external fiber grating by optical pulse trains with a peak power of  $\sim 1$  mW and repetition rate varying from 115.2 MHz to 3168 MHz. Enhanced self-seeding ranges of 3 MHz with side-mode suppression ratios better than 15 dB were achieved. The switching of the LD was realized with the power ratio of an On/Off power ratio of the dominant mode as high as 19 dB. This laser may have considerable potential applications where any detrimental RF electromagnetic interference is forbidden.

## References:

1. Y. C. Lee and C. Shu, *IEEE Photonics Technol. Lett.* **7**, 275 (1995).
2. D. Huhse, M. Schell, W. Utz, D. Bimberg, J. A. R. Williams, L. Zhang, and I. Bennion, *Appl. Phys. Lett.* **69**, 2018 (1996).
3. H. Ding, S. P. Li, Z. J. Fang, and K. T. Chan, *IEEE Photonics Tech. Lett.*, in printing, 1997.
4. A. Jourdan, P. Doussiere, D. Leclerc, S. Gurib, F. Masetti, C. Joergensen, T. Durhuus, B. Mikkelsen, S. L. Danielsen, K. Stubjkaer, N. Vojdani, F. Ratovelomanana, A. Enard, M. Schilling, K. Wunstel, W. Idler, G. Morthier, R. Baets, and D. Chiaroni, *Fiber and Integrated Optics*, **15**, 1993 (1996).

## Application of semiconductor lasers to agile optical phased arrays

Richard L. Fork and Vahid R. Riasati  
University of Alabama in Huntsville  
Huntsville, AL 35899

We examine an array of coupled modelocked semiconductor lasers combining close packing density with very specifically controlled linear and nonlinear behavior. The application provides an optical analog of agile phased array microwave radar. A particular concern is pulse forming and true time delay for any array of short optical pulses. In essence this requires phaselocking the entire set of modes of an array of physically distinct microlaser oscillators into a quasi-stable state and then rapidly reconfiguring that phaselocking along a well controlled trajectory to a different, and also quasi-stable, state.

Mastery of techniques for generating and shaping pulses of a few optical cycles[1], reductions in the number of quanta required for laser action[2] fabrication of densely packed arrays of microlaser oscillators[2]; demonstration of a micro-optical delay line susceptible of integration with a microresonator[3]; demonstration of synchronization of pulse envelopes in physically distinct modelocked laser oscillators[4]; demonstration of phase locking of the optical carrier fields in physically distinct modelocked laser oscillators[4]; and a detailed analysis of nonlinearly coupled optical pulses propagating on coupled guides[5] suggest that the demanding task of constructing an agile optical phased array technology can be seriously addressed. This is essentially a modelocked time dependent version of a supermode strategy developed earlier by Yariv and coworkers[6].

We show in Fig. 1a simulation of a simple two pulse array and the trajectories of the pulses under controls that move the pulses, stabilize the pulse relation in local time, and then move the pulses again. By rapidly reconfigurable we mean that an array of pulses (produced in an array of microlasers, Fig. 1b), would be capable of being formed, configured into a quasi-stable state, and then reconfigured to a new quasi-stable state within a short time, e.g. order of a microsecond or less. The main point of this feature is to gain improved agility as compared to current methods of beam scanning and also to provide non-mechanical beam steering. Non-mechanical scanning is particularly useful, e.g., for small spacecraft where inertial requirements favor non-mechanical controls. Special needs, such as separate control of group and phase delay, lengthening of microresonators, and avoidance of traditional phaselocking strategies are discussed. The task is very demanding; however, the recent advances, experiments, and simulations are encouraging.

### References

1. R.L. Fork, C.H. Brito Cruz, P.C. Becker, and C.V. Shank, "Compression of optical pulses to six femtoseconds by using cubic phase compensation", *Optics Letters* **12**, 483-5 (1987).
2. D. L. Huffaker, L. A. Graham, and D.G. Deppe, "Fabrication of High-Packing-Density Vertical Cavity Surface-Emitting Laser Arrays Using Selective Oxidation", *IEEE Photonics Technology Letters*, **8**, 596-8 (1996).
3. M. Scalora, R. J. Flynn, S. B. Reinhardt, R. L. Fork, M. J. Bloemer, M. D. Tocci, C. M. Bowden, H.S. Ledbetter, J. M. Bendickson, J. P. Dowling, and R. P. Leavitt, "Ultrashort pulse propagation at the photonic band edge: Large tunable group delay with minimal distortion and loss", *Physical Review E* **54**, R1078-R1081 (1996).
4. Song Wu, Sandra L. Smith, and Richard L. Fork, "Kerr-lens-mediated dynamics of two nonlinearly coupled mode-locked laser oscillators", *Optics Letters* **17**, 276-8 (1992). Also the PhD thesis by Wu.
5. S.L. Doty, J.W. Haus, Y.J. Oh and R.L. Fork, "Soliton interactions on dual core fibers", *Physical Review* **51E**, 709-717 (1995).
6. E. Kapon, J. Katz, and A. Yariv, "Supermode analysis of phase-locked arrays of semiconductor lasers", *Optics Letters* **10**, 125-127 (1984)

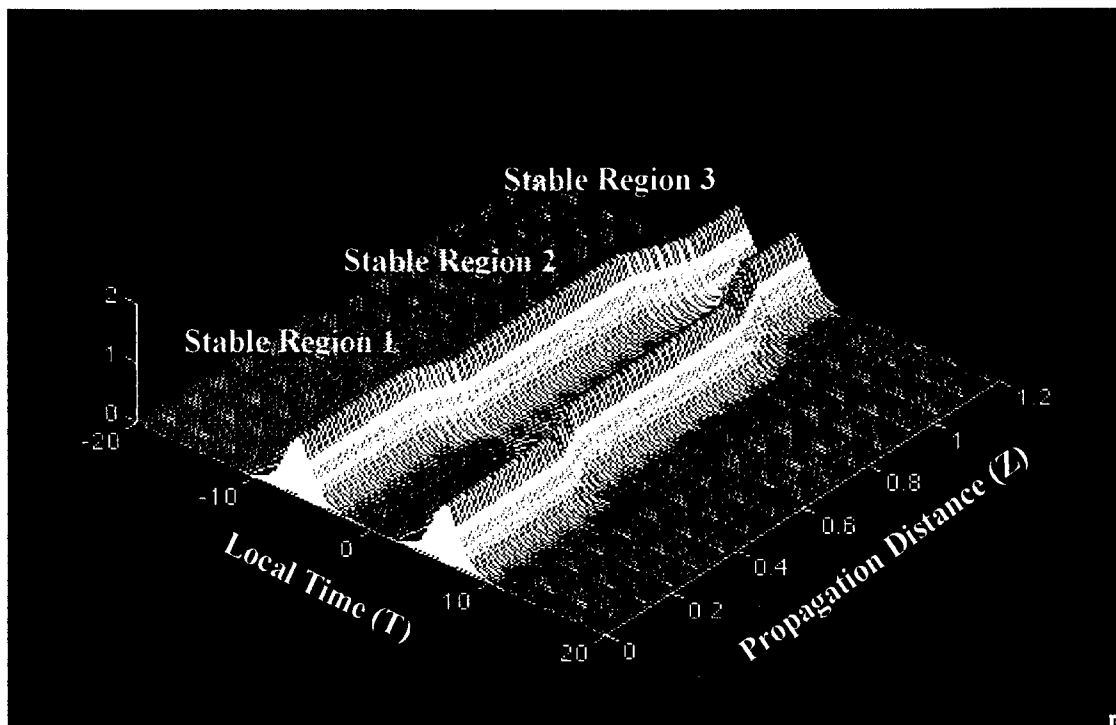


Fig. 1a. Perspective view of two pulses in two separate, but coupled, modelocked laser oscillators exhibiting controlled nonlinear dynamics within the local time of the two pulse array.

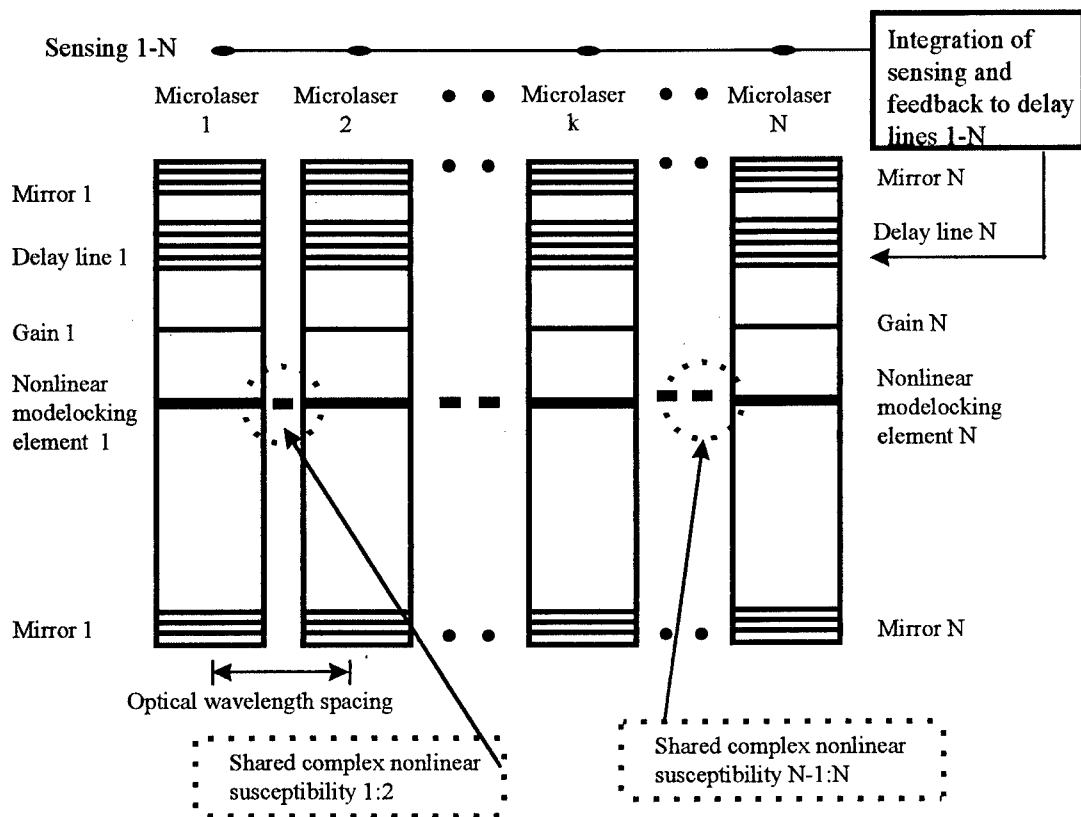


Fig. 1b. Array of coupled modelocked microlasers using feedback controlled group and phase delay in combination with a specifically designed shared complex nonlinear susceptibility.

## COMPOUND CAVITY SEMICONDUCTOR LASER (CCSL)

S. Kinugawa, T. Saito, S. Mattori, K. Miyagi, A. Taniguchi

Research Laboratory of ANRITSU CORPORATION

1800 Onna, Atsugi, Kanagawa, 243 Japan

### Introduction:

An external cavity laser is very attractive due to its narrow oscillation line width and wide wavelength tuning range<sup>1</sup>. Lately, to meet the rapid increase in demand, wide-band WDM optical communication networks<sup>2</sup> are required. A wavelength tunable laser using an external cavity is useful for measuring components of WDM systems, because the system needs over several tens nm wavelength range. However, use of this laser in this field is restricted by mode jumping and wavelength drift caused by instability of the optical cavity constructed from mechanical parts. Considerable work has been devoted to avoid this wavelength instability<sup>3,4</sup>, but sufficient stability has not been obtained yet.

This paper reports a Compound Cavity Semiconductor Laser (CCSL) with a feedback cavity added to the external cavity laser. This scheme improves the selectivity of the external cavity mode. As a result, the CCSL has long-term wavelength stability and continuous wavelength tuning without suffering from mechanical instability.

### Experimental setup:

The configuration of the CCSL is shown in Figure 1. The external-cavity laser consists of a 1.55- $\mu\text{m}$  BH semiconductor laser and a 1100/mm diffraction grating in a Littrow configuration. The facet of the semiconductor laser opposite the diffraction grating is coated with anti-reflective film. The output laser light is supplied by a mirror (30% reflectivity) within the external cavity. The feedback cavity is closed by the feedback mirror and the other facet (coated with low reflection (LR) film=10%) of the semiconductor laser. The feedback mirror is coated for a reflection >97% and is controlled by a piezoelectric ceramic. The length of the external cavity and feedback cavity is 40 mm and 4 mm. The two cavities have free-spectral ranges (FSR) equal to 30 pm and 200 pm, respectively. The pass-band of the diffraction grating is 200 pm. Figure 2 shows the relative positions of the gain profiles. One mode of the external cavity can not be selected by the diffraction grating only, because a few modes fall within the passband of the diffraction grating and the mechanical movement of the diffraction grating lacks repeatability. Meanwhile, in the CCSL, one external cavity mode is selected not by the passband of the diffraction grating, but by a feedback cavity mode extracted from the feedback spectrum with the passband of the diffraction grating. Therefore, the CCSL has less strict requirements for the passband, mechanical repeatability

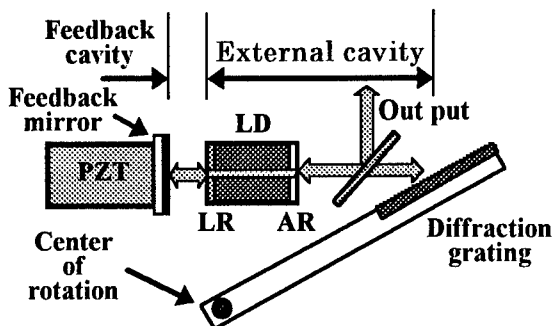


Fig. 1 Configuration of CCSL

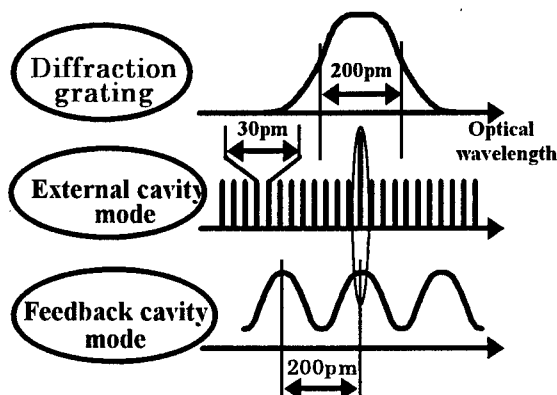


Fig. 2 Relative position of the gain profile

and stability of the diffraction grating.

#### Result:

Figure 3 shows the characteristic wavelength change by rotating the diffraction grating with a fixed feedback mirror. In this case, the wavelength change is stepwise with a periodic 200-pm wavelength jump. This feature can be explained by selection of feedback cavity mode in sequence according to the rotation of the diffraction grating. The wavelength change of about 200-pm within a single step is caused by wavelength pulling of the diffraction grating. This wavelength pulling occurs because the feedback power is not strong enough to completely dominate the oscillating wavelength with the feedback cavity. Therefore, it should be suppressed by using LR to lower reflectivity. Figure 4 shows the wavelength change caused by moving the feedback mirror using a voltage-controlled piezoelectric ceramic with a fixed diffraction grating. We confirmed that the external cavity mode within the region of the diffraction grating passband could be selected by the feedback cavity. In this experiment, six external-cavity modes spaced at 30 pm were selected within 200 pm. Moreover, we performed an experiment on continuous-wavelength tuning by moving both the feedback mirror and the diffraction grating synchronously. Figure 5 compares the wavelength-sweep characteristics of a conventional external cavity laser (a) and the CCSL (b). It clearly shows that the external cavity laser is unstable in several points, but the CCSL exhibits continuous tuning over 10 nm smoothly (limited by the movement range of the piezoelectric ceramic). Consequently, we confirmed that the CCSL is superior in stable continuous wavelength tuning.

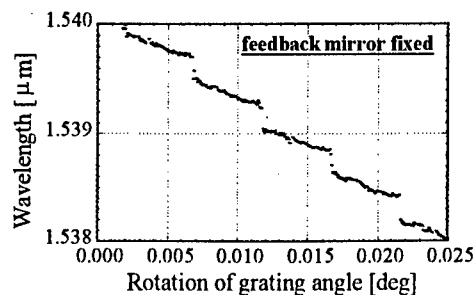


Fig. 3 Wavelength change with diffraction grating

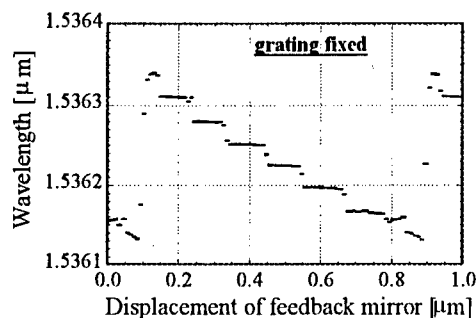
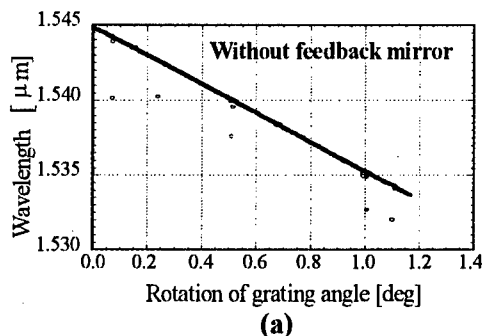
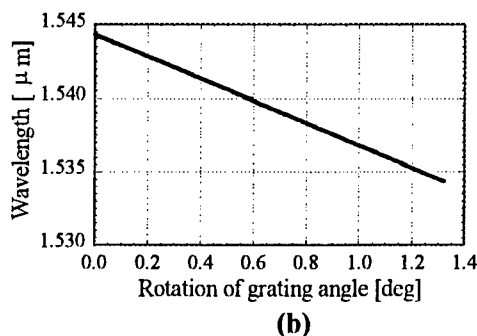


Fig. 4 Wavelength change with feedback mirror



(a)



(b)

Fig. 5 Tuning curves of lasing wavelength  
(a) external cavity laser (b) CCSL

#### References:

1. F. FAVER et al., : 82nm of continuous tunability for an external cavity semiconductor-laser, *Electron. Lett.*, 27, pp. 183-184, 1991
2. R.W.TKACH,et al., : One-third terabit/s transmission through 150km dispersion-managed fiber, *Proceedings of ECOC 1995*, vol.4 (PD), Sept. pp.45-48,1995
3. S. NAUTOV, et al., : A 670nm external-cavity single mode diode laser continuously tunable over 18GHz range, *Optics Communications* 107) pp.83-87, 1994
4. B. MAISENBACHER, et al., : Tunable laser sources for optical amplifier testing, *Hewlett-Packard Journal*, Feb., 1993

## A Diode Laser With An External High-Q Microcavity

V.V.Vasil'ev, V.L.Velichansky, A.V.Yarovitsky

P.N.Lebedev Physics Institute, Leninsky pr.53, 117924, Moscow, Russia

L.Hollberg,

National Institute of Standards and Technology, Boulder, CO, 80303, USA

M.L.Gorodetsky, V.S.Ilchenko

M.V.Lomonosov Moscow State University, Moscow, Russia

The applications of diode lasers (DL) have recently become much wider because methods for linewidth narrowing have been developed. One of the most effective methods relies on the optical feedback. Two modifications providing the same degree of narrowing are known: 1) an increase of the cavity Q-factor by increasing the cavity length without a significant change of the number of passes (strong coupling to an external cavity [1]); 2) weak coupling to an external high-Q multipass cavity. In the latter case a confocal or a fibre ring interferometers are used [2,3]. Unfortunately the linewidth is decreased at the expense of the increase of laser dimensions.

We report on using a fused silica microsphere with the diameter of 370  $\mu\text{m}$  as an external high-Q cavity. The 'whispering gallery' modes of such a sphere reveal Q factor in excess of  $10^9$  [4]. Light was coupled in and out of a sphere with the aid of a coupling prism, and the degree of coupling was varied by fine control of the gap between the prism and the sphere. The internal losses of the WG mode are very low and its Q factor depends strongly on coupling. For weak coupling when the linewidth of the WG mode ceases to depend on the degree of coupling the Q factor was  $10^9$  as measured with an independent reference laser.

The radiation of a LTO24MDO diode laser (with a solitary linewidth of about 20 MHz, 780 nm, 20 mW) was collimated with NA = 0.65 objective lens, sent to the optical isolator with controlled suppression of the feedback, and was focused with another objective lens on the internal surface of the prism in the region closest to the sphere. The resonance coupling to the whispering gallery mode was detected as a dip in the reflected intensity (frustrated total internal reflection). The counterpropagating wave needed for optical feedback was generated in a sphere via Rayleigh backscattering [5,6].



When the feedback was blocked by the isolator and the frequency of the solitary laser (operating in a single longitudinal mode) was tuned by the current, a 20 MHz resonance was displayed as a dip in the reflected intensity. Its width was determined by the linewidth of the laser. With a decreasing of the isolation we observed dramatic increase of the 'width of resonance' corresponding to the locking of the laser frequency to a WG mode. The ratio of the tuning rates without - and with feedback,  $S = (dv_0/dI)/(dv_{ext}/dI)$ , was found to be greater than 100 ( $I$  is laser current,  $v_0$  - solitary laser frequency,  $v_{ext}$  - frequency of the laser coupled to an external microsphere). Thus, for the white spectral distribution of the phase noise we might expect  $(1+S)^2$  decrease of the laser linewidth, i.e. it should be less than 2 kHz.[ 1]

This locking was found to be phase sensitive and a standard technique of the DL - sphere distance stabilization [2,3] was applied to provide reliable regime and direct linewidth measurements by heterodyne technique. An extended cavity laser was used as a local oscillator. The beat note width was about 100 kHz, however the measurements were made without any special protection against vibration and acoustic perturbations, and the spectrum was additionally broadened by the technical noise. To decrease it we locked two independent solitary lasers to different modes of the same sphere by using the same coupling lens and prism. The cross talking was suppressed by exciting two orthogonally polarized WG modes. Some of the technical noise was then correlated and the width of the beat note spectrum was decreased to 20 kHz, quite close to the estimate given above. In our experiments we made no attempt to utilize small dimensions of the sphere in order to reduce the dimensions of the whole system. In the report we will consider possible techniques of direct coupling of a laser and a microsphere. This approach can provide very small lasers with extremely high coherence.

#### References

- [1] V.L.Velichansky, A.S.Zibrov, V.S. Kargopol'tsev et al, Sov. Techn. Phys. Lett. v.4, 438 (1978); E.M. Belenov, V.L.Velichansky, A.S.Zibrov, et al, Sov J. Quantum Electron, v.13, 792 (1983)
- [2] B.Dahmany, L.Hollberg, R.Drullinger, Opt. Letts., v.12, 876, (1987); P.Laurent , A.Clairon, C.Breant, IEEE J. Quantum Electron., v.25, 1131 (1989).
- [3] A.G.Bulushev, E.M.Dianov, A.V.Kuznetsov, O.G.Okhotnikov, Sov J. Quantum Electron, v.19, 479 (1989).
- [4] V.B.Braginsky, M.L.Gorodetsky, V.S.Ilchenko Phys. Lett. A 137, 393 (1989)
- [5] V.S.Ilchenko, M.L.Gorodetsky, Laser Phys. v.2, 1004 (1992)
- [6] D.S.Weiss, V. Sandoghar, J.Hare, et al, Opt.lett. v.20, 1835 (1995)

## Type-II Quantum Well and Interband Cascade Lasers for the Mid-IR

J. R. Meyer, C. L. Felix, and I. Vurgaftman  
Code 5613, Naval Research Laboratory, Washington, DC 20375

C.-H. Lin, B. H. Yang, R. Q. Yang, and S.-S. Pei  
Space Vacuum Epitaxy Center, University of Houston, Houston, TX 77204

Since mid-IR (3-5  $\mu\text{m}$ ) lasers tend to be bulky, inefficient, and complex at present, compact, reliable semiconductor sources will find wide use once their levels of performance become adequate. For example, there is considerable demand associated with chemical sensing for pollution monitoring, leak detection, chemical process control, *etc.*, since many molecular absorption lines (e.g.,  $\text{CO}_2$ ,  $\text{CO}$ ,  $\text{CH}_4$ ,  $\text{N}_2\text{O}$ ,  $\text{HCN}$ ,  $\text{NH}_3$ ) are 2-5 orders of magnitude stronger in the mid-IR than in the near-IR where efficient diode lasers are already available. High-power mid-IR sources are also needed for infrared countermeasures against heat-seeking missiles, IR illumination, and laser surgery. While mid-IR semiconductor lasers have progressed rapidly in recent years, none of the devices reported to date have come close to meeting the requirement for high cw output powers at ambient or thermoelectric cooler temperatures ( $\geq 200$  K). However, our modeling projects that this objective should be achievable using novel type-II quantum well lasers (T2QWLs) and type-II interband cascade lasers (T2ICLs). Here we report simulation results, along with promising preliminary experimental data.

The T2QWL design with 4 constituents in each period of the active region combines the advantages of excellent carrier confinement, large optical matrix elements despite the spatially-indirect band alignment, the potential for significant suppression of Auger losses, and a 2D density-of-states for both electrons and holes. Initial optically-pumped T2QWLs have displayed ambient-temperature operation out to 4.5  $\mu\text{m}$ , and  $T_{\text{max}} = 350$  K for  $\lambda = 3.2$   $\mu\text{m}$  is the highest reported to date for any semiconductor laser emitting beyond 2.5  $\mu\text{m}$ . Figure 1 shows that for pulsed operation, peak output powers exceeding 1 W are obtained at  $\lambda \approx 4.5$   $\mu\text{m}$  even at  $T_{\text{op}}$  up to 260 K. We have quite recently demonstrated electrically-pumped T2QWLs, with  $T_{\text{max}}$  up to 245 K at 2.8  $\mu\text{m}$  and 185 K at 3.5  $\mu\text{m}$ .

Because of the small energy of each emitted photon, bipolar mid-IR diode lasers may never achieve cw output powers approaching 1 W. However, the multi-stage T2ICL is projected to produce much higher powers due to electron recycling, *i.e.*, the emission of more than one photon per injected electron, while eliminating the non-radiative phonon relaxation path of the intersubband-based quantum cascade laser. From the theoretical L-I curves in Fig. 2, note that the T2ICL is expected to have a much lower threshold current, higher operating temperature, and higher cw output power ( $> 0.5$  W at 300 K) than the bipolar T2QWL. Preliminary experimental demonstration of a T2ICL has recently been reported.<sup>1</sup>

1. C.-H. Lin, R. Q. Yang, D. Zhang, S. J. Murry, S.-S. Pei, A. A. Allerman, and S. R. Kurtz, submitted to Electron. Lett.

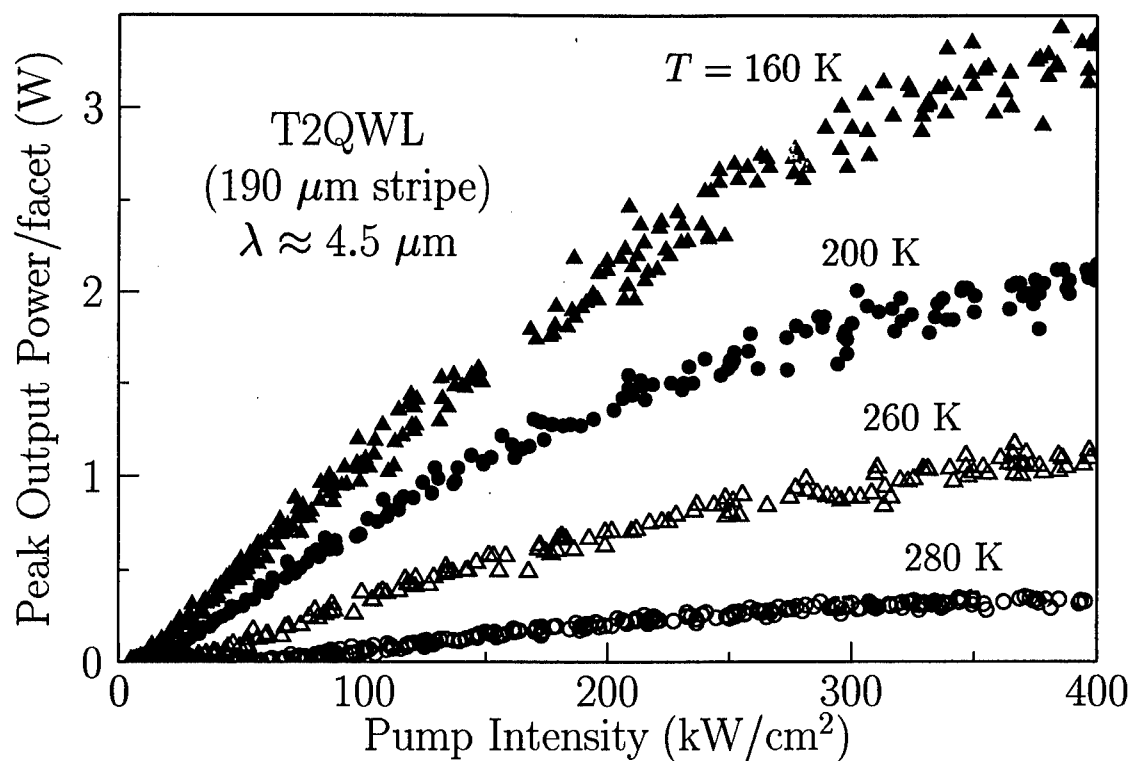


Figure 1. Peak output power per facet vs optical pump intensity at various temperatures.

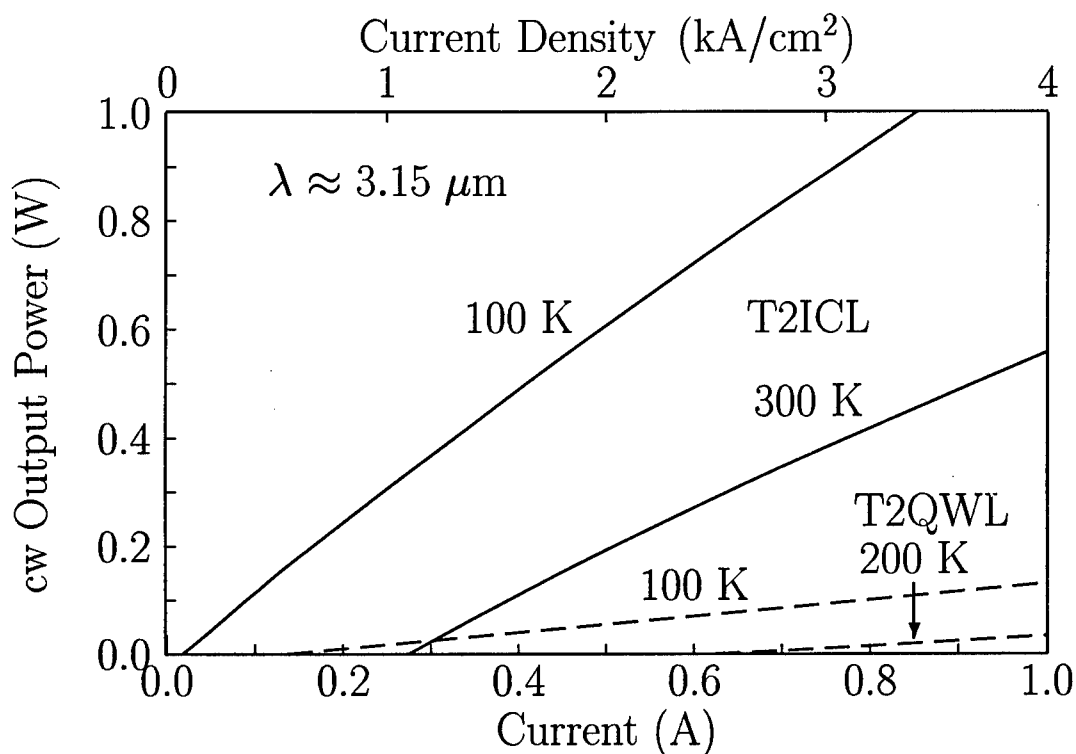


Figure 2. Theoretical cw output power per facet vs injected current density for a T2ICL and a T2QWL. Cavity lengths are 500 μm and stripe widths are 50 μm.

**Tunable sources and quantum cascade lasers in the mid-IR**

*Claire Gmachl, Jérôme Faist, Carlo Sirtori, Federico Capasso, Deborah L. Sivco, James N. Baillargeon, Albert L. Hutchinson, and Alfred Y. Cho*

Bell Laboratories, Lucent Technologies  
700 Mountain Avenue, Murray Hill, NJ 07974

High power, room temperature operation of a quantum cascade (QC) laser emitting at  $\lambda \sim 5 \mu\text{m}$  has recently been reported. This laser is based on a vertical transition and is optimized for high temperature operation by a design that reduces thermal backfilling and enhances injection efficiency – through a funnel injector and a so-called ‘three well’ active region.

The design further incorporates a molecular beam epitaxy grown InP top cladding which exhibits a much lower thermal resistance than the previously used ternary cladding material and significantly improves the high temperature performance of the laser devices. In pulsed operation, maximum peak output powers around 200 mW at 300 K and 100 mW at 320 K are observed. The devices are further tested at and above room temperature with a comparatively large (3.3 %) duty cycle. The high peak powers then translate into average powers in the 2-10 mW range. The devices are also operated in continuous wave (cw) with a maximum operating temperature of 140 K [1]. This is the first demonstration of high power, room-temperature operation of a mid-infrared semiconductor source.

Room temperature operation of a QC laser has also been obtained in devices operating in the second atmospheric window namely at  $\lambda \sim 8.5 \mu\text{m}$  [2]. The design is based on a ‘two well’ vertical active region with emphasis on optimized resonant tunneling injection. Pulsed operation displays a peak optical power of 15mW at 300K. Continuous wave operation is obtained up to 110 K. QC lasers with emission wavelengths as long as  $11.2 \mu\text{m}$  have been designed and tested [3], yielding a peak power of 50 mW at 110 K under pulsed operation and 7 mW at 10K in cw. This demonstrates that the QC laser is a powerful light source in the mid-IR with widely taylorable emission wavelength, by suitable quantum design from  $\sim 4$  to  $11 \mu\text{m}$  using the same hetero-structure material.

Recent developments as the design and fabrication of QC distributed-feed-back (QC-DFB) lasers are reported. Adding the DFB feature to QC lasers emitting at 5 and  $8 \mu\text{m}$  yields stable and continuously tunable single-mode operation up to room temperature. First results show a single-mode tuning range of  $\sim 100 \text{ nm}$  over a temperature range from 77 to 300 K for a QC-DFB emitting at  $8 \mu\text{m}$ .

- [1] J. Faist, F. Capasso, C. Sirtori, D. L. Sivco, J. N. Baillargeon, A. L. Hutchinson, S. N. G. Chu, and A. Y. Cho, “High power Mid-Infrared ( $\lambda \sim 5 \mu\text{m}$ ) quantum cascade lasers operating above room temperature”, *Appl. Phys. Lett.*, vol. **68**, 3680 - 3682, 1996
- [2] C. Sirtori, J. Faist, F. Capasso, D. L. Sivco, A. L. Hutchinson, and A. Y. Cho, “Mid-Infrared ( $8.5 \mu\text{m}$ ) Semiconductor Lasers Operating above Room Temperature”, *accepted in IEEE Photon. Techn. Lett.*
- [3] C. Sirtori, J. Faist, F. Capasso, D. L. Sivco, A. L. Hutchinson, and A. Y. Cho, “Pulsed and Continuous-Wave Operation of Long Wavelength Infrared ( $\lambda = 9.3 \mu\text{m}$ ) Quantum Cascade Lasers”, *IEEE J. Quantum Electron.*, vol. **QE 33**, pp. 89 - 93, 1997; C. Sirtori, J. Faist, F. Capasso, D. L. Sivco, A. L. Hutchinson, and A. Y. Cho, “Long wavelength infrared ( $\lambda \sim 11 \mu\text{m}$ ) quantum cascade lasers”, *Appl. Phys. Lett.*, vol. **69**, 2810 - 2812, 1996

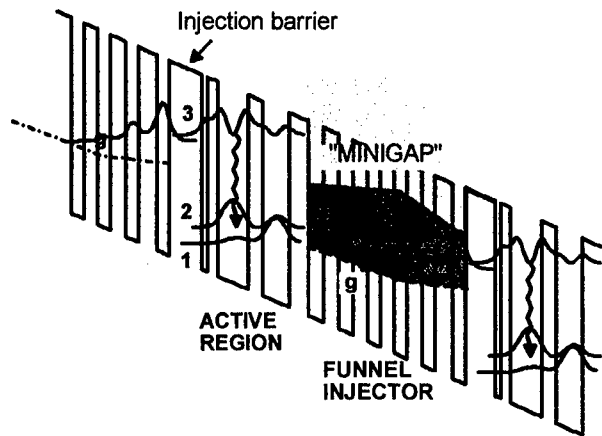


**Fig. 1:** Schematic conduction band diagram (partial) at threshold electric field of the active region of a QC laser emitting at  $\sim 5 \mu\text{m}$ . The wavy arrow indicates the laser transition. The moduli squared of the relevant wavefunctions are shown. The area denoted “miniband” represents the energy range and spatial extension of band-like states in the funnel injector. This superlattice is also designed to create a “minigap” preventing carriers from escape from level 3. The layer sequence of one period of the  $\text{Al}_{0.48}\text{In}_{0.52}\text{As}/\text{Ga}_{0.47}\text{In}_{0.53}\text{As}$  structure, in nanometers, left to right starting from the injection barrier is (5.0/0.9), (1.5/4.7), (2.2/4.0), (3.0/2.3), (2.3/2.2), (2.2/2.0), (2.0/2.0), (2.3/1.9), (2.8/1.9). [1]

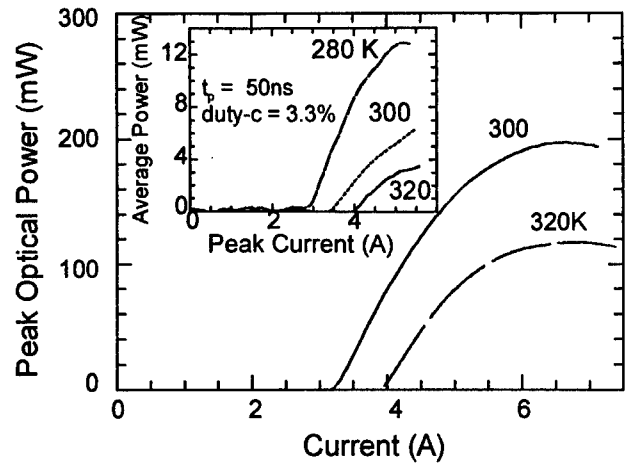


**Fig. 2:** Main graph: Collected pulsed optical power from a single facet versus injection current for the QC-laser of figure 1. The heat sink temperatures are 300 and 320 K. The collection efficiency is estimated to  $\sim 70\%$ . The device is 2.9 mm long and  $14 \mu\text{m}$  wide. Inset: Average power as a function of peak current for a device driven at high duty-cycle. The pulse width is 50 ns and the repetition rate 670 kHz. The heat sink temperatures are indicated as 280, 300 and 320 K.

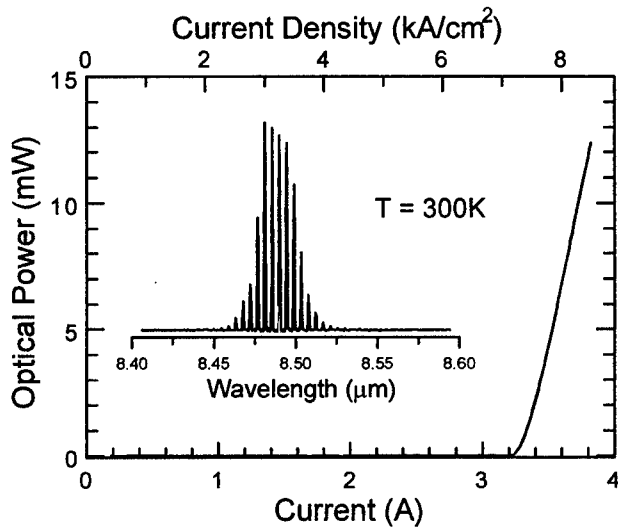


**Fig. 3:** Main graph: Collected peak optical power from a single facet versus drive current for a QC-laser emitting at  $\sim 8.5 \mu\text{m}$ . Inset: High resolution spectrum of the device at 3.6 A.

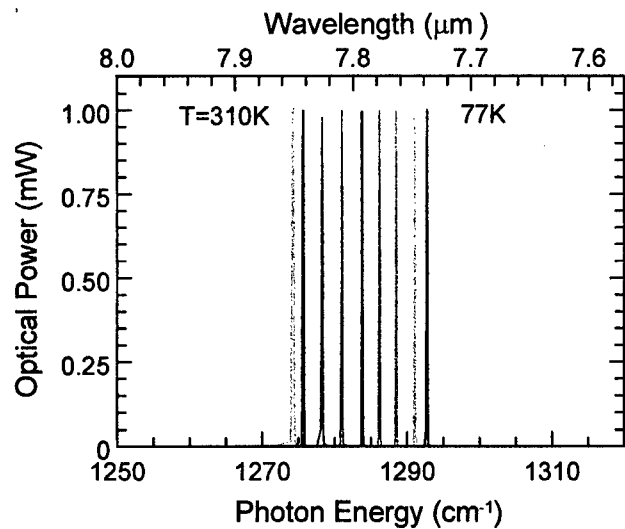


**Fig. 4:** High resolution spectra (9 spectra overlaid) of a QC-DFB laser emitting around  $7.8 \mu\text{m}$ . The single-mode emission is tuned with heat-sink temperature (77 K to 310 K).

## Measurement of $^{13}\text{CH}_4/^{12}\text{CH}_4$ ratios in air using diode-pumped $3.3\ \mu\text{m}$ difference-frequency generation in PPLN

<sup>1</sup>S. Waltman, <sup>2</sup>K. P. Petrov, <sup>3</sup>E. J. Dlugokencky, <sup>4</sup>M. Arbore, <sup>4</sup>M. M. Fejer,  
<sup>2</sup>F. K. Tittel, and <sup>1</sup>L. W. Hollberg

<sup>1</sup>National Institute of Standards and Technology, Boulder, CO 80303-3337

<sup>2</sup>Rice Quantum Institute, Rice University, Houston, TX 77251-1892

<sup>3</sup>National Oceanic and Atmospheric Administration, Boulder, CO 80303-3337

<sup>4</sup>Edward L. Ginzton Laboratory, Stanford University, Stanford, CA 94305-4085

Methane has a significant effect on the radiative balance of the troposphere and stratosphere because it has a strong absorption at  $7.66\ \mu\text{m}$  where carbon dioxide and water absorb only weakly. Accurate measurements of the abundance of methane are thus of considerable interest to climatologists.<sup>1</sup> Previously, we demonstrated a spectrometer capable of producing fast, accurate measurements of the methane mixing ratios in natural air samples. This system demonstrated a relative accuracy of less than  $10^{-9}$  mol/mol (1 ppb by volume),<sup>2</sup> which is comparable to what can be achieved using non-spectroscopic methods. This system employed bulk periodically poled lithium niobate pumped by a solitary diode laser at 808 nm and a diode-pumped monolithic ring Nd:YAG laser at 1064 nm, and a multi-pass absorption cell with 18 m path length.

We generated approximately 1  $\mu\text{W}$  of infrared radiation at  $3019\ \text{cm}^{-1}$  using 21 mW from a grating-tuned extended-cavity diode laser at 806 nm and 382 mW from a diode-laser-pumped Nd:YAG laser at 1064 nm to pump a periodically poled lithium niobate crystal. At this wavelength, a coincidence between the Q(1) line of  $^{12}\text{CH}_4$  and the R(0) line of  $^{13}\text{CH}_4$  allows both lines to be observed in a single 10 GHz frequency scan of the difference frequency and avoids significant interference from other lines. The difference frequency output is monitored by a liquid- $\text{N}_2$ -cooled InSb detector and sent through a commercial multi-pass cell with an 18 m path length to a second liquid- $\text{N}_2$ -cooled InSb detector. The signal from the first detector is used to stabilize the amplitude of the generated light by controlling the power of the Nd:YAG beam with an acousto-optic modulator. Background interference fringes from the multi-pass cell are reduced by vibrating it with an electromagnetic actuator at the frequency of a mechanical resonance in the mirror mounts.

A typical spectral trace is shown in Figure 1. The cell contained a sample of natural air at a

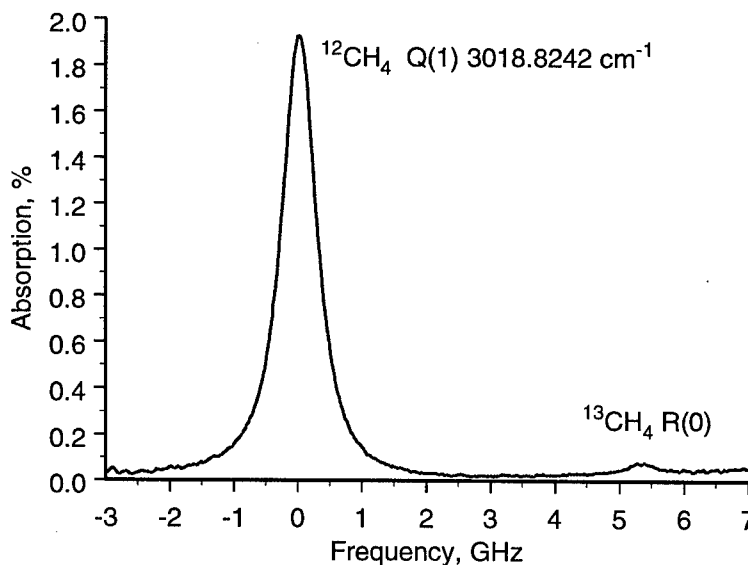


Figure 1-Direct absorption spectrum of methane in natural air at 13 kPa (100 Torr) in a multi-pass cell with 18 m path length.

pressure of 13 kPa (100 Torr). Total measurement time was 60 s, during which 1000 sweeps were averaged resulting in a noise bandwidth of 1.6 Hz. The peak CH<sub>4</sub> absorption amplitudes were determined by a nonlinear least squares fit to Voigt line profiles. The <sup>13</sup>CH<sub>4</sub>/<sup>12</sup>CH<sub>4</sub> ratios were then computed using Hitran catalog values for the line strengths.<sup>3</sup>

The absorbance ratio for the trace shown in Figure 1 is  $54 \pm 3$ , which yields a concentration ratio of  $95 \pm 5$ . This corresponds to an isotope value relative to the PeeDee belemnite (PDB) standard of  $-66 \pm 44$  per mil. The expected isotope value is  $-47 \pm 2$  per mil. The accuracy of our measurement is limited by the signal-to-noise ratio (SNR) in the acquired spectra, and the SNR is limited primarily by detector noise.

Once waveguide PPLN crystals become available, it should be simple to generate enough 3  $\mu$ m power to have shot noise be the dominant limit, even with a longer path length. It should be possible to improve the accuracy of this measurement by an order of magnitude before interference fringes from scattered light in the multi-pass cell become the dominant limit.

Our accuracy for measuring the isotope value relative to PDB of  $\pm 44$  per mil is roughly comparable to that achieved by Bergamaschi, Schupp, and Harris using a lead-salt tunable diode-laser absorption spectrometer.<sup>4</sup> They demonstrated an accuracy of  $\pm 0.5$  per mil on samples which had 50 ppm CH<sub>4</sub>. Our system would have an accuracy of  $\pm 1.4$  per mil when analyzing sample of that concentration. Using sample processing and concentration and an isotope ratio mass spectrometer, Stevens and Rust achieved an accuracy of  $\pm 0.06$  per mil.<sup>5</sup> We do not envision being able to achieve that kind of accuracy for methane carbon isotope measurements without concentrating the gas sample.

Because this system is compact, uses all solid-state lasers, and could be made transportable, it has potential applications for field measurements where rapid, nondestructive concentration and isotope ratio measurements are needed. Even though it is not competitive with state-of-the-art nonoptical instruments, this system can measure <sup>13</sup>CH<sub>4</sub>/<sup>12</sup>CH<sub>4</sub> ratios at CH<sub>4</sub> concentrations of only  $1.6 \cdot 10^{-6}$  mol/mol without gas processing.

## References

1. E. J. Dlugokencky, L. P. Steele, P. M. Lang, K. A. Masarie, "The growth rate and distribution of atmospheric methane," *J. Geophys. Res.* **99**, 17021 (1994).
2. K. P. Petrov, S. Waltman, E. J. Dlugokencky, M. Arbore, M. M. Fejer, F. K. Tittel, and L. W. Hollberg, "Precise measurement of methane in air using diode-pumped 3.4  $\mu$ m difference-frequency generation in PPLN," *Applied Physics B*, **64** No. 5 (in press) (1997).
3. L. S. Rothman, et al., "The HITRAN molecular database: editions of 1991 and 1992," *J. Quant. Spectrosc. Radiat. Transf. (UK)* **48**, 469 (1992).
4. P. Bergamaschi, M. Schupp, G. Harris, "High precision direct measurements of <sup>13</sup>CH<sub>4</sub>/<sup>12</sup>CH<sub>4</sub> and <sup>12</sup>CH<sub>3</sub>D/<sup>12</sup>CH<sub>4</sub> ratios in atmospheric methane sources by means of a long-path tunable diode laser absorption spectrometer," *Appl. Opt.* **33**, 7704-7716 (1994).
5. C. M. Stevens, F. E. Rust, "The carbon isotopic composition of atmospheric methane," *J. Geophys. Res.* **87** 4879 (1982).

## Monitoring Trace Gases with Antimonide Diode Lasers

Daniel B. Oh and Alan C. Stanton

Southwest Sciences, Inc.  
1570 Pacheco St., Suite E-11  
Santa Fe, New Mexico 87505

### Abstract

Trace gas monitoring with antimonide diode lasers combined with high sensitivity absorption detection techniques is described. Our work in progress targets NO, CO, H<sub>2</sub>O and H<sub>2</sub>CO detection under reduced pressure sampling conditions.

### Summary

Semiconductor diode lasers, including lead salt lasers operating at wavelengths beyond 3  $\mu\text{m}$  and InGaAlP, GaAlAs, or InGaAsP lasers operating at wavelengths less than 2  $\mu\text{m}$ , have been used extensively for measurement of trace gases by optical absorption.<sup>1</sup> The inherently narrow linewidths of these light sources, combined with high sensitivity detection techniques such as wavelength modulation spectroscopy<sup>2-3</sup> or frequency modulation spectroscopy,<sup>4-5</sup> provides a capability for the highly selective and sensitive measurement of a wide range of species important in atmospheric and combustion research, environmental monitoring, and process monitoring. The lead salt lasers, accessing vibrational fundamental bands, generally permit the highest detection sensitivity. However, development of commercial diode laser-based instrumentation for environmental or industrial applications has focused on the use of the near-infrared wavelength devices due to their characteristics of room temperature operation, compatibility with silica optical fibers, and availability of single mode operating devices.

Several research groups have been pursuing the development of semiconductor lasers with operating wavelengths in the 2 to 4  $\mu\text{m}$  range based on III-V antimonide materials systems.<sup>6-10</sup> Devices that exhibit room temperature cw operation have been demonstrated at the short wavelength end of this range, and recent results suggest that at least thermoelectrically-cooled operation should be possible at wavelengths beyond 3  $\mu\text{m}$ .<sup>9-10</sup> For detection of several species of combustion and environmental interest (e.g. carbon monoxide, nitric oxide, methane and formaldehyde), such lasers offer the promise of access to much stronger absorption bands than can be measured with shorter wavelength communication lasers, while retaining the practical advantages of room temperature or thermoelectrically cooled operation. For example, the first overtone band of CO near 2.3  $\mu\text{m}$  that is accessible with antimonide lasers is a factor of 160 times stronger than the third overtone band near 1.57  $\mu\text{m}$ . Although the potential of antimonide lasers for gas sensing applications is usually cited as a principal motivation for their development, examples of such applications are not evident in the literature. Recently, the measurement of a water vapor absorption line near 2.65  $\mu\text{m}$  using an



antimonide laser was briefly described.<sup>11</sup> We reported the first laboratory measurement of nitric oxide gas (NO) using an antimonide laser operating in the 2.65  $\mu\text{m}$  region.<sup>12</sup> By using high frequency wavelength modulation spectroscopy with second harmonic detection, a detection sensitivity for NO of 15 ppm-meter was achieved. Spectral interferences from water vapor, which absorbs strongly in this wavelength region, could be avoided by careful selection of the NO analysis line and by sampling the gas to be analyzed into a reduced pressure cell.

In this presentation, we will describe our current efforts to extend the NO measurement to combustion emissions monitoring and we will also discuss the results of formaldehyde ( $\text{H}_2\text{CO}$ ) detection in the 2 – 3  $\mu\text{m}$  region using antimonide diode lasers. We will also describe our efforts in developing high sensitivity monitors of CO near 2.3  $\mu\text{m}$  and  $\text{H}_2\text{O}$  near 2.65  $\mu\text{m}$ .

## References

- . D. S. Bomse, "Diode lasers: finding trace gases in the lab and the plant," *Photonics Spectra* **29**, No. 6, 88 – 94 (1995) and references therein.
- . J. A. Silver, "Frequency-modulation spectroscopy for trace species detection: theory and comparison among experimental methods," *Appl. Opt.* **31**, 707 – 717 (1992).
- . D. S. Bomse, J. A. Silver, and A. C. Stanton, "Frequency modulation and wavelength modulation spectroscopies: comparison of experimental methods using a lead-salt diode laser," *Appl. Opt.* **31**, 718 – 731 (1992).
4. P. Werle, F. Slemr, M. Gehrtz, and C. Braüchle, "Quantum-limited FM-spectroscopy with a lead-salt diode laser," *Appl. Phys. B* **49**, 99 – 108 (1989).
5. D. E. Cooper and T. F. Gallagher, "Double frequency modulation spectroscopy: high modulation frequency with low-bandwidth detectors," *Appl. Opt.* **24**, 1327 – 1334 (1985).
6. A. N. Baranov, A. N. Imenkov, M. P. Mikhailova, and Yu. P. Yakovlev, "Semiconductor lasers and photodiodes for gas analysis in the spectral range 1.8 – 2.5  $\mu\text{m}$ ," in *Tunable Diode laser Applications*, A. I. Nadezhdinskii, A. M. Prokhorov, eds., *Proc. Soc. Photo-Opt. Instrum. Eng.* **1724**, 78 – 82 (1992).
7. S. R. Kurtz, R. M. Biefeld, L. R. Dawson, K. C. Baucom, and A. J. Howard, "Midwave (4  $\mu\text{m}$ ) infrared lasers and light-emitting diodes with biaxially compressed InAsSb active regions," *Appl. Phys. Lett.* **64**, 812 – 814 (1994).
8. Lee, P. K. York, R. J. Menna, R. U. Martinelli, D. Z. Garbuzov, S. Y. Narayan, and J. C. Connolly, "Room-temperature 2.78  $\mu\text{m}$  AlGaAsSb/InGaAsSb quantum-well lasers," *Appl. Phys. Lett.* **66**, 1942 – 1944 (1995).
9. H. Chow, R. H. Miles, T. C. Hasenberg, A. R. Kost, Y. -H. Zhang, H. L. Dunlap, and L. West, "Mid-wave infrared diode lasers based on GaInSb/InAs and InAs/AlSb superlattices," *Appl. Phys. Lett.* **67**, 3700 – 3702 (1995).
10. H. K. Choi, G. W. Turner, M. J. Manfra, and M. K. Connors, "175 K continuous wave operation of InAsSb/InAlAsSb quantum-well diode lasers emitting at 3.5  $\mu\text{m}$ ," *Appl. Phys. Lett.* **68**, 2936 – 2938 (1996).
11. R. U. Martinelli, "Mid-infrared wavelengths enhance trace-gas sensing," *Laser Focus World* **32**, No. 3, 77 – 81 (March, 1996).
12. D.B. Oh and A. C. Stanton, "Measurement of nitric oxide with an antimonide diode laser," *Appl. Opt.*, in press (1997).

ThD1 (Invited)  
3:30pm - 4:00pm

## SPECTROCHEMICAL APPLICATIONS OF SEMICONDUCTOR LASERS

J. Koch<sup>a</sup>, K. Niemax<sup>a,b</sup>, B. Ocker<sup>a</sup>, H.D. Witzemann<sup>b</sup>, A. Zybin<sup>a</sup>

<sup>a</sup>*Institute of Spectrochemistry and Applied Spectroscopy, Bunsen-Kirchhoff-Str. 11, D-44139 Dortmund, Germany*

<sup>b</sup>*Institute of Physics, University of Hohenheim, Garbenstrasse 30, D-70599 Stuttgart, Germany*

Semiconductor laser diodes of the AlGaAs and InGaAsP type combine the special spectroscopic properties of tunable, cw lasers, such as narrow band width and high spectral radiation density, with properties which are important for compact and routinely operated spectrochemical instruments of high detection sensitivity. Such technical properties are, for example, rapid wavelength tunability by diode current, low amplitude noise, high stability, long lifetime, low price and small size. General aspects of diode laser application in element analysis are given in a recent review [1].

It is planned to present and discuss the following topics:

- 1.) Wavelength modulation diode laser atomic absorption spectrometry (WM-DLAAS) using flames and graphite tube atomizers and coupling of WM-DLAAS with high pressure liquid chromatography (HPLC).
- 2.) WM-DLAAS of non-metals, such as Cl, Br, C, H and S, in low-pressure plasmas and the coupling of WM-DLAAS with gas chromatography (GC). In particular, solution of complex analytical problems in biological samples and plastic recycling by GC-WM-DLAAS will be shown.
- 3.) Isotope selective DLAAS and WM-DLAAS in low-pressure graphite furnaces and FANES sources (FANES: Furnace Atomic Non-thermal Excitation Spectroscopy). Isotope selectivity allows calibration of DLAAS measurements and correction of chemical and physical matrix effects in DLAAS by isotope dilution.
- 4.) Remote measurements of the isotope ratios  $^{235}\text{U}/^{238}\text{U}$  in waste-glass by laser ablation and diode laser induced fluorescence (DLIF) in the laser produced plasma.

[1] K. Niemax, A. Zybin, C. Schnürer-Patschan and H. Groll, *Anal.Chem.* **68** (1996) 351A-356A.

## Compact, All-Diode-Laser, Optical Frequency Reference Based on Laser-Trapped Atomic Calcium

C.W. Oates, M. Stephens, and L.W. Hollberg

Time and Frequency Division  
National Institute of Standards and Technology  
Boulder, CO 80303  
Tel: (303)-497-7654, FAX (303)-497-7845

An important application of diode lasers in the standards community is the development of the next generation of frequency/wavelength references, where semiconductor laser technology will enable higher performance in portable, inexpensive, and reliable systems. At NIST we are working on an all-diode-laser, optical frequency reference based on the  $^1S_0$ - $^3P_1$  intercombination line in Ca at 657 nm. This transition is one of those recommended for the realization of the meter, and its absolute frequency has been measured with an uncertainty of 450 Hz, the most precise of any visible reference.<sup>1</sup>

Our work has addressed several important challenges. First of all, we have stabilized the frequency of a 657 nm extended-cavity diode laser to <100 Hz to allow resolution of the 400 Hz natural linewidth of this transition. Second, we have implemented a master-oscillator power-amplifier (MOPA) at 657 nm in order to produce 20 mW of usable light needed for spectroscopy of this weak transition. Finally, we have generated 35 mW of light at 423 nm (through frequency doubling of an 846 nm high power diode laser) and used it in a magneto-optic trap (MOT) which can provide samples of up to  $2 \times 10^7$  Ca atoms. The use of trapped atoms for our spectroscopic sample offers the extended interaction time needed for sub-kilohertz resolution and greatly reduced systematic effects. With this system we have observed Ca resonances as narrow as 6 kHz and should be able to reduce this further in the very near future.

To generate the frequency-stabilized light at 657 nm (see Figure 1), we start with a grating-tuned extended-cavity diode laser (ECDL), which yields 3 mW output power and a laser linewidth of ~100 kHz. After passing the beam through an optical isolator (50 dB isolation), we split the light into two paths, one for frequency stabilization and the other for spectroscopy. In the first path, 1 mW of light goes through a double-passed acousto-optic modulator (AOM) (for precise tuning of the laser frequency) to a high finesse Fabry-Perot cavity (50 kHz fringe linewidth). Our cavity consists of two mirrors optically contacted to a ultra-low expansion (ULE) spacer, which is placed inside a thermally and vibrationally isolated vacuum can. Using FM optical heterodyne techniques we derive an error signal which we filter and then feed back to the diode laser current (to correct fast laser frequency fluctuations) and to a PZT on the laser feedback mirror (to correct slow drifts). With the laser locked, the error signal indicates residual frequency fluctuations of

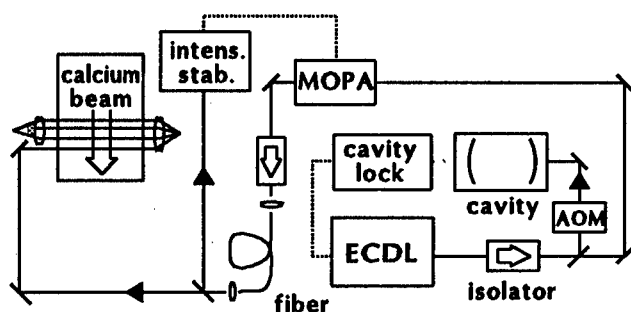


Figure 1 Diagram of 657 nm diode laser setup for optical Ramsey spectroscopy of a Ca atomic beam.

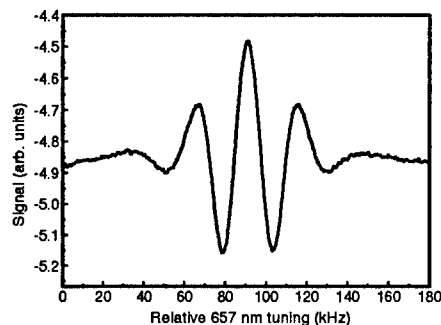


Figure 2 Optical Ramsey fringes at 657 nm taken with setup in Figure 1.

< 100 Hz. In the second path we send 1.3 mW to injection-seed a MOPA, so we can increase the power for the spectroscopy. This MOPA system produces 240 mW at 657 nm and adds negligible frequency noise to the light. As a first test of this system we sent the MOPA output through an optical fiber to an optical Ramsey fringe spectrometer, which used four interaction zones with a Ca atomic beam to probe the  $^1S_0$ - $^3P_1$  ( $m=0$ - $m=0$ ) transition. With 8 mW of probe power we were able to obtain Ramsey lineshapes with good contrast and a high signal-to-noise ratio. Figure 2 shows a scan taken at 11.5 kHz resolution with a data acquisition time of 1 minute to average 40 scans. Our resolution was limited by the fast atom transit time and the geometry of our setup. Using this lineshape as a reference we were able to characterize the long term stability of our frequency-stabilized diode laser system.

To achieve higher resolution we have constructed a Ca MOT. Previously, three Ca MOTs have been demonstrated, all of which used dye lasers at 423 nm to trap atoms from a slowed atomic beam.<sup>2,3</sup> In order to have a simpler, more compact system, we have designed a Ca trap apparatus which uses frequency-doubled diode laser light for cooling and trapping. As shown in Figure 3, a grating-tuned ECDL provides stable tunable light, which we use to injection lock a high-power slave diode laser. 5 mW of injection power produces 150 mW of slave output at 846 nm. We correct the slave laser's astigmatic and asymmetric spatial mode with an anamorphic prism pair and a cylindrical lens. After passing this beam through an optical isolator, we have 105 mW incident on a ring build-up cavity containing a 1 cm KNbO<sub>3</sub> non-linear crystal. With a build-up factor of  $\sim 20$  we generate 35 mW of stable 423 nm light.

For our atom trap, we modified a simple MOT design demonstrated for lithium<sup>4</sup> (and recently for calcium by workers at PTB<sup>2</sup>) which relies on trapping atoms directly from a short (12 cm) atomic beam. We find that adding a single-frequency slowing beam along the atomic beam axis leads to an 8-fold increase in the number of trapped atoms. We collect about  $2 \times 10^7$  atoms with the trap light detuned 35 MHz red of the  $^1S_0$ - $^1P_1$  cooling transition and a magnetic field gradient of 12 mT/cm. Figure 4 shows a trapped sample of  $>10^6$  Ca atoms, one of the first demonstrations of laser trapping with frequency-doubled diode lasers. We have performed optical Ramsey spectroscopy upon the trapped atoms and have obtained features as narrow as 6 kHz, suitable for use as a high precision frequency reference.

#### References:

1. H. Schnatz, B. Lipphardt, J. Helmcke, F. Riehle, G. Zinner, Phys. Rev. Lett. 76, 18(1996).
2. Th. Kisters, K. Zeiske, F. Riehle, and J. Helmcke, Appl. Phys. B59, 89(1994).
3. Takayuki Kurosu and Fujio Shimizu, Japanese J. Appl. Phys. 29, L2127(1990).
4. Brian P. Anderson and Mark A. Kasevich, Phys. Rev. A50, R3581(1994).

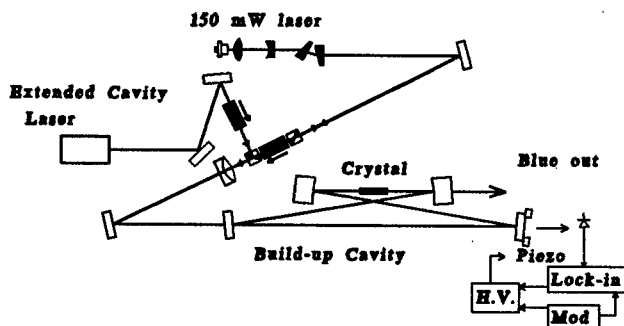


Figure 3 Frequency-doubling of 846 nm diode laser light to generate 35 mW of 423 nm cooling light.

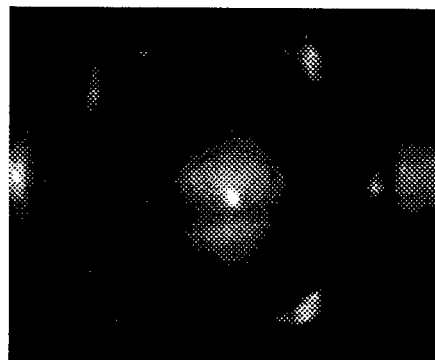


Figure 4 Ca MOT using frequency-doubled diode lasers. The central bright spot is fluorescence from  $>10^6$  atoms.

## **Coherent transient measurements with a semiconductor diode laser**

Yong-qing Li and Min Xiao

Department of Physics, University of Arkansas, Fayetteville, AR 72701

Tel: (501) 575-6568; Fax: (501) 575-4580

Email: yli@comp.uark.edu; mxiao@comp.uark.edu

Semiconductor diode lasers have been widely used in atomic physics and quantum optics [1-3]. Advanced semiconductor lasers have the capability of modulation in intensity or optical frequency at the rate greater than a few GHz by modulating the driving current. This characteristics makes semiconductor laser diodes ideal light sources in the study of optical coherent transient phenomena with the time scale ranging from few milliseconds to sub-nanoseconds [4-7]. In this paper, we discuss the applications of semiconductor lasers in coherent transient measurements and report our experimental results.

The applications of semiconductor lasers in coherent transients are based on the fast frequency-switching and fast frequency-scanning characteristics of laser diodes. A typical technique is as following: a diode laser (solitary or external cavity diode laser) is biased to have a desired oscillation frequency (for a given temperature and DC bias current) and, then, a step-function pulse current with fast rise or fall time is applied to modulate the bias current. This pulse current leads to a fast switching both in the oscillation frequency and in the intensity of the diode laser and then leads to a fast scanning in the frequency.

The frequency-switching technique of semiconductor lasers has been used to measure coherent transient behaviors (e.g., optical free-induced decay, nutation, and photon echo) of atoms [4-6] and solid materials [7]. The fast frequency-switching of a diode laser is related to the carrier effect, e.g., the pulse current causes a fast change in carrier concentration which leads to a fast change in refraction index and, therefore, in oscillation frequency. A typical frequency shift as a function of the pulsed current is a few tens MHz/mA for the laser diode used in references [4] and [5]. Therefore, for the pulsed current with a few mA, the diode laser frequency is switched to a few hundred MHz away from its original frequency without significant change in its intensity. This frequency-switching technique is suitable for using in coherent transient measurements with the time scale from few nanoseconds [4, 5] to few microseconds [7].

Following the step pulse current, the laser frequency is not only switched to a new value (frequency-switching due to the carrier effect), but also changed in time (fast frequency-scanning) due to the temperature modulation effect. When the laser frequency is swept quickly across an atomic transition (with a time scale much shorter than the

atomic decay time), the transient absorption of the atoms is a coherent process. This leads to a new coherent spectroscopy technique, i.e., transient absorption spectroscopy, which is different from the conventional steady-state (cw) absorption spectroscopy. The experimental results on Rb atoms using this technique are shown in Fig. 1.

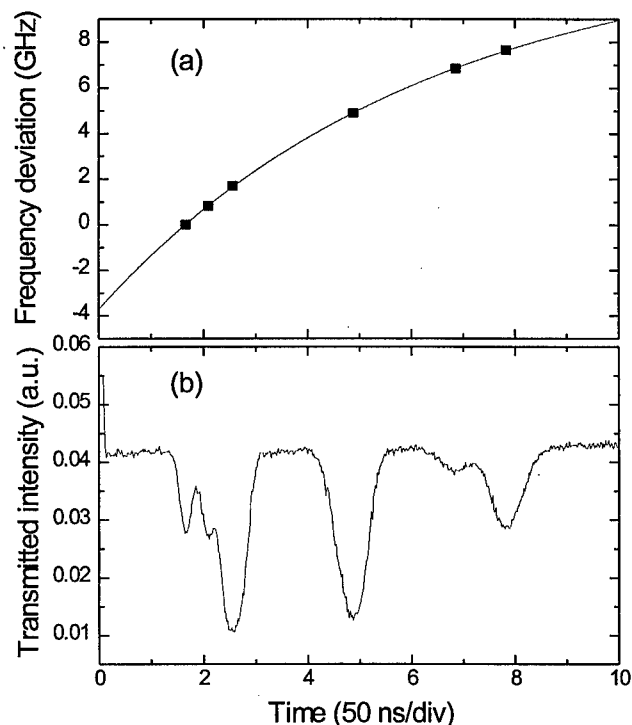


Fig.1 Transient absorption spectroscopy of Rb atoms at 794.8 nm. The bias current of 150 mA was modulated by a step-function pulse current with an amplitude of 26 mA, width of 500 ns, and period of 50  $\mu$ s.

(b) Transmitted intensity v.s. time. The hyperfine structures of Rb D1 line are displayed. The lifetime of Rb D1 line is 29.4 ns.

(a) Laser frequency deviation v.s. time. The solid curve is an exponential fit.

We acknowledge the funding supports from NSF and ONR. We acknowledge Ms. Lady Oak Arnold of Hewlett-Packard for the loan of HP8133A pulse generator.

1. C. E. Wieman and L. Hollberg, Rev. Sci. Instrum. **62**, 1-20 (1991).
2. W.H. Richardson, S. Machida, and Y. Yamamoto, Phys. Rev. Lett. **66**, 2867 (1991).
3. Y.Q. Li, P. Lynam, M. Xiao, and P. J. Edwards, Phys. Rev. Lett. **78**, 3105 (1997).
4. Y.Q. Li and M. Xiao, "Transient inversionless amplification in rubidium atoms by laser frequency-switching", in *Coherence and Quantum Optics VII*, Proceedings of the Seventh Rochester Conference on Coherence and Quantum Optics, held at the University of Rochester, June 7-10, 1995, eds. by J.H. Eberly, L. Mandel, and E. Wolf, Plenum Press, New York, pp.709-710.
5. Y.Q. Li, W.H. Burkett, and M. Xiao, Opt. Lett. **21**, 982 (1996).
6. P. Dube, M.D. Levenson, and J.L. Hall, Opt. Lett. **22**, 184 (1997).
7. R.M. Macfarlane and M. Zhu, Opt. Lett. **22**, 248 (1997).

## Monitoring of Molecular Species using Near-Infrared Extended Cavity Diode Lasers

H. R. Simonsen, J. Henningsen, and T. Møgelberg  
Danish Institute of Fundamental Metrology  
Building 307, Anker Engelunds Vej 1  
DK-2800 Lyngby, Denmark  
Tel.: +45 4593 1144 Fax: +45 4593 1137  
E-mail: hs@kelvin.dfm.dtu.dk

Near infrared diode lasers are attractive for spectroscopic applications due to their good spectral purity and low amplitude noise. They operate at room temperature with single-mode output power of milliwatts, and are adapted to fibre optic technology. Wavelength tunability is achieved using an extended cavity configuration. We report on a system based on high resolution infrared spectrometry in the 1.5 - 1.6  $\mu\text{m}$  region where several gases have overtone or combination absorption bands. In monitoring applications toxic and flammable gases like CO and  $\text{H}_2\text{S}$  are of particular interest. CO detection is aimed at detecting fires with special reference to smouldering combustion within the insulating layers of equipment, whereas  $\text{H}_2\text{S}$  is a major health hazard on oil rigs producing sour oil.

An experimental setup used for optimum selection of wavelengths is shown in Fig. 1. Light from an extended cavity diode laser (ECL), tunable from 1.51 to 1.59  $\mu\text{m}$ , is coupled to a fibre optic cable and distributed to several cells. About 10% of the power is directed through two 15 cm cells with  $\text{C}_2\text{H}_2$  and  $\text{H}_2\text{S}$ . This arm is used for wavelength calibration based on strong  $\text{C}_2\text{H}_2$  absorption lines between 1.51 and 1.54  $\mu\text{m}$ , and on  $\text{H}_2\text{S}$  lines which can be observed above 1.55  $\mu\text{m}$ . The second arm consists of a longer cell of length  $\approx 1.3$  m which can be filled with various gases. We have recorded absorption spectra of  $\text{H}_2\text{S}$ , CO,  $\text{CO}_2$  and  $\text{H}_2\text{O}$  in the wavelength range 1.51 to 1.59  $\mu\text{m}$ , where the latter molecules are included since they are potentially interfering with any atmospheric monitoring.

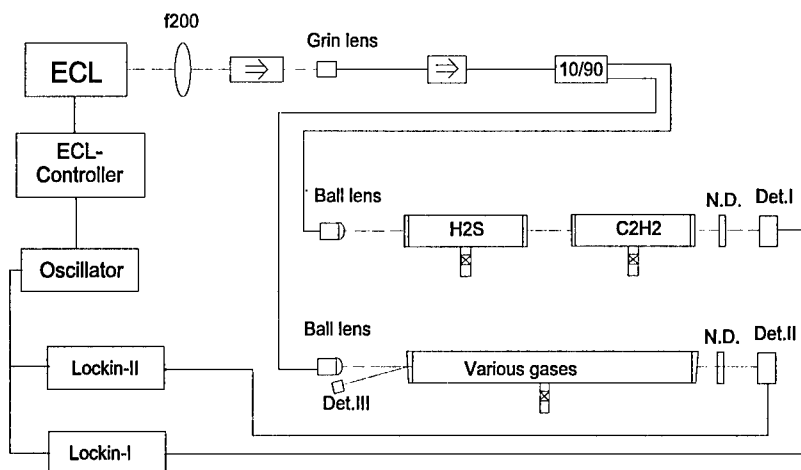


**Figure 1.** Experimental setup used to study various molecular gases with  $\text{C}_2\text{H}_2$  and  $\text{H}_2\text{S}$  as calibration gases. The absorption features are detected using a second derivative wavelength modulation technique.

Spectra were recorded at a pressure of 300 mBar with second derivative technique, using a modulation frequency of 370 Hz with an amplitude of 4 GHz. Fig. 2 shows the spectrum of  $\text{H}_2\text{S}$  and CO between 1.560 and 1.570  $\mu\text{m}$ , recorded by stepping the laser grating linearly in time. The wavelength axis was generated by identifying a number of  $\text{H}_2\text{S}$  lines in the FTIR spectrum recorded by Lechuga-Fossat et al [1,2], and using the corresponding wavelengths and step numbers for a third order polynomial fit. The

relative accuracy obtained in this way is better than  $1.5 \times 10^{-5}$ , corresponding to less than the pressure broadened linewidth.

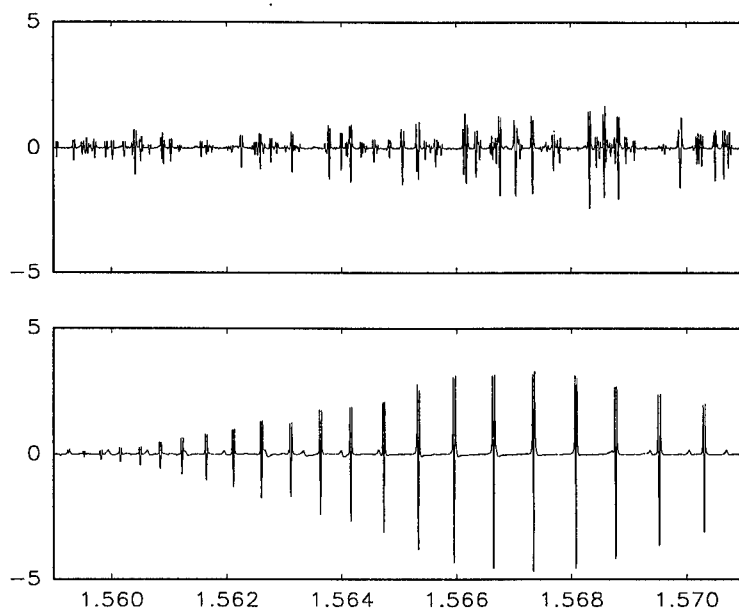


**Figure 2.** Second-derivative spectrum of CO (lower trace) and H<sub>2</sub>S (upper trace) in the wavelength range from 1.56 to 1.57  $\mu\text{m}$ .

- [1] L.Lechuga-Fossat, J.-M. Flaud, C.Camy-Peyret, P.Arcas and M. Cuisenier, "The H<sub>2</sub>S spectrum in the 1.6 micron spectral region", *Mol.Phys.*, 61,23-32 (1987)  
[2]. J.-M. Flaud, personal communication

This work was supported in part by the European Community under Contract No. OG-0269-95.



## **The applications of diode lasers to frequency standards and optical frequency standards at CMS**

Mao-Sheng Huang, Wen-Ling Yang, Yu-Ping Lan, Tzeng-Yow Lin  
Center for Measurement Standards, ITRI, Taiwan

In the last few years, CMS (Center for Measurement Standards in Taiwan) had devoted to the development of some of the Recommended Radiations of length standards. Most radiations at CMS were gas lasers. Recently, solid state lasers and semiconductor lasers have been highly improved in performance, thus they could be widely used in many applications in measurement standards. To fit the future needs, we have planned to build up our Iodine stabilized diode pump Nd-YAG laser and begun to use diode lasers in the research on measurement standards.

There are two fields in CMS, that use laser diode quite often. One is the field for the Cesium atomic fountain clock and the other is the field for laser trapping and cooling of Calcium. In this article, we would like to show how we use the laser diode in these researches.

The core technology of both the Cesium Atomic Fountain and Calcium Trap is the laser cooling and trapping which need six laser beams with frequencies to be red detuned from resonance. In the former case, the laser diode used at CMS was a Cesium stabilized DBR laser that was frequency stabilized on the side of the saturation absorption peaks of Cesium. The frequency of the laser could be tuned by the current of the solenoid which surrounded on a reference Cesium vapor cell. For the latter case, the cooling and trapping laser was frequency doubled from 844nm diode laser that was injection locked to a grating feedback low power diode laser. The laser diode used as the detection beams of the Cesium atomic fountain was a grating feedback DBR laser. The linewidth of the laser was reduced by the extended external cavity, and the frequency of the laser was lock to a Cs vapor cell by the feedback of the error signal to the current source of the diode laser. In contrast, the linewidth reduction of the laser diode used as the spectroscopy beam of the Ca trap was more complicated since the requirement of the beam for very narrow linewidth. It was a 657 nm diode laser with grating feedback. The laser was phase locked to a high Finesse Fabry-Perot cavity. The error signal was generated by the beat of the beam directly reflected from the front mirror and the beam coming back from the cavity. The error signal with quicker response went back to the current source of the diode laser and that with slower response went to the PZT driver of the grating. Similar laser linewidth reduction system were also demonstrated by some other groups.

Besides the Cesium Atomic Fountain and the Calcium trap, we are also interested in other applications. For instance, in the measurement of optical frequency, we would like to have a tunable laser diode with more stable frequency and less linewidth. For practical use of industry, we are going to develop a less expensive stabilized laser diode for interferometers.

# **ADVANCED SEMICONDUCTOR LASERS AND APPLICATIONS**

**Friday, 15 August 1997**

## **Sessions:**

- FA:    Device Theory**
- FB:    Device Characteristics**
- FC:    High-Brightness Sources**
- FD:    High Power Sources**

## **Friday Papers Not Available**

- FC1 "New Advances in High Power, High Brightness Diode Laser",  
*Robert Lang, SDL, Inc., San Jose, CA*
- FD2 "Laser Diode Bar Lifetime Testing: The User's Perspective", *F.C.Way,*  
*Decade Optical Systems, Inc., Albuquerque, NM and*  
*S.G.Post, USAF Phillips Laboratory, Kirtland AFB, NM*

## THE ORIGINS OF QUANTUM NOISE IN PHOTONICS

Charles H. Henry

*Bell Laboratories, Lucent Technologies, Murray Hill, NJ 07974-0636*

Rudolf F. Kazarinov

*Bell Laboratories, Lucent Technologies, Breinigsville, PA 18031-9359*

We will try to explain the origins of quantum noise and how it happens that quantum noise in lasers and amplifiers can be described by classical noise sources.

Classical noise is due thermal motion. Quantum noise has a different origin, it results from fluctuations that we associate with the Heisenberg uncertainty principle. For example, consider a model of an atom consisting of an electron in a potential well. Suppose the electron is its ground state. As a result of the confinement, the electron has momentum fluctuations. There is an energy associated with these fluctuations which raises the ground state in energy above that of the bottom of the well. The frequency spectrum of the momentum fluctuations can be found by calculating the correlation function of the momentum operator at two times. This calculation shows that the momentum fluctuations are composed of all the frequencies of transitions from the ground state to excited states. Thus momentum fluctuations occur at optical frequencies. The electron is charged, so there is a current associated with the electrons momentum. We call this fluctuating current a "spontaneous current". It is a source of quantum noise.

Maxwell's equations hold in the quantum theory. For radiation they reduce to a wave equation for the vector potential with a spontaneous current source. The solution of this equation is a field radiating from the atom and carrying away energy. It thus appears that an atom in its ground state will lose energy.

This is prevented by the other source of quantum noise: vacuum fluctuations. The field of radiation can be expanded into modes. In free space, the modes are transverse plain waves. The field of each mode oscillates sinusoidally at the mode frequency like a simple harmonic oscillator. It is well known that a quantum treatment of a mechanical simple harmonic oscillator results in an evenly spaced set energy levels. By postulating that the mode field amplitude and its time derivative are operators with commutation rules similar to those of position and momentum, the mode also acquires an evenly spaced set of energy levels. Each energy level is interpreted as a different number of photons in the mode.

Like the atomic ground state, the mode ground state of zero photons has an uncertainty related fluctuation associated with it, the field of "vacuum fluctuations" and these fluctuations raise the energy of the ground state above the minimum classical energy of zero. The atom is bombarded by vacuum fields from the continuum of modes of free space. Some of this energy is absorbed by the atom and this absorption exactly cancels the energy loss by the radiation of spontaneous currents, stabilizing the atomic ground state.

When the electron is in an excited state, vacuum fields are not absorbed, instead they stimulate spontaneous emission. The radiation emitted by the spontaneous current is also spontaneous emission, so spontaneous emission has two sources. Dalibard et al. [1]. have argued that the two sources contribute equally the spontaneous emission rate.

As an example of how vacuum fields and spontaneous currents create noise, let us consider a noise free optical signal traveling down an absorbing optical waveguide. The signal field

is attenuated. The incident vacuum field is also attenuated, however, it is replenished by spontaneous current emission from the absorbing atoms. The beating of the signal and vacuum fields causes fluctuations in the energy flux which is the shot noise observed when the signal is detected by an ideal opaque photodetector. If the photodetector is not opaque, there is additional noise due to fluctuations in the rate of optical absorption caused by the beating of the signal field and spontaneous currents within the detector. The latter noise accounts for shot noise when the photodetector is nearly transparent.

The spontaneous current can be thought of as a quantum Langevin force. However, unlike classical Langevin forces, spontaneous currents and other physical quantities are described in the quantum theory by non-commuting operators instead of by numbers. The spontaneous currents generate non-commuting fields. Consequently, the average of a pair of positive and negative frequency field components depends on their order, whereas the corresponding average of classical fields is order independent. This is necessary to explain the properties of quantized radiation. However, a laser mode above threshold contains many photons and we expect it to behave classically and laser noise is successfully modeled with classical Langevin forces. How do non-commuting spontaneous currents give rise to classical commuting Langevin forces in lasers?

To answer this question, we consider a simple laser model with a gain medium composed of two level atoms. Electrons in the upper level contribute to gain and electrons in the lower level contribute to loss. The non-commuting contributions of gain and loss to the Langevin force correlation functions are of opposite sign. As power increases above threshold, gain approaches loss and the non-commuting contributions nearly cancel, leaving Langevin forces that may be regarded as classical and that generate classical fields.

A similar cancellation results in a classical noise field in a traveling wave optical amplifier. The incident vacuum field is amplified as it propagates through the amplifier and the fields emitted by spontaneous currents within the amplifier are amplified. The order-dependent field averages of these two contributions to amplified spontaneous emission have opposite signs and nearly cancel for large amplification, leaving a noise field that can be regarded as classical.

In summary, there are two sources of quantum noise: spontaneous currents and vacuum fluctuations. Together, they account for the stability of the atomic ground state, spontaneous emission, shot noise and noise in lasers and amplifiers. Detailed derivations of these results are given in our review paper on "Quantum Noise in Photonics" [2].

---

[1] J. Dalibard, J. Dupont-Roc and C. Cohen-Tannoudji, *J. Phys. (Paris)* vol. 43, 1617 (1982).

[2] C. H. Henry and R. F. Kazarinov, *Rev. Mod. Phys.*, vol. 68, No. 3, pp. 801-853, (1996).

# Classical corpuscular optical theory of squeezed states of light

P. Gallion and F. J  r  mie

*D  partement Communications, CNRS, URA 820,  
Ecole Nationale Sup  rieure des T  l  communications  
46 Rue Barrault, 75634 Paris Cedex 13 France  
tel.:(+33) 0. 45.81.77.02*

## Summary

Semi-classical theory of semiconductor laser noise considers the spontaneous emission fluctuations as the major noise source [1]. Arnaud has recently proposed a description of semiconductor laser noise without quantification of the optical field where the fundamental noise source is the shot noise associated with the field to absorbing atom conversion [2]. We propose a classical corpuscular theory in which a laser beam is considered as a flow of classical particles without mutual interaction. The intrinsic field fluctuations are described as the shot noise associated with the photon production or absorption. The noise linked to mirror losses is taken into account in the form of partition noise [3]. It can be represented by a partition Langevin noise force linked to laser facet reflections as in figure 1.

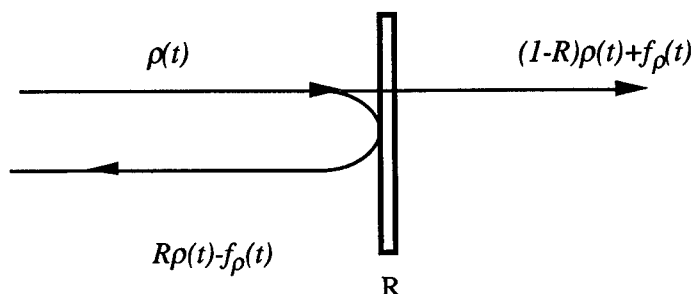


Figure 1: Model of partition noise

The langevin noise force satisfies the relations:

$$\langle f_{\rho}(t) \rangle = 0 \quad \text{and} \quad \langle f_{\rho}(t) f_{\rho}^*(t - \tau) \rangle = \overline{\Delta \rho^2} \delta(\tau) = \bar{\rho} \cdot R \cdot (1 - R) \delta(\tau)$$

where  $\langle \rangle$  represents the time average,  $R$  the laser power reflection coefficient and  $\rho(t)$  the photon flux. In this representation, as for vacuum fluctuation the anticorrelation of the reflected and transmitted powers provide a feedback signal which can correct the fluctuations resulting from the partition noise. Such a noise force is to be used for the laser facet reflection but also for the noise associated to the non-resonant internal loss, which can also be described by a beam splitting.

Fluctuations of the stored energy and emitted power of a semiconductor laser are derived with this description [5]. The theory allows the description of the non-classical states of light, and its results agree with quantum theory. For quiet pumping conditions [4] and for a high reflection coated Fabry-Perot laser, 50% of internal photon noise suppression is obtained. For high power and low frequency, the output photon noise is determined by the ratio between the overall photon lifetime and the mirror loss photon lifetime. For low internal loss, it can be reduced below the shot noise limit as presented in figure 2.

The effect of attenuation on the propagation of a laser fluctuations inside an absorbing medium is studied using the concept of partition noise. This leads to the invariance of a suitably defined Relative Intensity Noise. To describe sub-Poissonian photon statistic a negative Relative Intensity Noise is formally introduced [6]. The semiconductor laser noise measurement with the

dual balanced detection technique is analysed using optical partition noise showing the optimum conditions for the squeezed light measurement.

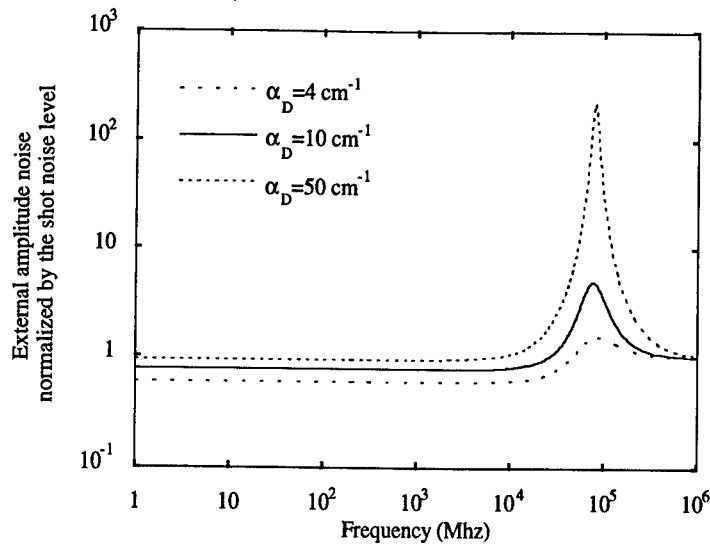


Figure 2: Normalized external amplitude noise for various values of internal loss

The low frequency intensity noise and the associated shot noise of a 1.55 mm compressive strained MQW DFB laser are measured with a dual balanced detection technique. Experimental results are presented in figure 3. The laser operates at room temperature and demonstrates 4 dB amplitude squeezing under quiet pumping conditions. Such efficient squeezing is achieved through an additional negative electrical feedback.

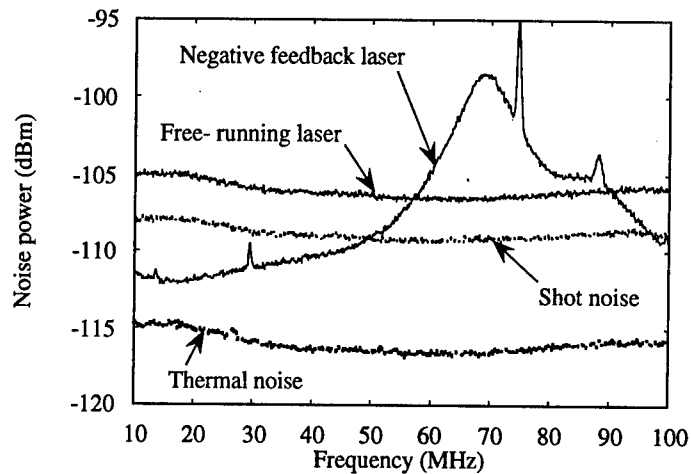


Figure 3: Intensity noise measurements of a 1.55 mm DFB laser

The authors would like to thank Alcatel Alsthom Research for the supplied lasers.

#### References

1. G.P. Agrawal and N.K. Dutta. Van Nostrand, Reinhold, New York (1986) Chap 6.
2. J. Arnaud, Phys. Rev. A, 45, No 3, pp 1775-1786 (1992).
3. R. Loudon and P. L. Knight, J. Mod. Opt, 34, p 709 (1987).
4. Y. Yamamoto, S.Machida, O.Nilsson, Phys. Rev. A, 34, No 5, pp 4025-4042 (1986).
5. P. Gallion, F. Jérémie and J.L. Vey. Opt. Quantum. Electron, 29, pp 65-70 (1997).
6. R. Schimpe, Zeitschrift für Physik B, Condensated Matter, 52, pp 289-294 (1983).

## Fine-Scale Analysis of Gain-Coupled MQW DFB Lasers

Alain Champagne, Jianyao Chen, Roman Maciejko and Toshihiko Makino\*

Optoelectronics Laboratory, Department of Engineering Physics, École Polytechnique  
P. O. Box 6079, Station "Centre-ville", Montréal, Québec, Canada H3C 3A7

\* Nortel Technology, P. O. Box 3511, Station C, Nepean, Ontario, Canada K1Y 4H7

In gain-coupled (GC) multiple-quantum-well (MQW) distributed feedback (DFB) lasers, phenomena on the submicron scale corresponding to quantum-well active regions with etched Bragg gratings have been shown to affect overall laser performance. Recently, we presented fine-scale bi-dimensional simulation results [1, 2], obtained below threshold, showing an enhancement of the gain coupling caused by a larger carrier injection in the thick section of the grating resulting in an improved single-mode yield. Technically, it is difficult to couple bi-dimensional fine scale analysis with longitudinal effects because of the huge discrepancy (3 orders of magnitude) between the grating period and the laser length. In this paper we present results combining submicron bi-dimensional modeling with a fine-scale longitudinal transfer matrix calculation, above threshold. This has the benefit of considering both the detailed bi-dimensional carrier behavior at the Bragg-wavelength scale and the larger scale DFB effects such as the longitudinal spatial hole burning and the non-uniform current injection along the the laser cavity.

We consider a  $1.55\text{ }\mu\text{m}$  laser with seven  $4.5\text{ nm}$  strained quantum-wells in which the top 3 wells are periodically etched (see Fig. 1) [1]. The barriers are  $10\text{ nm}$  thick and have an emission wavelength of  $1.10\text{ }\mu\text{m}$ . For a given applied bias on the laser, 2D calculations over one grating period are performed for a number of different values of the photon density covering the range expected to occur along the laser cavity. Once the 2D carrier distribution (see Fig. 2) is known for different photon densities, one can establish a relation between the photon density and the average gain in the high and the low sections of the grating as shown in Fig. 3. This relation is used to calculate the effective indices in the high and the low grating sections which are fed into the transfer-matrix computation to determine the longitudinal mode profile and the lasing wavelength for a given applied bias. From the known photon density distribution (see Fig. 4), one can construct the longitudinal distribution of any quantity given by the 2D calculation such as the injected current, and the carrier densities as shown in Fig. 5 and 6.

From Fig. 2 and 6, one can see that the carrier density is significantly larger in the high grating sections than in the lower ones which causes a gain-coupling enhancement. Fig. 6 also shows that the ratio between the carrier density in the high and the low grating section is position dependent due to longitudinal spatial hole burning. The model can also incorporate leakage currents which ought to be a very important consideration for high temperature operation.

This paper is thus the first one to deal with bi-dimensional local effects on such a fine scale in conjunction with global DFB laser features.

- [1] D. M. Adams, T. Makino, A. Champagne and R. Maciejko, "Yield Enhancement Due to Carrier-Injection Behavior in Truncated-Well Gain-Coupled DFBs", Paper CMF3, CLEO/QELS'96, Anaheim, California, June 2-7, 1996.
- [2] A. Champagne, R. Maciejko and T. Makino, "Enhanced Carrier Injection Efficiency from Lateral Current Injection in Multiple-Quantum-Well DFB Lasers", Photonics Technology Letters, Vol. 8, No. 6 June 1996.



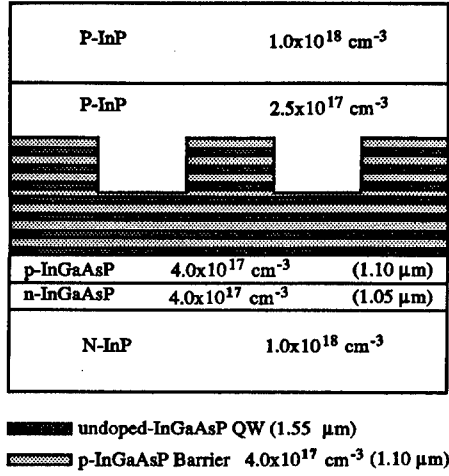


Fig. 1: Schematic diagram of the device structure.

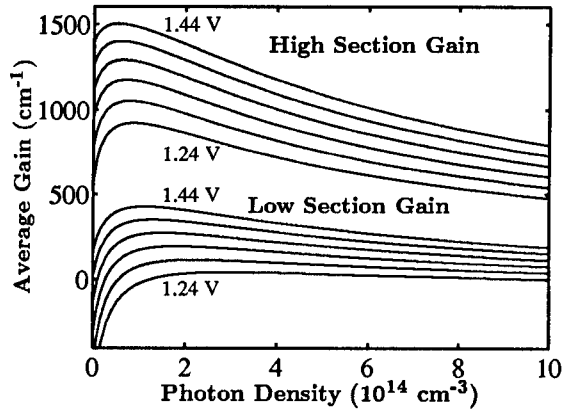


Fig. 3: Average gain as a function of the photon density for different applied bias values from 1.24 to 1.44 V, 0.04 V apart.

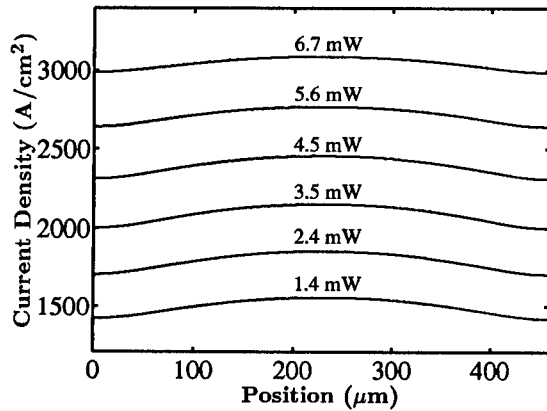


Fig. 5: Injected current density along the laser cavity for different output powers.

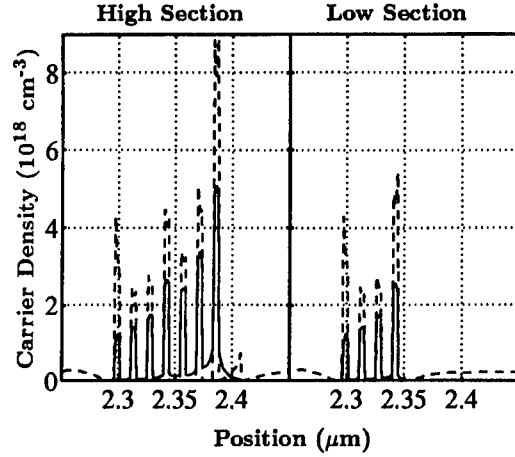


Fig. 2: Typical carrier density distribution. The solid and the dashed lines are, respectively, the electron and the hole concentrations.

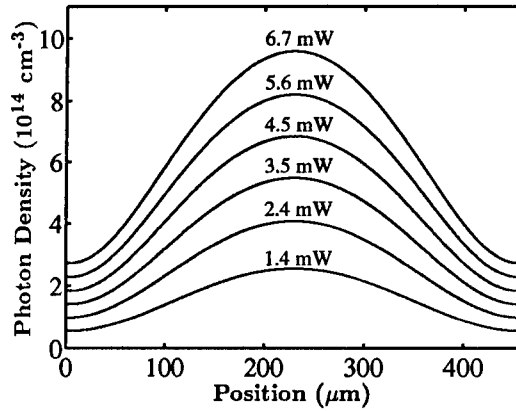


Fig. 4: Photon density along the laser cavity for different applied bias values. The corresponding total output power is also indicated.

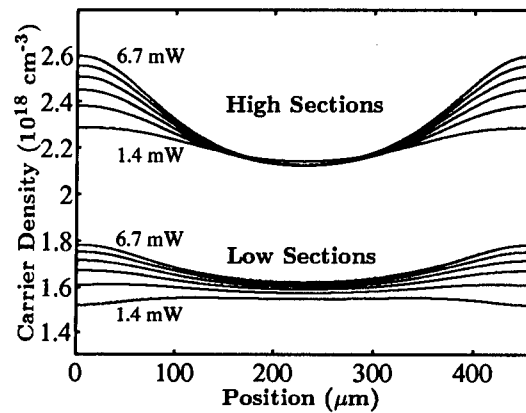


Fig. 6: Average electron density in the high and the low sections of the grating for different output powers as in Fig. 4 and 5.

## A Quantum-Well Laser Model for SPICE-Like Simulators

Paul Kerstetter  
School of Electrical & Computer Engineering  
Georgia Institute of Technology  
Atlanta, GA 30332-0250

Giorgio Casinovi  
Info Tech & Telecommunications Lab  
Georgia Tech Research Institute  
Atlanta, GA 30332-0800

Optoelectronic systems can be intricate and difficult to analyze. With the necessary integration of new devices as well as with the increase in complexity of optoelectronic systems, analysis and design of such systems has become a lengthy and time-consuming effort. However, the use of efficient computer simulation tools with accurate device models can help alleviate such problems. Currently we are developing an optoelectronic system simulator that makes use of a new quantum-well laser model.

The quantum-well laser model is based upon the semiconductor laser rate equations given in [1]. These equations are:

$$\frac{dN}{dt} = \frac{I}{qV} - \frac{N}{\tau_s} - g(N - N_o)(1 - \epsilon S)S \quad \frac{dS}{dt} = \Gamma g(N - N_o)(1 - \epsilon S)S - \frac{S}{\tau_p} + \frac{\Gamma \beta N}{\tau_s} \quad (1)$$

Where  $N$  is the density of electrons in the conduction band,  $I$  is the injection current and  $S$  is the density of photons in the lasing mode. With these rate equations an approach similar to that found in [2] was used to develop the model. That is the rate equations were manipulated into a current-voltage relationship for the laser. Then a circuit model was developed from the current-voltage relation. However, intensity is used as the output variable in our simulator so that the following equation was used to convert from photon density to average intensity:

$$S = 4 \frac{I_{int} \lambda}{c^2 h} \quad (2)$$

Where  $I_{int}$  is the intensity,  $\lambda$  is the wavelength,  $c$  is the speed of light and  $h$  is Planck's constant.

The rate equations used for the laser model are problematic to simulators that use Newton's method. This is because the equations have multiple solutions making it possible for the simulator to seek out the wrong solution. As an example consider the steady-state case with zero gain compression. The rate equations for this case can be manipulated into the following form:

$$I = \frac{((1 - \beta)(N^2 - NN_o)\tau_p g \Gamma - N)qV}{\tau_s ((N - N_o)\tau_p g \Gamma - 1)} \quad (3)$$

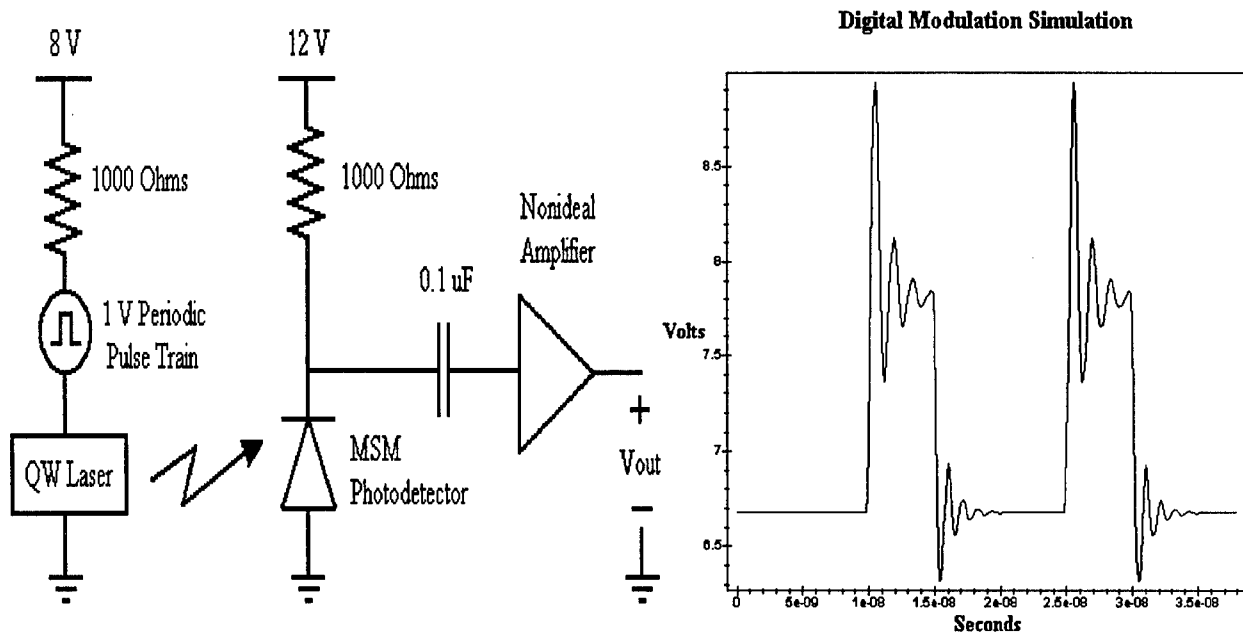
From equation 3, it is apparent that  $N$  has two solutions. However, the correct solution is bounded by two asymptotes. Thus, a test can be performed to see if the simulator solution lies

on the correct side of the asymptotes. If the test fails, the simulator can reset its solution to a value equal to the asymptote or to a value that lies within the neighborhood of the correct solution. The test equations are given below:

$$N \leq N_o + \frac{1}{\Gamma g \tau_p} \quad I \geq -\frac{qV(\Gamma g \tau_p N(\beta-1) + \beta)}{\Gamma \tau_p \tau_s g} \quad (4)$$

These equations help the simulator converge to the correct solution for the steady-state case without gain compression and may also be used to help find the correct initial conditions for transient analysis. When gain compression is introduced, a solution exists that has a vertical asymptote of  $N=N_o$ . However, in practice the electron density is not perfectly clamped at threshold as this solution suggests [3]. Thus another solution must be sought that is a closer match to what is observed.

In order to test the quantum-well laser model, a MSM photodetector model was developed from the nonlinear conductance given in [4]. An additional detector capacitance and back-to-back diode structure was added in parallel to the conductance. A test circuit that includes these models is shown below along with the simulation results for the circuit's output voltage.



- [1] D. Gao et al., "Modeling of Quantum-Well Lasers for Computer-Aided Analysis of Optoelectronic Integrated Circuits", IEEE J. Quantum Electron., QE-26, p.1206-1216, 1990.
- [2] D. Dodds and M. Sieben, "Fabry-Perot Laser Diode Modeling", IEEE Photonics Technology Letters 7, p. 254-256, 1995.
- [3] R. Nagarajan, "Effects of Carrier Transport on Injection Efficiency and Wavelength Chirping in Quantum-Well Lasers", IEEE J. of Quantum Electron., QE-29, p. 1601-1608, 1990.
- [4] E. Sano, "A Device Model for MSM Photodetectors and its Applications to Optoelectronic Integrated Circuit Simulation", IEEE Transactions Electron Devices 9, p. 1964-1968, 1990.

## **Beam Propagation Modelling of Tapered Waveguide Lasers.**

K.A. Williams, I.H. White and A. Wonfor.

Centre for Communications Research, Department of Electrical and Electronic Engineering, University of Bristol, Bristol BS8 1TR, UK.

Tapered waveguides are now widely implemented to increase the single lobe output power of semiconductor lasers [1]. Models to optimise their design have however been limited to single pass amplifier design [2], and the simulation of transient laser phenomena [3,4]. This paper presents a dynamic beam propagation model which is sufficiently advanced to allow the optimised design of high power low divergence tapered waveguide lasers. This has been achieved by extending a beam propagation model for semiconductor lasers [4,5] to include the spatially resolved temperature profile [2], and a temperature dependant gain [6]. Design parameters such as the optimum facet reflectivity, taper angle and waveguide dimensions for low far field divergence and high continuous wave power can thereby be calculated.

The model has been used to simulate the performance of a tapered waveguide laser where a short nontapered region is included to define the spatial mode. Such a device is shown schematically in figure 1. The local temperature is calculated from the difference between injected electrical power, and generated optical power, and is plotted in figure 2 in degrees Celsius above the ambient temperature. Under lasing conditions, the temperature rise at the centre of the waveguide is observed to be lower than at the edge of the waveguide, as a direct result of the narrow optical filament.

Device performance has been characterised in terms of the broadening in the far field pattern for both increases in bias current and facet reflectivity. Figure 3 (i) shows the dependence of far field angle on bias current for a low reflectivity of 0.6%. The far field is observed to broaden with increasing current, eventually leading to multimode operation. The broadening is seen to result from a confinement of the optical mode to the centre of the cavity at higher currents. Figure 3 (ii) highlights the broadening in the far field pattern observed for an increase in facet reflectivity for values of up to 3%. The far field width at the full width at half maximum is calculated to increase to in excess of 5 degrees for facet reflectivities of 3%.

The broadening in far field patterns originates largely from transverse mode spatial hole burning, especially evident in the spatially resolved carrier density profiles. The carrier densities at the facet are shown in figure 4 to highlight this. The dashed carrier density profile for the lower reflectivity device shows reduced transverse nonuniformity under the waveguide. The role of local temperature, and gain on mode formation will therefore be discussed, in the context of laser waveguide design, along with supporting experimental data at the meeting.

The authors acknowledge D.J. Robbins and J.J. Lewandowski of GMMT Ltd for scientific discussions.

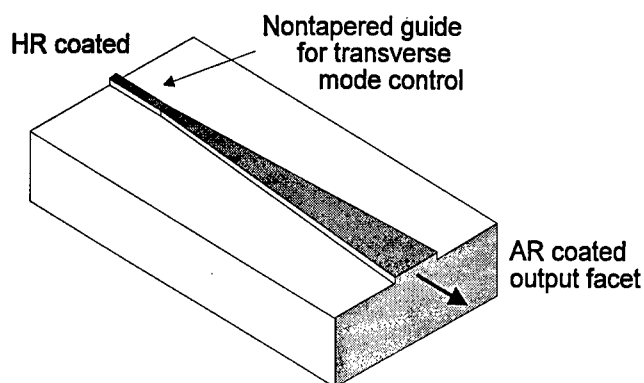


Figure 1: Schematic diagram for the modelled tapered waveguide laser showing the straight guide region for mode control.

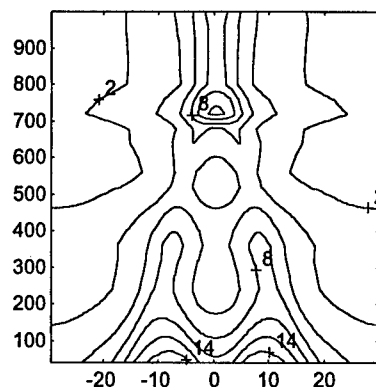


Figure 2: Temperature profile for tapered laser, with temperature in degrees above the mount level.

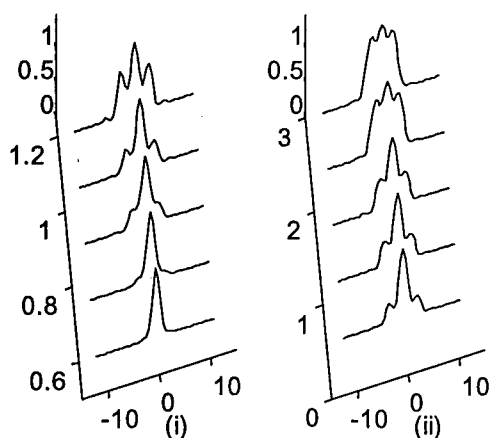


Figure 3 : Normalised far field intensity patterns plotted in degrees as a function of :  
(i) DC bias current in amps, and  
(ii) reflectivity in percent.

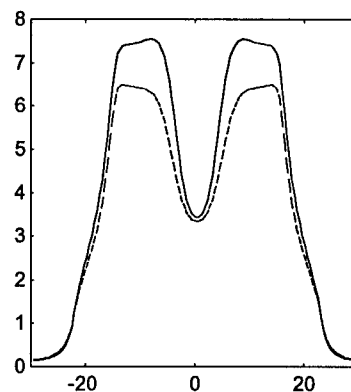


Figure 4 : Carrier density profiles (units  $10^{18} \text{ cm}^{-3}$ ) at the facet for : (i) low reflectivity laser and  
(ii) high reflectivity laser, highlighting the enhanced spatial hole-burning.

1. Walpole, J., Optical and Quantum Electronics, 28, 623-645, 1996.
2. Lang, R.J. et al., IEEE Journal of Quantum Electronics, 29, 2044-2051, 1993.
3. Jiang, Z. et al., OSA topical meeting, Keystone CO, 20, 136-138, 1995.
4. Williams, K.A. et al., IEEE Photonics Technology Letters, 9, 167-169, 1997.
5. Agrawal, G.P., IEEE Journal of Lightwave Technology, 2, 537-543, 1984.
6. Wang, J. et al., IEEE Journal of Lightwave Technology, 5, 184-189, 1987.

## Wide Temperature Range Operation of DFB Lasers at 1.3 $\mu\text{m}$ Wavelength

T. R. Chen  
Ortel Corporation  
2015 W. Chestnut St., Alhambra, CA 91803

### Summary

DFB lasers operating in a wide temperature range, normally between  $-45^{\circ}\text{C}$  and  $+85^{\circ}\text{C}$ , without TE cooler provide low noise, cost-effective light sources for interactive analog distribution networks. The elimination of TE coolers may also improve the overall system reliability.

InGaAsP/InP strained multiquantum well laser structure has been proved to be a promising candidate for wide temperature range operation. DFB lasers operation in a temperature range between  $-60^{\circ}\text{C}$  and  $+110^{\circ}\text{C}$ , with a sidemode suppression ratio better than 40 dB was demonstrated.

These lasers showed very low threshold current (1.4 mA at  $20^{\circ}\text{C}$  and 7.2 mA at  $80^{\circ}\text{C}$ ), high slope efficiency (0.65 mW/mA at  $20^{\circ}\text{C}$  and 0.53 mW/mA at  $80^{\circ}\text{C}$ ), low noise ( $\text{RIN} < -155$  dB/Hz) and low distortion ( $\text{CSO} < -50$  dBc,  $\text{CTB} < -65$  dBc between  $-45^{\circ}\text{C}$  and  $+85^{\circ}\text{C}$ ).

In this talk, advances in wide temperature DFB lasers will be reviewed. The principles for wide temperature range operation of a DFB laser will be addressed. Important issues such as maintaining singlemode operation across a wide temperature range, temperature sensitivity of threshold current and slope efficiency of a DFB laser, low distortion in a wide temperature range and reliability of wide temperature DFB lasers will be discussed.

The author would like to acknowledge the support of Rome Labs under contract #F30602-95-C-0182. I would also like to thank my colleagues Dr. P. C. Chen, Dr. J. Ungar, Dr. W. Hsin, Mr. S. Oh, Mr. H. Luong and Dr. N. Bar-Chaim, for their contribution in many ways.

## Longitudinal Effects on *SMSR* in Gain-Coupled DFB Lasers

Jianyao Chen, Roman Maciejko and Toshihiko Makino\*

Optoelectronics Laboratory, Department of Engineering Physics, École Polytechnique  
P. O. Box 6079, Station "Centre-ville", Montréal, Québec, Canada H3C 3A7

\* Nortel Technology, P. O. Box 3511, Station C, Nepean, Ontario, Canada K1Y 4H7

Gain-coupled DFB lasers have a complicated modal interaction influenced by the effects of spatial hole burning (SHB) and nonlinear gain compression (NGC) because of the carrier-dependent longitudinally distributed structures [1]. In order to obtain a better understanding of the high single mode performance of gain-coupled DFB lasers, we perform a self-consistent multimode analysis using spatially dependent rate equations for the carrier density  $N$  and the modal photon number  $I_i$  at steady state:

$$\gamma_i I_i = R_{sp}^i \quad (1)$$

$$J(z) = R[N(z)] + \frac{1}{A_c} G[N(z), S(z)] \sum_i |Z_i(z)|^2 I_i \quad (2)$$

together with the coupled wave equations:

$$\frac{dZ_i^+}{dz} + j[\beta_i(z) - \beta_0 + j\frac{\gamma_i}{2v_g}]Z_i^+ = -jK_i(z)Z_i^- \quad (3)$$

$$-\frac{dZ_i^-}{dz} + j[\beta_i(z) - \beta_0 + j\frac{\gamma_i}{2v_g}]Z_i^- = -jK_i(z)Z_i^+ \quad (4)$$

where  $R_{sp}^i$  is the spontaneous emission rate coupled into the corresponding mode [2] and  $\gamma_i$  is defined as the decay rate of the DFB mode.  $J(z)$ ,  $R[N(z)]$  and  $G[N(z), S(z)]$  are the laser pumping rate, the spontaneous carrier recombination rate and the net stimulated emission rate, respectively.  $S$  represents the distribution of the total photon density in the laser.  $v_g$  and  $A_c$  denote the group velocity of light in the laser and the cross section area of the laser waveguide, respectively.  $\beta_0$  is the Bragg wavenumber of the DFB structure.  $\beta_i(z)$  and  $K_i(z)$  represent the modal propagation constant and the DFB coupling coefficient as usual.

By transforming the coupled wave equations (3) and (4) into an  $F$ -matrix form and solving them with equations (1) and (2) simultaneously, we can obtain the self-consistent multimode solutions for the gain-coupled DFB lasers, including the SHB and NGC effects. Moreover, the side mode suppression ratio (*SMSR*) in the DFB laser can also be determined by:

$$SMSR_{\pm L/2} = \frac{P_{\pm L/2}^m}{P_{\pm L/2}^s} = \frac{\gamma_s \omega_m R_{sp}^m |Z_m^\pm(\pm L/2)|}{\gamma_m \omega_s R_{sp}^s |Z_s^\pm(\pm L/2)|} \quad (5)$$

where the superscripts and subscripts  $m$  and  $s$  are used to denote the main mode and side mode, respectively.  $\pm L/2$  represents the values at the right and left end facets, respectively.

Our self-consistent analysis reveals that longitudinal SHB has a significant effect on side mode suppression in gain-coupled DFB lasers. For the lasers with a large coupling strength  $|K|L$ , the intensity of the lasing mode is usually concentrated at the center of the DFB cavity. The longitudinal SHB effect induces a concave index distribution along the

laser waveguide. Therefore, the resonance conditions of DFB modes are changed and the stimulated emission of short wavelength modes is enhanced. The results in Fig. 1 show that, with the same coupling strength  $|K|L$  at threshold, antiphase gain-coupled DFB lasers produce higher  $SMSR$  values than their inphase gain-coupled counterparts because of the SHB effect. However, when  $|K|L$  is small ( $< 1.6$ ), the light intensity is higher at the two ends of the cavity. Then, the SHB effect induces a convex index distribution in the DFB cavity, which strongly favours the long wavelength DFB mode. When  $|K|L$  is small enough, the effect can even overcome the modal selection effect of the gain grating [3] and causes long wavelength lasing in antiphase gain-coupled lasers.

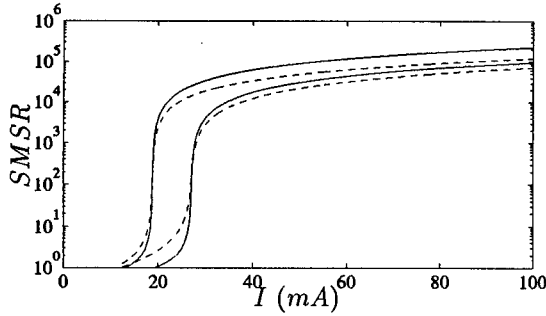


Fig. 1  $SMSR$  in gain-coupled DFB lasers. Solid line: antiphase gain-coupled; dashed line: inphase gain-coupled. The curve sets with a higher and lower thresholds correspond to  $|K|L = 2$  and  $|K|L = 3$ , respectively.

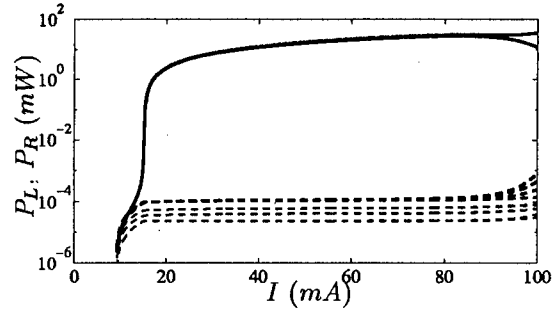


Fig. 2 Modal power evolution with bias current in an antiphase gain-coupled DFB laser with  $|K|L = 4$  and  $\epsilon_N = 5 \times 10^{-17} \text{ cm}^3$ . Solid line: lasing mode; dashed lines: side modes.

NGC also affects inphase and antiphase gain-coupled DFB lasers differently. Since the lasing mode is dominant and stable in inphase gain-coupled DFB lasers, the effect normally induces a gain variation within the region where the intensity of the lasing mode is high. In turn, this affects the lasing mode most and does not influence the side mode much. Self-consistent calculations indicate that NGC only reduces the  $SMSR$  slightly in inphase gain-coupled DFB lasers. However, in antiphase gain-coupled DFB lasers, the nonuniform gain variation induced by the NGC effect can further deteriorate the modal stability and cause the side modes to grow (see Fig. 2). This strongly degrades the side mode suppression in antiphase gain-coupled DFB lasers.

## References

- [1] T. Makino, "Mechanism for high single-mode stability of gain-coupled DFB lasers with periodically etched quantum wells", *Electron. Lett.*, Vol. 31, pp. 1579–1581, 1995.
- [2] B. Jonsson, A. J. Lowery, H. Olesen and B. Tromborg, "Instabilities and nonlinear L-I characteristics in complex-coupled DFB lasers with antiphase gain and index gratings", *IEEE J. Quantum Electron.*, Vol. 32, pp. 839–850, 1996.
- [3] J. Chen, A. Champagne, R. Maciejko, and T. Makino, "Improvement of single-mode gain margin in gain-coupled DFB lasers", *IEEE J. Quantum Electron.*, Vol. 33, pp. 33–40, 1997.



## Low short term timing jitter in an integrated monolithic extended cavity semiconductor mode-locked laser.

A. Wonfor, B. Zhu, I. H. White, R.V. Pentty.

Centre for Communications Research, University of Bristol, Queens Building, University Walk,  
Bristol. BS8 1TR. U.K.

Low timing jitter is required for low error rate communications in high capacity communications systems and for fast sampling applications. In particular return to zero (RZ) optical time division multiplexed (OTDM) schemes require low jitter between one pulse and the next in the pulse train so that the skirts of neighbouring pulses do not interfere with each other. We define this form of jitter to be short term jitter. However, techniques of jitter measurement using microwave spectra [1] or direct detection with a fast sampling oscilloscope provide no information about jitter on pulse repetition period timescales. Whilst spectral jitter measurements show jitter of several picoseconds, new measurements of jitter between one pulse and the next show jitter of significantly less than one picosecond.

A jitter measurement testbed, shown in Figure 1, has been developed which employs a Mach-Zehnder interferometer to enable measurement of jitter between neighbouring pulses in a train. The mode-locked laser input is fed through a 3dB coupler with one fixed length arm. The other arm is of variable length, employing a fibre phase shifter, additional fibre delay, and a final variable optical bulk delay. The two arms are then combined with another 3dB coupler and then undergo amplification with an EDFA and are measured with an SHG autocorrelator.

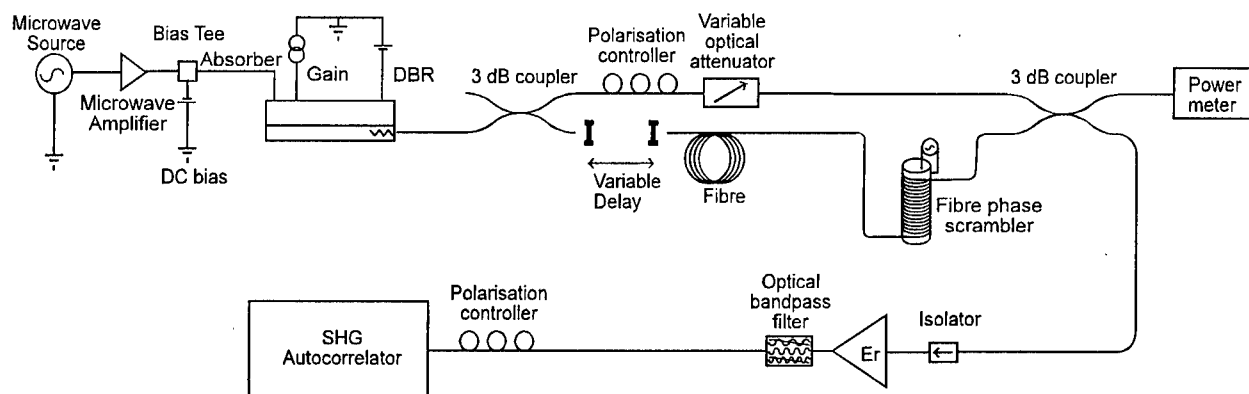


Figure 1 Experimental arrangement for short term jitter measurement.

The delay introduced in one arm of the interferometer allows the overlap of two pulse trains, one delayed by an integer number of pulse periods with respect to the other. The jitter between the pulse trains causes a broadening of the autocorrelation trace which allows measurement measurement of the short term jitter at the given delay.

Measurements have been performed on a monolithically integrated active/passive cavity MQW laser, actively mode-locked at 10GHz via modulation of an absorber section [2]. Optimisation of the drive conditions to the gain, DBR and absorber sections has enabled sub-10ps pulses to be produced.

Figure 2 shows both the measured pulsewidth of the overlapped pulse trains and time-resolved jitter for the mode-locked laser as a function of delay. There is no detectable time resolved jitter until a time delay of 1ns is introduced, the jitter then increasing until it reaches a plateau of 2.3ps after 150ns. This is in good agreement with the 2.8ps broadband jitter measured for this laser using the microwave spectrum technique [1].

A model has been developed using travelling wave rate equations and including the effect of self modulation, gain nonlinearities, a distributed Bragg reflector and noise sources. Figure 3 shows preliminary results of simulations using this model of time resolved jitter for varying pulse train delays. Here time resolved jitter is not significant until 1ns delay, the simulation having a similar form to the experimental results. The simulation results suggest that spontaneous emission is the dominant cause of jitter in this laser, with carrier dynamics having a time constant of the order of 1ns.

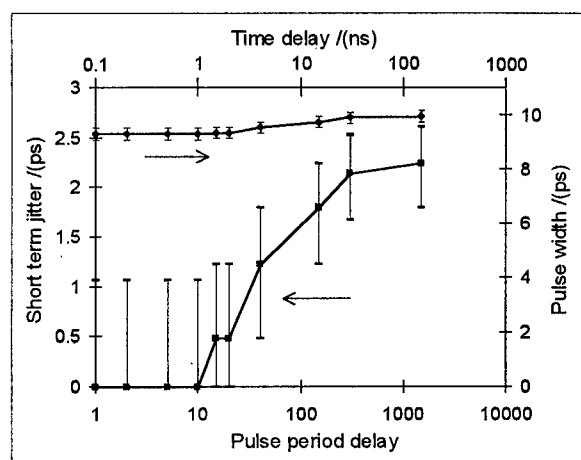


Figure 2 Pulsewidth and short term jitter versus time delay.

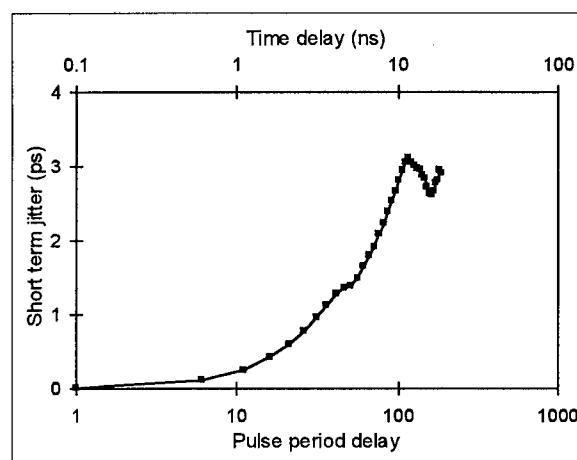


Figure 3 Simulated short term jitter versus time delay.

The laser output has low pulse to pulse timing jitter and is thus usable with clock recovery circuits which are often sensitive to short term jitter. This is not obvious from broadband microwave jitter measurements, which predict similar jitter values as delay resolved jitter measurements with a long delay between pulses.

Short term jitter has been measured in an extended cavity mode-locked laser operating at a pulse repetition frequency of 10 GHz, exhibiting FWHM pulsewidths of less than 10 ps. Timing jitter is insignificant until a time delay of greater than 1 ns is introduced. This is attributed to spontaneous emission, confirming simulation results.

In conclusion although uncorrelated jitter of several picoseconds is measured for this device, the short term timing jitter is shown to be significantly sub-picosecond, using a new direct measurement technique.

#### References

- 1 Lach, E., Baums, D., Hache, C., Haisch, H., Kühn, E., Satzke, K., Schilling, M., Weber, J. and Zielinski, E. *Proceedings of ECIO '95*, Delft. April 3-6 1995. (1995).
- 2 Leep, D.A. and Holm, D.A., *Appl Phys Lett* 60 2451-2453 (1992).

## MEASUREMENT OF SELF-PHASE MODULATION IN A SEMICONDUCTOR OPTICAL AMPLIFIER USING A MACH-ZEHNDER INTERFEROMETER

A.DJALALI-VALI, P.GALLION, D.ERASME, C.CHABRAN

Département Communications, CNRS, URA 820  
Ecole Nationale supérieure des Télécommunications  
46, Rue Barrault - 75634 PARIS Cedex 13, France  
tel.: (33) 1.45.81.78.98

Semiconductor optical amplifiers (SOAs) are very attractive for fiber optical communication systems, because of their small size, low power consumption, and optical gain. However, non-linearities caused by signal induced carrier density modulation must be taken into account. Nevertheless, for some applications like in Sagnac interferometer, they can be used as an useful effect, for optical switching or wavelength converter. Theoretically, they appear as frequency deviation peaks at the leading and trailing edge of a pulse travelling through SOAs. An experimental set-up is used, in order to measure this effect confirming theoretical predictions. Furthermore, signal induced phase shift dependence on bias current of the SOA is presented.

### PRINCIPLE OF MEASUREMENT

The main idea is based on the injection of a quasi zero chirped optical pulse in a SOA. The frequency deviations appearing at the leading and trailing edge of the pulse are measured through a Mach-Zehnder interferometer.

A DFB laser ( $\lambda=1559$  nm), is externally modulated by an electro-optical modulator. Moreover, the optical pulse is amplified by an erbium doped amplifier. The latter is previously saturated by a pump laser and does not introduce additional chirp. As expected, a quasi zero chirped pulse is generated. The SOA (an Alcatel Alsthom laser) presents a bulk active layer. The optical gain for the TE mode is slightly higher (typically 2 dB more than for the TM mode). At the operating laser wavelength, the estimated optical gain is 12 dB.

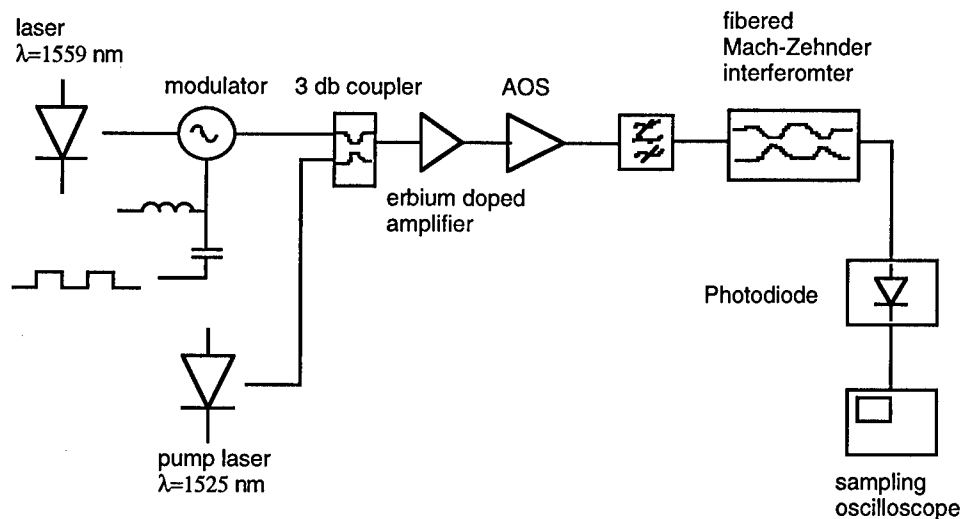


Figure 1. Experimental set-up

At the SOA's output, the chirp induced by carrier density modulation, is measured through a fibered Mach-Zehnder which includes a tuneable delay  $\tau$ . Besides the interference signal  $P_{\text{int}}(t)$ , each branch can be isolated in order to measure the signal  $P(t)$  and the delayed signal  $P(t+\tau)$  separately. Thus, the instantaneous frequency deviation can be calculated from:

$$\Delta f = \frac{P_{\text{int}}(t) - [P(t) + P(t + \tau)]}{4\pi\tau\vartheta\sqrt{P(t)P(t + \tau)}}$$

where  $\vartheta$  is the visibility of the interferometer.

## RESULTS AND DISCUSSION

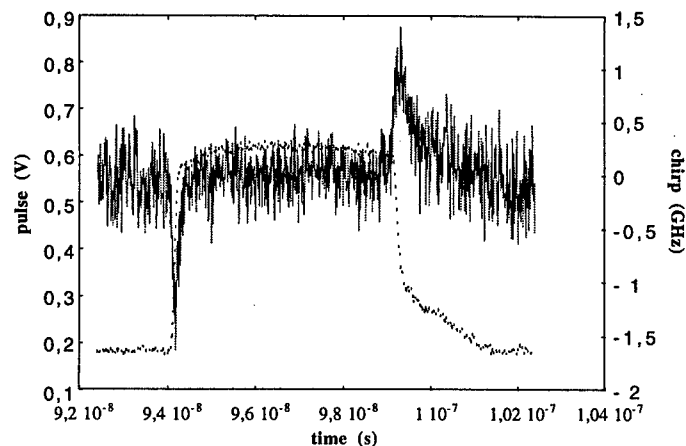


Figure 2. The frequency deviation (continuous line) induced by a square pulse (dotted line) is negative at the leading edge and positive at the trailing edge.

The chirp is measured for the same pulse at the SOA's input and for various bias currents. Figure 3 presents averaged frequency deviation at the leading edge of the pulse for 100mA, 90mA and 80mA bias currents of the SOA for an estimated injected power excursion of 100  $\mu$ W. The self phase modulations are  $0.6\pi$ ,  $0.8\pi$ , and  $0.9\pi$  respectively.

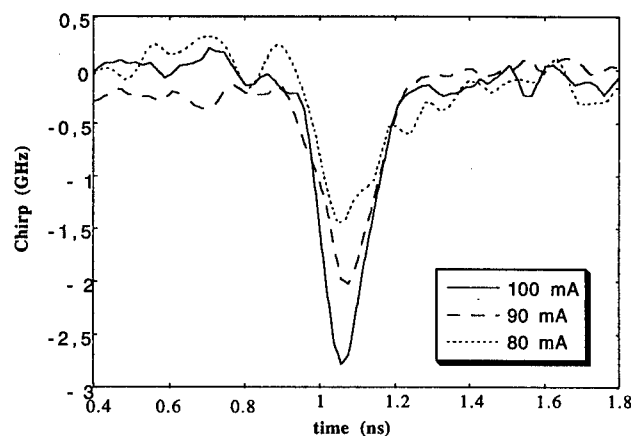


Figure 3. Chirp at the leading edge for various bias currents of the SOA.

The carrier density modulation induced chirp in a SOA is presented in Figure 2. The optical power increase at the leading edge of the pulse reduces the carrier density inside the SOA, thus the optical gain, and refractive index increases. The result is a negative frequency deviation at the leading edge. At the trailing edge, the opposite phenomena takes place and a positive chirp appears. The transit self phase modulation through a SOA can be calculated from the chirp by simple integration.

An increasing bias current of SOA leads to an increasing chirp amplitude. In the same way, the self-phase modulation increases. In conclusion, it is seen that a low optical power (an averaged power of only 200  $\mu$ W in our experiment) is enough to cause an important self-phase modulation. Moreover, it can be used in view of future applications like in Sagnac interferometer for optical switching or wavelength converter.

## REFERENCES

1. T.Durhuus, B.Mikkelsen, C.Joergensen, S. Lykke Danielsen, and K.E Stubkjaer, "All-Optical Wavelength Conversion by Semiconductor Optical Amplifiers", Journal of Lightwave Technology, vol. 14, no. 6, June 1996.
- 2.D.Baney, "Modélisation et caractérisation de la réponse FM des lasers a contre réaction distribuée mono et multi-section" - Phd Thesis, Telecom PARIS 90 E015.
3. J.Buus, "Single Frequency Semiconductor Laser", Chap .5, Publication of SPIE, Washington USA.

## **Novel Mechanism for Ultrafast Optical Nonlinearity in Semiconductor Laser Amplifier Using Assist Light**

**Munefumi Tsurusawa, Masashi Usami and Yuichi Matsushima**  
**KDD R&D Laboratories**  
**2-1-15 Ohara Kamifukuoka-shi, Saitama 356, Japan**

Optical nonlinearity in semiconductor laser amplifier (SLA) or saturable absorber (SA) is promising for optical gate including DEMUX as well as noise reduction and optical reshaping. As far as using real excitation process, however, the operating speed is limited by the carrier lifetime ( $\sim 1\text{ns}$ ). Therefore, the reduction of the carrier lifetime in the waveguide is requisite for the applications of ultra-high speed optical communication and signal processing, in which all-optical function is required. Although, there have been several approaches for reduction of the recovery time of SA [1-3], they are still not sufficient for ultra-high repetition rate ( $>100\text{Gbps}$ ) due to carrier accumulation effect [1,2] or heating problem [3]. In this paper, we propose a novel mechanism using the assist light for reduction of the carrier lifetime in SLA as a saturable absorber. Original idea is that the excess carriers quickly vanish by means of the stimulated recombination utilizing the CW assist light.

Figure 1 shows (a) the experimental configuration and (b) the simplified gain curve in the forward biased SLA to explain the principle. The device was the ridge waveguide InGaAs/InGaAsP MQW laser amplifier (gain peak= $1.58\mu\text{m}$ ). Measurements were carried out by a conventional cross-polarized pump-probe technique using 100fs pulse with a repetition rate of 80MHz. A CW additional light with longer wavelength (assist light) was superimposed to the front facet of the SLA. The steady state gain profile, under which the probe/pump pulse( $\lambda_1$ ) is absorbed, is shown by the solid line. The wavelength of the assist light( $\lambda_2$ ) is set at the transparent point on the curve [4]. Immediately after a pump (signal) pulse is passing through the SLA, the carrier population increases due to the absorption hence the probe transmission increases and the positive gain is generated for the assist light, which is shown by the dashed line. Then the gain profile quickly goes back to the steady state by means of the stimulated emission due to the assist light.

Figure 2 shows the normalized optical nonlinearity  $\Delta T$ , which is the change in the probe transmission, as a function of pump-probe delay time. The transparent wavelength of the CW assist light was  $1.56\mu\text{m}$  when operated at 10.7mA injection. The pump pulse energy was 1.7 pJ and the wavelength was  $1.53\mu\text{m}$ . The 1/e recovery time was drastically reduced by superimposing the assist light.

Figure 3 shows the 1/e recovery time  $\tau_r$  as a function of the assist light power. The recovery time  $\tau_r$  was reduced from 600ps to 70ps as increasing the assist light power, since the total quantity of stimulated recombinations seems to be proportional to the number of incident photons.

Figure 4 shows the device length dependence of the recovery time  $\tau_r$  and the optical nonlinearity at  $t=0$ . Injected current into each device was determined to make the waveguide transparent for the assist light. Shorter recovery time was obtained for shorter device length. Note that large optical nonlinearity  $\Delta T(0)$  was obtained for shorter  $L$ . In other words, the required pump energy is decreased to obtain the same  $\Delta T(0)$ , which gives shorter  $\tau_r$ . Consequently, much further reduction of lifetime is expected for shorter device.

We have proposed and first demonstrated a novel mechanism for ultrafast optical nonlinearity in semiconductor laser amplifiers as saturable absorbers. We have obtained the reduced carrier lifetime of less than 70ps by stimulated recombination due to a novel assist light. The further reduction of lifetime can be expected for shorter device. This novel mechanism is promising for ultra-high repetition-rate gate function and noise reduction function, because there is little heat generation process through this fast stimulated emission.

## References

1. S. Nakamura, K. Tajima and Y. Sugimoto, Appl. Phys. Lett. 66, 2457(1995)
2. A. Takeuchi, T. Inata, Y. Sugiyama, Y. Nakata, S. Nakamura, and S. Muto, Jpn. J. Appl. Phys.,31, L669(1992)
3. A. Hirano, H. Tsuda, K. Hagimoto, R. Takahashi, Y. Kawamura and H. Iwamura, Electron. Lett., 31, 736(1995)
4. R.J. Manning and D.A.O. Davies, Opt. Lett., 19, 889(1994)

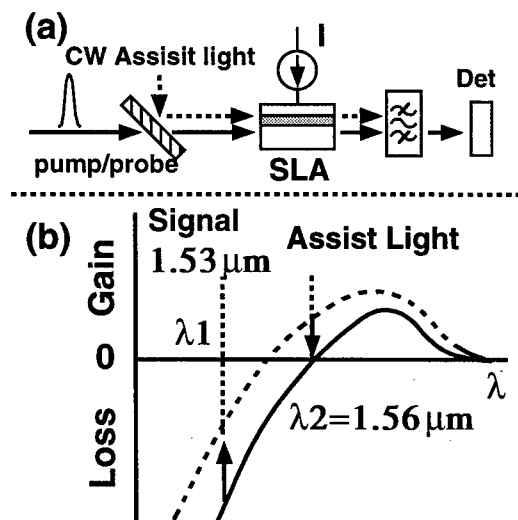


Fig.1 (a) Experimental configuration (b) Simplified gain curve of forward biased SLA

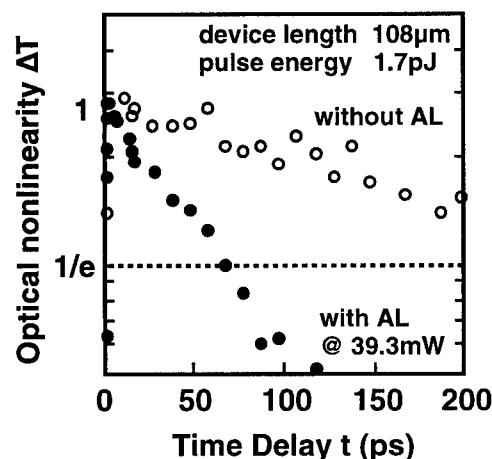


Fig.2 Time dependence of optical nonlinearity  $\Delta T$  with/without CW assist light.

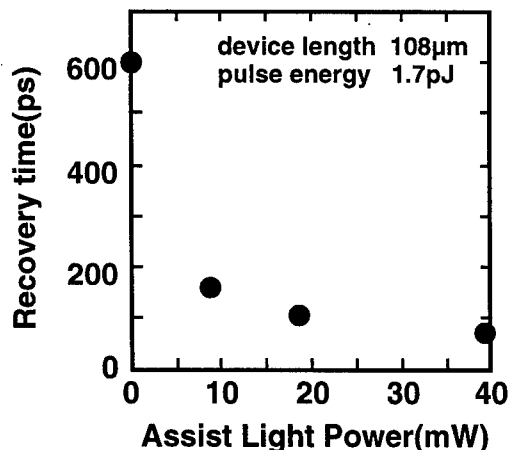


Fig.3 1/e recovery time as a function of the CW assist light power.

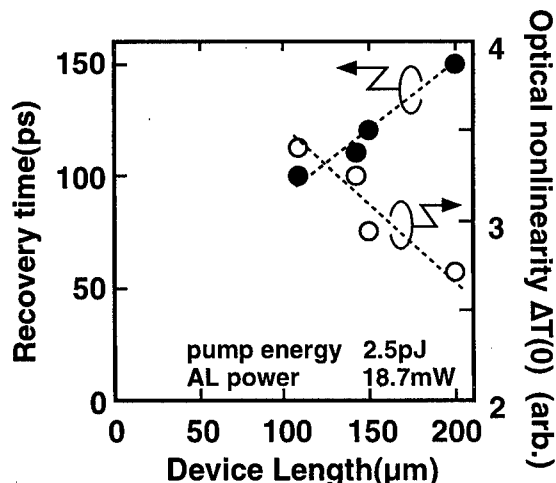


Fig.4 Device length dependence of the 1/e recovery time and optical nonlinearity at  $T=0$ .

## Applications of lasers for printing

Dave Kessler  
Hard Copy & Display Technology Division  
Imaging Research and Advanced Development  
Eastman Kodak Company

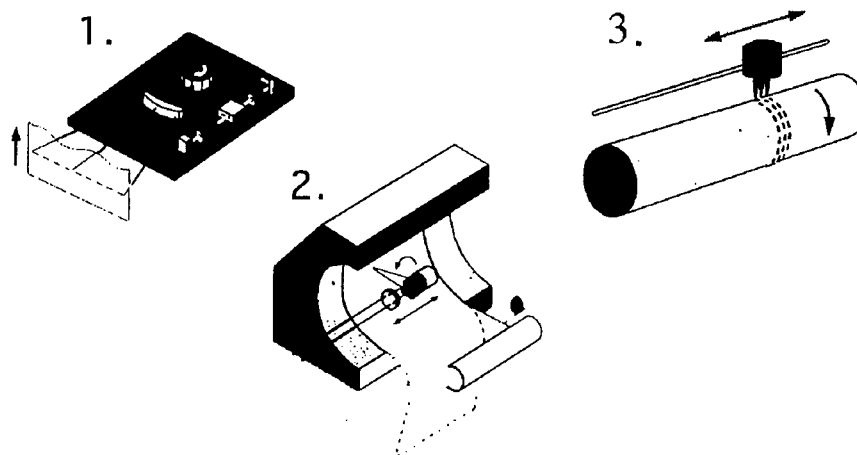
Address: David Kessler  
Building 65, Research Labs  
Rochester, NY 14650-1822  
E-mail: Dkessler@kodak.com

### Abstract:

Laser printing is an active and growing field. Many different lasers are used, from low-power single mode to high-power laser bars. Different printing applications will be described with emphasis on the required characteristic of the laser.

### Summary:

Laser printing is an active and growing field. There are three basic printing configurations: (1) the flying spot printer, (2) the internal drum printer and (3) the external drum printer. The most common one, the flying spot configuration is used in desktop printers where the laser beam is deflected by a polygon. This application uses a relatively low-power single mode laser mainly for line art monochrome printing at relatively low resolutions of 300 dots per inch. The laser is current-modulated at two levels (1 bit).



The flying spot configuration is also used in more challenging applications such as in continuous tone hospital printers where the lasers are modulated at up to 12 bits to produce high-quality monochrome images. The optical requirements for achieving artifact-free prints are quite demanding. Raster placement accuracy must be less than one percent of the raster pitch. Laser noise, back reflection, thermal drifts, and mode hopping can produce objectionable printing defects. Continuous tone color printers on silver halide materials use three lasers at three different wavelengths combined for printing on photographic film or paper. These printers use externally modulated gas and solid state lasers for the green and blue. Reliable, cost-effective, directly modulatable, laser sources would be preferable. Flying spot printers cannot provide resolution and format sizes needed in the graphic arts. Internal drum printers common for imagesetting use single-mode lasers at relatively low power levels. Systems using processless media usually need higher power, typically a few Watts. Fiber lasers seem to be a promising practical solution for this printing configuration.

External drum printers use large slowly turning drums. For practical printing speed, multi-spot printing heads are needed. High-power lasers are needed when dry media, such as thermal dye ablation or thermal dye transfer, are used for color proofers and platesetters. There are three kinds of laser thermal printing heads for external drum printers. The most common is the one using multi-mode pigtailed fibers. Another approach is to use laser bars to illuminate a spatial light modulator that is imaged onto the media. A third approach is to use a monolithic laser diode array with a number of independently modulated beams so as to reduce laser packaging cost. High-power, inexpensive arrays of single-mode laser diodes, when available, would enable better printing heads with higher resolution and larger depth of field.

The paper will explore the design tradeoffs associated with the currently available lasers and those on the wish list of the printer designer. Some relevant laser printing systems will be shown and discussed.



**Narrow-Linewidth, High-Brightness Laser Diode Arrays**

A. Schoenfelder, S.D. DeMars, and R.J. Lang

SDL, Inc., 80 Rose Orchard Way, San Jose, CA 95134

Phone: (408) 943-9411, Fax: (408) 943-1070

High-brightness, high-power diode laser arrays are expanding their role in pumping multi-level solid-state laser systems. Various advanced solid-state laser systems take advantage of strong but narrow absorption lines and thus, demand a very small linewidth of the pump source. Conventional diode laser bars cover only the lower part of required brightness range and have typically a broad emission spectrum. In this work, we describe a laser diode array source consisting of broad area laser diodes utilizing an angled-grating distributed feedback ( $\alpha$ -DFB) structure operating at a wavelength of 960.5 nm, which is an absorption line for Er:YAG solid-state material lasing near 3  $\mu\text{m}$ . Because the gain for this laser transition is quite low, the performance is strongly dependent upon the spectral and spatial quality of the pump beam. In order to obtain adequate power from the laser, a pump source is required which could deliver several Watts of power into a 50  $\mu\text{m}$  spot within less than 0.3 NA with a spectral bandwidth of  $<1$  nm at precisely 960.5 nm.

The  $\alpha$ -DFB laser combines the high power capacity of a broad area stripe device with grating-induced mode control yielding diffraction-limited and narrow-linewidth performance at high power levels. The grating is oriented at an angle with respect to the facets, and therefore provides not only longitudinal, but also *lateral* mode control. Single  $\alpha$ -DFB laser diodes were recently demonstrated to produce a collimated 1 W cw single-frequency ( $>40$  dB), single-lobed beam with a diffraction-limited lateral  $1/e^2$  divergence of  $0.29^\circ$  (5 mrad) at 980 nm.<sup>1</sup> Recently, we reported for the first time  *$\alpha$ -DFB laser diode arrays* with a maximum cw output power of 13.5 W at 980 nm.<sup>2</sup> The device exhibited very uniform lateral  $1/e^2$  divergence and emission wavelength distribution across the array.

In this work, we present the performance characteristics of an  $\alpha$ -DFB laser diode array with higher brightness at 960.5 nm. The arrays consists of 11 elements on a 0.5 cm wide bar. The device structure was described previously.<sup>2</sup>

The cw light output versus current (L-I) characteristic and the spectrum at an output power level of 4 W cw at a temperature of  $8^\circ\text{C}$  are shown in Figs. 1 and 2, respectively. The device was temperature-tuned to a peak emission wavelength of 960.5 nm. The output power exceeds 5 W cw. The device exhibits a spectral width of less than 1 nm measured at the -30 dB points. A temperature increase to room temperature red-shifts the emission spectrum by about  $+0.08$  nm/ $^\circ\text{C}$  but does not otherwise affect the device performance parameters significantly. The lateral far-field intensity profiles at various bias currents are shown in Fig. 3. The device exhibits a full width (FW)  $1/e^2$  divergence of only  $0.33^\circ$  up to 5 W cw output power.

Utilizing a 1-D cylindrical lens we collimated the raw output power and measured the collimated beam power versus current characteristics in a distance of 5 cm (lower curve in Fig. 1). We focused the collimated beam with an 8 mm focal length aspheric lens into a 50  $\mu\text{m}$  spot with less than 0.3 NA at 4+W cw output power.

In conclusion, we have demonstrated a new type of broad area narrow-linewidth, high-brightness laser array with an angled-grating distributed feedback structure. The authors

would like to thank Renny Fields and Todd Rose from The Aerospace Corporation for valuable discussions.

<sup>1</sup> S.D. DeMars *et al.*: "Angled grating distributed feedback laser with 1 W cw single-mode, diffraction-limited output at 980 nm," *Techn. Digest CLEO '96*, paper CTuC2, pp.77-78, 1996

<sup>2</sup> A. Schoenfelder *et al.*: "Ultra-High Brightness, High Power Broad Area Laser Diode Arrays," *Techn. Digest of IEEE Int. Semiconductor Laser Conference '96, Haifa, Israel*, post deadline paper PDP7, pp. 16-17, 1996

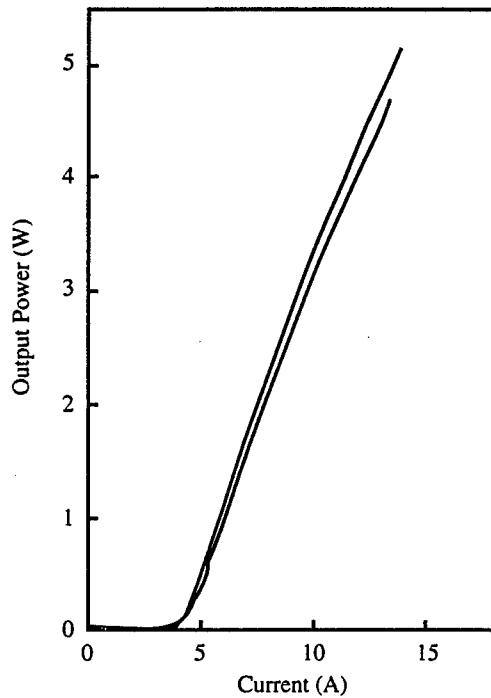


Fig.1. Light-current characteristic of an  $\alpha$ -DFB array. Upper curve: raw output power. Lower curve: power in the collimated beam.

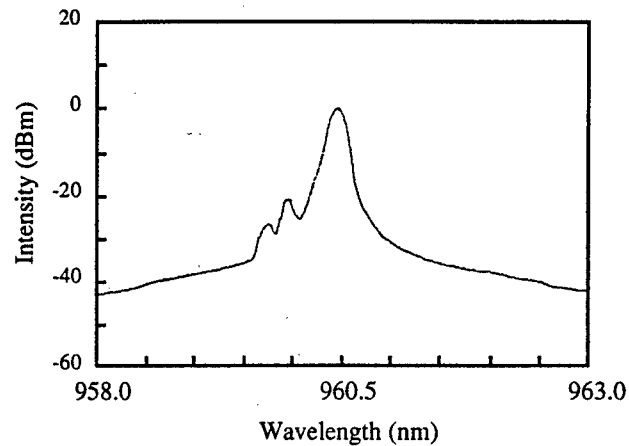


Fig.2. Spectrum at a raw output power of 4.0 W.

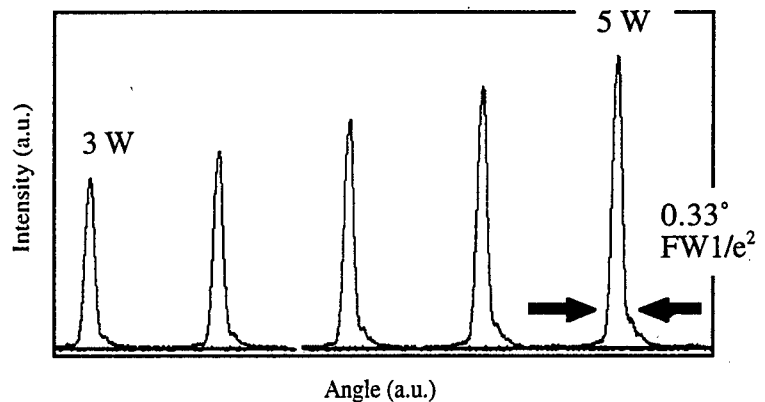


Fig.3. Farfield profile in the lateral (horizontal) direction at various cw output power levels.

## High-power, Diffraction-limited InGaAsP Flared Unstable Resonators at 840 nm

Vincent V. Wong, Hanmin Zhao, Stephen O'Brien, Mehrdad Ziari, Robert J. Lang and Jean-Marc Verdiell  
SDL, Inc., 80 Rose Orchard Way, San Jose, CA 95134, Ph: (408) 943-9411, FAX: (408) 943-1070

Jean-Luc Archambault

SDL Optics, Inc., 6703 Rajpur Place, Saanichton, BC, Canada V8M 1Z5, Ph: (604) 544-2244, FAX: (604) 544-2225

### Summary

Previously, we reported on the first demonstration of  $>1.0$  W cw diffraction-limited from an InGaAsP flared amplifier at 780 nm.<sup>1</sup> In this paper we report on the high-power, diffraction-limited performance of InGaAsP/GaAs flared devices in three configurations: a Fabry-Perot (FP) unstable resonator, a fiber Bragg grating wavelength-stabilized laser and an external grating tunable laser. In all three configurations over 1.0 W cw diffraction-limited was obtained with up to 2.0 W cw diffraction-limited from FP unstable resonators. In addition, temperature-insensitive operation and wavelength tunability was achieved using the fiber Bragg grating and external grating, respectively.

The epitaxial structure, grown on a GaAs substrate by MOCVD, consists of a separate-confinement heterostructure with a compressively-strained InGaAsP quantum well ( $\lambda \sim 840$  nm) bounded by an InGaAsP waveguide and InGaP cladding layers. This InGaAsP epitaxial material was processed into flared gain elements, consisting of a single mode waveguide integrated with a flared gain region. Figure 1(a) shows an L-I curve of an Al-free flared unstable resonator under cw operation. The device threshold and slope efficiency are 1.1 A and 0.95 W/A, respectively. The operating wavelength is approximately 852 nm and the spectral width is approximately 4 nm, as shown in the inset. The wavelength shift as a function of device temperature was measured to be 0.3 nm/ $^{\circ}$ C, and the lasing wavelength shifted by 2.5 nm as the output power was increased to 2.0 W. Figure 1(b) shows a reimaged cw far-field profile parallel to the *pn*-junction plane of the device at power levels ranging from 0.5 W to 2.0 W. The profiles remain single-lobed and diffraction-limited throughout with approximately 81% of the power within the central lobe. The peak intensity of the main lobe increases linearly with the total output power, indicating that the Strehl ratio ('power-in-the-bucket') remains approximately constant over the operating range of the device.

By incorporating a fiber Bragg grating into the laser cavity as a rear reflector, the output spectrum of the Fabry-Perot unstable resonator can be both stabilized and narrowed.<sup>2,3</sup> Figure 2 shows the L-I curve of the fiber grating stabilized laser. The lasing threshold and slope efficiency are 1.4 A and 0.9 W/A, respectively. Over 1.0 W cw diffraction-limited is obtained at a current of approximately 2.4 A. The insets to the figure show both the output spectrum and far-field profile of the device. The amplified spontaneous emission is suppressed by over 35 dB. Multiple longitudinal modes of the external cavity are visible in the spectrum; however, essentially all of the power is contained within the 0.4 nm bandwidth of the fiber grating. The wavelength shift as a function of the flared amplifier chip temperature was investigated with no measurable shift of lasing wavelength over the temperature range from 20 $^{\circ}$ C to 65 $^{\circ}$ C. In addition, the wavelength shift as a function of the fiber grating temperature was measured to be 0.0056 nm/ $^{\circ}$ C. The far-field profile of the device is shown at a current of 2.0 A and was single-lobed and diffraction-limited throughout the operating range of the device. To our knowledge, this is the highest power demonstrated from a diffraction-limited fiber grating stabilized laser source.

Tunability of the spectral output of InGaAsP flared gain elements can be achieved with a diffraction grating in an external cavity configuration.<sup>4</sup> Figure 3(a) plots the L-I curve of the device. The lasing threshold and slope efficiency are 1.0 A and 0.7 W/A, respectively. Over 1.0 W cw diffraction-limited is obtained at a current of approximately 2.5 A. The inset to Figure 3(a) shows the far-field profile, which is single-lobed and diffraction-limited, for the device at various operating currents. Figure 3(b) plots the operating current as a function of wavelength at a constant output power of 0.5 W for the external grating tunable laser. The inset to Figure 3(b) shows the output spectrum of the device operating in a single longitudinal mode at a wavelength of approximately 838 nm and with a sidemode suppression ratio of greater than 30 dB.

In summary, InGaAsP/GaAs flared gain elements have demonstrated over 2.0 W cw diffraction-limited at an operating wavelength of 840 nm. This represents the highest diffraction-limited output power reported in the Al-free materials system. Fiber Bragg grating and external grating cavity configurations incorporating these gain elements have also demonstrated over 1.0 W cw of diffraction-limited power, temperature-insensitive operation and tuning ranges of 20 nm. The authors would like to thank J. Kern for expert technical assistance. This work was supported by the Advanced Research Projects Agency and U. S. Army Missile Command under contract #DAAH01-95-C-R177.

## References

- (1) S. O'Brien, *et al.*, CLEO 1995, Baltimore, MD, paper CThP5.
- (2) D. Mehuys, *et al.*, Patent #5,537,432 (July 16, 1996).
- (3) D. Hargreaves, *et al.*, OFC 1996, paper ThG3.
- (4) D. Mehuys, *et al.*, *Elec. Lett.*, vol. 29, p. 1254, 1993.

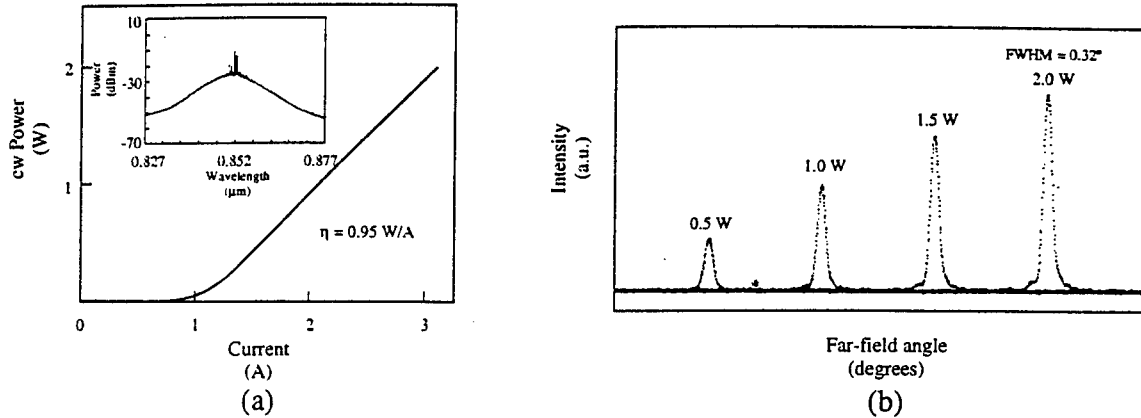


Figure 1. Device characteristics of an InGaAsP Fabry-Perot unstable resonator: (a) L-I curve and spectrum (inset); (b) Far-field profile at various operating powers.

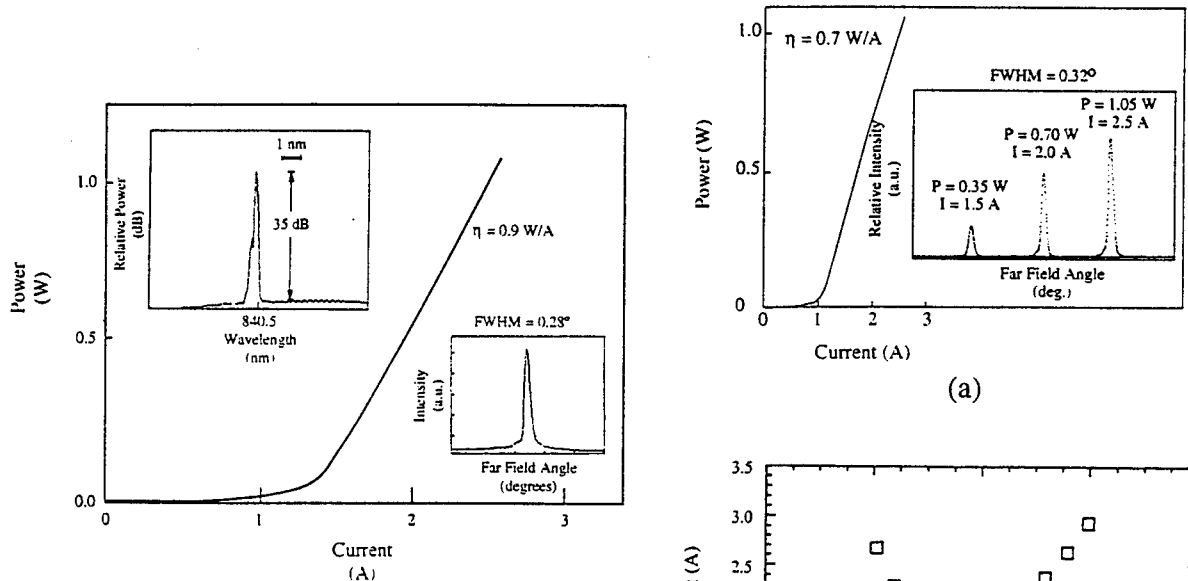


Figure 2. Device characteristics of an InGaAsP fiber Bragg grating stabilized laser: L-I curve, spectrum (inset) and reimaged far-field profile (inset).

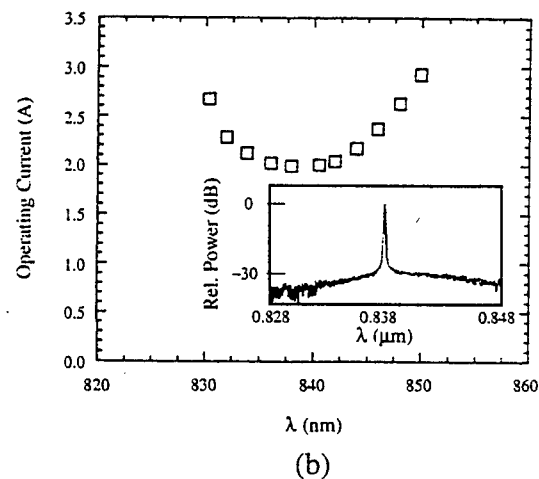


Figure 3. Device characteristics of an InGaAsP external grating tunable laser: (a) L-I curve and reimaged far-field profiles (inset); (b) Operating current as a function of wavelength at a constant output power of  $0.5 \text{ W}$  cw and spectrum (inset)

## High-Performance Al-free Diode Lasers

L. J. Mawst

University of Wisconsin-Madison  
1415 Engineering Dr., Madison WI 53706

### ABSTRACT

Broad Area, 100  $\mu\text{m}$ -stripe lasers, with Al-free active regions operating at a wavelength of 0.98  $\mu\text{m}$  (0.81  $\mu\text{m}$ ), provide high CW powers: 8W (5W) and "wallplug" efficiencies: 66% (45%). At 0.81  $\mu\text{m}$ , the devices are potentially twice as reliable as Al-containing active-layer devices.

The growth of InGaAsP alloys lattice-matched to a GaAs substrate is very attractive as an aluminum-free alternative to the conventional AlGaAs-based materials for diode laser structures. For wavelengths  $< 0.84 \mu\text{m}$ , conventional lasers structures utilize  $\text{Al}_x\text{Ga}_{1-x}\text{As}$  active regions. Replacing the  $\text{Al}_x\text{Ga}_{1-x}\text{As}$  active region with InGaAsP, more than doubles the power density at catastrophic optical mirror damage (COMD)<sup>1</sup>. Other advantages include: (1) significantly lower series resistance<sup>2</sup> and higher thermal dissipation characteristics<sup>3</sup> result from the higher electrical and thermal conductivity<sup>4</sup> of InGaP compared with AlGaAs; (2) The use of the InGaAsP-based material system, as opposed to InGaAs/AlGaAs, allows for the possibility of introducing strain-compensated active regions for high performance and reliability<sup>5</sup>; and (3) advanced single-mode, index-guided, laser structures generally require multiple growth steps, making the AlGaAs based material system difficult to use because of the high oxidation rate of AlGaAs<sup>6</sup>. By contrast, the low oxidation rate of InGaP, makes the Al-free material system desirable for the growth of complex-index guided structures.

Using a broad-waveguide design<sup>7,8</sup>, Al-free InGaAs/InGaAsP/InGaP ( $\lambda=980\text{nm}$ ) diode lasers have been grown by low-pressure MOCVD. These structures have demonstrated record performance in terms of CW output power<sup>9</sup> (8.5 W) and total power conversion efficiencies (66%)<sup>10</sup>. A comparison of COMD power density levels for strained-layer InGaAs quantum-well lasers in the AlGaAs-based and Al-free material systems reveal no significant differences. Thus, in the wavelength region  $\lambda > 0.88 \mu\text{m}$  (i.e. InGaAs active), Al-free structures exhibit output powers similar to conventional InGaAs/AlGaAs-based structures. However, the lower series resistance and ability to easily perform regrowth in the Al-free material system are advantageous.

Extending the Al-free material system into the shorter wavelength ( $< 0.87 \mu\text{m}$ ) region, requires the use of an InGaAsP quantum well. The conventional AlGaAs-based 0.78-0.81  $\mu\text{m}$  diode laser structure utilizes an  $\text{Al}_x\text{Ga}_{1-x}\text{As}$  quantum well, which leads to long-term reliability problems. In this wavelength region, the use of an Al-free active region offers potential long-term reliability at twice the output power of AlGaAs-based lasers. However, as yet, the performance of InGaAsP/InGaP/GaAs lasers has not surpassed that of AlGaAs-based lasers because the small bandgap differences of Al-free devices cause severe carrier leakage. As a result, threshold-current densities,  $J_{\text{th}}$ 's, have

been high (400-450A/cm<sup>2</sup> for 1mm-long devices) and the threshold-current characteristic temperature,  $T_0$ , has had low values (70-80K)<sup>11</sup> with the notable exception of tensile-strained quantum well devices<sup>12</sup>:  $J_{th}=310\text{A/cm}^2$  and  $T_0=102\text{K}$ . To reduce carrier leakage, we have employed  $\text{In}_{0.5}(\text{Ga}_{0.5}\text{Al}_{0.5})_{0.5}\text{P}$  cladding layers. The structure is shown in Fig. 1a. The broad waveguide provides a low internal loss coefficient ( $\alpha_i=3\text{cm}^{-1}$ ) and a large equivalent (transverse) spot size ( $0.5\mu\text{m}$ ), enabling high output powers and narrow transverse beamwidths ( $\Theta_{\perp}=35^\circ$ ). The optical confinement factor for this structure is 3%. As a result of the higher bandgap  $\text{In}_{0.5}(\text{Ga}_{0.9}\text{Al}_{0.1})_{0.5}\text{P}$  reducing carrier leakage into the waveguide,  $T_0$  for 1mm-long devices increases to 140K compared to 120K for devices with  $\text{In}_{0.5}\text{Ga}_{0.5}\text{P}$  confining layers.  $J_{th}$  is  $290\text{A/cm}^2$  for 1mm-long devices. For 1.2mm-long devices under cw operation, slope efficiencies (both facets) are relatively high (1W/A) and the series resistance is  $0.14\Omega$ . Then, as shown in Fig. 1b, at  $20^\circ\text{C}$  we obtain 5W cw (both facets) from uncoated,  $100\mu\text{m}$ -stripe devices.

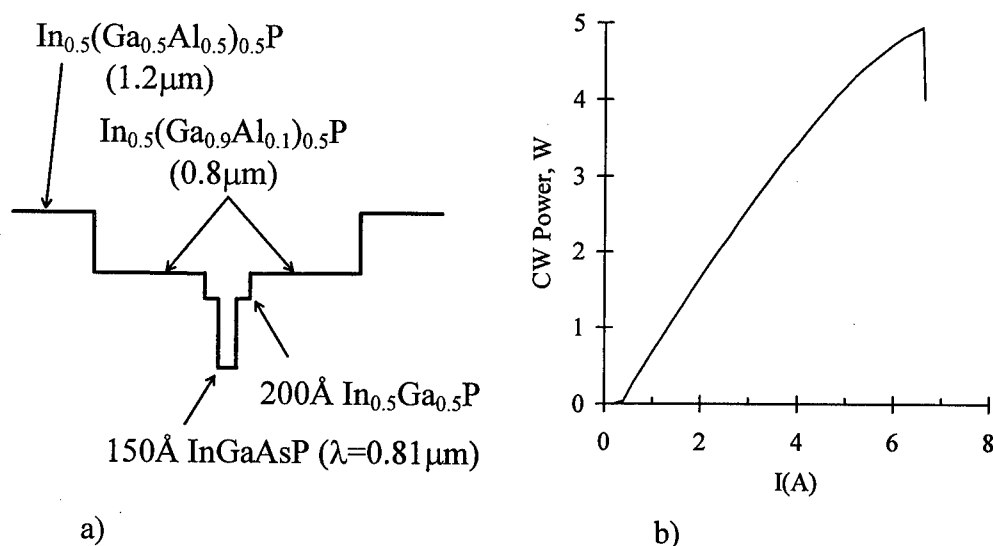


Fig. 1  $0.81\mu\text{m}$ -emitting Al-free active-region lasers: (a) schematic representation; (b) CW light-current characteristic at  $20^\circ\text{C}$  for a 1.2 mm-long,  $100\mu\text{m}$ -aperture, uncoated-facet laser.

1. J. K. Wade et al., Appl. Phys. Lett., **70**, 149(1997).
2. J. Diaz, et al, IEEE Photon. Tech. Lett., vol. **6**, 132(1994).
3. J. Diaz, Proceedings of LEOS'94, paper SL13.3, Boston, Mass., Nov., 1994.
4. W. Nakwaski, J. Appl. Phys., vol. **64**, 159(1988).
5. T. Fukunaga, et al, Appl. Phys. Lett., **69**, 248(1996).
6. A. Bhattacharya, et al, Electron. Lett., **32**, 657(1996).
7. D. Z. Garbuzov, et al, Proc. SPIE **2682**, 20(1996).
8. I. B. Petrescu-Prahova, et al, IEICE Trans. Electron. **E77-C**, 1472(1994).
9. L. J. Mawst, et al, Appl. Phys. Lett., **69**, 1532(1996).
10. D. Botez, et al, Electron. Lett., **32**, Oct. 10, 1996.
11. W. E. Plano et al., IEEE Photonics Technol. Lett. **6**, 465 (1994)
12. K. Uppal et al., IEEE Photon. Technol. Lett. **7**, 1128 (1995).

**Performance tests of quasi-CW laser diode pump arrays conducted or sponsored by NASA Goddard Space Flight Center**

Michael Krainak, Robert Afzal, Mark Stephen

*NASA Goddard Space Flight Center  
Greenbelt, Maryland 20771*

Gerald Browder, James Haden, Nils Carlson

*SDL Inc.  
80 Rose Orchard Way  
San Jose, California 95134-1365*

**Abstract**

We present tests of 100 W/bar quasi-CW laser diode arrays conducted, at SDL Inc. (at various deratings with constant junction temperature) and NASA Goddard, to assist in designing lasers for use in space.

Several performance tests of quasi-CW laser diode pump arrays have been conducted<sup>1</sup> and documented. Space flight missions<sup>2</sup> are being considered which require diode lifetimes in excess of 2 billion shots with little available (greater than one billion shot) reliability data.

For the vendor conducted test (denoted Test 1), one SDL-3257-H6 device was started at 100 W quasi-CW power, one SDL-3257-H6 device at 80 W quasi-CW power, and one SDL-3257-H6 device at 60 W quasi-CW power. Before the test began, the shot repetition rate was adjusted such that the device junction temperature was 30 C for every device. These devices were kept at these optical powers throughout the test (i.e., constant optical power). The pump diode laser pulse width was chosen as 200 microseconds for all devices. The 100 W/bar device operated with a 450 Hz repetition rate (9% duty factor), the 80 W/bar device operated with a 533 Hz repetition rate (11.2% duty factor), and the two 60 W/bar devices operated with a 750 Hz repetition rate (15 % duty factor). The Test 1 data is shown in Figure 1. The Test 1 constant peak optical power lifetest shows a 5 to 7 times increase in the expected lifetime for the SDL Inc. laser diode pump arrays (rated at 100 W peak optical power per bar) when they are derated to 80 W and 60 W respectively. All of the bars operated with less than 20% degradation for over 2 billion shots. Predicted lifetimes exceed 20 billion shots for the bars that were derated to 60 W.

The lifetime of the laser diodes varies inversely to the power loading at the facet and follows the power law:

$$Life(P_1) = Life(P_2) \times \left[ \frac{P_2}{P_1} \right]^n \quad (1)$$

The data was normalized relative one of the devices and the ratio of life time was plotted as a function of the ratio of operating peak optical power. It was found that the lifetime does vary inversely with optical power as in equation (1) with  $n \cong 3.5$ .

NASA Goddard conducted an independent laser diode performance test in at the NASA Goddard site. This test is described as follows. The NASA Goddard (Test 2) lifetest program used the Spectra Diode Lab 100 Watt Peak Power Quasi-CW laser diode arrays. Initially, one SDL-3252-C3 package device was run for approximately 42 weeks (7 months). In this case we chose the vendor recommended repetition rate of 200 Hz. The diode was water cooled with the water kept at a constant temperature of 25 C. The diode optical power, current level, temperature and shot count were monitored and recorded twice a day. In addition, the room temperature and humidity were also monitored and recorded twice a day. A fail-safe circuit was developed so that the laser diode array power supply would automatically be shut off when the diode temperature exceeded 30 C. This prevented thermal runaway (catastrophic failure) if the water chiller failed.

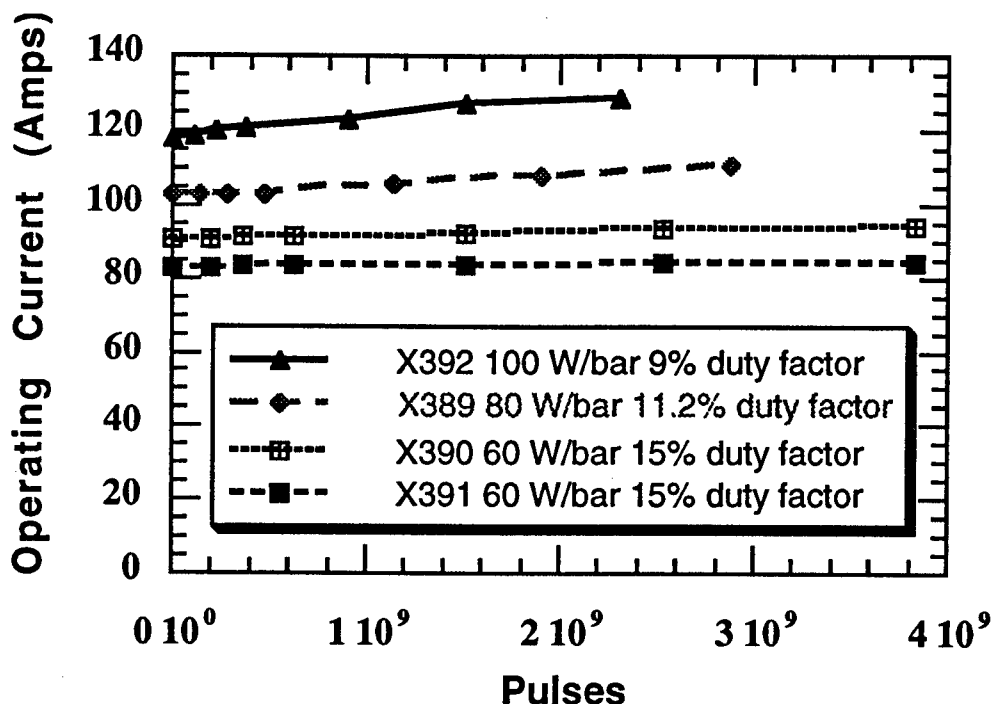


Figure 1. Vendor (SDL Inc.) performance test data of quasi-CW laser diode arrays (product is rated at 100 W/bar) with operating conditions as noted

The resulting test data from the initial run of the NASA Goddard in-house test showed a 20% degradation in diode power at ~5 billion shots.

Proof-of-principle reliability data now exists for the long term operation of the 100 W/bar quasi-CW product. In a third published NASA Goddard in-house test<sup>3</sup>, the same SDL Inc. quasi-CW 100 W/bar rated laser diode product performance was measured and the 22.8% degradation EOL exceeded 7 billion shots.

#### References

1. Haden et al., Proc. SPIE Vol. 2382, p. 2-21, Laser Diodes and Applications, Kurt J. Linden; Prasad R. Akkapeddi; Eds., (1995)
2. D. Schneider. Scientific American pp. 112-117 March 1997.
3. J. L. Dallas, R. S. Afzal, M. A. Stephen, Applied Optics Vol. 35 No. 9 1427 (1996).



# AUTHOR INDEX

<b>A</b>		<b>G</b>		<b>L</b>	
Afzal, R.	FD3	Gallion, P.	FA2,FB4	Laperle, C.	ThA2
Arbore, M.	ThC3	Gmachl, C.	ThC2	Lau, K.Y.	WB1
Archambault, J.L.	FC4	Gorodetsky, M.L.	ThB5	Li, Y.Q.	ThD3
		Grabherr, M.	WB4	Li, S.	ThB2
				Lin, C.-H.	ThC1
				Lin, T.-Y.	ThD5
<b>B</b>		<b>H</b>		<b>M</b>	
Baillargeon, J.N.	ThC2	Haden, J.	FD3	Maciejko, R.	FA3,FB2
Ballantyne, J.M.	WB2	Hall, K.L.	ThA1	Makino, T.	FA3,FB2
Browder, G.	FD3	Heerlein, J.	WB4	Matsushima, Y.	FB5
		Henningsen, J.	ThD4	Mattori, S.	ThB4
<b>C</b>		Henry, C.H.	FA1	Matuura, S.	ThA3
Capasso, F.	ThC2	Hidaka, T.	ThA3	Mawst, L.J.	FD1
Carlson, N.	FD3	Hollberg, L.W.	ThA4	McKillop, J.	WA3
Casinovi, G.	FA4		ThC3,ThD2,ThB5	Meyer, J.R.	ThC1
Chabran, C.	FB4	Huang, M.-S.	ThD5	Miles, R.	WB3
Chan, K.T.	ThB2	Hutchinson, A.L.	ThC2	Miyagi, K.	ThB4
Champagne, A.	FA3			Mogelberg, T.	ThD4
Chang-Hasnain, C.J.	WB1			Muller, R.S.	WB1
Chen, T.R.	FB1	<b>I</b>		<b>N</b>	
Chen, J.	FA3,FB2	Ilchenko, V.S.	ThB5	Niemax, K.	ThD1
Cho, G.	WA2	Imai, K.	ThB1		
Cho, A.Y.	ThC2	Ishibashi, A.	WA1		
Connolly, R.J.	WA2				
		<b>J</b>		<b>O</b>	
<b>D</b>		Jäger, R.	WB4	Oates, C.W.	ThD2
DeMars, S.D.	FC3	Jeremie, F.	FA2	Ocker, B.	ThD1
Ding, H.	ThB2	Ji, C.	WB2	Oh, D.B.	ThC4
Djalali-Vali, A.	FB4			Ohtsu, M.	ThB1
Dlugokencky, E.J.	ThC3	<b>K</b>		Okuyama, H.	WA1
Durville, F.M.	WA2	Kazarinov, R.F.	FA1	O'Brien, S.	FC4
		Kerstetter, P.	FA4		
<b>E</b>		Kessler, D.	FC2	<b>P</b>	
Erasme, D.	FB4	Kiang, M.H.	WB1	Pei, S.S.	ThC1
		Kinugawa, S.	ThB4	Penty, R.V.	FB3
<b>F</b>		Kitching, J.	ThA4	Petrov, K.P.	ThC3
Faist, J.	ThC2	Koch, J.	ThD1	Poirier, M.	ThA2
Fejer, M.M.	ThC3	Kourogi, M.	ThB1		
Felix, C.L.	ThC1	Krainak, M.	FD3		
Ferre-Pikal, E.	ThA4			<b>R</b>	
Fork, R.L.	ThB3	<b>L</b>		Rediker, R.R.	WA2
Francis, D.A.	WB1	Lan, Y.P.	ThD5	Riasati, V.R.	ThB3
		Lang, R.J.	FC1,FC3,FC4		
		Lantis, J.	WA2		

# AUTHOR INDEX

## S

Saito, T.	ThB4
Sakai, K.	ThA3
Schoenfelder, A.	FC3
Schwaitzberg, S.D.	WA2
Simonsen, H.R.	ThD4
Sirtori, C.	ThC2
Sivco, D.L.	ThC2
Stanton, A.C.	ThC4
Stephens, M.	ThD2, FD3
Svilans, M.	ThA2

## T

Tani, M.	ThA3
Taniguchi, A.	ThB4
Tetu, M.	ThA2
Tittel, F.K.	ThC3
Tsurusawa, M.	FB5

## U

Unger, P.	WB4
Usami, M.	FB5

## V

Vasil'ev, V.V.	ThB5
Velichansky, V.L.	ThB5
Verdiell, J.M.	FC4
Vurgaftman, I.	ThC1

## W

Walls, F.	ThA4
Waltman, S.	ThC3
Way, F.	FD2
White, I.H.	FB3
White, I.H.	FA5
Widiatmoko, B.	ThB1
Williams, K.A.	FA5
Wizemann, H.D.	ThD1
Wonfor, A.	FB3
Wonfor, A.	FA5
Wong, V.V.	FC4

## X

Xiao, M.	ThD3
----------	------

## Y

Yang, R.Q.	ThC1
Yang, B.H.	ThC1
Yang, W.L.	ThD5
Yarovitsky, A.V.	ThB5

## Z

Zhao, H.	FC4
Zhu, B.	FB3
Ziari, M.	FC4
Zybin, A.	ThD1

**1997 DIGEST  
of the IEEE/LEOS  
Summer Topical Meetings  
11-13 August 1997**

**Gallium Nitride Materials,  
Processing, and Devices**

**at  
THE QUEEN ELIZABETH HOTEL  
MONTREAL, QUEBEC, CANADA**

**IEEE Catalog Number: 97TH8276  
Library of Congress: 97-70754**

The papers in this book make up the digest of the meeting mentioned on the cover and title page. They reflect the authors' opinions and are published as presented and without change in the interest of timely dissemination. Their inclusion in this publication does not necessarily constitute endorsement by the editors, the Institute of Electrical and Electronics Engineers, Inc.

Copyright and reprint permissions: Abstracting is permitted with credit to the source. Libraries are permitted to photocopy beyond the limits of U.S. copyright law for private use of patrons those articles in this volume that carry a code at the bottom of the first page, provided the per-copy fee indicated in the code is paid through the Copyright Clearance Center, 222 Rosewood Drive, Danvers MA 01923. Instructors are permitted to photocopy isolated articles for noncommercial classroom use without fee. For other copying, reprint or republication permission, write to IEEE Copyrights Manager, IEEE Service Center, 445 Hoes Lane, P.O. Box 1331, Piscataway NJ 08855-1331.

© 1997 by The Institute of Electrical and Electronics Engineers, Inc. All right reserved.

IEEE Catalog Number: 97TH8276

ISBN:	0-7803-3891-X	Softbound Edition
	0-7803-3892-8	Microfiche Edition

Library of Congress: 97-70754

Additional copies can be ordered from:

IEEE Service Center  
445 Hoes Lane  
P.O. Box 1331  
Piscataway, NJ 08855-1331  
Tel: (732) 981-1393  
Fax: (732) 981-9667



# **GALLIUM NITRIDE MATERIALS, PROCESSING AND DEVICES**

## **Co-Chairs:**

P. Daniel Dapkus, *University of Southern California, Los Angeles, CA*  
Steven DenBaars, *University of California Santa Barbara, CA*

## **Program Committee:**

James Coleman, *University of Illinois, Urbana, IL*  
Russell Dupuis, *University of Texas, Austin, TX*  
Tom Kuech, *University of Wisconsin, Wisconsin, IL*  
Ted Moustakas, *Boston University, Boston, MA*  
Richard Miles, *SDL Inc., San Jose, CA*  
Peter Zory, *University of Florida, Gainesville, FL*

# **TABLE OF CONTENTS**

## **Wednesday, 13 August 1997**

### **Session WA: Epitaxial Growth I**

WA1	Crystal Growth and Conductivity Control of Group-III Nitride Semiconductors and Their Application To Short Wavelength Laser Diodes . . . . . (paper not available)	
WA2	MBE Growth of GaN . . . . .	3
WA3	Gas Phase Reactions of Trimethylgallium, Ammonia and Trimethylamine: Growth Chemistry and Reactor Models . . . . . (paper not available)	
WA4	Optical Properties of InGaN Double Heterostructures and Quantum Wells Grown by Metalorganic Chemical Vapor Deposition . . . . .	5
WA5	On The Incorporation of As in GaN Films by Conventional MOCVD . . . . .	8

### **Session WB: Epitaxial Growth II**

WB1	Growth and Characterization of Bulk Crystals, Thin Films, and Patterned Structures of AlN, GaN, and $Al_xGa_{1-x}N$ on SiC(0001) Substrates and Device-related Research . . . .	9
WB2	Growth of GaN on (0001) Sapphire by MOCVD Using A Multilayer Approach in A Closed Space Showerhead Reactor . . . . .	10
WB3	A Comparison of Silicon and Oxygen Doping of GaN and Optical and Electrical Properties of Deposited Layers . . . . .	11
WB4	Optimized Conditions for Flow Modulated Epitaxy of GaN . . . . .	13
WB5	The Effects of Boundary Layer and Thermal Gradient Upon GaN Growth . . . . .	15

## **Thursday, 14 August 1997**

### **Session ThA: Nitride Based Devices**

ThA1	CW Operation of InGaN MQW Laser Diodes . . . . .	19
ThA2	Fabrication of High Power GaN LEDs and HEMTs . . . . . (paper not available)	
ThA3	Substrate Effects on GaN Photodetector Performance . . . . .	21
ThA4	Hybrid Organic-inorganic GaN LED Based Color Downconversion for Displays . . . .	22

### **Session ThB: Epitaxial Growth III**

ThB1	MOCVD Growth, Characterization and Stability of High Quality InGaN MQW Structures . . . . .	24
ThB2	Barrier and Well Width Study of InGaN/GaN Multiple Quantum Wells . . . . .	25
ThB3	MOVPE Growth of High Quality InGaN Films and InGaN/GaN Quantum Wells . . . .	27
ThB4	Phase Separation in Bulk InGaN and Quantum Wells Grown by Low Pressure MOCVD . . . . .	29
ThB5	Effects of Well Thickness on the Light Emission in InGaN/GaN and GaN/AlGaIn Multiple Quantum Wells . . . . .	31

# TABLE OF CONTENTS

## Session ThC: GaN Substrate Issues

ThC1	MOCVD Growth of GaN on Alternative Substrates . . . . .	(paper not available)
ThC2	Exotic and Mundane Substrates for Gallium Nitride Heteroepitaxy . . . . .	33
ThC3	A New Compliant Substrate Approach for the Growth GaN Growth on Si by Metal Organic Chemical Vapor Deposition . . . . .	(paper not available)
ThC4	Surface Morphology and Structure of AlN Films grown on Si(111) .	(paper not available)

## Session ThD: "Optical Gain in Widebandgap Materials

ThD1	Optical Gain in GaN Based Semiconductors . . . . .	35
ThD2	Gain Spectroscopy on InGaN Quantum Well Diodes . . . . .	37
ThD3	Theory of Gain in InGaN Quantum Well Lasers . . . . .	39
ThD4	Coulomb Attraction Effects of CdZnSe Quantum Well Lasers . . . . .	41

## Friday, 15 August 1997

## Session FA: Characterization of GaN

FA1	Materials Characterization for GaN Laser Diodes . . . . .	(paper not available)
FA2	Characterization of Mid-gap States in n-type GaN With Optical-Isothermal Capacitance Transient Spectroscopy . . . . .	45
FA3	Stimulated Emission From Optically Pumped Cubic GaN on GaAs (100) Substrate . .	47
FA4	Spectral Reflectivity Monitoring of GaN growth . . . . .	49
FA5	In-situ Reflectance Monitoring and Characterization of GaN Grown by MOCVD . . . .	50

## Session FB: Characterization and Fabrication of GaN

FB1	Characterization of As-Grown and Ion-Implanted GaN by Photoluminescence and Photoluminescence Excitation Spectroscopy . . . . .	52
FB2	A Fabrication of GaN Micro-Lenses . . . . .	54
FB3	Low Damage Patterning of III-N Materials For Contact Deposition By Low Energy Electron Enhanced Etching (LE4) in DC Plasma . . . . .	(paper not available)
FB4	Raman Spectroscopy of Mg-doped GaN: Shift of the $A_1(\text{LO})$ Phonon . . . . .	56
FB5	Calculation of Spinodal Decomposition Temperature in Cubic Ternary Nitride Materials Including Coherency Stress and Spontaneous Ordering . . . . .	58





**GALLIUM NITRIDE MATERIALS,  
PROCESSING AND DEVICES**

**Wednesday, 13 August 1997**

**Sessions:**

**WA:    *Epitaxial Growth I***

**WB:    *Epitaxial Growth II***

## Wednesday Papers Not Available

- WA1      “Crystal Growth and Conductivity Control of Group-III Nitride Semiconductors and Their Application To Short Wavelength Laser Diodes”, *Isamu Akasaki, Meijo University, Nagoya,*
- WA3      “Gas Phase Reaction of Trimethylgallium, Ammonia and Trimethylamine: Growth Chemistry and Reactor Models”, *S.A. Safvi, D. Saulys, and T. F. Kuech, University of Wisconsin Madison, WI and J.R. Redwing, and M.A. Tischler, Epitronics/ATMI, Danbury, CT*

### MBE Growth of GaN

M.A.L. Johnson, Zhonghai Yu, N.A. El-Masry, Jr., J.W. Cook, Jr., and J.F. Schetzina  
Department of Physics, North Carolina State University, Raleigh, NC 27695-8202  
PH: 919-515-3314; FAX: 919-515-7667; e-mail: jan\_schetzina@ncsu.edu

GaN has been grown by MBE at growth rates up to 1  $\mu\text{m/hr}$  and at temperatures up to 1000  $^{\circ}\text{C}$  using a new rf nitrogen plasma source developed by EPI, Inc. The EPI source employs a pyrolytic boron nitride plasma reaction chamber that eliminates gas leakage. This "unibulb" construction gives rise to higher pressures and longer confinement times within the reaction chamber. Optical emission spectra show that the nitrogen plasma is very rich in nitrogen atoms and 1st-positive series metastable (long-lived) molecules (3.95 eV binding energy), both of which constitute "active nitrogen:" and contribute to the high growth rates. The GaN films show excellent optical properties and can be doped n-type with Si and p-type with Mg at high temperatures.

The doping of GaN with Mg to produce p-type material for device applications is poorly understood at present. Many researchers have reported difficulty in obtaining highly-doped material. In addition, increasing the Mg flux during growth sometimes produces n-type material-- rather than the expected p-type doping. This phenomenon has been attributed to compensation effects at high Mg incorporation levels. At NCSU, we have studied MBE growth of GaN:Mg systematically for a wide range of Mg oven temperatures, corresponding to different Mg fluxes during MBE film growth. At high Mg fluxes we also obtain n-type GaN. However, on the basis of PL and TEM studies, along with C-V and SIMS measurements, we propose a entirely new explanation for this observed anomalous behavior. Under optimum growth conditions, SIMS measurements show Mg levels of  $\sim 5 \times 10^{19} \text{ cm}^{-3}$ , corresponding to hole concentrations of about  $5 \times 10^{17} \text{ cm}^{-3}$ . Low temperature photoluminescence measurements yield an optical ionization energy for the Mg acceptor in GaN of about 224 meV.

Special techniques have been developed for the growth of InGa<sub>N</sub> quantum wells. The growth of high quality InGa<sub>N</sub> is complicated by thermodynamic limitations: InN is unstable and tends to dissociate at typical MBE growth temperatures of 600-800 $^{\circ}\text{C}$ . Furthermore, the surface energies of InGa<sub>N</sub> are such that the indium tends to coalesce into metal droplets rather than migrate freely to lattice incorporation sites. The formation of indium droplets results in a low incorporation rate of indium in the growing film and a weak photoluminescence (PL) signal dominated by deep level emission. To overcome these difficulties, we have developed a modulated beam technique which employs alternating layers of (In,Ga)<sub>N</sub> and (Ga)<sub>N</sub>, analogous to the techniques used for the growth of InGa<sub>N</sub> by MOVPE. The intermittent deposition of a brief Ga<sub>N</sub> layer stabilizes the indium containing layer before droplets can nucleate and results in high quality epitaxy. Factors which influence the InGa<sub>N</sub> composition include the metal flux ratios, substrate temperature, and the relative lengths of the beam modulation periods. RHEED analysis indicates a two dimensional growth surface during modulated beam deposition. In particular, we observe streaky (1x1) RHEED patterns during deposition of the InGa<sub>N</sub> layer alternating with a streaky (1x3) RHEED pattern during the Ga<sub>N</sub> layer as the quantum well is built up. Ga<sub>N</sub>/InGa<sub>N</sub> quantum well structures have been synthesized which emit narrow (FWHM  $\sim 20\text{-}30 \text{ nm}$ ) electroluminescence in the violet-to-green spectral regions at room temperature.

Work supported by DARPA, ARO, ONR, and Cree Research internal funds.

## Optical Emission Spectrum (400 W; $5 \times 10^{-5}$ Torr)

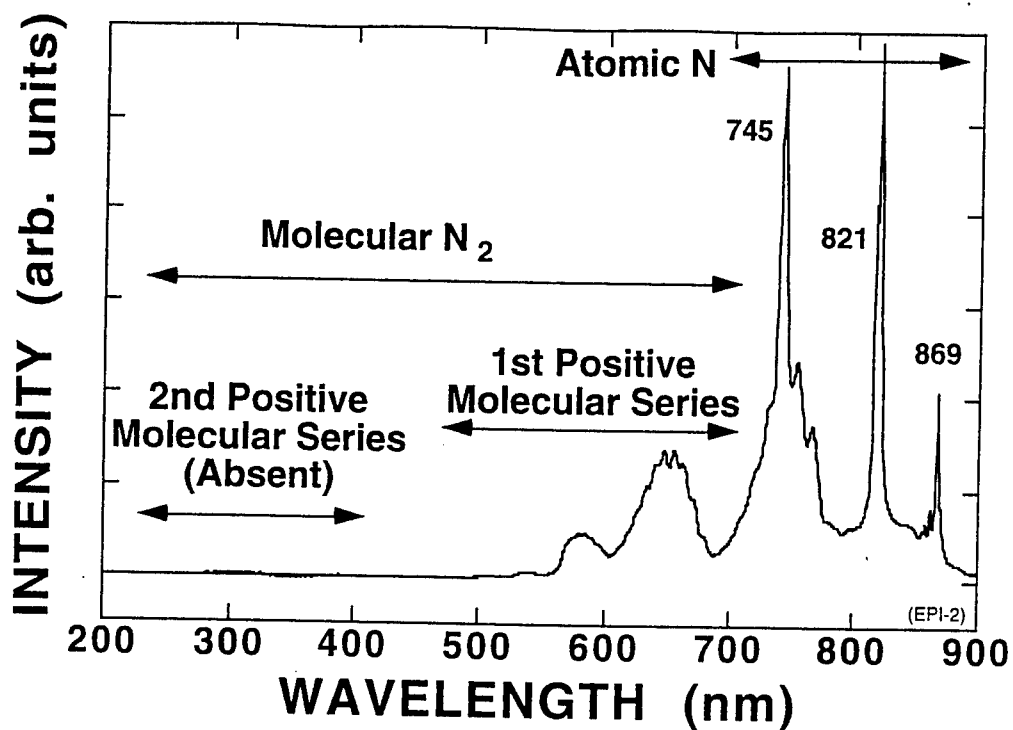
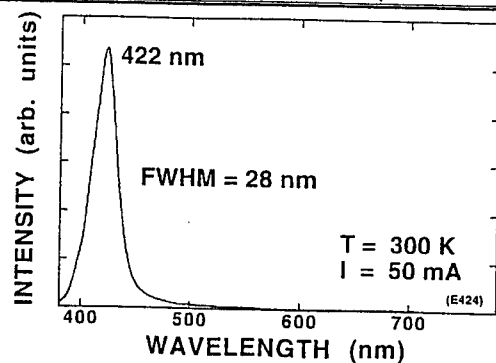


Figure 1. Optical emission spectrum from EPI nitrogen rf plasma source.

GaN/InGaN/GaN SQW Structure (21% Indium)



GaN/InGaN/GaN SQW Structure (22% Indium)

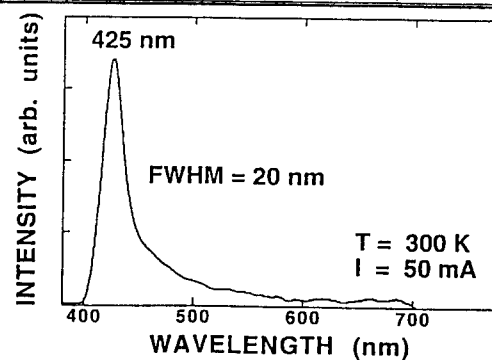


Figure 2. Electroluminescence from InGaN quantum well structures

***Optical Properties of InGaN Double Heterostructures and Quantum Wells  
Grown by Metalorganic Chemical Vapor Deposition***

R. D. Dupuis<sup>+</sup>, P. A. Grudowski, C. J. Eiting, J. Park, B. S. Shelton, and D. J. H. Lambert

Microelectronics Research Center

The University of Texas at Austin, Austin TX 78712-1100

and

I. Shmagin and R. M. Kolbas

Department of Electrical Engineering

North Carolina State University, Raleigh NC 27695-7911

High-quality III-V nitride epitaxial films and heterostructures are of great importance for a wide variety of electronic and optoelectronic devices. In this talk, data are presented on the optical and structural properties of  $\text{In}_x\text{Ga}_{1-x}\text{N}/\text{GaN}$  heteroepitaxial films and  $\text{In}_x\text{Ga}_{1-x}\text{N}/\text{In}_y\text{Ga}_{1-y}\text{N}$  heterostructures and quantum wells grown by low-pressure ( $P_{\text{tot}} = 76\text{-}100$  Torr) metalorganic chemical vapor deposition (MOCVD). The epitaxial films are deposited on  $\text{Al}_2\text{O}_3$  substrates in an EMCORE rotating-disk reactor using TMGa, TMAI, TMIIn, and  $\text{NH}_3$  using both  $\text{H}_2$  and  $\text{N}_2$  carrier gases employing a variety of  $\text{In}/[\text{In}+\text{Ga}]$  molar flow ratios, V/III flow ratios, temperatures, growth rates, and ammonia sources.

The InGaN growth rate, alloy composition, and optical quality are found to depend upon the growth temperature ( $730^\circ\text{C} < T_g < 810^\circ\text{C}$ ) and the In incorporation is strongly dependent upon growth kinetics. The films have been characterized by room-temperature (300K) and low-temperature (77K and 4.2K) photoluminescence (PL), cathodoluminescence (CL), high-resolution X-ray diffraction, secondary-ion mass spectrometry, and transmission electron microscopy. 300K PL spectra of single-heterostructure InGaN/GaN films and double heterostructures show relatively narrow linewidths with the narrowest FWHM (for a given alloy composition) measured for films grown at the higher temperatures (e.g.,  $\lambda = 401.0$  nm, FWHM = 13.6 nm). Optically pumped stimulated emission at 77K has been observed under pulsed excitation conditions from a single-heterostructure InGaN/GaN film at a wavelength of 402.0 nm.

The 300K PL spectra from 10-period InGaN/InGaN MQW structures ( $\sim 5$  nm  $\text{In}_{0.15}\text{Ga}_{0.85}\text{N}$  wells,  $\sim 10$  nm  $\text{In}_{0.05}\text{Ga}_{0.95}\text{N}$  barriers) grown at  $T_g \sim 760^\circ\text{C}$ - $790^\circ\text{C}$  exhibit intense band-related emission. Five-period InGaN/GaN MQW structures (10 nm  $\text{In}_{0.15}\text{Ga}_{0.85}\text{N}$  wells and 10 nm GaN barriers) grown at  $810^\circ\text{C}$  show bright  $\sim 430$  nm 300K PL emission with linewidths of  $\sim 35$  nm. Narrow 4.2K PL spectra for the bulk InGaN layers (FWHM = 5.8 nm for  $x = 0.11$ ) and the MQW heterostructures have been observed. 300K CL measurements reveal spatially uniform luminescence from the single layers and QW structures with no evidence of In segregation observed at magnifications up to  $\sim 100\text{KX}$ .

Undoped GaN films have 300K PL linewidths as narrow as  $\sim 2.9$  meV and net carrier concentrations in the range  $|N_d - N_a| \sim 1 \times 10^{17} \text{ cm}^{-3}$ . We have investigated the effect of Si doping upon the optical properties of GaN and InGaN films and InGaN/GaN MQW structures and have found that Si doping increases both the peak and integrated PL intensity relative to unintentionally doped films with a corresponding increase in the FWHM depending upon the doping density. *p*-type Mg-doped films have also been grown and characterized.

High-resolution X-ray diffraction characterization of InGaN MQW wafers reveals zero-, 1st-, and 2nd-order superlattice peaks. These data are used to determine the average

composition and the period of the MQW structures. X-ray diffraction reciprocal space maps also show the degree of mosaicity and strain in the crystalline structure of the GaN layer and the InGaN quantum wells. We will discuss the effect of strain and mosaic structure upon the optical properties of these films.

*\*Work supported in part by ARO, DARPA, Ford Motor Co., NSF, ONR, and The State of Texas.*

*\*Contact: Phone: 512 471-0537; FAX: 512 471-8575; e-mail: dupuis@mail.utexas.edu*

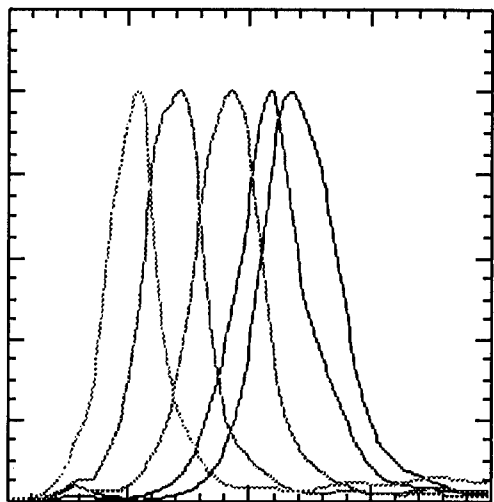


Figure 1. 300K PL spectra of InGaN/GaN single heterostructures grown on sapphire.

grown with constant V/III ratio ( $\sim 5400$ ) and In/III ratio ( $\sim 0.65$ ).

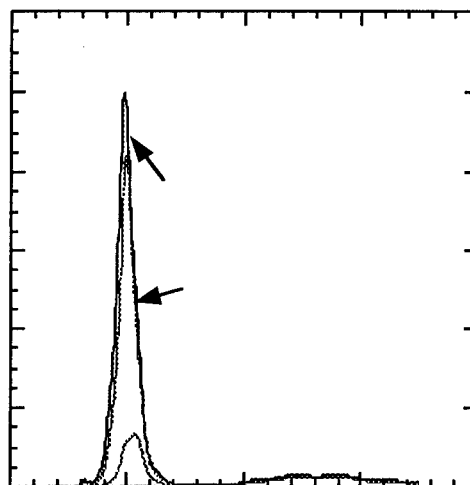


Figure 2. 300K PL spectra of doped and undoped 5-period MQW structures grown at  $790^\circ\text{C}$  with 5 nm  $\text{In}_{0.15}\text{Ga}_{0.85}\text{N}$  wells and 7.5 nm  $\text{In}_{0.07}\text{Ga}_{0.93}\text{N}$  barriers.

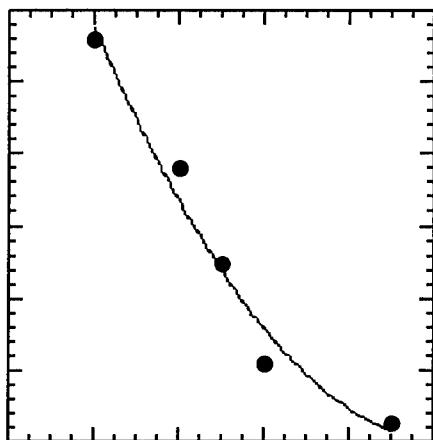


Figure 3. 300K PL peak wavelength vs. growth temperature for InGaN single layers

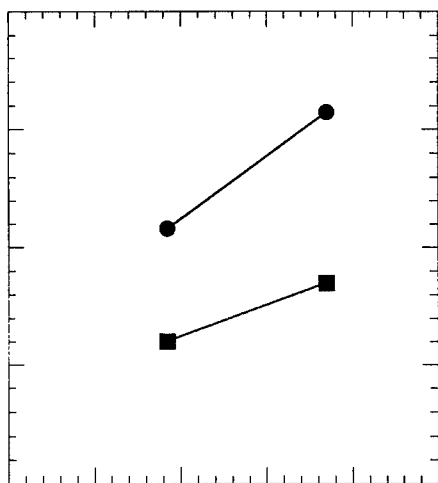


Figure 4. 300K PL peak wavelength vs. TMGa molar flow for InGaN single layers showing the effect of the InGaN growth rate on the In incorporation.

## On the Incorporation of Arsenic (As) in GaN Films By Conventional MOCVD

X. Li, S. Kim, S. G. Bishop and J. J. Coleman

Microelectronics Lab, University of Illinois, Urbana, IL 61801

There has been considerable interest in  $\text{GaAs}_x\text{N}_{1-x}$  and related quaternary semiconductor compounds, because they in principle bridge the gap between GaAs and GaN both in emission energy and in lattice parameter, and may be suitable for devices operating over a broad wavelength range. Unfortunately, theoretical calculations indicate a huge composition-dependent optical bowing coefficient in GaAsN alloys<sup>1</sup> and an extremely small solubility of As in GaN or N in GaAs.<sup>2</sup> Experimental studies using an active nitrogen (N) source by molecular beam epitaxy (MBE)<sup>3-6</sup> or plasma-assisted metalorganic chemical vapor deposition (MOCVD)<sup>7</sup> have also proven the downward band bowing and the difficulties of incorporating N in GaAs. So far, no experimental results have been reported on the N-rich end of the alloy. Furthermore, using conventional MOCVD for the growth of GaAsN has not been demonstrated.<sup>8</sup>

We report on the As incorporation in GaN films by atmospheric pressure MOCVD using  $\text{AsH}_3$  and  $\text{NH}_3$  as the As and N sources, respectively. The effect of growth parameters on the incorporation efficiency, including growth temperature, growth rate, layer thickness, ratio of  $\text{AsH}_3$  and  $\text{NH}_3$  flows for single layer growth, and the effect of growth interruption for multilayer growth, have been investigated. Of particular interest is the incorporation of As at a doping level. The optimum growth condition for the doping of As in GaN producing strong luminescence at a characteristic emission wavelength ( $\sim 480$  nm) has been identified. The characteristic emission has been attributed to excitons bound at As isoelectronic impurities.<sup>9,10</sup> Arsenic (As) concentration and its depth distribution are measured by SIMS. The crystal quality after As incorporation is demonstrated by X-ray diffraction rocking curve. Room temperature and low temperature cathodoluminescence (CL), photoluminescence (PL) spectroscopy and imaging are used to characterize the optical properties. Results will be compared with As ion implanted GaN.

<sup>1</sup> S. H. Wei and A. Zunger, *Phys. Rev. Lett.* **76**, 664 (1996).

<sup>2</sup> Y. C. Kao, T. P. E. Broekaert, H. Y. Liu, S. Tang, I. H. Ho, and G. B. Stringfellow, *Mater. Res. Soc. Symp. Proc.* **423**, 355 (1996).

<sup>3</sup> W. G. Bi and C. W. Tu, *Appl. Phys. Lett.* **70**, 1608 (1997).

<sup>4</sup> Z. Z. Bandic, R. J. Hauenstein, M. L. O'steen, and T. C. McGill, *Mater. Res. Soc. Symp. Proc.* **449**, 209 (1997).

<sup>5</sup> T. S. Cheng, C. T. Foxon, L. C. Jenkins, S. E. Hooper, J. W. Orton, S. V. Novikov, T. B. Popova, and V. V. Tet'yakov, *J. Cryst. Growth* **158**, 399 (1996).

<sup>6</sup> M. Kondow, K. Uomi, T. Kitatani, S. Watahiki, Y. Yazawa, *J. Cryst. Growth* **164**, 175 (1996).

<sup>7</sup> M. Sato, *J. Cryst. Growth* **145**, 99 (1994).

<sup>8</sup> Growth of GaPN with 0.4% N using DMHy as N source by MOCVD has been demonstrated by S. Miyoshi, H. Yaguchi, K. Onabe, R. Ito, and Y. Shiraki, *J. Cryst. Growth* **145**, 87 (1994).

<sup>9</sup> J. I. Pankove and J. A. Hutchby, *J. Appl. Phys.* **47**, 5387 (1976).

<sup>10</sup> R. D. Metcalfe, D. Wickenden, and W. C. Clark, *J. Lumin.* **16**, 405 (1978).



WB1 (Invited)  
3:30pm - 4:00pm

**GROWTH AND CHARACTERIZATION OF BULK CRYSTALS, THIN FILMS  
AND PATTERNED STRUCTURES OF AlN, GaN AND  $\text{Al}_x\text{Ga}_{1-x}\text{N}$   
ON SiC(0001) SUBSTRATES AND DEVICE-RELATED RESEARCH**

Robert. F. Davis, C. M. Balkas, L. Bergman\*, M.D. Bremser, O.H. Nam, W.G. Perry, I. Shmagin<sup>§</sup>, Z. Sitar, B. L. Ward\*, T. Zheleva, R. Kolbas<sup>§</sup>, R. Nemanich\*, Departments of Materials Science and Engineering, Box 7907; \*Physics, Box 8202; and <sup>§</sup>Electrical and Computer Engineering, Box 7911, North Carolina State University, Raleigh, NC, 27695

Department of Materials Science and Engineering, North Carolina State University, Raleigh, NC \*  
Department of Physics, North Carolina State University, Raleigh, NC, <sup>§</sup>Department of Electrical and Computer Engineering, North Carolina State University, Raleigh, NC, 27695

Single crystals of AlN to 1 mm thickness were grown at 1950-2250°C on 10x10 mm<sup>2</sup> 6H-SiC substrates via sublimation-re-condensation. Most crystals were 0.3mm - 1mm thick transparent layers completely covering the substrates. Raman, optical and TEM results will be presented. Single crystals of GaN were grown by subliming powders of this material under NH<sub>3</sub>. Raman and photoluminescence results will be shown.

Monocrystalline thin films and heterojunctions of GaN and  $\text{Al}_x\text{Ga}_{1-x}\text{N}$  alloys ( $0.05 \leq x \leq 0.96$ ) were grown via OMVPE on 6H-SiC(0001) substrates at 1050-1100°C with (GaN) or without (alloys) an  $\approx 100$  nm thick, monocrystalline AlN(0001) buffer layer pre-deposited at 1100°C. Cross-sectional TEM revealed threading dislocations ( $\mathbf{b} = 1/3[1210]$ ) having a density in films grown on the on-axis substrates of  $10^6 - 10^8/\text{cm}^2$  or  $\leq (10^2 - 10^3)/\text{cm}^2$  than for films deposited simultaneously on the vicinal substrates. Both materials were free of low-angle grain boundaries and associated oriented domains. Biaxial strains resulting from mismatches in thermal expansion coefficients and lattice parameters in 22 GaN films, and measured via changes in the c-axis lattice parameter, were both tensile and compressive. Thus, the residual strain due to lattice mismatch was not completely relieved by defect formation. The PL spectra of the GaN films revealed strong bound excitonic emission with a FWHM value of 4 meV. Marked variations in the free excitonic emission and the c-axis lattice parameter with film stress were observed. A plot of near band-edge emission energy (determined by cathodoluminescence) vs. alloy composition revealed a negative bowing parameter. Controlled n-type, Si-doping in GaN was achieved for net carrier concentrations ranging from approximately  $1 \times 10^{17} \text{ cm}^{-3}$  to  $1 \times 10^{20} \text{ cm}^{-3}$ . Magnesium-doped, p-type GaN was achieved with  $n_A - n_D \approx 3 \times 10^{17} \text{ cm}^{-3}$ ,  $\rho \approx 7 \Omega\text{-cm}$  and  $\mu \approx 3 \text{ cm}^2/\text{V}\cdot\text{s}$ . N-type (silicon) and p-type (magnesium) doping was achieved for  $\text{Al}_x\text{Ga}_{1-x}\text{N}$  for  $0.12 \leq x \leq 0.42$  and  $x \leq 0.13$ , respectively.

Selective growth of GaN and  $\text{Al}_{0.2}\text{Ga}_{0.8}\text{N}$  has been conducted on stripe and circular patterned GaN/AlN/6-H-SiC multilayer substrates. Growth morphologies on stripe patterns changed with their widths and the flow rate of TEG. Uniform hexagonal pyramid arrays of undoped GaN and Si-doped GaN were successfully grown on 5  $\mu\text{m}$  circular patterns. Field emission measurements of a Si-doped GaN hexagonal pyramid array exhibited a turn-on field of 14 V/ $\mu\text{m}$  for an emission current of 10.8 nA at an anode-to-sample distance of 27  $\mu\text{m}$ .

Platinum-based ohmic and rectifying contacts have been fabricated via electron beam evaporation surfaces cleaned via Si deposition/flash evaporation techniques. Room temperature resistivities of the former were 0.1-1  $\text{ohm}\cdot\text{cm}^2$ ; however, they increased during annealing above 700°C as a result of significant chemical interdiffusion. The leakage currents of the latter contacts were  $< 1 \text{ nA}$  at -10V. The breakdown voltage was  $\approx 40\text{V}/\text{cm}^2$ . The results of additional electronic, device-related and device studies will also be reported.

**WB2**

**4:00pm - 4:15pm**

**Growth of GaN on (0001) sapphire by MOCVD using a multilayer approach in a closed space showerhead reactor**

**J. T. Kobayashi, N. P. Kobayashi and P. D. Dapkus  
Compound Semiconductor Laboratory  
Department of Materials Science and Engineering  
University of Southern California SSC 510, MC 0483  
Los Angeles, CA 90089-0483**

**X. Zhang and D. H. Rich  
Photonic Materials and Devices Laboratory  
Department of Materials Science and Engineering  
University of Southern California SSC 510, MC 0483  
Los Angeles, CA 90089-0241**

The growth behavior of GaN grown on (0001) sapphire substrates by atmospheric pressure metalorganic chemical vapor deposition (MOCVD) in a closed space showerhead reactor has been studied. The unique characteristics of this reactor include minimal reactant mixing in the gas phase, spatially segregated exposure of the surface to reactants and relatively uniform growth. A multiple buffer layer and overgrowth layer strategy that results in the formation of featureless layers of high quality GaN on sapphire and other substrates has evolved from the optimization of growth in this reactor using slow rotation speeds and hydrogen carrier gas. These layers form as a result of the selective lateral growth and merging of uniform height three dimensional islands and subsequent two dimensional growth.

In this talk, we will discuss dependence of this growth mode on various reactor parameters including reactant flows, carrier gas, rotation speed and separation between the showerhead and substrate. These parameters all effect the hydrodynamics and chemical reaction pathways of this unique reactor design. We will discuss how the growth conditions affect the formation of the three dimensional islands and how the variation in the density and the size of the islands at the initial stages of overlayer growth affect the coalescence of the islands and the surface morphology and electrical, structural and optical quality of the GaN overlayer.

**P. Daniel Dapkus  
W. M. Keck Professor of Engineering  
Departments of Electrical Engineering  
and Materials Science  
University of Southern California  
504 Powell Hall  
Los Angeles, CA 90089-0271**

## A comparison of silicon and oxygen doping of GaN and optical and electrical properties of deposited layers

R. Niebuhr, B. Wachtendorf, D. Schmitz, R. Beccard, H. Jürgensen  
AIXTRON Semiconductor Technologies, Kackerstrasse 15-17, 52072 Aachen, Germany

B. Santic, P. Schlotter, M. Meier, U. Kaufmann, K.H. Bachem  
Fraunhofer-Institute for Applied Solid State Physics, Tullastr. 72, 79108 Freiburg, Germany

The purpose of the experiments presented in this paper is to study the effects of intentional oxygen and silicon doping on the properties of GaN layers. We will report for the first time on the comparison of these dopants and the doping of GaN with oxygen using  $N_2O$

About the influence of oxygen doping on deposited layers only little has been reported so far. This question is of considerable interest as in earlier works a high residual background density of n-type carriers has been reported [1], [2], which was tentatively attributed to the presence of nitrogen vacancies. Recent theoretical studies [3] show that an isolated vacancy is not likely to be responsible for this behaviour. On the other hand a low formation energy of oxygen in GaN is claimed which should be of comparable size as that for silicon doping [4], or under certain growth conditions even lower. According to these studies oxygen is a possible candidate to cause the residual n-type doping as already suggested in [5]. To shed some more light on this issue in the present study the influence of oxygen on the electrical and optical properties of GaN has been examined. For comparison silicon doped layers have been grown with carrier concentrations up to  $3 \times 10^{18} \text{ cm}^{-3}$ . At these samples the influence on the carrier concentration on the excitonic luminescence was studied for both dopants.

The silicon and oxygen doped GaN layers have been grown by low pressure MOCVD on c-plane 2" sapphire wafers. The GaN layers were grown on a low temperature AlN nucleations layer of about 300 Å thickness using TMG and TMA, respectively and especially purified ammonia as nitrogen precursor. The carrier gas was high purity nitrogen. Silan ( $SiH_4$ ) and laughing gas ( $N_2O$ ) were used as doping gases for silicon and oxygen doping, respectively.

The doped layers were characterized by low temperature photoluminescence and hall effect measurements. The later were performed in Van Der Pauw geometry (4-point) using Ti/Al contacts which showed for both types of layers ohmic behaviour.

Undoped layers have shown a high resistivity ( $> 20 \text{ k}\Omega/\text{square}$ ) and a very low background carrier concentration. The photoluminescence spectra were dominated by excitonic recombination. Besides free excitonic emission (A and B exciton) the spectra showed also excitons bound to residual donors. With increasing  $SiH_4$  concentration a linear increase in the carrier concentration was observed. Furthermore the emission wavelength of the donor bound exciton decreased while at the same time the FWHM

increased. The decreasing emission wavelength is tentatively attributed to a general narrowing of the bandgap which is caused by many-particles effects and a corresponding bandgap renormalisation. At a carrier concentration of  $3 \times 10^{18} \text{ cm}^{-3}$  the shift of the excitonic peak amounted to 35 meV.

The oxygen doped layers showed also n-type behaviour. The carrier concentration increased with increasing dopant gas concentration, which ranged between 25 and 400 ppm in the gas phase. The measured carrier concentration was between  $4 \times 10^{16}$  and  $3 \times 10^{18} \text{ cm}^{-3}$ , correspondingly. In contrast to the silicon doped samples a non-linear dependence of the carrier concentration on the gas phase concentration was observed. Furthermore the observed carrier mobility is about one order of magnitude smaller than that of comparable silicon doped samples. The observed low temperature photoluminescence spectra show a donor bound exciton besides the free A and B exciton. No deep level emission was observed. With increasing carrier concentration the intensity of the donor bound exciton increases while the intensity of the free excitons decreases. Both lines show a clear shift to lower energy with increasing carrier concentration which is also tentatively attributed to bandgap renormalisation effects, like in the silicon doped samples. The shift is also of comparable size at comparable carrier concentrations. The observed spectra allow for the interpretation, that oxygen forms a shallow donor state in GaN, like silicon. This is in accordance with arguments referring to the covalent radius of nitrogen and oxygen from which a substitutional incorporation appears to be likely. Judging from the similar electronegativities of nitrogen and oxygen a shallow donor behaviour of oxygen in GaN can be argued. SIMS measurements performed at the oxygen doped layers show that the doping efficiency of oxygen is comparable to the efficiency of silicon. Furthermore the chemically incorporated oxygen found by SIMS shows in comparison to the carrier concentration observed by Hall measurements a high degree of activation of about 50 % which also supports the interpretation that oxygen forms a shallow donor level in GaN.

- /1/ H.P. Maruska, J.J. Tietjen, Appl. Phys. Lett. 15 (1969) 327
- /2/ J.I. Pankove, S. Bloom, G. Harbeke, RCA Review 36 (1975) 163
- /3/ J. Neugebauer, C.G. van de Walle, Phys. Rev. B 50 (1994) 8067
- /4/ J. Neugebauer, C.G. van de Walle, Proc. 22th Int. Conf. Physics of Semiconductors, pp. 2327 World Scientific, Singapore (1995)
- /5/ W. Seifert, R. Franzfeld, E. Butter, Crystal Res. Technol. 18 (1983) 383

## Optimized Conditions for Flow Modulation Epitaxy of GaN

D.T. Emerson, J.A. Smart & J.R. Shealy

*School of Electrical Engineering, Cornell University, Ithaca, NY 14850*

H.S. Kong & J.A. Edmond

*CREE Research, Durham, NC 27713*

Flow modulation epitaxy (FME) has been employed previously to synthesize III-V arsenides and phosphides.[1,2] However, the ability of FME to extend growth to lower temperatures than those required for conventional organometallic vapor phase epitaxy (OMVPE) has only recently been explored for the synthesis of nitride based semiconductors.[3] Because, in part, of the importance of low temperature growth to the synthesis of indium-containing group III-nitrides, this growth technique should be explored further.

We report on the FME of group III-nitride compounds on sapphire and silicon carbide substrates. Materials include unintentionally doped as well as silicon- and magnesium-doped GaN and AlGaN. As depicted schematically in figure 1, two types of growth cycles were chosen for comparison between conventional OMVPE and FME. In one cycle, group III and group V reactant pulses are injected together into the reaction cell; this cycle can be thought of as conventional OMVPE with growth interruptions since growth is always group V rich. In the second cycle, more like the conventional FME process, group III and group V pulses are separately introduced to the reaction cell. In both cycles, a small group V background is maintained at all times to prevent the decomposition of the growth surface between the main group V pulses. Using these growth cycles, we studied the effect of growth temperature, growth rate, flow modulation cycle duration, ammonia flux (during both the group III-rich and group V-rich cycles), and n- or p-doping level on material properties. Epitaxial layers and heterostructures are assessed using room temperature photoluminescence, atomic force microscopy, capacitance-voltage measurements, and double crystal x-ray diffraction.

Although our data clearly demonstrates that the III-nitride mass transport limited growth regime is extended to lower growth temperatures when the conventional FME growth cycle is employed, this study reveals that the flow modulation scheme required for the growth of nitrides can differ substantially from that necessary for the synthesis of arsenides and phosphides. Nevertheless, the systematic exploration of growth cycle parameters allows the development of an optimized, high throughput FME growth process.

[1] Y. Kobayashi, T. Makimoto, Y. Yamauchi and Y. Horikoshi, *J. Appl. Phys.* **66**, 640 (1989).

[2] B.L. Pitts, D.T. Emerson and J.R. Shealy, *Appl. Phys. Lett.* **61**, 2054 (1992).

[3] S. Keller, U.K. Mishra, and S.P. DenBaars, *8th Biennial Workshop on OMVPE*, April 13-17, 1997, Dana Point, CA.

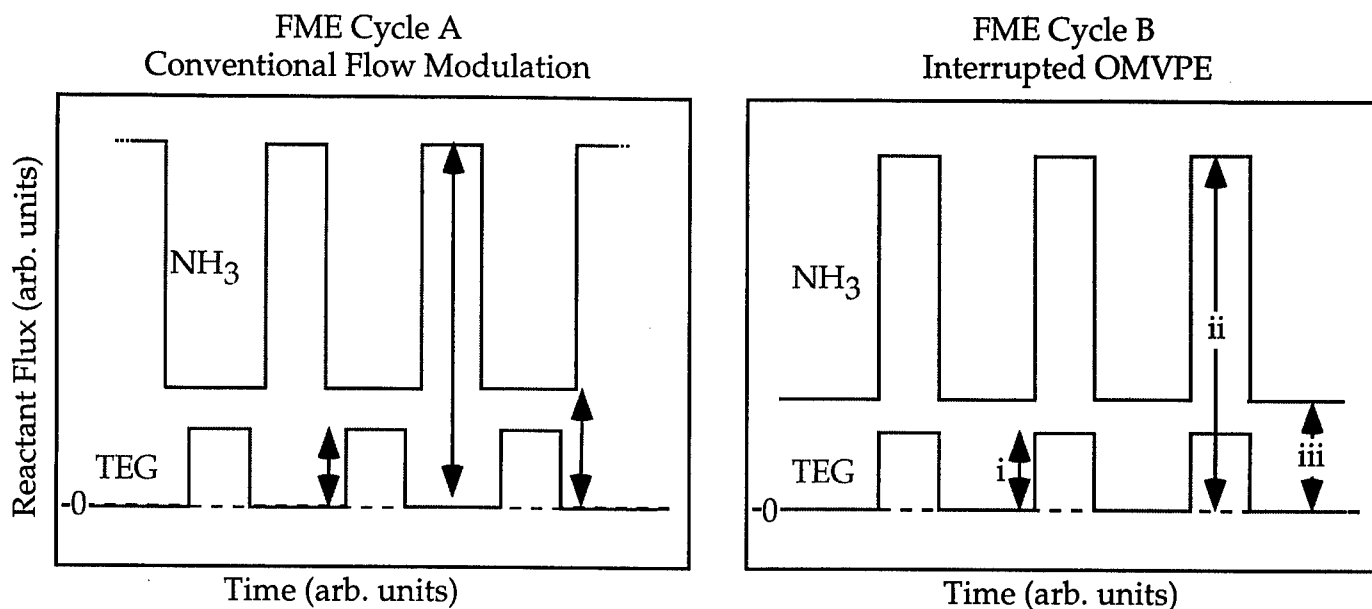


**Figure 1.** Growth cycles investigated for the growth of III-N in this study. Relative heights of the (i) group III pulse, (ii) main group V pulse, and (iii) uniform group V background are as indicated. The '0' reference level indicates reactant flow to vent. Dopants may be injected during the group III or group V cycle.

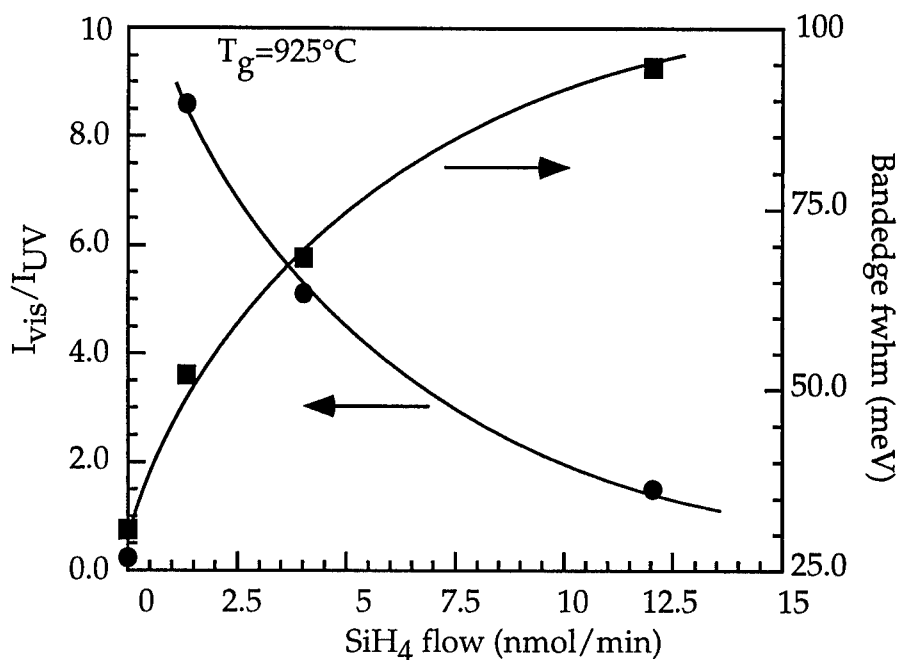


**Figure 2.** Optical properties of GaN:Si films prepared using growth cycle B. Heavier doping levels result in a decrease in yellow emission ( $I_{\text{vis}}$ ) relative to that of the bandedge ( $I_{\text{uv}}$ ).

## The effects of boundary layer and thermal gradient upon GaN growth

S. R. Chung<sup>a</sup>, J. C. Chen<sup>a</sup>, and T. L. Worchesky<sup>b</sup>

<sup>a</sup>CSEE Department, University of Maryland Baltimore County, Baltimore, Maryland, 21228

<sup>b</sup>Physics Department, University of Maryland Baltimore County, Baltimore, Maryland, 21228

### Introduction

Gallium nitride (GaN) is a very promising material for short wavelength optoelectronic devices. Recently, much progress has been made on device fabrication [1], but little is still known about the growth parameters of GaN. We have studied two of the parameters effecting the growth of high quality GaN. The boundary layer plays an important role in the growth of most III-V materials [2] but no data is currently available upon it's effect on GaN growth. Likewise, very few results are available on the effect of the thermal gradient [3] upon the growth of single crystal GaN.

### Experiment

An atmospheric pressure MOCVD reactor was used for the deposition of undoped GaN onto sapphire (0001) substrates. The sapphire substrates were degreased in solvents and soaked in HCl:HNO<sub>3</sub> (3:1) solution before loading into the horizontal reactor. Before the growth of epitaxial layer, a thin layer of GaN was deposited as the buffer layer. The buffer was deposited for 2 minutes at 490 °C by feeding trimethylgallium (TMG), ammonia (NH<sub>3</sub>), and nitrogen (N<sub>2</sub>) into the reactor. After the buffer layer, the epitaxial layer growth occurred at 1050 °C by feeding TMG, NH<sub>3</sub>, and H<sub>2</sub>. Three different susceptor configuration was used for the growth. As shown in Fig. 1, the sapphire substrates were placed between the lower susceptor and the upper susceptor. The lower susceptor was graphite while the upper susceptor was interchanged between graphite, quartz, or no susceptor.

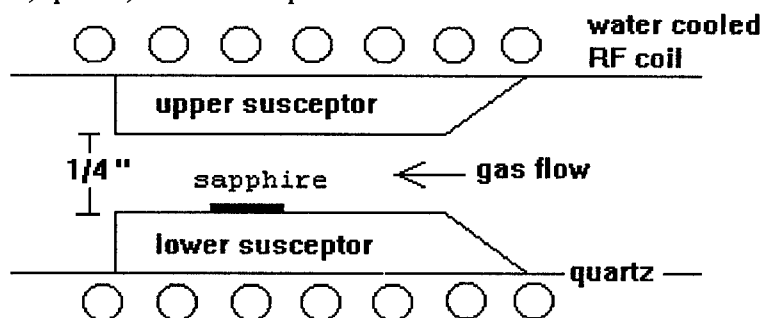


FIG. 1. Three different susceptor configuration was used by changing the upper susceptor to graphite, quartz or none. The lower susceptor was graphite.

### Results

The thickness of the films were 3 to 4  $\mu\text{m}$  after 60 minutes of growth. The films also showed a smooth mirror-like morphology on the surface. The samples were characterized by

room temperature photoluminescence (PL), double crystal x-ray diffraction (DCXRD), and C-V measurements.

The PL measurement was performed with 325 nm HeCd laser and the band edge luminescences are displayed in Fig. 2. To obtain an accurate measurement of the FWHM, a curve was fitted to the data.

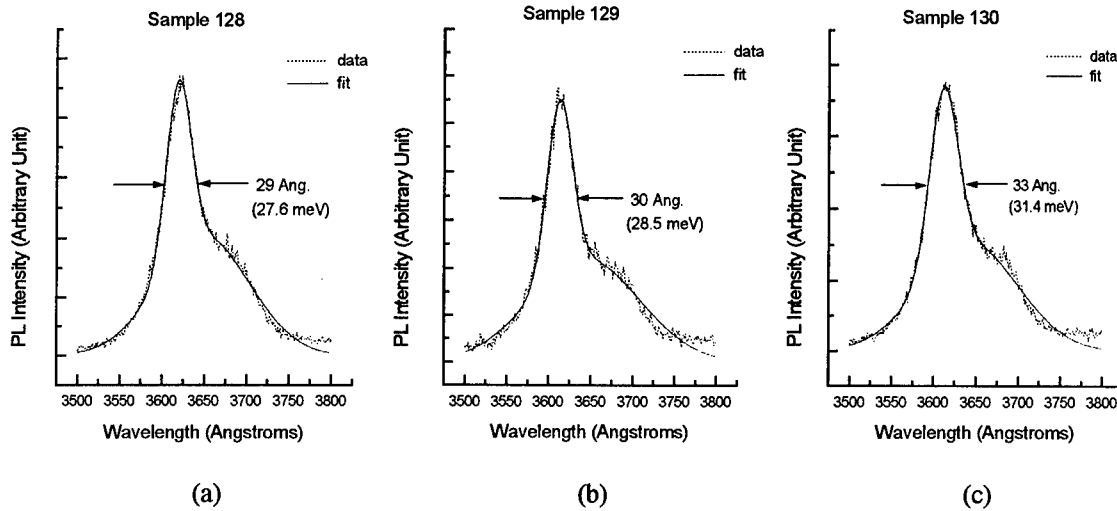


FIG. 2. RT PL spectrum of the band edge emission for growth with different upper susceptors [(a) graphite, (b) quartz, and (c) none].

Table I shows a similar trend for X-ray (DCXRD) and C-V measurements.

Table I. Summary of experimental results.

GaN experiment (upper susceptor)	X-ray (FWHM), arcsec	$n, \text{cm}^{-3}$	PL (band edge FWHM), meV
graphite	367	$2.5 \times 10^{17}$	27.6
quartz	418	$2.5 \times 10^{17}$	28.5
none	491	$3.5 \times 10^{17}$	31.4

## Conclusions

As indicated by Table I, the quality of the film difference between the graphite and the quartz upper susceptor growth is minimal. Thus, the difference in thermal gradient, when quartz is used instead of graphite, plays minimal role. However, a significant difference exists between the upper susceptor experiments and no upper susceptor experiment. If no upper susceptor is used, the boundary layer is larger [2]. Hence, lowering of the boundary layer by narrowing the gas flow channel plays an important role in increasing the quality of GaN growth.

## References

- [1] S. Nakamura, *Adv. Mater.* **1996**, 8, 8
- [2] G. B. Stringfellow, *Organometallic Vapor Phase Epitaxy* (Academic Press, San Diego, 1989).
- [3] S. Fisher, C. Wetzel, W. L. Hansen, E. D. Bourret-Courchesne, B. K. Meyer, E. E. Haller, *Appl. Phys. Lett.* **69**, 2716 (1996).



**GALLIUM NITRIDE MATERIALS,  
PROCESSING AND DEVICES**

**Thursday, 14 August 1997**

**Sessions:**

- ThA: Nitride Based Devices**
- ThB: Epitaxial Growth III**
- ThC: GaN Substrates Issues**
- ThD: Optical Gain in Widebandgap  
Materials**

## Thursday Papers Not Available

- ThA2      “Fabrication of High Power GaN LED’s and HEMTs”,  
*U. Mishra, Y.Wu, P.Kozody, S.Keller, B.Keller, J.Speck and  
S.DenBaars, University of California, Santa Barbara, CA*
- ThC1      “MOCVD Growth of GaN on Alternative Substrates”,  
*J. Redwing, Epitronics/ATMI, Danbury, CT*
- ThC3      “A New Compliant Substrate Approach for the Growth GaN  
Growth on Si by Metal Organic Chemical Vapor Deposition”,  
*N.P. Kobayashi, J.T. Kobayashi, P.D. Dapkus, W.J. Choi,  
A. Bond, X. Zhang, and D.H. Rich, University of California,  
Los Angeles, CA*
- ThC4      “Surface Morphology and Structure of AlN Films grown on  
Si(111)”, *N. Perkins, E. Rehder, K. Dunn, S.E. Babcock,  
T.F. Kuech, Univeristy of Wisconsin, Madison, WI*

## CW operation of InGaN MQW laser diodes

SHUJI NAKAMURA

Department of Research and Development, Nichia Chemical Industries, Ltd.,

491 Oka, Kaminaka, Anan, Tokushima 774, Japan

Phone: +81-884-22-2311

Fax: +81-884-23-1802

e-mail: shuji@nichia.co.jp

Major developments in wide-gap III-V nitride semiconductors have recently led to the commercial production of high-brightness blue/green light-emitting diodes (LEDs) and to the demonstration of room-temperature (RT) bluish-purple laser light emission in InGaN/GaN/AlGaN-based heterostructures under pulsed currents and continuous-wave (CW) operation. The radiative recombination of the spontaneous and stimulated emission of the InGaN MQW LEDs and LDs was attributed to excitons (or carriers) localized at deep traps (250 meV) which originated from the In-rich region in the InGaN wells acting as quantum dots [1,2]. The fundamental properties of semiconductor lasers are specified by the optical gain. Recently, RT CW operation of the InGaN MQW LDs with a lifetime of 35 hours has been achieved [3]. Here, we report the optical gain and the emission characteristics of InGaN single-quantum-well (SQW) LEDs and RT CW-operated MQW LDs.

Photocurrent spectra of the InGaN SQW LEDs and MQW LDs were measured at RT. The Stokes shifts of the energy difference between the absorption and the emission energy of the blue/green InGaN SQW LEDs and MQW LDs were 290, 570 and 190 meV, respectively. Both spontaneous and stimulated emission of the LDs originated from this deep localized energy state which is equivalent to a quantum dot-like state. The emission spectra of the LDs under RT CW operation showed periodic subband emissions with an energy separation of 2-5 meV which were different from a longitudinal mode. When the temperature or the operating current of the LDs was varied, a mode hopping of the emission wavelength between these periodic subband emissions was observed. The carrier lifetime and the threshold carrier density were estimated to be 2-10 ns and  $1 \times 10^{20}/\text{cm}^3$ , respectively. For the measurement of the gain spectra of the LDs, the Hakki-Paoli technique was used. The differential gain coefficient, the transparent carrier density, threshold gain and internal loss were estimated to be  $5.8 \times 10^{-17} \text{ cm}^2$ ,  $9.3 \times 10^{19} \text{ cm}^{-3}$ ,  $5200 \text{ cm}^{-1}$  and  $43 \text{ cm}^{-1}$ , respectively.

- [1] S. Chichibu, T. Azuhata, T. Sota, and S. Nakamura, Appl. Phys. Lett., 69, 4188 (1996).
- [2] Y. Narukawa, Y. Kawakami, M. Funato, Sz. Fujita, Sg. Fujita, and S. Nakamura, Appl. Phys. Lett., 70, 981 (1997).
- [3] S. Nakamura, M. Senoh, S. Nagahama, N. Iwasa, T. Yamada, T. Matsushita, Y. Sugimoto, and H. Kiyoku, Appl. Phys. Lett., 70, 1417 (1997).

**Substrate effects on GaN photodetector performance**

Gary M. Smith, Joan M. Redwing, Jeff S. Flynn, Vivek M. Phanse & Robert P. Vaudo  
Epitronics / ATMI  
7 Commerce Drive, Danbury, CT 06810  
(203) 794-1100 Voice, (203) 830-4116 FAX  
e-mail: gsmith[atmi.com]

Solar-blind UV photodetectors have a number of applications including missile detection, flame sensing, and solar UV monitoring. The III-V nitrides are ideal for these applications due to their wide bandgaps, making detectors transparent to visible and infrared radiation. There have been several publications on photoconductive GaN detectors on sapphire substrates but the effects of defect density on device performance have not been investigated. In this paper we describe the operation of GaN detectors grown by MOCVD on sapphire, SiC, and thick HVPE GaN base layers and compare the device performance of the detectors on each of these substrates.

The dislocation density of GaN layers grown by MOCVD on heteroepitaxial substrates such as sapphire and SiC is determined by the lattice mismatch, nucleation technique, and GaN layer thickness. Typical dislocation densities for GaN on sapphire are in the range of  $1\text{E}10\text{ cm}^{-2}$  due to the substantial lattice mismatch between the two materials (13.8%). In this study, we have investigated the use of two different substrates which enable a reduction in the dislocation density compared to sapphire: SiC substrates, which have a closer lattice match to GaN (3.4%), and thick HVPE-grown GaN layers on sapphire with dislocation densities in the range of  $1\text{E}8 - 1\text{E}9\text{ cm}^{-2}$ .

Photoconductive detectors were fabricated on each of the substrates by forming interdigitated electrodes using standard photolithography, metallization and lift-off procedures. The structure consists of a  $3\text{ }\mu\text{m}$  thick highly resistive ( $> 10^5\text{ }\Omega\text{-cm}$ ) GaN layer that is grown by MOCVD on the three substrates. The Ti/Al electrodes are  $5\text{ }\mu\text{m}$  wide with 10 or 20  $\mu\text{m}$  spacings. The square detector dimensions are 0.5 mm, 1 mm, and 1.5 mm on a side.

Preliminary measurements have been performed on the detectors. The detectors on SiC showed a slightly higher responsivity and sharper wavelength cutoff than did the detectors on sapphire. Further, the dynamic range of these detectors indicate that the detectors on SiC substrates have a more linear response to intensity variations than do detectors on sapphire which have a square root dependence on the intensity.

Further device characterization, including results on the detectors grown on HVPE GaN base layers will be discussed. In addition, a direct comparison will be made between the device results on identical structures grown on sapphire, SiC, and HVPE GaN base layers.

ThA4

9:45am - 10:00am

***Hybrid organic-inorganic GaN LED based color downconversion for displays***

S. Guha, N. A. Bojarczuk, R. Haight

IBM Research Division, IBM T. J. Watson Research Center, Yorktown Heights, NY 10598

The availability of small short wavelength III-N light sources have opened up new possibilities for applications involving color conversion. As a new application, consider the hybrid organic-inorganic structure shown in Figure 1 which consists of a GaN based LED emitting in the blue to uv coupled with an organic thin film with high fluorescence efficiency. Upon operation, the organic film absorbs the electroluminescence and emits in the green to red, resulting in color down conversion. Such a hybrid device is simple and has potential application as units for small full color pixelated displays for mobile applications. An array of identical GaN light emitters may be used as a substrate for deposition and patterning of appropriate emissive organic layers to form a full color display. Advantages over fully organic displays is that the electrical transport is confined to the robust GaN part, since organic films have poor electrical transport properties and degrade under electrical operation due to moisture. Advantages over fully semiconductor based displays is that different LEDs emitting different wavelengths do not have to be pieced together: the GaN LED is used as a skeleton to which an appropriate organic layer is simply added for the desired color. We demonstrate the operation of such hybrid LED units below and discuss applicability for displays.

A number of laser dyes have been examined as the organic thin films. These are either deposited by vacuum evaporation or spun on using a polymer matrix and an appropriate organic solvent. Depositions of the organic films were made on (i) soda lime glass substrates, or (ii) taking a commercial Nichia LED, stripping it out of its epoxy bubble and evaporating the dye film directly on top of the LED p-contact. While the latter is the more direct technique, the former is more convenient for rapid evaluation of different organic films. To form a hybrid unit, a Nichia LED was brought into proximity contact with the organic film deposited on a glass substrate, so that after absorption of the electroluminescence, the fluorescence is collected through the glass.

As an illustrative example, we show color conversion to orange using the laser dye 4-Dicyanomethylene -2-methyl-6-(p-dimethylaminostyryl)-4H-pyran (DCM). Figure 2a shows the electroluminescence spectrum from a Nichia LED. When a 2.5 micron thick DCM evaporated dye film is placed in front of it, the blue electroluminescence is absorbed and the DCM fluoresces in the orange, resulting in color conversion, as is seen in figure 2b). While dye molecules have been typically used as gain media for lasers and have extremely high (>90%) fluorescence efficiencies, pure dye films are very poor fluorescers due to the Forster effect, where an excited dye molecule transfers its excitation to a neighbouring molecule instead of relaxing radiatively. If the dye molecules are sufficiently close together, the excitation can then migrate till it is quenched at a non-radiative site. We have therefore examined the use of host-dopant combinations where both host and dopant are dye molecules: the host absorbs the GaN electroluminescence and transfers it to the dopant dye molecule. If the dopant molecules are far apart (with a distance greater than the critical Forster radius) then transfer effects are negligible and the dopant molecules recombine radiatively with high fluorescence efficiencies. Clearly, a number of conditions have to be met. Firstly, the host dye should absorb the electroluminescence significantly. Secondly, the excitation should be transferred to the dopant dye molecule: i.e. the

host emission spectrum and the dopant absorption spectrum should have appreciable overlap. Thirdly, the dopant should have a large Stoke shift to avoid self quenching. As an example, Figure 2c show the results from a DCM (0.4%)/Coumarin7(8%)/polymer film. In this case a blocking filter is placed between the Nichia diode and the organic film to eliminate the significant long wavelength ( $>520$  nm) content of the Nichia electroluminescence which remains unabsorbed. In this case DCM is the dopant dye, while Coumarin7 is the host dye. Coumarin 7 absorbs significantly at  $\sim 460$  nm and fluoresces at  $\sim 490$  nm in solution. On the other hand, DCM absorbs at  $\sim 480$  nm while it fluoresces at  $\sim 580$  nm: the conditions for host-dopant matching are thus reasonably met. As figure 2c shows, the blue electroluminescence is absorbed and the film fluoresces  $\sim 580$  nm.

The host-dopant films are significantly brighter and externally measured fluorescence efficiencies measured with a large area Si photodiode are in the 10-15% range. Recall that total internal efficiency limits the light extraction from a thin film: for a uniform thin film a simple estimate gives the total light extraction (from one surface) fraction at  $\sim 12\%$  for a film with a refractive index of 1.5. This number will be somewhat higher for rougher films, and due to scattering effects. Thus, our measured external efficiencies indicate quite high internal fluorescence efficiencies. The hybrid organic-inorganic nitride based LEDs are thus promising as units for small full color displays.

Figure 1: Schematic of a hybrid unit.

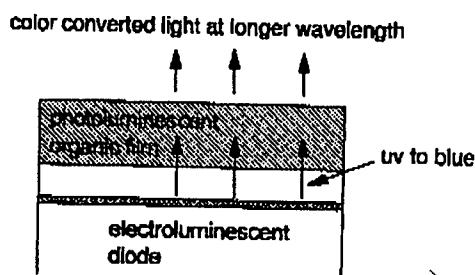
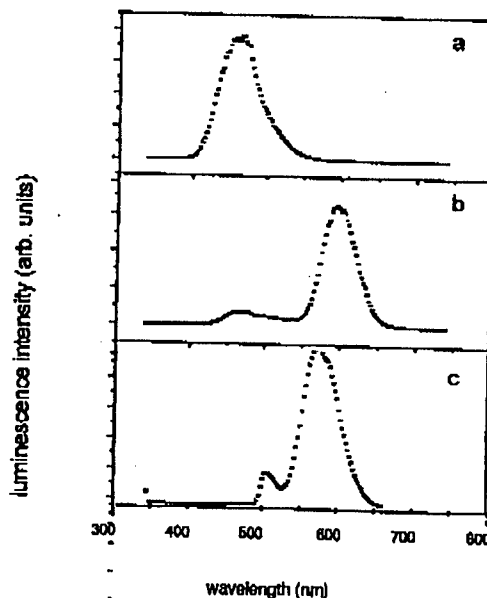


Figure 2: Luminescence spectra of (a) a Nichia LED; (b) Nichia LED with a 2.5 micron DCM film; and (c) Nichia LED with a DCM/Coumarin7/polymer film. Note that a blocking filter is placed between the LED and the film in c to cut off long wavelength ( $>520$  nm) electroluminescence.



**ThB1 (Invited)**  
**10:30am - 11:00am**

**MOCVD Growth, Characterization and Stability of High Quality  
InGaN MQW Structures**

J.C. Ramer and S.D. Hersee,  
Center for High Technology Materials,  
1313 Goddard SE,  
Albuquerque, NM 87106  
505-272-7823  
shersee@chtm.unm.edu

**Abstract**

High quality InGaN MQW structures (with In<sub>0.03</sub>Ga<sub>0.97</sub>N barriers and In<sub>0.18</sub>Ga<sub>0.82</sub>N wells) have been grown in which the FWHM of the room temperature PL spectrum is as low as 14 nm for a 10 period MQW structure. This paper will discuss the effects of growth rate, temperature and carrier gas (H<sub>2</sub> vs. N<sub>2</sub>) on InGaN composition and quality.

In addition to characterization by X-ray diffraction and photoluminescence we will demonstrate the usefulness of grazing incidence X-ray reflectivity (GIXR) as a new tool for the characterization of InGaN MQW structures. It will be shown that InGaN MQW structures with QW's as thin as 20Å can be grown with monolayer abrupt interfaces. MQW samples grown with no H<sub>2</sub> present during the InGaN growth will be compared to similar samples grown more conventionally, using H<sub>2</sub> as the pick-up flow through the MO bubblers.

The paper will also discuss the role of H<sub>2</sub> and temperature in the stability of heterointerfaces when high temperature cap layers are grown on top of the MQW region.



## Barrier and Well Width Study of InGaN/GaN Multiple Quantum Wells

A.C. Abare, S. Keller, M.P. Mack, L.A. Coldren, and S.P. DenBaars  
Electrical & Computer and Material Departments, University of California,  
Santa Barbara, CA 93106

InGaN multiple quantum wells have proven critical for the achievement of laser diodes in the (Ga,Al,In)N system.<sup>12</sup> We have studied the effects of barrier width and well width in MQW structures for use in laser diodes.

Atmospheric pressure MOCVD using trimethylgallium (TMGa), trimethylindium (TMIn), ammonia, and disilane as precursors was employed to grow the epitaxial films. The samples were grown on c-plane sapphire. The sapphire was first exposed to H<sub>2</sub> at 1050 °C. Growth was initiated with a 190 Å GaN nucleation layer deposited at 525 °C. The temperature was subsequently increased to 1060 °C and a 2.5 μm GaN layer was grown. The MQW structure, to be described below, was grown on this thick GaN layer. For the growth of the InGaN/GaN superlattice the temperature was lowered to 790 °C. During the InGaN wells, the input flows of TMGa and TMIn were 0.3 and 10 μmol/min, respectively. The barriers had a TMGa flow of 0.3 μmol/min and were doped with silicon to a carrier concentration of approximately 10<sup>18</sup> cm<sup>-3</sup>. The ammonia was 0.4 mol/min throughout. Following the MQW structure, a 120 Å Al<sub>0.1</sub>Ga<sub>0.9</sub>N layer was grown at low pressure. The temperature was then increased to 1060 °C under NH<sub>3</sub> for the growth of a 0.1 μm Al<sub>0.1</sub>Ga<sub>0.9</sub>N layer.

Two growth series were done to investigate the effects of the quantum well width and the barrier width. All structures consisted of 14 quantum wells. For the well width study, the barrier width was held at 50 Å while the well widths were made to be 10, 20, 30, 40, and 50 Å. The barrier width series had 20 Å wells and barriers of 10, 30, 70 and 90 Å. As mentioned above, a high temperature (HT) layer was grown above the MQW

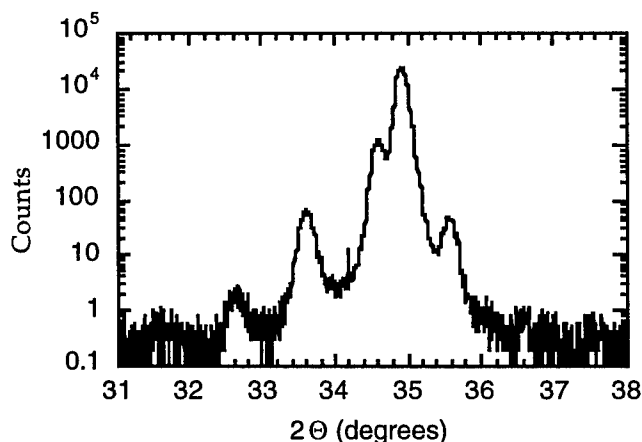


Figure 1 X-ray 2θ-w scan.

structure. While this step could cause some degradation in the MQW, it is salient since laser structures require this HT overlayer.

A bulk calibration samples of 800 Å InGaN was grown prior to the well width study. This film was grown under the same conditions as the well layer. X-ray diffraction was used to determine the indium composition. Assuming that the 800 Å film is completely relaxed and that Vegard's law holds, we obtain a value of approximately 0.2 for  $x_{\text{In}}$ . X-ray diffraction was also used to characterize the MQW structures. Figure 1 shows the  $2\theta - \omega$  scan for the sample with 40 Å wells and 50 Å barriers. Several superlattice fringes are visible. The  $x_{\text{In}}$  and superlattice period (well + barrier width) were determined assuming relaxed films and Vegard's law. These values agree with predicted growth rates and  $x_{\text{In}}$  from the calibration sample within experimental error.

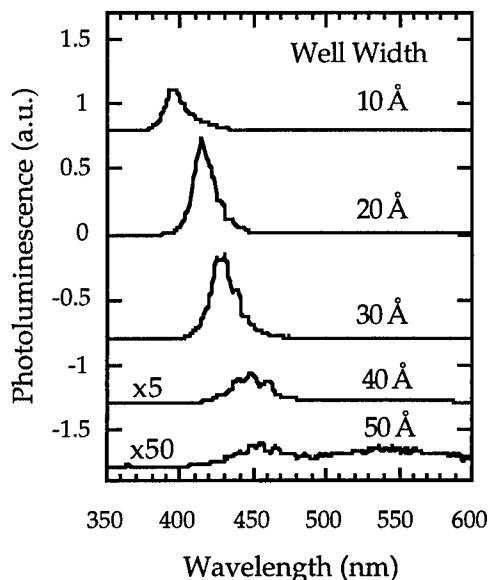


Figure 2 RT Photoluminescence.

also show an increase in FWHM and reduction of PL peak intensity. This is most likely a combined effect of degradation during the HT layer and effects of strain. The barrier width series showed improved performance for the thicker barriers. The PL peak intensity monotonically increases and FWHM decreases.

Based on photoluminescence, our results suggest a well width of 20 Å with a barrier width greater than 50 Å.

Room temp. photoluminescence (RT PL) was measured using a He-Cd laser with excitation density of approximately 200 W/cm<sup>2</sup>. This is shown in Figure 2 for the well width study. Optical interference can be seen due to the epitaxial layer on sapphire. A blue shift with reduction in well width is clearly seen. This shift matches with the quantum mechanical confinement using the effective mass approximation.

For the well width study, the 20 Å well width showed highest performance with the highest peak intensity and narrow emission. For the thinner 10 Å well, the FWHM increases presumably due to the interface roughness and the PL peak intensity reduces. The thicker wells

<sup>1</sup> Nakamura et al. *The Blue Laser Diode*. Springer-Verlag Berlin Heidelberg (1997).

<sup>2</sup> K. Itaya et al., *Jpn. J. Appl. Physics.*, 35, L1315, (1996).

## MOVPE growth of high quality InGaN films and InGaN/GaN Quantum Wells.

W. Van der Stricht, I. Moerman, P. Demeester

*University of Gent-IMEC, Department on Information Technology, Sint-Pietersnieuwstraat 41, 9000 Gent, Belgium.  
Tel: + 32 9 264 3316, Fax: + 32 9 264 3593, e-mail: piet.demeester@intec.rug.ac.be*

E.J. Thrush, J. A. Crawley

*Thomas Swan & Co. Ltd, Button End, Harston, Cambridge, CB2 5NX, United Kingdom.  
Tel: + 44 1223 87 2282, Fax: + 44 1223 871714, e-mail: ejthrush@dial.pipex.com*

### Summary

Recently the group III-nitrides (In, Ga)N have attracted much attention because of the high potential for the fabrication of light emitting devices operating in the red to ultraviolet wavelength range. Despite the recent success in realizing devices, only few reports have been made on growth of InGaN. In this paper growth of high quality InGaN films on (0001) sapphire substrates by atmospheric pressure organometallic vapor phase epitaxy in a close spaced vertical rotating disk reactor is investigated [1]. The effect of the growth temperature, V/III ratio and rotation speed is investigated. Some early results on InGaN/GaN quantum well structures are also discussed.

The InGaN films were deposited on GaN layers, because the lattice constant of InGaN is closer to GaN than sapphire. The growth was performed with a high indium source flow rate and nitrogen carrier. This is necessary because the indium incorporation is very low at growth temperatures in the range of 700 to 850 °C [2]. Typical flow rates for carrier, NH<sub>3</sub>, TMG and TMI are 4 l/min, 2.5 l/min, 5.6 μmol/min and 22.7 μmol/min. The indium incorporation was determined for several growth temperatures. Figure 1 clearly

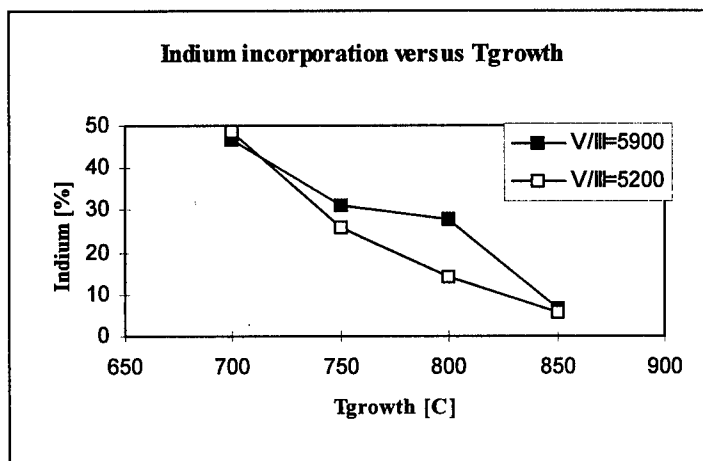


Figure 1: Indium incorporation in InGaN bulk layers.

illustrates a decreasing indium incorporation efficiency for increasing growth temperatures. A higher V/III ratio seems to enhance the Indium incorporation slightly. The indium content of the bulk InGaN films was calculated using room temperature photoluminescence measurements [3].

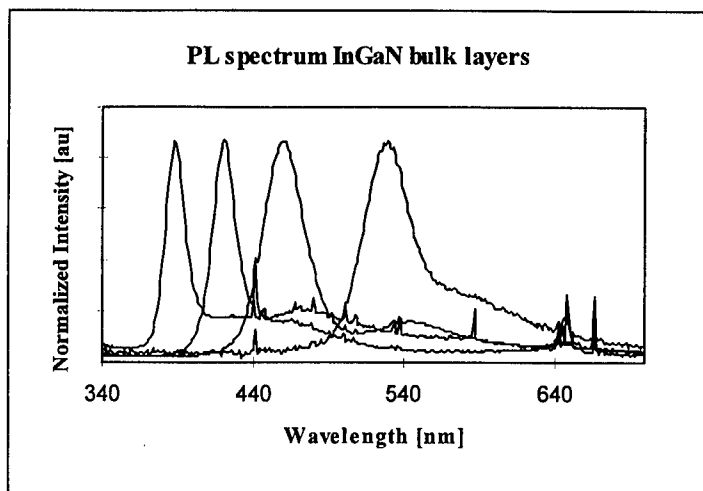


Figure 2: PL spectra of InGaN bulk layers.

intensities of the PL-spectra were normalized for comparison. For InGaN films with a high indium content the band-edge intensity usually decreases and the FWHM of the peak increases linearly with the composition. The optical quality of the InGaN films could be improved further by optimizing the growth conditions, which include: rotation speed, V/III ratio and nitrogen carrier flow.

Some efforts have been made to grow InGaN/GaN single and multi-quantum well structures. The approximately 5 nm thick InGaN wells have GaN barriers grown at the InGaN growth temperature ( $\pm 800$  °C) to prevent indium evaporation during the temperature ramp to GaN growth temperatures ( $\pm 1070$  °C). The quantum wells were covered with a GaN cap layer of approximately 30 nm thickness. Because the single InGaN wells were undoped the photoluminescence is typically very weak and show

strong deep level emission. However InGaN/GaN multi-quantum well structures exhibit a strong emission, as illustrated in figure 3. To conclude we can state that high quality InGaN films with high indium composition have been grown and that the preliminary results on InGaN/GaN quantum well structures are very promising.

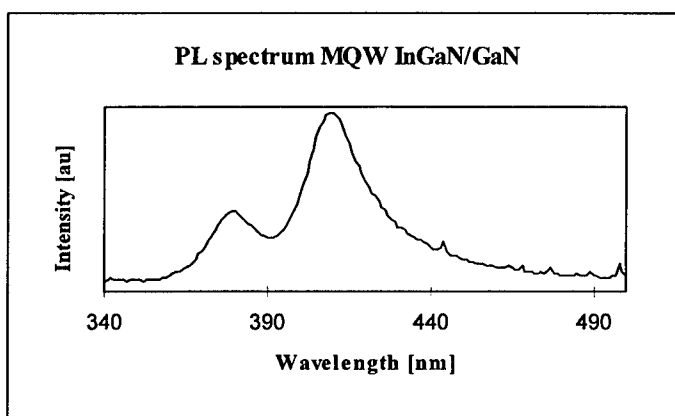


Figure 3: PL-spectrum InGaN/GaN MQW-structure.

## References.

- [1] W. Van der Stricht, I. Moerman, P. Demeester, J. A. Crawley, E.J. Thrush, J. Cryst. Growth 170 (1997), 344.
- [2] S. Nakamura and T. Mukai, Jpn. J. Appl. Phys.(1992), L1457
- [3] S. Nakamura, T. Mukai, M. Senoh, S Nagahama and N. Iwasa, J. Appl. Phys. 74 (1993), 3911.

ThB4

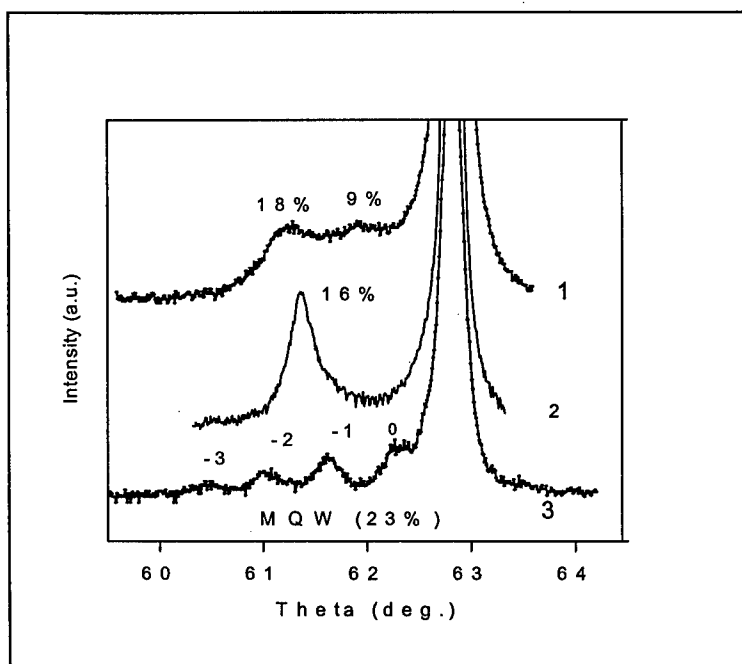
11:30am - 11:45am

### Phase Separation in Bulk InGaN and Quantum Wells Grown by Low Pressure MOCVD

C. A. Tran, R. F. Karlicek Jr., M. Schurman, T. Salagaj, A. Thompson and R. Stall  
Emcore Corp., 394 Elizabeth Ave. Somerset, NJ 08873

We have grown high quality InGaN layers and InGaN/GaN multiple quantum wells for blue LED applications. The degree of phase segregation of InGaN in bulk InGaN layers depends on the TMI and TMG flow rates as well as the growth temperature. Even for films without indium droplets on the surface, X-ray diffraction (XRD) reveals the coexistence of different indium compositions in the films. In this case photoluminescence of the films is red-shifted with respect to the wavelength calculated using the indium composition determined by XRD. The same observation is made for the multiple quantum wells, where phase segregation can significantly reduce interface abruptness. Using the same growth conditions as used for bulk InGaN layer growth, indium incorporation is significantly increased when growing quantum wells, where indium concentration variations within the wells may cause localization effects for excitons. It can explain the observed blue shift of electroluminescence

wavelength on function of driving current in blue LEDs, where multiple quantum wells are used as active layers. Under optimal growth conditions, multiple quantum wells with very well defined XRD satellite peaks and with PL in



wavelength range of (440-470 nm) can be achieved without any observable degree of indium phase segregation.

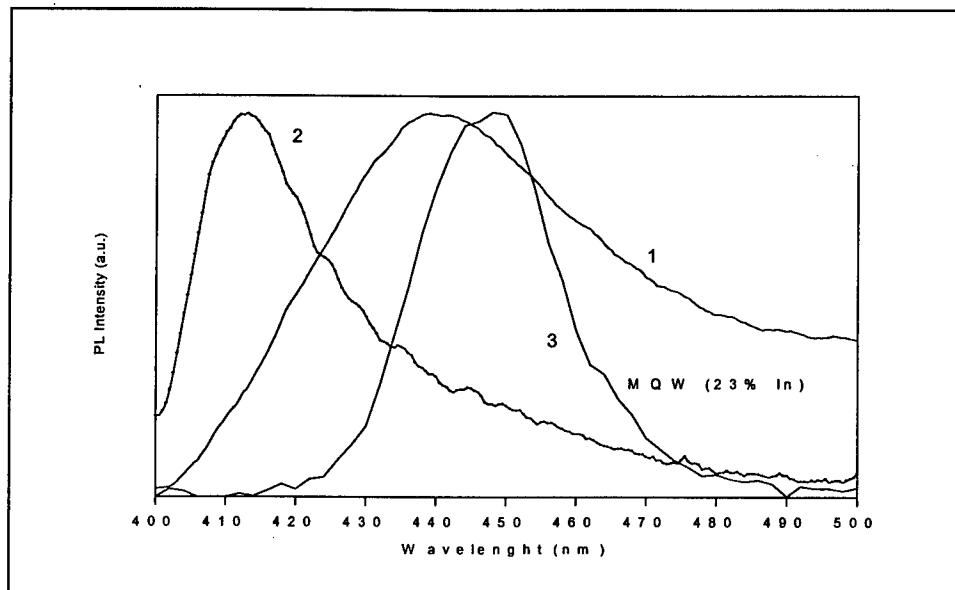


#### Figure Captions

XRD and room-temperature PL of 1) InGaN single layer with Indium phase segregation (9% and 18% Indium) 2) InGaN single layer InGaN (16% Indium) without phase segregation and 3) InGaN/GaN MQW (23% Indium) without phase segregation. In sample No.1, photoluminescence is red-shifted by 25 nm with respect to the wavelength calculated using the indium composition determined by XRD.

**Effects of Well Thickness on the Light Emission in  
InGaN/GaN and GaN/AlGaN Multiple Quantum Wells**

M. Smith, K. C. Zeng, J. Y. Lin, and H. X. Jiang

Department of Physics, Kansas State University, Manhattan, KS 66506-2601

A. Salvador, G. Popovici, H. Tang, W. Kim, and H. Morkoc

Materials Research Laboratory and Coordinated Science Laboratory, University of Illinois at  
Urbana-Champaign, Urbana, Illinois 61801

A. Khan and Q. Chen

APA Optics Inc., Blaine, MN 55449

**Summary**

Picosecond time-resolved photoluminescence (TRPL) has been employed to study the effects of well thickness on the light emission properties and recombination dynamics in  $\text{In}_x\text{Ga}_{1-x}\text{N}/\text{GaN}$  and  $\text{GaN}/\text{Al}_x\text{Ga}_{1-x}\text{N}$  multiple quantum wells (MQWs) grown both by metal-organic chemical vapor deposition (MOCVD) and reactive molecular beam epitaxy (MBE). In this work we present results from a set of MOCVD grown  $\text{In}_x\text{Ga}_{1-x}\text{N}/\text{GaN}$  and a set of MBE grown  $\text{GaN}/\text{Al}_x\text{Ga}_{1-x}\text{N}$  MQW samples with well thicknesses varying from 20 to 90 Å. Results from these MQW samples are compared with each other and also to InGaN and GaN epilayers to extrapolate the mechanisms and quantum efficiency of the optical emission in these structures. The implications of these results on device applications, in particular for blue LEDs and laser diodes will be discussed.

1.  $\text{In}_x\text{Ga}_{1-x}\text{N}/\text{GaN}$  MQW. The MQW sample with 25 Å well thickness showed only intrinsic localized exciton emission from the well region at low temperatures with recombination lifetimes in the sub-nanosecond scale, demonstrating high crystalline quality of the MQW structures. The MQW sample with 45 Å well thickness showed emission lines from both the well and barrier regions. For the MQW sample with 90 Å well thickness, an impurity related transition was observed to be dominant in its emission lines. In summary, our results have revealed that (i) the optical transitions in both the 25 Å and 45 Å well MQW samples were blue

shifted with respect to the  $\text{In}_x\text{Ga}_{1-x}\text{N}$  epilayer, however, no such blue shift was evident for the 90 Å well MQW sample, (ii) radiative recombination is dominant at low temperatures for the 25 Å well and 45 Å well MQW samples, and (iii) in 45 Å well MQW, the carrier transfer rate from the barrier to the well is strongly temperature and excitation intensity dependent.

2. GaN/Al<sub>x</sub>Ga<sub>1-x</sub>N MQW. In GaN/AlGaN MQWs, the dominant emission lines always resulted from the well region. In MQWs with well thicknesses of 20 and 25 Å, the emission lines at low temperatures were due to localized excitons. On the other hand, the band-to-impurity recombination dominated at low temperatures in MQWs with well thicknesses larger than 50 Å. In summary, our results have revealed that (i) the optical transitions in both the 20 Å and 25 Å well MQW samples were blue shifted with respect to the GaN epilayer, however, no such blue shift was evident for the MQW samples with well thicknesses greater than 50 Å, (ii) the localized exciton recombination lifetimes in MQWs of narrow well thicknesses increased linearly with temperature up to 60 K, which was a hallmark of radiative recombination in MQWs, and (iii) impurity related transitions, most likely the band-to-impurity transitions, were the dominant emission lines in MQWs of large well thicknesses ( $> 50$  Å).

All of these results can be explained by the concepts of the critical thickness of the MQWs. For both InGa<sub>x</sub>N/GaN and GaN/AlGa<sub>x</sub>N MQWs, below the critical thickness (e.g., in MQWs with 20 - 30 Å well thicknesses), intrinsic localized exciton transitions with expected quantum confinement (or blue shift) were observed. Above the critical thickness, structural defects and spatial nonuniformity were introduced, which caused impurity related transitions to be dominant with no evident of blue shift.

In terms of device applications, these results suggest that the better configuration for LED and laser diodes is to use multiple quantum wells of narrow well widths. The quantum efficiency is expected to be reduced dramatically when the well thickness becomes larger than a certain value since the band-to-impurity transition is less efficient compared with that of the excitonic transitions.



ThC2 (Invited)  
2:00pm - 2:30pm

## Exotic and Mundane Substrates for Gallium Nitride Heteroepitaxy

*Eric Hellman*

Bell Laboratories, Lucent Technologies\  
700 Mountain Ave.  
Murray Hill, New Jersey 07974 USA

### *Abstract*

It is often asserted that the principal obstacle to the epitaxial growth of high quality gallium nitride is the lack of a lattice matched substrate. Although this view is overly simplistic and underly factual, it conveys the correct impression that the most commonly used substrate, sapphire, has many shortcomings. Are there substrates to improve on sapphire? We have studied the growth of gallium nitride on a variety of materials, including ZnO, LiGaO<sub>2</sub>, LiAlO<sub>2</sub>, ScMgAlO<sub>4</sub>, Si, garnets and spinels. By growing on a variety of materials, we can assess the relative importance of lattice match, thermal expansion match, chemical stability and compatibility, polarity, and even cost of a substrate on the ensuing growth.

### *Lattice Match*

The case of SiC is a good example of the weak effect of lattice mismatch on epitaxial film quality. Although the lattice misfit of SiC to GaN is -3.5% compared to -13.7% for sapphire, only one group in the world has been able to obtain GaN epitaxial films on SiC of quality comparable to the Nichia films on sapphire. This is probably due to the high cost of SiC substrates on the commercial market. It is probably better to optimize film quality by making hundreds of growth runs than it is to use a substrate with smaller lattice match. Even smaller misfits do not make for better growth. We have shown[1] that (1 0 0)  $\beta$ -LiAlO<sub>2</sub> substrates do not even favor the growth of a structurally matched orientation of GaN with 0.1% $\times$ 1.2% misfit. In principle, though, it should be noted that given comparable experience, the growth of GaN should be better on a substrate where the misfit is not so large. We demonstrate the usefulness of a substrate with a +1.8% misfit for GaN, ScMgAlO<sub>4</sub>. [2] Commercial quality substrates of this material have recently been produced.

### *Structure Match and Chemical Compatibility*

The importance of structure match is perhaps most apparent when considering the substrates that don't work. For example, garnets have reasonably good lattice matches and chemical compatibility to GaN, but do not work as substrates. Oxides with close-packed oxygen lattices seem to be good candidates. Spinel can work extremely well[3], but some, such as iron spinels, don't, apparently because of chemical incompatibility.

### *Polarity*

Growth on the different polar surfaces of substrates such as AlN, ZnO[4] and LiGaO<sub>2</sub> has begun focussing attention on the importance of knowing which face of the GaN is being grown. Surprisingly, the question of which surface is which is still a matter of controversy, [5,6], although a consensus is building that MOCVD films and MBE films grown with ammonia are predominantly Ga-face. (The direction from gallium to nitrogen is along the substrate normal)

### *Cost*

To this date, the reigning champion in the GaN substrate race is sapphire. The big advantages of sapphire are its strength, chemical inertness, its ready availability and good quality, and its low price. All

of these attributes are improved upon by another substrate, silicon. Recently, AlN of high quality has been produced on (111) silicon.[7,8] If sapphire works so well despite its drawbacks, perhaps silicon could work too.

### References

- [1] E.S. Hellman, Z. Liliental-Weber D. N. E. Buchanan, unpublished.
- [2] E. S. Hellman, C. D. Brandle, L. F. Schneemeyer, D. Wiesmann, I. Brener, T. Siegrist, G. W. Berkstresser, D. N. E. Buchanan, E. H. Hartford, Jr., *MRS Internet J. Nitride Semicond. Res.* **1**, 1 (1996).
- [3] Shuji Nakamura, Masayuki Senoh, Shin-ichi Nagahama, Naruhito Iwasa, Takao Yamada, Toshio Matsushita, Hiroyuki Kiyoku, Yasunobu Sugimoto, *Appl. Phys. Lett.* **68**, 2105-2107 (1996).
- [4] E. S. Hellman, D. N. E. Buchanan, D. Wiesmann, I. Brener, *MRS Internet J. Nitride Semicond. Res.* **1**, 16 (1996).
- [5] F.A. Ponce, D.P. Bour, W.T. Young, M. Saunders, J.W. Steeds, *Appl. Phys. Lett.* **69**, 337-339 (1996).
- [6] Z. Liliental-Weber, S. Ruvimov, Ch. Kisielowski, Y. Chen, W. Swider, J. Washburn, N. Newman, A. Gassmann, X. Liu, L. Schloss, E. R. Weber, I. Grzegory, M. Bockowski, J. Jun, T. Suski, K. Pakula, J. Baranowski, S. Porowski, H. Amano, I. Akasaki, *Mater. Res. Soc. Symp. Proc.* **395**, 351 (1996).
- [7] M. Sanchez et. al. unpublished
- [8] E. S. Hellman and D. N. E. Buchanan, unpublished.

### Optical Gain in GaN Based Semiconductors

K. Domen, K. Horino, A. Kuramata, and T. Tanahashi  
Fujitsu Laboratories Ltd.  
10-1 Morinosato-Wakamiya, Atsugi 243-01, Japan

Since successful lasing has been reported for wurtzite (WZ) GaN and related materials,<sup>1-3</sup> researchers are now interested in exploring the possibility of reducing the threshold current density ( $J_{th}$ ). In this paper, we focus on this point by calculating the optical gain. We discuss the reduction in  $J_{th}$  on the c-plane, and we investigate the anisotropic strain effect on the  $(1\bar{1}00)$  plane.

WZ-nitrides reportedly require a high carrier density to generate optical gain.<sup>4</sup> Fig. 1 shows the optical gain of bulk GaN. It has a transparent carrier density ( $N_{tr}$ ) of about  $6 \times 10^{18} \text{ cm}^{-3}$ . This is because effective masses are large in both the conduction and valence bands, and there are three valence bands close to the band edge. Besides, the heavy hole (HH) and light hole (LH) bands are not separated by the quantum effect or strain effect on the c-plane.<sup>5</sup> All of these facts cause quantum well (QW) structure of nitrides to have a larger  $N_{tr}$  and a shorter radiative lifetime than conventional III-V materials. As a result,  $\text{In}_{0.05}\text{GaN}/\text{Al}_{0.05}\text{GaN}$ -QW has a 7 times larger transparent current density than that of  $\text{Ga}_{0.5}\text{In}_{0.5}\text{P}/(\text{Al}_{0.3}\text{Ga}_{0.7})\text{InP}$ -unstrained QW. We calculated the  $J_{th}$  of the InGaN single-layer QW (SQW) as a function of the well width in Fig. 2.  $J_{th}$  has a smallest value of around  $1 \text{ kA/cm}^2$  at about 4 nm. In spite of all these demerits described above,  $J_{th}$  is still a factor of 2 higher than for the unstrained-GaN MQW.<sup>6</sup> This is due to the large optical gain as shown in Fig. 1. So a SQW is sufficient to generate the threshold gain, while GaInP needs a 3-layer MQW. However, even if the threshold gain is sufficiently lowered, the reduction of  $J_{th}$  will hit a limit of around  $1 \text{ kA/cm}^2$  as far as we grow films on the c-plane, because the strain effect on the c-plane is not so large.<sup>5</sup>

The biaxial strain on the c-plane does not separate HH and LH because they are equivalent orbital functions in the isotropic energy structure of the hexagonal c-plane. We propose introducing the anisotropic strain in the c-plane utilizing the growth of  $(1\bar{1}00)$ -oriented GaN films,<sup>7</sup> where the c-plane is perpendicular to the growth plane. We calculated the valence band structures with anisotropic strain in the c-plane using the  $k \cdot p$  method by Bir and Pikus.<sup>8</sup> First we show the change in energy levels in the valence band at  $\Gamma$  ( $k = 0$ ) with strain in the a-axis,  $\epsilon_x$  (Fig. 3). We fixed the strain in the c-axis,  $\epsilon_z$ , at 0 % for clarity. We assumed the free-standing strain,  $\epsilon_y$ , along the b-axis which represents the growth direction. We found that both compressive and tensile strains split the HH and LH bands. This is explained as follows. At a strain of 0%, both HH and LH consist of two p-like orbital functions in the c-plane,  $|x\rangle$  along a-axis and  $|y\rangle$  along b-axis, like  $|x+iy\rangle$ . Since the hexagonal energy structure is isotropic in the c-plane,  $|x\rangle$  and  $|y\rangle$  are equivalent orbital functions. Therefore HH and LH are equivalent at  $\Gamma$ . When only the a-axis strain is applied, that is,  $\epsilon_x \neq \epsilon_y$ ,  $|x\rangle$  is no longer equivalent to  $|y\rangle$ . Hence, HH and LH split from each other and become  $|x\rangle$ - and  $|y\rangle$ -like functions, respectively. When  $\epsilon_x$  is compressive,  $\epsilon_y$  is tensile. Then the energy for  $|x\rangle$  goes up and that for  $|y\rangle$  goes down. When  $\epsilon_x$  is tensile, vice versa. Next, we examined the band structures at various strains from compressive to tensile (Fig. 4). We found another effect of isotropic strain in the c-plane; the relative position of HH and LH is reversed by the tensile strain. To reduce the transparent density, LH is preferable for the topmost band in order to reduce density of states at the band edge. We calculated the optical gain (Fig. 5). With the anisotropic strain in the c-plane, we obtained a transparent carrier density that was half that with no strain.

In summary, the growth of isotropic films in the c-plane limits the lowest value of  $J_{th}$  to around  $1 \text{ kA/cm}^2$ . On the other hand, growth on  $(1\bar{1}00)$  with anisotropic strain in the c-plane is significantly effective in reducing the threshold current density of the nitride lasers.

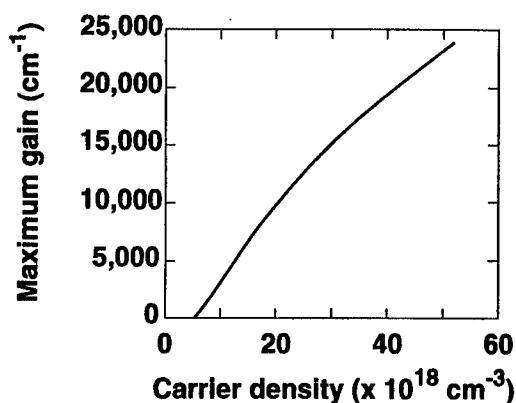


Fig. 1. Optical gain of bulk GaN as a function of carrier density.

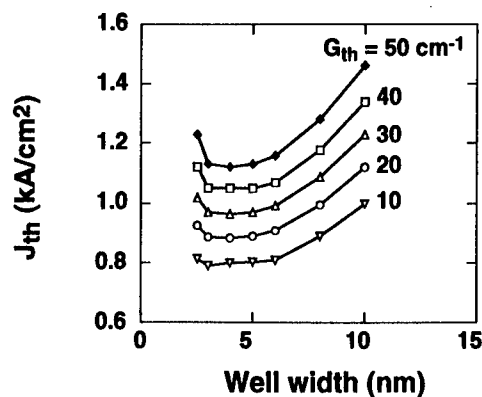


Fig. 2. Threshold current density versus SQW well width at various threshold gain.

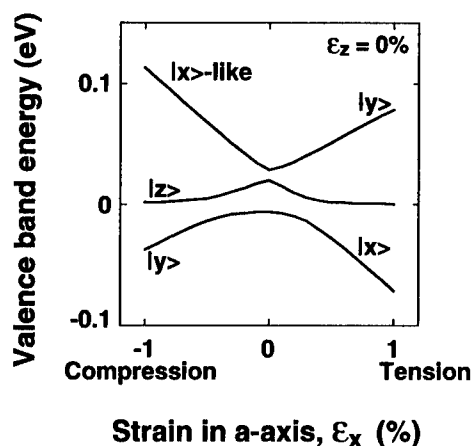


Fig. 3. Change of valence band energy level by strain in a-axis,  $\epsilon_x$ .

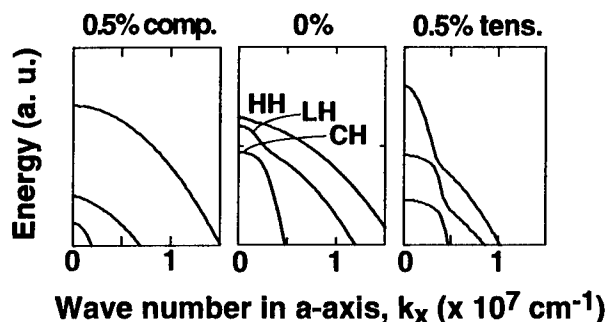


Fig. 4. Influence of a-axis strain on valence band structure.  $\epsilon_z$  is fixed at 0 %.

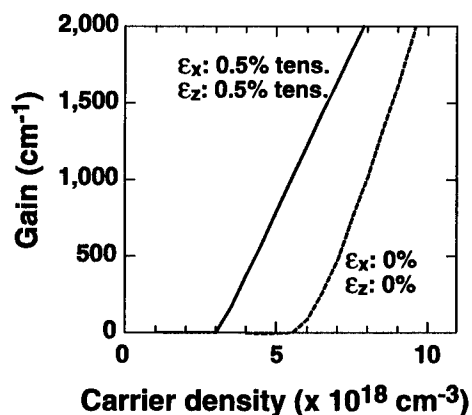


Fig. 5. Optical gain with strain of  $\epsilon_z = \epsilon_x = 0.5\%$  tensile. Dashed line is that with no strain.

#### References

- <sup>1</sup>S. Nakamura et al., Jpn. J. Appl. Phys. 35, L74 (1996).
- <sup>2</sup>I. Akasaki et al., Electron. Lett. 32, 1105 (1996).
- <sup>3</sup>K. Itaya et al., Jpn. J. Appl. Phys. 35, L1315 (1996).
- <sup>4</sup>S. Kamiyama et al., Jpn. J. Appl. Phys. 34, L821 (1995).
- <sup>5</sup>M. Suzuki et al., Jpn. J. Appl. Phys. 35, 1420 (1996).
- <sup>6</sup>K. Domen et al., Digest of 52nd Device Research Conference, IIA-5 (1994).
- <sup>7</sup>K. Horino et al., Proceedings of the International Symposium on Blue Laser and Light Emitting Diodes, We-P32 (1996).
- <sup>8</sup>G. L. Bir and G. E. Pikus, Symmetry and Strain-Induced Effects in Semiconductors (Wiley, New York, 1972).

## Gain Spectroscopy on InGaN quantum well diodes

M. Kuball, Y.-K. Song, and A. V. Nurmikko

*Department of Physics, Brown University, Providence, RI 02912*

S. P. DenBaars

*Department of Materials and Electrical Engineering, University of California, Santa Barbara, CA 93106*

One major question that has emerged with the demonstration of the InGaN QW diode injection laser [1] concerns the relationship between a macroscopic device parameter, such as the threshold current density, and the optical gain viewed at a microscopic level. At present, the optical gain, when normalized to the threshold electron-hole pair density, is about one order of magnitude higher in the InGaN QW laser than in the ZnCdSe QW laser [2], although the two wide gap alloys are rather similar at the level of the virtual crystal approximation (effective masses, etc.). As is well known, the GaN-based heterostructures house a wide range of crystalline defects which appear to impact the active physical properties and device performance in a surprisingly mild manner. The specific issue that is raised in paper concerns the correlation between compositional disorder in the InGaN QW on atomic scale with that of optical gain and associated e-h pair dynamics. There is plenty of evidence to date that InGaN, at In-composition exceeding a few atomic percent, is not a simple random alloy. For example, linear optical probes (luminescence, absorption, reflectance) exhibit spectral linewidths on the order of 100 meV, well in excess of estimates obtained from models based on random potential fluctuations in the cation composition.

We have performed a range of optical characterization experiments whose focus has been to examine spectroscopic details of the optical gain in a *pn*-junction device [2]. The device material used in these studies was grown by metalorganic chemical vapor deposition (MOCVD) on sapphire at UCSB and contained an active region composed of five nominally 25-Å-thick  $\text{In}_{0.20}\text{Ga}_{0.80}\text{N}$  quantum wells with 45-Å-thick GaN barriers within an AlGaIn/GaN *pn*-junction heterostructure. As LEDs, these devices have exhibited quantum efficiencies of several percent. Photocurrent (PC) and electroreflectance (ER) spectroscopy establish a useful baseline for the measurement of the distribution of electronic states at the conduction and valence band edges. Figure 1 shows an example of a room temperature PC spectrum exhibiting a pronounced disorder induced tail that penetrates deeply into the bandgap (on the order of 100-

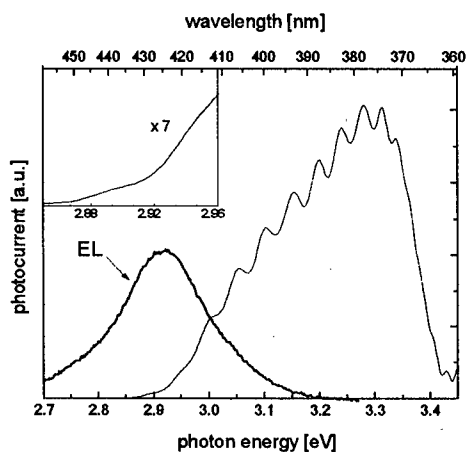


Fig. 1. Photocurrent spectrum (solid line) of a InGaN QW diode. The inset shows details of the PC spectrum on the low energy tail. The dotted line is the electroluminescence spectrum.

200 meV). The LED emission originates from these states which can be viewed as localized [4]. However, since the radiative lifetimes are quite long (several nsec and beyond) [4], it is unclear at this time whether e-h pair correlations (excitonic effects) are important in the recombination process. To calibrate the vertical scale of Fig. 1 a single pass transmission experiment was performed at 3.3 eV yielding an absorption coefficient of  $(5 \pm 0.5) \times 10^4 \text{ cm}^{-1}$ . No obvious features associated with quantum confinement of excitons are discernible in the absorption spectrum. Also electroreflectance measurements on similar samples have not yielded clear evidence for the QW exciton state. Arguments have been made recently that such states can be seen in InGaN QWs in photovoltage and electroabsorption measurements [3]; however, more detailed experiments are here clearly necessary.

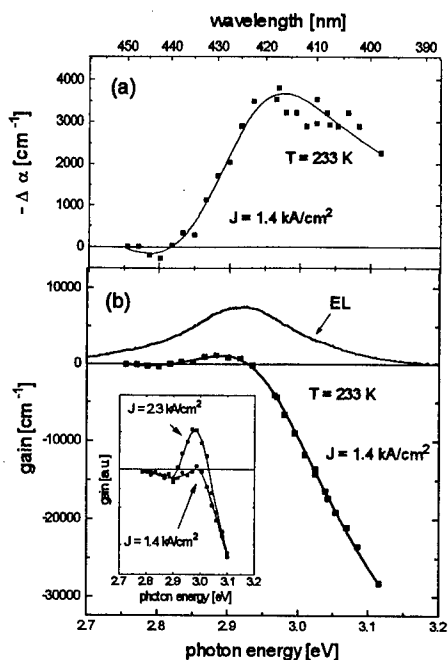


Fig. 2. (a) Differential absorption spectrum of a device at  $T=233$  K (squares) at a current density of  $J=1.4$  kA/cm<sup>2</sup>. (b) Actual gain/absorption spectrum at this current density, in comparison with the EL spectrum (dotted line). The inset shows the gain spectrum well above the transparency region for another device.

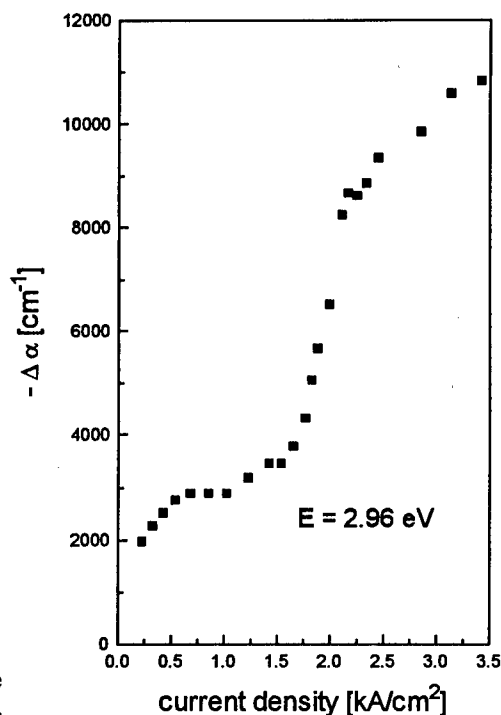


Fig. 3. Maximum of the differential absorption spectrum  $-\Delta\alpha$  as a function of current density.

Optical gain experiments have been performed in a single pass geometry through the QW heterostructure (direction perpendicular to the layer plane) on the device under pulsed forward bias. Figure 2(a) shows the injection induced changes  $-\Delta\alpha$  in the absorption coefficient at a current density of  $1.4$  kA/cm<sup>2</sup>. The actual gain spectrum is presented in Fig. 2(b), obtained from Fig. 2(a) by comparing  $-\Delta\alpha$  with the absorption coefficient shown in Fig. 1. For the active InGaN, we find that transparency condition is reached at an injection level of approximately  $1.4$  kA/cm<sup>2</sup> at near room temperature. At injection levels reaching  $5$  kA/cm<sup>2</sup> (corresponding to an estimated e-h pair density well in excess of  $1 \times 10^{19}$  cm<sup>-3</sup>), maximum gain coefficients of approximately  $5000$  cm<sup>-1</sup> have been measured. The gain spectra are broad, on the order of  $100$  meV, emerging on the low energy side of the LED spectrum. From the evolution of the gain, i.e., the injection induced changes  $-\Delta\alpha_{\text{peak}}$  in the absorption coefficient shown in Fig. 3, and the gain spectrum with increasing current density, we speculate that significant initial injection is necessary to fill the disorder broadened joint density of electronic states, before useful inversion is reached and values of the gain coefficient can be obtained which are required for an actual laser device. Note the sublinear 'plateau' in Fig. 3 in the range of  $J=0.6$ – $1.4$  kA/cm<sup>2</sup>. However, once the true gain regime is achieved  $-\Delta\alpha_{\text{peak}}$  starts increasing nearly linearly, before showing signs of a sublinear behavior at the highest current densities probably due to thermal effects. At high e-h pair densities encountered major question remains open as to whether the electronic states remain localized or acquire a (at least partially) extended (delocalized) character. Experiments to identify a possible 'mobility edge' are under way.

This work was supported by DARPA (N00014-92-J1893), ONR and NSF. M.K. acknowledges the support from the Alexander von Humboldt foundation (Germany).

- [1] S. Nakamura et al., Appl. Phys. Lett. **69**, 1568 (1996).
- [2] M. Kuball et al, Appl. Phys. Lett. **70**, 2580 (1997).
- [3] S. Chichibu et al., Appl. Phys. Lett. **69**, 4188 (1996).
- [4] E. S. Jeon et al., Appl. Phys. Lett. **69**, 4194 (1996).

ThD3

4:30pm - 4:45pm

Theory of gain in InGaN quantum well lasers

W.W.Chow and A. F. Wright  
Sandia National Laboratories  
Albuquerque, NM 85718-0601, U. S. A.

A. Girndt, F. Jahnke, and S.W.Koch  
Department of Physics and Material Sciences Center  
Philipps University  
Renthof 5, 35032 Marburg, Germany

To analyze experimental results in group-III nitride lasers, it is necessary to be able to predict their gain spectra accurately. Both excitons and electron hole plasma play important roles in the optical properties of group-III nitride compounds, even under typical lasing conditions of high carrier density and high temperature.<sup>1</sup> Also, inhomogeneous broadening is present, due to localization effects from dimensional or compositional variations in the quantum wells.<sup>2</sup> This paper describes a consistent treatment of the above effects.

Our approach is based on a Hamiltonian that includes the Coulomb interaction energy among carriers. This approach gives a consistent account of the many-body effects due to excitons and an electron-hole plasma. These effects include band gap renormalization, polarization dephasing, thermalization to quasi-equilibrium carrier populations and screening.<sup>3</sup> Using the many-body Hamiltonian, we derive the coupled quantum mechanical equations of motion for the gain medium variables. These equations are solved numerically for the steady state solutions, from which the homogeneously broadened small signal gain spectrum is extracted. The inhomogeneously broadened spectrum is determined from a statistical average of the homogeneously broadened ones.

The spectra in Fig. 1a are computed for a 4nm  $\text{In}_{0.1}\text{Ga}_{0.9}\text{N}/\text{Al}_{0.2}\text{Ga}_{0.8}\text{N}$  quantum well structure and different carrier densities. The hole energy dispersions and optical dipole matrix element are computed using a  $6\times 6$  Luttinger-Kohn Hamiltonian and the envelope approximation. Input parameters are the bulk wurtzite material parameters. The figure shows the exciton resonance at low densities and  $T = 300\text{K}$ . At high densities the exciton resonance vanishes and gain appears (see inset). The spectrum at carrier density  $N = 6\times 10^{12}\text{cm}^{-2}$  shows  $>100\text{meV}$  gain peak redshift relative to the unexcited quantum well bandgap energy, due to the bandstructure, Coulomb interactions and inhomogeneous broadening. The inhomogeneous broadening is assumed to come from a 15% standard deviation in the Indium concentration.

Figure 1b shows that inhomogeneous broadening reduces the gain, and shifts the spectrum towards lower energy. The red shift of the gain peak relative to the unexcited quantum well band gap ranges from  $70\text{meV}$  for the homogeneously broadened case to  $>200\text{meV}$  for  $>50\%$  compositional fluctuation.

In summary, our approach is based on the Semiconductor Bloch Equations with carrier correlation effects treated at the level of quantum kinetic theory in the Markovian limit. It gives a consistent description of plasma and excitonic effects, which play important roles in the optical properties of group-III nitride lasers. The effects of inhomogeneous broadening due to compositional variation are also discussed.

This work was supported in parts by the U. S. Department of Energy under contract No. DE-AC04-94AL85000, the Deutsche Forschungsgemeinschaft (Germany), and the Leibniz Prize.

### References

1. W. W. Chow, A. Knorr and S. W. Koch, Appl. Phys. Lett. **67**, 754, 1995.
2. S. Nakamura, Proc. SPIE, **2693**, 36, 1996.
3. F. Jahnke, *et al*, Phys. Rev. Lett. **77**, 5257, 1996.

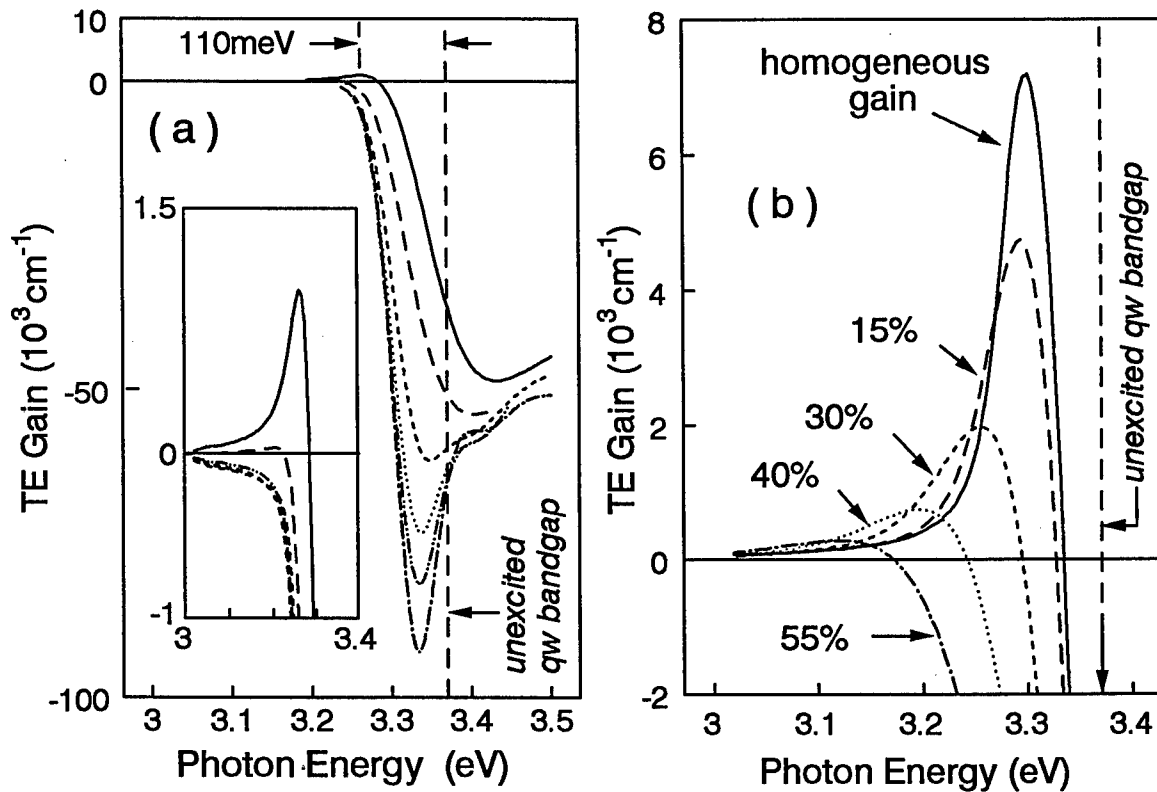


Fig. 1. (a) Calculated TE gain spectra for a 4nm  $\text{In}_{0.1}\text{Ga}_{0.9}\text{N}/\text{A}_{0.2}\text{Ga}_{0.8}\text{N}$  quantum well at  $T = 300\text{K}$  and densities  $N = 0.1, 0.5, 1.0, 2.0, 4.0,$  and  $6 \times 10^{12} \text{ cm}^{-2}$ . The inset shows the gain portion of the spectra. (b) TE gain spectra at  $N = 8 \times 10^{12} \text{ cm}^{-2}$  and different amount of inhomogeneous broadening due to compositional variation.



## Coulomb Attraction Effects in CdZnSe Quantum Well Lasers

P. S. Zory <sup>a</sup>, C. F. Hsu <sup>a</sup>, P. Rees <sup>b</sup> and M. A. Haase <sup>c</sup>

<sup>a</sup> Dept. of Electrical and Computer Engineering, University of Florida, Gainesville, FL 32611

<sup>b</sup> School of Electrical and Computer Systems, University of Wales, Bangor, UK

<sup>c</sup> 3M Scientific Research Lab, 3M Center 201-1N-35, St. Paul, MN 55144

**Abstract:** It is shown that Coulomb attraction in the electron-hole plasma in CdZnSe quantum wells plays an important role in determining the observed blue-shift in lasing wavelength with increasing carrier density. The relationship between Coulomb attraction and excitonic gain is also discussed.

### 1. Introduction

A simple method for testing the validity of one's laser model is to see how well it predicts the dependence of lasing wavelength on cavity length. Using a single particle theory [1] modified by the effects of carrier scattering (CS) and bandgap renormalization (BGR) [2], it was found that the "slope" of the predicted dependence was opposite in sign to the measured slope for CdZnSe quantum well (QW) cleaved facet lasers. Previous work using a many body theory in which CS, BGR and the effects of Coulomb attraction were included [3], also predicted the opposite slope. In Section 2, we show that when the effects of Coulomb attraction (Coulomb enhancement = CE) are included in our theory, the slope has the correct sign and the correct magnitude to within about 30% [4]. For carrier densities ( $N$ ) below the transparency level ( $N_t$ ), the inclusion of CE in these models [3, 4] causes a resonance-like feature, resembling an exciton-peak, in the absorption spectrum. The relationship of this feature to reports of "excitonic lasing" in CdZnSe lasers at room temperature [5, 6] is discussed in Section 3.

### 2. Lasing Wavelength vs. Cavity Length

For typical cleaved facet lasers, the lasing energy  $E$ , which is the photon energy at the peak of the output power spectrum, is determined by the spectral location of the peak of the gain curve. This value of  $E$  for a given cavity length  $L$  can be predicted using the standard relation between threshold gain and cavity losses in conjunction with the theory [4]. As mentioned in Section 1, the predicted dependence of  $E$  on  $1/L$  (the solid line in Fig. 1a) is opposite in sign to the experimental data (3 data points in Fig 1) when CS and BGR are taken into account. When CE is included (Fig. 1b), the calculated "slope" has the correct sign and the correct magnitude to within about 30% of the experimental slope. The small discrepancy between the predicted absolute values of  $E$  and the measured values could be rectified by making a small adjustment to any one of a number of QW bandgap determining parameters such as QW material composition, degree of biaxial compression, QW thickness, band offsets, etc. Adjustments of this type do not change, in any significant way, the slope of the  $E$  vs.  $1/L$  prediction.

Figure 1a

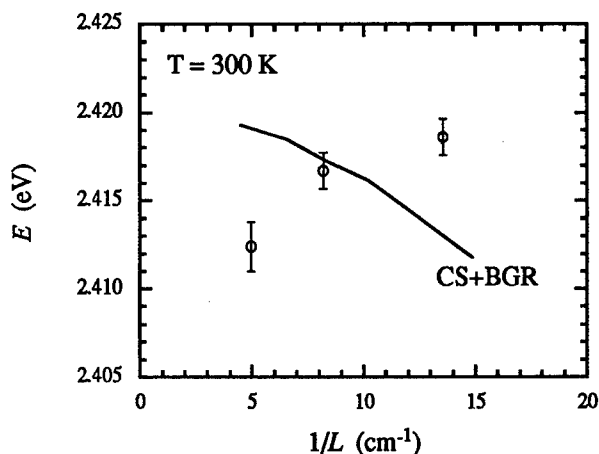
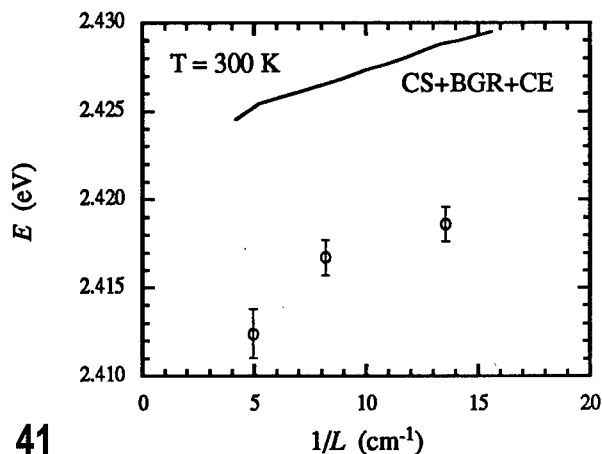


Figure 1b



### 3. Coulombic Attraction and Excitonic Gain

As shown in previous work [3, 4], CdZnSe laser models with CE included predict resonance-like absorption features for  $N < N_x$ . Such features are usually referred to as “exciton peaks” in experimental absorption spectra. In the specific case calculated in [3] for an 8 nm thick CdZnSe laser operating at a QW material gain of  $1000 \text{ cm}^{-1}$ , the gain peak (located at photon energy  $E$ ), is red-shifted 36 meV with respect to the absorption peak (located at  $E_x$ ) and about 75 meV with respect to the unexcited C1-HH1 CdZnSe bandgap ( $E_{g1}$ ). As shown in Fig. 2 and also in [4], we obtain a similar result for a 4 nm thick CdZnSe laser. This particular arrangement of energies with comparable separations has been observed in room temperature experiments using CdZnSe QW lasers [5, 6].

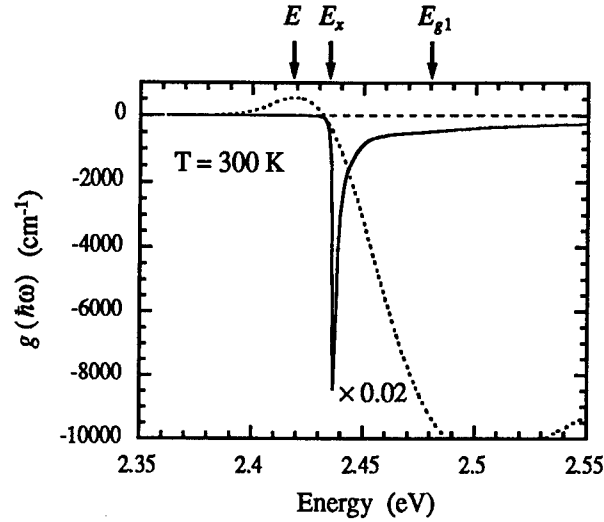


Figure 2

Since the measured  $E$  is close to  $E_x$  and far from  $E_{g1}$ , it is natural to think that the gain mechanism is somehow related to the phenomenon causing the sharp absorption peak. Since such peaks are usually attributed to exciton absorption, one can go one step further and say that the gain mechanism in CdZnSe lasers is excitonic in nature. However, since the CE-model used to generate Fig. 2 does not contain excitons and is in good agreement with experiment, it would appear that it is incorrect to say that excited excitons are the source of optical gain in room temperature CdZnSe lasers. What one can say is that conventional electron-hole plasma theory [1, 2] can be used to simulate the operation of CdZnSe QW lasers provided Coulomb attraction effects [3] are taken into account.

**Acknowledgment:** This work was supported by ONR/DARPA Grant No. N00014-92-J-1895.

### References

1. S. W. Corzine, R. H. Yan, and L. A. Coldren, *Quantum Well Lasers*, ch. 1, P. S. Zory, Ed. New York: Academic Press, 1993.
2. M. Asada, *Quantum Well Lasers*, ch. 2, P. S. Zory, Ed. New York: Academic Press, 1993.
3. W. W. Chow, and S. W. Koch, "Many-body Coulomb effects in room-temperature II-VI quantum well semiconductor lasers," *Appl. Phys. Lett.*, vol. 66, pp. 3004-3006, 1995.
4. C. F. Hsu, P. S. Zory, P. Rees, and M. A. Haase, "Coulomb enhancement in CdZnSe single quantum well lasers," *SPIE Proceedings*, vol. 3001, 1997.
5. J. Ding, H. Jeon, T. Ishihara, M. Hagerott, and A. V. Nurmikko, H. Luo, N. Samarth, and J. K. Furdyna, "Excitonic gain and laser emission in ZnSe-based quantum wells," *Phys. Rev. Lett.*, vol. 69, pp. 1707-1710, 1992.
6. J. Ding, M. Hagerott, P. Kelkar, A. V. Nurmikko, D. C. Grillo, L. He, J. Han, and R. L. Gunshor, "Role of Coulomb-correlated electron-hole pairs in ZnSe-based quantum-well diode lasers," *Phys. Rev. B*, vol. 50, pp. 5787-5790, 1994.

**GALLIUM NITRIDE MATERIALS,  
PROCESSING AND DEVICES**

**Friday, 15 August 1997**

**Sessions:**

**FA:    *Characterization of GaN***

**FB:    *Characterization and  
Fabrication of GaN***

## Friday Papers Not Available

- FA1      "Materials Characterization for GaN Laser Diodes",  
*N. Johnson, Xerox PARC, Palo Alto, CA*
- FB3      "Low Damage Patterning of III-N Materials For Contact  
Deposition By Low Energy Electron Enhanced Etching (LE4) in  
DC Plasma", *H.P. Gillis, University of California, Los Angeles,  
CA and D.A. Choutov and K.P. Martin, Georgia Technical  
Institute, Atlanta, GA*

## Characterization of mid-gap states in n-type GaN with optical-isothermal capacitance transient spectroscopy

Peter Hacke and Hideyo Okushi

*Electrotechnical Laboratory, 1-1-4 Umezono, Tsukuba-shi, Ibaraki-ken 305 Japan  
[evehp@etl.go.jp, tel 81 298-58-5417, fax 81 298-58-5419]*

Deep levels are often deleterious to efficiency and speed of semiconductor devices. n-type GaN frequently exhibits broad yellow photoluminescence emission and has been observed to become semi-insulating when the donor concentration is reduced below a certain threshold.<sup>1</sup> These phenomena are likely to be caused by deep levels acting as luminescent recombination centers and carrier compensation sites. Further, GaN deposited on lattice and thermal mismatched substrates such as sapphire exhibit high dislocation density. Despite the successful operation of light emitting diodes with such material,<sup>2</sup> influence of crystallographic defects on electronic properties is probable.

In this work, the deep level band structure of unintentionally doped n-type GaN grown by HVPE and MOVPE is demonstrated. Optical-isothermal capacitance transient spectroscopy (O-ICTS)<sup>3</sup> is used to simultaneously observe thermal and optical emission processes from deep levels. The key benefit of this technique found when applied to GaN is that deep levels can be distinguished spectroscopically by their characteristic emission time constant. The O-ICTS spectra can be deconvoluted to estimate the concentrations and ionization energies of deep levels with a high degree of confidence.

In the 143 K O-ICTS spectra (shown in Fig. 1 for the HVPE case), carriers from the relatively shallow level E1 (activation energy 0.22 eV) are thermally emitted to the conduction band, whereas those from E2 are detected with optical excitation of greater than ~0.85 eV. The concentrations of these levels tend to be higher in HVPE-grown GaN, but are nevertheless of generally low concentration in the  $10^{14} \text{ cm}^{-3}$  range. They may originate from impurities, such as those contained in the hot quartz tube of the HVPE deposition system.

With O-ICTS, carriers from what apparently is a broad deep level (E5) are photoionized to the conduction band in the range of ~1.6 to ~2.5 eV; the broad yellow photoluminescence in unintentionally doped n-type GaN may originate from this deep level as it is the dominant deep level common to all such material. We observe the concentration of E5 to be about  $1 \times 10^{15} \text{ cm}^{-3}$  in ~100  $\mu\text{m}$  thick HVPE-grown GaN, but it is found to be more than three times greater in our MOVPE-GaN samples grown on sapphire. The total measured deep level concentration is thus lower in the HVPE sample. This is consistent with the high mobilities<sup>4,5</sup> (about  $2000 \text{ cm}^2/\text{V}\cdot\text{s}$  at the low temperature peak), sharp bound exciton photoluminescence line widths<sup>4</sup> (2.58 meV), and good Schottky barrier device properties<sup>6</sup> achievable with HVPE grown GaN. The fact that E5 photoionizes in a broad manner suggests the origin to be extended defect states such as those associated with dangling bonds,<sup>7</sup> rather than a highly localized energy state such as that of an impurity related point defect.

It is seen that the photoionization time of E5 is rapid compared to the shallower E2 level with 2.0 eV incident photon energy. This indicates E5 possesses a larger optical cross section at this energy and is therefore expected to be the more optically and electronically active deep level.

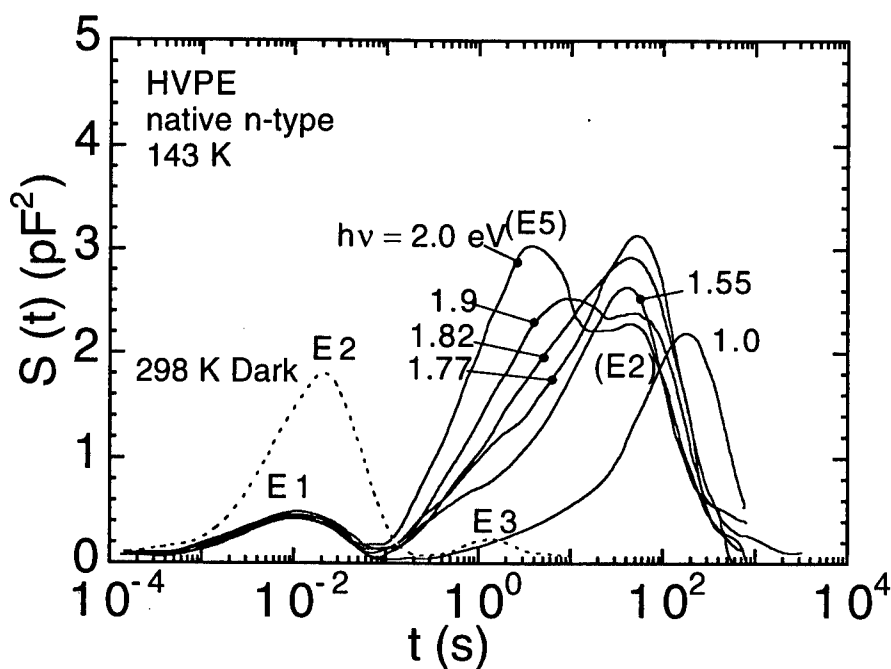


Fig. 1. Development of the ICTS spectra as a function of incident photon energy, where  $S(t) = t[d\Delta C^2(t)/dt]$ . The dark spectrum with thermoionized levels E2 and E3 is shown for comparison (dotted line). With 1.0 eV illumination, a peak consisting largely of the E2 level is seen. The relatively shallow E1 (0.22 eV) is quickly thermoionized at 143 K and its position is thus independent of photon energy. On increased incident photon energy to 2.0 eV, a peak consisting largely of the dominant E5 level is seen to develop on the left (fast) side of E2, indicating E5 has a relatively large optical cross section. This peak continues to increase in amplitude with higher incident photon energy to about 2.5 eV.

- 1 P. Hacke, A. Maekawa, N. Koide, K. Hiramatsu, and N. Sawaki, Jpn. J. Appl. Phys. 33, 6443 (1994).
- 2 S. Lester, F. Ponce, M. Craford and D. Steigerwald, Appl. Phys. Lett. 66(1995) 1249.
- 3 H. Okushi and Y. Tokumaru and H. Naka, Semicond. Sci. Technol. 7, A196 (1992).
- 4 T. Detchprohm, K. Hiramatsu, H. Amano and I. Akasaki, Appl. Phys. Lett. 61, 2688 (1992)
- 5 W. Götz, L. Romano, N. Johnson, J. Walker, D. Bour and R. Molnar, presented at the Fall 1996 MRS Meeting, Boston.
- 6 P. Hacke, T. Detchprohm, K. Hiramatsu, N. Sawaki, Appl. Phys. Lett. 63, 2676 (1993).
- 7 H. Okushi, Phil. Magazine B, 52, 33 (1985).

## Stimulated emission from optically pumped cubic GaN on GaAs (100) substrate

Atsushi Nakadaira and Hidenao Tanaka

NTT Integrated Information & Energy Systems Laboratories

3-9-11, Midori-cho, Musashino-shi, Tokyo 180, Japan

E-mail: nakadair@ilab.ntt.co.jp

Group III-nitrides are attractive for use in light emitting devices. It is well known that zinc-blende type III-nitrides can be grown on substrates that have a cubic lattice. However, it has been difficult to grow high-quality crystals. Recently we reported that the molar ratio of precursors played an important role in determining the quality of cubic GaN and that the optical properties of cubic III-nitrides could be considerably improved<sup>1</sup>. On the other hand, there have been no reports of stimulated emission from cubic III-nitride alloys. In the case of hexagonal III-nitride alloys, measurements<sup>2,3</sup> of optically pumped stimulated emission have been used to determine if the crystal quality is sufficient for a laser diode. We report here the observation of stimulated emission from optically excited cubic GaN.

We prepared a cubic GaN sample by low-pressure metalorganic vapor-phase epitaxy. We first grew GaN on GaAs (100) substrate at 570°C; next, a GaN layer at 950°C; then AlGaIn at 950°C; and finally GaN at 950°C again. Thicknesses of these layers were 10, 120, 120, and 750 nm, respectively. The AlGaIn layer prevented the GaAs substrate from becoming rough at high temperature, and thus improved the surface flatness of the final cubic GaN layer. This sample was cleaved parallel to the [011] direction of the GaAs substrate. The cleaved surface of the layers was as flat as that of the GaAs substrate. The cavity length of the sample was 1.3 mm.

The sample that was mounted on a heat-sink was optically pumped with a pulsed nitrogen laser, whose wavelength was 337.1 nm. The repetition rate was 10 Hz and the pulse width was

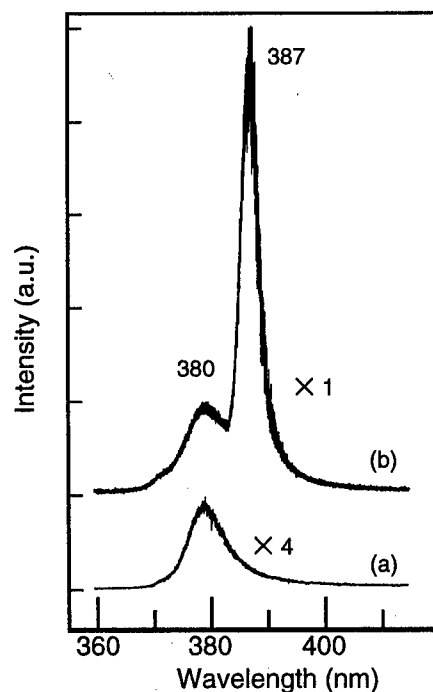


Figure 1. Emission spectra from cubic GaN when excitation power density was (a) 0.78 and (b) 5.7 MW/cm<sup>2</sup>.

about 5 ns. The photoluminescence from the cleaved facet of the specimen was observed when the heat-sink was cooled to 34 K with a cryostat. Figures 1 (a) and (b) show emission spectra when excited power was 0.78 and 5.7 MW/cm<sup>2</sup>, respectively. The spectrum of emission at excitation power of 0.78 MW/cm<sup>2</sup> exhibits a broad and weak emission peak at 380 nm. On the other hand, the peak narrowed on the longer-wavelength side when the excitation power was 5.7 MW/cm<sup>2</sup>. The peak position was 387 nm. The output power characteristics are shown in figure 2. The output power increased super-linearly as excitation power increased. The threshold excitation power density was estimated to be 2.4 MW/cm<sup>2</sup>. The emission whose peak was 387 nm was almost completely TE polarization mode, while the emission whose peak was 380 nm showed no linear polarization. The TE polarization indicates that the emission concerned a Fabry-Perot cavity and a waveguide.

In conclusion, we have observed the first stimulated emission from a cleaved zinc-blende GaN specimen by optical excitation. The emission showed 1) narrowing of the spectrum width compared with that of spontaneous emission, 2) super-linear output-power dependence on excited power density, and 3) TE-polarization above the threshold excitation power density, which was 2.4 MW/cm<sup>2</sup> when the heat-sink temperature was 34 K. These results are encouraging for the development of laser diodes using cubic III-nitrides.

## REFERENCES

- <sup>1</sup> A. Nakadaira and H. Tanaka, J. Electron. Mater. **26**, 320 (1997).
- <sup>2</sup> R. Dingle, K. L. Shaklee, R. F. Leheny, and R. B. Zetterstorm, Appl. Phys. Lett. **19**, 5 (1971).
- <sup>3</sup> S. T. Kim, H. Amano, I. Akasaki, and N. Koide, Appl. Phys. Lett. **64**, 1535 (1994).

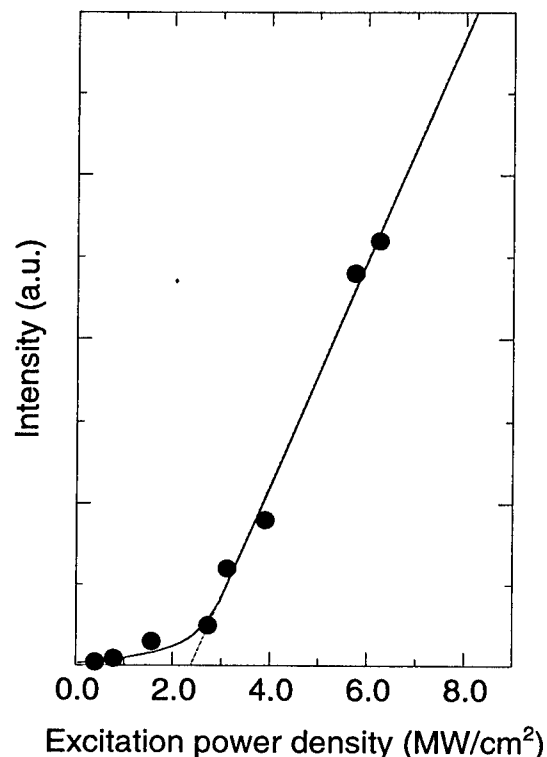


Figure 2. Output emission intensity dependence on the excitation power density.



### Spectral Reflectivity Monitoring of GaN Growth

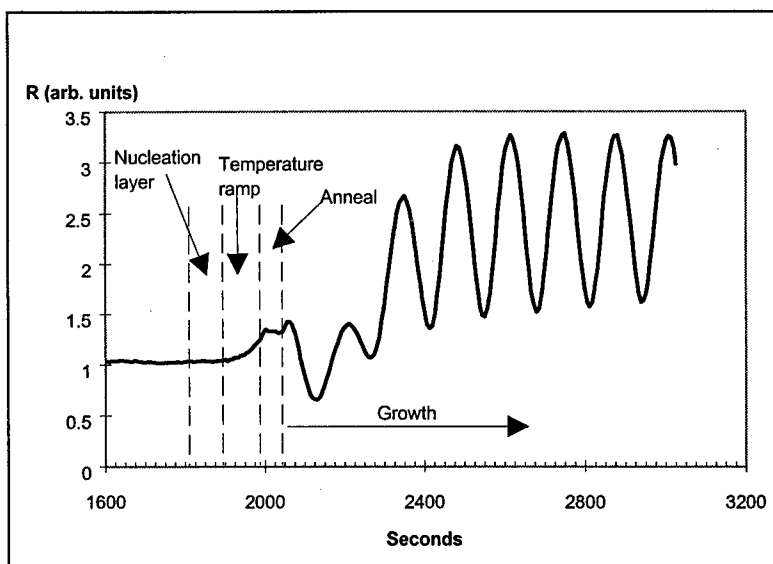
R. F. Karlicek, Jr., C. A. Tran, M. Schurman, T. Salagaj and I. Ferguson

EMCORE Corporation  
394 Elizabeth Avenue  
Somerset, NJ 08873  
Tel: (908) 271 9090  
Fax: (908) 271 9686

The use of *in situ* spectral reflectance for monitoring the growth of GaN is described. By using this method to measure the growth of GaN nucleation layers at several temperatures and reactor pressures, the activation energy for the growth of the GaN nucleation layer versus temperature was determined to be 126 kJ/mole, independent of growth pressure over the range of 55 to 200 torr. During the growth of GaN, the nucleation layer is too thin to be measured using interferometry, but reflectivity measurements during the initial stages of high temperature GaN growth immediately following nucleation layer deposition probe the initial GaN surface morphology. While the final, thick GaN films are specular, the amount of time needed to create a smooth reflective growing surface can range from 100 to 1000 seconds. The required time is inferred from the development of good GaN surface reflectivity with intense interference fringes as shown in the figure at the right for the growth of a simple undoped GaN layer.

The recovery rate of this surface depends on factors known to influence GaN electrical and optical properties, such as substrate cleaning, nitridization and nucleation layer growth conditions. Undoped GaN films grown under conditions yielding a rapid recovery of the surface reflectivity tend to be highly

resistive, while films grown with a slower rate of smoothing tend to have higher background carrier concentrations and higher room temperature mobilities. This suggests that the rate of formation of the smooth GaN surface at elevated temperatures is related to the grain size and defect structure of the final film. These factors are found to be important in the growth of high quality films including the growth of GaN:Mg and simple LED structures.



***In-Situ Reflectance Monitoring and Characterization of GaN grown by MOCVD***

Jung Han, R. M. Biefeld, J. C. Zolper

M. H. Crawford, and D. M. Follstaedt

Sandia National Laboratories\*

P. O. Box 5800, Albuquerque, NM 87185-0601

Despite rapid progress in the development of optoelectronic and electronic devices based on wide bandgap III-nitride semiconductors, growth of GaN by MOCVD (by far the most effective means of GaN material synthesis) has remained largely a "black-box" process. The optimization and exploration of the vast parameter space has depended solely on *ex-situ* characterization with growth recipes to a great extent confined to the so called "two-step" nucleation procedure first proposed by Akasaki et. al. We showed previously that, due to a well-behaved, laminar gas flow pattern in the high-speed rotating-disk MOCVD reactor, it is possible to avoid undesirable coatings and to preserve optical access to the growth surface. An *in-situ* optical reflectometer was employed in this work to probe and extract information such as growth rates, deposition uniformity, and morphological evolution during the initial hetero-nucleation of GaN on sapphire.

Two different nucleation procedures have been evaluated. In an attempt to optimize the reflectance (intensity) transient, for the first method we adopted a "ramp-and-nucleate" procedure in which the beginning of TMGa flow (at  $\sim 500^\circ\text{C}$ ) was followed immediately by a temperature ramp to the final growth temperature ( $\sim 1030^\circ\text{C}$ ). It is worth noting that there is little or no surface roughening, as judged by the nearly ideal reflectance oscillations (see Figure 1), throughout this nucleation procedure which normally yield a specular surface morphology. The other procedure investigated was the conventional "two-step" approach with well-defined deposition of a low-temperature GaN bufer, followed by a growth interruption for a temperature ramp. In this case the high temperature growth is often initiated by various degrees of roughening due to a strongly 3-dimensional island nucleation. The subsequent coalescence of nucleation islands can be seen by a recovery of reflectance intensity before the reflectance reaches a periodic oscillatory pattern (see Figure 2).

The two surface morphological transitions at the nucleation stage resulted in different microstructures. Cross-sectional TEM revealed a large difference in the density and nature of dislocations. The sample with nearly no nucleation roughening (Sample A) had a density of edge-type dislocations along the c-axis of around  $5 \times 10^9 \text{ cm}^{-2}$  and a density of dislocations with a screw component (screw-type) of around  $7 \times 10^8 \text{ cm}^{-2}$ . (The thickness of the specimen was determined by convergent-beam electron diffraction.) On the other hand the two-step nucleation procedure used for Sample B yielded dislocation densities of around  $4 \times 10^8 \text{ cm}^{-2}$  each for the edge-type and the screw-type dislocations. Previous TEM work by other groups suggested that the edge-type dislocations may be due to the presence of twist domain boundaries, e.g., columnar domains with the c-axis aligned and some finite in-plane misalignment, while the screw-type dislocations arise from tilt domain boundaries. The attempt to maintain a smooth morphological transition on the scale of optical wavelengths during Sample A growth possibly produced a high density of "twisted nuclei". Alignment of the c-axis among these nuclei could have preserved the nucleation morphology yet resulted in a high density of edge-type dislocations. The two-step nucleation procedure seems to facilitate an initial morphological roughening during high-temperature growth that we interpret as the formation of tilted (mis-aligned along c-axis) domains. Generation of screw-type dislocations associated with the initial roughening could promote the interaction and annihilation of the dislocations during the island coalescence stage.

The observed reduction in defect density resulted in the improvement of optical and electrical properties. Room-temperature electrical properties (electron concentration and mobility) were improved from  $0.5\text{--}1 \times 10^{18} \text{ cm}^{-3}$  and  $250 \text{ cm}^2/\text{V}\cdot\text{sec}$  to  $1 \times 10^{17} \text{ cm}^{-3}$  and  $460 \text{ cm}^2/\text{V}\cdot\text{sec}$ . Low-temperature (4K) PL linewidth was reduced from around 15 meV to 4.5 meV with the additional appearance of free-exciton emission peaks. We will also present correlation of the *in-situ* optical reflectance measurement with

surface AFM measurements at various stages during the roughening-recovery transient. The use of *in-situ* monitoring not only enhances process control and reproducibility, it also provides links between the resulting material's properties and growth parameters and surface kinetics.

\*Sandia is a multiprogram laboratory operated by Sandia Corporation, a Lockheed Martin Company, for the United States Department of Energy under Contract DE-AC04-94AL85000.

Figure 1.

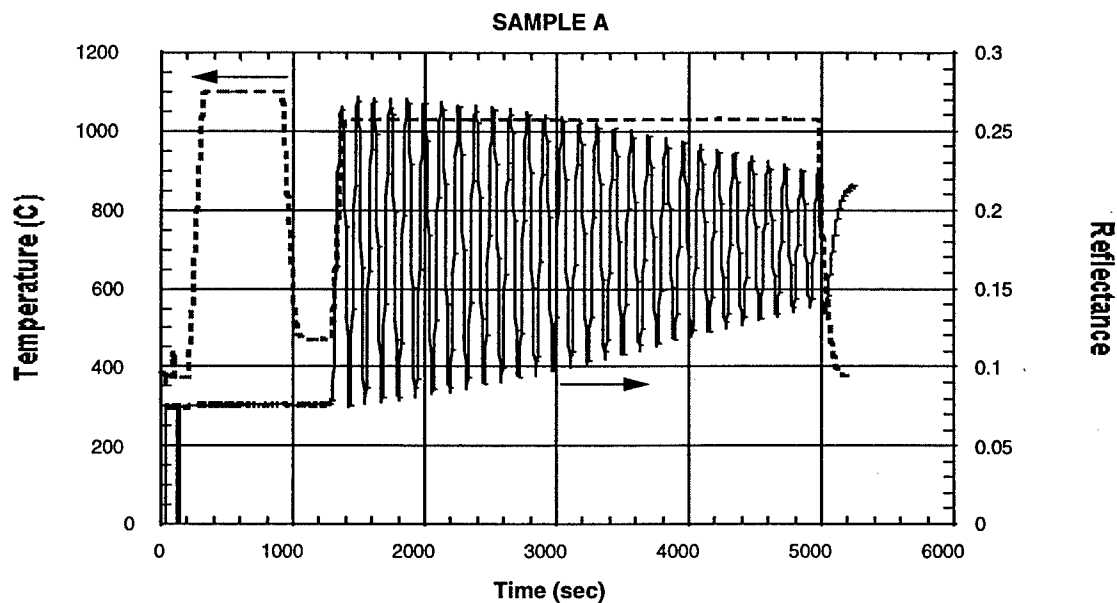
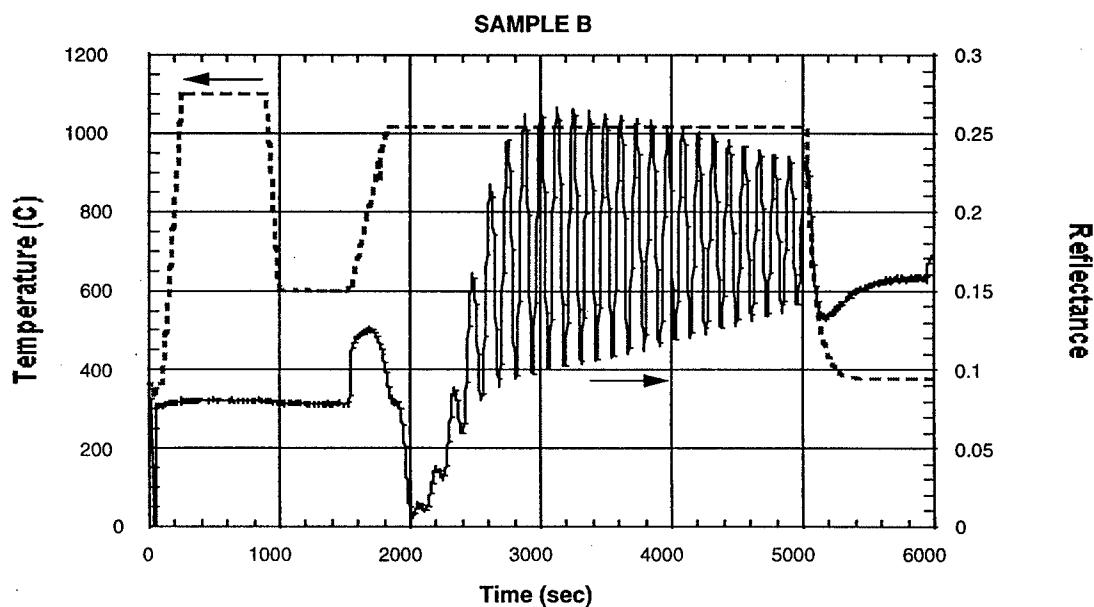


Figure 2.



**Characterization of As-Grown and Ion-Implanted GaN by Photoluminescence and Photoluminescence Excitation Spectroscopy\***

S. Kim, S.J. Rhee, D.A. Turnbull, E.E. Reuter, X. Li, J.J. Coleman, S.G. Bishop

*Microelectronics Laboratory  
University of Illinois at Urbana-Champaign  
Urbana, IL 61801*

Photoluminescence (PL) and photoluminescence excitation (PLE) spectroscopy have been used to characterize as-grown and ion-implanted epitaxial films of GaN grown on sapphire and SiC substrates by MOCVD, and on sapphire substrates by HVPE. Our studies have included a variety of near-band edge PL bands and deeper PL bands such as the ubiquitous yellow band which is present at varying strength in most as-grown films of GaN, and several types of deep emission bands introduced by the implantation of Er, Cr, and isovalent impurities such as As and P. PLE spectroscopy of the deep PL bands such as the yellow band, the broad implantation-induced defect bands, and the intra-f-shell emissions of  $\text{Er}^{3+}$  has been used to detect extrinsic (below gap) absorption bands due to defects and impurities over an extremely broad spectral range. Comparison of the PLE spectra of these deep PL bands and the temperature dependences of the PL and PLE spectra provide new insights concerning the competing excitation and recombination mechanisms for the deep centers in as-grown and ion-implanted GaN.

Fig. 1 shows examples of the broad yellow band emission peaking near 560 nm (2.2 eV) observed in GaN samples obtained from several sources. These spectra also exhibit a low energy band or tail on the yellow band (~600-800 nm) that corresponds to the 670 nm (1.84 eV) PL band reported in GaN films grown by HVPE<sup>1</sup>. The temperature dependence of the PL and PLE spectra of the yellow and red PL bands has been investigated in the 6K to 296K range. As the temperature increases through the 150 K to 300 K range, both the yellow band and the red band exhibit an exponential decrease in intensity characterized by a 32-33 meV thermal activation energy. This is consistent with established values of the calculated effective mass binding energy for the shallow donor, and values of the shallow donor binding energy inferred from the  $\text{I}_2$  donor bound exciton and FTIR spectra.<sup>2-4</sup> Although there is evidence<sup>2-4</sup> for the existence of multiple donors in GaN, our observation of a ~34 meV thermal quenching energy for both the yellow and red PL bands and the extraction of a comparable quenching energy from the data of Ogino and Aoki<sup>5</sup> seem to indicate that the recombination mechanism or path for these pervasive broad, defect PL bands involves the 34 meV shallow donor only.

The PLE spectra of the integrated yellow and red PL bands at temperatures ranging from 6K to 296K are shown in Fig. 2. At low temperatures the PLE spectra exhibit near band edge features characteristic of a combination of interband absorption and absorption by free and bound excitons<sup>6</sup> (~30-35 meV below the 3.5 eV band gap). There is also a weak low energy tail in the PLE spectrum extending ~110 meV below the gap. With increasing temperature the band gap shifts to lower energy, and the below gap PLE spectrum broadens and grows in intensity relative to the above gap excitation as an increasing fraction of donors are thermally ionized and give rise to extrinsic (below gap) optical absorption.<sup>7</sup> At 296 K the PLE spectrum is dominated by a broad peak or band which extends at least as far below the gap as the weak PLE tail does at 6K.

PL and PLE spectroscopy have been carried out at 6K on the 1540 nm  $^4\text{I}_{13/2}$  to  $^4\text{I}_{15/2}$  emission of  $\text{Er}^{3+}$  in Er-implanted films of GaN grown by metal-organic chemical vapor deposition (MOCVD). PLE has detected several broad below-gap absorption bands which excite three distinct site-selective  $\text{Er}^{3+}$  PL spectra (Fig. 3). The excitation of the site-selective Er PL bands involves optical absorption by defects with subsequent nonradiative transfer of the energy to nearby  $\text{Er}^{3+}$  luminescence centers. Proximity to or complexing with a specific defect perturbs the crystal field at the Er site and induces the site-selective, characteristic spectral distribution of the  $^4\text{I}_{13/2}$  to  $^4\text{I}_{15/2}$  radiative transitions of  $\text{Er}^{3+}$ . The spectral position and lineshape of the PLE spectrum of one of the

site-selective PL bands suggest that an exciton bound at this Er site is involved in the excitation mechanism.<sup>8</sup>

The isovalent anion impurities P and As have been ion implanted into MOCVD films of GaN, and As has been introduced by doping during growth. These dopants can be expected to manifest radiative recombination characteristic of excitons bound at isoelectronic impurities<sup>9</sup>. Each isovalent impurity produces a distinctive emission band with wavelength determined by the binding energy of the isoelectronic trap created by incorporation of the impurity in the GaN lattice. Proper selection of isovalent dopants may enable the wavelengths of the emission bands to be tailored throughout the visible spectral range without significantly altering the electrical characteristics of the material since the dopants are isovalent, i.e. they are not active as donors or acceptors. For example, the 6K cathodoluminescence (CL) spectra of P- and As-implanted samples of MOCVD-grown GaN are dominated by broad peaks at 2.97 eV and 2.64 eV, respectively, consistent with earlier work. Apparently because of ion-implantation damage, PL spectra from these samples were quite weak. Incorporating isoelectronic impurities through in-situ doping eliminates the damage due to ion implantation, and recent samples of GaN films doped with As during MOCVD growth exhibit a strong 2.56 eV PL band at room temperature.

1. W. Gotz et al., Appl. Phys. Lett. 69, 242 (1996).
  2. B.K. Meyer et al., Solid State Commun. 95, 597 (1995).
  3. U. Kaufmann et al., Mat. Res. Soc. Symp. Proc. Vol. 395 (MRS 1996) pg. 633.
  4. B.K. Meyer, Mat. Res. Soc. Symp. Proc., MRS Meeting (Boston 1996), in press.
  5. T. Ogino and M. Aoki, Jap. J. Appl. Phys. 19, 2395 (1980).
  6. D.M. Hofmann et al., Phys. Rev. B 52, 16702 (1995).
  7. M. Banas et al., Mat. Res. Soc. Symp. Proc. Vol. 395 (MRS 1996) pg. 583.
  8. P. Wellman et al., Mat. Res. Soc. Symp. Proc. Vol. 422 (MRS 1996) pg. 255.
  9. R.D. Metcalfe, D. Wickenden, and W.C. Clark, J. Lumin. 16, 405-415 (1978).
- \* Supported by DARPA (MDA 972-94-1-0004) and the Joint Services Electronics Program.

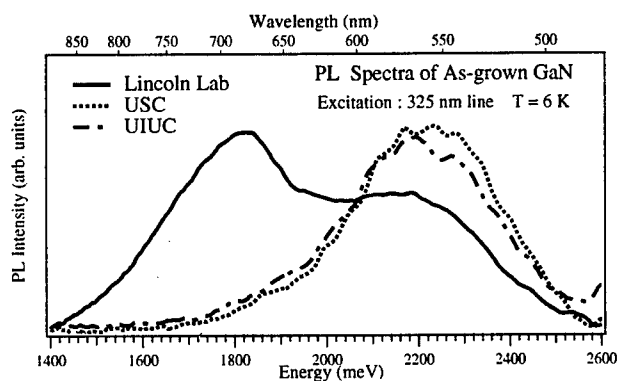


Fig. 1

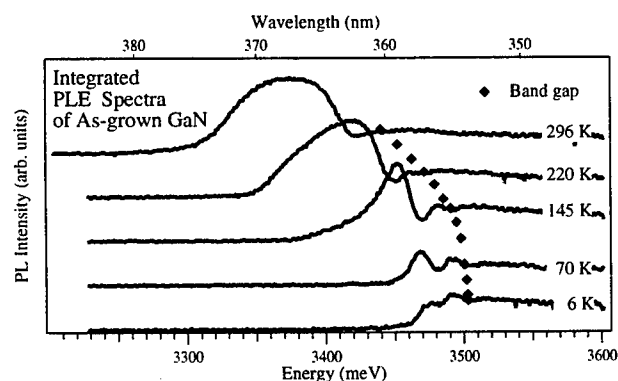


Fig. 2

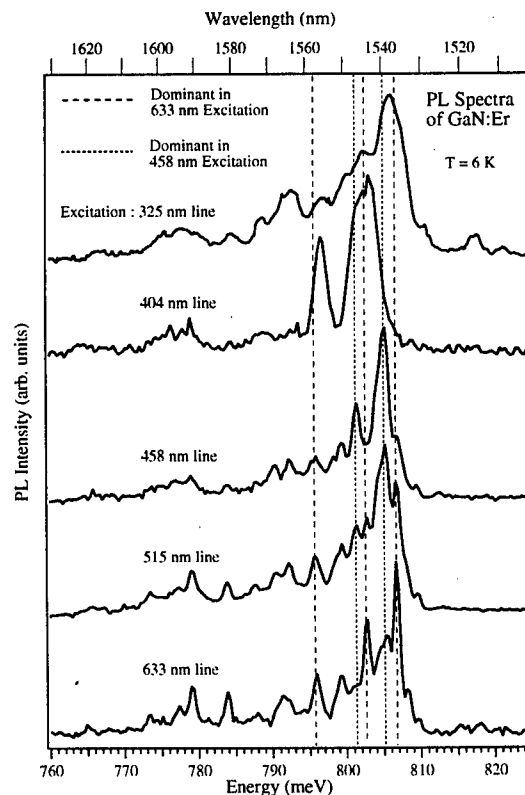


Fig. 3

## A Fabrication of GaN Micro-lens

Taek Kim, Jinseok Khim, Soohee Chae, and Taeil. Kim

Photonics Lab., Samsung Advanced Institute of Technology, P.O. Box 111, Suwon, 440-600 KOREA

Tel : +82-331-280-8234, Fax : +82-331-280-9357, email : taek@saitgw.sait.samsung.co.kr

Hyeon -Soo Kim, Young-Jun Lee, and Geun-Young Yeom

Department of Materials Engineering, Sung Kyun Kwan University, Suwon, 440-746, KOREA

Tel : +82-331-290-7418, Fax : +82-331-290-7410

The group III-nitrides are very promising materials for optoelectronic devices light emitting diodes (LEDs)<sup>1</sup> and laser diodes (LDs)<sup>2</sup> in the UV to green wavelength region. To realize these devices, development of GaN dry etching technique is essential. While most dry etching studies have been concentrated on anisotropic, preferential etching using highly selective etch masks such as metals and/or SiO<sub>2</sub><sup>3</sup>, we present a novel process of fabricating GaN convex micro-lenses using non-selective etching. The process was consisted of the thermal re-flowing of sacrificial photoresist (P.R) and non-selective dry etching technique. The GaN lenses could be applied to the surface of GaN-based LEDs to give directionality and improve the external quantum efficiency by reducing the amounts of total reflection which could be absorbed by defects in the crystal. Such elements also could be fabricated on the cavities of a variety of microcavity structures, such as vertical cavity surface emitting laser diodes (VCSELs), asymmetric Fabry-Perot modulators, resonant cavity LEDs, and resonant cavity photodetectors<sup>4</sup>.

In Figure 1, a brief fabrication scheme is illustrated. At first, circular shaped P.R was patterned on GaN film using standard photolithography. 1.1  $\mu\text{m}$ -thick Shipley S-1400-27 P.R was used in this experiment. The GaN samples used in this study were grown on c-plane sapphires by metal organic chemical vapor deposition (MOCVD). After patterning, the P.R was thermally re-flowed to make a lens shape at 200 °C for 2 minutes. The SEM image of the P.R lens is shown in Figure 2-a. During the thermal re-flowing, the surface tension of the P.R makes smooth and circular lens shape automatically.

We used ICP RIE for the non-selective etching. To generate inductively coupled plasmas, 13.56MHz rf inductive power was applied to a planar spiral Cu coil separated by a 1cm-thick quartz window at the top of the process chamber after the introduction of process gas combinations. Separate 13.56MHz rf power was also applied to the bottom electrode, where the substrates are located, to generate a dc self-bias voltage. Cl<sub>2</sub> was used as the main etching gas while the operating pressure was kept at 10 mTorr. The inductive power was set to 800 W. The dc-self bias voltages measured using a high voltage probe were changed from 0 to 150 V to control the selectivity between GaN and the P.R. In Figure 3, the etching rates of the GaN and the P.R as a function of bias voltage were shown. As shown in Figure 3, almost no-selectivity was found at zero bias. However, the etching rates were too slow (150 Å/min for GaN and 180 Å/min for P.R). In the low bias voltage range, the etch rates of GaN were higher than those of the P.R. However, the etching rate of P.R increased faster than that of GaN with increasing bias voltage. At the bias voltage of -75 V, the etching rates of the P.R came to close to those of GaN. In the range of bias voltage over than -100 V, the etching rates of the P.R became faster than those of GaN. At the bias voltage of -75 and -100 V, the ratios of the etching rate of the GaN to

the P.R were 1.05 and 0.96, respectively. Therefore, it should be noted that the curvature of lenses can be controlled by choosing a proper bias voltage. The SEM images of Figure 2-b and -c were taken from the sample etched for 5 and 10 minutes under the bias voltage of -100 V. In the case of 5 minute etched sample, the P.R was not completely etched and remained on the top of the lens. However a smooth lens shape was obtained and no discontinuity between the P.R and the GaN film was observed. Thus, we could confirm that the etching condition had no selectivity and was suitable for the purpose of fabricating lenses. For the 10 minutes etched sample, the P.R was completely etched resulting in the convex GaN micro-lens with a diameter of 7  $\mu\text{m}$ . The thickness of the lens at the center was 1  $\mu\text{m}$ .

In conclusion, we have fabricated GaN micro-lenses. We have varied the selectivity between a P.R and GaN by varying ICP RIE etching condition, ie bias voltage. The fabricated lenses showed a good convex lens shape with a soothe surface.

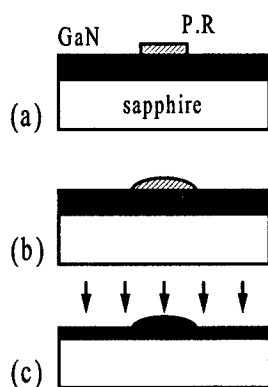


Figure 1. Schemetic diagrams illustrating a brief fabrication procedure.  
a) after photolithography.  
b) after thermal treatment of P.R.  
c) after non-selective etching.

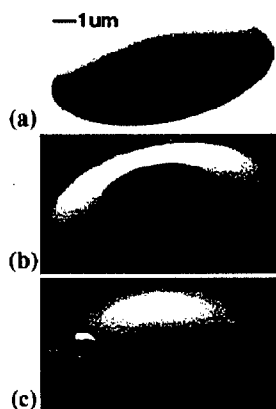


Figure 2. SEM images of GaN lenses  
a) P.R after thermal treatment  
b) 5 min, and c) 10 min etched  
GaN lens at a bias voltage of  
-100 V.

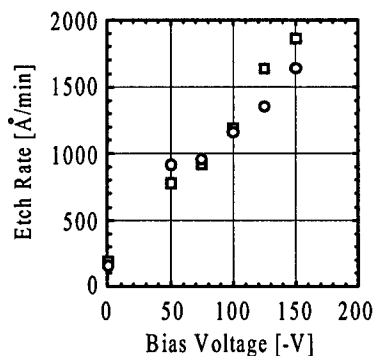


Figure 3. The etching rates of GaN and P.R as a function of bias voltage. The inductive power was 800 W and the operating pressure was 10 mTorr.

## REFERENCES

- [1] Shuji Nakamura, Takashi Mukai, and Masayuki, Senoh, Appl. Phys. Lett. **64**, 1687 (1994)
- [2] Shuji Nakamura, Masayuki Senoh, Shin-ichi, Nagahama, Naruhito Iwasa, Takao Yamada, Toshio Matsushita, Hiroyuki Kiyoku, and Yasunobu, Sugimoto, Jpn. J. Appl.Phys. Vol. 35 (1996) pp.L74 - L76
- [3] A.T. Ping, I. Adesida, and M. Asif Khan. Appl. Phys. Lett. **67**, 1250 (1995)
- [4] O. Blum, K.L. Lear, H.Q. Hou, and M.E. Warren. Electron. Lett. **32**, 406 (1996)

**Raman spectroscopy of Mg-doped gallium nitride:  
shift of the  $A_1(\text{LO})$  phonon**

J. C. Burton, S. Cohen, S. J. Lukacs, F. H. Long\*

Department of Chemistry, Rutgers University, P.O.Box 939, Piscataway, NJ 08855

S. Liang and Y. Lu

Department of Electrical and Computer Engineering, Rutgers University, Piscataway, NJ 08855

Y. Li and C. Tran

Emcore Corp., 394 Elizabeth Ave., Somerset, NJ 08873

\*To whom correspondence should be addressed.

E-mail address fhlorg@rutchem.rutgers.edu

For the development of improved devices, the control and understanding of the electrical properties of nitride semiconductors is essential. Although significant progress has been made in recent years, the p-type doping of nitride semiconductors has proven to be challenging.<sup>1</sup> It has been found necessary to anneal the sample after growth at moderate (700°C-900°C) temperatures in order to electrically activate the dopants.<sup>2</sup> In order to help in the development of improved p-type doped GaN and other group III-nitrides, we have undertaken a study of the Raman spectroscopy of p-type doped GaN under a variety of processing conditions.

Raman spectroscopy has been used for several earlier studies of nitride semiconductors.<sup>3-10</sup> In this paper, we report studies of the wavelength dependence of Mg-doped (p-type) GaN Raman spectra for samples that have been annealed at different temperatures.

Samples of p-type doped GaN on sapphire substrate were used. The Mg doped GaN samples were prepared by means of low pressure MOCVD process. From one initial sample, four different samples were generated. One sample was analyzed as grown, while the other three were each annealed under  $\text{N}_2$  for four minutes at one of the following temperatures: 500°C, 700°C and 900°C.

We have performed an extensive study of the wavelength dependence of the GaN Raman spectrum at energies well below the absorption band edge. Careful inspection of the  $A_1(\text{LO})$  peak at around  $737\text{ cm}^{-1}$  reveals a small shift to higher frequencies as the laser is tuned to higher energies. The laser energy dependence of the  $A_1(\text{LO})$  and  $E_2$  Raman peaks for native GaN sample is shown in Figure 1. Upon tuning the laser from 2.18 eV (568.2 nm) to 2.60 eV (476.5 nm), the  $A_1(\text{LO})$  phonon shifts approximately  $2.5\text{ cm}^{-1}$ . This observed  $2.5\text{ cm}^{-1}$  dispersion of the  $A_1(\text{LO})$  phonon is well outside our experimental error of  $0.5\text{ cm}^{-1}$ . We have also noted the same type of shift in unannealed p-type samples, but to a slightly smaller degree,  $2.0\text{ cm}^{-1}$ . Furthermore, we note that the  $E_2$  Raman active vibration at  $568\text{ cm}^{-1}$  does not shift, within experimental error, when the laser energy is varied.

The effects of thermal annealing on the  $A_1(\text{LO})$  and  $E_2$  phonons have been examined. We have found that the observed dispersion in the  $A_1(\text{LO})$  phonon is very sensitive to thermal annealing. The sample annealed at 500°C exhibits a shift of slightly smaller magnitude to that which we observed in the unannealed sample shown in Figure 2. However, after annealing at 700°C there is no evidence of change, within experimental error, in the  $A_1(\text{LO})$  mode frequency with excitation energy. At 900°C, the  $A_1(\text{LO})$  phonon increases in frequency to  $737\text{ cm}^{-1}$  for 2.34 eV excitation, other energies are the same as before. We also note that although the  $E_2$  phonon modes do not shift with laser energy, the average value of the  $E_2$  phonon frequency clearly increases with higher annealing temperature. By analogy with the experiments in <sup>10</sup>, the increase in the  $E_2$  phonon frequency is consistent with a increase of biaxial lattice strain upon thermal



annealing. Therefore the shift observed in the  $A_1(\text{LO})$  phonon is most likely not directly associated with stress.

The observed resonance effects in the GaN Raman spectra are consistent with inhomogeneous broadening. The clearly observable shift of the  $A_1(\text{LO})$  phonon with the laser energy suggests that there are electronic states inside the GaN band gap. Associated with these band gap states are a distribution of vibrational frequencies. The lack of a shift in the high frequency  $E_2$  mode with laser excitation energy is consistent with the physical picture that only the LO phonons are strongly coupled to the electrons. The existence of states inside the band gap, i.e., band tails, for GaN is supported by photothermal deflection<sup>11</sup> and photoconductivity<sup>12</sup> experiments. These studies found that band tail states were very prominent in GaN and sensitive to thermal annealing. Because we have also observed similar shifts in the  $A_1(\text{LO})$  phonon frequency for native and n-type doped samples, we do not attribute the observed resonances in the Raman spectra to states associated with the doping. It is possible that the band tail states are associated with the large electron-phonon coupling typical of nitride semiconductors. The origin of the band tail states will be the subject of further investigation.

Acknowledgment is made to the donors of the Petroleum Research Fund, administered by the ACS, for partial support of this research. FHL would also like to thank the Rutgers University Research Council for their generous support of this work.

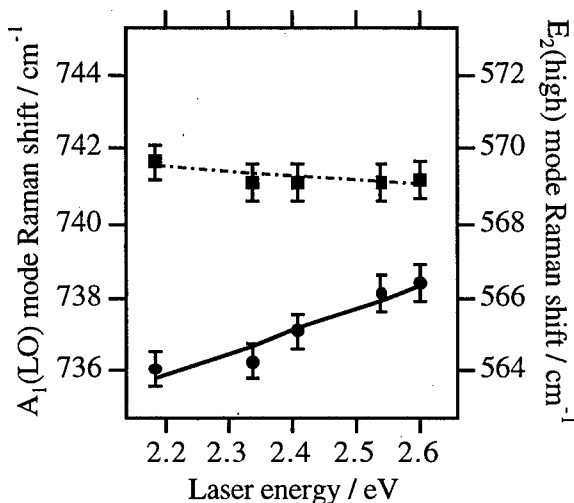


Figure 1

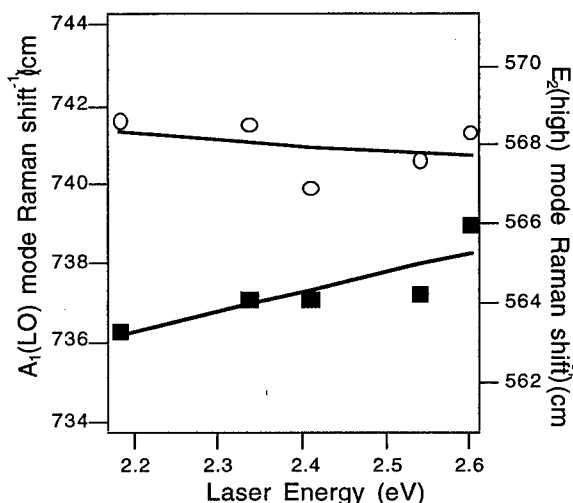


Figure 2

1. Amano, H., Kito, M., Hiramatsu, K. & Akasaki, I. *Jpn. J. Appl. Phys.* **28**, L2112-L2114 (1989).
2. Nakamura, S., Iwasa, N., Senoh, M. & Mukai, T. *Japanese Journal of Applied Physics* **31**, 1258-1266 (1992).
3. Giehler, M., Ramsteiner, M., Brandt, O., Yang, H. & Ploog, K.H. *Appl. Phys. Lett.* **67**, 733-735 (1995).
4. Murugkar, S., Merlin, R., Botchkarev, A., Salvador, A. & Morkoç, H. *J. Appl. Phys.* **77**, 6042-6043 (1995).
5. Kozawa, T., et al. *J. Appl. Phys.* **75**, 1098 (1994).
6. Ramsteiner, M., Menniger, J., Brandt, O., Yang, H. & Ploog, K.H. *Applied Physics Letters* **69**, 1276-1278 (1996).
7. Behr, D., Wagner, J., Schneider, J., Amano, H. & Akasaki, I. *Appl. Phys. Lett.* **68**, 2404-2406 (1996).
8. Kuo, H.-R., Feng, M.-S., Guo, J.-D. & Lee, M.-C. *Japanese Journal of Applied Physics* **34**, 5628-5632 (1995).
9. Kirillov, D., Lee, H. & Harris, J.S., Jr. *J. Appl. Phys.* **80**, 4058-4062 (1996).
10. Demangeot, F., et al. *M.R.S. Internet Journal of Nitride Semiconductor Research* **1**, 23 (1996).
11. Ambacher, O., et al. *Solid State Commun.* **97**, 365-370 (1996).
12. Qiu, C.H., Hoggatt, C., Melton, W., Leksono, M.W. & Pankove, J.I. *Appl. Phys. Lett.* **66**, 2712-2714 (1995).

## Calculation of Spinodal Decomposition Temperature in Cubic Ternary Nitride Materials Including Coherency Stress and Spontaneous Ordering.

V.A. Elyukhin\*, E.A. Avrutin\*\*, J.H. Marsh\*\*, E.L. Portnoi\*,

\*. A.F. Ioffe Physico-Technical Institute, St. Petersburg 194021, RUSSIA

\*\*Dept. of Electronics & Electrical Engineering, University of Glasgow, Glasgow G12 8QQ, Scotland, UK

**1. Background and introduction.** The issues of reliability, device lifetime and degradation are extremely important in group III nitride devices. One of the physical processes likely to influence the corresponding properties of devices based on ternary nitride compounds, especially those containing indium, i.e.  $In_xGa_{1-x}N$ ,  $In_xAl_{1-x}N$  [1], is *spinodal decomposition* of the ternary material, i.e. the decomposition of the material into two phases, also ternary, with gradually diverging compositions. The process is gradual and thresholdless and may take place in a complete working device, especially in LED's or lasers where high current densities increase the mobilities of individual atoms. The decomposition would influence the operating characteristics of the device and may speed up degradation. It is therefore highly advisable that the materials used for device fabrication are stable with respect to spinodal decomposition; e.g. that the intended operation temperature range is *above* the characteristic decomposition temperature of the material. This characteristic temperature may be calculated, for a given material composition, using the methods of statistical mechanics [2-3]; such a calculation for nitrides was recently reported [2]; however, it did not include the effects of coherency stress which exists in alloys consisting of materials with different lattice constants and stabilises the structure against spinodal decomposition [3]. Also, the reported calculation [2] applied only to completely random ternary (quasi-binary) solutions; there is strong indication that ternary nitrides may be grown as *spontaneously ordered* materials, or superstructures of CuPt-type. Here, we present a calculation of spinodal decomposition temperatures for a variety of nitride compounds taking into account both the coherency stress and an arbitrary degree of ordering and show that, for a given composition, superstructures tend to have lower decomposition temperatures than random alloys and may therefore be advantageous.

**2. Theoretical:** The decomposition temperature for a ternary  $A_xB_{1-x}C$  material (for our purposes, the materials  $A$  and  $B$  are two metals, i.e.  $In$ ,  $Al$  or  $Ga$ , the material  $A$  listed first being the one with the larger lattice constant, and  $C$  is nitrogen) is defined from a condition [3]:

$$d^2f/dx^2=0 \quad (1)$$

with  $f$  the Helmholtz free energy (per mole) of the material, given by :

$$f=U_i+U_c-TS \quad (2)$$

where  $U_i$  and  $U_c$  are the internal energy of mixing and the energy due to coherency stress, both per mole, respectively;  $T$  is temperature and  $S$  the configurational entropy; from (1) and (2) the decomposition temperature is easily defined explicitly as

$$T = (d^2U_i/dx^2 + d^2U_c/dx^2) / d^2S/dx^2 \quad (3)$$

To calculate the internal energy of mixing of the ordered material which is due to short-range deformations in the crystal lattice, we consider the metal sublattice as consisting of two equivalent sublattices  $a$  and  $b$  with (111) orientation. Single layer ordering makes it possible for each  $A$  atom to have three  $B$  and one  $A$  atoms as nearest neighbours (and vice versa). Then we can define probabilities  $W_{Aa}, W_{Ab}, W_{Ba}, W_{Bb}$  where, for example,  $W_{Aa}$  is the probability of the arrangement of an  $A$  atom on the  $a$  sublattice and the rest are defined in a similar manner. We consider *cubic* nitrides which, although thermodynamically metastable, may have a number of advantages, for device applications, over the stable and more conventional hexagonal modification. The explicit expressions for the probabilities  $W_{Aa} \dots W_{Bb}$  for a cubic, partially ordered ternary alloy are, for  $0 < x < 0.5$  :

$$W_{Aa} = x + xr, W_{Ab} = x - xr, W_{Ba} = 1 - x - xr, W_{Bb} = 1 - x + xr \quad (4a-d)$$

and for  $0.5 < x < 1$  :

$$W_{Aa} = x + (1-x)r, W_{Ab} = x - (1-x)r, W_{Ba} = 1 - x - (1-x)r, W_{Bb} = 1 - x + (1-x)r \quad (5a-d)$$

where  $r$  is the long-range order parameter  $0 < r < 1.0$ ,  $r=0$  corresponding to a completely random alloy and  $r=1$  to an ideal superstructure. Furthermore, we consider five types of tetrahedral cells in the crystal structure - 4A, 3A1B, 2A2B, 1A3B and 4B - and two types of arrangement of these cells for ordered alloys, namely:

type 1: three atoms from the tetrahedral cell are placed on the sublattice  $a$  and one atom on  $b$ ;

type 2: one atom from the tetrahedral cell is placed on the sublattice  $a$  and three atoms on  $b$ .

The concentrations of tetrahedral cells for the type 1 are then calculated as :

$$P_{4A}^1 = W_{Aa}^3 W_{Ab} ; \quad P_{3A1B}^1 = W_{Aa}^3 W_{Bb} + 3 W_{Aa}^2 W_{Ab} W_{Ba} ;$$

$$P_{2A2B}^1 = 3 W_{Aa} W_{Ab} W_{Ba}^2 + 3 W_{Bb} W_{Ba} W_{Aa}^2 ; \quad P_{1A3B}^1 = W_{Ba}^3 W_{Ab} + 3 W_{Bb} W_{Ba}^2 W_{Aa} ; \quad P_{4B}^1 = W_{Ba}^3 W_{Bb} \quad (6a-e)$$

and for the type 2 as:

$$P_{4A}^2 = W_{Aa} W_{Ab}^3 ; \quad P_{3A1B}^2 = W_{Ab}^3 W_{Ba} + 3 W_{Ab}^2 W_{Aa} W_{Bb} ;$$

$$P_{2A2B}^2 = 3 W_{Aa} W_{Ab} W_{Bb}^2 + 3 W_{Bb} W_{Ba} W_{Ab}^2 ; \quad P_{1A3B}^2 = W_{Bb}^3 W_{Aa} + 3 W_{Bb}^2 W_{Ba} W_{Ab} ; \quad P_{4B}^2 = W_{Bb}^3 W_{Ba} \quad (7a-e)$$

The internal energy is expressed as

$$U_i = \frac{1}{2} \sum_{j=1}^5 (P_j^1 + P_j^2) U_{ij} \quad (8)$$

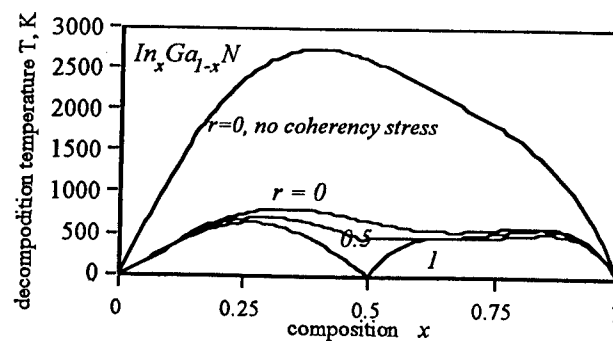
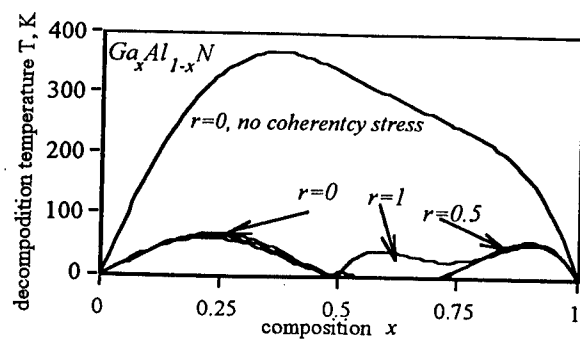
where the sum is over all five types of tetrahedral cells, each of the parameters  $U_{ij}$  is the deformation energy of the tetrahedral cell of the  $j$ th kind; the expressions for these energies were calculated previously using the valence-force-field model [4, 5]. For the energy  $U_i$  associated with the coherency stress, we also use the expressions available in the literature [3]. Finally, the factor in (3) associated with the configurational entropy is given by :

$$d^2S/dx^2 = -R[2/x + (1+r)^2/(1-x-xr) + (1-r)^2/(1-x+xr)]/2 \quad (x < 0.5) \quad (9a,b)$$

$$d^2S/dx^2 = -R\{(1-r)^2/[x+(1-x)r] + (1+r)^2/[x-(1-x)r] + (1-r)^2/[1-x-(1-x)r] + (1+r)^2/[1-x+(1-x)r]\}/2 \quad (x > 0.5)$$

with  $R$  the universal thermodynamical constant.

**3. Results and discussion:** using the approach outlined above, we calculated the temperatures of spinodal decomposition for a range of materials and an arbitrary value of the long-range order parameter  $r$ . Typical curves are shown in the Figures below; more results will be shown at the Meeting. As expected, for  $Ga_{1-x}Al_xN$  alloys, given the close lattice constants of  $Ga$  and  $Al$ , the strains are small and the decomposition temperatures relatively low, with or without the account of ordering; account of coherency strain brings them down from around room temperature to several tens of Kelvins or even negative values. For alloys containing indium, the situation is more complex. Here, also, taking into account coherency stress decreases the calculated decomposition temperature. However, for most composition values and especially with no, or weak, ordering (small  $r$ ) the predicted decomposition temperatures are still higher than room temperature, which means devices fabricated from these materials can likely to degrade fast, which has been indeed observed [1]. In strongly ordered materials, the decomposition temperatures are decreased; in particular, with high values of the long-range order parameter, i.e. with a nearly ideal superstructure, the decomposition temperatures see a pronounced dip around  $x=0.5$  indicating that materials with these composition may be fairly stable. It may be therefore advisable to target the formation of indium nitride superstructures in the technological process. The analysis of spinodal decomposition in hexagonal group III nitrides, presently more common, is reserved for future work, but we expect the results to be qualitatively similar.



- [1] R. Singh, D. Doppalapudi, T.D. Moustakas, Appl. Phys. Lett., **69**, 1996, pp.2388-2390.
- [2] I-hsiu Ho, G.B. Stringfellow, Appl. Phys. Lett., **69**, 1996, pp. 2701-2703.
- [3] J.W. Cahn, Acta Metall., **10**, 1962, pp.179-183.
- [4] V.A.Elyukhin, L.P. Sorokina, Sov. Phys. Dokl., **31**, 1986, pp. 342-344
- [5] V.A. Elyukhin, S.A. Nikishin, Semicond.Sci. Technol., **11**, 1996, pp.917-920.

# AUTHOR INDEX

## A

Abare, A.C. ThB2  
Akasaki, I. WA1  
Amano, H. WA1  
Avrutin, E.A. FB5

## B

Babcock, S.E. ThC4  
Bachem, K.H. WB3  
Balkas, C.M. WB1  
Beccard, R. WB3  
Bergman, L. WB1  
Biefeld, R.M. FA5  
Bishop, S.G. WA5, FB1  
Bojarczuk, N. A. ThA4  
Bond, A. ThC3  
Bremser, M.D. WB1  
Burton, J.C. FB4

## C

Chae, S. FB2  
Chen, J.C. WB5  
Choi, Won-Jin ThC3  
Choutov D.A. FB3  
Chow W.W. ThD3  
Chung, S.R. WB5  
Cohen, S. FB4  
Coldren, L.A. ThB2  
Coleman, J.J. WA5, FB1  
Cook, Jr., J.W. WA2  
Crawford, M.H. FA5

## D

Dapkus, P. D. WB2, ThC3  
Davis, R.F. WB1  
Demeester, P. ThB3  
DenBaars, S.P. ThA2, ThB2  
Domen, K. ThD1  
Dunn, K. ThC4  
Dupuis, R.D. WA4

## E

Edmond, J.A. WB4  
Eiting, C.J. WA4  
El-Masry, Jr., N.A. WA2  
Elyukhin, V.A. FB5  
Emerson, D.T. WB4

## F

Ferguson I. FA4  
Flynn, J.S. ThA3  
Follstaedt, D.M. FA5

## G

Gillis, H.P. FB3  
Girndt, A. ThD3  
Grudowski, P.A. WA4  
Guba, S. ThA4

## H

Hacke P. FA2  
Haight, R. ThA4  
Han J., FA5  
Hellman, E. ThC2  
Hersee, S.D. ThB1  
Horino, K. ThD1  
Hsu, C.F. ThD4

## J

Jahnke, F. ThD3  
Jurgensen, H. WB3  
Jiang, H.X. ThB5  
Johnson, M.A.L. WA2  
Johnson N. FA1

## K

Karlicek Jr., R.F. ThB4, FA4  
Kaufmann, U. WB3  
Keller, S. ThA2, ThB2  
Keller, B. ThA2

Khim, J. FB2  
Kim, S. FB1, WA5  
Kim, H.-S. FB2  
Kim, T. FB2  
Kim W. ThB5  
Kobayashi, J. T. WB2, ThC3  
Kobayashi N. P. WB2, ThC3  
Koch, S.W. ThD3  
Kolbas, R. WB1  
Kong, H.S. WB4  
Kozodoy, P. ThA2  
Kuball, M. ThD2  
Kuech, T.F. WA3, ThC4  
Kuramata, A. ThD1

## L

Lambert, D.J.H. WA4  
Lee, Y.-J. FB2  
Li, X. FB1, WA5  
Li Y. FB4  
Liang, S. FB4  
Lin, J.Y. ThB5  
Long, F.H. FB4  
Lu, Y. FB4  
Lukacs, S.J. FB4

## M

Mack, M.P. ThB2  
Marsh, J.H. FB5  
Martin, K. P. FB3  
Meier, M. WB3  
Mishra, U.K. ThA2  
Moerman, I. ThB3  
Morkoc, H. ThB5

## N

Nakadaira A. FA3  
Nakamura, S. ThA1  
Nam, O.H. WB1  
Nemanich, R. WB1  
Niebuhr, R. WB3  
Nurmikko A. ThD2

# AUTHOR INDEX

## O

Okushi, H. FA2

## P

Park, J. WA4  
Perkins, N. ThC4  
Perry, W.G. WB1  
Phanse, V.M. ThA3  
Popovici, G. ThB5  
Portnoi, E.L. FB5

## R

Ramer, J.C. ThB1  
Redwing, J. ThC1  
Redwing, J. M. ThA3  
Redwing, J.R. WA3  
Rees, P. ThD4  
Rehder, E. ThC4  
Reuter, E.E. FB1  
Rhee, S.J. FB1  
Rich, D. H. WB2,ThC3

## S

Safvi, S.A. WA3  
Salagaj T. ThB4, FA4  
Salvador, A. ThB5  
Santic, B. WB3  
Saulys, D. WA3  
Schetzina, J.F. WA2  
Schlotter, P. WB3  
Schmitz, D. WB3  
Schurman, M. ThB4,FA4  
Shealy, J.R. WB4  
Shelton, B.S. WA4  
Shmagin, I. WB1  
Sitar, Z. WB1  
Smart, J.A. WB4  
Smith, G. M. ThA3  
Smith, M. ThB5  
Song, Y.-K. ThD2  
Speck, J. ThA2  
Stall, R. ThB4

## T

Tanahashi, T. ThD1  
Tanaka, K. FA3  
Tang, H. ThB5  
Thompson, A. ThB4  
Tischler M.A. WA3  
Tran, C.A. ThB4  
Tran, C.A. FA4  
Tran, C. FB4  
Turnbull, D.A. FB1

## V

Van der Stricht, W. ThB3  
Vaudo, R.P. ThA3

## W

Wachtendorf, B. WB3  
Ward, B.L. WB1  
Worchesky, T.L. WB5  
Wright, A.F. ThD3  
Wu, Y. ThA2

## Y

Yeom, G.-Y. FB2  
Yu, Z. WA2

## Z

Zeng, K.C. ThB5  
Zhang X. WB2,ThC3  
Zheleva, T. WB1  
Zolper, J.C. FA5  
Zory P.S. ThD4